

AD-A128 683

TRANSACTIONS OF THE CONFERENCE OF ARMY MATHEMATICIANS  
(28TH) HELD AT BETHESDA MARYLAND ON 28-30 JUNE 1982(U)  
ARMY RESEARCH OFFICE RESEARCH TRIANGLE PARK NC FEB 83

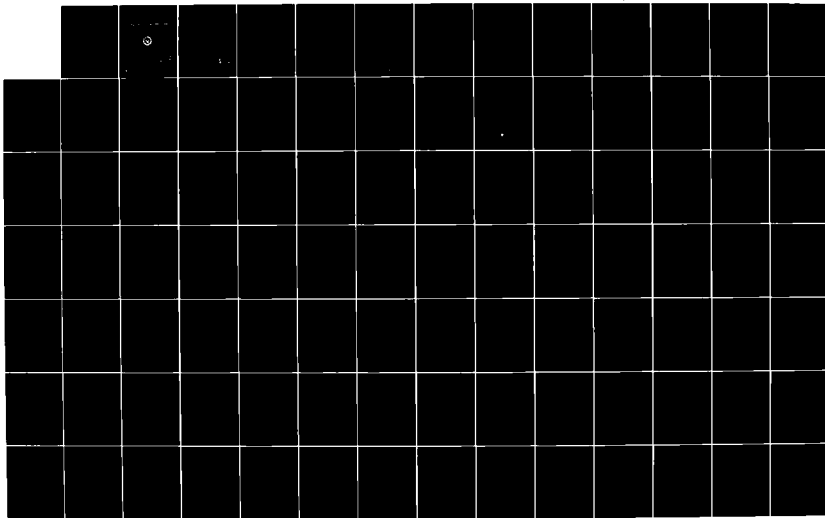
1/6

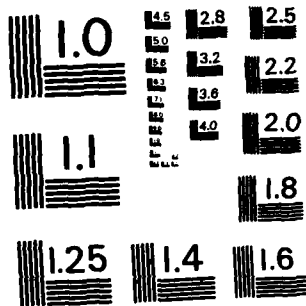
UNCLASSIFIED

ARO-83-1

F/G 12/1

NL





MICROCOPY RESOLUTION TEST CHART  
NATIONAL BUREAU OF STANDARDS-1963-A

12

ARO Report 83-1

**TRANSACTIONS OF THE TWENTY - EIGHTH  
CONFERENCE OF ARMY MATHEMATICIANS**

AD A 128 683



Approved for public release; distribution unlimited.  
The findings in this report are not to be construed  
as an official Department of the Army position, un-  
less so designated by other authorized documents.

DTIC  
APR 18 1983  
S A

DTIC FILE COPY

Sponsored by  
The Army Mathematics Steering Committee  
on behalf of  
THE CHIEF OF RESEARCH, DEVELOPMENT  
AND ACQUISITION

88 04 18 081

COMPONENT PART NOTICE (CON'T)

AD#:	TITLE:
AD-P001 030	A New Flight Instability Affecting Spinning Projectiles Having Non-Rigid Payloads.
AD-P001 031	Terrain Mesoroughness Description and Its Application to Mobility and Cover.
AD-P001 032	A Spatial Domain Walsh Feature Set.
AD-P001 033	Multiple Model Adaptive Filter for Tank Fire Control and Its Microprocessor Implementation.
AD-P001 034	Large Deformations and Stability Axisymmetric Mooney Membranes - Finite Element Solutions.
AD-P001 035	Structural Analysis of a Mine with Two Viscoelastic Explosive Fills.
AD-P001 036	Formation of Singularities for a Conservation Law with Memory.
AD-P001 037	Theories for Control of Neurotransmitter Release and for Two Problems in Physical Chemistry.
AD-P001 038	Linearized Dynamics of Shearing Deformation Perturbing Rest in Viscoelastic Materials.

Accession For	
NTIS GRA&I	<input checked="" type="checkbox"/>
DTIC TAB	<input type="checkbox"/>
Unannounced	<input type="checkbox"/>
Justification	
By	
Distribution/	
Availability Codes	
Dist	Avail and/or Special
A	

**DTIC**  
**ELECTRIC**  
**S** JUN 1 1983 **D**  
**A**

## COMPONENT PART NOTICE

THIS PAPER IS A COMPONENT PART OF THE FOLLOWING COMPILATION REPORT:

(TITLE): Transactions of the Conference of Army Mathematicians (28th) Held at  
Bethesda, Maryland on 28-30 June 1982.

(SOURCE): Army Research Office, Research Triangle Park, NC.

TO ORDER THE COMPLETE COMPILATION REPORT USE AD-A128 683.

THE COMPONENT PART IS PROVIDED HERE TO ALLOW USERS ACCESS TO INDIVIDUALLY AUTHORED SECTIONS OF PROCEEDINGS, ANNALS, SYMPOSIA, ETC. HOWEVER, THE COMPONENT SHOULD BE CONSIDERED WITHIN THE CONTEXT OF THE OVERALL COMPILATION REPORT AND NOT AS A STAND-ALONE TECHNICAL REPORT.

THE FOLLOWING COMPONENT PART NUMBERS COMPRISE THE COMPILATION REPORT:

AD#:	TITLE:
AD-P001 010	Linear Evolution of Data with Microstructure and Applications.
AD-P001 011	Inhomogeneous Diffusion (Particularly in Inhomogeneous Polymer Membranes or Slabs).
AD-P001 012	Aerodynamic Breakup of Viscoelastic Solutions.
AD-P001 013	Transport-Theoretic Analysis of Pulse Propagation through a Random Cloud of Scatterers.
AD-P001 014	Analysis of Multilayer Dielectric Waveguide Structures.
AD-P001 015	Calculation of Advective Mass Transport in Heterogeneous Media.
AD-P001 016	Electric Theory of Osmosis for Dilute Saline Solutions.
AD-P001 017	Free Boundary Problem in Newtonian Flow.
AD-P001 018	Evolution of Near Chapman-Jouget Deflagrations.
AD-P001 019	Eine Kleine Eigenvalueproblem (A Simple but Informative Nonlinear Eigenvalue Problem).
AD-P001 020	The Evolution of a Gas Bubble in a Closed Volume of Stirred Liquid.
AD-P001 021	On Growth Processes of Condensation Aerosols.
AD-P000 022	Modeling of Flow Interaction of a Liquid Jet with a Contaminant Droplet.
AD-P001 023	Viscous Flow of a Droplet on a Flat Surface.
AD-P001 024	Cavitating Flow with Surface Tension.
AD-P001 025	Stress Solutions at Bondline-Boundary Intersections in Composite Materials.
AD-P001 026	A Functional Stress Intensity Approach to Multiply Cracked, Partially Autofrettaged Cylinders.
AD-P001 027	Two-Phase Flow of Liquid Propellant Guns by Space Mean Approach.
AD-P001 028	Calculation of Legendre Functions on the Cut for Integral Order and Complex Degree by Means of Gauss Continued Fractions.
AD-P001 029	The Best Possible Class of Initial Values for the Porous Medium Equation in $R(N)$ .

This document has been approved  
for public release and sale; its  
distribution is unlimited.

U. S. ARMY RESEARCH OFFICE

Report No. 83-1

February 1983

TRANSACTIONS OF THE TWENTY-EIGHTH CONFERENCE  
OF ARMY MATHEMATICIANS

Sponsored by the Army Mathematics Steering Committee

Host

U. S. Army Research Office

held at

Uniformed Services University of Health Sciences  
Bethesda, Maryland  
28-30 June 1982

Approved for public release; distribution unlimited.  
The findings in this report are not to be construed  
as an official Department of the Army position un-  
less so designated by other authorized documents.

U. S. Army Research Office  
P. O. Box 12211  
Research Triangle Park, NC 27709

## FOREWORD

The Twenty-Eighth Conference of Army Mathematicians, like all the others in this series, had many papers on the applications of mathematics. In most cases these applications were to problems that arose in Army laboratories. Since one mathematical idea can apply to many different disciplines, the successful treatment of a problem at one installation often enables a scientist at another installation to handle an entirely different assignment. This all helps to shorten the time between the creation of new ideas and their applications. Today, with the increasing momentum of scientific activity, the speed of applications has increased. This is in contrast with the following known case. The time between the mathematical presentation of all the properties of conics, by the Greek geometer Appollonius, and their application to the orbits of the planets, by the German mathematical physicist Johannes Kepler, was 1800 years.

The host of this conference was the U. S. Army Research Office (ARO) and it was held on 28-30 June 1982 at the Uniformed Services University of Health Sciences in Bethesda, Maryland. The Army Mathematics Steering Committee (AMSC), sponsor of these Army-wide conferences, would like to thank this university for the use of its excellent facilities. Members of the AMSC would also like to thank Mr. Wendell Young of the Uniformed Services University for making several rooms available for the conduction of this meeting and for the many other services he performed in our behalf.

The theme of <sup>this</sup> ~~the 28th~~ Conference was "Mathematical Problems in Diffusion, Transport and Mixing". Special emphasis was given to problems of viscoelastic fluids, stability and fluid mixing in containers and propagation in complex media. A list of the invited speakers along with the titles of their addresses ~~are noted below~~. These gentlemen as well as authors of several of the solicited papers stressed the ideas expressed in the theme of the meeting.

### Speakers and Affiliation

Professor George Papanicolaou  
Courant Institute of Mathematical  
Sciences

Professor James Brock  
University of Texas at Austin

Professor S. H. Davis  
Northwestern University

Professor D. D. Joseph  
University of Minnesota

Professor Lee Segel  
Weizmann Institute and  
Rensselaer Polytechnic Institute

*follows -*

### Title

CONVECTION OF MICROSTRUCTURE;

AEROSOL DYNAMICS;

SPREADING OF LIQUID FILMS:  
BIFURCATION AND STABILITY STUDIES;

RHEOLOGY OF VISCOELASTIC FLUIDS; and

ANALYSIS OF NEUROTRANSMITTER  
RELEASE.

Members of the AMSC would like to take this opportunity to thank the speakers and all the other individuals who contributed to the success of this meeting. They have requested that these proceedings be issued to enable those scientists that could not attend, as well as those present, to have a summary of the conference. They would also like to thank Mrs. Sherry Duke of the Army Research Office for her excellent secretarial work in connection with this and the other two Army-wide conferences. Attendees appreciated all the help she gave them during the course of this meeting.



Accession For	
NTIS Grant	<input checked="" type="checkbox"/>
DTIC TAB	
Unannounced	
Justification	
Re	
Distribution/	
Availability Codes	
Avail and/or	
Dist	Special
A	

TABLE OF CONTENTS\*

<u>Title</u>	<u>Page</u>
Foreword . . . . .	iii
Table of Contents . . . . .	v
Program . . . . .	
Non Linear Evolution of Data with Microstructure and Applications G. C. Papanicolaou . . . . .	1
Inhomogenous Diffusion (Particulariy in Inhomogeneous Polymer Membranes or Slabs) H. L. Frish . . . . .	5
Aerodynamics Breakup of Viscoelastic Solutions Joseph E. Matta . . . . .	13
X Ray Tracing Methods for Calculation of Atmospheric Refracion Eugene A. Margerum . . . . .	31
A Transport-Theoretic Analysis of Pulse Propagation Through a Random Cloud of Scatterers I. M. Besisris, W. E. Kohler and A. I. Tsolakis . . . . .	47
Analysis of Multilayer Dielectric Waveguide Structures J. M. Zavada and S. T. Peng . . . . .	57
Calculation of Advective Mass Transport in Heterogeneous Media Charles J. Daly . . . . .	73
An Electric Theory of Osmosis for Dilute Saline Solutions Donal L. Buttz . . . . .	91
A Free Boundray Problem in Newtonian Flow W. G. Pritchard, Yuriko Renardy, and L. R. Scott . . . . .	125
Evolution of Near Chapman-Jouget Deflagrations D. S. Stewart and G. S. S. Ludford . . . . .	133
Eine Kleine Eigenvalueproblem (A Simple but Informative Nonlinear Eigenvalue Problem) B. A. Fleishman and P. W. Davis . . . . .	143
The Evolution of a Gas Bubble in a Closed Volume of Stirred Liquid Peter Tikuisis and Charles A. Ward . . . . .	157

\*This Table of Contents lists only the papers that are published in this Technical Manual. For a list of all the papers presented at the Twenty-Eighth Conference of Army Mathematicians see the copy of the Agenda.

On Growth Processes of Condensation Aerosols J. R. Brock . . . . .	173
Modeling of Flow Interaction of a Liquid Jet with a Contaminant Droplet Lang-Mann Chang . . . . .	189
Viscous Flow of a Droplet on a Flat Surface Donald A. Drew . . . . .	205
Cavitating Flow with Surface Tension Jean-Marc Vanden-Broeck . . . . .	219
Stress Solutions at Bondline-Boundary Intersections in Composite Materials Oscar L. Bowie, Colin E. Freese, and Dennis M. Tracey . . . . .	237
X Thermo-Elastic-Plastic Analysis of a Thick-Walled Cylinder with Temperature-Dependent Yield Stress P. C. T. Chen . . . . .	249
A Functional Stress Intensity Approach to Multiply Cracked, Partially Autofrettaged Cylinders S. L. Pu . . . . .	263
Two-Phase Flow of Liquid Propellant Guns by Space Mean Approach R. Yalamanchili . . . . .	285
Calculation of Legendre Functions on the Cut for Integral Order and Complex Degree by Means of Gauss Continued Fractions Alexander S. Elder, James N. Walbert, and Eric C. Benck . . . . .	297
The Best Possible Class of Initial Values for the Porous Medium Equation in $R^N$ Michael G. Crandall . . . . .	335
A New Flight Instability Affecting Spinning Projectiles Having Non-Rigid Payloads Miles C. Miller . . . . .	341
Terrain Mesoroughness Discription and Its Application to Mobility and Cover Richard A. Weiss . . . . .	353
X Interval Bounds for Stationary Values of Functionals L. B. Rall . . . . .	389
A Spatial Domain Walsh Feature Set Charles R. Giardino, Frank P. Kuhl, T. A. Grogan, and O. Robert Mitchell . . . . .	397

Multiple Model Adaptive Filter for Tank Fire Control and Its Microprocessor Implementation P.T. Yip . . . . .	409
Solution of a Hyperbolic Volterra Equation by Finite Difference Scheme Peter Markowich and Michael Rennardy . . . . .	415
Large Deformations and Stability of Axisymmetric Mooney Membranes -- Finite Element Solutions A. R. Johnson . . . . .	431
Structural Analysis of a Mine with Two Viscoelastic Explosive Fills Aaron D. Gupta . . . . .	451
Formation of Singularities for a Conservative Law with Memory Reza Malek-Madani and John A. Nohel. . . . .	477
Theories for Control of Neurotransmitter Release and for Two Problems in Physical Chemistry Lee A. Segel . . . . .	489
Linearized Dynamics of Shearing Deformation - Perturbing Rest in Viscoelastic Materials A. Narain and D. D. Joseph . . . . .	499
Attendance List . . . . .	513

28TH CONFERENCE OF ARMY MATHEMATICIANS

MONDAY  
28 June 1982

0815-0845 REGISTRATION

0845-0900 OPENING REMARKS

0900-1000 GENERAL SESSION I

CHAIRPERSON - Dr. Edward Ross, US Army Natick Research  
& Development Laboratories, Natick,  
Massachusetts

TITLE CONVECTION OF MICROSTRUCTURE

SPEAKER Professor George Papanicolaou, Courant Institute of  
Mathematical Sciences, New York University, New York

1000-1030 BREAK

1030-1200 SPECIAL SESSION A

CHAIRPERSON - Mr. Arthur Stuempfle, Chemical Systems Laboratory,  
Aberdeen Proving Ground, Maryland

SOME ASPECTS OF INHOMOGENEOUS DIFFUSION

Dr. H. L. Frisch, State University of New York-Albany,  
Albany, New York

AERODYNAMIC BREAKUP OF VISCOELASTIC SOLUTIONS

Dr. Joseph Matta, Chemical Systems Laboratory, Aberdeen  
Proving Ground, Maryland

ON THE INFLUENCE OF CONTACT ANGLE HYSTERESIS ON STATIC  
MENISCI

Professor Elizabeth B. Dussan V., University of Pennsylvania,  
Philadelphia, Pennsylvania

1200-1330 LUNCH

**REMOVED PAGE LABEL-NOT FILLED**

1330-1515

TECHNICAL SESSION I

CHAIRPERSON - Dr. Dennis Tracey, US Army Materials and  
Mechanics Research Center, Watertown,  
Massachusetts

RAY TRACING METHODS OF ATMOSPHERIC REFRACTION

Dr. Eugene A. Margerum, Center for Geodesy, US Army  
Engineer Topographic Laboratories, Ft. Belvoir, Virginia

A TRANSPORT-THEORETIC ANALYSIS OF PULSE PROPAGATION THROUGH  
A RANDOM CLOUD OF SCATTERERS

Professors A. I. Tsolakis, I. M. Besieris and W. E. Kohler,  
Virginia Polytechnic Institute and State University,  
Blacksburg, Virginia

ANALYSIS OF MULTI-LAYER DIELECTRIC WAVEGUIDE STRUCTURES

Dr. J. M. Zavada, US Army Armament R&D Command, Dover,  
New Jersey and Dr. S. T. Peng, Polytechnic Institute of  
New York, Brooklyn, New York

CALCULATION OF ADVECTIVE MASS TRANSPORT IN NONHOMOGENEOUS  
MEDIA

Dr. Charles J. Daly, US Army Cold Regions Research and  
Engineering Laboratory, Hanover, New Hampshire

AN ELECTRIC THEORY OF OSMOSIS FOR DILUTE SALINE SOLUTIONS

Dr. Donald L. Buttz, US Army White Sands Missile Range,  
White Sands Missile Range, New Mexico

1330-1515

TECHNICAL SESSION II

CHAIRPERSON - Dr. San Li Pu, Benet Weapons Laboratory,  
Watervliet, New York

A FREE BOUNDARY PROBLEM IN NEWTONIAN FLOW

Dr. Yuriko Renardy, University of Minnesota, Minneapolis,  
Minnesota

EVOLUTION OF NEAR CHAPMAN-JOUGET DEFLAGRATIONS

Professor D. S. Stewart, University of Illinois-Urbana  
Urbana, Illinois and Professor G.S.S. Ludford, Cornell  
University, Ithaca, New York

SPLINE FUNCTION APPROXIMATIONS FOR ORDINARY DIFFERENTIAL EQUATIONS

Dr. Shih C. Chu, US Army Armament R&D Command, Dover,  
New Jersey

EINE KLEINE EIGENVALUE PROBLEM

Professor Paul Wm. Davis, Worcester Polytechnic Institute,  
Worcester, Massachusetts and Professor Bernard A. Fleishman,  
Rensselaer Polytechnic Institute, Troy, New York

THE REVOLUTION OF A GAS BUBBLE IN A CLOSED VOLUME OF STIRRED LIQUID

Dr. Peter Tikuisis, Defence and Civil Institute of  
Environmental Medicine, Downsview, Ontario, Canada and  
Dr. C. A. Ward, University of Toronto, Toronto, Ontario,  
Canada

1515-1545

BREAK

1545-1645

GENERAL SESSION II

CHAIRPERSON - Dr. Stephen S. Wolff, US Army Research Office  
and Ballistic Research Laboratory

AEROSOL DYNAMICS

Professor James Brock, University of Texas at Austin,  
Austin, Texas

TUESDAY  
29 June 1982

0830-1000

SPECIAL SESSION B

CHAIRPERSON - Dr. Norman Banks, Ballistic Research Laboratory,  
Aberdeen Proving Ground, Maryland

MODELING OF FLOW INTERACTION OF A LIQUID JET WITH A  
CONTAMINANT DROPLET

Dr. Lang-Mann Chang, Ballistic Research Laboratory, Aberdeen  
Proving Ground, Maryland

VISCOUS FLOW OF A DROPLET ON A FLAT SURFACE

Dr. Donald A. Drew, Mathematics Research Center, University  
of Wisconsin-Madison, Madison, Wisconsin

THE INFLUENCE OF SURFACE TENSION ON NONLINEAR FREE SURFACE FLOWS

Dr. Jean-Marc Vanden-Broeck, Mathematics Research Center,  
University of Wisconsin-Madison, Madison, Wisconsin

1000-1030

BREAK

1030-1200

TECHNICAL SESSION III

CHAIRPERSON - Dr. James Thompson, US Army Tank-Automotive  
Command, Warren, Michigan

STRESS SOLUTIONS AT BONDLINE-BOUNDARY INTERSECTIONS IN  
COMPOSITE MATERIALS

Drs. Dennis M. Tracey and Colin Freese, US Army Materials and  
Mechanics Research Center, Watertown, Massachusetts

THERMO-ELASTIC-PLASTIC ANALYSIS OF A THICK-WALLED CYLINDER  
WITH TEMPERATURE-DEPENDENT YIELD STRESS

Dr. P.C.T. Chen, Benet Weapons Laboratory, Watervliet,  
New York

A FUNCTIONAL STRESS INTENSITY APPROACH TO MULTIPLE CRACKED,  
PARTIALLY AUTORETTAGED, CYLINDERS

Dr. S. L. Pu, Benet Weapons Laboratory, Watervliet, New York

TWO-PHASE FLOW OF LIQUID PROPELLANT GUNS BY SPACE MEAN  
APPROACH

Dr. R. Yalamanchili, US Army Armament R&D Command, Dover,  
New Jersey

1030-1200

POSTER SESSION

CALCULATION OF LEGENDRE FUNCTIONS ON THE CUT FOR INTEGRAL  
ORDERS AND COMPLEX DEGREE BY MEANS OF GAUSS CONTINUED  
FRACTIONS

Messrs. Alexander S. Elder, James N. Walbert, and Eric C.  
Benck, Ballistic Research Laboratory, Aberdeen Proving  
Ground, Maryland

MEASUREMENTS OF THE RHEOLOGICAL PROPERTIES OF SIMULANTS

Dr. S. J. Armour, Department of National Defence, Ralston,  
Alberta, Canada

SOLUTIONS OF THE POROUS MEDIUM EQUATION ON  $R^N$  WITH GROWING DATA

Professor Michael G. Crandall, Mathematics Research Center,  
University of Wisconsin-Madison, Madison, Wisconsin

COMPUMATH

Mr. Donald L. Gilman, Institute for Scientific Information,  
McLean, Virginia

1200-1330

LUNCH

1330-1530

SPECIAL SESSION C

CHAIRPERSON - Dr. Billy Jenkins, IIS Army Missile Command,  
Redstone Arsenal, Alabama

A NEW FLIGHT INSTABILITY AFFECTING SPINNING PROJECTILES  
HAVING NON-RIGID PAYLOADS

Dr. Miles C. Miller, Chemical Systems Laboratory, Aberdeen  
Proving Ground, Maryland

STABILITY ANALYSIS OF THE MOTION OF CONFINED ROTATING FLUIDS

Drs. Thorwald Herbert and William Saric, Virginia Polytechnic  
Institute and State University, Blacksburg, Virginia

ROTATING FLUID PROBLEMS IN LIQUID-FILLED PROJECTILES

Dr. Raymond Sedney, Ballistic Research Laboratory, Aberdeen  
Proving Ground, Maryland

MEASUREMENT OF YAW MOMENTS FOR LOW REYNOLD NUMBER ROTATING FLOWS

Dr. William P. D'Amico, Jr., Ballistic Research Laboratory,  
Aberdeen Proving Ground, Maryland

1530-1545

BREAK

1545-1645

GENERAL SESSION III

CHAIRPERSON - Dr. Raymond Sedney, Ballistic Research Laboratory,  
Aberdeen Proving Ground, Maryland

SPREADING OF LIQUID FILMS: BIFURCATION AND STABILITY STUDIES

Professor S. H. Davis, The Technological Institute,  
Northwestern University, Evanston, Illinois

WEDNESDAY  
30 June 1982

0830-1030

TECHNICAL SESSION IV

CHAIRPERSON - Mr. Arthur Hausner, Harry Diamond Laboratory,  
Adelphi, Maryland

TERRAIN MESOROUGHNESS DESCRIPTION AND ITS APPLICATION TO  
MOBILITY AND COVER

Dr. Richard A. Weiss, US Army Engineer Waterways Experiment  
Station, Vicksburg, Mississippi

INTERVAL BOUNDS FOR STATIONARY VALUES OF FUNCTIONALS

Professor Louis B. Rall, Mathematics Research Center,  
University of Wisconsin-Madison, Madison, Wisconsin

A WALSH FEATURE SET FOR CLOSED CONTOURS

Dr. Charles Giardina, Fairleigh-Dickinson University,  
Teaneck, New Jersey and Dr. Frank Kuhl, US Army Armament  
R&D Command, Dover, New Jersey

MULTIPLE MODEL ADAPTIVE FILTER FOR TANK FIRE CONTROL AND  
ITS MICROPROCESSOR IMPLEMENTATION

Dr. Pak T. Yip, US Army Armament R&D Command, Dover,  
New Jersey

APPLICATION OF ARTIFICIAL INTELLIGENCE CONCEPTS IN PRUNING  
HYPOTHESIS TREES

Dr. T. Posbergh, US Army Armament R&D Command, Dover,  
New Jersey

0830-1030

TECHNICAL SESSION V

CHAIRPERSON - Mr. Donald Neal, US Army Materials and  
Mechanics Research Center, Watertown,  
Massachusetts

NUMERICAL STUDY OF A MODEL EQUATION FOR VISCOELASTIC LIQUIDS

Dr. Michael Renardy, University of Minnesota, Minneapolis,  
Minnesota

LARGE DEFORMATIONS AND STABILITY OF AXISYMMETRIC MOONEY  
MEMBRANES - FINITE ELEMENT SOLUTIONS

Dr. Arthur R. Johnson, US Army Natick Research and  
Development Laboratories, Natick, Massachusetts

STRUCTURAL ANALYSIS OF A MINE WITH TWO VISCOELASTIC  
EXPLOSIVE FILLS

Dr. Aaron Das Gupta, Ballistic Research Laboratory,  
Aberdeen Proving Ground, Maryland

COUPLED THERMOELASTODYNAMIC WAVE PROPAGATION

Mr. Julian L. Davis, US Army Armament R&D Command, Dover,  
New Jersey

FORMATION OF SHOCKS FOR NONLINEAR CONSERVATION LAWS WITH  
MEMORY

Professor Reza-Malek Madani, Virginia Polytechnic Institute  
and State University, Blacksburg, Virginia and Professor  
John Nohel, Mathematics Research Center, University of  
Wisconsin-Madison

1030-1100

BREAK

1100-1200

GENERAL SESSION IV

CHAIRPERSON - Dr. Jagdish Chandra, US Army Research Office,  
Research Triangle Park, North Carolina

RHEOLOGY OF VISCOELASTIC FLUIDS

Professor D. D. Joseph, University of Minnesota, Minneapolis,  
Minnesota

1200-1300

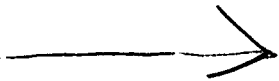
ANALYSIS OF NEUROTRANSMITTER RELEASE

Professor Lee A. Segel, Weizmann Institute  
and Rensselaer Polytechnic Institute

1300-1315

ADJOURN

AD P 0 0 1 0 1 0



Non linear evolution of data with  
microstructure and applications

G. C. Papanicolaou  
Courant Institute, New York University

The well known calculation of the Reynolds stress tensor that can be found for example in [1] goes as follows.

Write the velocity field  $u(t,x)$  in the form

$$u = \bar{u} + u' = \text{mean} + \text{fluctuating field}$$

where the mean of  $u'$ ,  $\overline{u'}$  is zero and insert this expression into the Navier-Stokes equations

$$u_t + u \cdot \nabla u + \nabla p = \nu \Delta u, \quad \nabla \cdot u = 0.$$

Taking averages yields the equation

$$\bar{u}_t + \bar{u} \cdot \nabla \bar{u} + \nabla \bar{p} = \nu \Delta \bar{u} + \nabla \cdot \tau, \quad \nabla \cdot \bar{u} = 0$$

where

$$\tau = -\overline{u' \otimes u'}$$

is the average of the tensor product of the fluctuating part of the velocity field. The tensor  $\tau$  is called the Reynolds stress tensor. Of course the equation for  $\bar{u}$  is not closed since it involves the unknown tensor  $\tau$ . One can obtain an equation for  $\tau$  in the usual manner which in turn is not closed because it involves products of three velocities

and so on. One has the usual closure problem of turbulence.

Very early on, and with substantial effectiveness, it was suggested that  $\tau$  be replaced by a known quantity of the form

$$(1) \quad \tau_{ij} = \nu_T(\bar{u}_{i,j} + \bar{u}_{j,i})$$

where the coefficient  $\nu_T$  is called the eddy or turbulent viscosity coefficient.\*

The question arises: to what extent is this simple closure hypothesis (1) valid if at all, and how can  $\nu_T$  be characterized in terms of more basic properties of the turbulent velocity field? This is at present very much an open question and will probably remain so for some time because the mathematical understanding of the Navier-Stokes equations is very incomplete.

Perhaps hypothesis (1) is not bad and may even be useful in many calculations. Unfortunately what one finds in experiments is that when (1) is used to calculate the drag on a body moving through a turbulent flow the coefficient  $\nu_T$  depends on the macroscopic geometry of the body. It is not a constant reflecting properties of the microstructure of the flow as one would expect.

Along another direction Saffman [3] approached the

---

\*For a recent review of such ideas see [2].

problem of calculating interesting flow quantities in turbulent fluids by writing down a phenomenological system of equations for several quantities that are not related directly to averages of the microscopic flow. Further applications are given by D. Knight [4] and one can see that in these works also the constants that enter into the equations have to be adjusted from problem to problem -- a very unsatisfactory situation!

We have tried to understand this difficulty by exploring a set of simpler problems as well as the Navier-Stokes equations. A report is given in [5] where a two-fluid approach is taken: we attempt to separate the dependence of  $v_T$  into parts that depend only on the microstructure and parts that depend on the macroscopic geometry.

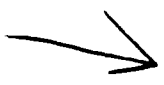
We have also given an account of the connection of the closure problem to homogenization and random media [6].

## References

- [1] A. Monin & A. Yaglom, Statistical Fluid Mechanics, MIT Press, 1971.
- [2] W. C. Reynolds, An. Rev. Fl. Mech. (1976), p. 183.
- [3] P. Saffman, Development of a complete model for the calculation of turbulent shear flow, Duke Turbulence Conference, 1976, Duke University Math. Series.
- [4] D. Knight and P. Saffman, Turbulent model predictions in flows with significant mean streamline curvature, AIAA 16th Aerospace Sciences meeting, Jan. 16-18, 1978.
- [5] D. McLaughlin, G. Papanicolaou and O. Pironneau, Convection of Microstructure, INRIA Congress 1981, North Holland, 1982 (R. Glowinsky, editor).
- [6] G. Papanicolaou and O. Pironneau, "On the asymptotic behavior of motion in random flows," in Stochastic Nonlinear Systems, edited by L. Arnold and R. Lefever, Springer, 1981, pp. 36-41.



AD P001011

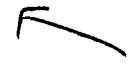


# INHOMOGENEOUS DIFFUSION (PARTICULARLY IN INHOMOGENEOUS POLYMER MEMBRANES OR SLABS)

H. L. Frish  
Department of Chemistry  
State University of New York at Albany  
1400 Washington Avenue  
Albany, N.Y. 12222

*The authors*  
ABSTRACT. ~~We~~ review briefly the inverse diffusion problem encountered in practice interpreting permeation and sorption measurements on inhomogeneous polymer membranes, films or slabs. ~~We~~ suggest some important open problems in this field.

*They*



There exists in many contexts interest in the diffusion of smaller molecules, the penetrants, in polymer membranes or films.<sup>1</sup> Polymer membranes or films are often used as protective barriers against the penetrant or to separate penetrant mixtures. These polymer membranes are often naturally inhomogeneous due to the presence of crystalline regions in the amorphous polymer matrix or regions of polymer - polymer phase separation if the film is made from a polymer alloy composite. Artificial inhomogeneities such as fillers and/or voids introduced with them are sometimes added to polymers to enhance their barrier properties or permselectivity. Lineal dimensions of these inhomogeneities are of the order of 0.01 - 100 m $\mu$  and in first approximation can be thought to be remain fixed in the sample without distortion in the course of the diffusion process.<sup>1</sup> A schematic diagram of such an inhomogeneous polymer is shown in Figure I below, with the cross-hatched area indicating crystallinity, the stippled region polymer phase separation and the dark particle a filler particle.

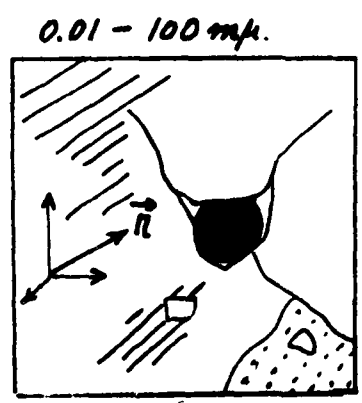


Figure I

The concentration  $c(\vec{r}, t)$  of the isothermally diffusing penetrant at any point  $\vec{r}$  at time  $t$  is governed by the irreversible thermodynamic relationships:

a) The flux  $\vec{J}(\vec{r}, t)$  of the penetrant is given by

$$\vec{J} = - \frac{D}{RT} \nabla(\Delta\mu) c = - Dk \nabla(c/k) \quad (1)$$

where  $\Delta\mu = RT \ln(c/k)$  is the chemical potential difference of the penetrant,  $c/k = a$  is the thermodynamic activity,  $T$  is the absolute temperature,  $R$  the gas constant,  $D = D(\vec{r}, c)$  the diffusion coefficient,  $k(\vec{r}, c)$  the partition coefficient (essentially the inverse activity coefficient) of the penetrant - polymer system, and

b) the equation of continuity

$$\frac{\partial c}{\partial t} = - \nabla \cdot \vec{J} \quad (2)$$

Combining eq. (1) with (2) yields

$$\frac{\partial c}{\partial t} = \nabla \cdot [Dk \nabla(c/k)] \quad (3)$$

which describes penetrant diffusion in such an inhomogeneous medium. Only in the case of (homogeneous) ideal Fickian diffusion, when  $D = D_0$ , a constant and  $k = k_0$ , a constant does eq. (3) reduce to the usual form of Fick's Second Law

$$\frac{\partial c}{\partial t} = D_0 \nabla^2 c \quad (4)$$

Besides suitable initial and boundary conditions (B.C.) eq. (3) can only lead to a well posed mathematical boundary value problem if the material coefficients describing the dispersal of the penetrant in the polymer,  $D(\vec{r}, c)$  and  $k(\vec{r}, c)$ , are known. Unfortunately, in practice, this is not the case and one has to deal with an inverse diffusion problem, which is to extract some information about  $D$  and  $k$  from standard permeation and sorption measurements. These permeation and sorption techniques were originally designed to study homogeneous polymer samples and thus one of the first tasks is to describe what functionals of  $D$  and  $k$  are contained in the collected data from such experiments.

In both sorption and permeation experiments an initially penetrant-free membrane, film or slab of the polymer sample of thickness  $l$  (which we take to lie along the  $x$  axis) and known cross-sectional area is rendered impermeable  $\partial c / \partial \vec{n} = 0$ , on the bounding surfaces normal to the  $x$  direction, where  $\vec{n}$  is the normal vector to these bounding surfaces. In a permeation experiment<sup>1</sup> the surface

$x = 0$  is brought into contact with a constant activity reservoir which maintains the penetrant concentration at a fixed value  $c_0$  at  $x = 0$ . The surface at  $x = l$  is in contact with a vacuum, i.e.  $c(x=l, t) = 0$ , and the amount of penetrant which flows through the surface  $x = l$ , per unit area up to time  $t$ ,  $Q(t)$  is monitored as a function of  $t$ . A schematic diagram of such a permeability cell is shown in Figure 2 below.

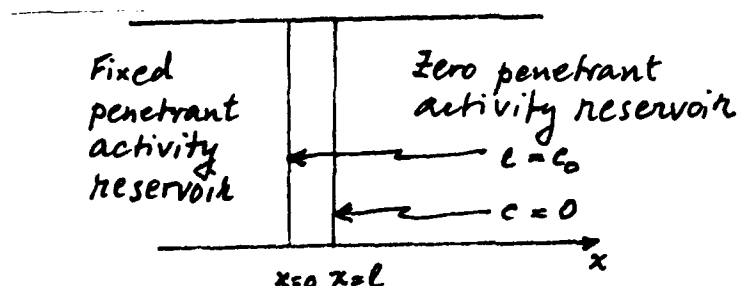


Figure 2

The remaining B.C. under which eq. (3) has to be solved are

$$c(\vec{r}, 0) = 0$$

$$c(x=0, t) = c_0$$

$$c(x=l, t) = 0$$

A schematic plot of  $Q(t)$  versus  $t$  is shown in Figure 3 below

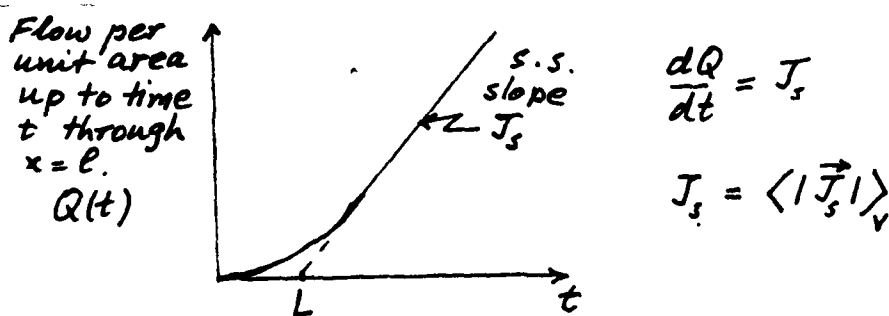


Figure 3

The steady state slope of this curve (i.e. of the straight line portion) provides  $J_s$  which used to define the steady state permeation diffusion coefficient  $D_s$  sometimes called the effective diffusion coefficient  $D_{eff}$ ,

$$\frac{J_s \ell}{C_0} = D_s = D_{eff} \quad (6)$$

The time intercept of the asymptote to the  $Q(t)$  curve defines the time-lag  $L$ . A time-lag diffusion coefficient  $D_L$  can be defined as

$$D_L = \ell^2 / 6L \quad (7)$$

For ideal Fickian diffusion ( $D = D_0$ ,  $k = k_0$ ) one has

$$D_0 = D_L = D_s \quad (8)$$

In general  $D_L$  and  $D_s$  are expected to be different functionals of  $k$  and  $D$ .

In a sorption cell measurement<sup>2</sup> an initially penetrant free film or slab of known cross-sectional area and width  $\ell$  is suspended in a constant activity reservoir and the net weight increase per unit area of the sample due to penetrant diffusion up to time  $t$ ,  $M_t$ , is recorded. A schematic diagram of the apparatus is shown in Figure 4 below:

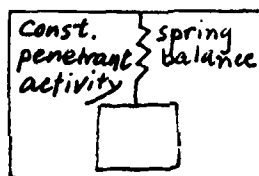


Figure 4

The remaining B.C. are

$$c(\vec{r}, 0) = 0$$

$$c = c_0 \text{ at } x = 0, \ell \quad (9)$$

$M_t$  is directly proportional to the volume average of  $c(\vec{r}, t)$ ,  $\langle c(\vec{r}, t) \rangle_v$ .

The data is often plotted as  $M_t / M_\infty$  versus  $(t/\ell^2)^{1/2}$  as shown schematically in Figure 5 below:

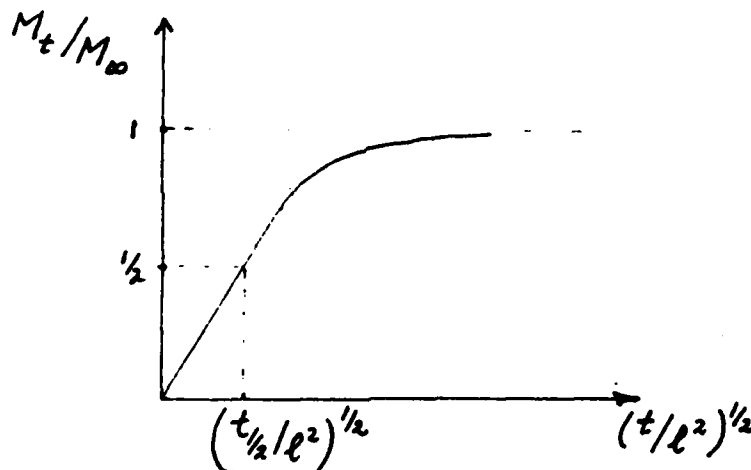


Figure 5 8

An initial time diffusion coefficient,  $D_I$ , is defined by

$$\left[ \frac{d (M_t/M_\infty)}{d (t^{1/2}/\ell)} \right]_{t \rightarrow 0}^2 \frac{\pi}{16} = D_I \quad (10)$$

Sometimes one employs also the "half time" diffusion coefficient defined by

$$D_{1/2} = \frac{0.04914}{t_{1/2} \ell^2} \quad (11)$$

where  $t_{1/2}$  is time taken for  $M_t/M_\infty = 1/2$ .

A long time diffusion coefficient,  $D_{l.t.}$ , can be obtained using the relation

$$- \left[ \frac{d}{dt} \ln (1 - M_t/M_\infty) \right]_{t \rightarrow \infty} \frac{\ell^2}{\pi} = D_{l.t.} \quad (12)$$

In the case of Ideal Fickian diffusion

$$D_0 = D_I = D_{1/2} = D_{l.t.}, \quad (13)$$

but for inhomogeneous diffusion  $D_I$ ,  $D_{1/2}$ ,  $D_{l.t.}$  are different functionals of  $D$  and  $k$ .

Results are only known for special cases:

Case 1. Concentration dependent diffusion coefficient for which  $D = D(c)$  and  $k = k(c)$ . This occurs with homogeneous polymer samples in which the penetrant "plasticizes" the sample and generally makes it easier for subsequent penetrant molecules to diffuse in the sample. Thus the only real inhomogeneity is due to the external penetrant concentration gradient impressed on the sample to study diffusion. Eq. (3) reduces in this case to the non-linear form of Fick's second law:

$$\frac{\partial c}{\partial t} = \frac{\partial}{\partial x} \left\{ \mathcal{D}(c) \frac{\partial c}{\partial x} \right\} \text{ in } 0 < x < \ell \quad (14)$$

with  $\mathcal{D}(c)$  given by

$$\mathcal{D}(c) = D(c) k(c) d(c/k(c)) / dc \quad (15)$$

For permeation (B.C. given by eq. (5) the steady-state version of eq. (14) is easily integrated to give the steady-state concentration,  $c_s$ , achieved as  $t \rightarrow \infty$ . The steady state permeation diffusion coefficient is simply a concentration averaged  $D(c)^2$

$$D_s = \frac{1}{c_0} \int_0^{c_0} \mathcal{D}(c) dc. \quad (16)$$

The time lag  $L$  is a simple functional of  $c_s$  and  $\mathcal{D}(c)$  as can be seen by direct

integration and integration by parts of eq. (14) and yields<sup>3</sup>.

$$D_L = \frac{\ell^2 \int_0^{c_0} \mathcal{D}(c) dc}{\int_0^{\ell} x c_s(x) dx}$$

$$= \frac{\left[ \int_0^{c_0} \mathcal{D}(c) dc \right]^3}{6 \int_0^{c_0} dc c \mathcal{D}(c) \int_c^{c_0} \mathcal{D}(u) du} \quad (17)$$

No exact analytical results are available for the sorption diffusion coefficients defined by equations (10), (11) and (12). Extensive numerical calculations suggest that<sup>4</sup>

$$D_I \approx \frac{5}{3} c_0 - \frac{5}{3} \int_0^{c_0} c^{2/3} \mathcal{D}(c) dc \quad (18)$$

and<sup>5</sup>

$$D_{l.t.} \approx \mathcal{D}(c_0) \quad (19)$$

Another practically interesting limiting case is:

Case 2. The Linear Inhomogeneous Medium for which  $D = D(\vec{r})$  and  $k = k(\vec{r})$  only. Experimentally this is achieved by carrying out permeation and sorption runs for different values of  $c_0$  and extrapolating the data to  $c_0 \rightarrow 0$ . Eq. (3) now reduces to a linear partial differential equation on which one can employ usefully a one sided Laplace transform with respect to time. In permeation there is no generally valid analytic expression for  $D_s$  for arbitrary random inhomogeneity distributions but there are special random geometries for which  $D_s$  is known or for which strict bounds for  $D_s$  are known. These results are summarized in references (1) and (4). Again one can show<sup>6</sup> by direct integration that for permeation (B.C. given by eq. (5))

$$\frac{D_L}{D_s} = \frac{1}{6} \left[ \frac{\langle c_s \rangle_v}{c_0} - \frac{\langle k \rangle_v \langle c_s^2 / k \rangle_v}{c_0^2} \right]^{-1} \quad (20)$$

Using an eikonal solution of the Laplace transformed eq. (3) and exact Laplace transform asymptotics for the  $t \rightarrow 0$  limit one can show that

$$D_I = \frac{1}{2} \left[ \frac{\langle D^{-1/4} k^{1/2} \rangle_0}{\langle (D^{3/4} k^{1/2})^{-1} \rangle_0} + \frac{\langle D^{-1/4} k^{1/2} \rangle_\ell}{\langle (D^{3/4} k^{1/2})^{-1} \rangle_\ell} \right]^2 / (\langle k \rangle_V)^2 \quad (21)$$

$$= \left[ \frac{\langle D^{-1/4} k^{1/2} \rangle_V}{\langle k \rangle_V \langle (D^{3/4} k^{1/2})^{-1} \rangle_V} \right]^2$$

where  $\langle \dots \rangle_0$  and  $\langle \dots \rangle_\ell$  stand for surface averages over  $x = 0$  and  $\ell$  respectively and the second equality only holds if the distribution is statistically homogeneous and isotropic. No analytic result for  $D_{\ell.t.}$  (cf. eq. (12) is known.

A specialization of Case 2 is:

Case 3. The Linear Laminated Medium for which  $D = D(x)$  and  $k = k(x)$  only. The Laplace transform of eq. (3) is now an ordinary linear second order differential equation. A variety of authors have obtained explicit results for this simple case which we list below: ( $P(x) = D(x)k(x)$ )

$$D_S = \ell^2 / \left[ \left( \int_0^\ell k(x) dx \right) \left( \int_0^\ell dx / P(x) \right) \right], \quad (22)$$

$$D_L = \ell^2 \int_0^\ell dx / P(x) / \left[ 6 \int_0^\ell \int_0^\ell \int_0^{x'} \frac{k(x'')}{P(x)P(x')} dx'' dx' dx, \right] \quad (23)$$

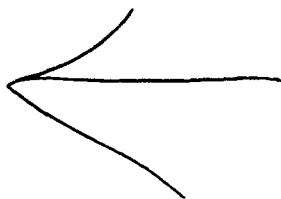
$$D_I = \left[ \frac{k(0) D^{1/2}(0) + k(\ell) D^{1/2}(\ell)}{\frac{2}{\ell} \int_0^\ell k(x) dx} \right]^2 \quad (24)$$

and  $D_{\ell.t.}$  estimates are available from WKB asymptotics. A natural inhomogeneity scale can be introduced in this case from measured  $D_S$  and  $D_L$  values.<sup>7-8</sup>

The principal open problems in this field deal with the meaning of the various experimentally measured diffusion coefficients  $D_S$ ,  $D_L$ ,  $D_I$ ,  $D_{\ell.t.}$ , etc. in the general case where  $D = D(\vec{r}, c)$  and  $k = k(\vec{r}, c)$  and neither  $D$  or  $k$  can be factored into a product of a function of  $\vec{r}$  and  $c$  only. Perhaps a completely different strategy for employing these measurements is required to extract useful information about the inhomogeneity distributions.

### References

- (1) Crank, J and Park, G. S. (eds), "Diffusion in Polymers", Academic Press, N.Y., 1968.
- (2) Barrer, R.M., Proc. Phys. Soc. 58, 321 (1946).
- (3) Frisch, H. L., J. Phys. Chem. 62, 93 (1957); J. Chem. Phys. 36, 510 (1962).
- (4) Crank, J., "The Mathematics of Diffusion", 2<sup>o</sup> Edit., Clarendon Press, Oxford, 1975.
- (5) Frensdorff, H.K., J. Polym. Sci. A2, 341 (1964).
- (6) Frisch, H. L. and Prager, S., J. Chem. Phys. 54, 1451 (1971).
- (7) Frisch, H. L. and Bdzil, J., J. Chem. Phys. 62, 4804 (1975).
- (8) Falkovitz, M. and Frisch, H. L., J. Membrane Sci., 10, 61 (1982).



AD P001012

AERODYNAMIC BREAKUP OF VISCOELASTIC SOLUTIONS

Joseph E. Matta  
Physics Branch  
Research Division  
Chemical Systems Laboratory, USAARRADCOM  
Aberdeen Proving Ground, Maryland 21010

ABSTRACT. A helium activated firing device was used to propel viscoelastic fluid slugs (350cc) to Mach 1 velocities. Aerodynamic forces disrupt the slug which eventually transforms into a cloud of droplets that fall on the ground below. Various concentrations and types of polymethyl methacrylate (PMMA) in diethylmalonate (DEM) were disseminated. The resultant average drop sizes for each trial were measured and shown to significantly increase with the addition of polymers. A correlation between average drop size and fluid viscosity was not observed. Both a relative relaxation time deduced from a simple die swell experiment and the first normal stress difference  $N_1$  correlated dissemination trials conducted at ambient temperatures. However, only the relative relaxation time correlation was consistent with breakup trials using heated fluids. Use of  $N_1$  for predicting particle size from dissemination tests employing heated viscoelastic fluids can produce considerable error.

I. INTRODUCTION: Aerodynamic forces are often used to break up liquids for various applications, e.g. paint spraying, fuel combustion, aircraft dissemination of bulk liquids for fire fighting and insecticide applications, etc. Although various studies dating back many years have been aimed at an understanding of the mechanics of aerodynamic liquid breakup, aside from low Reynold's number jet breakup (Rayleigh), only empirical models exist to describe such behavior. For newtonian liquids the resultant drop sizes (the usual dependent variable of interest) is correlated to the liquid density, surface tension, viscosity, and relative air velocity.

However, when newtonian liquids are subjected to a relatively high air velocity, small particles normally result. For various applications this is often undesirable. Small drops remain air borne for a considerable time and often fail to impact on the intended location. Various investigators<sup>1-3</sup> have shown by adding polymer to the solution one can significantly increase the particle size and thus reduce the settling time. The addition of polymer results in a non-Newtonian, viscoelastic fluid. The breakup mechanisms of polymer solutions are very complicated. Not only are the fluids elastic but usually also thixotropic in behavior.

A recent wind tunnel study<sup>1</sup> was conducted to investigate the effect of viscoelasticity on the resultant drop size. Various viscoelastic fluids with similar densities and surface tensions were injected concurrently into a high velocity airstream. It was possible to correlate the dissemination with the fluid relaxation time  $(\theta/\theta_{0.5\%})^*$  deduced from a simple die swell experiment. In addition to  $(\theta/\theta_{0.5\%})$ , the first normal stress difference  $N_1$  measured at 500 sec<sup>-1</sup> also correlated the breakup results; but since considerable uncertainty exists over the breakup deformation rate, the shear rate independent  $(\dot{\gamma}/\dot{\gamma}_{0.5\%})$  was considered preferable over  $N_1$  for predicting particle size. However, it was suggested that dissemination of heated fluids would enable a comparison of the validity of the two correlating variables, since  $N_1$  decreases much more rapidly

\* A relative relaxation time was calculated for each fluid from the amount of shift necessary to superimpose all the die swell curves onto the chosen, 0.5% PMMA/DEM, swell curve.

than does ( $\theta/\theta_{0.5\%}$ ) with an increase in temperature. This report describes such an experiment where viscoelastic fluids both at ambient and elevated temperatures were disseminated. Correlations between resultant drop sizes and various rheological properties were evaluated.

In contrast to the earlier effort where small diameter (<5 cm) viscoelastic ligaments were slowly ejected into a high velocity airstream (200 m/sec), this study describes a system where 7.6 cm diameter viscoelastic slugs (350 cc) were ejected with high velocities (Mach 1) into ambient air. This system was developed to more closely simulate high speed delivery conditions for large bulk liquid quantities and yet provide a relatively inexpensive and reproducible testing procedure.

### III. EXPERIMENT:

A. Test Procedure: A helium activated firing device was used to project liquid slugs that were 7.6 cm in diameter to Mach 1 velocities (Figure 1). The primary component of the firing device is a 7.6 cm solenoid valve. To the breach side is attached a cylindrical gas reservoir 14 cm in diameter and 61 cm long. The aluminum barrel has a smooth bore (7.6 cm ID) that measures 1.8 meters in length. The solenoid actuates within 9 milliseconds, opening a clear path between the pressurized gas reservoir and the barrel.

Before loading the test liquid, a polyethylene cylinder is inserted down into the barrel to act as a pusher on the test fluid when the pressurized helium is released. The cylinder has an attached O-ring seal to prevent intermixing of the liquid and gas. The liquid is then simply poured into the inclined barrel through a loading port just in front of the pusher. When the gun is actuated the pusher cylinder accelerates and forms the liquid into a cylindrical slug prior to exiting the muzzle. After the slug exits the gun barrel, aerodynamic forces begin to disrupt the slug which eventually transforms into an aerosol of droplets that fall on the ground below. The gun barrel is vertically inclined 20 degrees from the horizontal plane to assure that complete aerodynamic breakup occurs before fallout and to spread the drop pattern over a sufficiently large area for proper sampling.

Before each firing, sampling cards mounted on plywood squares ( $92 \text{ cm}^2$ ) were placed on the ground to form a sampling array ( $100 \text{ m}^2$ ) in which card spacing in the lateral and flight direction was 3.0 and 2.4 m, respectively. In addition, spin samples were used along the axis of flight and two neighboring rows. The spin samplers are designed to permit sampling and avoid stain overlap that would otherwise occur in the high density deposition areas. These spin samplers consisted of a circular ( $30.5 \text{ cm}$  diameter) paper sheet rotating (10 rpm) under a cover having a sector shape ( $58 \text{ cm}^2$ ) opening. As the drops settle towards the ground a new portion of the sampling sheet is continually exposed. This decreases the density of droplet deposition and loss of data due to overlap that would occur were the drops allowed to cumulatively impact on a stationary sampling area.

After each firing, the drop impacted witness cards were collected and allowed to dry. The resulting circular drop stains were later sized on a Quantimet 720 Image Analyzer\* and converted to actual drop diameters using a previously determined spread factor relationship. Figure 2 shows a typical spread factor regression obtained for measured stain diameters of known drop sizes. A cumulative mass probability plot was then prepared to determine the resultant mass median diameter (MMD) of the aerosol

\* Manufactured by Cambridge Instruments, Monsey, New York.

cloud that was generated in each test. By assuming the droplets collected on each sample card were representative of the surrounding area the sampling efficiency of the experiment was estimated comparing the calculated mass deposited on the ground with the actual fluid quantity disseminated (370 gms). The calculated disseminated mass was obtained by summing the products of each measured mass density deposition with the mesh sampling area. The ratio of the measured with the actual disseminated mass is referred to as the mass recovery.

As a data gathering tool and to provide a pictorial history of the dissemination process, two high speed cameras recording at 3000 frames per second with overlapping fields of view are employed. Timing dot generators were used in conjunction with the cameras to accurately determine the framing rate necessary for establishing liquid velocity. A meter scale was placed at the line of fire as a distance reference. In order to highlight the liquid mass on film, a white cloth was suspended behind the path of the liquid slug at the same angle of trajectory. A series of timing devices were integrated into a common firing box to properly sequence the start of the cameras and the firing of the gun. The films were later analyzed on a Tele-Cordex film reader which permitted determination of liquid velocity and other visible aspects of the dissemination process.

Test Fluids: The solvent used in the study was diethylmalonate, DEM, which was converted into a viscoelastic liquid by the addition of various concentrations and types of polymethyl methacrylate to give a range of liquid characteristics. The polymers used included: (a) a polymer of high molecular weight,  $6 \times 10^6$ , obtained from Rohm and Haas Co. referred to as PMMA, (b) a copolymer of medium molecular weight,  $1.9 \times 10^6$ , composed of 80% PMMA and 20% poly (ethyl/butyl acrylate), also from Rohm and Haas, and used at a 5.2% concentration and (c) DuPont's Elvacite 2041 at 9.8% concentration, the lowest molecular weight,  $4 \times 10^5$ , powder tested. Two percent Calco Oil Blue ZV was added to all solutions to enhance drop stain measurements. Both the density ( $1.05 \text{ g/cc @ } 25^\circ\text{C}$ ) and surface tension ( $30.4 \text{ dyne/cm @ } 30^\circ\text{C}$ ) were similar for all the tested fluids.

The viscosity,  $\eta$ , and first normal stress difference  $N_1$  of the test fluids were measured using a Weissenberg Model R-18 Rheogoniometer with a .5 degree cone angle (Figure 3 & 4). The shear rate was increased until an observable flow instability occurred. The polymer solutions are viscoelastic as shown by their viscosity variation with shear rate and their measurable first normal stress difference.

The die swell ratio was measured for the fluids over a shear range of 500 to 5000  $\text{sec}^{-1}$  (Figure 5). The swell ratio  $D_j/D_N$  was determined from the maximum diameter along the jet  $D_j$  and the inner diameter of the nozzle  $D_N$ . The fluid was ejected vertically downward from a 7.6 cm reservoir through either a 1.78 or 1.27 mm nozzle with length to diameter ratios of 85 and 120, respectively. No dependence of swell on nozzle diameter was observed. The swell-shear behavior is similar for all the fluids except the most elastic (2.1% PMMA), which appeared to exhibit some sort of instability towards the higher shear rates. Assuming the swell is dependent only on Weissenberg number ( $\theta^j$ ) one can calculate a relative relaxation time for each liquid by the amount of horizontal shift required to superimpose all the curves. The 0.5% PMMA fluid was chosen as the reference fluid to which other curves were shifted. The essentially parallel die swell curves result in relative relaxation times that are independent of shear rate (table 1).

**III. RESULTS:** Cumulative mass probability plots for each dissemination trial indicate that log-normal distributions adequately describe the resultant drop sizes. Figure 6 shows such a plot for the Elvacite dissemination trials. From the plot the mass median diameter MMD was determined graphically at the 50% point of the cumulative mass. The geometric standard deviation  $\sigma_g$  is given approximately by the diameter ratios

corresponding to the 84/50 or 50/16 percent cumulative mass values<sup>4</sup>. Similar plots for each fluid tested were made and results are summarized in table II. For the majority of tests the mass measured was within 30 percent of the actual dispersed mass, although greater deviations were occasionally observed for the more elastic fluid trials, where the larger drops reduced the sampling accuracy.

It is obvious from the data in table II that viscosity alone does not account for the increase in resultant particle size. The 1.0 and 1.5 percent PMMA solutions have lower and/or nearly similar viscosities, respectively than the copolymer and Elvacite solutions but yet the resultant MMDs are considerably larger for the PMMA solutions.

Correlations of the MMDs values obtained and the liquids' rheological properties were attempted in terms of both the relative relaxation time (figure 7) and first normal stress difference  $N_1$  measured at  $500 \text{ sec}^{-1}$  (figure 8). The solid lines are the least square regressions and the dashed lines represent the 95% confidence limits.

The  $500 \text{ sec}^{-1}$  shear rate\* was chosen since it provides the best correlation between MMD and  $N_1$ . As in the wind tunnel work<sup>1</sup>, both variables correlate with the MMD results. However, in the present field study, greater sensitivity with  $N_1$  and  $(\theta/\theta_{0.5\%})$  is observed, which is probably a scaling effect. For the tests using the helium gun, the range in resultant MMDs varied about an order of magnitude, while in the wind tunnel study where smaller initial ligament diameters of the same fluids were disseminated, a variation of only a factor of two was observed.

Although both parameters appear to correlate dissemination results, rheological measurements at elevated temperatures indicate that  $N_1$  decreases more rapidly with temperature than does  $(\theta/\theta_{0.5\%})$ . Thus, dissemination of heated fluids should enable a distinction to be made between the two correlating variables. Both first normal stress and die swell measurements were made for the 2.1% PMMA solution at various temperatures up to  $90^\circ\text{C}$ \* over the shear rate range indicated in Figures 9 & 10. From these results,  $N_1$  ( $500 \text{ sec}^{-1}$ ) is shown to be more sensitive to temperature changes than  $(\theta/\theta_{0.5\%})$  (Figure 11). With a  $70^\circ\text{C}$  increase,  $N_1$  decreases about an order of magnitude more than  $(\theta/\theta_{0.5\%})$ .

A series of dissemination trials were conducted with the 2.1% PMMA solution at

\* The error bars shown for the data points were estimated from their respective mass recovery values. It was assumed that the average percent difference between the actual and measured mass for each trial is approximately three times the error of the MMD calculation since drop mass varies as the cube of the diameter. An additional 5% error was included to account for the uncertainty associated with graphical determination of the MMD from these cumulative plots.

\*\* This value is not obviously unrealistic since a 2 msec breakup time estimated from the inverse of the  $500 \text{ sec}^{-1}$  rate (i.e. assuming the process time is inversely proportional to the deformation rate) does not appear inconsistent with the data obtained from the dissemination films. However, without knowledge of the breakup kinetics deformation rate estimates involve considerable conjecture.

\* Due to fluid stability it was not possible to measure  $N_1$  above  $65^\circ\text{C}$ .

various temperatures, and the results are shown in table III. For these tests, the fluid was heated before being poured into the barrel, and the barrel itself was wrapped with a heating coil to prevent the liquid from cooling. Temperatures were measured through the filling port immediately before dissemination. Figures 7 and 8 show how the MMDs compare with the earlier correlations found for  $N_1$  and  $(\theta/\theta_{0.5\%})$  at ambient temperatures. As can be seen, the MMDs for the heated fluid trials agree considerably better with the  $(\theta/\theta_{0.5\%})$ , rather than the  $N_1$  correlation and thus  $(\theta/\theta_{0.5\%})$  is preferable for resultant particle size predictions. The small deviation from the regression line for the heated fluids is not unexpected, because of the slight cooling that may occur during the dissemination process.

**IV. DISCUSSION:** Since the breakup results correlate with the relative relaxation time rather than the fluid shear viscosity one might expect the extensional fluid behavior to significantly influence the atomization process. Attempts were made to correlate the dissemination trials using the transient convected Maxwell expression<sup>5</sup> for the elongational viscosity,  $\eta_E$  i.e.,

$$\eta_E = \eta \left\{ \frac{2}{1 - 2\theta_M \dot{\epsilon}} [1 - \exp(-[1 - 2\theta_M \dot{\epsilon}]t/\theta_M)] + \frac{1}{1 + \theta_M \dot{\epsilon}} [1 - \exp(-[1 + \theta_M \dot{\epsilon}]t/\theta_M)] \right\}$$

where  $\dot{\epsilon}$  and  $\theta_M$  are the elongation rate and Maxwell relaxation time, respectively. Choosing an elongation rate of about  $30 \text{ sec}^{-1}$  it is possible to correlate the ambient dissemination trials with the predicted elongational viscosity at a time = .1 sec. However, the heated fluid trials were not consistent with this correlation.

The failure is not too surprising when one considers the high degree of nonlinearity probably occurring during atomization. Various other constitutive equations may better describe the breakup process. Currently we plan to estimate the extensional behavior of the tested solutions using the BKZ model<sup>6</sup> by measuring the elastic strain energy function from a stress relaxation experiment.

Although we have not yet found an elongational viscosity expression to correlate all of our breakup trials, the relative relaxation time deduced from the die swell experiment is consistent with the elongational breakup mechanism if one considers the swell phenomenon as an extensional effect. Recently, Tanner<sup>8</sup> has suggested this by associating the die swell behavior of liquids with the outer sheath extension of the ejected fluid rather than the usually proposed elastic recoil effect. Furthermore, since the fluids are extruded vertically downward the gravitational force tends to stretch the jet and is possibly responsible for the observed correlation with breakup results.

In any case, although the relationships between dissemination and the die swell mechanism is not clearly understood, the relaxation time does correlate breakup results and as a figure of merit alone is considered a viable parameter for resultant viscoelastic particle size predictions. Both our earlier wind tunnel<sup>1</sup> results and the dissemination tests discussed in this study indicate that the use of the relative relaxation time is preferable to  $N_1$  for predicting particle size. Not only is the relaxation time shear rate independent, thus eliminating any need for estimating the shear rate of the breakup process, but the relaxation time parameter also correlates with both the ambient and heated temperature results. The use of  $N_1$  for predicting particle size when heated fluids are disseminated can produce considerable error. In addition, reliable high shear rate  $N_1$  measurements are impossible to obtain with the current state-of-the-art techniques.

### References

1. J.E. Matta, Journal Applied Polymer Science, Vol 27, 397-405, 1982.
2. J.W. Hoyt, J.J. Taylor, and R.L. Altman, J. Rheol. 24(5), 685-699, 1980.
3. J.D. Wilcox, R.K. June, and H.A. Brown, J. Appl Polym Sci, 13, 1-6, 1961.
4. G. Gerdan, "Small Particle Statistics", pp 96-97, Academic Press, 2nd Edition, N.Y., N.Y., 1960.
5. M. Denn and G. Marrucci, AICHE J., 17, 101 - 103, (1971).
6. J. Dealy, J. Polymer Engineering and Science, Vol II, No. 6, 433-445, 1971.
7. B. Bernstein, E.A. Kearsley and L.J. Zapas, Trans. Soc. Rheol. 7, 391, 1963.
8. R.I. Tanner, Journal of Non-Newtonian Fluid Mechanics, 6, 289-302, (1980).

Table I: The Relative Relaxation Times Deduced From a Die Swell Experimental Using Disseminated Test Fluids

<u>Test Fluid at 21°C</u>	<u><math>\theta/\theta_{0.5\%}</math></u>
0.5% PMMA	1.0
1.0% PMMA	4.3
1.5% PMMA	10.0
2.1% PMMA	26.6
5.2% Copolymer	2.0
9.8% Elvacite	2.0

Table II: Field Dissemination Results - Ambient Conditions

<u>TEST #</u>	<u>Fluid</u>	<u>% Recovery</u>	<u>MMD, <math>\mu\text{m}</math></u>	<u><math>\sigma_g</math></u>
1	0.5% PMMA	81	340	2.2
2	0.5% PMMA	78	370	1.8
3	1.0% PMMA	84	1450	2.7
4	1.0% PMMA	72	1200	3.0
5	1.5% PMMA	61	1700	2.3
6	1.5% PMMA	101	2450	3.3
7	2.1% PMMA	160	4100	2.8
8	2.1% PMMA	150	4100	2.8
9	5.2% Copolymer	107	480	2.2
10	5.2% Copolymer	81	430	2.0
11	9.8% Elvacite	102	420	1.6
12	9.8% Elvacite	62	460	1.6

Table III: Heated 2.1% PMMA Dissemination Results

<u>Test #</u>	<u>Temperature, <math>^{\circ}\text{C}</math></u>	<u>% Recovery</u>	<u>MMD, <math>\mu\text{m}</math></u>	<u><math>\sigma_g</math></u>
13	38	115	3800	3.0
14	68	81	1070	2.3
15	68	106	1450	2.5
16	68	102	1500	2.5
17	95	83	820	2.2

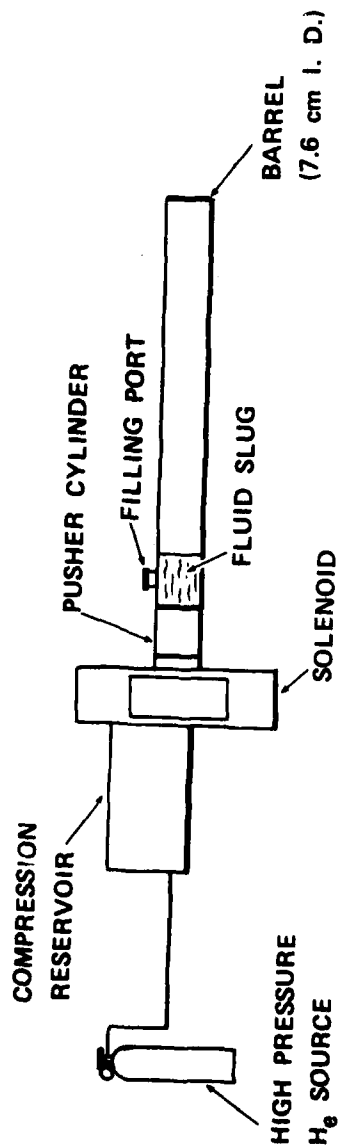


Figure 1: A sketch of the 7.6 cm I.D. Helium gun used to disseminate test fluids.

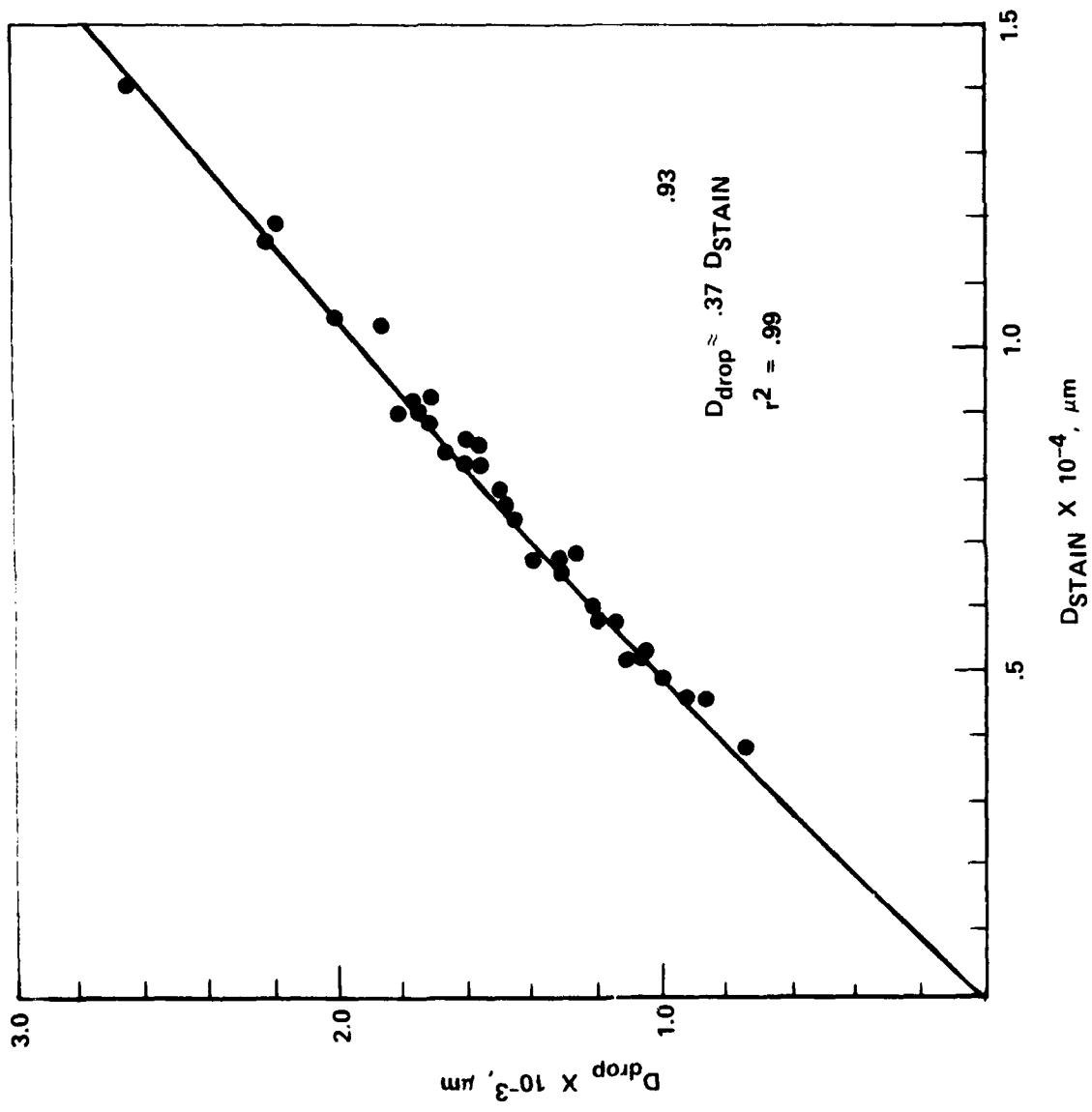


Figure 2: Measured drop versus stain diameter for 1.5% PMMA/DEM solution,  $D_{\text{drop}} = 0.37 D_{\text{stain}}$  .93

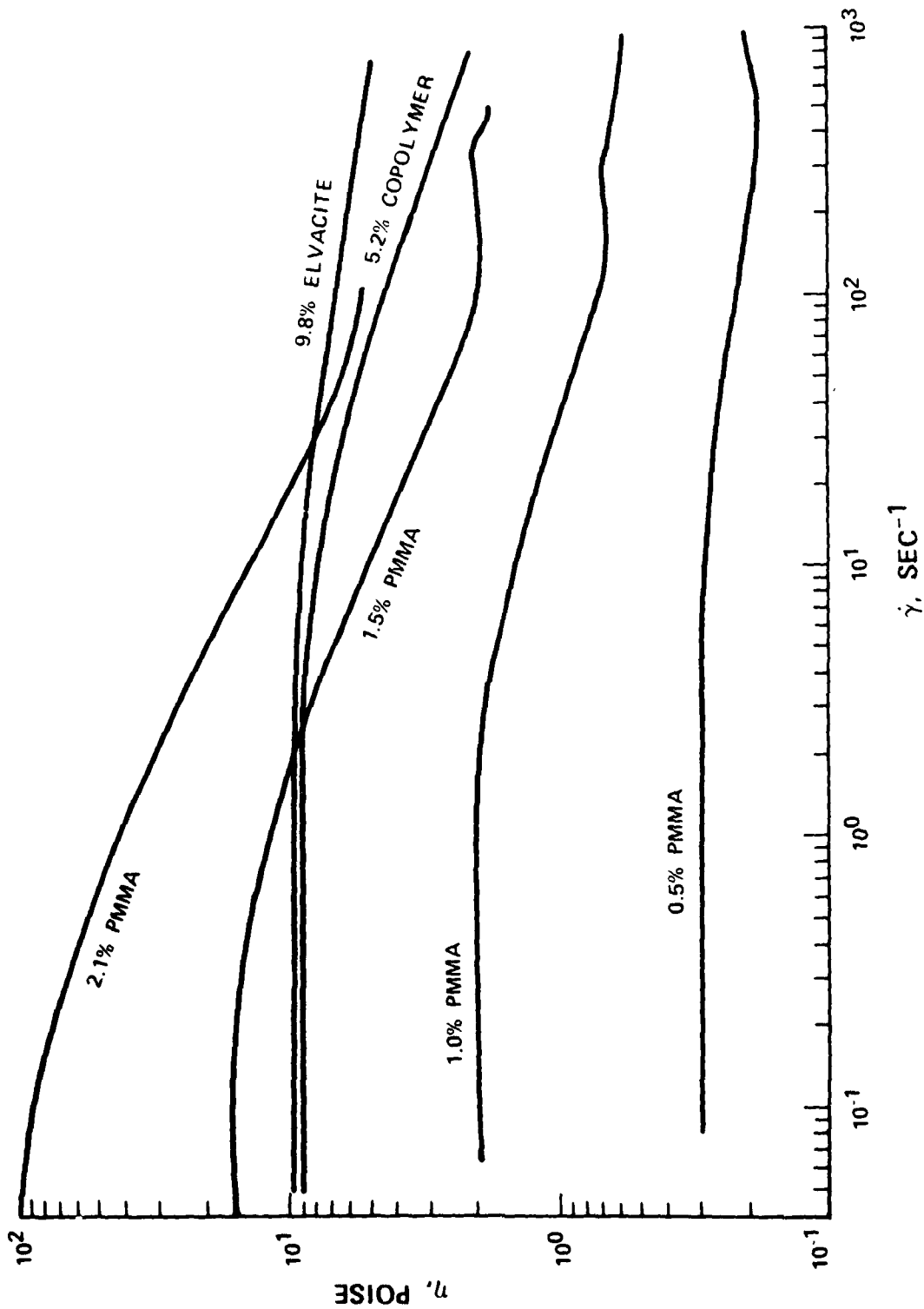


Figure 3: Viscosity versus shear rate for the viscoelastic test fluids measured on a cone and plate viscometer

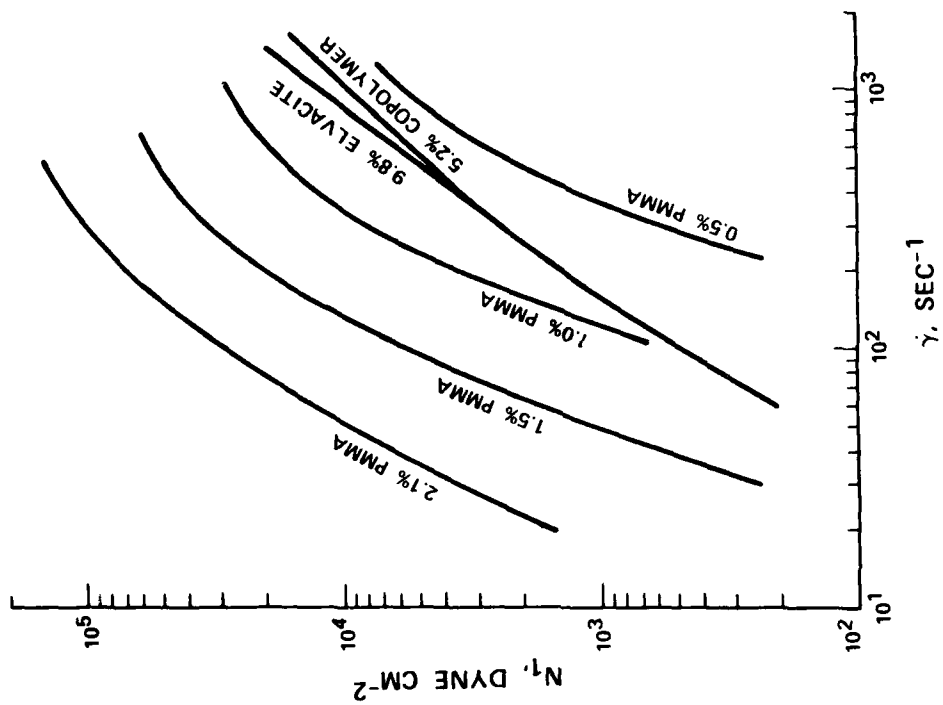


Figure 4: First normal stress difference versus shear rate for viscoelastic test fluids measured on a cone and plate viscometer.

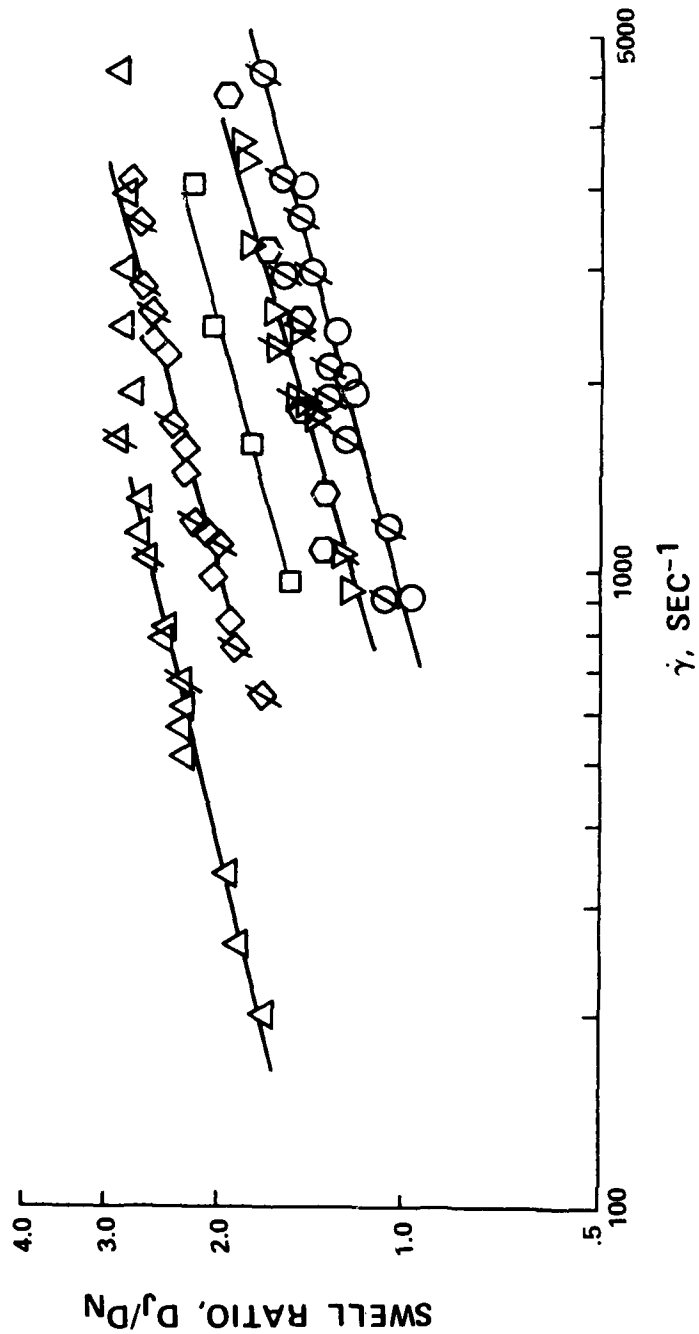


Figure 5: Die swell measurements of disseminated test fluids. Test conditions:  
 ( / ) indicates 1.27 mm, I.D. nozzle otherwise 1.78mm; (O) 0.5% PMMA; (□) 1.0% PMMA; (◇) 1.5% PMMA; (△) 2.1% PMMA; (○) 5.2% Copolymer; (▽) 9.8% ELVACITE.

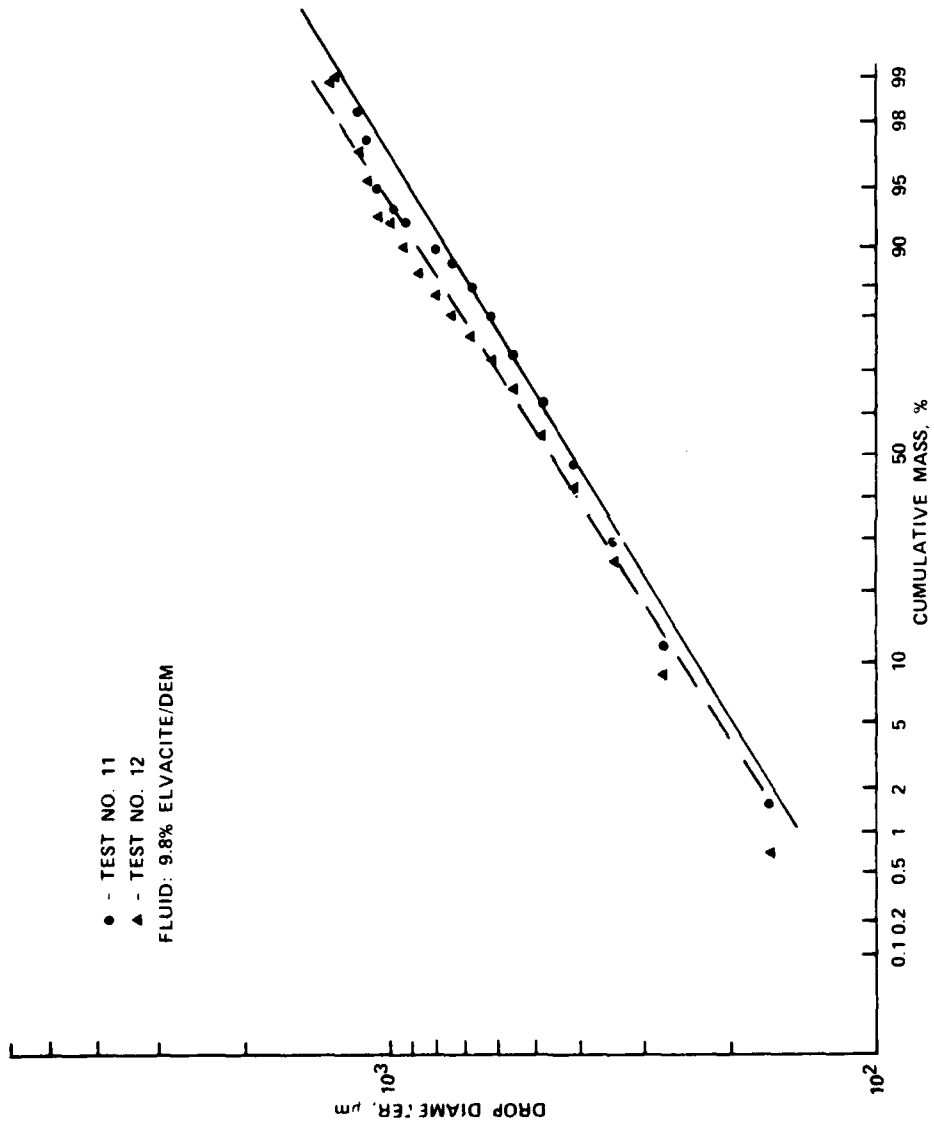


Figure 6: Cumulative probability plot for a disseminated 9.8% ELVACITE fluid.

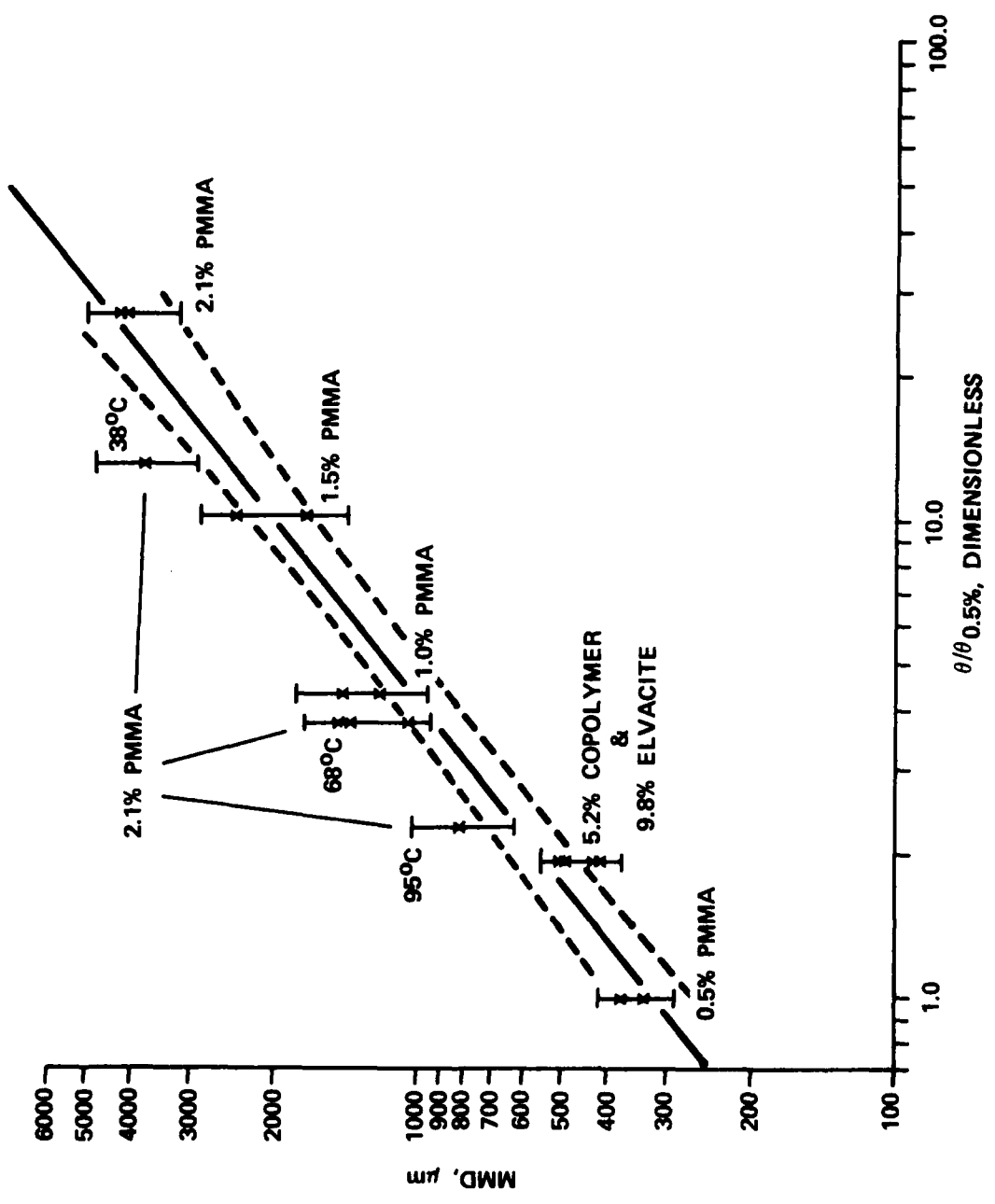


Figure 7: Correlation of MMD versus relative relaxation time.

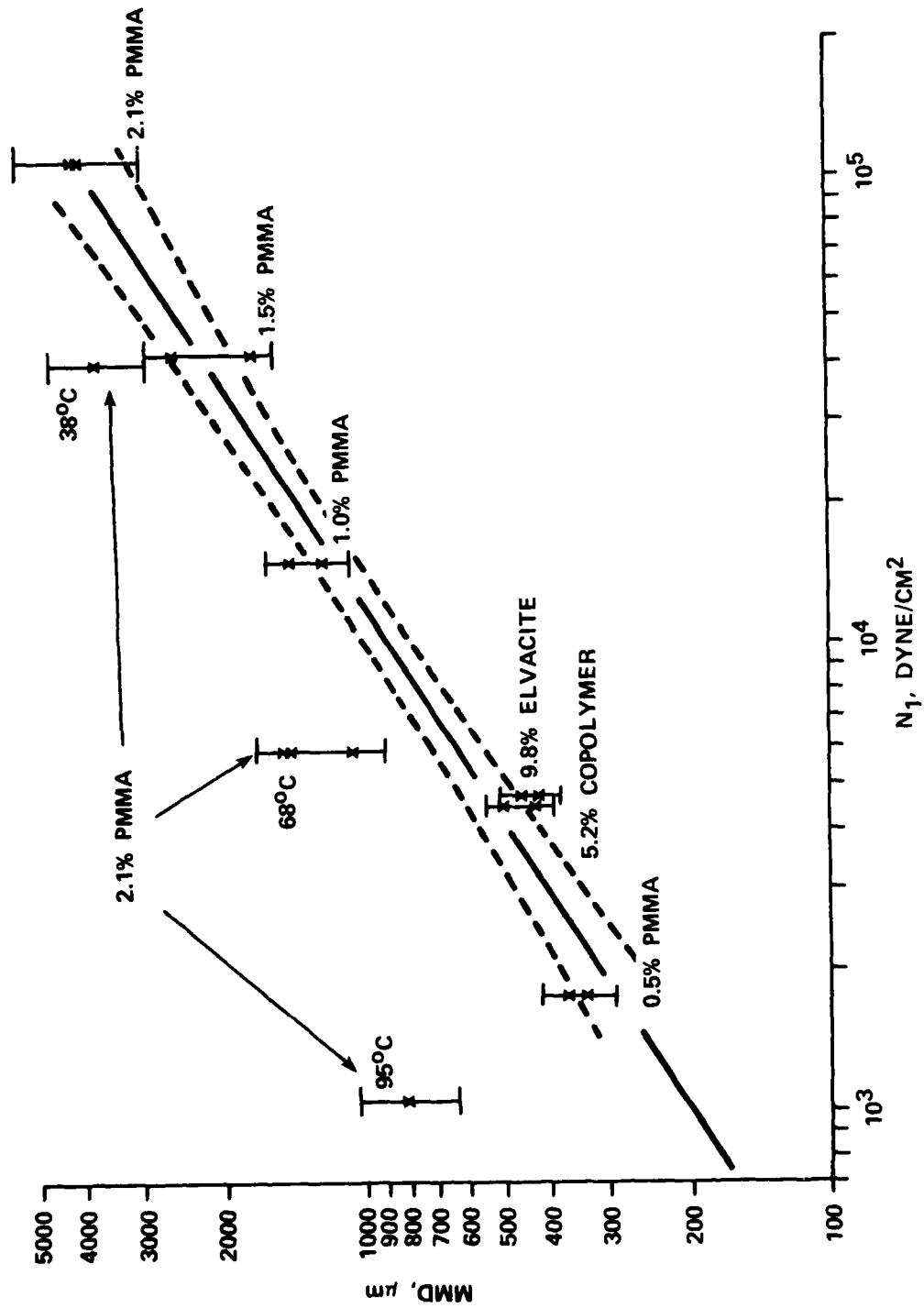


Figure 8: Correlation of MMD versus first normal stress difference ( $500 \text{ sec}^{-1}$ ).

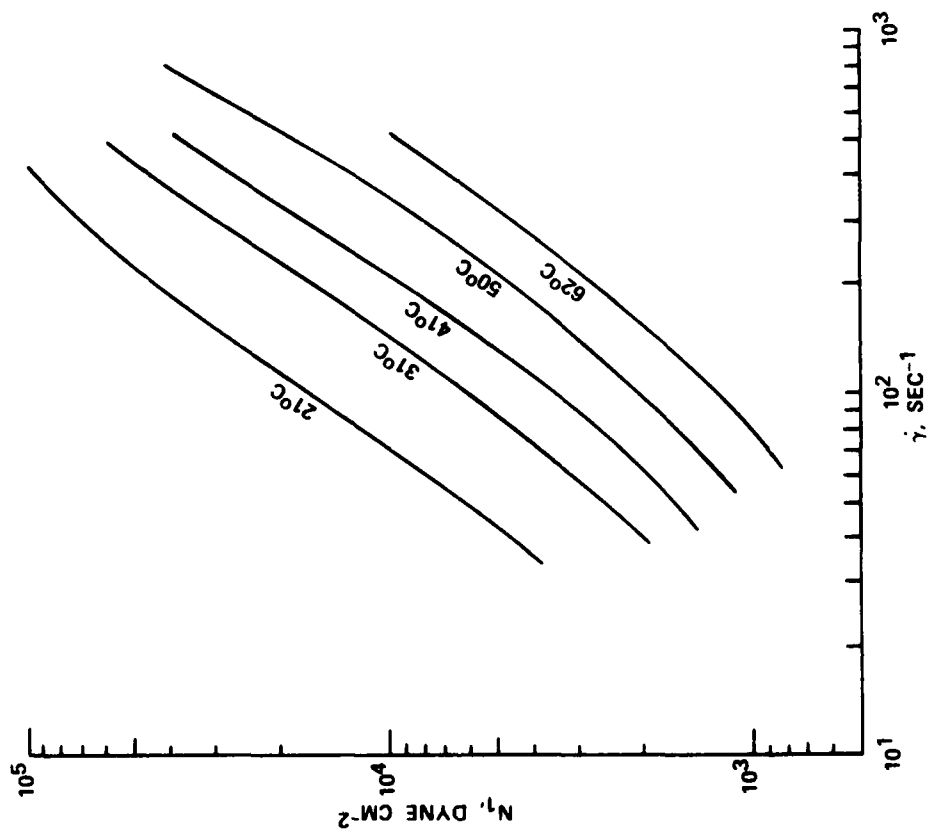


Figure 9: First normal stress difference for 2.1% PMMA solution at various fluid temperatures.

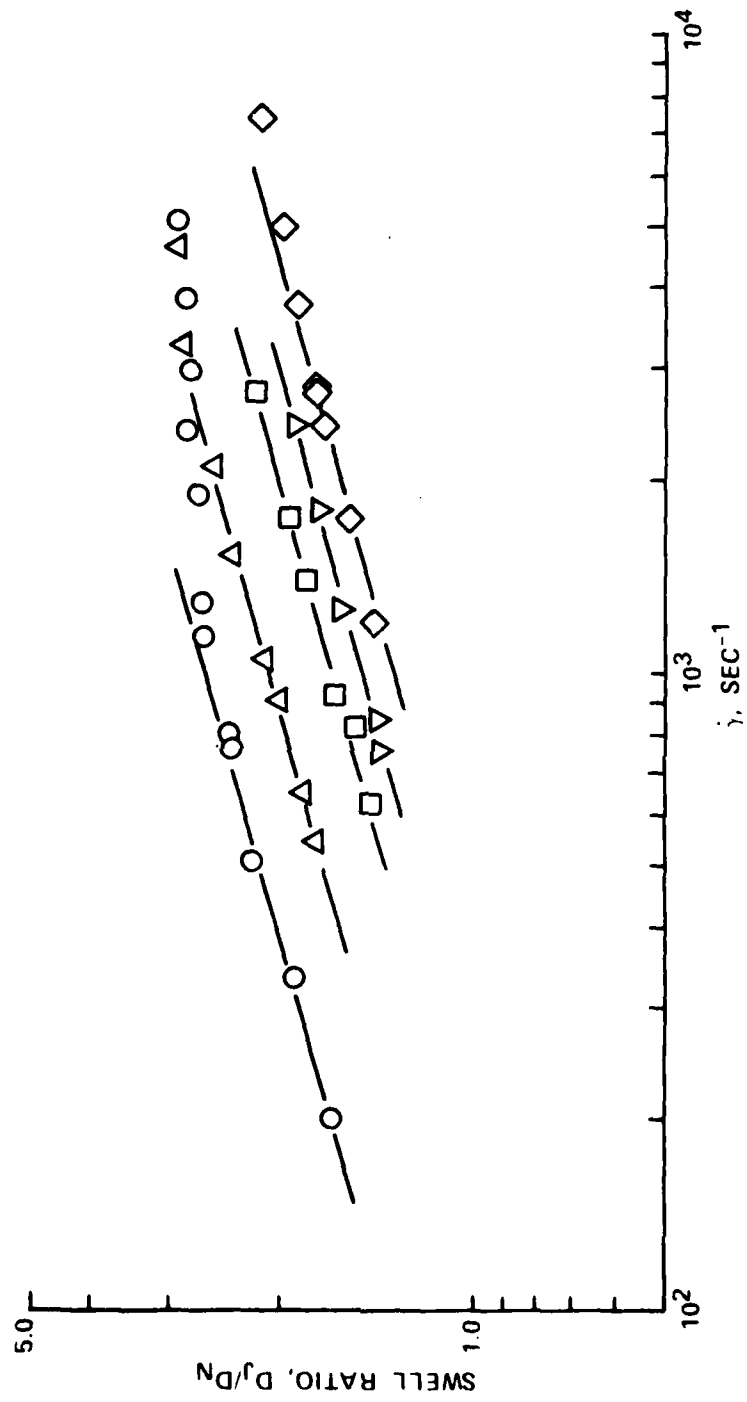


Figure 10: Die swell measurements of the 2.1% PMMA solution at various fluid temperatures.

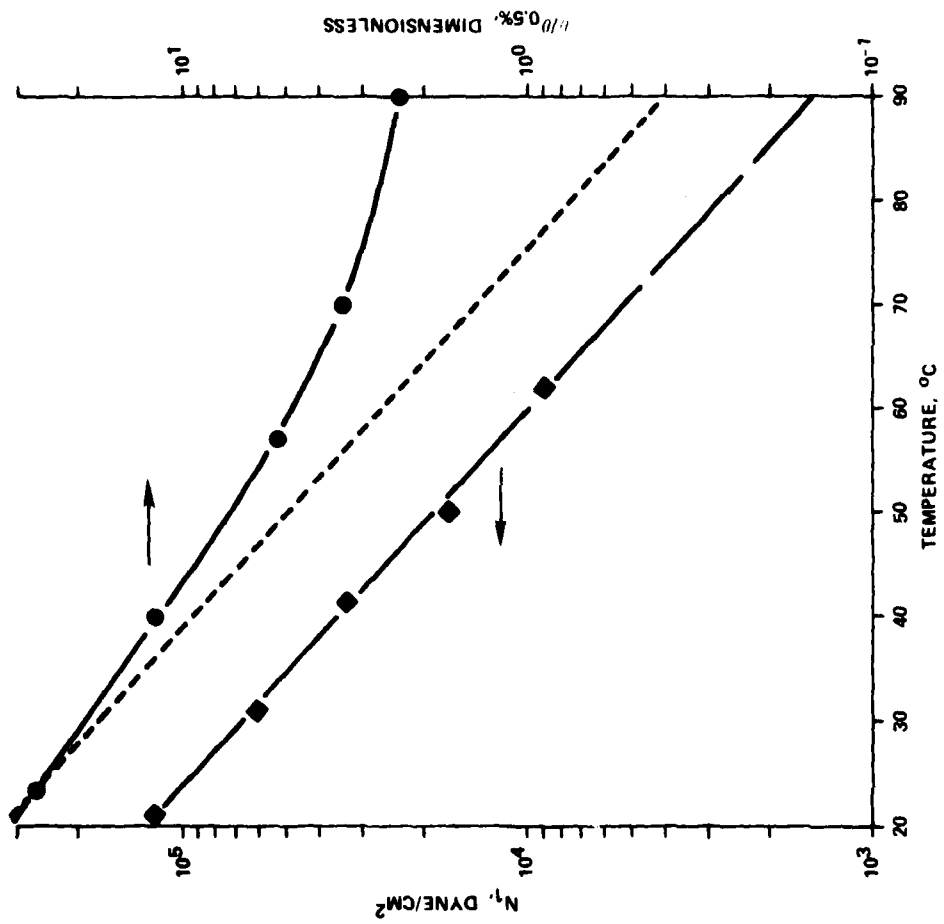
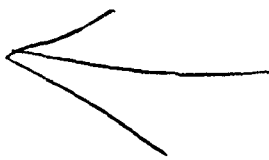


Figure 11: A comparison of the first normal stress difference and the relative relaxation time versus temperature.



dup 2

RAY TRACING METHODS FOR CALCULATION  
OF ATMOSPHERIC REFRACTION

Eugene A. Margerum

U. S. Army Engineer Topographic Laboratories  
Fort Belvoir, Virginia 22060

ABSTRACT

Equations for tracing rays through an atmospheric medium of continuously variable refractive index are obtained in spherical coordinates from Fermat's principle by applying the Euler equation. By introducing canonical variables they are reduced to a set of first order differential equations in normal form, suitable for stepwise numerical integration. Altitude and azimuth angles are introduced and a transformation is derived for determining the refraction errors, including lateral refraction, from the integrated results. The spherically symmetrical case is considered in more detail and leads to an equation for the error in altitude angle expressible as a quadrature over the radial coordinate. A perturbation formula for obtaining the part of the refraction error due to differences between an actual atmospheric profile and some standard atmospheric profile is derived by taking the functional (or variational) derivative. The resulting integral over the radial coordinate has a particularly simple form.

## RAY TRACING IN SPHERICAL COORDINATES

According to Fermat's principle<sup>(1)</sup> (also referred to as the principle of least time), the ray joining any two arbitrary points,  $P_1$  and  $P_2$ , is determined by the condition that its optical length

$$S = \int_{P_1}^{P_2} n \, ds \quad (1)$$

be stationary as compared with the optical lengths of arbitrary neighboring curves joining  $P_1$  and  $P_2$ . If the refractive index  $n$  is considered to be a given smooth continuous function of position and the location along the path is given in terms of a parameter  $t$ , then an actual ray path must furnish an extremum

$$\delta \int_{P_1}^{P_2} n(r, \theta, \phi) S(r, \theta, \dot{r}, \dot{\theta}, \dot{\phi}) dt = 0 \quad (2)$$

where spherical coordinates are indicated with

$$\frac{ds}{dt} = S(r, \theta, \dot{r}, \dot{\theta}, \dot{\phi}) = \sqrt{\dot{r}^2 + r^2 \dot{\theta}^2 + r^2 \sin^2 \theta \dot{\phi}^2} \quad (3)$$

and where the dots indicate differentiation with respect to  $t$ . The partial derivatives

$$\begin{aligned} \frac{\partial S}{\partial r} &= \frac{r(\dot{\theta}^2 + \sin^2 \theta \dot{\phi}^2)}{S}, & \frac{\partial S}{\partial \dot{r}} &= \frac{\dot{r}}{S} \\ \frac{\partial S}{\partial \theta} &= \frac{r^2 \sin \theta \cos \theta \dot{\phi}^2}{S}, & \frac{\partial S}{\partial \dot{\theta}} &= \frac{r^2 \dot{\theta}}{S} \\ \frac{\partial S}{\partial \phi} &= 0, & \frac{\partial S}{\partial \dot{\phi}} &= \frac{r^2 \sin^2 \theta \dot{\phi}}{S} \end{aligned} \quad (4)$$

will be useful in evaluating the Euler equations in the derivation that follows.

Taking

$$f(r, \theta, \phi, \dot{r}, \dot{\theta}, \dot{\phi}) = n(r, \theta, \phi) S(r, \theta, \dot{r}, \dot{\theta}, \dot{\phi}) \quad (5)$$

in equation 2, the rays must lie along curves satisfying an Euler equation for each coordinate

$$\frac{d}{dt} \left( \frac{\partial f}{\partial \dot{r}} \right) - \frac{\partial f}{\partial r} = 0$$

$$\frac{d}{dt} \left( \frac{\partial f}{\partial \dot{\theta}} \right) - \frac{\partial f}{\partial \theta} = 0 \quad (6)$$

$$\frac{d}{dt} \left( \frac{\partial f}{\partial \dot{\phi}} \right) - \frac{\partial f}{\partial \phi} = 0$$

or by making use of the relations given in equations 4 and 5

$$\frac{d}{dt} \left( n \frac{\dot{r}}{S} \right) - S \frac{\partial n}{\partial r} - n \frac{r(\dot{\theta}^2 + \sin^2 \theta \dot{\phi}^2)}{S} = 0$$

$$\frac{d}{dt} \left( n \frac{r^2 \dot{\theta}}{S} \right) - S \frac{\partial n}{\partial \theta} - n \frac{r^2 \sin \theta \cos \theta \dot{\phi}^2}{S} = 0 \quad (7)$$

$$\frac{d}{dt} \left( n \frac{r^2 \sin^2 \theta \dot{\phi}}{S} \right) - S \frac{\partial n}{\partial \phi} = 0$$

By taking the parameterization to be given in terms of arc length  $s$  along a ray

$$t = s$$

$$S = \frac{ds}{dt} = 1 \quad (8)$$

the differential system for the rays is simplified by eliminating the radicals appearing in  $S$  above.

$$\frac{d}{ds} (nr) - \frac{\partial n}{\partial r} - nr(\dot{\theta}^2 + \sin^2 \theta \dot{\phi}^2) = 0$$

$$\frac{d}{ds} (nr^2 \dot{\theta}) - \frac{\partial n}{\partial \theta} - nr^2 \sin \theta \cos \theta \dot{\phi}^2 = 0 \quad (9)$$

$$\frac{d}{ds} (nr^2 \sin^2 \theta \dot{\phi}) - \frac{\partial n}{\partial \phi} = 0$$

If a canonical system of variable is introduced where

$$\begin{aligned}
 p_r &= nr \\
 p_\theta &= nr^2 \dot{\theta} \\
 p_\phi &= nr^2 \sin^2 \theta \dot{\phi}
 \end{aligned}
 \tag{10}$$

the corresponding first order differential system is easily put in normal form.

$$\begin{aligned}
 \dot{p}_r &= \frac{1}{nr^3} (p_\theta^2 + \frac{p_\phi^2}{\sin^2 \theta}) + \frac{\partial n}{\partial r} \\
 \dot{p}_\theta &= \frac{\cos \theta}{nr^2} \frac{p_\phi^2}{\sin^3 \theta} + \frac{\partial n}{\partial \theta} \\
 \dot{p}_\phi &= \frac{\partial n}{\partial \phi} \\
 \dot{r} &= \frac{p_r}{n} \\
 \dot{\theta} &= \frac{p_\theta}{nr^2} \\
 \dot{\phi} &= \frac{p_\phi}{nr^2 \sin^2 \theta}
 \end{aligned}
 \tag{11}$$

This system is suitable for numerical integration by many standard methods including the Runge-Kutta method. The equations are not completely independent but are inter-related by the implicit relationship from equations 3 and 8

$$\dot{r}^2 + r^2 \dot{\theta}^2 + r^2 \sin^2 \theta \dot{\phi}^2 = 1
 \tag{12}$$

which requires that the sum of the squares of the local direction cosines of the tangent to the ray at any point be unity. This permits the integration

to be initiated from a knowledge of position coordinates and two angles sighted along a ray; for example altitude and azimuth angles. It can also facilitate the change of independent variable from  $s$  to one of the coordinates if desired; for example if it is desired to increment the radial distance  $r$  in fixed predetermined amounts. In such a case, the six equations given by 11 are reduced to five. For a general integration with  $s$  as the independent variable, the initial conditions consist of the coordinates  $r, \theta, \phi$  and the direction cosines  $\alpha_r, \alpha_\theta, \alpha_\phi$ , related to the conjugate variables, as follows.

$$\begin{aligned}
 \alpha_r &= \frac{dr}{ds} & p_r &= nr\alpha_r \\
 \alpha_\theta &= r \frac{d\theta}{ds} & p_\theta &= nr\alpha_\theta \\
 \alpha_\phi &= r \sin\theta \frac{d\phi}{ds} & p_\phi &= nr \sin\theta \alpha_\phi
 \end{aligned}
 \tag{13}$$

The altitude angle  $a$  and azimuth angle  $A$  are given by

$$\begin{aligned}
 \sin a &= \alpha_r \\
 \tan A &= \pm \frac{\alpha_\phi}{\alpha_\theta}
 \end{aligned}
 \tag{14}$$

where the ambiguity of sign must be rectified to conform with the spherical coordinates, since various defining conventions are used for azimuth. By making use of the identity

$$\alpha_r^2 + \alpha_\theta^2 + \alpha_\phi^2 = 1
 \tag{15}$$

it is easy to obtain the direction cosines in terms of altitude and azimuth.

$$\begin{aligned}
 \alpha_r &= \sin a \\
 \alpha_\theta &= \cos a \cos A \\
 \alpha_\phi &= \pm \cos a \sin A
 \end{aligned}
 \tag{16}$$

## ATMOSPHERIC REFRACTION INCLUDING LATERAL REFRACTION

Assuming the quantities  $\frac{\partial n}{\partial r}$ ,  $\frac{\partial n}{\partial \theta}$ ,  $\frac{\partial n}{\partial \phi}$  are known functions of position, a ray may now be traced up through the atmosphere by using the system of equations 11, for any starting location  $r_o$ ,  $\theta_o$ ,  $\phi_o$  and direction  $\alpha_{r_o}$ ,  $\alpha_{\theta_o}$ ,  $\alpha_{\phi_o}$ . Assuming the initial altitude angle is great enough that atmospheric ducting and subsequent return of the ray does not occur, the ray eventually will emerge from the atmosphere at some location  $r_f$ ,  $\theta_f$ ,  $\phi_f$  with local direction coordinates  $\alpha_{r_f}$ ,  $\alpha_{\theta_f}$ ,  $\alpha_{\phi_f}$ . In order to determine the amount of bending of the ray, it is necessary to know the transformation of the final direction coordinates back into the initial frame. This transformation will now be obtained. For a general position vector  $\vec{R}$  given in rectangular components but expressed in spherical coordinates

$$\vec{R} = \hat{i} r \sin \theta \cos \phi + \hat{j} r \sin \theta \sin \phi + \hat{k} r \cos \theta . \quad (17)$$

A local reference frame of unit vectors  $\hat{r}$ ,  $\hat{\theta}$ ,  $\hat{\phi}$  maybe defined by

$$\begin{aligned} \hat{r} &= \frac{\partial \vec{R}}{\partial r} / \left| \frac{\partial \vec{R}}{\partial r} \right| = \hat{i} \sin \theta \cos \phi + \hat{j} \sin \theta \sin \phi - \hat{k} \cos \theta \\ \hat{\theta} &= \frac{\partial \vec{R}}{\partial \theta} / \left| \frac{\partial \vec{R}}{\partial \theta} \right| = \hat{i} \cos \theta \cos \phi + \hat{j} \cos \theta \sin \phi + \hat{k} \sin \theta \\ \hat{\phi} &= \frac{\partial \vec{R}}{\partial \phi} / \left| \frac{\partial \vec{R}}{\partial \phi} \right| = -\hat{i} \sin \phi + \hat{j} \cos \phi \end{aligned} \quad (18)$$

If the unit direction vector of the ray

$$\hat{\alpha} = \alpha_r \hat{r} + \alpha_\theta \hat{\theta} + \alpha_\phi \hat{\phi} \quad (19)$$

is expressed in terms of the initial frame, the components are found to depend on the cosines of angles between the initial and current frame vectors

$$\begin{aligned}
\hat{\alpha}' &= \hat{r}'_o [(\hat{r} \cdot \hat{r}'_o) \alpha_r + (\hat{\theta} \cdot \hat{r}'_o) \alpha_\theta + (\hat{\phi} \cdot \hat{r}'_o) \alpha_\phi] \\
&+ \hat{\theta}'_o [(\hat{r} \cdot \hat{\theta}'_o) \alpha_r + (\hat{\theta} \cdot \hat{\theta}'_o) \alpha_\theta + (\hat{\phi} \cdot \hat{\theta}'_o) \alpha_\phi] \\
&+ \hat{\phi}'_o [(\hat{r} \cdot \hat{\phi}'_o) \alpha_r + (\hat{\theta} \cdot \hat{\phi}'_o) \alpha_\theta + (\hat{\phi} \cdot \hat{\phi}'_o) \alpha_\phi]
\end{aligned} \tag{20}$$

where the direction cosines involved are readily obtained from equations 18 applied at the initial and current positions. (The prime added to  $\hat{\alpha}'$  is to avoid confusion with the starting direction  $\hat{\alpha}_o$ ).

$$\begin{aligned}
\hat{r} \cdot \hat{r}'_o &= \sin \theta \sin \theta_o \cos (\phi - \phi_o) + \cos \theta \cos \theta_o \\
\hat{r} \cdot \hat{\theta}'_o &= \sin \theta \cos \theta_o \cos (\phi - \phi_o) - \cos \theta \sin \theta_o \\
\hat{r} \cdot \hat{\phi}'_o &= \sin \theta \sin (\phi - \phi_o) \\
\hat{\theta} \cdot \hat{r}'_o &= \cos \theta \sin \theta_o \cos (\phi - \phi_o) - \sin \theta \cos \theta_o \\
\hat{\theta} \cdot \hat{\theta}'_o &= \cos \theta \cos \theta_o \cos (\phi - \phi_o) + \sin \theta \sin \theta_o \\
\hat{\theta} \cdot \hat{\phi}'_o &= \cos \theta \sin (\phi - \phi_o) \\
\hat{\phi} \cdot \hat{r}'_o &= -\sin \theta_o \sin (\phi - \phi_o) \\
\hat{\phi} \cdot \hat{\theta}'_o &= -\cos \theta_o \sin (\phi - \phi_o) \\
\hat{\phi} \cdot \hat{\phi}'_o &= \cos (\phi - \phi_o)
\end{aligned} \tag{21}$$

By applying equations 20 and 21 to the emerging ray direction  $\hat{\alpha}'_f$ , the components referred to the initial frame can be expressed in matrix form as given by equation 22.

$$\begin{bmatrix} \alpha'_{rf} \\ \alpha'_{\theta f} \\ \alpha'_{\phi f} \end{bmatrix} = \begin{bmatrix} \sin \theta_f \sin \theta_o \cos (\theta_f - \theta_o) + \cos \theta_f \cos \theta_o & \cos \theta_f \sin \theta_o \cos (\theta_f - \theta_o) - \sin \theta_f \cos \theta_o & -\sin \theta_o \sin (\theta_f - \theta_o) \\ \sin \theta_f \cos \theta_o \cos (\theta_f - \theta_o) - \cos \theta_f \sin \theta_o & \cos \theta_f \cos \theta_o \cos (\theta_f - \theta_o) + \sin \theta_f \sin \theta_o & -\cos \theta_o \sin (\theta_f - \theta_o) \\ \sin \theta_f \sin (\theta_f - \theta_o) & \cos \theta_f \sin (\theta_f - \theta_o) & \cos (\theta_f - \theta_o) \end{bmatrix} \begin{bmatrix} \alpha_{rf} \\ \alpha_{\theta f} \\ \alpha_{\phi f} \end{bmatrix} \tag{22}$$

It was found that the transformation matrix could be factored as

$$\begin{bmatrix} \alpha'_{rf} \\ \alpha'_{\theta f} \\ \alpha'_{\phi f} \end{bmatrix} = \begin{bmatrix} \sin \theta_o & \cos \theta_o & 0 \\ \cos \theta_o & -\sin \theta_o & 0 \\ 0 & 0 & 1 \end{bmatrix} \begin{bmatrix} \cos \phi_o & \sin \phi_o & 0 \\ 0 & 0 & 1 \\ -\sin \phi_o & \cos \phi_o & 0 \end{bmatrix} \begin{bmatrix} \cos \phi_f & \sin \phi_f & 0 \\ \sin \phi_f & -\cos \phi_f & 0 \\ 0 & 0 & 1 \end{bmatrix}$$

$$\begin{bmatrix} \sin \theta_f & \cos \theta_f & 0 \\ 0 & 0 & -1 \\ \cos \theta_f & -\sin \theta_f & 0 \end{bmatrix} \begin{bmatrix} \alpha_{rf} \\ \alpha_{\theta f} \\ \alpha_{\phi f} \end{bmatrix} \tag{23}$$

or alternatively in the form given by equation 24 as probably the most convenient for computations.

$$\begin{bmatrix} \alpha'_{rf} \\ \alpha'_{\theta f} \\ \alpha'_{\phi f} \end{bmatrix} = \begin{bmatrix} \sin \theta_o & \cos \theta_o & 0 \\ \cos \theta_o & -\sin \theta_o & 0 \\ 0 & 0 & 1 \end{bmatrix} \begin{bmatrix} \cos(\phi_f - \phi_o) & \sin(\phi_f - \phi_o) & 0 \\ 0 & 0 & 1 \\ \sin(\phi_f - \phi_o) & -\cos(\phi_f - \phi_o) & 0 \end{bmatrix}$$

$$\begin{bmatrix} \sin \theta_f & \cos \theta_f & 0 \\ 0 & 0 & -1 \\ \cos \theta_f & -\sin \theta_f & 0 \end{bmatrix} \begin{bmatrix} \alpha_{rf} \\ \alpha_{\theta f} \\ \alpha_{\phi f} \end{bmatrix} \tag{24}$$

Returning to equation 14, the vertical refraction correction is given by

$$a'_f - a'_o = \arccos \alpha'_{rf} - \arccos \alpha_{ro} \tag{25}$$

and the lateral refraction error by

$$A'_f - A_o = \arctan \left( \pm \frac{\alpha'_{\phi f}}{\alpha'_{\theta f}} \right) - \arctan \left( \pm \frac{\alpha_{\phi o}}{\alpha_{\theta o}} \right) \tag{26}$$

$$= \pm \arctan \left( \frac{\alpha'_{\phi f} \alpha_{\theta o} - \alpha_{\phi o} \alpha'_{\theta f}}{\alpha'_{\theta f} \alpha_{\theta o} - \alpha_{\phi o} \alpha'_{\phi f}} \right)$$

where the sign again depends on the convention used for azimuth

THE SPHERICALLY SYMMETRICAL CASE

For the case where the refractive index depends only upon  $r$ , equations 9 become

$$\begin{aligned} \frac{d}{ds}(nr\dot{\theta}) - \frac{\partial n}{\partial r} - nr(\dot{\theta}^2 + \sin^2 \theta \dot{\phi}^2) &= 0 \\ \frac{d}{ds}(nr^2\dot{\theta}) - nr^2 \sin \theta \cos \theta \dot{\phi}^2 &= 0 \\ nr^2 \sin^2 \theta \dot{\phi} &= C_1 \end{aligned} \tag{27}$$

where an integral has been found for the last equation. The coordinate system may be chosen so that initially  $\frac{d\phi}{ds} = 0$ . Then,  $C_1 = 0$  and  $\frac{d\phi}{ds}$  vanishes identically

$$\phi = \phi_0 = \text{constant} \tag{28}$$

and the problem is reduced to two dimensions. Using the fact that  $\dot{\phi} = 0$ , the second equation of 27 becomes integrable.

$$nr^2 \frac{d\theta}{ds} = C_2 \tag{29}$$

Inserting the resultant value for  $\frac{d\theta}{ds}$  into the first equation of 27 (together with  $\dot{\phi} = 0$ ) yields the following relationship.

$$\frac{d}{ds}\left(n \frac{dr}{ds}\right) - \frac{\partial n}{\partial r} - \frac{C_2^2}{nr^3} = 0 \tag{30}$$

Multiplying by  $n$  and using the relationship  $\frac{d}{ds} = \frac{dr}{ds} \frac{d}{dr}$ ,

$$n \frac{dr}{ds} \frac{d}{dr}\left(n \frac{dr}{ds}\right) - n \frac{dn}{dr} - \frac{C_2^2}{r^3} = 0 \tag{31}$$

and integrating yields

$$\left(n \frac{dr}{ds}\right)^2 - n^2 + \frac{C_2^2}{r^2} = C_3 \tag{32}$$

If  $\frac{C_2^2}{r^2}$  is replaced by  $(nr \frac{d\theta}{ds})^2$  from equation 29, it is found that

$$n^2 \left[ \left( \frac{dr}{ds} \right)^2 + \left( r \frac{d\theta}{ds} \right)^2 - 1 \right] = C_3. \quad (33)$$

The quantity in square brackets must vanish because arc length  $s$  is defined by  $ds = \sqrt{dr^2 + r^2 d\theta^2}$  and hence  $C_3 = 0$ . It then also follows that equations 29 and 30 (in  $r$  and  $\theta$ ) are not independent. As a matter of convenience, equation 29 will be used and the geometrical relations between  $dr$ ,  $ds$  and  $d\theta$  will be exploited.

As demonstrated in Figure 1, a star is observed at the apparent position  $A_1$  given by angle  $\psi_0$ .

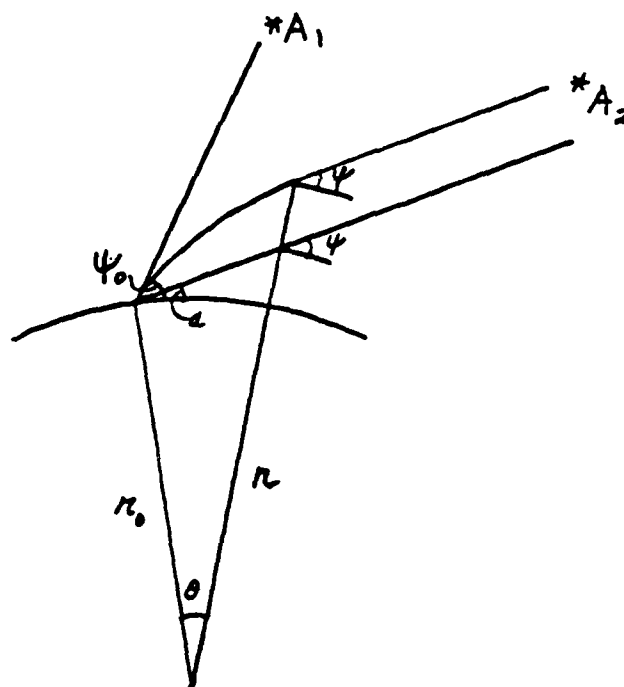


Figure 1 - Geometrical Parameters for the Atmospheric Ray Path

If no atmosphere were present, the actual position  $A_2$  would coincide with  $A_1$ . For a ray travelling in the reverse direction and emanating at the surface at angle  $\psi_0$  in a medium with variable refractive index, the ray path is curved and its inclination  $\psi$  at  $r$  is given by

$$nr\left(r \frac{d\theta}{ds}\right) = nr \cos \psi = C \quad (34)$$

from equation 29 where the constant is determined from the initial values of  $n$ ,  $r$  and  $\psi$ .

$$C = n_0 r_0 \cos \psi_0 \quad (35)$$

After passing through the region of variable index, the ray will emerge at  $r_f$ ,  $\theta_f$  in the direction  $\psi_f$  toward  $A_2$ . By the optical Principle of Reversibility, an object at  $A_2$  would be observed to have elevation  $\psi_0$ , whereas, if the refractive index were constant (atmosphere removed) it would have its true elevation angle  $a$ . As layers of variable refractive index are added in the reversed ray system,  $a$  would change and so in this inbedded sense can be regarded as a function of  $r$ .

From Figure 1,

$$a = \psi - \theta \quad (36)$$

or

$$\frac{da}{dr} = \frac{d\psi}{dr} - \frac{d\theta}{dr} \quad (37)$$

and  $a$  may be determined by integrating equation 37. By rewriting equation 34 in the form

$$nr^2 \frac{dr}{ds} \frac{d\theta}{dr} = C \quad (38)$$

and using the fact that  $\sin \psi = \frac{dr}{ds}$ , an expression for  $\frac{d\theta}{dr}$  is found

$$\sin \psi \frac{d\theta}{dr} = \frac{C}{nr^2} \quad (39)$$

By differentiating equation 34 in the form

$$\cos \psi = \frac{C}{nr} \quad (40)$$

an expression containing  $\frac{d\psi}{dr}$  is obtained.

$$\sin \psi \frac{d\psi}{dr} = \frac{C}{nr^2} + \frac{C}{n^2r} \frac{dn}{dr} \quad (41)$$

Combining equations 39 and 41

$$\sin \psi \left( \frac{d\psi}{dr} - \frac{d\theta}{dr} \right) = \frac{C}{n^2r} \frac{dn}{dr} \quad (42)$$

and using the fact that

$$\sin \psi = \sqrt{1 - \cos^2 \psi} = \sqrt{1 - \left(\frac{C}{nr}\right)^2} \quad (43)$$

an expression for  $\frac{da}{dr}$  is readily found.

$$\frac{da}{dr} = \frac{C \frac{dn}{dr}}{n^2r \sqrt{1 - \left(\frac{C}{nr}\right)^2}} = \frac{\frac{r}{C} \frac{dn}{dr}}{\frac{nr}{C} \sqrt{\left(\frac{nr}{C}\right)^2 - 1}} \quad (44)$$

If this expression is integrated by parts from  $r_0$  to  $r_f$ , the value for the observational error is found

$$\delta a = a_f - a_0 = \int_{r_0}^{r_f} \frac{\frac{r}{C} \frac{dn}{dr}}{\frac{nr}{C} \sqrt{\left(\frac{nr}{C}\right)^2 - 1}} dr \quad (45)$$

$$\delta a = \text{arcsec} \left( \frac{nr_f}{C} \right) - \text{arcsec} \left( \frac{n_0 r_0}{C} \right) - \int_{r_0}^{r_f} \frac{dr}{r \sqrt{\left(\frac{nr}{n_0 r_0}\right)^2 \sec^2 \psi_0 - 1}} \quad (46)$$

where  $a_0 = \psi_0$ ,  $r_0$ ,  $n_0$ , and  $a_f$ ,  $r_f$ ,  $n_f$ , are initial and final values and where  $C$  is given by equation 35.

$$\delta a = \text{arcsec} \left( \frac{n_f r_f}{n_0 r_0} \sec \psi_0 \right) - \psi_0 - \int_{r_0}^{r_f} \frac{dr}{r \sqrt{\left( \frac{n r}{n_0 r_0} \sec \psi_0 \right)^2 - 1}} \quad (47)$$

For determination of  $\delta a$  by numerical integration, equation 45 should be preferable to equation 47 by virtue of its simplicity and certainly a need to carry fewer significant figures. It can be easily evaluated with the trapezoidal rule, using a linear interpolation for  $\frac{dn}{dr}$ . For higher degree approximations, standard spline methods are suggested. Although it can be integrated by quadrature formulae (e.g. Newton-Cotes), equation 47 appears to offer no distinct advantage.

#### PERTURBATION OF THE SOLUTION

The refractive index function  $n(r)$  is given a variation  $\epsilon m(r)$  and the new error in altitude angle is obtained from equation 45

$$J = \int_{r_0}^{r_f} \frac{\frac{r}{C} \frac{d\tilde{n}}{dr}}{\frac{\tilde{n}r}{C} \sqrt{\left( \frac{\tilde{n}r}{C} \right)^2 - 1}} dr \quad (48)$$

where

$$\tilde{n}(r) = n(r) + \epsilon m(r) \quad (49)$$

and

$$\frac{d\tilde{n}}{dr} = \frac{dn}{dr} + \epsilon \frac{dm}{dr} \quad (50)$$

By making use of equation 50 and the following Taylor expansion in  $\epsilon$ ,

$$\frac{\frac{r}{c}}{\frac{\tilde{n}r}{c}\sqrt{(\frac{\tilde{n}r}{c})^2 - 1}} = \frac{\frac{r}{c}}{\frac{nr}{c}\sqrt{(\frac{nr}{c})^2 - 1}} - \frac{\frac{r}{c} \left(\frac{mr}{c}\right) \left[2\left(\frac{nr}{c}\right)^2 - 1\right]}{\left(\frac{nr}{c}\right)^2 \left[\left(\frac{nr}{c}\right)^2 - 1\right]^{3/2}} \epsilon + 0(\epsilon^2) \quad (51)$$

the expression given below is obtained for the perturbed (or varied) integral

$$J = \int_{r_0}^{r_f} \frac{\frac{r}{c} \frac{dn}{dr}}{\frac{nr}{c}\sqrt{(\frac{nr}{c})^2 - 1}} dr + \epsilon \int_{r_0}^{r_f} \left\{ \frac{-\frac{r}{c} \left(\frac{mr}{c}\right) \left[2\left(\frac{nr}{c}\right)^2 - 1\right]}{\left(\frac{nr}{c}\right)^2 \left[\left(\frac{nr}{c}\right)^2 - 1\right]^{3/2}} \frac{dn}{dr} + \frac{\frac{r}{c}}{\frac{nr}{c}\sqrt{(\frac{nr}{c})^2 - 1}} \frac{dm}{dr} \right\} dr \quad (52)$$

$$+ 0(\epsilon^2)$$

In equation 52, the full variation is obtained for  $\epsilon = 1$  and the conditions that the first order term give a good representation of the corresponding variation in  $J$  are

$$\epsilon m(r) \ll n(r)$$

$$\epsilon \frac{dm}{dr} \ll \frac{dn}{dr} \quad (53)$$

where  $\epsilon$  has been carried in equation 52 mainly for purposes of identification.

By differentiation and a considerable amount of algebraic manipulation, the following identity may be obtained

$$\frac{\frac{r}{c} \frac{dm}{dr}}{\frac{nr}{c} \sqrt{\left(\frac{nr}{c}\right)^2 - 1}} = \frac{d}{dr} \left[ \frac{\frac{mr}{c}}{\frac{nr}{c} \sqrt{\left(\frac{nr}{c}\right)^2 - 1}} \right] + \frac{\frac{m}{c} \left(\frac{nr}{c}\right)}{\left[\left(\frac{nr}{c}\right)^2 - 1\right]^{3/2}} + \frac{\frac{r}{c} \left(\frac{mr}{c}\right) \left[2\left(\frac{nr}{c}\right)^2 - 1\right]}{\left(\frac{nr}{c}\right)^2 \left[\left(\frac{nr}{c}\right)^2 - 1\right]^{3/2}} \frac{dn}{dr} \quad (54)$$

and this is useful in further simplifying the form of the integral.

$$J = \int_{r_0}^{r_f} \frac{\frac{r}{c} \frac{dn}{dr}}{\frac{nr}{c} \sqrt{\left(\frac{nr}{c}\right)^2 - 1}} dr + \epsilon \int_{r_0}^{r_f} \frac{\frac{m}{c} \left(\frac{nr}{c}\right)}{\left[\left(\frac{nr}{c}\right)^2 - 1\right]^{3/2}} dr + \epsilon \left[ \frac{\frac{mr}{c}}{\frac{nr}{c} \sqrt{\left(\frac{nr}{c}\right)^2 - 1}} \right]_{r_0}^{r_f} + O(\epsilon^2) \quad (55)$$

By assuming the value of  $m$  to vanish at the endpoints,

$$m(r_0) = m(r_f) = 0 \quad (56)$$

the quantity bracketed in equation 55 will also vanish. For the upper endpoint, this is a reasonable assumption since the refractive index should assume the value for vacuum and variation or perturbation is not reasonable. For the lower endpoint, it is necessary on practical grounds, since any variation of refractive index will disturb the value of  $C$  (initial condition) used throughout the entire range of integration.

The first term of equation 55 is the unperturbed error. The integral in the second term is known as the variational or functional derivative of J of first order. Taking  $\epsilon = 1$  and ignoring higher order terms yields the first order or linear perturbation of J.

$$\delta J \cong \int_{r_0}^{r_f} \frac{\frac{m}{c} \left(\frac{nr}{c}\right)}{\left[\left(\frac{nr}{c}\right)^2 - 1\right]^{3/2}} dr \quad (57)$$

It can be used for approximately determining refraction errors in the altitude angle due to differences between the actual refractive index profile and the profile of some standard atmospheric model.

#### REFERENCES

1. An Introduction to Hamiltonian Optics - H. A. Buchdahl, Cambridge Univ. Press, 1970.
2. The Optics of Rays, Wavefronts and Caustics - O. N. Stavrovdis, Academic Press, 1972.
3. Propagation of Short Radio Waves - ed. by Donald E. Kerr, McGraw-Hill, 1951.
4. Principles of Optics - Max Born and Emil Wolf, Pergamon Press, 1965.
5. Mathematical Theory of Optics - R. K. Luneburg, Univ. of California Press, 1966.
6. Geodesy - G. Bomford, Oxford University Press, 1971.
7. Mathematical Geodesy - Martin Hotine, ESSA Monograph 2, 1969.
8. Physics of the Air - W. J. Humphreys, McGraw-Hill, 1940.
9. U.S. Standard Atmosphere, 1962 - under sponsorship of National Aeronautics and Space Administration, United States Air Force, United States Weather Bureau.
10. Introduction to Meteorological Optics - R. A. R. Tricker, Elsevier, 1971.
11. System Identification, Methods and Applications - Harriet H. Kagiwada Addison-Wesley, 1974.
12. Compendium of Spherical Astronomy - Simon Newcomb, Dover, 1960.

AD P001013

A TRANSPORT-THEORETIC ANALYSIS OF PULSE PROPAGATION THROUGH  
A RANDOM CLOUD OF SCATTERERS

I. M. Besieris, W. E. Kohler and A. I. Tsolakis\*  
Virginia Polytechnic Institute and State University  
Blacksburg, VA 24061

**ABSTRACT.** A systematic development from the Dyson equation and the two-frequency Bethe-Salpeter equation of a two-frequency radiative transfer equation suitable for pulsed waves in the presence of a random distribution of absorptive discrete scatterers with pair correlations is presented. The main strength of the radiative transfer theory expounded here stems from the fact that it is applicable under conditions of large-angle scattering, statistical inhomogeneities and statistical anisotropies. It accounts, also, for regular refraction (variable scatterer density,) absorption and frequency offsets.

**I. INTRODUCTION.** Multiple scattering by a random distribution of discrete scatterers has been studied extensively over the past thirty five years, primarily because of its relevance to a large number of pressing applied problems that arise in radio physics and engineering. Fundamental work on multiple scattering of scalar waves by a distribution of uncorrelated scatterers was initiated by Foldy [1] and has been developed further by Lax [2] and Twersky [3]. Based on these original contributions, a great number of applications have appeared in the literature [cf., for example, Refs. 4-7] involving both the coherent field and the incoherent intensity. The problem of assessing the multiple scattering effects on scalar and vector waves in the presence of random distributions of correlated scatterers is more challenging. Basic contributions along this direction have been made by Twersky [8], Bringi *et al.* [9] and Tsang and Kong [10] in connection with the coherent field, and by Barabanenkov [11], Barabanenkov and Finkel'berg [12] and Watson *et al.* [13] in connection with the incoherent field intensity.

The motivation for our work is based on the absence of a second-order statistical theory for studying pulse propagation through random distributions of correlated scatterers. Such a theory is necessary for the development of predictive models pertinent to (1) pulsed electromagnetic propagation through complex natural media (e.g., rain, fog, sandstorms, vegetation); (2) the analysis of obscuration and detection techniques; (3) remote sensing and identification of aerosol clouds; (4) scattering clouds consisting of complicated individual scatterers (lossy, anisotropic, frequency-sensitive, possibly aligned, pair-correlated) with gross macroscopic structure (finite extent and variable number density).

\*Present address: Bell Laboratories, Holmdel, NJ 07733.

Our specific goal in this exposition is to derive systematically a radiative transfer equation for the two-frequency incoherent intensity function (a quantity related to the two-frequency mutual coherence function and, hence, to second-order pulse statistics.) The derivation is limited to scalar pulsed waves propagating through a random distribution of absorptive scatterers with pair correlations.

The proposed radiation transport equation is based on the Dyson and Bethe-Salpeter equations at the level of the direct interaction and ladder approximations, respectively. If, in addition to pair correlations, the assumptions are made that the number of scatterers is large and the average distance between any two scatterers is large compared with a reference wavelength, the Dyson and Bethe-Salpeter equations are analogous to those associated with a continuous random medium with fluctuations of the permittivity which are distributed according to a normal law and with a deterministic profile directly linked to the number of scatterers per unit volume.

The transition from the Dyson and Bethe-Salpeter equations to the two-frequency radiative transfer equation is effected by a continuous stochastic transport theory that was originally introduced by Barabanov et al. [14] and subsequently extended to the two-frequency context by Besieris and Kohler [15-17]. As in their case, our derivation differs markedly from the usual procedures for obtaining classical radiation transport equations; the latter rely mostly on considerations of energy balance, with no explicit "microscopic" interpretation given to the extinction and scattering coefficients.

In the following we present a sketch of the proposed two-frequency radiation transport theory, with primary emphasis on the underlying assumptions and the physical interpretation of the various terms entering into the final transport equation.

II. FIRST AND SECOND ORDER COHERENCE FUNCTIONS FOR A RANDOM DISTRIBUTION OF PAIR-CORRELATED SCATTERERS, PART A: ANISOTROPIC SCATTERING. The derivation of the Dyson equation for the mean field and the Bethe-Salpeter equation for the mutual coherence tensor under conditions of anisotropic scattering and in the presence of pair correlations among scatterers is based on the Twersky procedure. The basic underlying assumptions are the following: (1) We ignore third-order scattering by two scatterers, fourth-order scattering by three scatterers, etc. (essentially the Twersky assumption); (2) All scatterers have the same shape, size and orientation distributions; (3) We consider only pair correlations and neglect all contributions from higher-order correlations; (4) The number of scatterers in a volume is infinite.

We resort, also, to the following notational definitions: (1)  $\underline{E}_a$ : incident electric field at position  $\underline{r}_a$ ; (2)  $\underline{E}^a$ : total electric at  $\underline{r}_a$ ;

(3)  $g_j^a \underline{E}^j$ : electric field at  $\underline{r}_a$  caused by the  $j$ th particle; (4)  $\langle\langle \dots \rangle\rangle$ : configurational averaging (over size, shape and orientation distributions); (5)  $\rho(\underline{r})$ : particle density function; (6)  $B'(\underline{r}_j, \underline{r}_k)$ : pair correlation function.

Under the aforementioned assumptions, the Dyson equation for the coherent vector-valued electric field assumes the form

$$\begin{aligned} \langle \underline{E}^a \rangle = & \underline{E}^a + \int d\underline{r}_j \langle\langle g_j^a \rangle\rangle \langle \underline{E}^j \rangle \rho(\underline{r}_j) \\ & + \int d\underline{r}_j \int d\underline{r}_k \langle\langle g_j^a \rangle\rangle \langle\langle G_k^j \rangle\rangle \langle \underline{E}^k \rangle B'(\underline{r}_j, \underline{r}_k) ; \end{aligned} \quad (2.1a)$$

$$\begin{aligned} \langle\langle G_k^a \rangle\rangle \equiv & \langle\langle g_k^a \rangle\rangle + \int d\underline{r}_l \langle\langle g_l^a \rangle\rangle \langle\langle G_k^l \rangle\rangle \rho(\underline{r}_l) \\ & + \int d\underline{r}_l \int d\underline{r}_m \langle\langle g_l^a \rangle\rangle \langle\langle G_m^l \rangle\rangle \langle\langle G_k^m \rangle\rangle B'(\underline{r}_l, \underline{r}_m) . \end{aligned} \quad (2.1b)$$

On the other hand, the Bethe-Salpeter equation for the mutual coherence tensor becomes

$$\begin{aligned} \langle \underline{E}^a \underline{E}^{b*} \rangle = & \langle \underline{E}^a \rangle \langle \underline{E}^{b*} \rangle + \int d\underline{r}_j \langle\langle G_j^a \rangle\rangle \langle \underline{E}^j \underline{E}^{j*} \rangle \langle\langle G_j^{b*} \rangle\rangle \rho(\underline{r}_j) \\ & + \int d\underline{r}_j \int d\underline{r}_m \langle\langle G_j^a \rangle\rangle \langle \underline{E}^j \underline{E}^{m*} \rangle \langle\langle G_m^{b*} \rangle\rangle B'(\underline{r}_j, \underline{r}_m) . \end{aligned} \quad (2.2)$$

A detailed derivation of Eqs. (2.1) and (2.2) is given in Ref. 18. The former is at the level of the direct interaction approximation, whereas the latter is at the level of the ladder approximation. Both are analogous to equations associated with a continuous random medium with fluctuations of the permittivity which are distributed according to a normal law and with a deterministic refractive profile directly linked to the number of scatterers per unit volume. It should be noted, however, that no counterpart to the second (collapsed) term on the right-hand side of (2.2) exists in the continuous random medium case. In the absence of pair correlations, i.e.,  $B'(\underline{r}_j, \underline{r}_m) = 0$ , (2.1) and (2.2) reduce to the equations derived previously by Twersky [cf. Ref. 19].

The vector-valued Dyson equation (2.1) and the tensor-valued Bethe-Salpeter equation (2.2) are the basic equations for deriving a tensor-valued radiative transfer equation for vector waves. Such a derivation is very complicated and will not be undertaken in this paper. Instead, Eqs. (2.1) and (2.2) will be "scalarized" in the next section. (A set of assumptions sufficient for such an approximation is given in the Appendix.) The resulting equations will form the basis for deriving a scalar radiation transport theory in Sec. IV.

III. FIRST AND SECOND ORDER COHERENCE FUNCTIONS FOR A RANDOM DISTRIBUTION OF PAIR-CORRELATED SCATTERERS, PART B: ISOTROPIC SCATTERING.

In the following, we shall assume that the scattering channel is tenuous, i.e., the distance between any two scatterers is much greater than a reference wavelength. We shall also assume scalar isotropic scattering. In the electromagnetic case this approximation arises if individual scatterer dimensions are small compared to wavelength and if "gross" depolarization effects are neglected. In the case of acoustic wave propagation, isotropic scattering takes place when individual scatterer dimensions are small compared to wavelength.

Under these assumptions, one deals, essentially, with a scalar wave theory. The Dyson equation (2.1) simplifies considerably and is rewritten below in a form suitable for our work in Sec. IV:

$$\begin{aligned}
 & [\nabla^2 + k^2 + 4\pi f \rho(\underline{r})] \langle E(\underline{r}, k) \rangle \\
 & = -4\pi f \int d\underline{r}' \langle\langle G'(\underline{r}, \underline{r}', k) \rangle\rangle \langle E(\underline{r}', k) \rangle B'(\underline{r}, \underline{r}') \quad ; \quad (3.1a)
 \end{aligned}$$

$$\begin{aligned}
 & [\nabla^2 + k^2 + 4\pi f \rho(\underline{r})] \langle\langle G'(\underline{r}, \underline{r}', k) \rangle\rangle \\
 & = -4\pi f \delta(\underline{r} - \underline{r}') - 4\pi f \int d\underline{r}'' \langle\langle G'(\underline{r}, \underline{r}'', k) \rangle\rangle \langle\langle G'(\underline{r}'', \underline{r}', k) \rangle\rangle B'(\underline{r}, \underline{r}'') \quad . \\
 & \hspace{20em} (3.1b)
 \end{aligned}$$

The notation is identical to the one used in the previous section, except that  $E$  and  $G'$  are now scalar-valued. The quantities  $k$  and  $f$  are respectively the wavenumber and a configurationally averaged scalar-valued scattering coefficient. The latter is independent of  $\underline{r}$ ; however, it may depend on  $k$  and, in general, is complex by virtue of the absorptive properties of the scatterers.

The scalar-valued Bethe-Salpeter equation for the two-frequency mutual coherence function  $\Gamma'(\underline{r}_1, \underline{r}_2, k_1, k_2) \equiv \langle E(\underline{r}_1, k_1) E^*(\underline{r}_2, k_2) \rangle$  can be written as follows:

$$\begin{aligned}
 & [(\nabla_{\underline{r}_1}^2 - \nabla_{\underline{r}_2}^2) + (k_1^2 - k_2^2) + 4\pi f \rho(\underline{r}_1) - 4\pi f^* \rho(\underline{r}_2)] \Gamma'(\underline{r}_1, \underline{r}_2, k_1, k_2) \\
 & = -4\pi \{ \rho(\underline{r}_1) f \langle\langle G'^*(\underline{r}_2, \underline{r}_1, k_2) \rangle\rangle \Gamma'(\underline{r}_1, \underline{r}_1, k_2) \\
 & \quad - \rho(\underline{r}_2) f^* \langle\langle G'(\underline{r}_1, \underline{r}_2, k_1) \rangle\rangle \Gamma'(\underline{r}_2, \underline{r}_2, k_1, k_2) \}
 \end{aligned}$$

$$\begin{aligned}
& -4\pi \int d\underline{r}' [f B'(\underline{r}_1, \underline{r}') - f^* B'(\underline{r}', \underline{r}_2)] [\langle\langle G'(\underline{r}_1, \underline{r}', k_1) \rangle\rangle \Gamma'(\underline{r}', \underline{r}_2, k_1, k_2) \\
& + \langle\langle G'^*(\underline{r}_2, \underline{r}', k_2) \rangle\rangle \Gamma'(\underline{r}_1, \underline{r}', k_1, k_2)] . \quad (3.2)
\end{aligned}$$

The derivation of (3.2) [cf. Ref. 18] incorporates a narrowband pulse assumption. In this case, the scattering coefficient  $f$  depends only on the prescribed carrier frequency.

The functional forms of Eqs. (3.1) and (3.2) are analogous to those derived by Besieris and Kohler [15,16] for acoustic wave propagation in a continuous random medium characterized by Gaussian fluctuations. As in the case of the more general equation (2.2), no counterpart of the first (collapsed) term on the right-hand side of (3.2) exists in the continuous random case. For  $k_1 = k_2$  and in the absence of pair correlations, i.e.,  $B'(\underline{r}_1, \underline{r}_2) = 0$ , Eqs. (3.1) and (3.2) reduce to relationships already available in the literature [cf. Ref. 19].

#### IV. TWO-FREQUENCY RADIATIVE TRANSFER EQUATION FOR A RANDOM DISTRIBUTION OF ABSORPTIVE SCATTERERS WITH PAIR CORRELATIONS: SCALAR WAVE THEORY.

In the Bethe-Salpeter equation (3.2) for  $\Gamma'(\underline{r}_1, \underline{r}_2, k_1, k_2)$  we introduce center-of-mass and difference coordinates and wavenumbers, viz.,  $\underline{R} \equiv (\underline{r}_1 + \underline{r}_2)/2$ ,  $\underline{r} \equiv \underline{r}_1 - \underline{r}_2$ ;  $k_s \equiv (k_1 + k_2)/2$ ,  $k_d \equiv k_1 - k_2$ , and use the notational definitions  $\Gamma'(\underline{r}_1, \underline{r}_2, k_1, k_2) \equiv \Gamma(\underline{R}, \underline{r}, k_s, k_d)$ ,  $B'(\underline{r}_1, \underline{r}_2) \equiv B(\underline{R}, \underline{r})$ ,  $\langle\langle G'(\underline{r}_1, \underline{r}_2, k) \rangle\rangle \equiv \langle\langle G(\underline{R}, \underline{r}, k) \rangle\rangle$ , and  $M(\underline{R}, \underline{r}, k) \equiv f \langle\langle G(\underline{R}, \underline{r}, k) \rangle\rangle B(\underline{R}, \underline{r})$ . We introduce, also, the Fourier transform pairs  $\Gamma(\underline{R}, \underline{r}, k_s, k_d) \longleftrightarrow f(\underline{R}, \underline{\kappa}, k_s, k_d)$ ,  $B(\underline{R}, \underline{r}) \longleftrightarrow \phi(\underline{R}, \underline{\kappa})$ , and  $M(\underline{R}, \underline{r}, k) \longleftrightarrow \tilde{M}(\underline{R}, \underline{\kappa}, k) = \tilde{M}'(\underline{R}, \underline{\kappa}, k) + i \tilde{M}''(\underline{R}, \underline{\kappa}, k)$ . It should be noted that  $M(\underline{R}, \underline{r}, k)$  is analogous to the "mass operator" entering into the Dyson equation in the case of smoothly inhomogeneous media. Furthermore, the quantity  $f(\underline{R}, \underline{\kappa}, k_s, k_d)$  is the two-frequency extension to the phase-space Wigner distribution function.

We consider next smoothly inhomogeneous media for which  $\Gamma(\underline{R}, \underline{r}, k_s, k_d)$ ,  $B(\underline{R}, \underline{r})$  and  $\langle\langle G(\underline{R}, \underline{r}, k) \rangle\rangle$  vary slowly with respect to the sum variable  $\underline{R}$ , and rapidly with respect to the difference variable  $\underline{r}$ . We make also two further assumptions: (1) the ratio of difference to sum wavenumbers is small compared to unity, i.e.,  $|k_d/k_s| \ll 1$ ; (2) the scattering and regular losses are small but not negligible. Within the framework of these restrictions scattering becomes significant [cf. Ref. 18 for details] on the "energy" surface

$$H'(\underline{R}, \underline{\kappa}, k_s) \equiv \frac{1}{2}[\kappa^2 - k_s^2 - 4\pi f_R \rho(\underline{R}) - 4\pi \tilde{M}'(\underline{R}, \underline{\kappa}, k_s)] = 0 , \quad (4.1)$$

which is independent of regular and scattering losses. The quantity  $f_R$  in (4.1) denotes the real part of the complex scattering coefficient  $f$ .

In the general case of statistically anisotropic pair correlations of the scatterers we seek a solution in the form

$$f(\underline{R}, \underline{\kappa}, k_s, k_d) = f_0(\underline{R}, \underline{\kappa}, k_s, k_d) + f_1(\underline{R}, \underline{\kappa}, k_s, k_d) \quad (4.2)$$

The first term on the right-hand side of (4.2) is the coherent part of the two-frequency Wigner distribution and is directly related to the solution of the Dyson equation (3.1). The incoherent part of the Wigner density function, on the other hand, is chosen as follows:

$$f_1(\underline{R}, \underline{\kappa}, k_s, k_d) = k_s |\nabla_{\underline{\kappa}} H'(\underline{R}, \underline{\kappa}, k_s)| |\nabla_{\underline{\kappa}} H'(\underline{R}, \underline{\kappa}, k_s)|^{-3} \\ \times \delta[H'(\underline{R}, \underline{\kappa}, k_s)] I(\underline{R}, \underline{s}, k_s, k_d); \quad \underline{s} = \underline{\kappa}/\kappa \quad (4.3)$$

The quantity  $I(\underline{R}, \underline{s}, k_s, k_d)$  is the two-frequency incoherent "ray" intensity at the point  $\underline{R}$  and in the direction of the unit vector  $\underline{s}$ .

Let, next,  $k_{\text{eff}}(\underline{R}, \underline{s}, k_s)$  denote the value of  $\kappa$  for which  $H'(\underline{R}, \underline{\kappa s}, k_s) = 0$ , and define an effective index of refraction as follows:

$$n_{\text{eff}}(\underline{R}, \underline{s}, k_s) = |\nabla_{\underline{\kappa}} H'(\underline{R}, \underline{\kappa s}, k_s)| / k_s; \quad \kappa = k_{\text{eff}}(\underline{R}, \underline{s}, k_s) \quad (4.4)$$

Let, finally,  $\theta(\underline{R}, \underline{s}, k_s)$  be the angle between the direction of the group and phase velocities. With these definitions in mind, the incoherent ray intensity  $I(\underline{R}, \underline{s}, k_s, k_d)$  is found to obey the two-frequency radiative transfer equation

$$n_{\text{eff}}^2(\underline{R}, \underline{s}, k_s) \frac{d}{dl} \{I(\underline{R}, \underline{s}, k_s, k_d) |\cos \theta(\underline{R}, \underline{s}, k_s)|^{-1} n_{\text{eff}}^{-2}(\underline{R}, \underline{s}, k_s)\} \\ = \{-4 f_I \rho(\underline{R}) - 4\pi \tilde{M}''[\underline{R}, k_{\text{eff}}(\underline{R}, \underline{s}, k_s) \underline{s}, k_s] + i \frac{1}{4} k_s k_d\} \\ \times k_s^{-1} n_{\text{eff}}^{-1}(\underline{R}, \underline{s}, k_s) I(\underline{R}, \underline{s}, k_d) \\ + 2|f|^2 k_s^{-2} \int_{\Omega} d\underline{s}' k_{\text{eff}}^2(\underline{R}, \underline{s}', k_s) n_{\text{eff}}(\underline{R}, \underline{s}, k_s) n_{\text{eff}}^{-3}(\underline{R}, \underline{s}', k_s)$$

$$\begin{aligned}
& \times |\cos \Theta(\underline{R}, \underline{s}', k_s)|^{-1} \{ \phi[\underline{R}, k_{\text{eff}}(\underline{R}, \underline{s}, k_s) \underline{s} - k_{\text{eff}}(\underline{R}, \underline{s}, k_s) \underline{s}'] + \rho(\underline{R}) \} \\
& \times I(\underline{R}, \underline{s}', k_s, k_d) \\
& + 2|f|^2 n_{\text{eff}}(\underline{R}, \underline{s}, k_s) |\cos \Theta(\underline{R}, \underline{s}, k_s)| \int_{R^3} d\underline{\kappa}' \{ \phi[\underline{R} - k_{\text{eff}}(\underline{R}, \underline{s}, k_s) \underline{s} - \underline{\kappa}'] \\
& + \rho(\underline{R}) \} f_o(\underline{R}, \underline{\kappa}', k_s, k_d) \quad , \quad (4.5)
\end{aligned}$$

where  $\Omega$  denotes the range of  $\underline{s}'$  over the surface of a unit sphere.

Equation (4.5) for the two-frequency incoherent intensity  $I(\underline{R}, \underline{s}, k_s, k_d)$  is the main result of this paper. In interpreting this equation, we should note the following: The left-hand side of the equation is a convective term; the ray paths correspond to an effective medium determined by the density of the scatterers  $\rho(\underline{R})$ , the scattering coefficient  $f$  and the spatial correlation function of the scatterers. [The quantity  $d\underline{\kappa}$  denotes the differential of a curvilinear ray passing through the point  $\underline{R}$  in the direction  $\nabla_{\underline{\kappa}} H'(\underline{R}, \underline{\kappa}, k_s)$ .] The first and second terms on the right-hand side of (4.5) are due respectively to regular and scattering losses; the third term arises because of frequency offsets; the fourth one is the scattering term; finally, the last one is the source term, representing the "feeding" of the incoherent intensity by the coherent part of the Wigner distribution function.

In order to compute the second-order pulse moment  $\langle E(\underline{r}_1, t_1) E^*(\underline{r}_2, t_2) \rangle$  at the receiver site, we must first find the two-frequency mutual coherence function  $E(\underline{r}_1, \omega_1) E^*(\underline{r}_2, \omega_2)$  and then perform a two-dimensional Fourier transform with respect to  $\omega_1$  and  $\omega_2$ . In the ladder approximation, the two-frequency mutual coherence function obeys the Bethe-Salpeter equation (3.2). The phase-space analog of the two-frequency mutual coherence function is the Wigner distribution  $f(\underline{R}, \underline{\kappa}, k_s, k_d)$ . The latter is decomposed in (4.2) into a coherent part, which is directly linked to the solution of the Dyson equation (3.1), and an incoherent part directly expressible [cf. Eq. (4.3)] in terms of the two-frequency ray intensity  $I(\underline{R}, \underline{s}, k_s, k_d)$ . The latter obeys the radiative transfer equation (4.5).

Not all the successive steps outlined in the previous paragraph need be followed for obtaining information about second-order pulse statistics. If, for example, such information is restricted to the incoherent part of  $\langle E(\underline{r}_1, t_1) E^*(\underline{r}_2, t_2) \rangle$ , direct usage can be made of the two-frequency ray intensity  $i(\underline{R}, \underline{s}, k_s, k_d)$ , as explained below.

Let  $\Gamma_i(\underline{R}, \underline{\kappa}, k_s, k_d) \leftrightarrow f_1(\underline{R}, \underline{\kappa}, k_s, k_d)$  denote the incoherent part of  $\Gamma(\underline{R}, \underline{\kappa}, k_s, k_d)$ . Then,

$$\Gamma_i(\underline{R}, \underline{r}, k_s, k_d) = \int_{\Omega} d\underline{s} k_s^{-2} n_{\text{eff}}^{-3}(\underline{R}, \underline{s}, k_s) k_{\text{eff}}^2(\underline{R}, \underline{s}, k_s) \times |\cos \theta(\underline{R}, \underline{s}, k_s)|^{-1} I(\underline{R}, \underline{s}, k_s, k_d) \exp\{i k_{\text{eff}}(\underline{R}, \underline{s}, k_s) \underline{s} \cdot \underline{r}\} , \quad (4.6)$$

which establishes a useful connection between the photometric ray intensity  $I(\underline{R}, \underline{s}, k_s, k_d)$  and the incoherent part of the two-frequency mutual coherence function.

V. CONCLUDING REMARKS. A radiative transfer equation for pulsed scalar waves in a random distribution of pair correlated absorptive scatterers has been derived systematically from the Dyson and Bethe-Salpeter equations. Detailed solutions -- both analytical and numerical -- are presently under consideration. An important question in this context is whether controlled experiments could be carried out so that comparisons would be made with theoretical results.

An open research area in propagation through random distributions of scatterers is the systematic derivation of a tensor transport theory from the Dyson equation (2.1) and the Bethe-Salpeter equation (2.2). Such a theory is of paramount importance for physical situations where anisotropic scattering and depolarization effects cannot be neglected.

ACKNOWLEDGMENTS. Research supported in part by the Army Research Office under contract No. DAAG 29-79-C-0085 and the Office of Naval Research under contract No. N00014-76-C-0056.

APPENDIX. Consider the case of Born approximation valid for single particle scattering together with the simplification

$$\int_{V_s} d\underline{r}' [\epsilon_r(\underline{r}') - 1] \exp\{ik(\hat{\underline{i}} - \hat{\underline{o}}) \cdot \underline{r}'\} \approx \int_{V_s} d\underline{r}' [\epsilon_r(\underline{r}') - 1] . \quad (A-1)$$

In this expression,  $V_s$  denotes the volume of the scatterer,  $\epsilon_r(\underline{r})$  is the relative permittivity of the scatterer, and  $\hat{\underline{i}}, \hat{\underline{o}}$  are respectively unit vectors along the incident and scattered directions. In this case, the tensor-valued quantity  $\langle\langle g_j^a \rangle\rangle$  obeys the equation

$$[\nabla_{\underline{r}_a} \times \nabla_{\underline{r}_a} \times (\cdot) - k^2 I] \langle\langle g_j^a \rangle\rangle = k^2 \xi \delta(\underline{r}_a - \underline{r}_j) I , \quad (A-2)$$

where

$$\xi = \xi' + i \xi'' = \langle\langle \int_{V_s} d\underline{r}' [\epsilon_{\underline{r}}(\underline{r}') - 1] \rangle\rangle \quad (\text{A-3})$$

and  $I$  is the unit tensor (dyadic).

Let

$$M^a(\cdot) = [\nabla_{\underline{r}_a} \times \nabla_{\underline{r}_a} \times (\cdot) - k^2(1 + \xi \rho(\underline{r}_a))I] \cdot \quad (\text{A-4})$$

Then, the Dyson equation (2.1) reduces to

$$M^a \langle \underline{E}^a \rangle = k^2 \xi \int d\underline{r}_k \langle \langle G_k^a \rangle \rangle \langle \underline{E}^k \rangle B'(\underline{r}_a, \underline{r}_k) ; \quad (\text{A-5a})$$

$$M^a \langle \langle G_j^a \rangle \rangle = k^2 \xi \delta(\underline{r}_a - \underline{r}_j) I + k^2 \xi \int d\underline{r}_m \langle \langle G_m^a \rangle \rangle \langle \langle G_j^m \rangle \rangle B'(\underline{r}_a, \underline{r}_m) \cdot \quad (\text{A-5b})$$

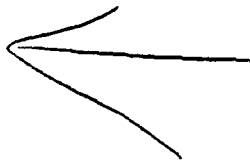
The Bethe-Salpeter equation (2.2) simplifies to

$$\begin{aligned} & M^a \langle \underline{E}^a \underline{E}^{b*} \rangle - \langle \underline{E}^a \underline{E}^{b*} \rangle M^{b*} \\ &= k_1^2 \xi \int d\underline{r}_j \langle \langle G_j^a \rangle \rangle \langle \underline{E}^j \underline{E}^{b*} \rangle B'(\underline{r}_a, \underline{r}_j) \\ &- k_2^2 \xi^* \int d\underline{r}_j \langle \underline{E}^a \underline{E}^{j*} \rangle \langle \langle G_j^{b*} \rangle \rangle B'(\underline{r}_j, \underline{r}_b) \\ &+ k_1^2 \xi \int d\underline{r}_j \langle \underline{E}^a \underline{E}^{j*} \rangle \langle \langle G_j^{b*} \rangle \rangle B'(\underline{r}_a, \underline{r}_j) \\ &- k_2^2 \xi^* \int d\underline{r}_j \langle \langle G_j^a \rangle \rangle \langle \underline{E}^j \underline{E}^{b*} \rangle B'(\underline{r}_j, \underline{r}_b) \\ &+ k_1^2 \xi \langle \underline{E}^a \underline{E}^{a*} \rangle \langle \langle G_a^{b*} \rangle \rangle - k_2^2 \xi^* \langle \langle G_b^a \rangle \rangle \langle \underline{E}^b \underline{E}^{b*} \rangle \cdot \end{aligned} \quad (\text{A-6})$$

If macroscopic depolarization effects are neglected, that is, if the approximation  $\nabla \times \nabla \times (\cdot) = \nabla[\nabla \cdot (\cdot)] - \nabla^2 I \approx \nabla^2 I$  can be justified, both equations (A-5) and (A-6) reduce to scalar relationships.

#### REFERENCES

1. L. O. Foldy, *Phys. Rev.* 67, 107 (1945).
2. M. Lax, *Rev. Mod. Phys.* 23, 287 (1951).
3. V. Twersky, *Proc. Am. Math. Soc.* 16, 84 (1969).
4. A. Ishimaru, *Proc. IEEE* 65, 1030 (1977).
5. K. Furutsu, *J. Math. Phys.* 21, 765, 2764 (1980); *J. Opt. Soc. Am.* 70, 360 (1980).
6. S. Ito and K. Furutsu, *J. Opt. Soc. Am.* 70, 365 (1980).
7. S. Ito, *Appl. Opt.* 20, 2706 (1981).
8. V. Twersky, *J. Math. Phys.* 19, 215 (1978).
9. V. N. Bringi, T. A. Seliga, V. K. Varadan and V. V. Varadan, "Bulk Propagation Characteristics of Discrete Random Media," in Multiple Scattering and Waves in Random Media, edited by P. L. Chow, W. E. Kohler and G. C. Papanicolaou (North-Holland Publishing Co., Amsterdam, 1981).
10. L. Tsang and J. A. Kong, *J. Appl. Phys.* 52, 5448 (1981).
11. Yu. N. Barabanenkov, *Sov. Phys. - Doklady* 12, 431 (1967).
12. Yu. N. Barabanenkov and V. M. Finkel'berg, *Sov. Phys. JETP* 26, 587 (1968).
13. K. M. Watson, *J. Math. Phys.* 10, 688 (1969); C. W. Law and K. M. Watson, *J. Math. Phys.* 11, 3125 (1970).
14. Yu. N. Barabanenkov, A. G. Vinogradov, Yu. A. Kravtsov and V. I. Tatarskii, *Izv. VUZ., Radiofiz.* 15, 1852 (1972).
15. I. M. Besieris and W. E. Kohler, "Derivation of the Two-Frequency Radiative Transfer Equation for a Statistically Inhomogeneous and Anisotropic Medium," *Proc. International U.R.S.I. Symp.*, Munich, Germany (1980).
16. I. M. Besieris and W. E. Kohler, "Two-Frequency Radiative Transfer Equation for a Statistically Inhomogeneous and Anisotropic Absorptive Medium," in Multiple Scattering and Waves in Random Media, edited by P. L. Chow, W. E. Kohler and G. C. Papanicolaou (North-Holland Publishing Co., Amsterdam, 1981).
17. I. M. Besieris, W. E. Kohler and H. Freese, "A Transport-Theoretic Analysis of Pulse Propagation Through Ocean Sediments," *J. Acoust. Soc. Am.* (to appear).
18. A. I. Tsolakis, "Multiple Scattering of Electromagnetic Waves by Distributions of Particles with Applications to Radio Wave Propagation Through Precipitation," Ph.D. Thesis, Virginia Polytechnic Institute and State University.
19. A. Ishimaru, Wave Propagation and Scattering in Random Media (Academic Press, New York, N.Y., 1978).



AD P001014

ANALYSIS OF MULTILAYER DIELECTRIC  
WAVEGUIDE STRUCTURES

J.M. Zavada  
US Army Armament R&D Command  
Dover, NJ 07801

S.T. Peng  
Polytechnic Institute of New York  
Brooklyn, NY 11201

ABSTRACT

Multilayer dielectric structures are analyzed to determine the optical waveguiding properties of the surface and leaky waves that can be supported by such structures. Each layer in these structures is assumed to have a uniform dielectric constant that may include an absorption term. Any finite number of layers can be treated by this analysis. The method of transmission line theory is applied to this problem in order to keep the formulation both tractable and general enough to include an arbitrary distribution of piecewise uniform dielectric constants in the multilayer structure. The resulting equations are placed into a simple form that is convenient for effective computer programming. A computer program based on these equations is developed and used to investigate optical waveguiding in representative multilayer structures.

## INTRODUCTION

The simplest version of an optical waveguide is a planar structure with an uniform dielectric constant (ref 1). For an electromagnetic wave to be guided in this structure, the dielectric constant must be larger than that of the adjacent media. The guided wave will then propagate in a zig-zag fashion within this structure undergoing total internal reflection at each interface.

There are two main problems with this type of optical waveguide. The first arises from surface and interfacial irregularities that scatter light out of the waveguiding region. This scattering can lead to large propagational losses and to poor signal/noise characteristics. The second is lack of phase coherence for modes of different order. This difficulty limits the use of such structures in multimode propagation and reduces the information content that can be transferred. Similar problems have been encountered with optical fibers used in communication systems and have led to the development of Graded Index (GRIN) or Self-Focusing (SELFOC) fibers (ref 2). The refractive index of these fibers is no longer uniform but varies according to a parabolic profile. Due to this index variation, light rays in the fiber are contained in a sinusoidal envelope. Since the light ray never touches the interface, scattering losses from surface irregularities are drastically reduced. Also, the index profile is adjusted to maintain phase coherence for a wide range of propagating modes.

While such advances have been made in the fabrication of cylindrical optical fibers, controlled index profiling has not as yet been achieved in planar optical waveguides. The reason for this lies in the considerable difficulty of introducing impurity atoms in a precise manner over a two dimensional region of several square centimeters.

Molecular beam epitaxy (MBE) is a vacuum deposition processing technique in which several different atoms or molecules can be deposited producing a film with the same crystalline structure as the substrate (epitaxial growth) (ref 3). MBE machines have been available for over a decade but the quality of the deposited films has often been erratic. Recent progress in vacuum technology has allowed the fabrication of high quality films in a reproducible manner.

With modern MBE machines, it is also possible to grow multilayer planar structures in which the optical or electronic doping in individual layers can be accurately specified. Dopant profiling of this type can lead to novel electro-optical devices for use in integrated optics and microelectronics. To effectively utilize the advantages of multilayer structures for guided wave applications, it is necessary to be able to determine the optical waveguiding characteristics of such structures. In this report an analysis of multi-

layer waveguiding structures is performed.

The scattering and guiding of electromagnetic waves by planar multilayer dielectric structures is a well known classical boundary-value problem in electromagnetics (refs 4 & 5). The formulation of such a problem is straightforward, but its complexity increases drastically with increasing number of layers. For a structure with a large number of layers, the analysis requires a special technique that will keep the complex problem tractable. In this work, the method of equivalent network (transmission-line) is applied together with the concept of the input impedance to the electromagnetic boundary-value problem. Such a network approach makes the formulation of the problem simple and particularly effective for developing computer programs that are needed for theoretical understanding as well as verification of experimental results in laboratories.

In principle, the planar multilayer dielectric structure can be formulated as an electromagnetic boundary-value problem for any structure parameters. However, for numerical analyses using a computer, such as the search for dispersion roots, an analytic solution often has to be put into different forms for different possible situations that may arise in a complex structure; otherwise, the numerical analyses may not always converge. Therefore, an essential part of this work is to develop a computer program that will automatically search for a suitable form of the analytic solution as the situation demands. Fortunately, the equivalent-network and input-impedance approach is versatile enough to permit an automatic search routine that ensures the convergence of the numerical analyses.

#### FORMULATION OF MULTILAYER DIELECTRIC STRUCTURE

A multilayer dielectric structure consisting of  $N$  uniform layers is shown in fig. 1. The dielectric constant and the thickness of the  $i$ -th layer from the top are  $E_i$  and  $t_i$ . Such a multilayer structure is placed on top a large substrate. The upper space above the structure may be a superstrate or simply air and its dielectric constant is denoted by  $E_a$  which may take any arbitrary value for a given material. Without the loss of generality, the substrate and the air region are assumed to be infinite in extent. If the uniform substrate has a finite thickness, for example, the substrate may then be considered as another layer below which is the unbounded air region, and the formulation to be presented below will still hold.

#### Equivalent Network for Multilayer Dielectric Structure

For the coordinate system chosen in fig. 1, the dielectric constant of the entire space is uniform in the  $xy$ -plane and varies only in the  $z$ -direction. For such a structure, we may consider the Transverse Electric (TE) and Transverse Magnetic (TM) modes

separately. If the electromagnetic fields are invariant along the y direction, we have, for each uniform region of dielectric constant  $E_i$ , the field representations:

$$\begin{matrix} (i) \\ E_y(x, z) = V_i(z) \exp(-jk_x x) \end{matrix} \quad (1)$$

$$\begin{matrix} (i) \\ H_x(x, z) = I_i(z) \exp(-jk_x x) \end{matrix} \quad (2)$$

$$\begin{matrix} (i) \\ H_z(x, z) = \frac{k_x}{k_0 Z_0} V_i(z) \exp(-jk_x x) \end{matrix} \quad (3)$$

for the TE modes and

$$\begin{matrix} (i) \\ H_y(x, z) = I_i(z) \exp(-jk_x x) \end{matrix} \quad (4)$$

$$\begin{matrix} (i) \\ E_x(x, z) = V_i(z) \exp(-jk_x x) \end{matrix} \quad (5)$$

$$\begin{matrix} (i) \\ E_z(x, z) = \frac{-k_x Z_0}{k_0 E_i} I_i(z) \exp(-jk_x x) \end{matrix} \quad (6)$$

for the TM modes. Here  $V_i(z)$  and  $I_i(z)$  are two unknown functions to be determined by substituting each of the two sets of field representations into Maxwell's equations and  $Z_0$  is the characteristic impedance of free space. In doing so, we obtain the transmission line equation, for the i-th layer (Reference 6):

$$\frac{d}{dz} V_i(z) = -jK_i Z_i I_i(z) \quad (7)$$

$$\frac{d}{dz} I_i(z) = -jK_i Y_i V_i(z) \quad (8)$$

$$K_i = (k_0^2 E_i - k_x^2)^{1/2} \quad (9)$$

$$\begin{aligned} Z_i &= \frac{k_0 Z_0}{K_i} \quad (\text{TE}) \\ Y_i &= \frac{K_i Z_0}{k_0 E_i} \quad (\text{TM}) \end{aligned} \quad (10)$$

where  $V_i$  for the electric field and  $I_i$  for the magnetic field are interpreted as the transmission line voltage and current, respectively;  $K_i$  is the characteristic propagation constant;  $Z_i$  is the characteristic impedance; and,  $Y_i$  is the characteristic admittance. The form of transmission line equations remains the same for any constituent layer, but the transmission line parameters depend on the dielectric constant of the layer  $E_i$  and on the parameters of the incident wave,  $k_0$  and  $k_x$ , as described by Eqs 9 and 10.

The boundary conditions at an interface between two media of different dielectric material require that the tangential field components be continuous across the interface. At the interface at  $z = z_i$  between the  $i$ -th and  $(i+1)$ st media, we must have, for the TE-mode:

$$E_y^{(i)}(x, z_i) = E_y^{(i+1)}(x, z_i) \quad (11)$$

$$H_x^{(i)}(x, z_i) = H_x^{(i+1)}(x, z_i) \quad (12)$$

Using eqs. (1) and (2), the last two equations result in:

$$V_i(z_i) = V_{i+1}(z_i) \quad (13)$$

$$I_i(z_i) = I_{i+1}(z_i) \quad (14)$$

which states the continuity of both transmission-line voltage and current at the junction representing the interface. This is true at every interface boundary. An equivalent network consisting of transmission line sections for the multilayer structure shown in fig. 1(a) can be given in fig. 1(b). It can be easily shown by the same procedure that the same equivalent network also holds for the TM mode, but the characteristic impedance of the transmission lines has to be modified according to eq 10.

#### Impedance Transformation of Transmission Line Section

The multilayer structure or the cascaded transmission line system, shown in fig. 1, may be analyzed by many different methods. The two most commonly employed ones are the transfer-matrix method and the impedance-transformation method (ref 7). Each method is applied to the terminal voltages and currents at the junctions. It should be noted that a junction can be either a natural one existing in the system or an artificial one created for the convenience of an analysis. The transfer-matrix method is useful in some situations, such as a system with fixed parameters. For the present problem of scattering and guiding of waves by a multilayer structure we are interested in the effect of changes in structure parameters. Therefore the transfer-matrix method is not suitable here. On the other hand, the impedance-transformation method is relatively simple and easy for numerical analyses. We shall employ exclusively the method of impedance transformation in this work.

A transmission-line of known propagation constant,  $K$ , and characteristic impedance,  $Z$ , is shown in fig. 2; it has a finite length  $t$  and is terminated by an output impedance,  $Z_{out}$ . The transmission-line voltage and current can be written as a superposition of a forward and backward traveling wave:

$$V(z) = Z(b \exp(jKz) + a \exp(-jKz)) \quad (15)$$

$$I(z) = a \exp(-jKz) - b \exp(+jKz) \quad (16)$$

where a and b are arbitrary constants. At the output end,  $z=t$ , the boundary condition is:

$$V(t) = Z_{out}I(t) \quad (17)$$

Substituting eqs 15 and 16 into eq 17, we obtain:

$$b = R \exp(-j2Kt) a \quad (18)$$

where R is the reflection coefficient at  $z = t$  and is defined by:

$$R = (Z_{out} - Z)/(Z_{out} + Z) \quad (19)$$

Finally, setting  $z = 0$  in eqs 15 and 16, taking the ratio of  $V(0)$  and  $I(0)$ , and making use of eqs 18 and 19, we obtain:

$$Z_{in} = V(0)/I(0) = Z (Z_{out} + jZ \tan Kt)/(Z + jZ_{out} \tan Kt) \quad (20)$$

which defines the impedance transformation between the input and output terminals of the transmission line section. This transformation formula will be used as a building block in the analysis of the cascaded transmission line system given in the next section.

#### GUIDANCE OF SURFACE AND LEAKY WAVES

Since the substrate region in fig. 1 is assumed to be semi-infinite in extent, the transmission line representing this region is likewise semi-infinite in length. The input impedance looking downward in fig. 1 is then given by the characteristic impedance of a semi-infinite transmission line:

$$Z_{in}^{(N+1)} = Z_s \quad (21)$$

Such an input impedance is actually the output impedance of the N-th section and the input impedance of the N-th section can be determined by using the transformation formula in eq 20. The input impedance then becomes the output impedance of the preceding (N-1)st section and the process may be repeated until the sections are exhausted. More specifically, the impedance transformation for each section can be given by:

$$Z_{in}^{(i)} = Z_i (Z_{out}^{(i)} + jZ_i \tan Kt_i)/(Z_i + jZ_{out}^{(i)} \tan Kt_i) \quad (22)$$

$$Z_{out}^{(i)} = Z_{in}^{(i+1)} \quad (22a)$$

$$t_i = z_i - z_{i-1} \quad (22b)$$

for any  $i=1,2,3,\dots,N$ . Thus, the input impedance at every junction may be assumed to be known.

Consider now a plane wave of amplitude  $a$  incident from the air region onto a multilayer structure, as shown in fig. 3(a). The angle of incidence is  $\theta$  and the reflected wave amplitude is  $b$ . In this case, we have:

$$k_x = k_0 (E_a)^{1/2} \sin \theta \quad (23)$$

With a given  $k_x$ , the transmission parameters can be determined by eqs 9 and 10. An equivalent network for the scattering of a plane wave by the multilayer structure is shown in fig. 3(b), with the incident and reflected wave amplitudes indicated. The voltage and current in the air region are given by:

$$V_a(z) = Z_a(a \exp(-jK_a z) + b \exp(+jK_a z)) \quad (24)$$

$$I_a(z) = a \exp(-jK_a z) - b \exp(+jK_a z) \quad (25)$$

At  $z=0$ , the voltage and current must satisfy the relation:

$$V_a(0) = Z_{in}^{(1)} I_a(0) \quad (26)$$

Substituting eqs 24 and 25 into eq 26, we obtain, after some manipulations:

$$(Z_{in}^{(1)} + Z_a)b = (Z_{in}^{(1)} - Z_a)a \quad (27)$$

In general, we then obtain:

$$b = R_{a1} a \quad (28)$$

where  $R_{a1}$  is the reflection coefficient of the multilayer structure and is defined by:

$$R_{a1} = (Z_{in}^{(1)} - Z_a) / (Z_{in}^{(1)} + Z_a) \quad (29)$$

In the absence of an incident wave ( $a=0$ ), and in order for eq 27 to have a non-trivial solution ( $b \neq 0$ ), we must have:

$$Z_{in}^{(1)} + Z_a = 0 \quad (30)$$

which defines the dispersion relation for surface and leaky waves guided by the multilayer structure. This dispersion relation is a

transcendental equation whose roots can be determined only by numerical methods, such as the Newton iteration method which has been successfully tested for the problem under investigation.

#### SAMPLE CALCULATIONS

Optical waveguides having an exponential variation in the dielectric function form a common class of inhomogeneous waveguiding structures. These waveguides can be produced either through in-diffusion of foreign atoms into an optically homogeneous medium, or by out-diffusion of certain atoms originally located in the medium. In either case, the variation in the dielectric function can be described by:

$$\begin{aligned} E(z) &= E_0 && \text{for } z < 0 \\ E(z) &= E_1 + E_2 \exp(-z/d) && \text{for } z > 0 \end{aligned} \quad (31)$$

where  $E_0$  is the dielectric constant of the superstrate region;  $E_1$  characterizes the substrate prior to diffusion;  $E_2$  is the maximum change due to diffusion; and,  $d$  is the transition length. Upon substituting eq 31 into Maxwell's equations, it is possible to obtain a closed form solution, in terms of Bessel functions, for the propagating waves. The allowed values for the propagation constants are then determined by finding the roots of these functions when the boundary conditions are satisfied at  $z = 0$ . This method has been utilized to analyze waveguides fabricated by in-diffusion of Se into CdS substrates (ref 8). In that analysis, the waveguiding region was specified by the following parameters:  $E_0 = 1$ ,  $E_1 = 6.1$ ,  $E_2 = 0.3$ ,  $d = 2.5$  microns, and the wavelength is 0.633 microns. Table 1 lists the propagation constants for the eight TE modes that can be supported by this waveguide.

In order to apply the multilayer formalism, developed in the previous two sections, to this type of waveguide, it is necessary to replace the continuous profile by a set of approximating steps. Table 2 indicates the dielectric constant and the thickness of each layer in the ten layer approximation to the exponential profile. Here the substrate region is labeled "A" and the air region is "S". When these parameters are used as inputs to the computer program, the TE propagation constants for the multilayer profile can be calculated. The values resulting from this calculation are shown in table 1 and are in very good agreement with the numbers determined by the continuous exponential profile solution. Since this latter method also involves numerical root finding procedures, it is somewhat difficult to state which method is more accurate. Probably the multilayer approach is more economical to use as it does not involve the computation of Bessel functions at each stage.

## CONCLUSIONS

The mathematical problem of determining the propagating modes in a multilayer dielectric waveguiding structure has been analyzed in this investigation. A solution to the problem has been derived based upon the method of equivalent network formulation used with the concept of input impedance matching. The analytical solution has been used to generate a computer program to calculate both the TE and the TM propagation constants in multilayer structures. The program can treat an arbitrary number of layers each characterized by a uniform dielectric constant that may include losses. Any piecewise continuous dielectric profile can, in principle, be represented by a structure consisting of  $N$  such layers, where  $N$  is an integer. As  $N$  becomes very large, the solution presented here approaches the WKB approximation to the electromagnetic boundary value problem. In its current form, the computer program has been shown to yield very accurate values for the propagation constants for a waveguide having an exponential dielectric profile. This program can be easily extended to calculate the field distribution within each dielectric layer. In this manner, complicated dielectric waveguiding structures can be analyzed to predict propagation constants for each polarization along with their associated modal patterns.

#### REFERENCES

1. D. Marcuse, Theory of Dielectric Optical Waveguides, Academic Press, New York, 1974.
2. M. S. Sodha and A. K. Ghatak, Inhomogeneous Optical Waveguides, Plenum, New York, 1979.
3. A. Y. Cho and J. R. Arthur, "Molecular Beam Epitaxy," Progress in Solid State Chemistry, chap. 10, Pergamon, New York, 1975.
4. L. M. Brekhovskikh, Waves in Layered Media, 2nd ED., Academic Press, New York, 1980.
5. J. F. Revelli, "Mode Analysis and Prism Coupling for Multilayered Optical Waveguides," Applied Optics, 20, 3158-3167 (1981).
6. G. C. Southworth, Principles and Applications of Waveguide Transmission, Van Nostrand, New York, 1950.
7. R. E. Collin, Foundations of Microwave Engineering, McGraw-Hill, New York, 1966.
8. E. Conwell, "Modes in Optical Waveguides Formed by Diffusion," Applied Physics Letters, 23, 328-329 (1973).

Table 1. Propagation constants for exponential profile

<u>TE mode number</u>	<u>Continuous profile</u>	<u>Multilayer profile</u>
0	2.508	2.508
1	2.495	2.495
2	2.486	2.487
3	2.480	2.480
4	2.476	2.476
5	2.473	2.473
6	2.471	2.471
7	2.470	2.470

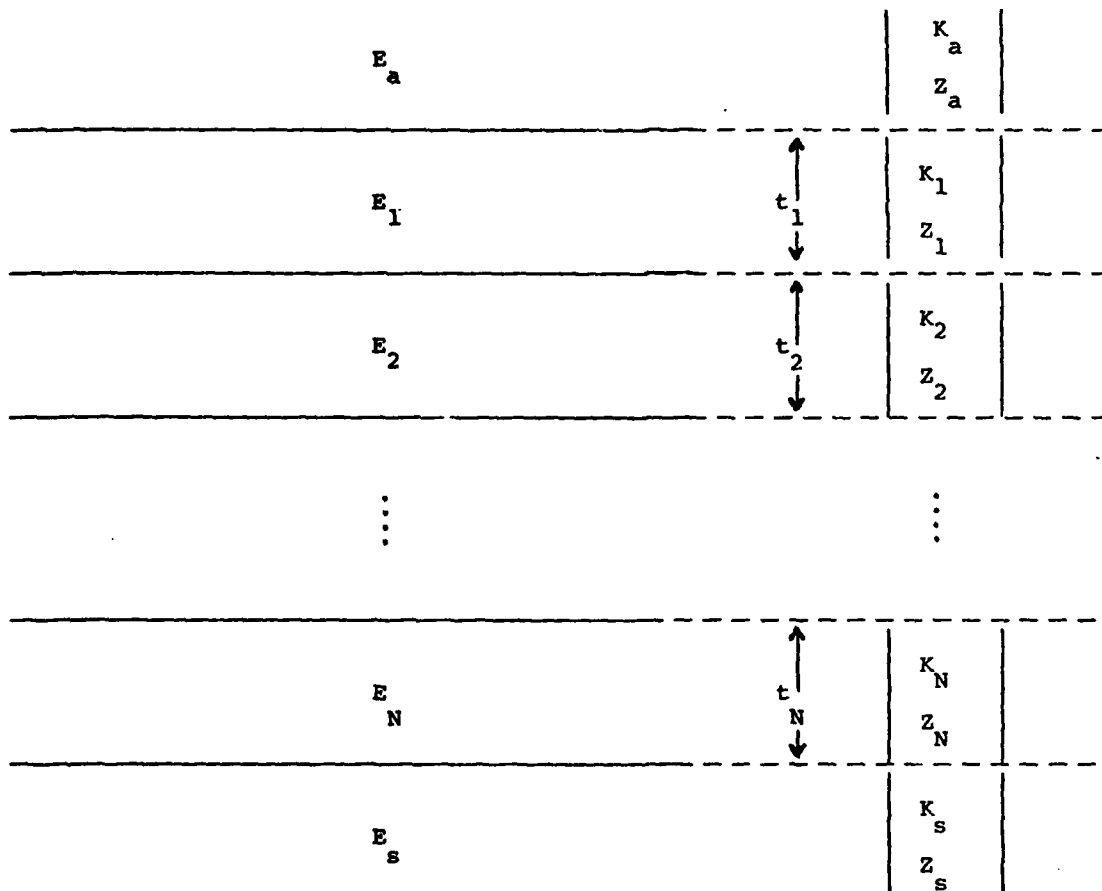
Table 2. Multilayer input data

EA = 6.10000 -0.00000

ES = 1.0 -0.0000

WAVELENGTH = 0.633

E 1 =	6.10309	-0.00000	T 1 =	2.40000
E 2 =	6.10962	-0.00000	T 2 =	2.00000
E 3 =	6.12141	-0.00000	T 3 =	2.00000
E 4 =	6.14398	-0.00000	T 4 =	1.60000
E 5 =	6.17398	-0.00000	T 5 =	1.00000
E 6 =	6.21036	-0.00000	T 6 =	1.00000
E 7 =	6.25819	-0.00000	T 7 =	0.80000
E 8 =	6.30930	-0.00000	T 8 =	0.60000
E 9 =	6.35564	-0.00000	T 9 =	0.40000
E10 =	6.40000	-0.00000	T10 =	0.20000



(a)

(b)

(a) Multilayer dielectric structure

(b) Equivalent transmission line network

Figure 1. Mathematical modeling of dielectric structure and its equivalent network

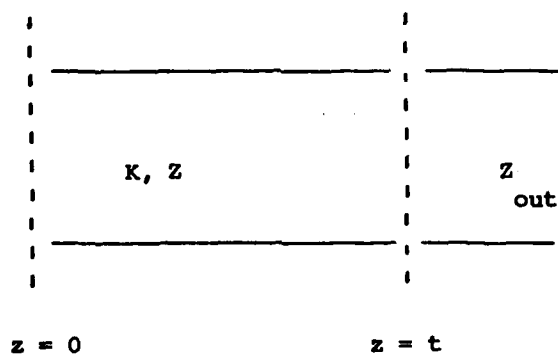
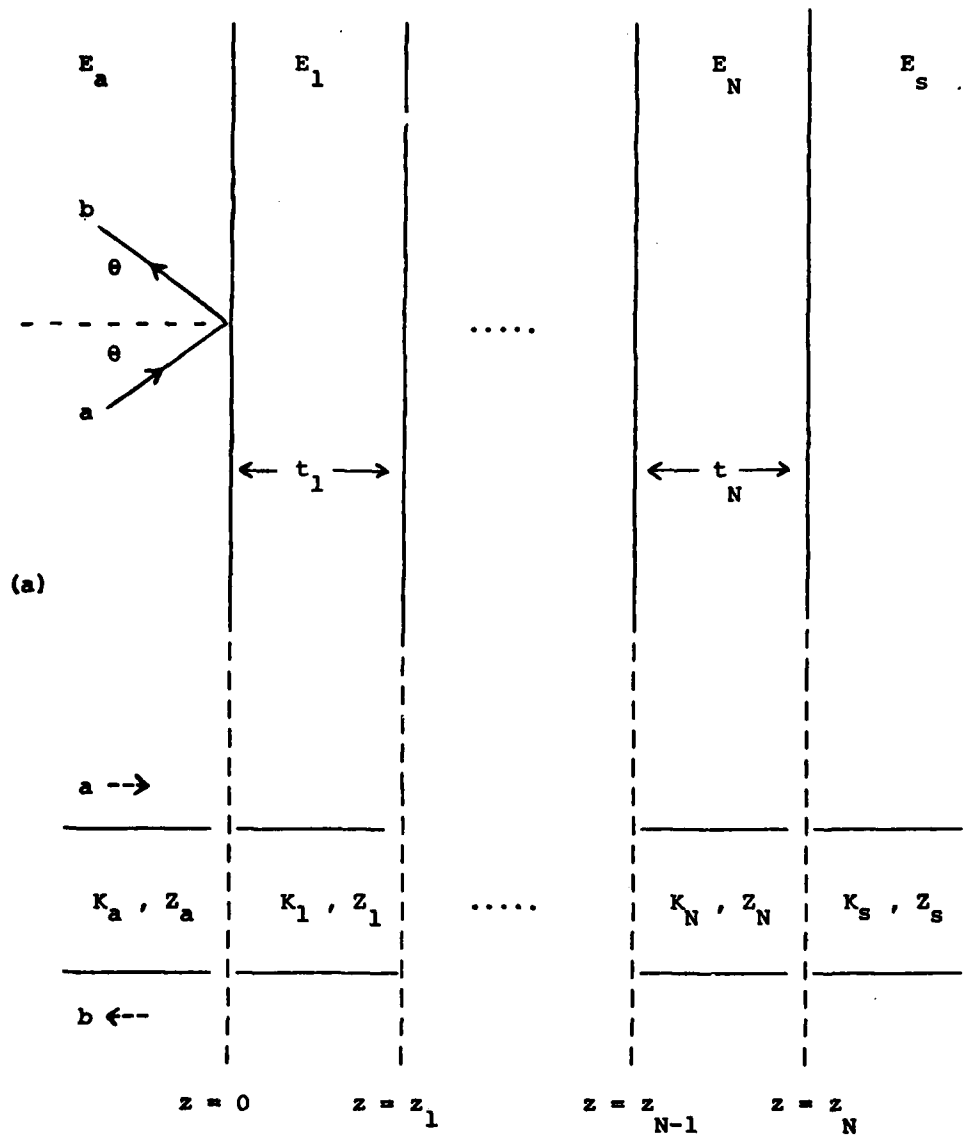


Figure 2. Transmission line section with termination



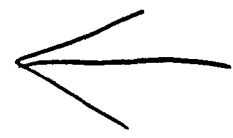
(a)

(b)

(a) Multilayer structure

(b) Equivalent network

Figure 3. Scattering of a plane wave by a multilayer structure and its equivalent network



AD P001015

CALCULATION OF ADVECTIVE MASS TRANSPORT IN HETEROGENEOUS MEDIA

Charles J. Daly  
Earth Sciences Branch  
Cold Regions Research and Engineering Laboratory  
Hanover, New Hampshire 03755

**ABSTRACT.** A coupled analytical/numerical procedure for prediction of solute transport in heterogeneous media is described. The procedure consists of an analytic solution of the hydraulic equations, followed by a numerical solution for solute transport using the method of characteristics. The characteristics are determined by fourth-order Runge-Kutta and predictor-corrector algorithms. Accuracy of solute transport calculation is enhanced by the fact that fluid velocity can be directly obtained at a priori undetermined points in the flow field.

The solute transport process is considered to be entirely advective, neglecting the effects of mechanical dispersion and molecular diffusion. Evidence is presented to demonstrate that purely advective processes in both heterogeneous and homogeneous media can produce large "apparent dispersion." Such dispersion is shown to be easily capable of overwhelming any reasonable estimates of dispersion or diffusion based upon laboratory analyses of homogeneous media. For groundwater contamination problems, it is concluded that precise definition of the spatial variability of hydraulic properties is crucial to the accurate determination of the trajectory of contaminated waters.

**BACKGROUND.** At the scale of individual grains, the transport of a conservative solute through a porous medium is clearly an advective phenomenon. Solute particles are wafted along by fluid as it flows over tortuous routes in the general direction of the potential gradient. Close observation of the movement of initially adjacent solute particles would reveal their tendency to become separated. Contributing to the separation one would observe: (a) random bifurcation of pore channels, (b) a large range of fluid velocities across individual pores, and (c) differences of fluid velocity from one pore to another. To a very minor extent, pore scale advection is supplemented by molecular diffusion.

For a fluid of nonuniform concentration which saturates a porous medium, the separation of solute particles amounts to mixing, resulting in changes of local solute concentration. Buyevich et al. (1969) noted that the pore scale advective mixing process is very much like the mixing resulting from ordinary fluid turbulence.

The usual material continuum approach to porous media modeling defines solute transport in terms of macroscale mass fluxes (Bachmat and Bear, 1964). Although the entire process is fundamentally advective at the pore scale, the macroscale description of advection can represent only an average transport, strictly in the direction of the potential gradient. The pore scale mechanisms listed above as (a) through (c) cannot be accounted for by macroscale advection alone.

RESEARCH REPORT R-64-101

Dispersion is an additional macroscale solute flux whose purpose is to account for the pore scale mechanisms which cause mixing. Dispersive flux is assumed to be proportional to concentration gradient.

Harleman et al. (1963), Klotz and Moser (1974), and others have conducted laboratory experiments on columns of homogeneous media to determine the relative magnitudes of macroscale advection and dispersion. Their results are presented as a correlation between the magnitude of dispersion, the potential gradient, and the physical properties of fluid and media.

Many investigators (e.g. Pinder, 1973; Konikow and Bredehoeft, 1974) have applied macroscale advection-dispersion models to field problems. Calibration of these models generally leads to the assumption of dispersive fluxes which are orders of magnitude greater than would be expected on the basis of lab analyses of porous material samples. Gelhar et al. (1979) reiterate the conclusion that this discrepancy is related to local heterogeneity of porous medium hydraulic properties. The experimental results of Skibitski and Robinson (1963) substantiate this by illustrating the dominant effect of heterogeneity on the transport of dye in sand flumes.

**THEORY.** The aim of this paper is to demonstrate a coupled analytical/numerical technique for predicting the transport of conservative solutes in heterogeneous media. The approach presumes that genuine dispersion is negligible compared to true macroscale advection when that advection fully accounts for heterogeneity and nonuniform flow.

In order to accurately determine the effect of heterogeneity on macroscale advection, an analytic solution for hydraulic potential is obtained. Application of Darcy's law yields an analytic expression for average linear velocity which can be evaluated at a priori unspecified points  $\vec{x}$ . As part of the technique, medium properties are accounted for as known (or interpolated) explicit functions of  $\vec{x}$ . Given an accurate description of flow field, streamlines are calculated by applying the method of characteristics. Advection is determined from the rates of flow along the streamlines.

Example problems are used to demonstrate the fact that genuine dispersion can be easily overwhelmed by the effects of heterogeneity and non-uniform flow. In each example, flow is assumed steady and horizontal. The analyses apply to confined aquifers and also to phreatic aquifers where the Dupuit assumptions and linear approximation are valid.

**Advection-dispersion equation (numerical solution).** The control volume approach can be used to derive the advection-dispersion equation (Daly, 1979):

$$\phi \frac{\partial C}{\partial t} - \nabla \cdot (DVC) + \vec{v} \cdot VC = \frac{\tilde{C}}{\rho} + q \frac{(\hat{C} - C)}{\rho} \quad (1)$$

where:

- $\phi$  = effective porosity, dimensionless;  
 $C$  = mass fraction of the pore fluid; the ratio of the mass of solute in a given volume to the total mass of fluid in that volume, dimensionless;  
 $D$  = dispersion coefficient tensor,  $L^2/T$ ;  
 $\vec{v}$  = specific discharge,  $L/T$ ;  
 $\tilde{C}$  = contaminant mass source/sink strength representing the exchange of mass between fluid and porous matrix,  $M/L^3T$ ;  
 $\rho$  = fluid density,  $M/L^3$ ;  
 $q$  = recharged fluid mass strength,  $M/L^3T \geq 0$ ;  
 $\hat{C}$  = mass fraction of recharged fluid, dimensionless.

Considering (1), it is clear that the effect of fluid withdrawals is not felt directly through the terms on the RHS of the equation. However, withdrawals do affect the transport by modifying the flow field (represented in (1) by  $\vec{v}$ ).

If dispersion is neglected compared to macroscale advection, (1) can be written, for the simple case of no source/sink terms, as:

$$\phi \frac{\partial C}{\partial t} + v_x \frac{\partial C}{\partial x} + v_y \frac{\partial C}{\partial y} = 0 \quad (2)$$

Application of the method of characteristics transforms (2) into the equivalent system of ordinary differential equations:

$$\frac{dx}{dt} = \frac{v_x}{\phi} \equiv f(x, y, t) \quad (3)$$

$$\frac{dy}{dt} = \frac{v_y}{\phi} \equiv g(x, y, t) \quad (4)$$

$$\frac{dC}{dt} = 0 \quad (5)$$

Equations (3) and (4) are used to determine the trajectories (also called the characteristic lines) of fluid particles in the flow field. Equation (5) is simply a statement of the fact that in the absence of sources or sinks the concentration of fluid particles remains constant. It is important to note that (3), (4), and (5) are not independent. Equation (5) is only valid along the trajectories defined by the joint solution of (3) and (4).

Determination of the trajectories of fluid particles is done by numerically solving the linked system of (3) and (4). A fourth order Runge-Kutta technique is used to start the procedure which can be continued

by a more efficient predictor-corrector scheme. The numerical solution method starts at a point  $(x_0, y_0)$  at time zero. The concentration is defined at all such points by an initial condition. Using a time step  $\Delta t$ , successive points  $(x_n, y_n)$  along the trajectory of the particle which began at point  $(x_0, y_0)$  are obtained. The Runge-Kutta algorithm for accomplishing this is:

$$x_{n+1} = x_n + \frac{1}{6} (a_1 + 2a_2 + 2a_3 + a_4) \quad (6)$$

$$y_{n+1} = y_n + \frac{1}{6} (b_1 + 2b_2 + 2b_3 + b_4) \quad (7)$$

where:

$$a_1 = \Delta t f(x_n, y_n, t_n) \quad (8)$$

$$b_1 = \Delta t g(x_n, y_n, t_n) \quad (9)$$

$$a_2 = \Delta t f(x_n + a_1/2, y_n + b_1/2, t_n + \Delta t/2) \quad (10)$$

$$b_2 = \Delta t g(x_n + a_1/2, y_n + b_1/2, t_n + \Delta t/2) \quad (11)$$

$$a_3 = \Delta t f(x_n + a_2/2, y_n + b_2/2, t_n + \Delta t/2) \quad (12)$$

$$b_3 = \Delta t g(x_n + a_2/2, y_n + b_2/2, t_n + \Delta t/2) \quad (13)$$

$$a_4 = \Delta t f(x_n + a_3, y_n + b_3, t_n + \Delta t) \quad (14)$$

$$b_4 = \Delta t g(x_n + a_3, y_n + b_3, t_n + \Delta t), \quad (15)$$

and  $f$  and  $g$  are defined in Equations (3) and (4).

Runge-Kutta algorithms belong to the set of self-starting numerical solution methods. Self-starting means that the determination of all successive points  $(x_n, y_n)$  requires only the starting point  $(x_0, y_0)$ . In other words, calculation of  $x_n$  and  $y_n$  depends only on the known values  $x_{n-1}$  and  $y_{n-1}$ . The set of non self-starting methods require the values  $(x_n, y_n)$  to be given at more than one point along the trajectory. For example, a fourth order predictor-corrector algorithm called Milne's method requires the values  $x_0, x_1, x_2, x_3, y_0, y_1, y_2, y_3$  to calculate successive values of  $x_n$  and  $y_n$ .

Beside the question of starting values, the efficiency of the calculation procedure is an important factor in selecting a numerical method. It turns out that Milne's algorithm is significantly more efficient than the Runge-Kutta method, although both are fourth-order accurate. One numerical procedure proposed in this paper is that which takes advantage of the Runge-Kutta self-starting feature and the efficiency of Milne's method. Given a starting point  $(x_0, y_0)$ , the Runge-Kutta procedure is used to obtain  $(x_1, y_1)$ ,  $(x_2, y_2)$ ,  $(x_3, y_3)$ . At that stage the necessary starting values are available for Milne's method which is then used to generate succeeding points.

Non self-starting methods typically assume constant  $\Delta t$ , whereas self-starting methods allow for change of  $\Delta t$  at each time step. For problems in which the frequent change of  $\Delta t$  is desirable, exclusive use of a self-starting method, such as the Runge-Kutta algorithm, is advised.

Milne's predictor-corrector method consists of two steps. First, predicted estimates of  $x_{n+1}$  and  $y_{n+1}$  are calculated. Let these be denoted  $x_{n+1}^*$  and  $y_{n+1}^*$ . Second, the predicted values are corrected to obtain the final values  $x_{n+1}$  and  $y_{n+1}$  at the end of a time step. The algorithm is :

$$x_{n+1}^* = x_{n-3} + \frac{4\Delta t}{3} [2x'_n - x'_{n-1} + 2x'_{n-2}] \quad (16)$$

$$y_{n+1}^* = y_{n-3} + \frac{4\Delta t}{3} [2y'_n - y'_{n-1} + 2y'_{n-2}], \quad (17)$$

then:

$$x_{n+1} = x_{n-1} + \frac{\Delta t}{3} [x_{n+1}^* + 4x'_n + x'_{n-1}] \quad (18)$$

$$y_{n+1} = y_{n-1} + \frac{\Delta t}{3} [y_{n+1}^* + 4y'_n + y'_{n-1}] \quad (19)$$

where:

$$x'_n = f(x_n, y_n, t_n) \quad (20)$$

$$y'_n = g(x_n, y_n, t_n) \quad (21)$$

Consideration of the Runge-Kutta and the Milne algorithms shows that Milne's method requires only two evaluations of  $f$  and  $g$  per time step, whereas Runge-Kutta requires four. This makes Milne's method more efficient.

Steady flow between a source/sink pair. Consider the steady flow of fluid between a line source and a line sink of equal strength =  $Q$ , separated by a distance =  $a$ . Let the source/sink pair be located in a homogeneous, isotropic medium of infinite extent, and saturated thickness

b. Suppose that at time zero the concentration of solute at the source is changed from zero to  $C_0$ .

The well-known time dependent solution for the concentration of fluid recovered at the sink depends on the travel time of fluid particles (e.g. Charbeneau and Street, 1979). Travel time  $t$  is expressed as a function of  $\theta$ , the direction of travel of a particle as it issues from the source. If the angle  $\theta$  is measured from a line between the source and sink, then:

$$t = \frac{\pi b \phi a^2}{Q} \frac{1}{\sin^2 \theta} [1 - \theta \cot \theta] \quad \theta > 0 \quad (22)$$

where  $\phi$  is the effective porosity. For  $\theta = 0$ , the minimal travel time  $t_m$  is:

$$t_m = \frac{\pi b \phi a^2}{3Q} \quad (23)$$

At time  $t > t_m$  the relative concentration of recovered fluid is:

$$\frac{C}{C_0} = \frac{1}{\pi} \theta(t) \quad (24)$$

where the function  $\theta(t)$  is defined by (22).

The analytical solution to the source/sink problem was compared with a numerical solution obtained via the method of characteristics and the Runge-Kutta algorithm. Variables were assigned the values:  $a = 500$  m,  $Q = 10000$  m<sup>3</sup>/days,  $b = 50$  m,  $\phi = 0.2$ . The numerical calculation began with  $\Delta t = 0.05$  day; subsequent values of  $\Delta t$  were selected so as to allow fluid particles to travel about 10 meters per time step. Both analytical and numerical results are plotted in Figure 1; note that the two solutions practically coincide.

Since the concentration of fluid recovered at the sink varies with time, the transport may be viewed as a mixing process. In fact, this mixing or "apparent dispersion" is obviously just the result of nonuniform flow. The source/sink example leads to the conclusion that unrepresented nonuniform flow may result in considerable unexplained "dispersion."

Transport in heterogeneous media. Consider the transport of a conservative solute in a two dimensional steady flow field. The flow domain is assumed to be rectangular,  $L$  by  $H$ , having the distributions of transmissivity and effective porosity as shown in Figures 2 and 3.

Solution of the transport problem begins with the determination of flow field, which in turn begins with finding the hydraulic potential. Using the linearized Boussinesq equation, Daly and Morel-Seytoux (1981) determined an analytic solution to this problem subject to the boundary conditions on the potential  $h$ :

$$h(0,y) = 0 \quad h(L,y) = \lambda$$

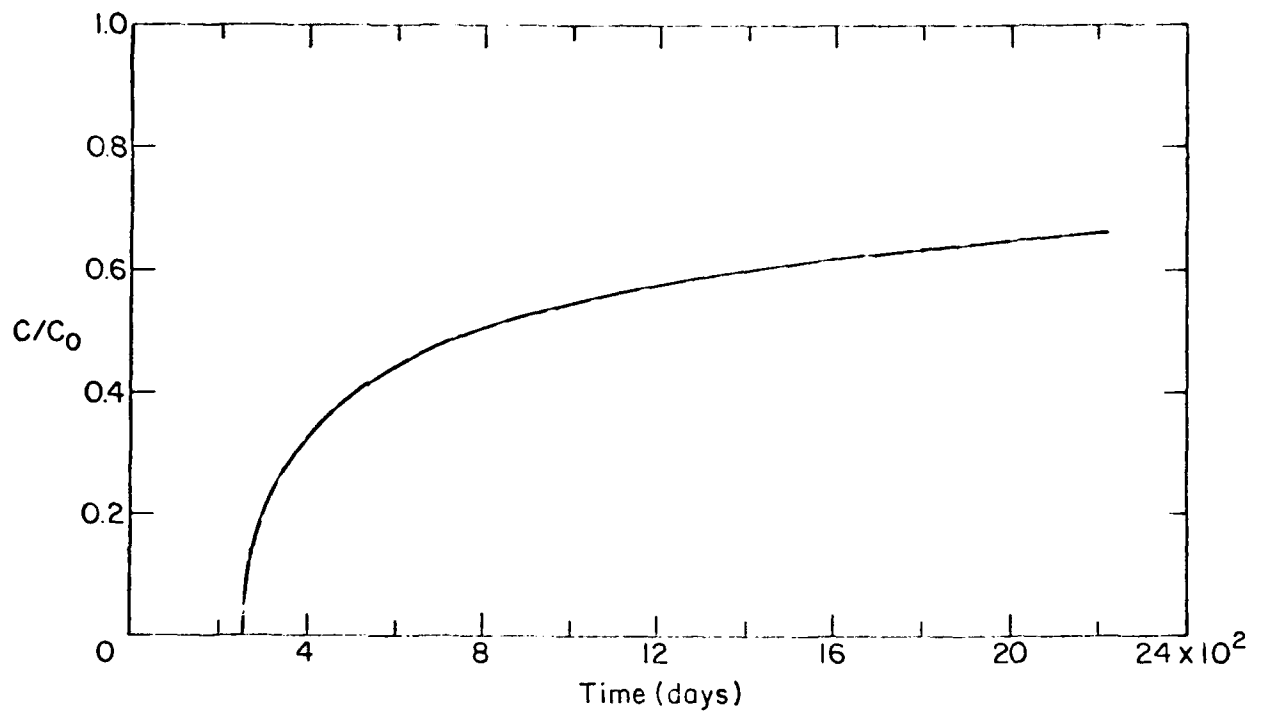


Figure 1. Relative concentration of fluid at the producing well of a source-sink pair.

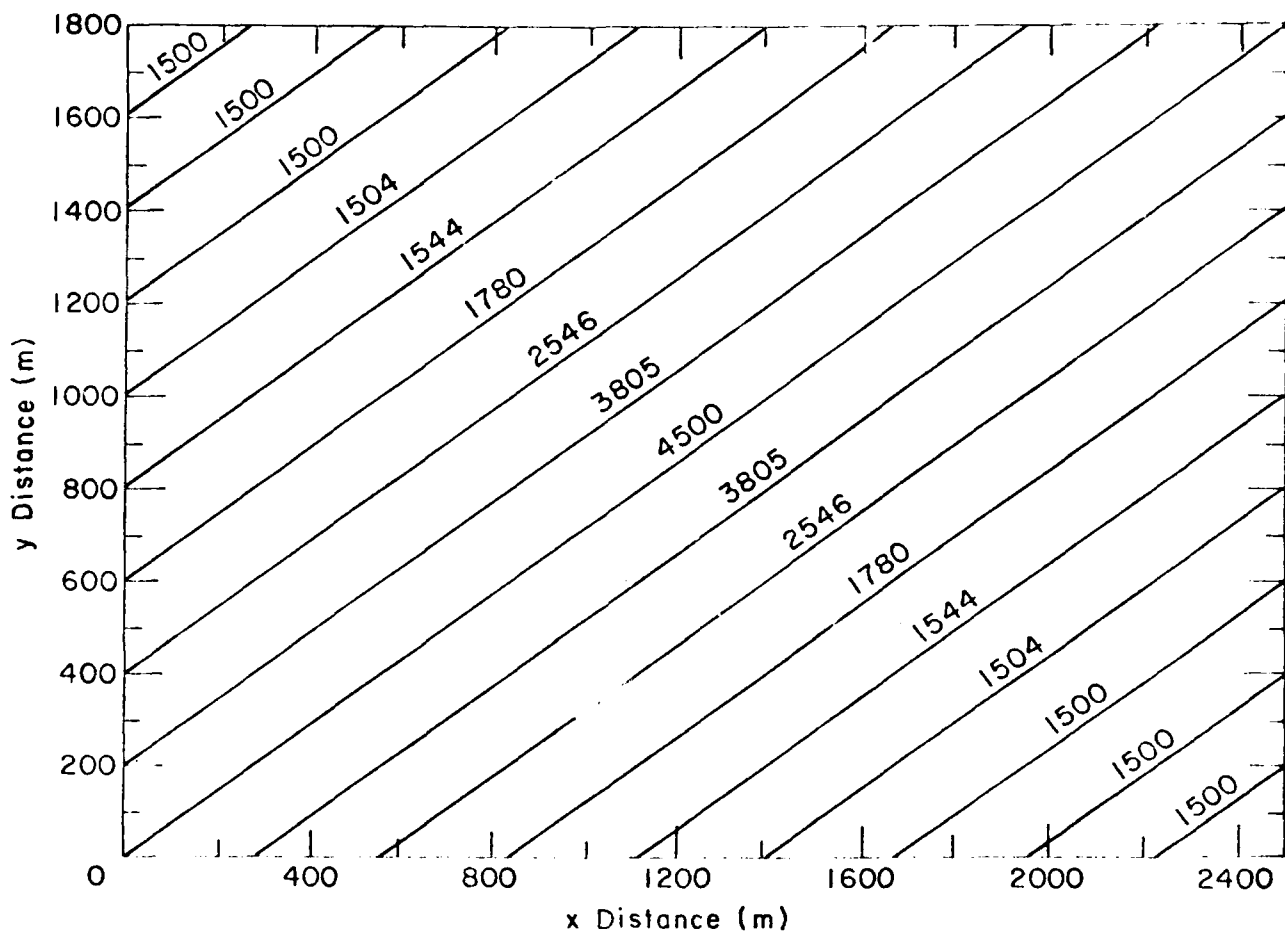


Figure 2. Distribution of aquifer transmissivity [ $\text{m}^2/\text{day}$ ].

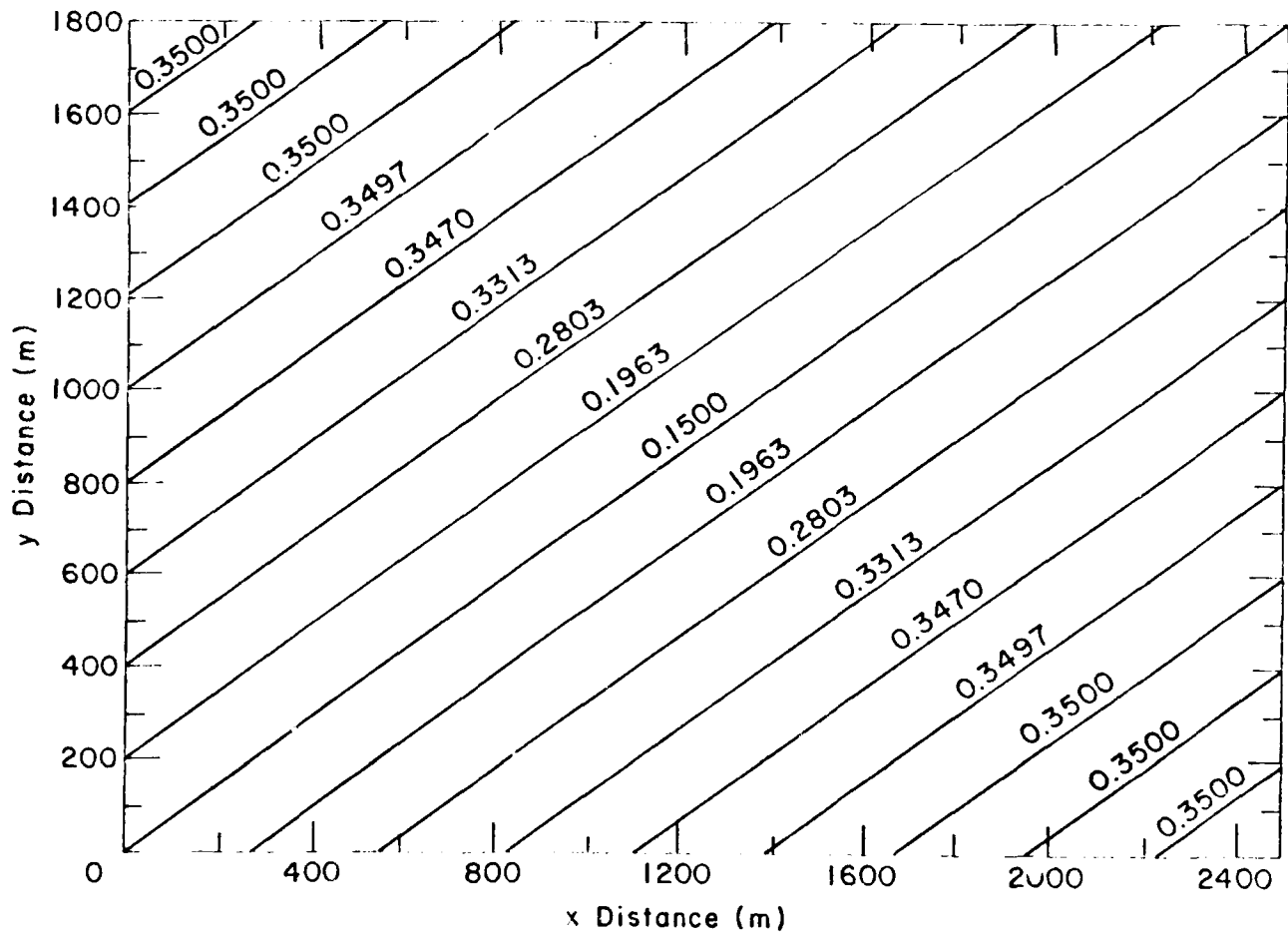


Figure 3. Distribution of aquifer porosity [dimensionless].

AD-A128 683

TRANSACTIONS OF THE CONFERENCE OF ARMY MATHEMATICIANS  
(28TH) HELD AT BETHESDA MARYLAND ON 28-30 JUNE 1982(U)  
ARMY RESEARCH OFFICE RESEARCH TRIANGLE PARK NC FEB 83

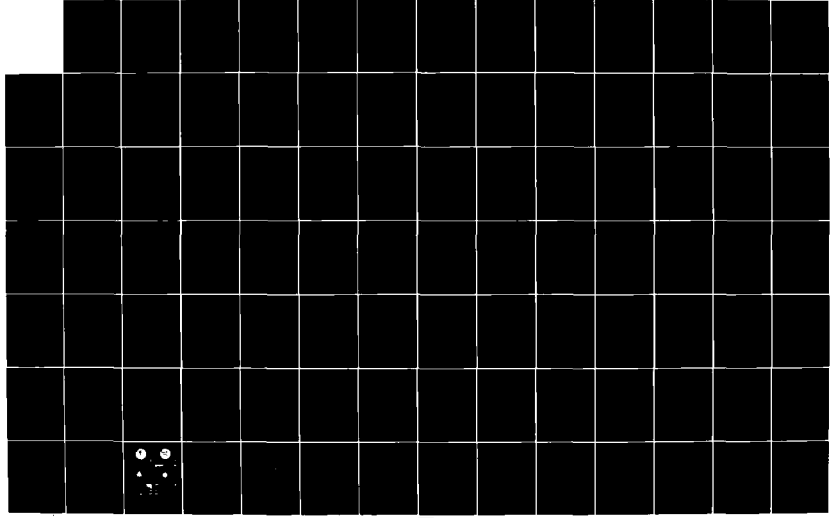
2/6

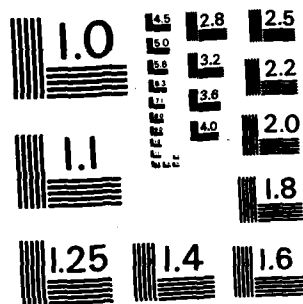
UNCLASSIFIED

ARO-83-1

F/G 12/1

NL





MICROCOPY RESOLUTION TEST CHART  
NATIONAL BUREAU OF STANDARDS-1963-A

$$\frac{\partial h}{\partial y}(x,0) = \frac{\partial h}{\partial y}(x,H) = 0 \quad (25)$$

Their solution is:

$$h(x,y) = \frac{2}{LH} \sum_{n=1}^N \Lambda(n,0) \sin \frac{n\pi x}{L} + \frac{x\lambda}{L} + \frac{4}{LH} \sum_{m=1}^M \sum_{n=1}^N \Lambda(n,m) \sin \frac{n\pi x}{L} \cos \frac{m\pi y}{H} \quad (26)$$

where the Fourier coefficients  $\Lambda$ , dependent on medium heterogeneity, are found by the application of an integral transform method.

The specific discharge (and average linear velocity) associated with the potential distribution of (26) is obtained from Darcy's law. Equation (26) is easily differentiated to yield the hydraulic gradient. For the problem presented here:  $L = 2500$  m,  $H = 1800$  m,  $\lambda = 10$  m, and saturated thickness is assumed constant and equal to 50 m. Figure 4 is a vector diagram of specific discharge.

The trajectories of fluid particles (located initially along the right hand vertical edge of Figure 4) were calculated by the Runge-Kutta, predictor-corrector method. A constant time interval of 100 days was used. The calculated trajectories define the streamlines shown in Figure 5; triangles are used to locate particles at 100-day intervals.

The movement of a sharp concentration front through the medium is shown in Figure 6. It is assumed that at time zero the concentration of fluid along the right hand boundary was instantaneously changed from zero to  $C_0$ . In the figure, the front is plotted at 200-day intervals. The movement of any particular point on the front is found by following that point along its associated streamline.

Consider the fluid which exits the porous medium at the left hand side of Figure 4. The average concentration of that fluid can be determined by calculating the time of breakthrough of many individual stream tubes. The ratio of the outflow produced by the tubes which have broken through to the total outflow can be obtained at any time. That ratio gives the relative concentration of the fluid flowing out of the medium. Using many more stream tubes than are shown in Figure 5, the calculation procedure was performed. The result is plotted as the solid line in Figure 7 (the "observed" breakthrough curve).

Using dispersion to account for the shape of the breakthrough curve.  
Suppose that the existing heterogeneity of the preceding problem is unknown. Suppose also that an experiment is conducted to determine a breakthrough curve; the result is the "observed" breakthrough curve of Figure 7.

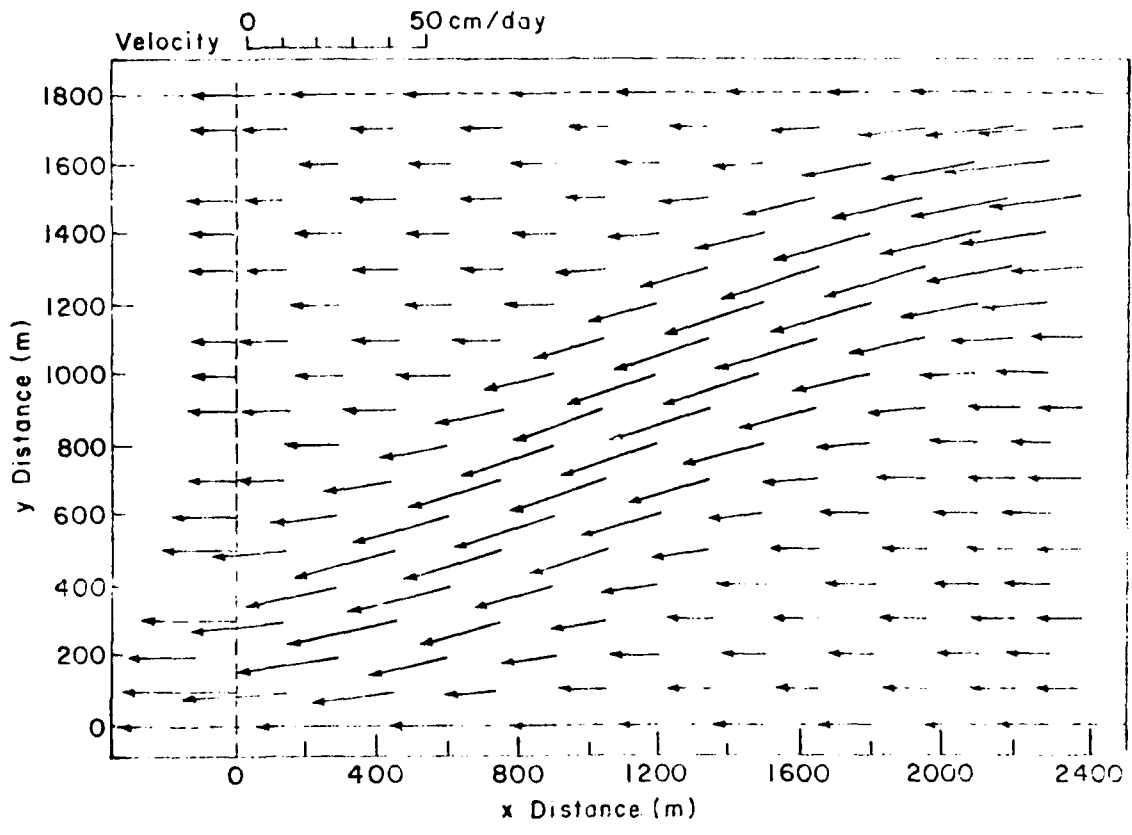


Figure 4. Specific discharge; flow pattern for two dimensional steady state flow.

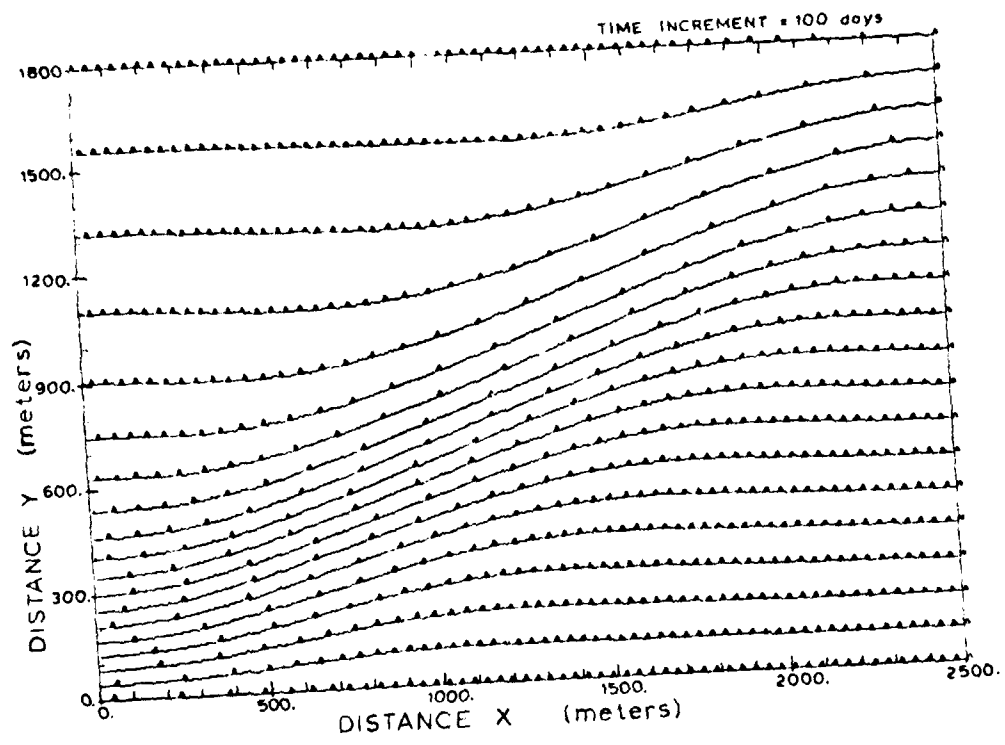


Figure 5. Streamline pattern for the flow field of Figure 4.

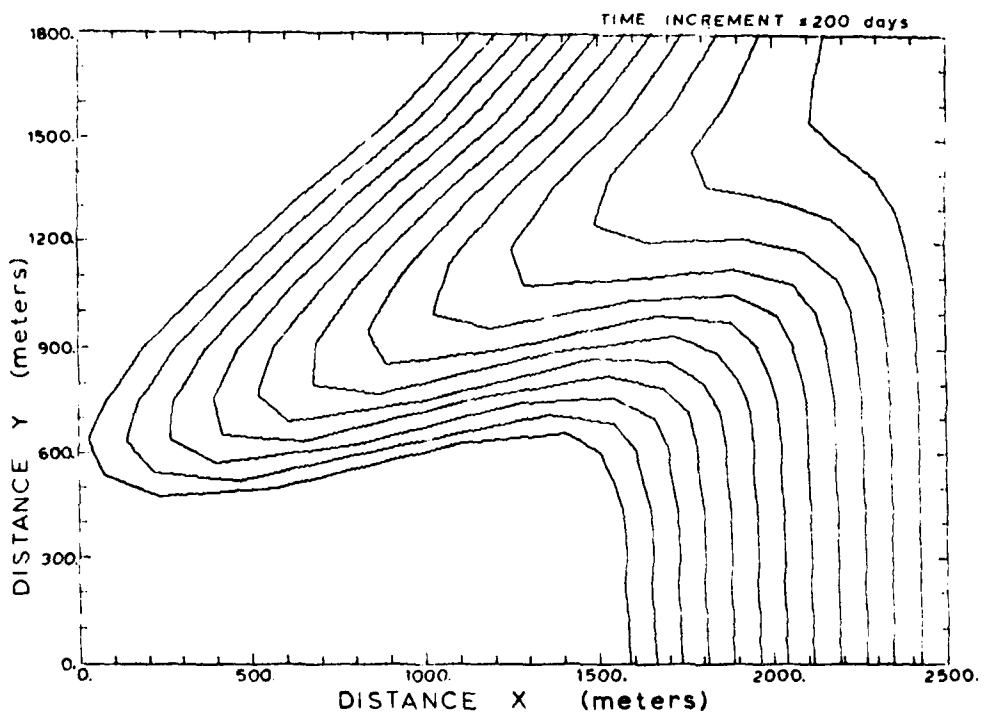


Figure 6. Movement of a solute front in the flow field of Figure 4.

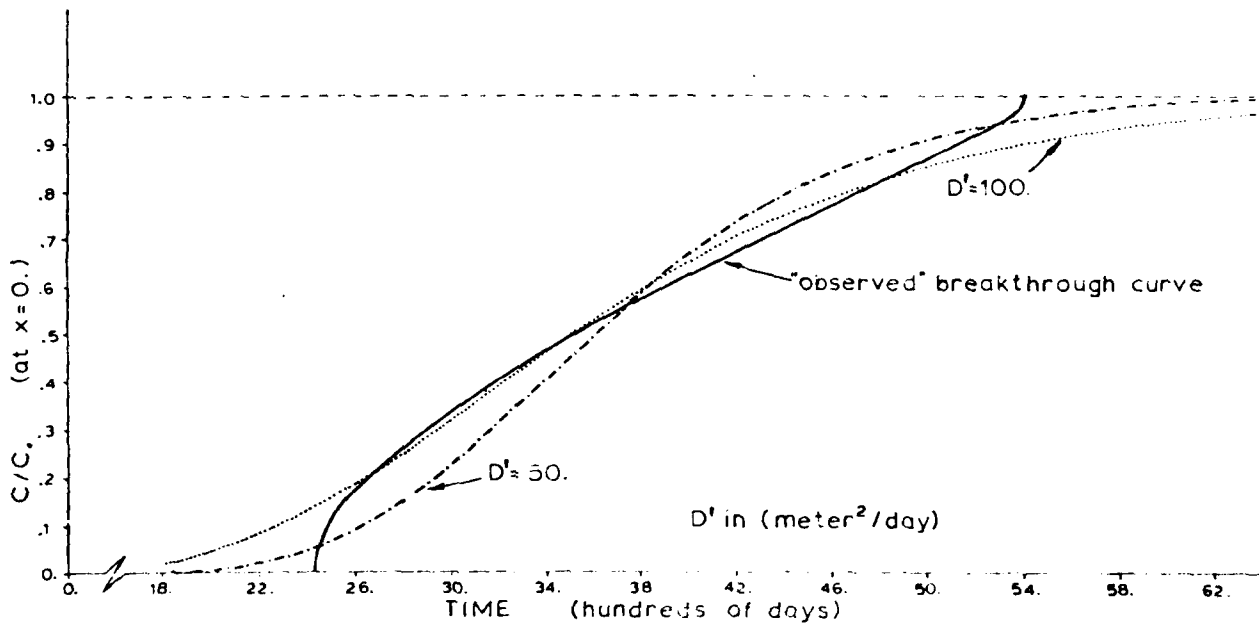


Figure 7. Breakthrough curves for the moving solute front of Figure 6.

If the porous medium were assumed homogeneous, all streamlines in Figure 5 would be parallel to the x axis. Flow would be steady and uniform and the problem could be considered one dimensional. A solution to the one dimensional advection-dispersion equation for steady flow has been obtained by Ogata and Banks (1961). The differential equation is:

$$\frac{\partial C}{\partial t} - D' \frac{\partial^2 C}{\partial x^2} + u \frac{\partial C}{\partial x} = 0 \quad u \geq 0 \quad (27)$$

subject to:

$$C(0,t) = C_0; \quad C(\infty,t) = 0 \quad (28)$$

and the initial condition:

$$C(x,0) = 0 \quad (29)$$

where  $u$  = average linear velocity;  $D' = D/\phi$ . After a change of origin, the solution for the breakthrough curve is: at  $x = 0$ :

$$\frac{C}{C_0} = \frac{1}{2} \operatorname{erfc} \frac{L-ut}{2\sqrt{D'T}} + e^{\frac{uL}{D'}} \operatorname{erfc} \frac{L+ut}{2\sqrt{D'T}} \quad (30)$$

For the problem considered here  $L = 2500$  meters and

$$u = \frac{v}{\phi} = 0.6745 \text{ m/day} \quad (31)$$

Several estimates of the coefficient  $D'$  can be made. The resulting breakthrough curves are plotted in Figure 7 for the estimates  $D' = 50$  and  $100 \text{ m}^2/\text{day}$ . Note that these two curves give an approximate fit to the observed breakthrough curve.

In a series of experiments dealing with one dimensional dispersion, Harleman et al. (1963) correlated dispersion coefficient with flow and media properties. A variety of unconsolidated materials were used. The flow and transport problem were such that the analysis of Ogata and Banks (1961) could be applied. Determining the breakthrough curve and the average linear velocity gave Harleman et al. the ability to estimate  $D'$  from Equation (30). Their correlation formula predicts for sand grains:

$$\frac{D'}{v} = 0.90 (R_{d50})^{1.2} \quad (32)$$

where:  $v$  is the kinematic viscosity [ $L^2/T$ ],

$$R_{d50} = \frac{|u|d_{50}}{v} \quad (33)$$

and  $d_{50}$  is the 50% grain size of the porous material.

If the shape of the observed breakthrough curve of Figure 7 is assumed to be the result of dispersion, (32) can be used to estimate  $d_{50}$  for the

porous material. With  $D' = 100 \text{ m}^2/\text{day}$ ,  $d_{50} = 49.32 \text{ m}$ ; for  $D' = 50 \text{ m}^2/\text{day}$ ,  $d_{50} = 27.68 \text{ m}$ .

CONCLUSIONS. The above results dramatically show that: (a) even modest heterogeneity of porous media properties cannot be properly accounted for by dispersion, and (b) genuine dispersion is easily overwhelmed by the effects of heterogeneity.

ACKNOWLEDGMENT. The author wishes to thank the U.S. Army Toxic and Hazardous Materials agency (USATHAMA) for funding the report of these results through project P387.05.0056.

#### REFERENCES

- Bachmat, Y., and J. Bear, 1964. The general equations of hydrodynamic dispersion in homogeneous, isotropic porous mediums, *Journal of Geophysical Research*, vol. 69, no. 12, pp. 2561-2567.
- Buyevich, Y.A., A.I. Loenov, and V.M. Safrai, 1969. Variations in filtration velocity due to random large scale fluctuations of porosity, *Journal of Fluid Mechanics*, vol. 37, pp. 371-381.
- Charbeneau, R.J., and K.L. Street, 1979. Modeling groundwater flow fields containing point singularities: streamlines, travel times, and breakthrough curves, *Water Resources Research*, vol. 15, no. 6, pp. 1445-1450.
- Daly, C.J., 1979. Analytical/numerical methods for groundwater flow and quality problems, doctoral dissertation, Colorado State University, Fort Collins, 167 pp.
- Daly, C.J., and H.J. Morel-Seytoux, 1981. An integral transform method for the linearized Boussinesq groundwater flow equation, *Water Resources Research*, vol. 17, no. 4, pp. 875-884.
- Gelhar, L.W., A.L. Gutjahr, and R.L. Naff, 1979. Stochastic analysis of macrodispersion in a stratified aquifer, *Water Resources Research*, vol. 15, no. 6, pp. 1387-1397.
- Harleman, D.R.F., P.F. Mehlhorn, and R.R. Rumer, 1963. Dispersion-permeability correlation in porous media, *Journal of the Hydraulics Division, ASCE*, vol. 89, no. HY2, pp. 67-85.
- Klotz, D., and H. Moser, 1974. Hydrodynamic dispersion as aquifer characteristic, *Isotope Techniques in Groundwater Hydrology*, vol. 2, International Atomic Energy Commission, pp. 341-354.
- Konikow, L.F. and J.D. Bredehoeft, 1974. Modeling flow and chemical quality changes in an irrigated stream-aquifer system, *Water Resources Research*, vol. 10, no. 3, pp. 546-562.
- Ogata, A., and R.B. Banks, 1961. A solution of the differential equation of longitudinal dispersion in porous media, U.S. Geological Survey Professional Paper 411-A.
- Pinder, G.F., 1973. A Galerkin finite element simulation of groundwater contamination on Long Island, New York, *Water Resources Research*, vol. 9, no. 6, pp. 1657-1669.
- Skibitski, H.E., and G.M. Robinson, 1963. Dispersion in groundwater flowing through heterogeneous materials, U.S. Geological Survey Professional Paper 386-B.

AD P001016



AN ELECTRIC THEORY OF OSMOSIS  
FOR DILUTE SALINE SOLUTIONS

DONALD L. BUTTZ

ANALYSIS DIVISION  
ARMY MATERIEL TEST AND EVALUATION DIRECTORATE  
US ARMY WHITE SANDS MISSILE RANGE,  
NEW MEXICO 88002

ABSTRACT

Osmosis can be redefined in electrical terms and can be explained by an electrostatic model. A formula for the variation of the dielectric coefficient with temperature is developed for water. A relationship for the osmotic pressures of dilute saline solutions is put forth as a theoretical result, given the volume, temperature, number of moles, and average inter-ionic distance. This theory assumes that the interionic distances are sufficiently large such that the osmotic pressure is proportional to the concentration at constant temperature. This paper describes osmosis through physical electrostatic theory as opposed to the usual chemical diffusion theory. A generalized mathematical model is developed which has application to osmosis for dilute saline solution.



REPRODUCED FROM ADP-1016

## CHAPTER I

### Introduction

Osmosis is the flow of a solvent through a semi-permeable membrane. A semi-permeable membrane is an ideal membrane which will permit the passage of the solvent but not of dissolved substance. There is a tendency for solutions separated by such a membrane to become equal in solute concentration; thus, a solvent will flow from a more dilute to a more concentrated solution and the solutions will tend to become equal in concentration. Osmotic pressure is the pressure which must be applied to a solution in order to prevent the flow of solvent through a semi-permeable membrane separating the solution and the pure solvent. The osmotic pressure, temperature and volume of a dilute solution of a non-electrolyte are connected by laws exactly similar to the gas laws, but this investigation is restricted to osmotic pressures produced by dilute salt solutions.

The purpose of this study is to explain osmosis of a dilute saline solution using an electrostatic model. Thus, osmosis should be understood as an electrical phenomenon. Therefore, a new definition of osmosis seems to be in order.

## CHAPTER II

### Electric Theory Background for Osmosis

Since the nature of the problem is electrostatic, let us state Maxwell's two postulates of electrostatics in differential form:

$$\nabla \cdot \mathbf{D} = \rho \quad (2-1)$$

$$\nabla \times \mathbf{E} = 0 \quad (2-2)$$

Where  $\mathbf{D}$  is the electric displacement and  $\mathbf{E}$  is the electric field strength. In free space,  $\mathbf{D}$  is related to  $\mathbf{E}$ , that is,

$$\mathbf{D} = \epsilon_0 \mathbf{E} \quad (2-3)$$

Let the potential of the electrostatic field be  $\phi$ .  $\mathbf{E}$  is related to  $\phi$  by the relation,

$$\mathbf{E} = -\nabla\phi \quad (2-4)$$

A liquid solvent has a dielectric coefficient,  $k_e$ . If the medium is homogeneous and has a dielectric coefficient, then  $\mathbf{D}$  and  $\mathbf{E}$  are related by the equation,

$$\mathbf{D} = k_e \epsilon_0 \mathbf{E} \quad (2-6)$$

and similarly for expression (2-2) we have,

$$\nabla \times k_e \mathbf{E} = 0$$

The equations (2-2) and (2-3) become

$$\nabla \cdot (k_e \mathbf{E}) = \frac{\rho}{\epsilon_0} \quad (2-7)$$

$$\nabla \times (k_e \mathbf{E}) = 0 \quad (2-8)$$

These relations hold provided that the solvent is an isotropic dielectric fluid and  $k_e$  is independent of the magnitude of the electric field strength.

Applying the divergence theorem to (2-7) we have,

$$\oint (k_e \mathbf{E}) \cdot d\mathbf{S} = \int \frac{\rho}{\epsilon_0} dv \quad (2-9)$$

and after rearrangement we arrive at the relation:

$$\mathbf{E} = \frac{e_i}{4\pi\epsilon_0 k_e r^2} \quad (2-10)$$

Multiplying equation (2-10) by  $e_j$ , we have the coulombic force between charge  $e_i$  and  $e_j$  in a dielectric medium.

That is,

$$F = \frac{e_i e_j}{4\pi\epsilon_0 k_e r^2} \quad (2-11)$$

The interaction energy between charges  $e_i$  and  $e_j$  in a dielectric is,

$$U = \frac{e_i e_j}{4\pi\epsilon_0 k_e r} \quad (2-12)$$

and analogously, the interaction energy between charges  $e_i$  and  $e_j$  in free space is,<sup>1</sup>

$$U = -\frac{e_i e_j}{4\pi\epsilon_0 r} + \frac{e_i e_j}{4\pi\epsilon_0 k_e r} \quad (2-13)$$

There are attractive and repulsive electrostatic forces

in (2-13). By analogy to the well-known potential energy of a pair of ions in an ionic crystal, we have the following graph:<sup>2</sup>

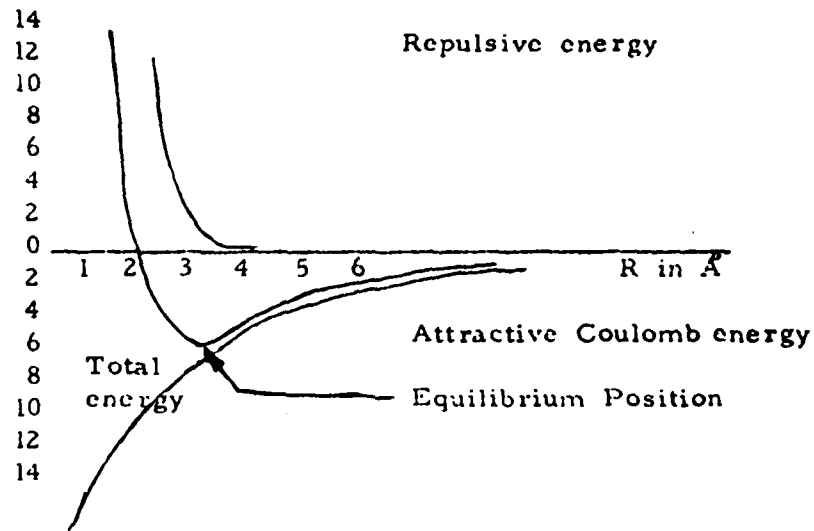


Figure 1 - Energy per ion pair of an ionic crystal, showing Madelung and repulsive contributions.

A salt is composed of ions forming an ionic crystal.

The main contribution to the binding energy of an ionic crystal is electrostatic and is called the Madelung energy.<sup>3</sup>

Let  $U_{ij}$  be the interaction energy between ions  $i$  and  $j$ .

$$U_{ij} = - \frac{e_i e_j}{4 \pi \epsilon_0 r_{ij}} \quad (2-14)$$

Let  $U_i$  be a sum of energy involving all interactions with ion  $i$ .

$$U_i = \sum_j U_{ij} \quad (2-15)$$

This sum includes all ions except  $i = j$ . The total lattice energy of a crystal is composed of  $N$  ion pairs or  $2N$  ions. The equation giving the total lattice or crystal energy for the formation of a mole of oppositely charged ions is,<sup>4</sup>

$$U_c = - \frac{N_0 A Z_+ Z_- e^2}{4 \pi \epsilon_0 r_0} \left( 1 - \frac{1}{n'} \right) \quad (2-16)$$

where,

$N_0$  = Avogadro's number

$A$  = Madelung constant

$Z_+$  = Charge on cation

$Z_-$  = Charge on anion

$e$  = Electronic charge

$n'$  = Empirical constant

$r_0$  = Nearest neighbor separation

For monovalent ions  $Z_+ = Z_- = 1$  and  $n'$  is on the order of 9. In this case equation (2-16) gives an approximate crystal lattice energy:

$$U_c = - \frac{N A e^2}{4 \pi \epsilon_0 r_0} \quad (2-17)$$

Thus, the chemical bond in the alkali halides is assumed to be strictly electrostatic. Also, we have as a first order approximation, assumed the ions to be point charges. The positive and negative ions can be described by Coulomb's Law. Note that a repulsive term operates to establish an equilibrium separation distance  $r_0$  between positive and

negative ions. The repulsive term is short range in its effect.

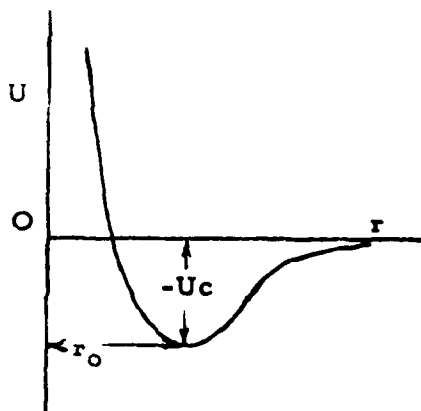


Figure 2 - Potential energy versus ionic separation.

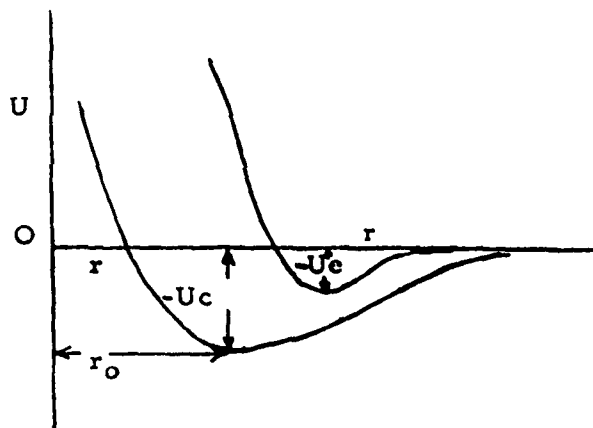


Figure 3 -  $U_c$  is reduced in a dielectric and becomes  $-U_e$ .

Work must be done to separate the positive and negative ions from each other. The amount of energy required per mole is called the lattice energy. As an example, the lattice energy of NaCl is 184 Kcal/mole.<sup>5</sup> When a salt is dissolved in a solvent, the electrostatic attraction between the ions is

reduced by a factor of  $1/k_e$  .

In order that dissolution may take place, solute-solute and solvent-solvent attractions must be overcome by solute-solvent attraction.<sup>6</sup> Ionic solutes are soluble in polar solvents such as water. Two classes of dielectrics exist, one polar and the other non-polar. The non-polar molecules are the ones in which the centers of the positive nuclei and the electron cloud are coincident. Non-polar molecules are usually symmetric, such as  $H_2$ ,  $N_2$ ,  $O_2$ , etc. Polar molecules do not have coincident centers.<sup>7</sup> Examples of these are:  $H_2O$ ,  $NaCl$ , etc. Under the influence of an electric field, the charges of a non-polar molecule become displaced. These non-polar molecules become polarized by the field and we have what is called induced dipoles. The restoring force between charges equals the force produced by the electric field. A dielectric consists of polar molecules, which have permanent dipoles and these dipoles are oriented at random due to thermal agitation with no external field present. Under the applied electric field, some orientation takes place. The stronger the field, the greater the number of dipoles pointing in the direction of the field. If a salt is dissolved in water, there is a force of attraction which pulls the water dipoles in the direction of the ions' electric field.

This force can be expressed as: <sup>8</sup>

$$F_x = \frac{\alpha \partial E^2}{2 \partial x} \quad (2-18)$$

where  $\alpha$ , is the polarizability.

The above shows that the force pulls the molecule in the direction in which the magnitude of the field increases most rapidly. The field of the ion varies as  $1/r^2$ , so that  $E^2$  varies as  $1/r^4$  taking the derivative with respect to  $x$  and multiplying by  $\alpha/2$  the force of attraction varies inversely as the fifth power of the distance, and the potential energy inversely as the fourth power: <sup>9</sup>

$$U = -\frac{1}{2} \cdot \frac{\mu^2 e^2}{3 k_b T (4 \pi \epsilon_0 k_e)^2} \frac{1}{r^4} \quad (2-19)$$

A dipole is acted on not only by a force, but also by a torque in an electric field, and this torque is proportional to the field strength rather than to its rate of change with position. The potential energy associated with this torque is,

$$U = -\mu E \cos \theta \quad (2-20)$$

The electric field due to a dipole radially outward is: <sup>10</sup>

$$E_r = \frac{2 \mu \cos \theta}{4 \pi \epsilon_0 k_e r^3} \quad (2-21)$$

The interacting force between an ion and a dipole in a dielectric  $k_e$  is:

$$F = \frac{2 e \mu \cos \theta}{4 \pi \epsilon_0 k_e r^5} \quad (2-22)$$

The  $\cos \theta$  represents a thermal average. To calculate this average we use the Boltzmann Distribution Law. The relative probability of finding a molecule in an element of solid angle  $d\Omega$  is proportional to  $\exp(-U/k_b T)$ , where  $U = -\mu E \cos \theta$ . Therefore, the thermal average for  $\cos \theta$  is as follows, <sup>11</sup>

$$\langle \cos \theta \rangle = \frac{\int_0^\pi e^{-\beta U} \cos \theta d\Omega}{\int_0^\pi e^{-\beta U} d\Omega} \quad (2-23)$$

where  $\beta = \frac{1}{k_b T}$

and  $d\Omega = 2 \pi \sin \theta \cdot d\theta$

after some manipulation, we find that

$$\langle \cos \theta \rangle = \frac{1}{3} \frac{\mu E}{k_b T} \quad (2-24)$$

Applying equation (2-24), equation (2-22) becomes,

$$F = \frac{2e\mu}{4\pi\epsilon_0 k_e r^3} \left( \frac{1}{3} \frac{\mu E}{k_b T} \right) \quad (2-25)$$

Recalling equation (2-10) and substituting into (2-25) we have,

$$F = \frac{2e\mu}{4\pi\epsilon_0 k_e r^3} \left( \frac{1}{3} \frac{\mu}{k_b T} \frac{e}{4\pi\epsilon_0 k_e r^2} \right) \quad (2-26)$$

Simplifying, we get

$$F = \left( \frac{2e^2 \mu^2}{3k_b T (4\pi\epsilon_0 k_e)^2} \right) \frac{1}{r^5} \quad (2-26)$$

and the ion-dipole interaction energy becomes,

$$U = - \frac{1}{2} \left( \frac{e^2 \mu^2}{3k_b T (4\pi\epsilon_0 k_e)^2} \right) \frac{1}{r^4} \quad (2-27)$$

This equation is identical to equation (2-19), arrived at by

two different approaches.

Equation (2-27) represents the interaction energy between one ion and one dipole. One would have to sum all the ion-dipole interactions for  $r$ , ranging from one ion to the nearest ion and then take into account all the ions in solution to calculate the total ion-dipole interaction energy simply by knowing the electrostatic binding energy before and after the salt is dissolved and finding the difference. This difference must be reduced by a factor due to thermal agitation opposing complete alignment of the dipoles with the ion field. Including this factor, a net energy for doing work in attracting the dipoles is determined. We have therefore excluded the work done to orient the dipoles. The other portion of the work does the actual pulling of the dipoles. From this information, we can calculate the osmotic pressure.

### Calculations

Recall equation (2-17)

$$U_c = - \frac{N_o A e^2}{4 \pi \epsilon_o r_o} \quad (2-28)$$

where,

A = Madelung constant (NaCl structure = 1.747565; CsCl structure = 1.76276)<sup>12</sup>

$N_o$  = Avogadro's number =  $6.0223 \times 10^{23}$  / mole

$r$  = Interionic separation

$$e = \text{Charge} = 1.602 \times 10^{-19} \text{ coulomb}$$

$U_c$  is the stored attractive potential energy before the solvent is introduced. After the solvent is introduced, the stored attractive potential energy is less by a factor  $1/k_e$ , so that the difference in these energies is the work done to pull and orient the solvent in the lattice.<sup>13</sup>

$$U_c = \left(1 - \frac{1}{k_e}\right) \text{ Joules/mole} \quad (2-29)$$

Given the number of moles of solute  $n$  of the salt, we can determine the total work done on the solvent.

$$U_T = U_c \left(1 - \frac{1}{k_e}\right) \cdot n \quad (2-30)$$

The fraction of the total work done on the solvent goes into atomic and orientation polarization.

$$\langle \cos \theta \rangle = \frac{1}{3} \frac{\mu E}{k_b T} \quad (2-31)$$

$$\mu = \text{dipole moment for H}_2\text{O} = 4.1 \times 10^{-30} \text{ coul-m.}$$

$$k_b = \text{Boltzmann's Constant} = 1.38 \times 10^{-23} \text{ Joule/}^\circ\text{K.}$$

$$T = 298^\circ\text{K or } 25^\circ\text{C.}$$

Since we are considering a solute saline solution, assume a reasonable ion separation of approximately  $10 \text{ \AA}$  for a concentration of 1 molar.<sup>14</sup> We can then proceed to calculate the

approximate E field strength for dilute cases:

$$E = \frac{c}{4\pi\epsilon_0 k_c r^2} \quad (2-32)$$

$$E = 0.184 \times 10^8 \text{ V/m} \quad (2-33)$$

$$\langle \cos \theta \rangle = \frac{1}{3} \frac{\mu E}{k_b T} = 6.115 \times 10^{-3} \quad (2-34)$$

This number is the fraction which accounts for orientation polarization of the solvent, provided it has a permanent dipole as for the case of water.<sup>15</sup>

By multiplying this fraction times the total work done on the solvent, we compute the work which tends to pull the solvent toward the ionic "crystal".

$$U_T \langle \cos \theta \rangle = U_C \left(1 - \frac{1}{k_e}\right) \cdot n \langle \cos \theta \rangle \quad (2-35)$$

Thus we have excluded the work to orient the solvent molecules.

$$U_C \left(1 - \frac{1}{k_e}\right) \cdot n \langle \cos \theta \rangle \quad (2-36)$$

By dividing this equation by the volume of the pure solvent, we have determined an energy density which is otherwise the osmotic pressure .

$$\pi_o = U_C \left(1 - \frac{1}{k_e}\right) \cdot n \langle \cos \theta \rangle / \tau \quad (2-37)$$

$U_c$  for NaCl is 180.5 kcal/mole. By converting to new units, it is

$$U_c = 7.46 \times 10^5 \text{ Joule/mole}$$

Given a 1 molal concentration, we can dissolve 1 mole of solute in 1000 grams of solvent. Therefore,  $n = 1$ .

The volume of 1000 grams of water is  $10^{-3} \text{ m}^3$ , hence,  
 $\tau = 10^{-3} \text{ m}^3$ .

We need to convert into atmospheres by dividing by  $1.013 \times 10^5 \text{ Nt/m}^2 \text{ atm}$ . Let  $\gamma = 1.013 \times 10^5 \text{ Nt/m}^2 \text{ atm}$ .

$$\pi_o = U_c \left(1 - \frac{1}{k_c}\right) \cdot n \langle \cos \theta \rangle / (\gamma \tau) \quad (2-38)$$

$$U_c = 7.46 \times 10^5 \text{ Joule/mole}$$

$$\left(1 - \frac{1}{k_c}\right) = .98723$$

$$k_c = 78.3 \text{ at } 25^\circ\text{C}$$

$$n = 1$$

$$\langle \cos \theta \rangle = 6.115 \times 10^{-3}$$

$$\gamma = 1.013 \times 10^5 \text{ Nt/m}^2 \text{ atm}$$

$$\tau = 10^{-3} \text{ m}^3$$

$$\pi_o = 44.46 \text{ atm}$$

$$\pi_o = 23.70 \text{ atm at } 0.535 \text{ (m), sea water concentration considering NaCl only.}$$

Given a volume of 1000 grams of water =  $10^3 \text{ cm}^3$ .

and taking the density of  $\text{H}_2\text{O}$   $1 \text{ gm/cm}^3 = 10^{-3} \text{ m}^3$ ,

$$\begin{aligned} \frac{1000 \text{ gm}}{1 \text{ gm/cm}^3} &= 10^3 \text{ cm}^3 \\ &= 10^3 \times 10^{-6} \text{ m}^3 \\ &= 10^{-3} \text{ m}^3 \end{aligned}$$

$$(m) = 1 \text{ mole} / 1000 \text{ gm}$$

$$\pi_0 = U_c \left(1 - \frac{1}{78.3}\right) \frac{Nt m n 6 \times 10^{-3}}{1.013 \times 10^5 \text{ Nt/m}^2 \text{ atm} (10^{-3} \text{ m}^3)}$$

$$\langle \cos \theta \rangle = .006 = E = \frac{4.1 \times 10^{-30} E}{12.33 \times 10^{-21}}$$

$$E = 0.18 \times 10^8 \text{ V/m}$$

$$r = 10 \text{ \AA}$$

## CHAPTER III

### Experimental Data

The following data is presented in tabular and graphical form. This data gives osmotic pressures as a function of molality. The osmotic pressures are listed in atmospheres at 25°C. Experimental data on the variation of the dielectric constant of water with temperature is provided. Also, an empirical relation is formulated to express that variation.

Figure 4 illustrates that for a dilute solution of NaCl the graph is reasonably linear.

In figure 5 we observe how osmotic pressure varies with molality for several salts.

TABLE 1 . - Osmotic Pressure of LiCl Solutions at 25°C.<sup>16</sup>

(m)	g	i = g.j	$\pi_0$
0.1	.939	1.378	4.58
0.2	.939	1.878	9.12
0.3	.945	1.890	13.88
0.4	.954	1.908	18.41
0.5	.963	1.926	23.6
0.6	.973	1.946	28.61
0.7	.984	1.968	33.65
0.8	.995	1.990	39.10
0.9	1.006	2.012	44.25
1.0	1.018	2.036	49.75
1.2	1.041	2.082	61.25
1.4	1.066	2.132	73.10
1.6	1.091	2.182	85.60
1.8	1.116	2.232	98.40
2.0	1.142	2.284	110.10
2.5	1.212	2.424	148.80
3.0	1.286	2.572	189.00
3.5	1.366	2.732	234.1
4.0	1.449	2.898	282.9
4.5	1.533	3.066	338.2
5.0	1.619	3.238	396.1
5.5	1.705	3.410	460.0
6.0	1.791	3.582	526.0

(m) = concentration  
 g = osmotic coefficient  
 j = 2 at infinite dilution i = 2  
 $\pi_0$  = i.(m). 24.5 osmotic pressure in atmospheres  
 $\tau$  = 298°K  
 $\rho$  = 10<sup>3</sup> Kg/m<sup>3</sup> H<sub>2</sub>O density  
 R = 8.314 Joules/mol°K  
 $\gamma$  = 1.013 x 10<sup>5</sup> Nt/m<sup>2</sup>atm  
 $\frac{\rho RT}{\gamma}$  = 24.5

TABLE 2. - Osmotic Pressure of NaCl Solutions at 25°C.<sup>17</sup>

(m)	g	$i = g.l$	$\pi_0$
0.1	0.932	1.864	4.56
0.2	0.925	1.850	9.04
0.3	0.922	1.844	13.55
0.4	0.920	1.840	18.02
0.5	0.921	1.842	22.6
0.6	0.923	1.846	27.12
0.7	0.926	1.852	31.80
0.8	0.929	1.858	36.37
0.9	0.932	1.864	41.20
1.0	0.936	1.872	45.80
1.2	0.943	1.886	55.50
1.4	0.951	1.902	65.25
1.6	0.962	1.924	75.5
1.8	0.972	1.944	85.9
2.0	0.983	1.966	96.2
2.5	1.013	2.026	124.1
3.0	1.045	2.090	153.2
3.5	1.080	2.160	185.1
4.0	1.116	2.232	218.9
4.5	1.153	2.306	254.1
5.0	1.192	2.384	293.0
5.5	1.231	2.462	332.0
6.0	1.271	2.542	374.0

TABLE 3 . - Osmotic Pressure of KCl Solutions at 25°C. <sup>18</sup>

(m)	$\rho$	$\rho \cdot \rho \cdot j$	$\pi_0$
0.1	0.927	1.854	4.54
0.2	0.913	1.826	8.95
0.3	0.906	1.812	13.31
0.4	0.902	1.804	17.70
0.5	0.899	1.798	22.1
0.6	0.898	1.796	26.4
0.7	0.897	1.794	30.79
0.8	0.897	1.794	35.1
0.9	0.897	1.794	39.46
1.0	0.897	1.794	44.0
1.2	0.899	1.798	52.8
1.4	0.901	1.802	62.0
1.6	0.904	1.808	71.0
1.8	0.908	1.816	80.0
2.0	0.912	1.836	90.0
2.5	0.924	1.848	113.0
3.0	0.937	1.874	138.0
3.5	0.950	1.900	163.0
4.0	0.965	1.920	188.0
4.5	0.980	1.960	216.0
5.0	- - -	- - -	- - -
5.5	- - -	- - -	- - -
6.0	- - -	- - -	- - -

TABLE 4 . - Osmotic Pressure of RbCl Solutions at 25°C. <sup>19</sup>

(m)	g	i = g . j	$\pi_0$
0.1	0.923	1.846	4.52
0.2	0.907	1.814	8.9
0.3	0.898	1.796	13.2
0.4	0.893	1.786	17.51
0.5	0.889	1.778	21.77
0.6	0.887	1.774	26.1
0.7	0.886	1.772	30.4
0.8	0.886	1.772	37.0
0.9	0.885	1.770	39.0
1.0	0.885	1.770	43.4
1.2	0.886	1.772	52.0
1.4	0.888	1.776	61.0
1.6	0.890	1.780	69.75
1.8	0.893	1.786	78.7
2.0	0.896	1.792	88.0
2.5	0.905	1.810	110.8
3.0	0.916	1.832	134.9
3.5	0.928	1.856	159.0
4.0	0.941	1.882	184.9
4.5	0.952	1.904	210.0
5.0	0.966	1.930	237.0
5.5	- - -	- - -	- - -
6.0	- - -	- - -	- - -

TABLE 5 . - Osmotic Pressure of CsCl Solutions at 25°C.<sup>20</sup>

(m)	g	$i = g \cdot j$	$\pi_0$
0.1	0.917	1.834	4.50
0.2	0.897	1.794	8.80
0.3	0.885	1.770	13.08
0.4	0.875	1.750	17.15
0.5	0.869	1.738	21.21
0.6	0.864	1.728	25.4
0.7	0.861	1.722	29.4
0.8	0.859	1.718	33.61
0.9	0.858	1.716	37.8
1.0	0.857	1.714	42.0
1.2	0.856	1.712	50.4
1.4	0.856	1.712	58.75
1.6	0.857	1.714	67.2
1.8	0.859	1.718	75.7
2.0	0.862	1.724	84.4
2.5	0.869	1.738	106.1
3.0	0.879	1.758	129.0
3.5	0.889	1.778	152.1
4.0	0.900	1.800	176.1
4.5	0.912	1.824	201.0
5.0	0.924	1.848	226.1
5.5	- - -	- - -	- - -
6.0	- - -	- - -	- - -

TABLE 6 . - Osmotic Pressure of NaCl Solutions at four different temperatures. <sup>21</sup>

(m)	25°C	40°C	60°C	100°C
0.001	0.05	0.05	0.05	0.06
0.01	0.47	0.49	0.52	0.57
0.05	2.31	2.41	2.53	2.75
0.10	4.56	4.76	5.00	5.42
0.20	9.04	9.44	9.93	10.74
0.40	18.02	18.84	19.83	21.45
0.60	27.12	28.40	29.92	32.35
0.80	36.37	38.14	40.22	43.48
1.00	45.80	48.08	50.76	54.87
2.00	96.2	101.3	107.3	115.9
3.00	153.2	161.6	171.0	184.2
4.00	218.9	230.5	243.3	260.8
5.00	295.2	309.4	325.2	346.5
6.00	384.1	400.2	418.0	442.2

TABLE 7 .- Osmotic Pressures for LiCl, NaCl, KCl, RbCl and CsCl.

(m)	LiCl	NaCl	KCl	RbCl	CsCl
0.1	4.58	4.56	4.54	4.52	4.50
0.2	9.12	9.04	8.95	8.90	8.80
0.3	13.83	13.55	13.31	13.2	13.08
0.4	18.41	18.02	17.70	17.51	17.15
0.5	23.6	22.6	22.1	21.77	21.21
0.6	28.61	27.12	26.4	26.1	25.4
0.7	33.65	31.80	30.79	30.4	29.4
0.8	39.10	36.37	35.1	34.7	33.61
0.9	44.25	41.20	39.46	39.0	37.8
1.0	49.75	45.80	44.0	43.4	42.0
1.2	61.25	55.50	52.8	52.0	50.4
1.4	73.10	65.25	62.0	61.0	58.75
1.6	85.60	75.50	71.0	69.75	67.2
1.8	98.40	85.9.	80.0	78.7	75.7
2.0	112.10	96.2	90.0	88.0	84.4
2.5	148.80	124.1	113.0	110.8	106.1
3.0	189.00	153.2	138.0	134.9	129.0
3.5	234.1	185.1	163.0	159.0	152.1
4.0	282.9	218.9	188.0	184.0	176.1
4.5	338.2	254.1	216.0	210.0	201.0
5.0	396.1	283.0	- - -	237.0	226.1
5.5	460.0	332.0	- - -	- - -	- - -
6.0	526.0	374.0	- - -	- - -	- - -

TABLE 8. Dielectric Constants of Water at various temperatures.<sup>22</sup>

t°C	k <sub>e</sub> <sup>*</sup>	k <sub>e</sub> <sup>†</sup>	k <sub>e</sub>
0	87.74	87.90	87.8
5	85.86	85.90	85.8
10	83.83	83.95	83.9
15	81.95	82.04	82.0
18	80.84	80.95	80.88
20	80.10	80.18	80.1
25	78.30	78.36	78.3
30	76.55	76.58	76.5
35	74.83	74.85	74.84
38	73.82	73.83	73.82
40	73.15	73.15	73.15
45	71.51	71.50	71.5
50	69.91	69.88	69.9
55	68.34	68.30	68.3
60	66.81	66.76	66.8
65	65.32	65.25	65.3
70	63.86	63.73	63.8
75	62.43	62.34	62.4
80	61.03	60.93	61.0
85	59.66	59.55	59.6
90	58.32	58.20	58.26
95	57.01	56.88	56.9
100	55.72	55.58	55.65

\* From data of Malmberg and Maryott (1956)

† From data of Owen, Miller, Milner and Cagan (1961)

k<sub>e</sub> An average of k<sub>e</sub><sup>\*</sup> and k<sub>e</sub><sup>†</sup>

From this data it can be shown that k<sub>e</sub> × T<sup>3/2</sup> is approximately a constant.

TABLE 9 . - Variation of  $k_e$  with temperature

$$k_e \times T^{3/2} = a$$

$k_e$	$t^{\circ}\text{C}$	T in $^{\circ}\text{K}$	$T^{3/2}$	$k_e \times T^{3/2}$
87.8	0	273	$4.50 \times 10^3$	$3.95 \times 10^5$
85.8	5	278	$4.64 \times 10^3$	$3.98 \times 10^5$
83.9	10	283	$4.74 \times 10^3$	$3.97 \times 10^5$
82.8	15	288	$4.88 \times 10^3$	$4.01 \times 10^5$
80.1	20	293	$5.04 \times 10^3$	$4.04 \times 10^5$
76.3	25	298	$5.15 \times 10^3$	$4.04 \times 10^5$
75.5	30	303	$5.30 \times 10^3$	$4.06 \times 10^5$
74.84	35	308	$5.42 \times 10^3$	$4.05 \times 10^5$
73.82	38	311	$5.51 \times 10^3$	$4.06 \times 10^5$
73.15	40	313	$5.56 \times 10^3$	$4.06 \times 10^5$
71.5	45	318	$5.69 \times 10^3$	$4.06 \times 10^5$
69.9	50	323	$5.83 \times 10^3$	$4.06 \times 10^5$
68.3	55	328	$5.94 \times 10^3$	$4.05 \times 10^5$
66.8	60	333	$6.12 \times 10^3$	$4.08 \times 10^5$
65.3	65	338	$6.25 \times 10^3$	$4.08 \times 10^5$
63.8	70	343	$6.29 \times 10^3$	$4.01 \times 10^5$
62.4	75	348	$6.53 \times 10^3$	$4.06 \times 10^5$
61.0	80	353	$6.66 \times 10^3$	$4.06 \times 10^5$
59.6	85	358	$6.83 \times 10^3$	$4.06 \times 10^5$
58.26	90	363	$6.95 \times 10^3$	$4.05 \times 10^5$
56.9	95	368	$7.10 \times 10^3$	$4.04 \times 10^5$
55.65	100	373	$7.25 \times 10^3$	$4.04 \times 10^5$

In Table 9 we see that  $k_e \times T^{3/2}$  is a constant  $\approx 4.04 \times 10^5$ .

TABLE 10 . - An Application of Equation (2-38) .

Salt	A	B	C	D	E	F
LiCl	193.9	191.42	$8.01 \times 10^5$	7.91	$7.91 \times 10^3$	47.46
NaCl	180.5	175.20	$7.40 \times 10^5$	7.36	$7.36 \times 10^3$	44.10
KCl	165.3	162.20	$6.79 \times 10^5$	6.70	$6.70 \times 10^3$	40.2
RbCl	158.1	156.08	$6.53 \times 10^5$	6.45	$6.45 \times 10^3$	38.7
CsCl	148.8	146.90	$6.15 \times 10^5$	6.07	$6.07 \times 10^3$	36.42

A = Lattice energies  $U_c$  in Kcal/mole<sup>23</sup>

B = Column A multiplied by  $(1 - 1/k_e)$   $k_e = 73.3$

C = Column B multiplied by 4184 Joule

D = Column C divided by  $1.013 \times 10^5$  Nt/m<sup>2</sup>atm

E = Column D multiplied by 1 mole/10<sup>-3</sup> m<sup>3</sup>

F = Column E multiplied by  $\langle \cos \theta \rangle = 6 \times 10^{-3}$

Column F expresses the osmotic pressure of each given salt in atmospheres for a concentration of 1 molal at 25°C.

From figure 5 , note the following linear relationships and the range of their approximate linearity at a constant temperature of 25°C.

Salt	Relation	Range of $m$
LiCl	$\pi_0 = 45.8 (m)$	0 to 0.2
NaCl	$\pi_0 = 45.2 (m)$	0 to 0.6
KCl	$\pi_0 = 41.0 (m)$	0 to 1.2
RbCl	$\pi_0 = 43.4 (m)$	0 to 1.4
CsCl	$\pi_0 = 42.0 (m)$	0 to 2.5

TABLE 11 .- Experimental and Calculated Lattice Energies of Alkali Halides (Kcal/mole).<sup>24</sup>

Salt	Experimental (Born-Haber Cycle)	Calculated (Simple Electrostatic Model)
LiCl	200.8	193.9
NaCl	184.1	180.5
KCl	167.6	164.3
RbCl	163.1	158.1
CsCl	150.5	148.8

TABLE 12 .- Interionic distances, electrostatic potentials, and ionic radii.<sup>25</sup>

Salt	$r_0$ in Å (Interionic Distance)	$\phi$ (Potential)	Radii in Å
LiCl	2.57	29.14	Li 0.68
NaCl	2.82	22.64	Na 0.98
KCl	3.147	18.79	K 1.33
RbCl	3.291	17.69	Rb 1.48
CsCl	- - -	16.58	Cs 1.68
			Cl 1.81

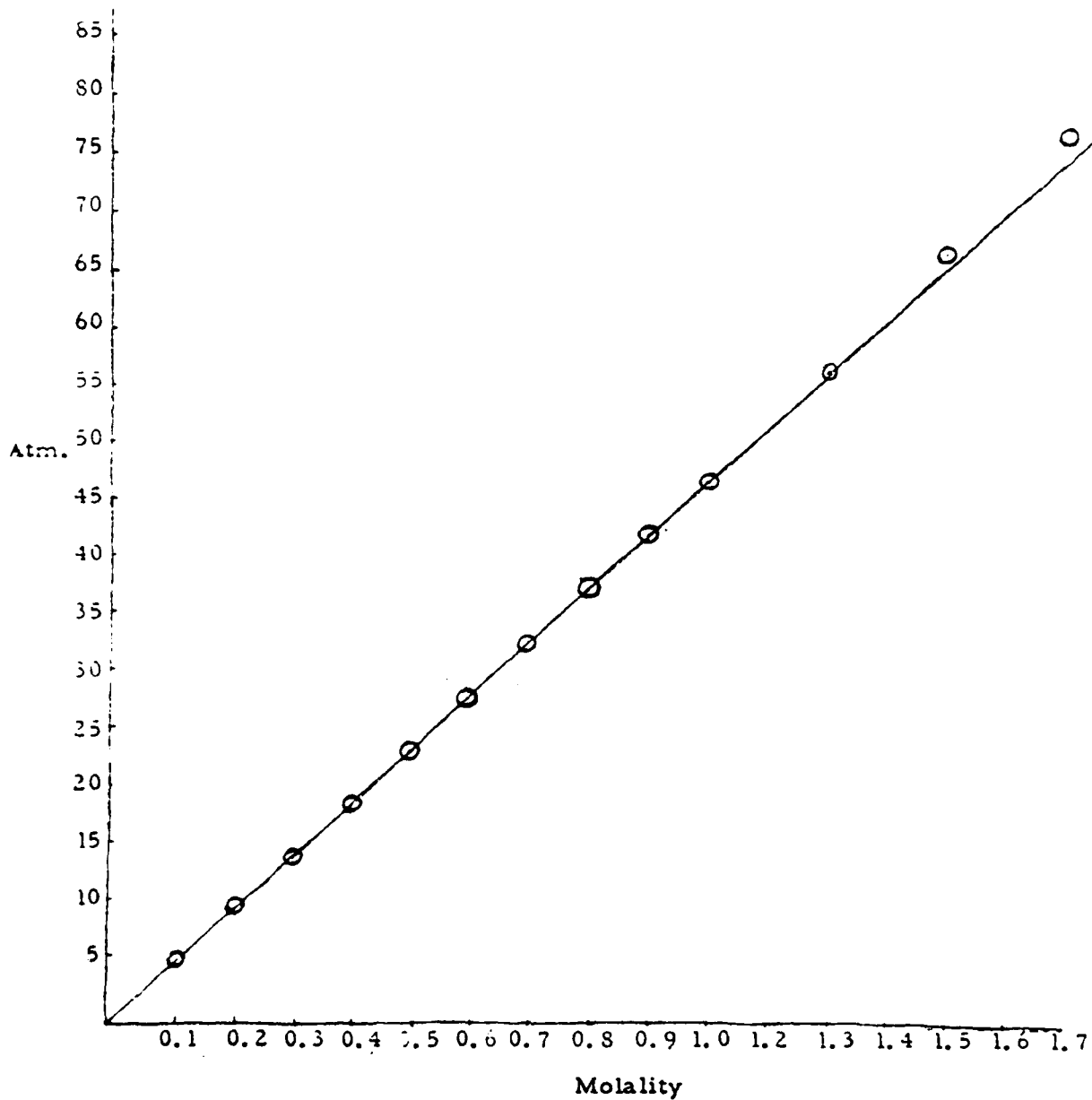


Figure 4 .- Osmotic Pressure of Sodium Chloride Solutions at 25°C .

For 0.533 (m), the osmotic pressure  $\pi_0$  is 24.21 atm.

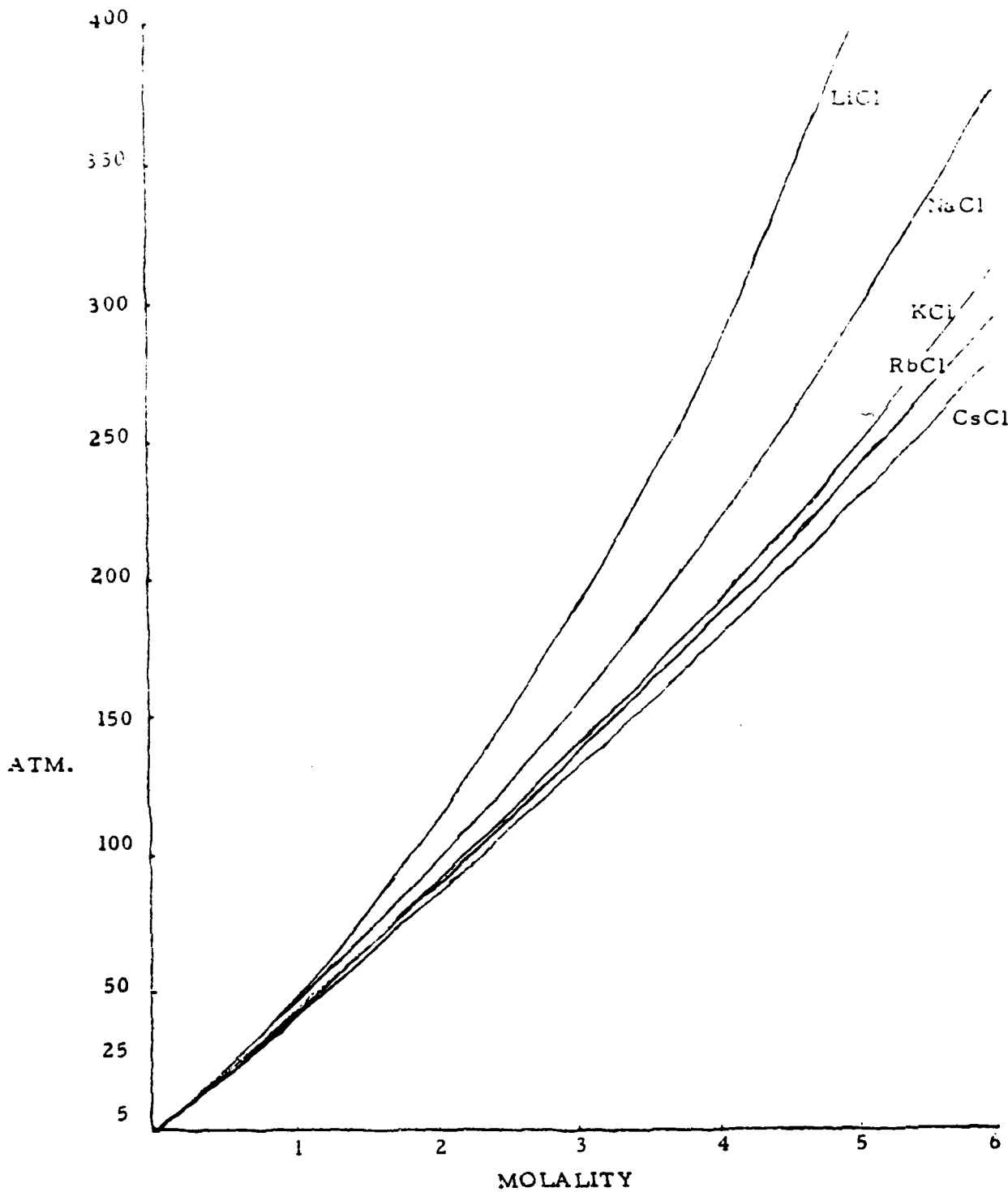


Figure 5 .- Osmotic Pressure vs. Molality for LiCl, NaCl, KCl, RbCl, and CsCl at 25°C.

## CHAPTER IV

### Discussion and Conclusions

The experimental values for the lattice energies for LiCl, NaCl, KCl, RbCl, and CsCl show a progressive increase. The charge densities for Lithium, Potassium, Sodium, Rubidium and Cesium in their ionic state show a progressive decrease. Then the electrostatic potentials for each would follow the same trend. Furthermore, the electric field strengths decrease as a consequence. Another deduction is that by an electrostatic model of ionic crystals, the electrostatic energies for LiCl, NaCl, KCl, RbCl and CsCl drop in that order. Consequently, we should expect the osmotic pressure for each salt to drop correspondingly, all other experimental conditions held equal. The data demonstrates this dramatically. Thus, any theory of osmosis must predict this trend. Equation (2-38) predicts osmotic pressures for the above salt solutions for dilute concentrations. So long as the ions in solution are sufficiently far apart, the osmotic pressure is directly proportional to the concentration. As seen in figure 4, this theory coincides closely with the data. The temperature dependence of equation (2-38) va-

ries in the following way:

$$\pi_0 = + \frac{N_b A e^3}{(4 \pi \epsilon_0)^2 r_b r^2} \left( \frac{\sqrt{T}}{a} - \frac{T^2}{a^2} \right) \frac{n}{\gamma T} \quad (2-39)$$

where  $a = 4.04 \times 10^5$

With additional investigation, one could lead to a more general equation than (2-39).

## REFERENCES

- <sup>1</sup>B. Mahan, University Chemistry (Reading, Massachusetts: Addison Wesley Publishing Company, Inc., 1965).
- <sup>2</sup>Charles Kittel, Introduction to Solid State Physics (New York: John Wiley and Sons, Inc. 1971).
- <sup>3</sup>Introduction to Solid State Physics (New York: John Wiley & Sons, Inc., 1971)
- <sup>4</sup>Paul Ander and Anthony J. Sonnessa, Principles of Chemistry, (New York: The Macmillan Company, 1965).
- <sup>5</sup>Michell J. Sienko and Robert A. Plane, Chemistry (New York: McGraw-Hill Book Company, 1966).
- <sup>6</sup>A. Laubengayer, General Chemistry ((New York: Holt, Rinehart and Winston, 1957).
- <sup>7</sup>Francis Weston Sears and Mark W. Zemansky, University Physics (Reading, Massachusetts: Addison-Wesley Publishing Company, Inc., 1964).
- <sup>8</sup>J. C. Slater, Introduction to Chemical Physics (New York: Dover Publications, Inc. 1939).
- <sup>9</sup>Introduction to Chemical Physics (New York: Dover Publications, Inc., 1939).
- <sup>10</sup>University Physics (Reading, Massachusetts: Addison-Wesley Publishing Company, Inc., 1964).
- <sup>11</sup>Introduction to Solid State Physics (New York: John Wiley & Sons, Inc., 1971).
- <sup>12</sup>Introduction to Solid State Physics (New York: John Wiley & Sons, Inc., 1971).
- <sup>13</sup>David Halliday and Robert Resnick, Physics Part II (New York: John Wiley & Sons, 1960).
- <sup>14</sup>R. A. Robinson and R. H. Stokes, Electrolyte Solutions (London: Butterworths Scientific Publications, 1959).

<sup>15</sup>F. O. Rice and Edward Teller, The Structure of Matter (New York: Science Editions, Inc., 1939).

<sup>16</sup>R. A. Robinson, Trans., Faraday Society, (1945) 41, 756.

<sup>16</sup>R. A. Robinson and P. A. Sinclair, Trans., Faraday Society, (1934), 56, 1830.

<sup>17</sup>R. A. Robinson, Trans., Roy. Soc. N. Z., (1945), 75, 203.

<sup>18</sup>R. A. Robinson, Trans. Roy. Soc. N. Z., (1945), 75, 203.

<sup>19</sup>R. A. Robinson, Ibid., (1937), 59, 84.

<sup>20</sup>R. A. Robinson and P. A. Sinclair, Ibid., (1934), 56, 1830.

<sup>21</sup>H. S. Harned and O. E. Schupp, Ibid., (1930), 52, 3836.

<sup>22</sup>J. Hamer, Handbook of Physics and Chemistry, ed. E. U. Condon and Hugh Odishaw, (New York: McGraw - Hill Company, 1958).

<sup>23</sup>J. Huheey, Inorganic Chemistry (New York: Harper & Row Publishers, 1972).

<sup>24</sup>Inorganic Chemistry (New York: Harper & Row Publishers, 1972).

<sup>25</sup>Introduction to Solid State Physics (New York: John Wiley & Sons, Inc., 1971).



AD P001017

A FREE BOUNDARY PROBLEM IN NEWTONIAN FLOW

W. G. Pritchard\*, Yuriko Renardy\*\*, L. R. Scott\*\*\*

ABSTRACT. The construction of a computer program or "code" to solve steady free surface flows with surface tension at small Reynolds numbers is described. The code uses fixed-point iteration for the nonlinearities in the Navier-Stokes equations and a second-order finite element scheme. Before using the code on general flow problems such as coating flows, it is necessary to test it as thoroughly and rigorously as possible. Numerical tests for such a code are usually only done against a previously computed approximate solution to the driven-cavity flow. However, <sup>the authors</sup> we have instead chosen to test ~~our~~ code against three flows for which exact solutions are known: the Couette-Poiseuille flow, the Jeffrey-Hamel flow and Richardson's stick-slip flow. Convergence tests are presented.

1. INTRODUCTION. An example of a flow we are interested in is the flow problem when fluid emerges from a nozzle at small Reynolds numbers. Attempts have been made to solve this problem by assuming that the fluid separates at the lip of the nozzle [1], [2]. Experimental work by Pritchard showed that this is not a valid assumption and Jean and Pritchard [3] have set this problem (see figure 1) in a way which could be demonstrated to provide a unique solution. They prescribe the contact angle. The separation point is then sought as part of the solution. Jean [4] gives the existence and uniqueness proofs for this. Similar results by quite different methods have also been obtained by Solonnikov. References to his work are in Jean's paper [4]. The only other free-surface study of this kind for which numerical schemes have been analyzed and tested appears to be by Cuvelier [5]. His exit boundary conditions are slightly different from ours.

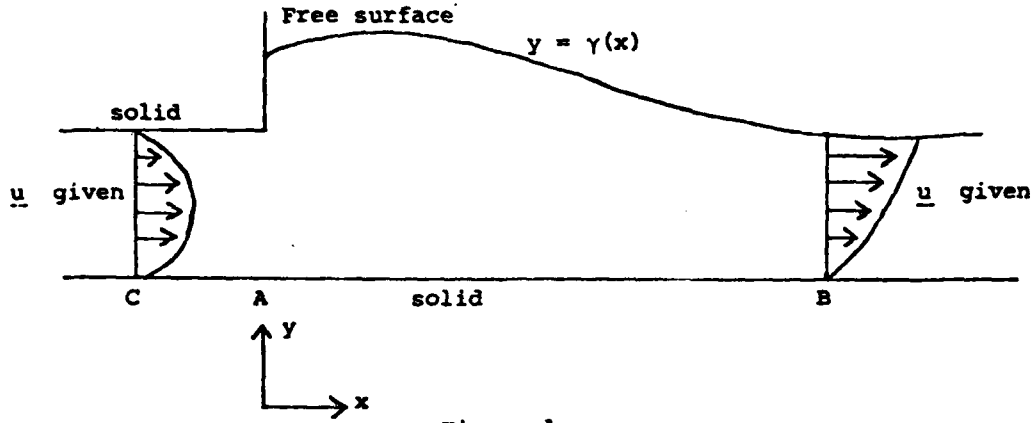


Figure 1

\* Department of Mathematics, University of Essex, U.K.

\*\* Mathematics Research Center, University of Wisconsin-Madison, 610 Walnut Street, Madison, WI 53706. Sponsored by the United State Army under Contract No. DAAG29-80-C-0041.

\*\*\* Department of Mathematics, University of Michigan, Ann Arbor, MI 48109.

2. EQUATIONS OF MOTION. The two-dimensional flow out of a nozzle onto a wall is shown in Figure 1. The velocity  $\underline{u}$  and pressure  $p$  satisfy the dimensionless Navier-Stokes equations:

$$\nabla^2 \underline{u} = \nabla p + \text{Re } \underline{u} \cdot \nabla \underline{u} \quad (1)$$

where the Reynolds number  $\text{Re}$  is  $UL/\nu$ ,  $U$  is a typical speed,  $L$  is a typical length scale,  $\nu$  is the kinematic viscosity, and incompressibility:

$$\nabla \cdot \underline{u} = 0 \quad (2)$$

The free-surface boundary conditions are: on  $y = \gamma(x)$ ,  $A < x < B$ ,

$$\underline{u} \cdot \underline{n} = 0 \quad (3)$$

$$\frac{\partial u_t}{\partial n} = 0 \quad (4)$$

$$T \cdot \frac{\gamma''}{(\sqrt{1+\gamma'^2})^3} = -p + 2 \frac{\partial u_n}{\partial n} \quad (5)$$

$$\left. \begin{array}{l} \gamma'(A) \\ \gamma(B) \end{array} \right\} = \text{given} \quad (6)$$

where  $T$  is the surface tension,  $u_n$  is the normal component of the velocity and  $\underline{n}$  is the unit normal vector pointing out of the fluid at the free-surface,  $u_t$  is the tangential component of velocity. The velocity fields at boundaries  $x = C$  and  $x = B$  are given. At the solid boundaries,  $\underline{u} = 0$ .

3. METHOD OF SOLUTION. The method of solution we propose is an iterative one. We first guess the shape of the free-surface. Secondly we compute the velocity and pressure fields using two of the free surface conditions: zero normal flow (3) and zero shear stress (4). Thirdly we compute a new free surface from conditions (5), (6) and (7). This iteration is continued. Under suitable conditions such as the presence of surface tension, low  $\text{Re}$  and a good enough initial guess for  $\gamma(x)$ , this scheme will converge to a unique solution [3]. This method has been found not to converge if the surface tension is too low [6]. Indeed, Jean's proof does not apply to flows with zero surface tension and it is not clear that a unique solution exists for such flows. Since the position of the boundary must be adjusted at each iterate, a finite element method was suggested. The zero shear stress condition then appears as a natural boundary condition in the variational formulation. For simplicity, we have used a second-order scheme. The most efficient in terms of work needed to compute the solution is a scheme analyzed by Crouzeix and Raviart [7] which is based on the Hodge decomposition. The domain is triangulated. A triangulation is shown in Figure 2.

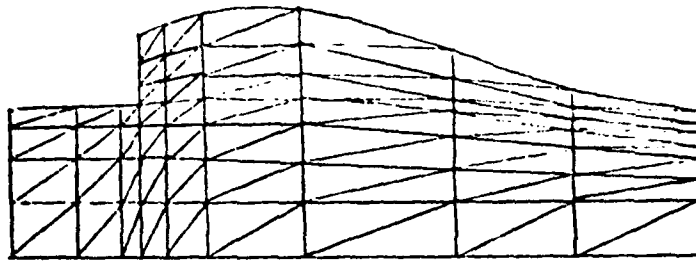


Figure 2

A weak formulation is: find velocity  $\underline{u} = \bar{\underline{u}} + \underline{q}$  and pressure  $p$ , where  $\underline{q}$  is a reference function and incorporates the boundary (denoted by  $\partial\Omega$ ) conditions,

$$\bar{\underline{u}} \in V, V = \{ \bar{\underline{u}} \in (H^1)^2 \mid \text{div } \bar{\underline{u}} = 0, \bar{\underline{u}} = 0 \text{ on } \partial\Omega - \gamma(x), \bar{\underline{u}} \cdot \underline{n} = 0 \text{ on } \gamma(x) \},$$

such that

$$-(\nabla \underline{u}, \nabla \underline{w}) = -(p, \nabla \cdot \underline{w}) + (\text{Re} \cdot \underline{u}, \nabla \underline{u}, \underline{w}) \quad (7)$$

for all  $\underline{w} \in W, W = \{ \underline{w} \in (H^1)^2 \mid \underline{w} = 0 \text{ on } \partial\Omega - \gamma(x), \underline{w} \cdot \underline{n} = 0 \text{ on } \gamma(x) \}$ . To solve for the velocity field, let the discretised  $\bar{\underline{u}}$  be  $\bar{\underline{u}} = \sum_{i=1}^N \alpha_i \phi_i$ . The  $N$

basis functions  $\phi_i$  and the  $N$  test functions  $\underline{w}$  are chosen to be nonconforming, discretely divergence free, and piecewise linear.

"Nonconforming" refers to the property that these functions do not have to be continuous across the edges of the triangles. However, they must satisfy compatibility conditions [7], which, for piecewise linear functions, is the continuity at the midpoints of the edges. "Discretely divergence-free" means, for piecewise linear functions, that  $\iint_{\mathcal{T}} \text{div } \underline{w} \, dx dy$  vanishes over each triangle. This is equivalent to: for each triangle,

$$\sum_{i=1}^3 w_n(m_i) |e_i| = 0 \text{ where } |e_i| \text{ is the length of the } i\text{th edge, } w_n(m_i) \text{ is}$$

the normal component of  $\underline{w}$  at the  $i$ th midpoint. The test function associated with a vertex  $V$  and the one associated with a midpoint  $M$  of an edge are shown in Figure 3.

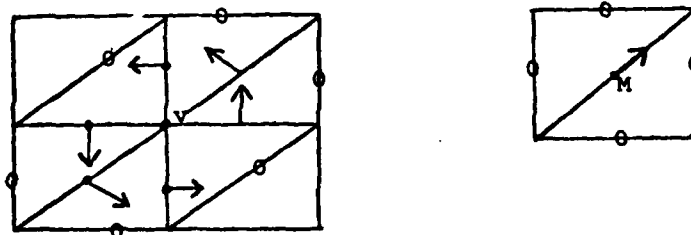


Figure 3

The pressure never enters in the calculation of the velocity field and we compute it only when it is needed, unlike methods where it is carried explicitly [8]. Since the applications we have in mind are at low  $Re$ , we merely use a straightforward fixed-point-iteration method, starting with an initial iterate at zero  $Re$ . Also, by concentrating on a near-Stokes problem, we can use very efficient solvers, such as conjugate gradients, for the linear algebra.

After the velocity field has been computed, we compute  $p$  by using a non-solenoidal piecewise linear vector  $\underline{w}$  (see Figure 4) in equation (7). The discretized pressure field is piecewise constant so that the integrals in (7) can be calculated explicitly. The pressure on one of the

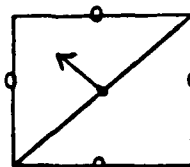
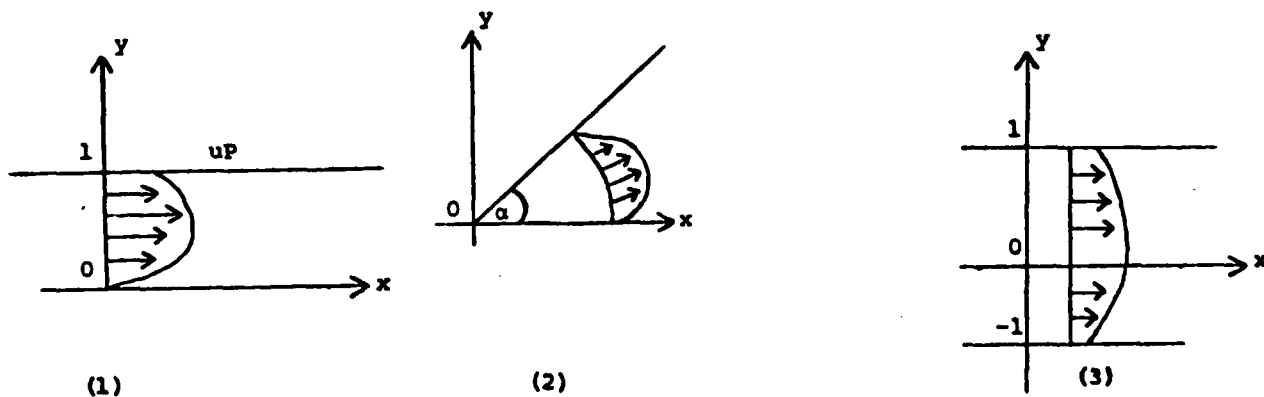


Figure 4

triangles will be prescribed, and then the code marches through the domain from there. The estimates for errors are given by Crouzeix and Raviart [7] for the Stokes problem and have been extended to the Navier-Stokes equations by Rannacher and Heywood [9].

**4. CONVERGENCE TESTS.** The three exact solutions used for the convergence tests describe Stokes flows. However, the discretization introduces perturbations and we can use these flows also to test the code for Navier-Stokes flows.



(1) Couette-Poiseuille flow. The upper wall at  $y = 1$  is moving with speed  $uP$  and there is a pressure gradient. The test area is a unit square with velocities prescribed on the boundaries. Figure 5 is a graph of

$\ln(h)$  verses  $\ln(L_2 \text{ error})$ ,  $h = \text{mesh size}$ , for  $Re = 1$ , showing that the error varies as  $h^2$ . For higher  $Re$  up to about 50, the method converged provided the fixed-point iteration was under-relaxed; that is, to calculate the  $n$ th iterate  $\underline{u}^{(n)}$ , replace  $\underline{u}^{(n-1)}$  in the nonlinear terms by  $\underline{u}^{(n-1)} + r(\underline{u}^{(n-1)} - \underline{u}^{(n-2)})$ ,  $0 < r < 1$ . The optimum value for  $r$  can be found by trial and error to lie in  $0.25 < r < 0.5$ . Convergence tests for the pressure code at  $Re = 0$  have confirmed the analysis [7] that the  $L_2$  error should be proportional to  $h$ .

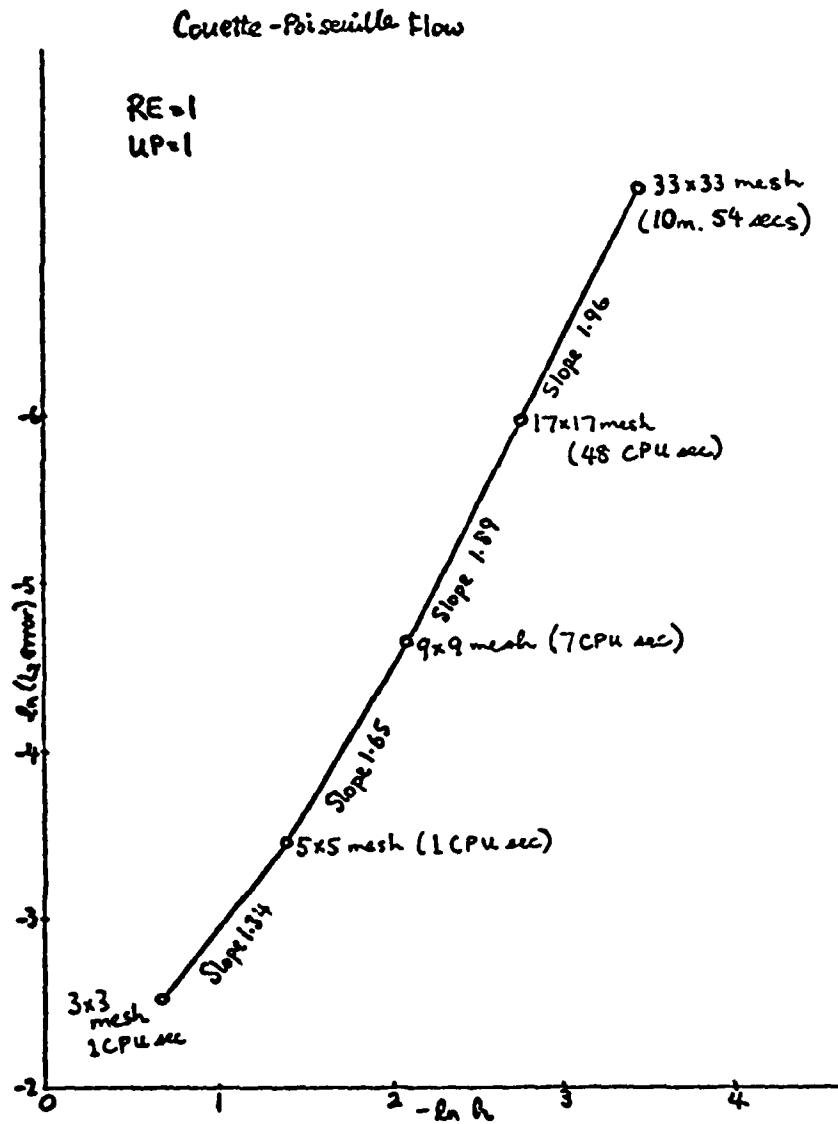


Figure 5

(2) Jeffrey-Hamel flow. This is purely radial flow into or out of two walls meeting at an angle  $\alpha$  at the origin where there is a source or sink. The test area was chosen to be a trapezoid one unit away from the origin and we have chosen to work with outgoing flow. The exact solution, in polar coordinates, is described by  $\underline{u} = (\frac{6V}{r} u(\theta), 0)$  where the Navier-Stokes

equations yield  $(u'' + 4u + 6u^2)(\theta) = C$  on  $0 < \theta < \alpha$ ,  $u(0) = u(\alpha) = 0$ . A finite-difference scheme was devised to generate the exact solution, using centered difference for  $u''$  and a Newton scheme for the nonlinearity. Figure 6 shows the  $\ln(L_2 \text{ error})$  vs  $\ln(h)$  for various  $Re$ . The  $Re$  here denotes an "average" Reynolds number. It shows that the second-order convergence is more asymptotic for higher  $Re$ . For the fixed-point iteration, under-relaxation was necessary for the  $Re$  larger than 0.082 and the number of iterations required increased to 12 for the  $17 \times 17$  mesh at  $Re = 18$ . A study is currently underway to record the behaviour of the code to different triangulations.

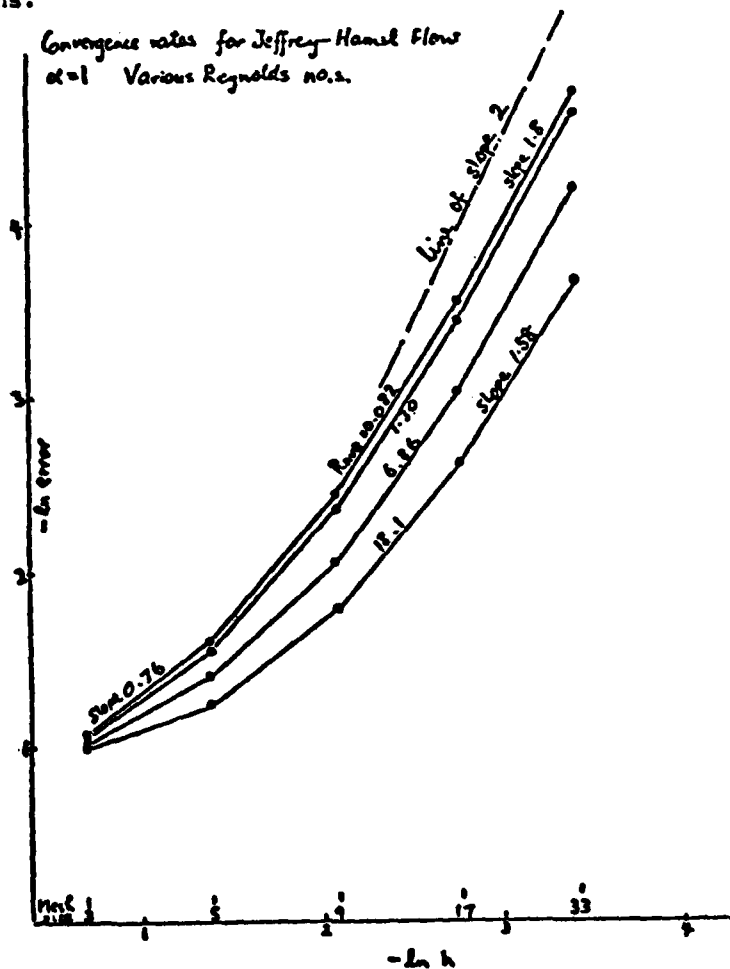


Figure 6

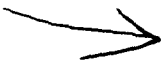


3

REFERENCES

1. Nickell, R. Z., Tanner, R. I. and Caswell, B. 1974. The solution of viscous incompressible jet and free-surface flows using finite-element methods. *J. Fluid Mech.* 65, 189-206.
2. Saito, H. and Scriven, L. E. Study of coating flow by the finite element method. *J. Comp. Phys.* Vol. 42, No. 1, July 1981, 53-75.
3. Jean, M. and Pritchard, W. G. 1980. The flow of fluids from nozzles at small Reynolds numbers. *Proc. Roy. Soc. London. A* 370, 61-72.
4. Jean, M. 1980. Free surface of the steady flow of a Newtonian fluid in a finite channel. *Arch. Rat. Mech. Anal.* Vol. 74, 197-217.
5. Cuvelier, C. 1981. On the numerical solution of a capillary free boundary problem governed by the Navier-Stokes equations. *Seventh International Conference on Numerical Methods in Fluid Dynamics*. Ed. Reynolds, W. C. and MacCormack, R. W. *Lecture Notes in Physics*, 141, Springer-Verlag, Berlin, 132-137.
6. Silliman, W. J. and Scriven, L. E. 1980. Separating flow near a static contact line: slip at a wall and shape of a free surface. *J. Comp. Phys.* Vol. 34, No. 3, 287-313.
7. Crouzeix, M. and Raviart, P.-A. 1973. Conforming and nonconforming finite element methods for solving the stationary Stokes equations, I. *R.A.I.R.O.*, R3, 33-76.
8. Taylor, C. and Hood, P. 1973. A numerical solution of the Navier-Stokes equations using the finite element technique. *Comp. & Fluids*, Vol. 1, 73-100.
9. Heywood, J. G. and Rannacher, R. 1982. Finite element approximation of the nonstationary Navier-Stokes problem I. *SIAM J. Num. Anal.*, April.
10. Richardson, S. 1970. A stick-slip problem related to the motion of a free jet at low Reynolds numbers. *Proc. Camb. Phil. Soc.* 67, 477.

AD P001018



EVOLUTION OF NEAR CHAPMAN-JOUGET DEFLAGRATIONS

D.S. Stewart  
Department of Theoretical and Applied Mechanics  
University of Illinois, Urbana-Champaign, IL 61801

<sup>†</sup>G.S.S. Ludford  
Department of Theoretical and Applied Mechanics  
Cornell University, Ithaca, NY 14853

**ABSTRACT.** In order to analytically investigate flame acceleration effects, Stewart and Ludford (1983a), (1983b) posed a model rationally derived from Arrhenius kinetics in which the temperature of the thin reaction zone is constant. For small heat-release during combustion this model has been shown to have a simple limiting form. In this paper we show that such a model leads to a Burger's equation for the evolution of disturbances moving with the flame when the flame has been accelerated close to its Chapman-Jouget value (the maximum steady deflagration velocity). The flame forms a moving boundary that imposes certain conditions on the solution. The problem thus posed is a moving boundary problem; the solution and the location of the flame are to be found simultaneously. Numerical results are given for examples of compressional and rarefactive disturbances applied to the unbounded Chapman-Jouget flame. Boundary effects are also investigated.

**I. INTRODUCTION.** A near Chapman-Jouget deflagration is a weak deflagration that travels at a speed close to the Chapman-Jouget (CJ) speed. An examination of the Rankine-Hugoniot relations, (Williams (1965)), shows that the CJ velocity represents the maximum velocity for steady deflagrations. The CJ value depends upon the amount of heat released by the reaction. In particular when this heat-release is small compared to the thermal energy of the mixture, characterized by a parameter  $\beta \ll 1$  (say), then the CJ value approaches the quiescent sound speed of the fluid far upstream. Also, the density, particle velocity and temperature are disturbed slightly from their quiescent values as well.

Based on these principles and other assumptions (one dimensionality, constant material properties, fuel into product and very fast Arrhenius kinetics among them) Stewart and Ludford (1983b) have shown that a Burger's-like equation governs the time dependent evolution of near CJ deflagrations.

The dimensionless density, fluid velocity, temperature and reduced mass fraction of the deficient reactant will be denoted by  $\rho$ ,  $v$ ,  $T$ ,  $Y$ . (The reduced mass fraction is the mass fraction of the reactant divided by its quiescent value.) The temperature and density units are the quiescent values. The velocity unit is the quiescent sound speed; the length unit is  $\lambda/c_p$ , where  $\lambda$  and  $c_p$  are respectively the thermal conductivity and the specific heat of the

<sup>†</sup>This work was supported by U.S. Army Research Office

fluid, and  $M$  (a mass flux) is the product of the quiescent density and the quiescent speed of sound. Finally, the time unit is formed by the ratio of the length and velocity units.

The reader is referred to the paper of Stewart and Ludford (1983b) for a more complete description of the results presented here.

## II. THE EVOLUTION EQUATION.

Let

$$\underline{u} = \begin{pmatrix} \rho \\ v \\ T \end{pmatrix} \quad (1)$$

be a vector that represent the state of the gas, (note that the mass fraction  $Y$  plays a passive role having the unburnt value  $Y_0$  upstream and the burnt value  $0$  downstream).  $v$  is the velocity of the deflagration.  $u = \underline{u}_0$  corresponds to quiescent conditions upstream and  $v = -1$  corresponds to a deflagration moving to the left at the quiescent speed of sound. Then, near CJ deflagrations can be characterized by

$$\underline{u} = \underline{u}_0 + f(\eta, T) \underline{r} \beta^{\frac{1}{2}} + \dots, \quad v = -1 + c(T) \beta^{\frac{1}{2}} + \dots, \quad (2)$$

where  $\underline{r}^T = (1, -1, \gamma-1)$  and  $\eta$  and  $T$  represent dimensionless space and time.  $f(\eta, T)$  and  $c(T)$  are specified by the problem

$$\begin{aligned} f_{,T} - c(T) f_{,\eta} - \frac{\gamma+1}{2} f f_{,\eta} &= \frac{\gamma}{2} f_{,\eta\eta}, \\ f(0, T) = 0, \quad f_{,\eta}(0^+, T) - f_{,\eta}(0^-, T) &= -Y_0/\gamma \\ f(\eta, 0) &= h(\eta). \end{aligned} \quad (3)$$

$Y_0/\gamma$  is a specified constant;  $\gamma$  is the ratio of specific heats of the mixture;  $h(\eta)$  is the initial data corresponding to the initial disturbance and it is assumed to satisfy the conditions on  $f$  at  $\eta = 0$ .

The steady solutions of (3) (Stewart, Kapila and Ludford (1983)) found by setting  $f_{,T} = 0$  and  $c$  constant, are

$$f = \begin{cases} 0 & \text{for } \eta < 0 \\ f_+ (1 - e^{\delta\eta}) / [1 - (f_+/f_-) e^{\delta\eta}] & \text{for } \eta > 0, \end{cases} \quad (4)$$

where

$$\delta = (\gamma + 1)(f_- - f_+)/2\gamma, \quad f_{\pm} = 2c\{-1 \mp \sqrt{1 - Y_0(\gamma + 1)/2c^2}\}/(\gamma + 1). \quad (5)$$

$c$  is supposed known and must be greater than or equal to the CJ value

$$c_{CJ} = \sqrt{Y_0(\gamma + 1)/2}. \quad (6)$$

Since (3a) is a Burger's equation, written in a frame moving with the deflagration, the Hopf-Cole transformation leads to a linear equation in the transform variable  $\phi$  and leads to simplification in further analytical and numerical treatment. Letting

$$f = 2\gamma\phi_{,n}/(\gamma + 1)\phi, \quad \text{i.e., } \phi = A(T)\exp\left[(\gamma + 1) \int_0^n f(\bar{n}, T) d\bar{n}/2\gamma\right], \quad (7)$$

Stewart and Ludford (1983b) showed that  $\phi$  satisfies

$$\begin{aligned} \phi_{,T} - c(T)\phi_{,n} &= \frac{Y}{2}\phi_{,nn} \quad \text{for } n < 0, \\ \phi_{,T} - c(T)\phi_{,n} &= \frac{Y}{2}\phi_{,nn} + Y_0(\gamma + 1)\phi/4\gamma \quad \text{for } n > 0, \\ \phi_{,n}(0, T) &= 0, \quad \phi(0^+, T) = \phi(0^-, T), \quad \phi(n, 0) = g(n), \end{aligned} \quad (8)$$

where  $h = 2\gamma g_{,n}/(\gamma + 1)g$ . Any solution of the problem (8) to within an unspecified constant corresponds to a solution of (3).

The steady solutions of (8) are simply

$$\begin{aligned} \phi &= 1 \quad \text{for } n \leq 0, \\ \phi &= (r_+ e^{-rn} - r_- e^{rn})/(r_+ - r_-) \quad \text{for } n \geq 0, \end{aligned} \quad (9)$$

where  $r_{\pm} = -c\{1 \pm \sqrt{1 - c_{CJ}^2/c^2}\}/\gamma$ . In particular when  $c = c_{CJ}$ ,  $r = r_+ = r_- = -c_{CJ}/\gamma$  and

$$\phi = (1 - rn)e^{rn}, \quad \text{for } n \geq 0. \quad (10)$$

**III. NUMERICAL RESULTS.** Various initial-value problems were solved by an implicit finite-difference scheme. An initial profile for the amplitude function  $f$  was chosen as well as an initial value of  $c$ . The corresponding  $\phi$ -profile for  $n < 0$  and  $n > 0$  were advanced independently to the next time step using condition (8c) and requiring that  $f$  remain constant at large positive and negative values of  $n$ ; i.e., definition (7a) with  $f$  fixed was the additional boundary condition at large  $n$ . At this stage the condition (8d) wasn't necessarily satisfied, the difference  $\phi(0^+, T) - \phi(0^-, T)$  generally

being non-zero. If the difference was non-zero, a new value of  $c$  was chosen and  $\phi$  was determined as before. The process was repeated until (8d) was satisfied to within a prescribed tolerance. (A secant root finding procedure to find the root of the difference was used to iterate for  $c$ ). The procedure was repeated at a new time step, and so on.

Some numerical experiments were performed by taking the initial profile of  $f$  to be the superposition of a disturbance on the steady profiles (4). It was decided to study the effect of compressional and rarefactive disturbances applied to the steady deflagrations. Since the initial data could be specified independently upstream and downstream, the effects of only an upstream disturbance (or only a downstream disturbance) could be studied as well as the effects of combined disturbances.

Physically, the pressure perturbation is the sum of the density and temperature perturbations since the ideal gas law  $P = \rho T$  holds ( $P$  being the dimensionless pressure). The  $\beta^{1/2}$  perturbation is then found from (2) to be  $\gamma f$ . Hence, increasing the value of  $f$  corresponds to increasing the pressure and vice-versa. Figure 1 shows an example of a steady deflagration,  $\gamma = 1.4$ ,  $c = 2$ ,  $Y_0 = 1$ , denoted by a dashed line; the deflagration is simply a rarefaction in the burnt region. Typical compressional and rarefactive disturbances that were applied singly, (e.g., a compression in the burnt region and no disturbance in the fresh) and in combination are shown as well.

Compressional disturbances applied singly, both in the fresh ( $n \leq 0$ ) and burnt ( $n \geq 0$ ) regions caused the flame to decelerate at first ( $c$  increasing) whence the flame returned to its original velocity and the profile for  $f$  relaxed to the steady profile. The opposite behavior was observed for rarefactive disturbances applied singly upstream and downstream.

When disturbances were applied in combination their effects were amplified or reduced depending on the single disturbance response. For example, rarefactive disturbances in the fresh and burnt regions both caused an acceleration. However, the combined effect of a fresh and burnt rarefaction caused the deflagration to accelerate to a larger velocity (smaller value of  $c$ ) than either disturbance applied singly. The numerical results for the example of Figure 1 are shown in Figures 2 and 3.

From these results, it appears that the acceleration response of these deflagrations is much more sensitive to disturbances in the burnt region than in the fresh. The extent of this sensitivity can only be established by additional numerical experimentation or further analytical results. Also, all the steady deflagrations examined numerically, including the limiting CJ deflagration, behaved similarly. In particular, the deflagrations seemed stable to imposed disturbances of the type considered here.

An additional numerical experiment was performed in which the boundary condition on  $f$ , far downstream, was varied in order to simulate the effect of a shock or piston emanating far downstream. In the first experiment the value of  $f$  at  $\eta = 10$  (say) was changed at a uniform rate from its steady value at  $T = 0$  to the value  $-1$  at  $T = .6$  and then held fixed for further time. This corresponds to imposing and maintaining a rarefaction on the burnt side. The results in Figure 4 show that it was possible to accelerate the deflagration and hold its velocity at a value above the CJ velocity. By varying the value of  $f$  at the boundary, different values of  $c$  could be attained.

Figure 5 shows the results when the value of  $f$  at  $\eta = 10$  (say) was increased at a constant rate to zero by  $T = 1.2$  and held fixed thereafter. This corresponds to an imposed compression far downstream. The amplitude of the solution in the burnt region seemed to decay to zero everywhere, while the speed gradually, then rapidly, decelerated ( $c$  increasing). This result is consistent with the earlier analysis by Stewart and Ludford (1983b) showing that no  $O(\beta^{1/2})$  perturbation occurs when the wave speed differs from its CJ value by an  $O(1)$  amount. Hence, as the velocity decelerates and its difference from  $-1$  can no longer be measured by the  $O(\beta^{1/2})$  perturbation  $c$ , then the solution must vanish.

#### REFERENCES

1. Stewart, D.S. & Ludford, G.S.S. 1983a. Fast deflagration waves, Journal de Mecanique (to appear).
2. Stewart, D.S. & Ludford, G.S.S. 1983b. The acceleration of fast deflagration waves, Z.A.M.M. (to appear).
3. Stewart, D.S., Kapila, A.K. & Ludford, G.S.S. 1983. Deflagrations and detonations for small heat release, (submitted for publication).
4. Williams, F.A. 1964. Combustion Theory. Reading, Massachusetts: Addison-Wesely Publishing Co., Ch. 2.

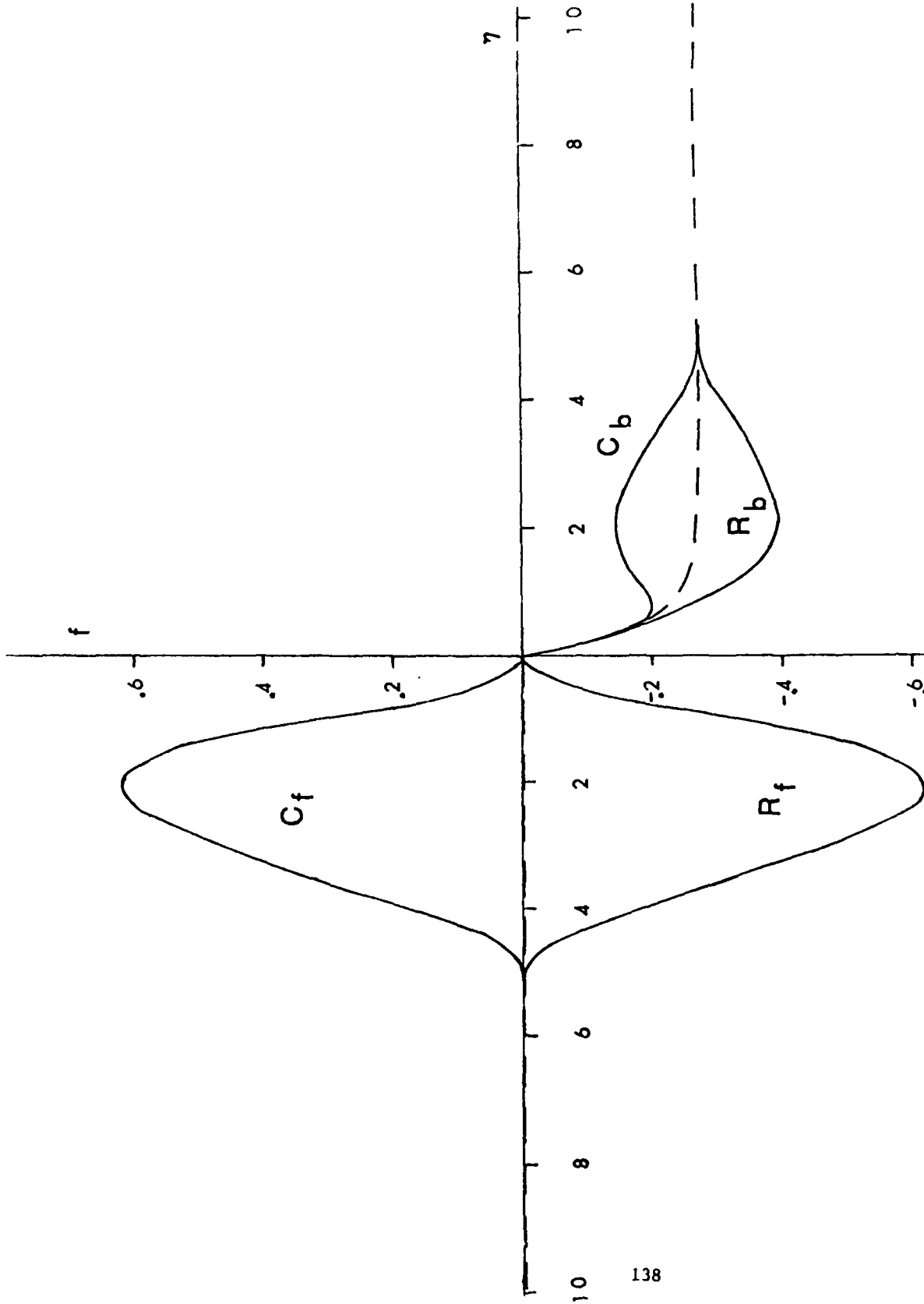


Figure 1. Steady deflagration (4) for  $\gamma = 1.4, c = 2, Y_0 = 1$  is shown by the dotted line. Initial disturbances are denoted by C for compression and R for rarefaction. Subscripts f and b correspond to fresh and burnt respectively. Disturbances were analyzed separately and in combination.

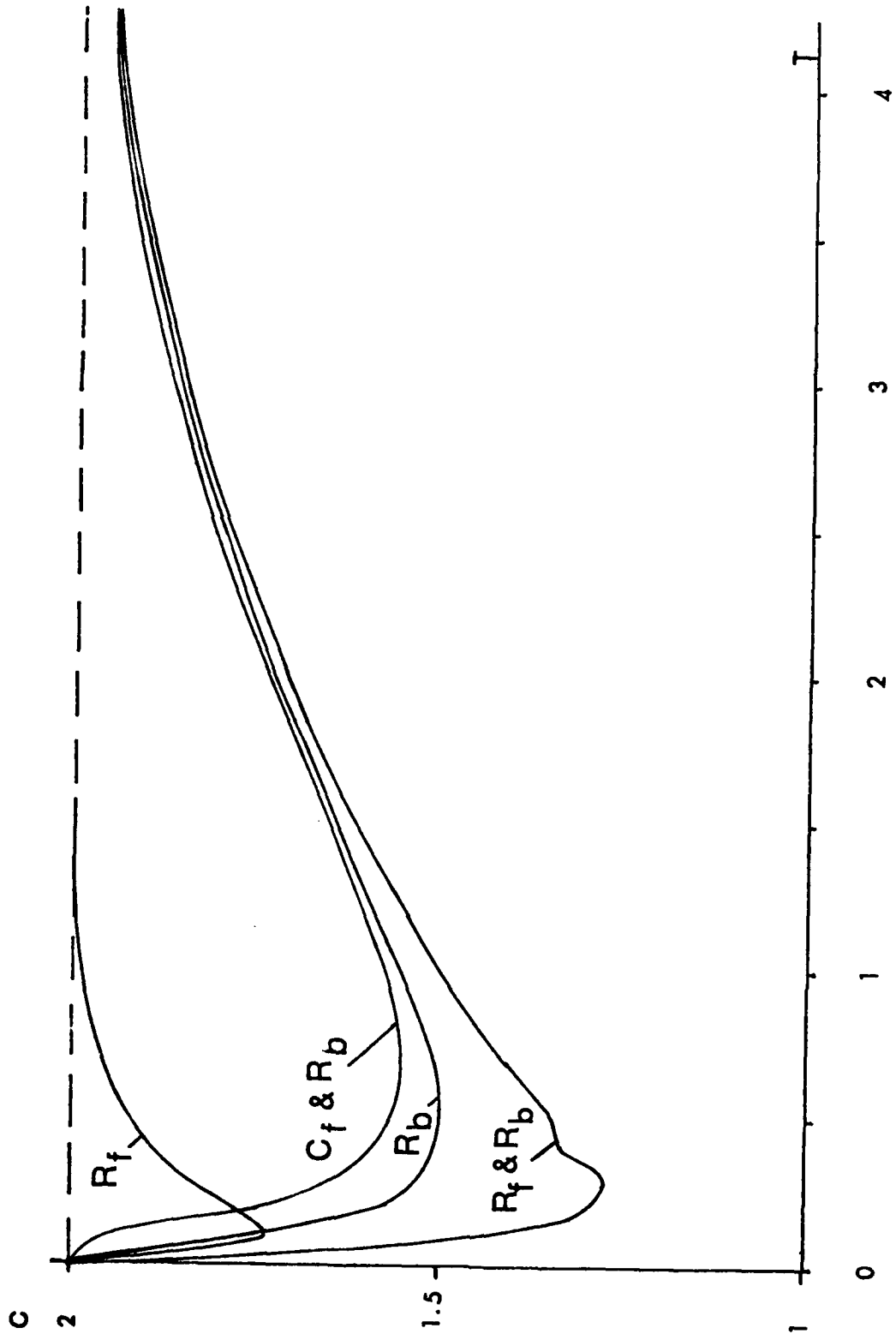


Figure 2. Examples of flame acceleration due to the initial disturbances of Figure 1. For example:  $R_f$  corresponds to initial data where disturbance  $R_f$  of Figure 1 is applied in the fresh region and no disturbance applied in the burnt.

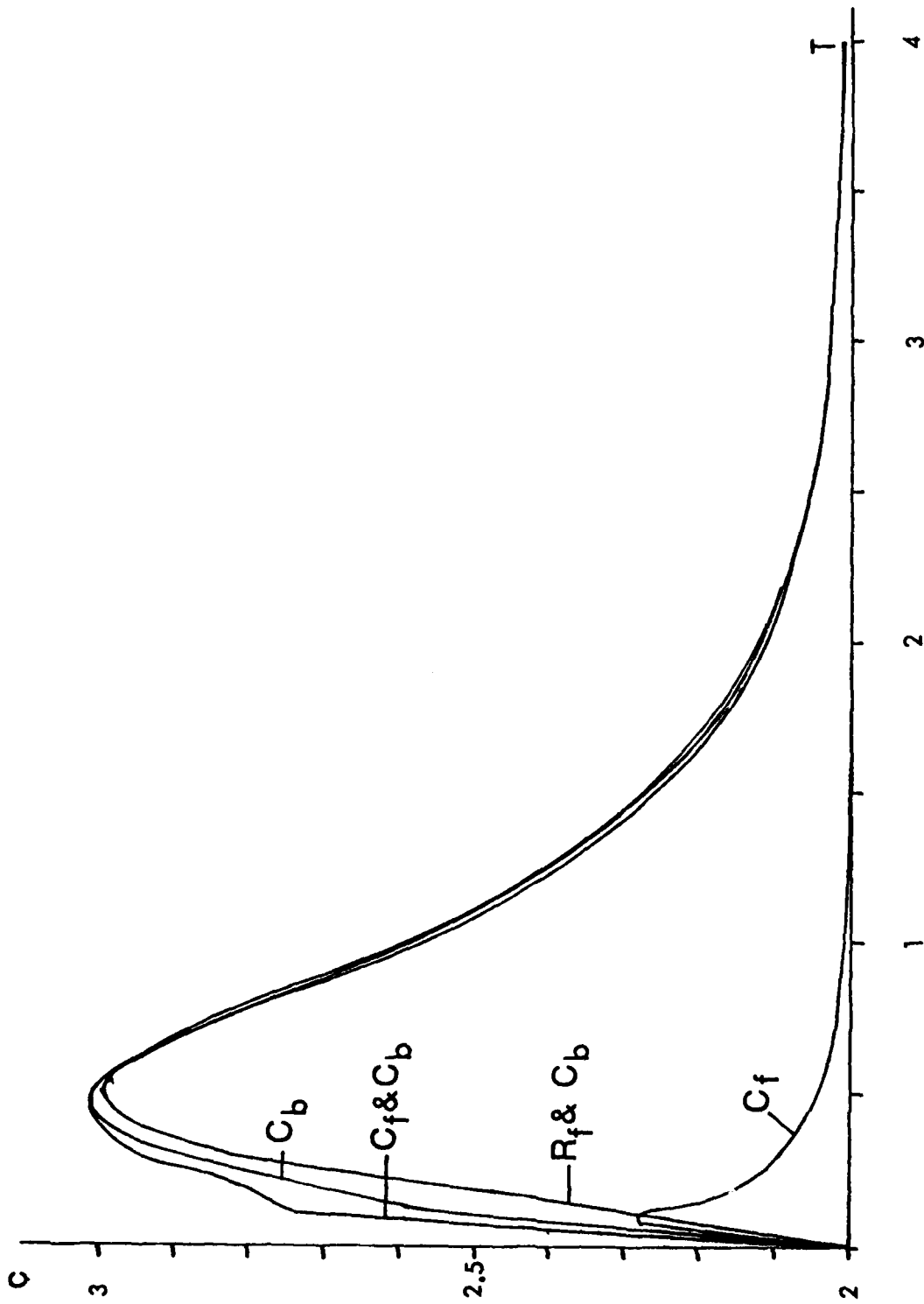


Figure 3. Example of flame deceleration due to the initial disturbances of Figure 1.

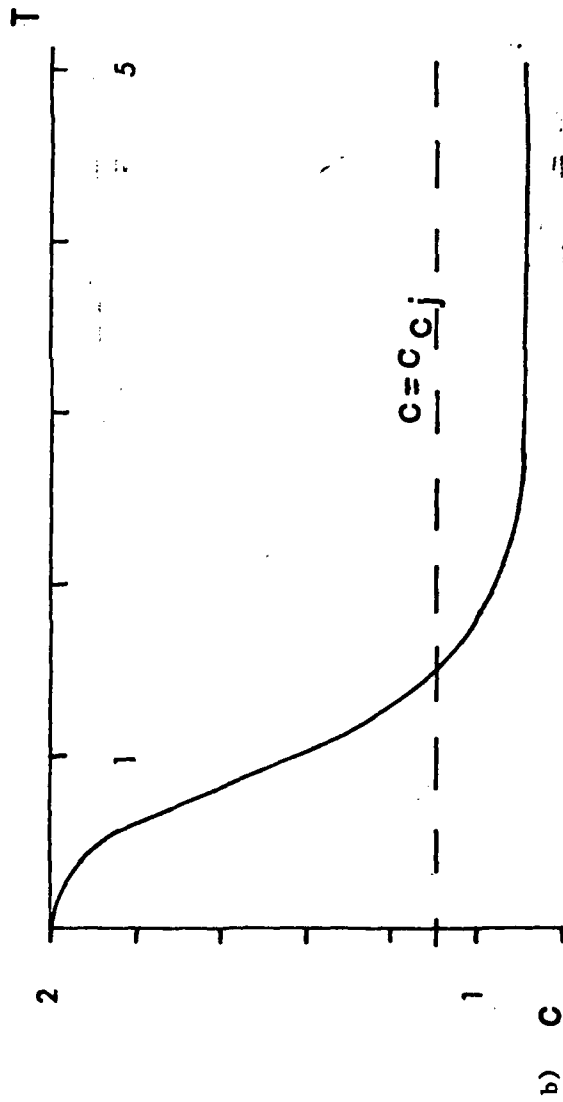
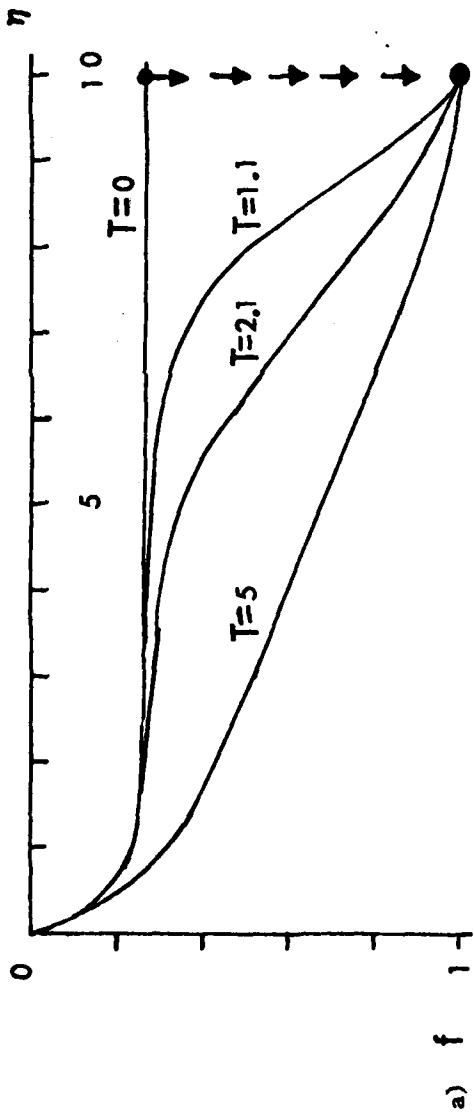


Figure 4a, b. Result of numerical experiment where  $f$  at  $\eta = 10$  is reduced uniformly from the initial steady value, ( $\gamma = 1.4, c = 2, Y_0 = 1$ ) to  $-1$  by  $T = .6$  and then held fixed. Figure 4a shows calculated profiles in the burnt region. Figure 4b shows  $c$  versus  $T$ .

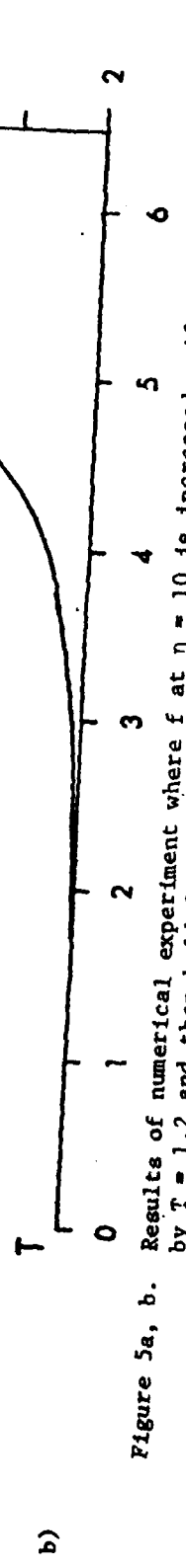
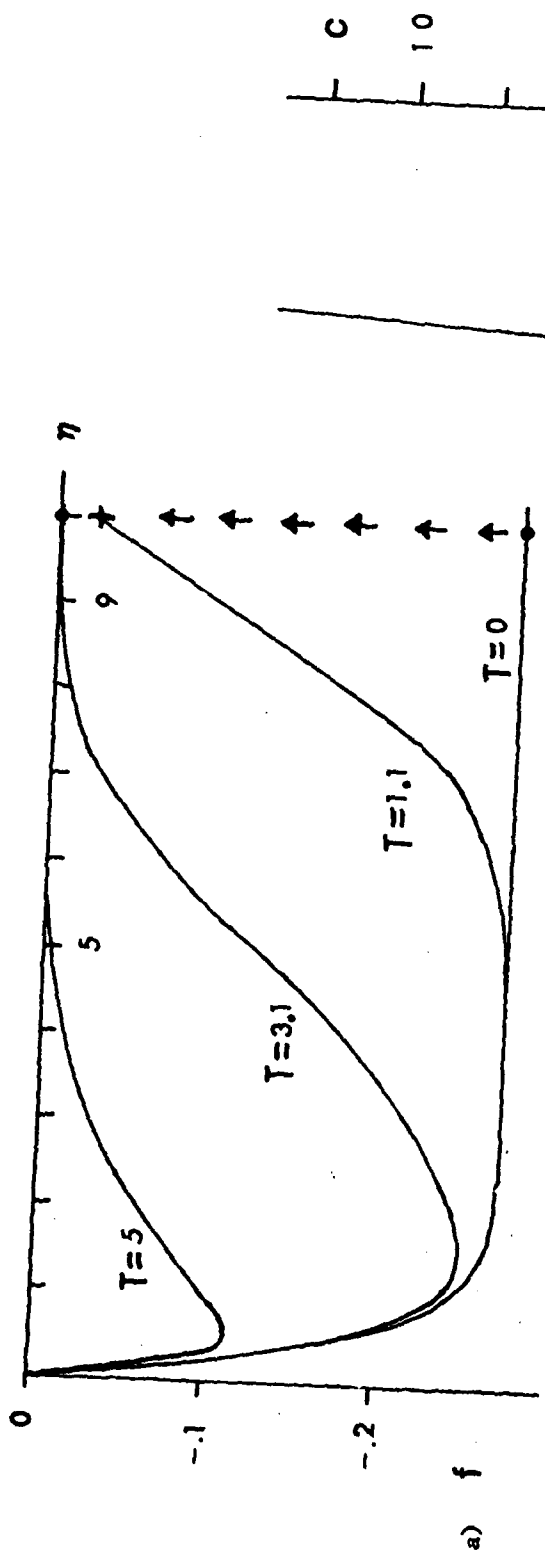


Figure 5a, b. Results of numerical experiment where  $f$  at  $\eta = 10$  is increased uniformly to  $f = 0$  by  $T = 1.2$  and then held fixed.  $\gamma = 1.4$ ,  $c = 2$ ,  $Y_0 = 1$ . Figure 5a shows the calculated profiles in the burnt region. Figure 5b shows  $c$  versus  $T$ .

AD P 0 0 1 0 1 9



Eine Kleine Eigenvalueproblem

(A Simple but Informative Nonlinear Eigenvalue Problem)

B. A. Fleishman  
Mathematical Sciences Department  
Rensselaer Polytechnic Institute  
Troy, NY 12181

P. W. Davis  
Mathematical Sciences Department  
Worcester Polytechnic Institute  
Worcester, MA 01609

ABSTRACT

The simple eigenvalue problem

$$-d^2u/dx^2 = \lambda \operatorname{sgn} u, \quad u(0) = u(1) = 0$$

*This paper*

( $\lambda$  a real parameter) exhibits a number of interesting properties of nonlinear Problems, some established here by elementary arguments. For each eigenvalue we find all eigenfunctions (an infinite number of them) in explicit form. As  $\lambda$  increases through 0, there is an exchange of stability: the trivial solution, formerly stable, becomes unstable while the maximal and minimal eigenfunctions ( $\lambda > 0$ ) are stable. The stability of non-extremal eigenfunctions is also discussed.

The work of the authors was supported by the U. S. Army Research Office under contract numbers DAAG-29-79-C-0012 and DAAG-29-81-K-0018, respectively.

## 1. Introduction

We consider here the nonlinear eigenvalue problem

$$-d^2u/dx^2 = \lambda \operatorname{sgn} u \quad (0 < x < 1) \quad (1)$$

$$u(0) = u(1) = 0 \quad (2)$$

where  $\operatorname{sgn} u = u/|u|$  for  $u \neq 0$  and  $\operatorname{sgn} 0 = 0$ ,  $x$  and  $u$  are real variables and  $\lambda$  is a real parameter. A number of properties characteristic of nonlinear problems are exhibited, and as will be seen, because of the special nature of the nonlinearity some properties are established by elementary arguments.

We find that all  $\lambda > 0$  are eigenvalues, and all eigenfunctions (a countable infinity) are found in explicit form. As  $\lambda$  increases through 0 there is an exchange of stability: the trivial solution, formerly stable, becomes unstable, while the maximal and minimal eigenfunctions (for  $\lambda > 0$ ) are stable. The stability of non-extremal eigenfunctions is also discussed. An iteration scheme based on problem (1-2) turns out to have interesting features. It is possible to follow in detail the development of an iterative sequence, and we are able to show for several important examples that iterative sequences converge in a finite number of steps.

Differential equations with signum nonlinearities were much studied in the 1950's and 60's as models of relay (or on-off) control systems [1,2]. In recent years discontinuous nonlinearities have arisen also in a variety of free boundary problems [4]. This investigation has originated from a desire to gain further insight into the special properties of nonlinear systems with discontinuous nonlinearities.

In Section 2 all eigenvalues and eigenfunctions are exhibited. Sections 3 and 4 contain general remarks about the iteration scheme and a few detailed examples. Questions of stability are addressed in Section 5. We restate here the results of a rigorous proof of stability of the maximal and minimal eigenfunctions, given elsewhere. For the non-extremal solutions, a linear stability analysis is developed in general and applied in a specific case.

## 2. Eigenvalues and Eigenfunctions

We first establish

Proposition 1. All  $\lambda > 0$  are eigenvalues of (1-2), and these are the only eigenvalues.

Proof. Clearly  $\lambda = 0$  is not an eigenvalue, for then the boundary value problem (1-2) has only the trivial solution. For fixed  $\lambda \neq 0$ , let

$$v(x) = u(x)/\lambda. \quad (3)$$

Substitution in (1) yields  $-v'' = \text{sgn}(\lambda v)$ . When  $\lambda < 0$ ,  $\text{sgn}(\lambda v) = -\text{sgn } v$  and we have to solve the boundary value problem

$$(\lambda < 0) \quad v'' = \text{sgn } v, \quad 0 < x < 1, \quad v(0) = v(1) = 0.$$

Then by a maximum principle argument it follows readily that  $v(x) \equiv 0$  is the only solution.

When  $\lambda > 0$ ,  $\text{sgn}(\lambda v) = \text{sgn } v$  and (1-2) reduces to

$$(\lambda > 0) \quad -v'' = \text{sgn } v, \quad 0 < x < 1, \quad v(0) = v(1) = 0. \quad (4)$$

This boundary value problem has been discussed in [4]. Assuming that a solution  $v(x)$  has constant sign, say  $v > 0$  (and therefore  $\text{sgn } v = 1$ ) on  $(0,1)$ , we find that  $v(x) = \frac{1}{2}x(1-x)$ . Hence, each  $\lambda > 0$  has associated with it the eigenfunction  $u(x) = \lambda v(x)$ , and the proof of Proposition 1 is complete.

It is not hard to see that there is also a solution of (4) of opposite sign. Thus, the problem (1-2) has two eigenfunctions

$$u(x) = \pm \lambda \phi_1(x), \quad \phi_1(x) \equiv \frac{1}{2}x(1-x). \quad (5)$$

In addition, there are solutions of non-constant sign (in fact, infinitely many), whose graphs are constructed by patching together parabolic arcs which are alternately concave up and concave down, at uniformly spaced points on the x-axis. As shown in [3], the following is true.

Proposition 2. For any given  $\lambda > 0$ , the totality of eigenfunctions is given by

$$u(x) = \pm \lambda \phi_n(x), \quad n = 1, 2, \dots,$$

where

$$\phi_n(x) = \frac{1}{2}(-1)^k \left(x - \frac{k}{n}\right) \left(\frac{k+1}{n} - x\right) \quad (6)$$

for  $k/n \leq x \leq (k+1)/n$ ,  $k = 0, 1, \dots, n-1$ , with

$$\max |\phi_n(x)| = 1/8n^2.$$

The graphs of  $\phi_1$ ,  $\phi_2$  and  $\phi_3$  are shown in Figure 1.

From now on, in considering iterative procedures and stability, we shall refer for convenience to problem (4) for  $v(x)$ , rather than to problem (1-2). There is no loss of generality since, as shown above, for fixed  $\lambda > 0$ ,  $v(x)$  is a solution of (4) if and only if  $u(x) = \lambda v(x)$  is a solution of (1-2).

### 3. Iteration: Description of Procedure; General Remarks

Since all the other solutions of (4),  $v = \pm\phi_n$ ,  $n = 2, 3, \dots$ , lie between  $\phi_1$  and  $-\phi_1$ , the latter two are, respectively, the "maximal" and "minimal" solutions of (4). If we had not found explicit representations of all these solutions by elementary means, it is reasonable to ask which, if any, might be determined, even approximately, by iteration.

Based on problem (4), we consider the sequence  $\{v_n(x)\}$ , where for  $n = 1, 2, \dots$ ,  $v_n(x)$  is the solution of

$$-v'' = \operatorname{sgn} v_{n-1} \quad (0 < x < 1), \quad v(0) = v(1) = 0, \quad (7)$$

and  $v_0(x)$  is a prescribed function. Solutions to (7) are required to be  $C^1$  and piecewise  $C^2$ . Since the right-hand side of the differential equation will always be a specific piecewise-constant function, the solution will always consist of quadratic and/or linear functions patched together smoothly at given values of  $x$ . It follows too that the solution will be unique.

Because we can find iterates in this problem explicitly, we shall be able to examine, in greater detail than is usually possible in nonlinear problems, the behavior of the iterative sequence for different choices of  $v_0$ . Another reason for studying such behavior is that it may give indications of stability properties for various solutions of (4).

We shall treat three choices of  $v_0$ : a)  $v_0$  has fixed sign, say  $v_0 > 0$ , on  $(0,1)$ ; b)  $v_0$  changes sign once in  $(0,1)$ ; c)  $v_0$  changes sign twice in  $(0,1)$ . These are illustrated in Figure 2.

#### 4. Iteration: Three Choices for $v_0$ .

a) Suppose  $v_0(x) > 0$  for  $0 < x < 1$ . Then  $\operatorname{sgn} v_0 \equiv 1$ , and as the solution of (7), we have  $v_1(x) = \frac{1}{2}x(1-x) = \phi_1(x)$ . Similarly  $v_2(x) = v_3(x) = \dots = \phi_1(x)$ . If  $v_0$  is negative on  $(0,1)$  then  $v_1(x) = -\phi_1(x)$ . The actual values of  $v_0(x)$  are irrelevant. In other words, if the initial iterate is positive-valued (resp. negative-valued) on  $(0,1)$ , the sequence of iterates converges to  $\phi_1$

(resp.  $-\phi_1$ ), and convergence takes place in one step! There is a suggestion here that the maximal/minimal solutions  $\pm \phi_1$  are stable in some sense (which is made precise in the next section and proved in [3]). In the same sense, the trivial solution  $v(x) \equiv 0$  would appear to be unstable, since if  $v_0$  is arbitrarily small in magnitude but positive-valued,  $v_1(x) = \phi_1(x)$ , while simply changing the sign of  $v_0$  yields  $v_1(x) = -\phi_1(x)$ .

b) Now we choose  $v_0$  close to  $\phi_2$  in its sign variation. As the simplest non-trivial choice for  $v_0$ , this case will be treated in detail. Specifically, suppose

$$v_0(x) > 0 \text{ on } I_\ell: 0 < x < x_0; v_0(x) < 0 \text{ on } I_r: x_0 < x < 1,$$

where  $x_0$  is a given number satisfying

$$1/2 < x_0 < 1.$$

It is helpful, but not necessary, to think of  $x_0$  as close to  $1/2$ .

Then from equation (7),  $v_1$  must satisfy

$$-v'' = 1 \text{ on } I_\ell, -v'' = -1 \text{ on } I_r, v(0) = v(1) = 0$$

with  $v$  and  $v'$  continuous at  $x_0$ . Note that we do not require  $v_1(x_0) = 0$ ; in fact the point of this calculation is to determine an  $x_1$  in  $(0,1)$  such that  $v_1(x_1) = 0$ . In general,  $x_1 \neq x_0$ .

Integrating twice, we have quadratic functions representing  $v_1$  on each of the intervals  $I_\ell$  and  $I_r$ ; imposing the boundary and continuity conditions, we obtain

$$v_1(x) = \begin{cases} -\frac{x^2}{2} - (x_0^2 - 2x_0 + \frac{1}{2})x & \text{on } \bar{I}_\ell: 0 \leq x \leq x_0 \\ \frac{x^2}{2} - (x_0^2 + \frac{1}{2})x + x_0^2 & \text{on } \bar{I}_r: x_0 \leq x \leq 1. \end{cases} \quad (8)$$

The graph of  $v_1$  consists of two parabolic arcs joined smoothly at  $(x_0, v_1(x_0))$ ; the arc on the left, concave downward, passes through

the origin, while the one on the right, concave upward, passes through the point (1,0).

As noted above,  $v_1(x_0) \neq 0$  (unless  $x_0 = 1/2$ ). The sign of  $v_1(x_0)$  determines the fate of the iterative sequence. For example, consider  $1/2 < x_0 < 1$ , and let  $x_1$  denote the zero of  $v_1$  in  $(0,1)$ :  $v_1(x_1) = 0$ . Now if  $v_1(x_0)$  is positive,  $v_1(x) > 0$  for  $0 < x \leq x_0$ . Hence, we expect  $1/2 < x_0 < x_1 < 1$ . Repeating the argument for successive iterates should show that their interior zeroes march off to the right. The iterates themselves should move away from  $\phi_2$ .

To demonstrate this result precisely, consider  $1/2 < x_0 < 1$ . Then (8) yields

$$v_1(x_0) = -x_0(x_0 - 1)(x_0 - \frac{1}{2}) > 0.$$

(Similarly,  $0 < x_0 < 1/2$  would imply  $v_1(x_0) < 0$ , which would lead to the zeroes of successive iterates marching off to the left toward 0 from  $1/2$ .)

Thus,  $v_1(x) > 0$  for  $0 < x \leq x_0$ . If  $v_1$  has a zero  $x_1$  in  $(0,1)$ , then it must lie in  $(x_0,1)$ . To determine  $x_1$  we must use from (8) the representation of  $v_1(x)$  on  $I_p$ . Setting

$$v_1(x_1) = \frac{x_1^2}{2} - (x_0^2 + \frac{1}{2})x_1 + x_0^2 = 0$$

gives  $x_1 = 1$  (which was built into the function  $v_1$ ) and

$$x_1 = 2x_0^2.$$

The simplicity of this relation between the zeroes of successive iterates has several immediate consequences of interest.

First, from  $x_0 > \frac{1}{2}$ ,  $2x_0 > 1$  we have  $x_1 = (2x_0)x_0 > x_0$ , in agreement with our previous conclusion.

Second, if  $x_0 \geq 1/\sqrt{2}$  then  $x_1 = 2x_0^2 \geq 1$ , which means that  $v_1$  has no zero in  $(x_0, 1)$ ,  $v_1$  is positive-valued throughout  $(0, 1)$ , and the next step of the iteration gives  $v_2 = \phi_1$ . In other words, if  $1/\sqrt{2} \leq x_0 < 1$ , the iteration scheme converges to  $\phi_1$ , and in two steps.

Finally, for any  $x_0$  in  $(1/2, 1)$ , repeating the previous argument gives for the zeroes  $x_n$  of successive iterates  $v_n$ ,

$$\begin{aligned} x_2 &= 2x_1^2 = 2^3 x_0^4, \\ x_3 &= 2x_2^2 = 2 \left[ 2^3 x_0^4 \right]^2 = 2^7 x_0^8, \\ \vdots \\ x_n &= 2^{(2^n - 1)} x_0^{(2^n)} = \frac{1}{2} (2x_0)^{2^n} \end{aligned}$$

Let  $N$  be the first integer  $n$  for which  $x_n \geq 1$ , or  $(2x_0)^{2^n} \geq 2$ . Then the sequence  $\{v_n\}$  converges to  $\phi_1$  in  $N + 1$  steps, where  $2^N \geq (\ln 2) / \ln(2x_0)$ .

On the other hand, if  $0 < x_0 < 1/2$  for  $v_0$  positive on  $(0, x_0)$  and negative on  $(x_0, 1)$ , since  $x_0, x_1, x_2, \dots$  march to the left with increasing  $n$ , the interval  $(0, x_n)$  on which  $v_n$  is positive gets smaller. Again convergence takes place in a finite number of steps, but now  $v_n \rightarrow -\phi_1$ .

c) Suppose  $v_0$  has two changes in sign:

$$v_0(x) \begin{cases} > 0, & 0 < x < x_0, \\ < 0, & x_0 < x < x_0^1, \\ > 0, & x_0^1 < x < 1, \end{cases}$$

where  $x_0$  is close to  $1/3$  and  $x_0^1$  is close to  $2/3$ . In its sign variation  $v_0$  is similar to  $\phi_3$  (see Figure 1 and Figure 2c).

Clearly there are more cases to consider here than in the previous example and in any case the algebra is messier.

Without showing the analysis (which is similar to that of the previous example) we describe here the results for two cases:

$$i) \quad 1/3 < x_0 < x_0^1 < 2/3,$$

$$ii) \quad x_0 < 1/3, x_0^1 > 2/3.$$

(Recall that  $\phi_3$  vanishes at  $x = 1/3$  and  $x = 2/3$ .)

Simply stated, the result for both cases is that the zeroes (if any) of successive iterates move steadily away from  $1/3$  and  $2/3$  respectively, toward the middle of the interval  $(0,1)$  in case i) and toward the ends of the interval in case ii). In each case, as long as an iterate has zeroes within  $(0,1)$  it resembles its predecessor in its sign variation. When an iterate is reached that has constant sign on  $(0,1)$ , then (as in the two prior examples) the next iterate is  $\phi_1$  or  $-\phi_1$ , the limit for that sequence.

In case i) the limit is  $\phi_1$ , while in case ii) it is  $-\phi_1$ . In either case convergence takes place in a finite number of steps.

## 5. Stability.

The behavior of iterative sequences in a nonlinear time-independent problem in approaching (resp. receding from) a particular solution of the problem corresponds frequently to the stability (resp. instability) of the latter as a steady state of a related time-dependent (parabolic) problem. Thus the iteration results in the previous section suggest that the maximal and minimal solutions  $\pm\phi_1$  of (4) are stable while  $\pm\phi_2, \pm\phi_3$  are unstable steady states of an appropriate parabolic problem.

In part a) the stability of  $\pm\phi_1$  is described, based on a rigorous analysis carried out previously [3]. In part b) a linearized stability analysis is formulated in general and then applied to a treatment of  $\pm\phi_2$ .

a) Consider the boundary-value problem in  $S: (0,1) \times (0,\infty)$

$$(PP) \begin{cases} \partial w / \partial t - \partial^2 w / \partial x^2 = \operatorname{sgn} w, & 0 < x < 1, t > 0, & (9) \\ w(0, t) = w(1, t) = 0, & t > 0, & (10) \\ w(x, 0) = f(x), & 0 < x < 1 & (11) \end{cases}$$

By a solution of (PP) we mean a function  $w(x, t)$  such that  $w$  and  $w_x$  are continuous in  $[0, 1] \times [0, \infty]$ ,  $w_t$  is continuous in  $S$ , (10-11) are satisfied, and at all points of  $S$  where  $w \neq 0$ ,  $w_{xx}$  is continuous and (9) holds.

Proposition 3. (see [3] for proof). For any continuously differentiable initial state  $f(x)$  which is positive-valued on  $(0, 1)$  and satisfies  $f(0) = f(1) = 0$ ,  $f'(0) > 0$ , and  $f'(1) < 0$ , the unique solution  $w(x, t)$  of (PP) approaches  $\phi_1(x)$  asymptotically (and uniformly in  $x$ ) as  $t \rightarrow \infty$ . Likewise,  $-\phi_1(x)$  is the uniform limit in time of initial states  $-f(x)$ , where  $f$  is as above.

b) A rigorous stability result of the type stated above for  $\pm\phi_1$  is not available for  $\pm\phi_n$ ,  $n > 1$ . For the latter, therefore, we resort to a formal linear stability analysis. After outlining the general procedures, we carry out the details in the case  $n = 2$ .

If  $v(x)$  is the particular solution of (4) whose stability is under study, we consider again (PP), the time-dependent version of (4), where now we take  $f(x)$  close to  $v(x)$ :

$$w(x, 0) = f(x) = v(x) + \epsilon y(x), \quad (11)'$$

$y$  an arbitrary bounded function.

Assuming a solution of the form  $w(x, t) = v(x) + \epsilon z(x, t)$ , we substitute for  $w$  in (9-10).

Using  $-v'' = \operatorname{sgn} v$  and retaining only terms linear in  $\epsilon$ , we find that  $z(x, t)$  satisfies

$$z_t - z_{xx} = 2\delta(v(x))z,$$

$$z(0, t) = z(1, t) = 0.$$

The delta function arises from a formal use of Taylor's theorem:

$$\begin{aligned} \operatorname{sgn}(v+\epsilon z) &\approx \operatorname{sgn} v + \epsilon z \left. \frac{d \operatorname{sgn} w}{dw} \right|_{w=v} \\ &= \operatorname{sgn} v + 2 \epsilon z \delta(v) \end{aligned}$$

(See [5] for similar treatment of a discontinuous nonlinearity.)

Finally, applying the method of separation of variables, with  $z(x,t) = e^{\lambda t} y(x)$ , leads to the eigenvalue problem

$$\begin{aligned} y'' + 2\delta(v(x))y &= \lambda y, \\ y(0) = y(1) &= 0 \end{aligned} \quad (12)$$

If this problem has a positive eigenvalue  $\lambda$ , with eigenfunction  $y(x)$ , then  $v(x)$  is unstable, in that the small initial perturbation  $\epsilon y(x)$  gives rise to the solution of (PP),  $w(x,t) = v(x) + \epsilon e^{\lambda t} y(x)$ , whose deviation from  $v(x)$  grows exponentially in  $t$ .

Let  $v(x) = \phi_2(x)$ . The only zero of  $\phi_2(x)$  in  $(0,1)$  is at  $x = 1/2$ ; then in equation (12),  $\delta(v(x)) = \delta(\phi_2(x)) = \delta(x - 1/2)/|\phi_2'(1/2)|$ . From (6) we see that  $\phi_2'(1/2) = -1/4$ . Finally, setting  $\lambda = \mu^2$  (for  $\lambda > 0$ ), we rewrite the eigenvalue problem in the form

$$\begin{aligned} y'' - \mu^2 y + 8\delta(x-1/2)y &= 0 \\ y(0) = y(1) &= 0 \end{aligned}$$

Solving the differential equation  $y'' - \mu^2 y = 0$  on  $(0,1/2)$  and  $(1/2,1)$  subject to the boundary conditions at each end, we have

$$y(x) = c_1 \sinh \mu x, \quad y'(x) = c_1 \mu \cosh \mu x, \quad 0 \leq x \leq 1/2,$$

$$y(x) = c_2 \sinh \mu(1-x), \quad y'(x) = c_2 \mu \cosh \mu(1-x), \quad 1/2 \leq x \leq 1.$$

Requiring that  $y$  be continuous on  $[0,1]$  gives  $c_1 = c_2$  ( $= 1$ , for convenience). The singularity prevents  $y'$  from being continuous. A jump condition on  $y'$  results from taking

$$\int_{\frac{1}{2}-\eta}^{\frac{1}{2}+\eta} [y''(x) - \mu^2 y(x) + 8\delta(x - 1/2)y(x)] dx = 0 \quad (\eta > 0)$$

and letting  $\eta \rightarrow 0$ . Since  $y(x)$  is continuous at  $x = 1/2$ , the integral of the second term goes to zero, and we have

$$y'(1/2+) - y'(1/2-) + 8y(1/2) = 0$$

The expressions for  $y(x)$  and  $y'(x)$  for  $x > 1/2$  and  $x < 1/2$  then yield

$$\mu [-\cosh(\mu/2) - \cosh(\mu/2)] = -8 \sinh(\mu/2)$$

or

$$\tanh(\mu/2) = \mu/4. \quad (13)$$

Since the graphs of  $s = \mu/4$  and  $s = \tanh \mu/2$  intersect in the first (and third) quadrant of the  $\mu, s$ -plane, equation (13) has non-zero real roots, say  $\pm\mu_0$ ; thus  $\lambda = \mu_0^2$  is a positive eigenvalue of problem (12), so that  $\phi_2$  is an unstable solution of (9-10-11). So is  $-\phi_2$ .

We have not carried out the details for the other  $\phi_n$ 's, but we suspect that  $\pm\phi_n$ ,  $n > 1$ , are all unstable.

### References

1. M. A. Aizerman and A. I. Lur'e, Methods for construction of periodic motions in piecewise-linear systems, in Analytical Methods in Theory of Nonlinear Vibrations, Proc. International Symposium on Nonlinear Vibrations, v. I, 1961, Izdat. Akad. Nauk Ukrain. SSR, Kiev, 1963, 27-50
2. B. A. Fleishman, Convex superposition in piecewise-linear systems, J. Math. Anal. and Appl. 6 (1963), 182-189
3. \_\_\_\_\_ and P. W. Davis, A simple boundary value problem with infinitely many solutions, submitted
4. \_\_\_\_\_ and T. J. Mahar, Analytic methods for approximate solution of elliptic free boundary problems, Nonlinear Analysis, Theory, Methods and Applications, 1 (1977), 561-569.
5. \_\_\_\_\_ and \_\_\_\_\_, A step-function model in chemical reactor theory: multiplicity and stability of solutions, Nonlinear Analysis, Theory, Methods, and Applications 5 (1981), 645-654

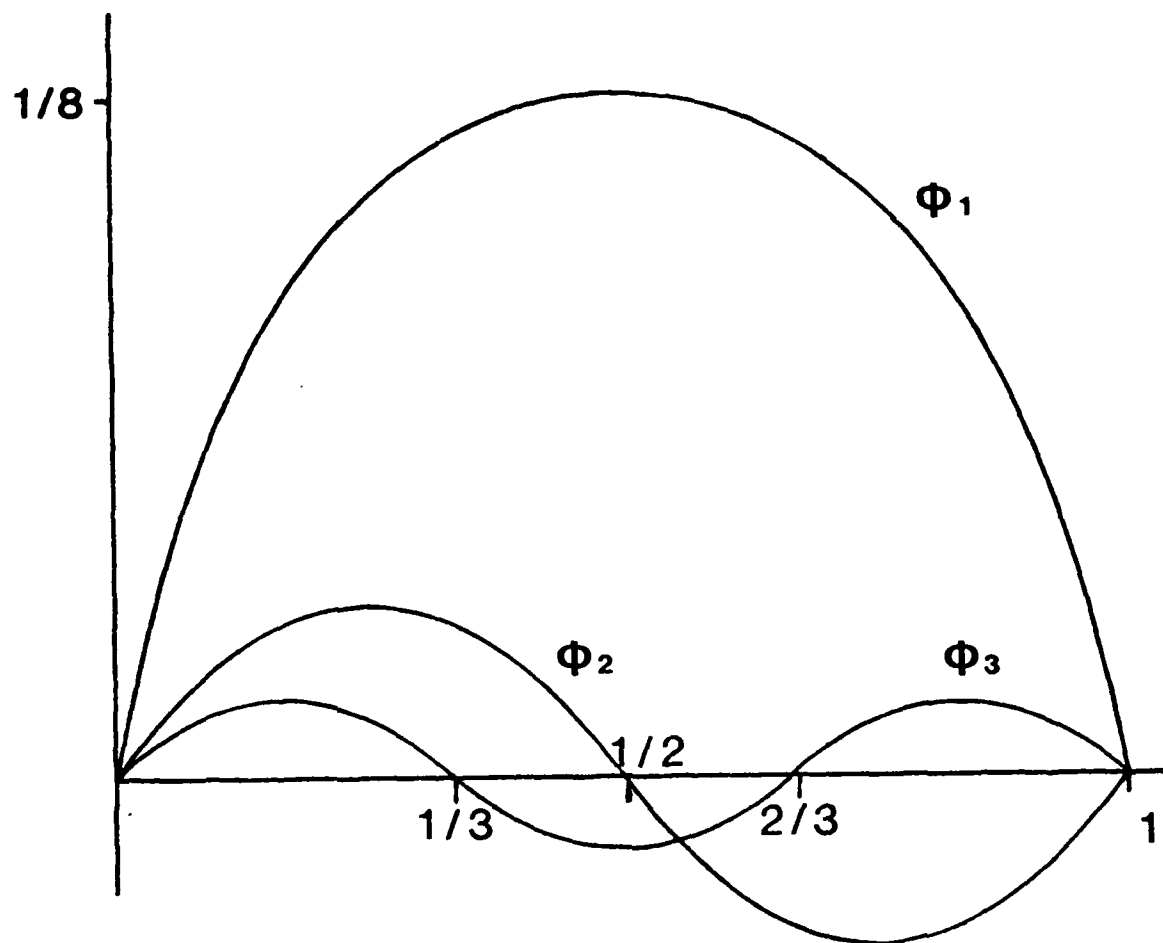


Fig. 1: The solutions  $\Phi_1$ ,  $\Phi_2$ ,  $\Phi_3$

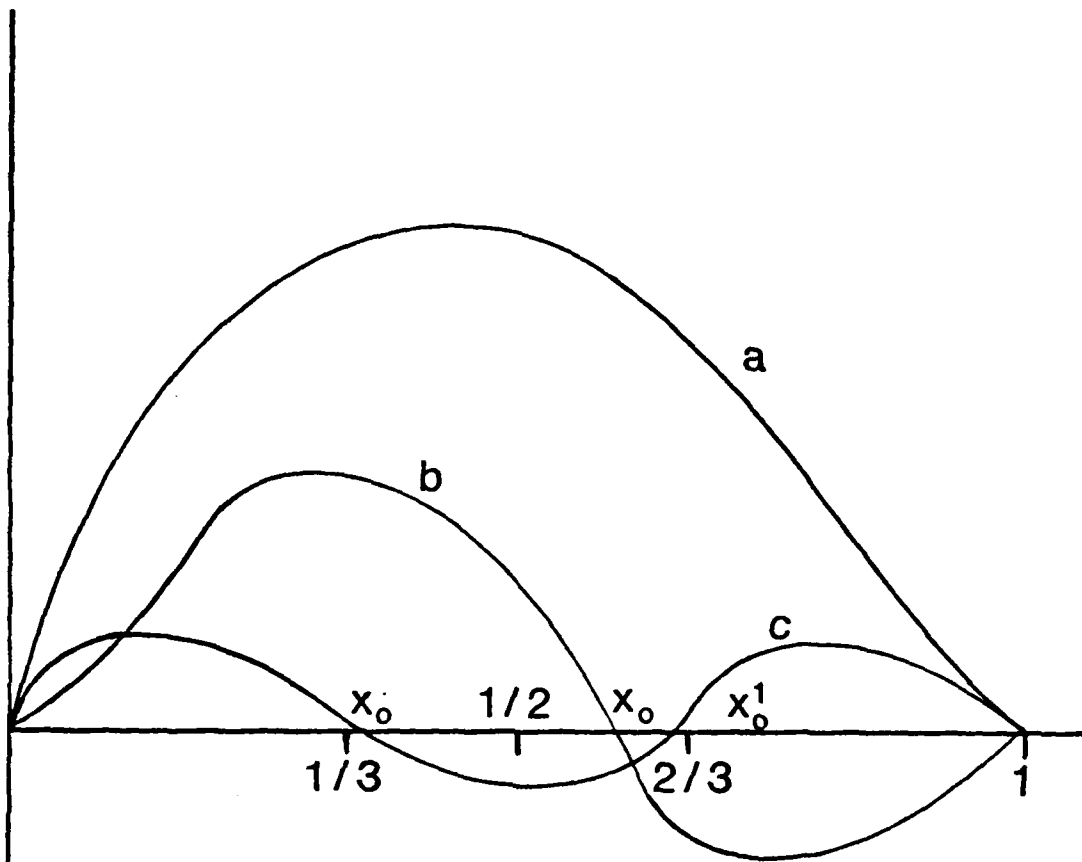


Fig. 2: Three examples of initial iterates



AD P001020

THE EVOLUTION OF A GAS BUBBLE IN A  
CLOSED VOLUME OF STIRRED LIQUID

Peter Tikuisis\* and Charles A. Ward  
Department of Mechanical Engineering  
University of Toronto  
Toronto, Ontario, Canada

\*Present Address: Defence & Civil Institute of Environmental Medicine  
1133 Sheppard Avenue West  
P.O. Box 2000  
Downsview, Ontario, Canada

ABSTRACT

The rate of bubble evolution and hence the rate of mass transport across a curved liquid-gas interface has been examined both theoretically and experimentally. The closed liquid volume constraint provides the mechanism by which the gas bubble may be placed initially in a state of stable equilibrium, thus allowing an accurate determination of the system parameters. The stirred liquid condition is measured with the use of laser-doppler anemometry. Through an experimental examination on the complete dissolution of nitrogen gas bubbles in water, the mechanism of mass transport is shown to be consistent with a model comprised of two processes: 1) the primary and rate-limiting process is modelled by the diffusion of gas through an unstirred liquid boundary layer whose thickness varies with bubble radius and 2) a second-order limitation is shown to be due to the condition of non-equilibrium of the gas component at the phase boundary. The non-linearity of mass transport is shown to increase as curvature of the liquid-gas interface increases.

## INTRODUCTION

A number of experimental studies have been conducted of bubbles in a stirred liquid [1-6], however none of the kinetic analyses have applied to the circumstance of a bubble contained in a volume of liquid closed to external mass transport or to those liquid-gas interfaces of large curvature. Here we consider the evolution of a bubble under such conditions. The closed volume constraint allows us to initially place the bubble in a state of stable equilibrium [7] and therefore the system parameters such as total gas content and liquid volume can be determined. We investigate two features previously not considered in this type of problem; firstly, we assume the existence of a thin unstirred layer of liquid of variable thickness at the bubble boundary (past expressions assume a constant thickness [8]) and secondly, we consider the interfacial resistance to mass transport across the liquid-gas phase boundary [9].

## MODEL EQUATIONS

We begin this study by considering the boundary value problem shown schematically in Fig. 1 in which a single bubble of radius  $R$  is immersed in a liquid of a finite volume and of radius  $b$ . It is assumed that the liquid surrounding the bubble is well-stirred except for a thin unstirred boundary layer of thickness  $\delta$ . The transport of gas through the unstirred liquid is governed by the following diffusion equation:

$$\frac{1}{r^2} \frac{\partial^2}{\partial r^2} (rc) = \frac{1}{D} \frac{\partial c}{\partial t} \quad R \leq r \leq R + \delta, t > 0, \quad (1)$$

subject to the following initial and boundary conditions:

$$c = c_0, \quad R \leq r \leq b, \quad t = 0, \quad (2)$$

$$c = c_\infty, \quad R + \delta \leq r \leq b, \quad t > 0, \text{ and} \quad (3)$$

$$c = c(R), \quad r = R, \quad t > 0, \quad (4)$$

where  $r$  is the radius taken from the centre of the bubble and  $c$  and  $D$  are, respectively, the concentration and diffusivity of the gas component in the liquid phase. This diffusion problem can be solved by an Integral Transform Method [10].

We depart from the conventional procedure of assuming that the gas component is in local equilibrium across the phase boundary and instead adopt the expression for the mass flux across the interface from a recently developed statistical rate theory [9]. The non-equilibrium mass flux is given by:

$$J_{g1} = k_{g1} [\alpha/c(R) - c(R)/\alpha], \quad (5)$$

where the rate constant,  $k_{g1}$ , is a property of the liquid-gas solution and  $\alpha$  is the gas solubility or that value of the gas concentration

that would be in equilibrium with the liquid-gas solution.

We introduce a second flux expression that arises from the diffusion of gas through the unstirred layer of liquid:

$$J_{g1} = -D(\partial c/\partial r)|_R, \quad (6)$$

where the gradient of gas concentration is determined through the solution of Eq. 1. By equating the two flux expressions, we obtain a quadratic expression for determining the dissolved gas concentration at the phase boundary, i.e.  $c$  at  $R$ :

$$c(R)^2 - (\gamma D/k_{g1})(\partial c/\partial r)|_R - \gamma^2 = 0. \quad (7)$$

For detail on the solution to the gas concentration gradient see Ref. 11.

We hypothesize the following formulation for the thickness of the unstirred layer of liquid around the bubble:

$$\delta = Z[1 - \exp(-R/Z)], \quad (8)$$

where the parameter  $Z$  is the unstirred layer thickness for a flat interface; that is, as the bubble radius tends to infinity. This expression is unique in that it also satisfies the constraint of

a vanishing unstirred layer as the bubble radius tends to zero; in fact, our expression suggests that the unstirred layer thickness approaches the bubble radius in that limit.

Finally, the evolution of the bubble is determined by equating the mass flow at the phase boundary to the net change of gas molecules in the gaseous phase:

$$dN_g/dt = -4\pi R^2 J_{g1} \quad (9)$$

We assume ideal gas behaviour and introduce the Laplace relationship to the above expression to obtain the following rate equation for bubble evolution:

$$dR/dt = kTJ_{g1}/(P - P_v + 4\gamma/3R) \quad (10)$$

where  $k$  is the Boltzmann constant,  $T$  is the temperature,  $P$  is the liquid pressure,  $P_v$  is the vapour pressure and  $\gamma$  is the liquid surface tension. Of all the parameters introduced in the theory, only the value of  $Z$  is unknown, all other parameters can be measured or predicted.

#### EXPERIMENTAL EXAMINATION OF BUBBLE EVOLUTION

A single bubble is generated in a water-nitrogen solution,

caught as a set of thin glass fibres and then lowered into a spherically shaped cavity of approximately 1.3 cc in volume. After positioning the bubble, more or less concentrically, the cavity is sealed and the liquid pressure is controlled to within 0.04 mmHg by a mercury plug in contact with a gas reservoir. A micro stir bar is rotated to ensure adequate mixing of the water-nitrogen solution. Greater detail on the experimental arrangement can be found in Ref. 7.

Laser-doppler anemometry [12] was used to measure the motion of liquid as it was stirred. It was found that the liquid motion was both laminar and sinusoidal, a finding consistent with all the stir rates measured, namely 2, 3, 4 and 5 Hz. An analysis of the fluid velocities indicates that the root mean square velocity of the fluctuating component exceeds the value of the mean flow for all stir rates. We conclude therefore, that although the flow is laminar, there is a good degree of mixing.

Once the bubble was stabilized in the cavity [7], the liquid pressure was increased and the bubble was allowed to dissolve away completely. Figure 2 shows the sequence of photographs taken during the complete dissolution of one such bubble. Note the various stages of bubble attachment to the glass fibres, labelled f1 through f4.

Figure 3 shows the measured values of the bubble radius, indicated by the circles, and the theoretical path of evolution, given

by the solid line, for a stirred liquid condition of 5 Hz. The solid line was obtained by numerical integration of the rate equation (Eq. 10) and by applying various values of  $Z$  until the best agreement was found through a least squares analysis. The slight deviation between the experiment and theory for bubble radii of less than 30  $\mu\text{m}$  may be due to the obstruction of mass transport by the presence of the glass fibres. Finally, the dashed line shows the thickness of the unstirred boundary layer.

Figure 4 shows the bubble dissolution for a stirred liquid condition of 2 Hz. The theoretical fit begins to deteriorate at a bubble radius of less than 100  $\mu\text{m}$ . This result is not surprising considering the assumption that the unstirred boundary layer is perfectly concentric. Since the flow of liquid has been shown to be laminar with superimposed sinusoidal oscillations, the streamlines of flow around the bubble are skewed, the degree depending upon the stir rate. For a low stir rate of 2 Hz, the assumption of a concentric unstirred liquid layer is therefore not consistent with the experimental result.

In Figure 5, the experimental results for bubble evolution in a stirred liquid condition of 3 Hz is shown to be in excellent agreement with the theoretical prediction. We consider the liquid to be well-stirred in this circumstance. For completeness, the rate of bubble evolution was documented for a stirred liquid condition of 4 Hz and again, excellent agreement between experiment and theory was obtained

as can be seen in Fig. 6. We emphasize that these experiments have been repeated and the results have been consistent.

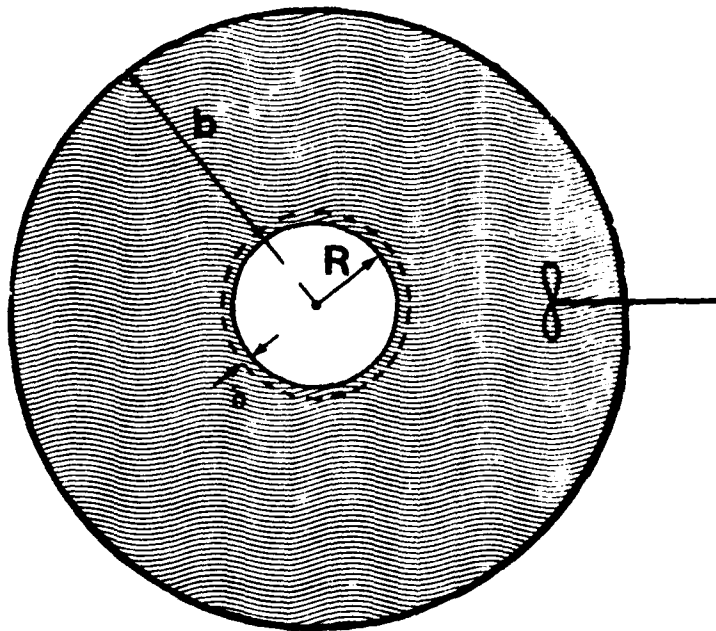
#### SUMMARY

Through a series of experiments, we have shown that the evolution of a bubble in a well-stirred liquid of finite volume can be modelled by assuming a thin unstirred layer of liquid of radial dependent thickness surrounding the bubble. It is to be noted that the unstirred layer thickness changes significantly only for small bubble radii. Less obvious is the finding that the non-equilibrium condition of mass transport across the phase boundary becomes increasingly important as the bubble radius decreases. It can be stated that for bubbles immersed in a stirred liquid, an unstirred liquid layer of constant thickness and a condition of local equilibrium of the gas component at the liquid-gas boundary are valid assumptions only if the bubble radius exceeds 300  $\mu\text{m}$ .

### References

1. D. Hammerton and F.H. Garner. *Trans. Instn. Chem. Engrs.* 32: 518 (1954).
2. J.H. Leonard and G. Houghton. *Chem. Eng. Sci.* 18: 133 (1963).
3. G.R. Garbarini and C. Tien. *Can J. Chem. Eng.* 47: 35 (1969).
4. W.T. Koetsier, D. Thoenes and J.F. Frankena. *Chem. Eng. J.* 5: 61 (1973)
5. K. Kiode, Y. Orito and Y. Hara. *Chem. Eng. Sci.* 29: 417 (1974).
6. M. Filla, J.F. Davidson, J.F. Bates and A. Eccles. *Chem. Eng. Sci.* 31: 359 (1976).
7. C.A. Ward, P. Tikuisis and R.D. Venter. *J. Appl. Phys.* (in press).
8. V.G. Levich. *Physicochemical Hydrodynamics*, Prentice-Hall, New Jersey, 1962, pg. 692.
9. C.A. Ward. *J. Chem. Phys.* 67: 229 (1977).

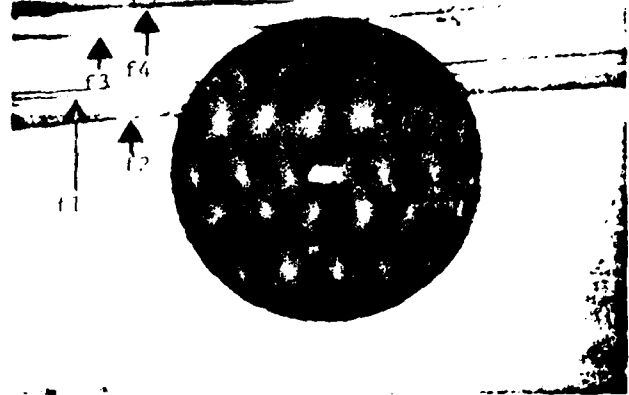
10. M.N. Ozisik. Boundary Value Problems of Heat Conduction. Int. Textbook, Pennsylvania, 1968, pg. 194.
11. P. Tikuisis, C.A. Ward and R.D. Venter. (Submitted for publication).
12. F. Durst, A. Melling and J.H. Whitelaw. Principles and Practice of Laser-Depler Anemometry. Academic Press, London, 1976, pg. 4.



Schematic of the geometry for the examination of bubble evolution. A single gas bubble of radius  $R$  is shown bounded by a thin unstirred layer of liquid of thickness  $\delta$  and immersed in a finite well-stirred liquid of radius  $b$ .



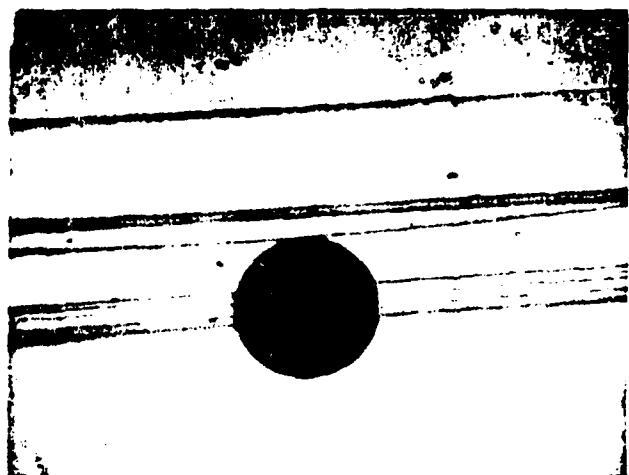
a)  $t = 0$



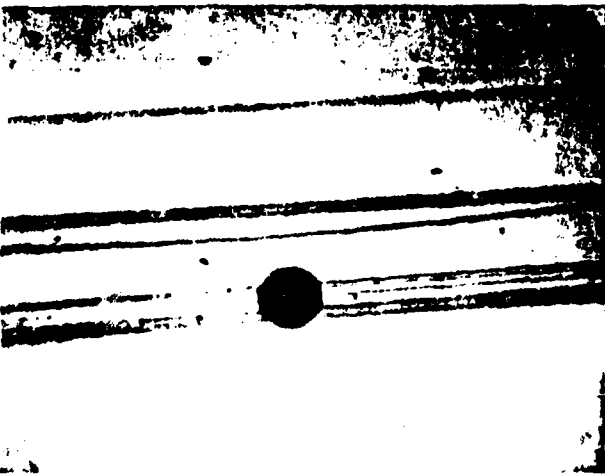
b)  $t = 0.5 \text{ min}$



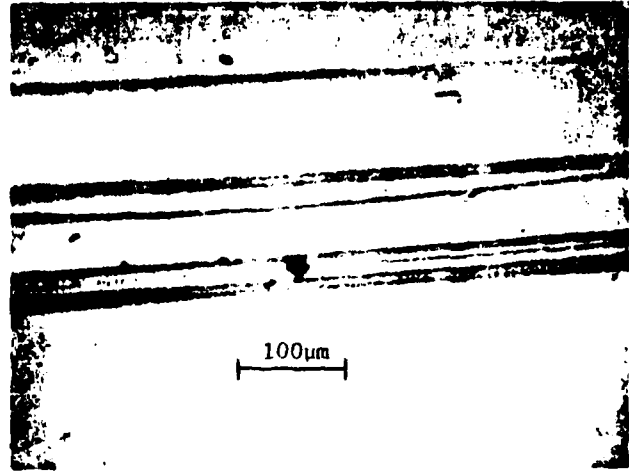
c)  $t = 20 \text{ min}$



d)  $t = 30 \text{ min}$



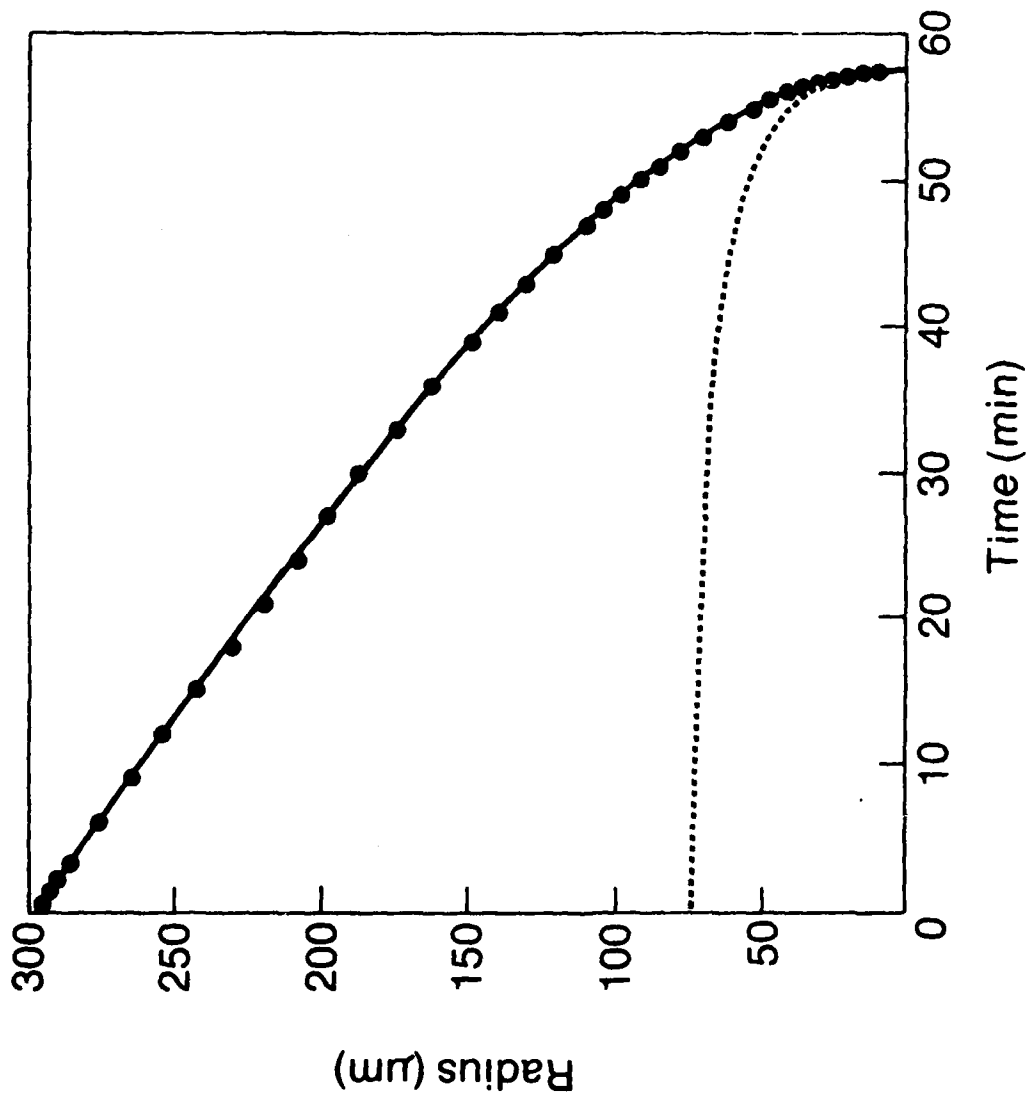
e)  $t = 40 \text{ min}$



f)  $t = 43 \text{ min}$

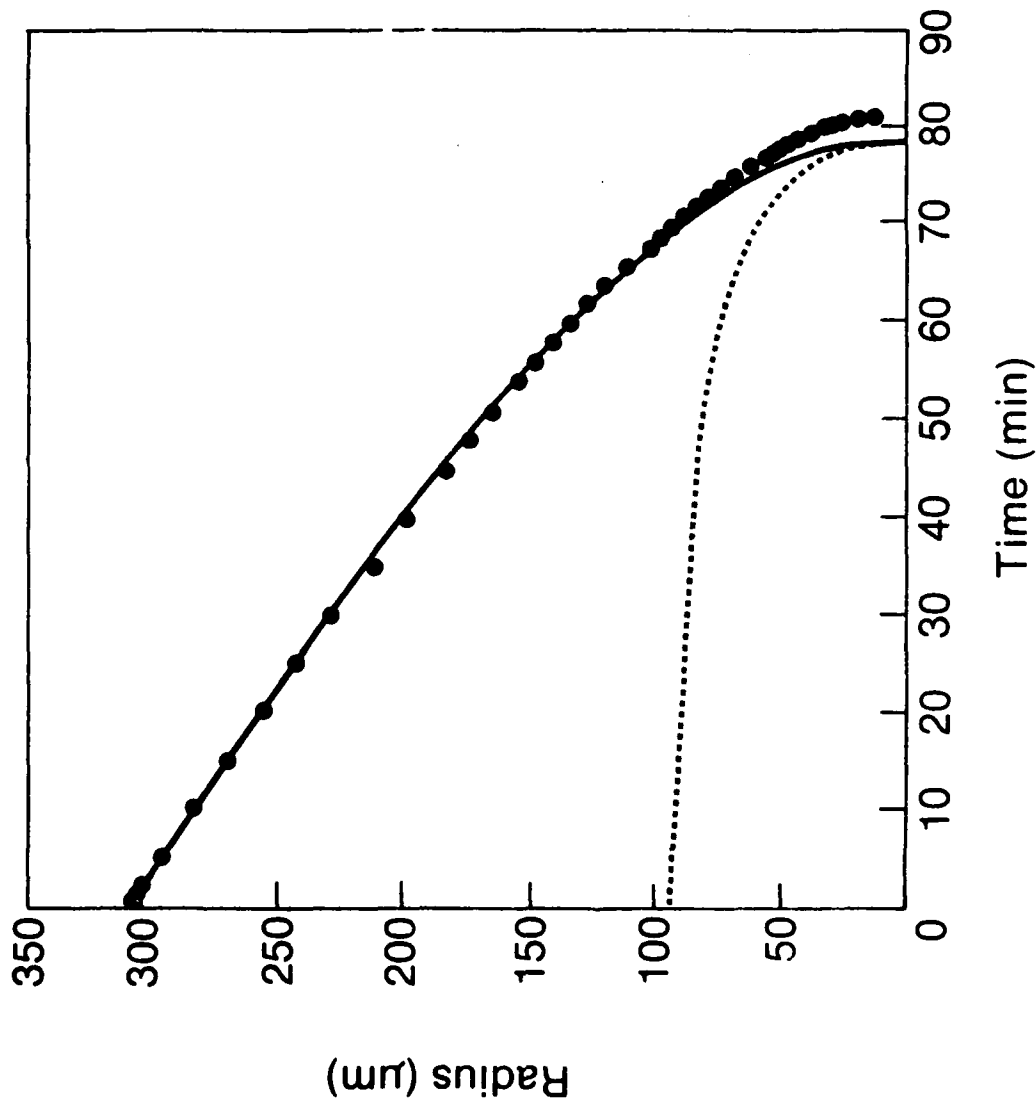
Sequence of photographs of the complete dissolution of a bubble in a water-nitrogen solution stirred at 5 Hz. The initial bubble radius was 298.4µm and the liquid pressure was increased from 743.55 mm Hg to 829.40 Hg. 168

**Figure 2**



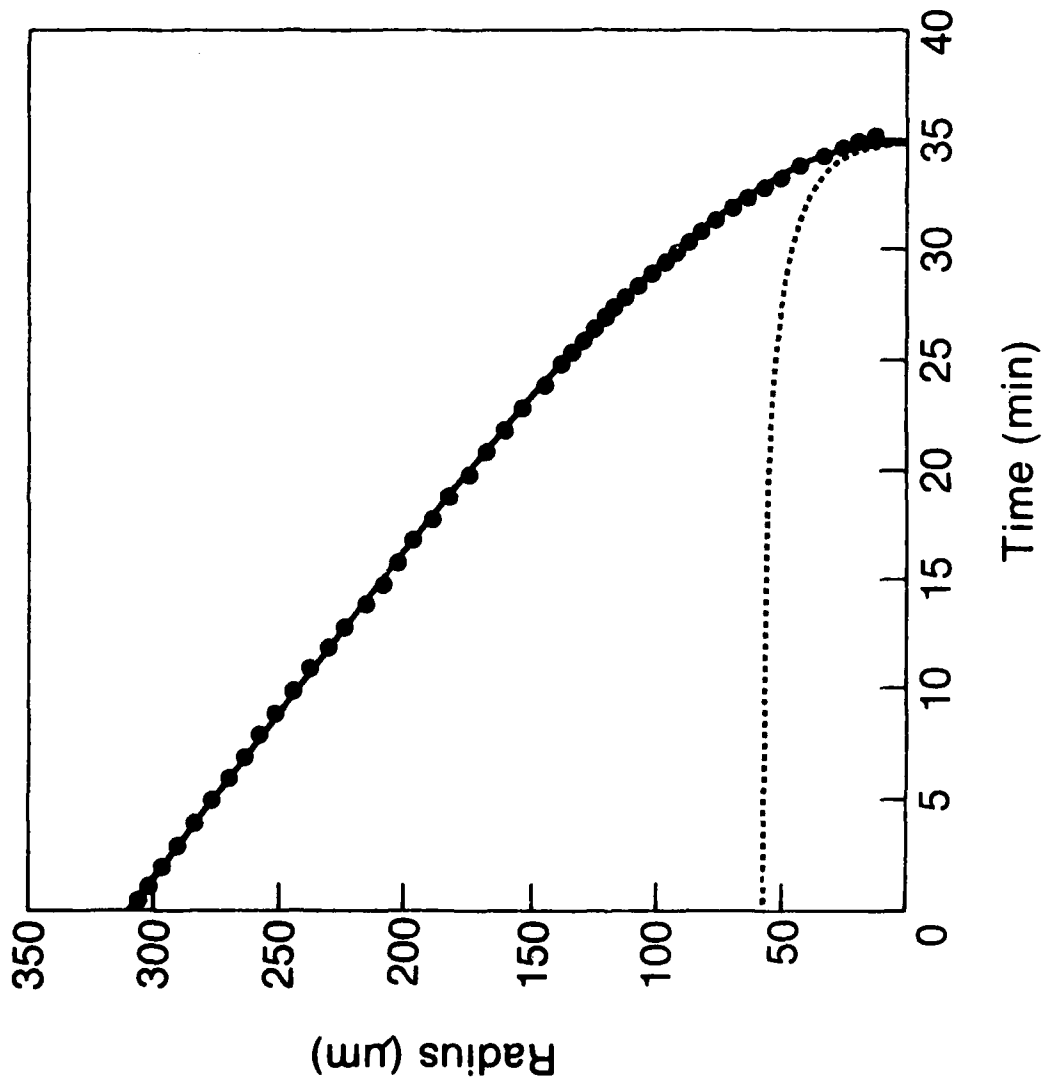
Measured bubble radii (•) during the evolution of a bubble in a water-nitrogen solution at 25°C and stirred at 5 Hz. The initial bubble radius was 326.5 μm and the liquid pressure was increased from 735.70 mmHg to 864.60 mmHg. The solid line shows the theoretical path of evolution and the dashed line shows the thickness of the unstirred layer of liquid around the bubble.

**Figure 3**



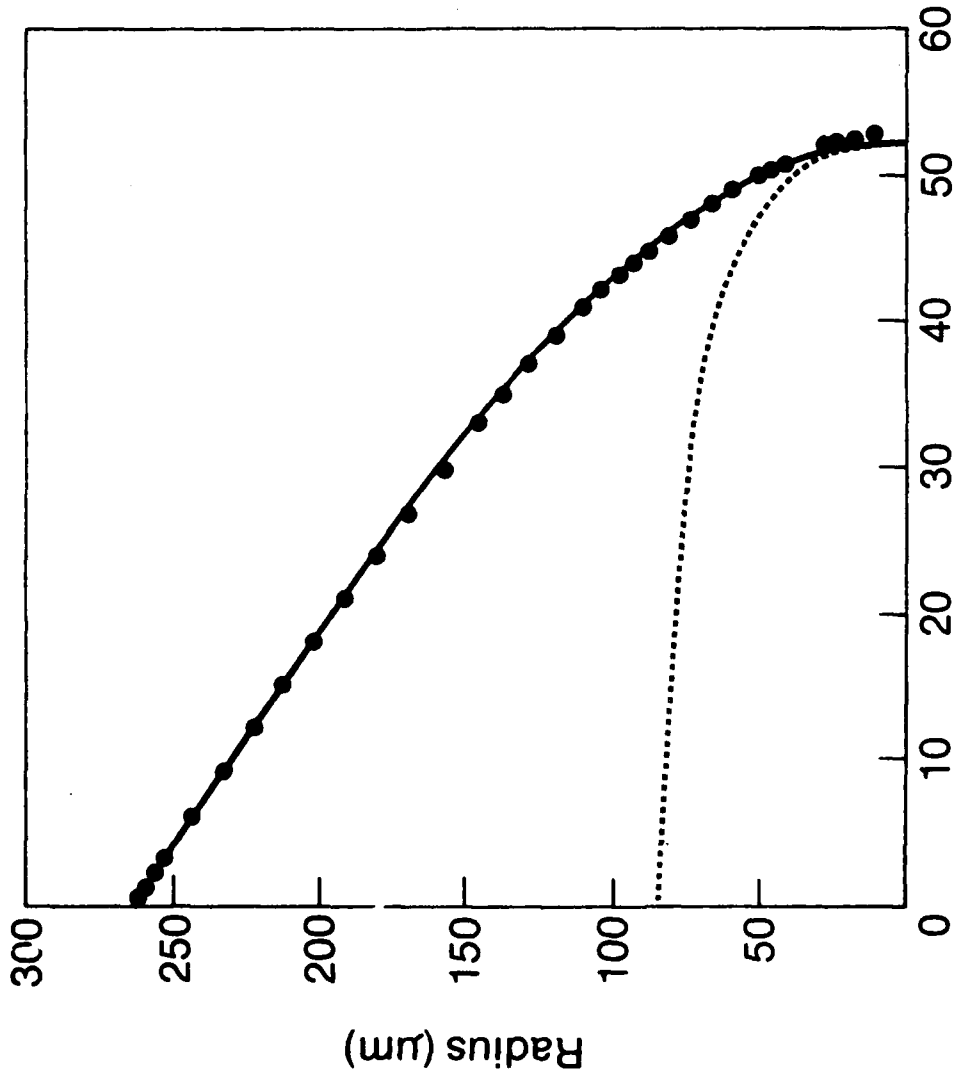
Measured bubble radii (•) during the evolution of a bubble in a water-nitrogen solution at 25°C and stirred at 2 Hz. The initial bubble radius was 320.2µm and the liquid pressure was increased from 783.63mmHg to 858.70mmHg. The solid line shows the theoretical path of evolution and the dashed line shows the thickness of the unstirred layer of liquid around the bubble

Figure 4



Measured bubble radii (•) during the evolution of a bubble in a water-nitrogen solution at 25°C and stirred at 3Hz. The initial bubble radius was 272.µm and the liquid pressure was increased from 761.02mmHg to 841.79mmHg. The solid line shows the theoretical path of evolution and the dashed line the thickness of the unstirred layer of liquid around the bubble.

**Figure 5**



Measured bubble radii (•) during the evolution of a bubble in a water-nitrogen solution at 25°C and stirred at 4Hz. The initial bubble radius was 306.5μm and the liquid pressure was increased from 770.81mmHg to 854.01mmHg. the solid line shows the theoretical path of evolution and the dashed line shows the thickness of the unstirred layer of liquid around the bubble.

Figure 6

AD P001021

ON GROWTH PROCESSES OF CONDENSATION AEROSOLS

J. R. Brock  
Chemical Engineering Department  
University of Texas  
Austin, Texas 78712

ABSTRACT. Aerosol particles formed by condensation of a vapor grow by the processes of coagulation and condensation/evaporation. Some properties of the evolution equations describing each of these processes are discussed. The complexity of the rate coefficients for these processes precludes general analytical solutions and necessitates numerical approximation. Some approaches to numerical analysis of the coagulation and condensation/evaporation processes are outlined briefly.

I. INTRODUCTION. An aerosol of coalescing (liquid) particles formed by nucleation from a single chemical species is usually characterized by its particle size distribution [1]. For such aerosols, the goal of simulation studies is to describe the evolution of this distribution. This evolution begins with the aggregation of monomeric molecular species at sufficiently high supersaturations to form stable particles which subsequently grow by the processes of coagulation and condensation/evaporation.

The description of the nucleation step in aerosol formation remains as one of the unsolved problems of classified physics [2]. Therefore, a complete theory of aerosol evolution is not now possible. However, an approximate theory is possible in the later evolutionary stages where coagulation and condensation/evaporation are the only growth processes in infinite, spatially homogeneous systems.

In this paper some aspects of aerosol growth by coagulation and condensation/evaporation are discussed. In the first section, the theories of Brownian coagulation and Knudsen condensation/evaporation are discussed. The rate coefficients of these processes are sufficiently complex that only numerical solution of the evolution equations of coagulation and condensation/evaporation is possible. Some numerical procedures are outlined in the final section.

II. COAGULATION AND CONDENSATION. The formation of particles in a condensing vapor is controlled by the vapor supersaturation,  $S$ . So long as  $S$  is greater than the critical supersaturation,  $S_c$  for that temperature, new particles will be created by nucleation.<sup>c</sup> For a spatially homogeneous, isothermal system prepared with an initial  $S > S_c$ ,

S will decrease as nucleation and condensation on existing stable particles continues. Eventually,  $S < S_c$  and production of new particles ceases. Subsequent to nucleation the stable particles grow by the coagulation and condensation/evaporation processes. In this section these are examined.

For a uniform system, after nucleation the evolution of the ultra-fine aerosol can be represented by the conservation equations in the continuous representation for the number density function  $n(x,t)$  and the vapor mass concentration,  $c$ . For a uniform system with no sources of particles:

$$\begin{aligned} \frac{\partial n(x,t)}{\partial t} = & (\frac{1}{2}) \int_{x^*}^x dx' b(x-x',x') n(x-x',t) n(x,t) \\ & - n(x,t) \int_{x^*}^{\infty} dx' b(x',x) n(x',t) \\ & - \frac{\partial}{\partial x} [\Psi(x,t) n(x,t)] \end{aligned} \quad (1)$$

where  $n(x,t) dx$  is the number of particles with masses in the range  $x$ ,  $dx$  at time  $t$ .  $x^*$  is the mass of the critical nucleus. For a uniform system,  $b(x',x)$  is the Brownian coagulation coefficient [3] given by the expression:

$$\begin{aligned} b(x',x) &= 4\pi(R + R') (D + D') \beta \\ \beta &= 1 / (1 + 4(D + D') / (x^{1/3} + x'^{1/3}) (\bar{v}^2 + \bar{v}'^2)^{1/2}) \\ x &= (4/3) \pi R^3 \rho; \quad \bar{v} = (8kT/\pi x)^{1/2}; \\ D &= (kT/6\pi\mu R) (1 + Kn (A + B e^{-CKn^{-1}})) \end{aligned} \quad (2)$$

where  $R$  is the radius of a particle of mass  $x$ ,  $\rho$  is the particle density,  $kT$  is the thermal energy,  $\mu$  the viscosity of the host gas, and  $Kn$  the Knudsen number. Here  $Kn = \bar{L}/R$ , where  $\bar{L}$  is the molecular mean free path of the host gas. The first and second terms on the right hand side of equation (1) represent the coagulation process. The third term represents the condensation/evaporation process, where  $\Psi$  is the rate coefficient [4]:

$$\begin{aligned} \Psi(x) &= \pi R^2 \bar{v}_1 c_v (S - e^{Ke}) \pi^{1/2} Kn \\ &\cdot \left[ \frac{1 + Kn \left(\frac{4\pi Kn}{3}\right) + 1.016}{\frac{4 Kn}{3} + 1} \right]^{-1} \end{aligned} \quad (3)$$

where:

$$\bar{V}_1 = \left( \frac{8kT}{\pi m_1} \right)^{1/2}; \quad Kn = L/R; \quad L = 2D_{1h} (m_1/2kT)^{1/2}; \quad S = c/c_v$$

$m_1$  is the molecular mass of the condensing monomer,  $D_{1h}$  is the diffusion of the monomer in the host gas and  $c_v$  is the vapor mass concentration corresponding to the vapor pressure  $V$  in the bulk condensate.  $Ke$  is the Kelvin number:  $Ke = 2\sigma\gamma/RkT$ , where  $\sigma$  is the surface tension and  $\gamma$  the molecular volume of the condensed state. Equation (1) is coupled to the vapor mass conservation equation:

$$\frac{\partial c}{\partial t} = - \int_{x^*}^{\infty} dx \Psi(x,c) n(x,t) - x^* \Psi(x^*,c) n(x^*,t) \quad (4)$$

where  $x^*$  represents the mass of the critical nucleus size so that evaporation from this size leads to unstable particles and an addition to the monomer concentration.

Some of the properties of these processes can be examined by considering the first two moments of (1) - the total number concentration,  $M_0$  and total mass concentration  $M_1$ :

$$M_0 = \int_{x^*}^{\infty} n(x,t) dx \quad (5)$$

$$M_1 = \int_{x^*}^{\infty} x n(x,t) dx \quad (6)$$

It is simple to show that the moment equations for (1) and (4) are [1]:

$$\begin{aligned} \frac{\partial M_0}{\partial t} = & -(\frac{1}{2}) \int_{x^*}^{\infty} \int_{x^*}^{\infty} dx' dx b(x',x) n(x,t) n(x,t) \\ & + \Psi(x^*,c) n(x^*,t) \end{aligned} \quad (7)$$

$$\frac{\partial M_1}{\partial t} = \int_{x^*}^{\infty} dx \Psi(x,c,t) n(x,t) + x^* \Psi(x^*,c) n(x^*,t) \quad (8)$$

As can be demonstrated easily (e.g. [1]) the coagulation process conserves particle mass and this term vanishes in obtaining equation (8).

Also, adding (4) and (8) gives:

$$\frac{\partial}{\partial t} (M_1 + c) = 0 \quad (9)$$

so that, as obvious from the specifications of the physical system, the total mass concentration of particles plus monomer is invariant. The number concentration,  $M(t)$  decreases not only by coagulation but also by the instability below  $x^*$ , which is determined by the critical supersaturation  $S_c$  for the system temperature,  $T$ . According to the classical theory, the radius of the critical nucleus,  $R^*$ , is:

$$R^* = 2\sigma\gamma/\kappa T \ln S_c \quad (10)$$

and therefore:  $x^* = (4/3) \pi R^{*3} \rho$

As particle growth proceeds at  $S < S_c$ , the point separating the regions of evaporation and condensation is given by:

$$R_0 = 2\sigma\gamma/\kappa T \ln S \quad (11)$$

since  $\Psi(R_0) = 0$ . As the stable particles grow by coagulation and condensation,  $R_0$  increases as  $S$  decreases. Clearly, as  $S \rightarrow 1$ ,  $R_0 \rightarrow \infty$ . In the initial stages of growth, particle sizes are small and those with radii  $R < R_0$  will evaporate rapidly when  $Ke \gg 1$ . This evaporation supplies monomeric vapor which permits condensation to proceed for particles with  $R > R_0$ .

In many applications monomeric vapor is not conserved as in the system described. Instead mixing with external streams may rapidly lower  $S$ , perhaps to the extent that  $S < 1$ . In this case the particles will, of course, only evaporate. If the vapor pressure of the substance composing the particles is very small relative to the time scale of interest, then evaporation may be neglected and coagulation will remain as the only growth process.

The work of Sutugin (e.g. [5]) has shown that under some conditions formation and growth of ultrafine particles will proceed entirely through the coagulation mechanism. Regardless of the process suppressing the condensation/evaporation process, it is of interest to consider briefly the characteristic features of the coagulation process.

In practice, one is often interested not in the details of  $n(x,t)$  during the nucleation regime or during early stages of growth but in the form of  $n(x,t)$  for long times - the asymptotic distribution. Several

questions can be posed: given an initial density function  $n(x,0)$  in a system in which only coagulation occurs, will the form of this density function be changed by coagulation, and if so what will be the form of the new function?

These questions can be studied in the case of coagulation in a uniform system in which the aerosol evolves according to equation (1) without the condensation/evaporation term:

$$\frac{\partial n(x,t)}{\partial t} = \left(\frac{1}{2}\right) \int_{x^*}^x dx' b(x-x',x') n(x-x',t) n(x',t) - n(x,t) \int_{x^*}^{\infty} dx' b(x',x) n(x',t) \quad (12)$$

subject to the initial condition  $n(x,0)$ . The questions posed have been investigated analytically by a number of investigators (e.g. [6], [7], [8]) for restricted forms of  $n(x,0)$  and restricted forms of  $b(x',x)$ . For Brownian coagulation with  $b(x',x)$  given by equation (2) and more complex density functions, it is only possible to study these questions by numerical analysis.

We have recently carried out [9] numerical investigations of equation (12) with  $b(x',x)$  given by equation (2) with the view of determining the existence of an asymptotic limit distribution  $n(x,t \rightarrow \infty)$  and the empirical distribution providing the best fit to  $n(x,t \rightarrow \infty)$ . This investigation used the five initial number density functions shown in Figure 1 in non-dimensional form for convenience: log normal, exponential, first-order gamma, gamma, and log gamma. Each of the five density functions has two adjustable parameters which were set by requiring that the mass concentration and geometric mean particle size be the same for each of the functions. In this example, after times in excess of  $10^3$  sec. the initial density functions are "forgotten" and all five are merged essentially into the same density function. The rate at which the five density functions approach each other can be seen from Figures 2, 3 and 4 for the moments  $M_2$ ,  $M_3$  and  $M_4$ . The log gamma function merges with the other four at a noticeably slower rate. This is caused by the long tail of this initial function.

The best fit of the asymptotic function approached by the initial functions is an important question because it is intuitively supposed in the literature that the log normal density function should describe aged condensation aerosols. Two tests have been used in determining the best empirical density function: closeness of fit and randomness of fit. Five candidate density functions were chosen for these tests: log normal, first-order gamma, gamma, log gamma, and beta of the second kind. These were chosen because they have been used in the literature by various investigators as representative of the density function of

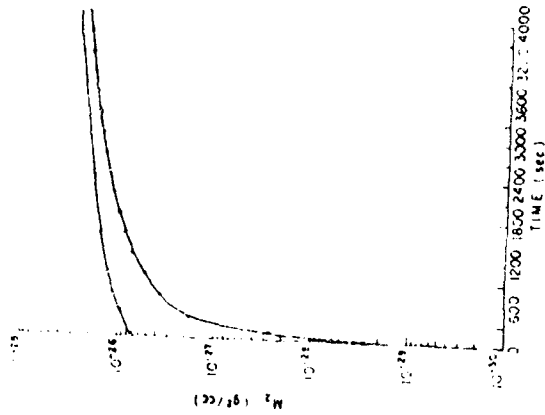


Figure 2. Effect of coagulation on second moments of five initial density functions as a function of time: approach to asymptotic limit distribution. See Fig. 1 for details.

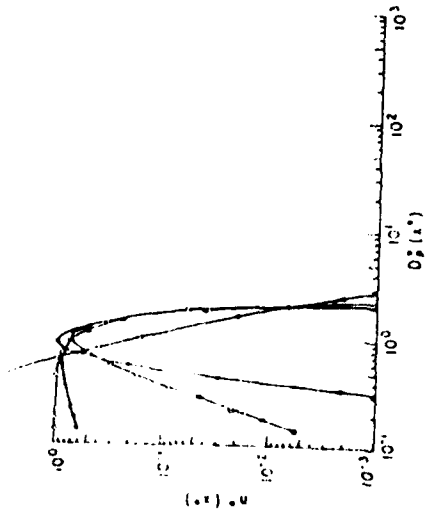


Figure 1. Reduced initial density functions used in study of asymptotic limit distributions for Brownian coagulation. Initial mass concentration =  $5E-11$  g/cc. Initial mean diameter =  $8E-7$  cm.

- Log normal
- ◇— Exponential
- First order gamma
- ▲— Gamma
- Log gamma

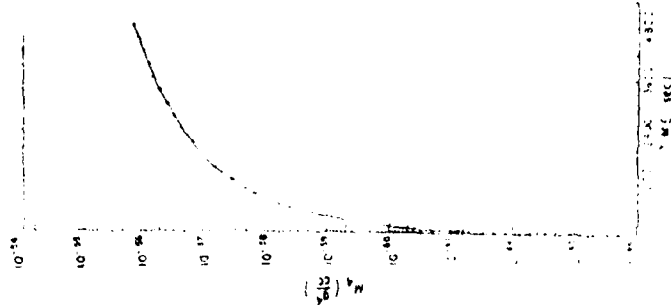


Figure 4. Effect of coagulation on fourth moment of initial density function as a function of time: approach to asymptotic limit distribution. See Fig. 1 for details.

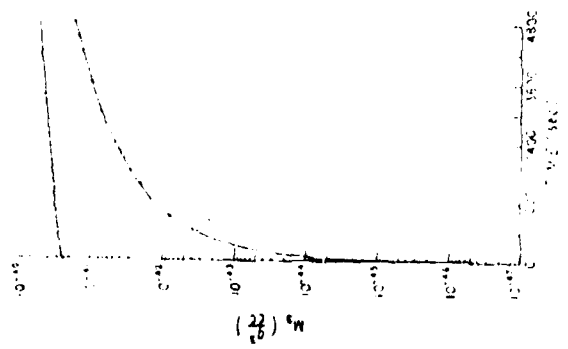


Figure 3. Effect of coagulation on third moments of five initial density functions as a function of time: approach to asymptotic limit distribution. See Fig. 1 for details.

AD-A128 683

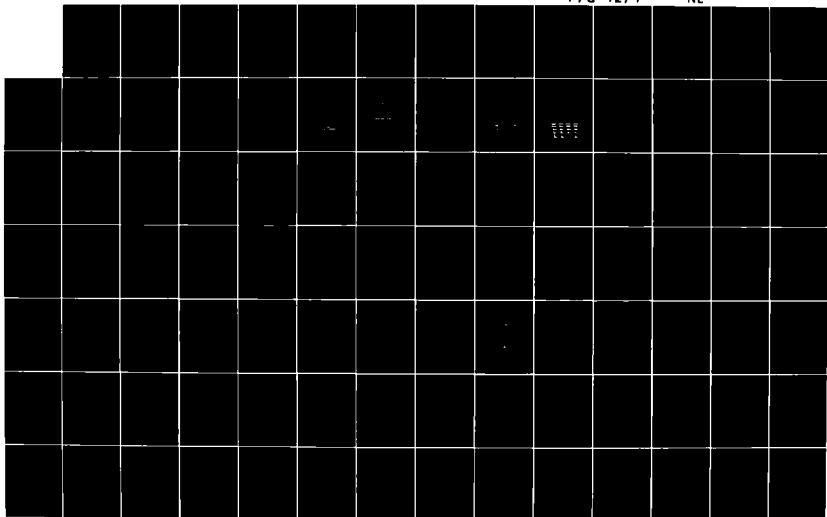
TRANSACTIONS OF THE CONFERENCE OF ARMY MATHEMATICIANS  
(28TH) HELD AT BETHESDA MARYLAND ON 28-30 JUNE 1982(U)  
ARMY RESEARCH OFFICE RESEARCH TRIANGLE PARK NC FEB 83  
ARO-83-1

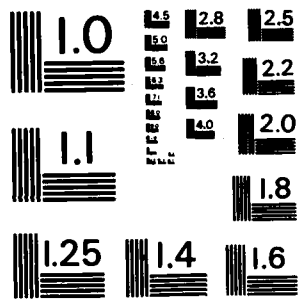
3/6

UNCLASSIFIED

F/G 12/1

NL





MICROCOPY RESOLUTION TEST CHART  
NATIONAL BUREAU OF STANDARDS-1963-A

condensation aerosols. By a variety of fitting procedures, it was determined that the log gamma density function was marginally superior to the log normal density function in providing an empirical fit to the numerical asymptotic limit function. Power spectral analysis of residuals revealed that the three other functions (first order gamma, gamma, beta of second kind) were consistently biased and were therefore unacceptable.

The various studies of asymptotic limit distributions produced by coagulation have all been initiated with unimodal or truncated density functions. The question arises as to the limit distribution for multimodal density functions. It has been pointed out [10] that the diagonal matrix elements of the Brownian coagulation coefficients are small in magnitude compared to the off-diagonal elements whose magnitudes are greatest between the smallest and largest particles. Therefore, growth in particle size within a mode is a slower process than the rate of attachment of particles of this mode by another mode of larger particles, if the number concentrations of the two modes are the same. This qualitative picture has been confirmed by numerical calculations [10], although the existence of an asymptotic limit was not investigated. The previous study [9] certainly suggests that a multimodal function will eventually approach a unimodal asymptotic limit function.

As coagulation of an aerosol with a unimodal density function proceeds, the characteristic time of coagulation  $t_{coag}$  increases. Approximately,  $t_{coag} \sim 1/bM_0$ . Coagulation can therefore be neglected when the interest is in times small in comparison with  $t_{coag}$ . For this situation, the evolution equation (1) reduces to:

$$\frac{\partial n(x,t)}{\partial t} = - \frac{\partial}{\partial x} [\Psi(x,S) n(x,t)] \quad (13)$$

which is coupled to the monomer conservation equation. In terms of the supersaturation ratio, S:

$$\frac{dS}{dt} = - \int_{x^*}^{\infty} dx \Psi(x,S,t) n(x,t) - x^* \Psi(x^*,S) n(x^*,t) \quad (14)$$

The condition  $n_{10} \ll n_h$  introduced at the beginning insures that the condensation/evaporation process is isothermal. Without this condition, equations (13) and (14) would be coupled to the energy conservation equation, as indeed is the case in consideration of rapid growth of aerosols.

If the supersaturation,  $S$ , is controlled externally equation (13) is decoupled from (14). In this case, the solution of (13) is very simple and can be effected by the method of characteristics. For two cases, similarity is easily demonstrated.

When  $S = S_0$ , a constant,  $\Psi$  given by equation (3) is a function only of  $x$ . With the transformations:

$$y = \int^x \frac{dx}{\Psi(x)}, \quad F = \Psi n, \quad \text{equation (13) becomes:}$$

$$\frac{\partial F}{\partial t} + \frac{\partial F}{\partial y} = 0 \quad (15)$$

which has the solution  $F = F_0(y-t)$  where  $F_0$  is some arbitrary initial function. Consequently:

$$n(x,t) = \frac{1}{\Psi(x)} F_0 \left( \int^x \frac{dx}{\Psi(x)} - t \right) \quad (16)$$

If  $S = S(t)$  where  $S(t)$  is determined by external variation, then similarity is also easily shown for the special case:  $\Psi = G(x)H(t)$ . This separation would be valid, for example, for  $\Psi$  given by equation (3) when  $S \gg Ke$ . With the transformations:  $y = \int^x \frac{dx}{G(x)}$ ,  $u = \int^t H(t)dt$ ,

$F = G(x)n$ , equation (13) becomes:

$$\frac{\partial F}{\partial u} + \frac{\partial F}{\partial y} = 0 \quad (17)$$

and  $F = F(y-u)$  so that:

$$n(x,t) = \frac{1}{G(x)} F_0 \left( \int^x \frac{dx}{G(x)} - \int^t H(t)dt \right) \quad (18)$$

Other special cases of similarity can be demonstrated. More generally, the solution of (13) is possible by standard procedures.

When  $S$  is not externally controlled, equations (13) and (14) are coupled and no simple solution appears to exist. Equations (13) and (14) with (3) are non-linear integro-differential equations and only numerical solution appears to be feasible. In the next part of this section, some approaches to this numerical problem will be considered briefly.

numerical accuracy.

The coagulation process can be simulated numerically with high accuracy. We have chosen methods which optimize both accuracy and efficiency. Accuracy has been studied ([10], [16]) by comparison with analytical solutions for restricted forms of  $b(x, x')$  and with Brownian coagulation, equation (2), by testing for conservation of mass. We use cubic spline for numerical quadrature and interpolation of the coagulation terms. Gear's method is used for time integration. Comparisons noted above show that simulation by these methods is accurate and reliable and that errors can be reduced to any desired level.

In comparison with the coagulation term, the condensation/evaporation term in equation (13) is deceptively simple in appearance. However, it is a first-order hyperbolic equation whose numerical solution is difficult, as evidenced by the numerous published attempts at numerical solution of similar hyperbolic equations (simulation of advection, for example). The difficulty lies in the fact that most numerical schemes for hyperbolic equations give rise to numerical dispersion and numerical diffusion. The numerical dispersion, due to the combination of large phase errors and insufficient damping of short waves, manifests itself by the unphysical wakes behind and ahead of the simulated regions of high concentration. Numerical diffusion lowers the peak values of the concentration distribution but increases the values around the peak. Numerical methods with "upwinding" can remove numerical dispersion but create unrealistic numerical diffusion [20]. Numerical methods without upwinding, such as the finite element method with linear basis functions ([20], [21], [22], [23]) do not introduce much numerical diffusion but create numerical dispersion. Such dispersion is undesirable for simulation or condensation/evaporation because the dispersion level increases with time and for prolonged simulations dispersion finally dominates and creates numerical instability. Also, numerical dispersion may erase the real "signatures" of the condensation/evaporation processes.

Many methods have been tried to reduce dispersion, such as by introduction of a dissipative term in the Galerkin finite element formulation ([21], [25]) or use of filtering schemes ([26], [27]). These have not been found to be suitable for condensation/evaporation simulation.

A robust numerical scheme for condensation/evaporation should be free of numerical dispersion while numerical diffusion is minimized. Eulerian numerical schemes create numerical dispersion whereas Lagrangian schemes do not suffer from this difficulty. Using Bonnerot and Jamet's approach [28], Varoglu and Finn [29] derived a finite element method incorporating characteristics for the diffusion-convection equation. This scheme is free of numerical dispersion. Recently, Neumann [30] derived an Eulerian-Lagrangian numerical scheme for the diffusion-convection equation, which is also free from numerical dispersion and controls numerical diffusion.

Numerical simulation of coagulation and condensation. A variety of methods have been proposed for numerical simulation of coagulation and condensation. Work before 1970 on coagulation has been reviewed by Drake [11]. Since this time, a large number of numerical studies have been carried out (e.g. [6], [10], [12], [13], [14], [15], [16]) in uniform systems. In view of the many numerical approximation schemes which have been proposed, it would be desirable to develop test problems for evaluating these schemes. For very large scale atmospheric aerosol dynamics simulations, approximate methods may be suitable, given the existing uncertainties in input data. The emphasis in this discussion will be on methods of high accuracy which we have employed in simulation studies.

Simulation of condensation aerosol dynamics involves particle radii covering around four orders of magnitude  $10^{-8}$  -  $10^{-4}$  cm. The logarithmic transformation suggested by Berry [17] has been employed by us in a number of studies (e.g. [9], [10], [16], [18], [19]):

$$x(J) = x(J_0) \exp(q(J-J_0)) \quad (19)$$

$J$  is a positive number greater than or equal to  $J_0$ .  $x(J_0)$  is the mass of a particle starting at  $J_0$ .  $q$  is a numerical parameter which can be selected to give equally spaced integer  $J$  values. From the definition of the density function,

$$n(x(J)) = g(J)/qx(J) \quad (20)$$

With (19) and (20), equation (1) becomes:

$$\begin{aligned} \frac{\partial g(J,t)}{\partial t} &= \int_{J_0}^J dJ' b_1(\tilde{J}, J') g(\tilde{J}, t) g(J', t) \\ &\quad - g(J, t) \int_{J_0}^{\infty} dJ' b(J, J') g(J', t) \\ &\quad - \frac{\partial}{\partial J} [\Psi(J)g(J)/qx(J)] \end{aligned} \quad (21)$$

and:  $J_u = J - \ln 2/q$ ,  $J \geq 2$ ;

$$\tilde{J} = J + (1/q) \ln [1 - \exp(q(J'-J))];$$

$$b_1(\tilde{J}, J') = x(J)/x(\tilde{J}) b(x-x', x'),$$

with  $b(x-x', x')$  given by equation (2). The adjustable parameter  $q$  has a great advantage in "fine tuning" for mass or diameter spacings to increase

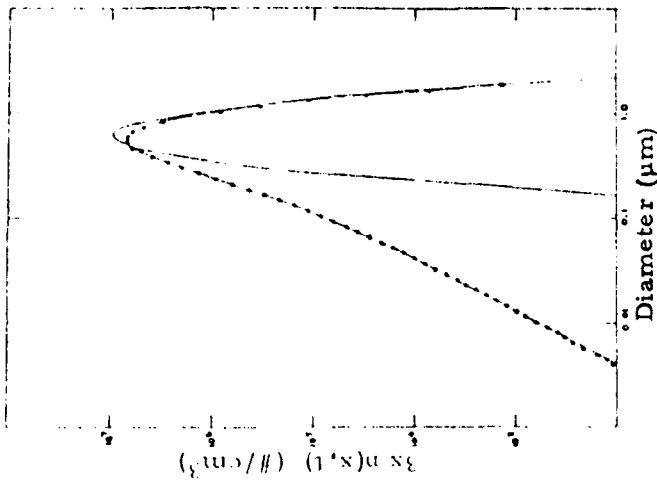


Figure 5. Comparison between linear finite element method and Tsang's method for numerical solution of condensation equation for continuum growth.

Figure 6. Application of Tsang's method for numerical solution of evaporation equation for continuum evaporation.

— Initial density function  
 - - - Exact analytical solution (t=1000 sec.)  
 . . . . . Numerical solution by Tsang's method (t=1000 sec.)

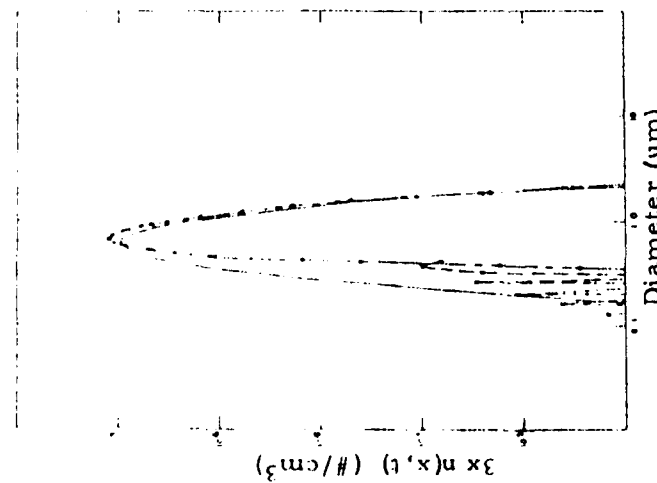


Figure 6. Comparison between linear finite element method and Tsang's method for numerical solution of evaporation equation for continuum evaporation.

Figure 7. Comparison between linear finite element method and Tsang's method for numerical solution of condensation equation for continuum growth.

— Initial density function  
 - - - Exact analytical solution (t=1000 sec.)  
 . . . . . Numerical solution by Tsang's method (t=1000 sec.)  
 xxx Numerical solution by finite element method (t=1000 sec.)

In our work, we have modified and combined Varoglu and Finn's method with Neumann's method because of the requirements of the condensation/evaporation term. This new method, Tsang's method, has been successful. Figure 5 shows a comparison between the linear finite element and our method for continuum ( $Kn \rightarrow 0$ ) condensation according to the law  $\Psi = \epsilon x^{1/3}$  with the analytical solution included for comparison. For the linear finite element method, the magnitude of dispersion increases with time. Tsang's method is more accurate than the linear finite element method over the whole computational domain. For continuum evaporation,  $\Psi = -\epsilon x^{1/3}$ , Tsang's method gives also good agreement with the analytical solution as shown in Figure 6.

These preliminary results are encouraging. Work is now underway on the numerical simulation of equations (1) and (4) using Tsang's method.

III. DISCUSSION. This brief exposition is intended only to suggest some of the interesting problems which remain in the dynamics of condensation aerosols. Here, only the simplest physical system has been discussed - that is, an aerosol of coalescing particles in a uniform system.

In the "real world" of shocks, flames and jets, highly non-uniform systems, the theoretical basis for studying aerosol dynamics is lacking except in certain special cases. An aerosol of particles which do not coalesce on collision presents special problems in analysis. As a result of the collisional process, such particles will form larger particles with complex morphology - chains, branched structures, random aggregates, etc. - whose description has not yet been achieved.

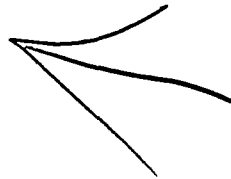
Owing to deficiencies which have yet to be overcome, the experimental study of aerosol dynamics with sufficient temporal and spatial resolution is not possible. This situation places special emphasis on theoretical analysis to lead the way. The description of the dynamics of high density condensation aerosols in non-uniform systems is a challenging problem for the future for workers in applied mathematics, non-equilibrium statistical mechanics and fluid dynamics.

ACKNOWLEDGMENT. This work was supported by the Chemical Systems Laboratory, U. S. Army, Aberdeen Proving Ground.

#### REFERENCES

1. Hidy, G. M. and Brock, J. R., The Dynamics of Aero-Colloidal Systems, Pergamon Press, Oxford, 1970.
2. Marlow, W. H. (Ed.), Aerosol Microphysics I, II, Springer-Verlag, Berlin, 1980.
3. Fuchs, N., Mechanics of Aerosols, Pergamon Press, Oxford, 1964.
4. Davis, E. J., Ravindran, P. and Ray, A. K., Chem. Eng. Commun. 5 251-268 (1980).
5. Sutugin, A. G., Lushnikov, A. A., and Chernyaeva, G. A., J. Aerosol Sci. 4 295-305 (1973).
6. Schumann, T., J. Roy. Met. Soc. 66 195 (1940).
7. Friedlander, S. K. and Wang, C. I., J. Colloid Interface Sci. 22 126 (1966).
8. Mulholland, G. W. and Baum, H. R., Phys. Rev. Letters 45 761-763 (1980).
9. Yom, K. and Brock, J. R., To be published.
10. Suck, S. H. and Brock, J. R., J. Aerosol Sci. 10 581-590 (1979).
11. Drake, R. in G. M. Hidy and J. R. Brock, Eds., Topics in Aerosol Research Vol. III, Pergamon, Oxford, 1971.
12. Sutugin, A. and Fuchs, N. A., J. Aerosol Sci. 1 287-293 (1970).
13. Bleck, R., J. Geophys. Res. 65 5165-5171 (1970).
14. Gelbard, F. and Seinfeld, J. H., J. Comp. Phys. 28 357-375 (1978).
15. Gelbard, F., Tambour, Y., and Seinfeld, J. H., J. Colloid Interface Sci. 76 541-556 (1980).
16. Middleton, P. B. and Brock, J. R., J. Colloid Interface Sci. 54 249 (1976).
17. Berry, E. X., J. Atmos. Sci. 24 688 (1967).
18. Tsang, T. H. and Brock, J. R., Atmos. Environ., in Press, 1982.

19. Tsang, T. H. and Brock, J. R., J. Appl. Optics, in Press, 1982.
20. Long, P. E. and Pepper, D. W., J. Appl. Meterol. 20 146-156 (1981).
21. Pepper, D. W. and Baker, A. J., Num. Heat Transfer 2 81-95 (1979).
22. Baker, A. J. and Solimon, M. O., J. Comp. Phys. 32 289-324 (1979).
23. Baker, A. J. and Solimon, M. O., Comp. Meth. Appl. Mech. Engr. 27 215-237 (1981).
24. Dendy, J. E., SIAM J. Num. Meth. 13 233-247 (1974).
25. Raymond, W. H. and Garder, A., Mon. Weath. Rev. 104 1583-1590 (1976).
26. Pepper, D. W., Kerr, C. D., and Long, P. E., Atmos. Environ. 13 223-237 (1979).
27. Orszag, S. A. and Gottlieb, D., Lecture Notes in Mathematics, #771, 381-389 (1981).
28. Bonnerot, R. and Jamet, P., Int. J. Num. Meth. Eng. 8 811-820 (1974).
29. Varoglu, E. and Finn, W. D. L., J. Comp. Phys. 34 371-389 (1980).
30. Neumann, S. P., J. Comp. Phys. 41 270-294 (1981).



AD P001022

MODELING OF FLOW INTERACTION OF A LIQUID JET  
WITH A CONTAMINANT DROPLET

Lang-Mann Chang  
Computational Interior Ballistics Branch  
Interior Ballistics Division  
US Army Ballistic Research Laboratory, ARRADCOM  
Aberdeen Proving Ground, Maryland 21005

**ABSTRACT.** Two flow models have been developed for investigation of the flow interaction of a liquid jet with a chemical contaminant droplet on a plane wall. This interaction is considered as a two-dimensional viscous flow problem. Computer plots are presented for the flow pattern and the evolution of the droplet upon jet impingement. Displacements and mean velocity of the droplet upstream edge are provided as functions of jet velocity and fluid viscosity. These values may be used for evaluation of the efficiency of jet impingement for decontamination. Typical instantaneous pressure distribution on the impingement wall is also given. Studies in progress will establish correlations between flow parameters, such as the incidence angle and the diameter of the jet, and the performance of jet impingement.

**I. INTRODUCTION.** The present investigation involves utilization of jet impingement for chemical decontamination. The procedure is to use the great force produced by the impingement of jets to remove chemical contaminant droplets from surfaces of a vehicle or equipment.

While falling through air, the contaminant droplets assume the shape of rain drops, with diameters ranging from 1 mm to 2 mm. After impact on a flat surface, each droplet may spread out to 2 - 4 mm in diameter and the average number density of droplets in a surface area of 10 cm by 10 cm is 4.2. Its viscosity may vary widely from 10 to 1000 times that of plain water primarily depending on the temperature.

If not removed, the contaminant may gradually penetrate into the surface and become permanent residue or after drying out may appear as a stain on the surface. A hazardous environment still exists. Of various methods proposed for removal of the contaminant, utilization of liquid jets appears to be the most effective and perhaps most economical at the current level of technological development. The liquid jet can easily break up the droplets and subsequently carry away the contaminant. A thorough clean-up of the surface can be achieved by moving the jet toward the contaminant droplets.

The task seems to be as simple as using a sink hose spray to wash a dish. However, little has been known about the flow interaction of the individual jets in the spray with the dirt droplets on the dish and about the effects of varying a flow parameter, such as the incidence angle of the jet, on the performance of the spray. In the battlefield, in particular, the supply of jet fluid as well as the power source for the pumping system could be very limited. As a result, the efficiency of the jet system in terms of decontaminating a larger area with least consumption of jet fluid and with shortest period of time to complete the mission is of great concern.

In the design of an highly efficient jet system, the following knowledge is vital: the general flow pattern, the evolution of the contaminant droplet, and the effect of varying each flow parameter on the flow. Though this information can be sought via experiments, the work will need very sophisticated instrumentation and will be very costly. As an alternative, computer simulations based on appropriate flow models will be a more desirable means. In fact, the method can provide much greater flexibility for examining areas of importance in the flow field and the results can provide better insights into flow phenomena. The computer results then can be checked by sample experiments for accuracy.

The present jet-contaminant flow consists of two fluids, namely the jet fluid and the contaminant, or three fluids if the ambient is treated as the third one. The two prime fluids are separated by interfaces and have free surfaces with the ambient. The flow is three-dimensional in nature and is highly transient. Much research work has been done in the past on jet impingement problems. However, very few involve a second fluid interacting with the jet in the impingement region. Historically, Taylor [1] remarked that in 1890 Michell [2] gave a solution for the pressure distribution on a flat plate when subjected to a two-dimensional, steady, incompressible, inviscid jet impingement. Nevertheless, it was not known how the solution was obtained until Taylor himself derived an expression for the pressure distribution. In recent years, most of the work in this area is relevant to the VTOL program (vertical takeoff and landing air craft) and are concentrated in impingements on a solid surface. Among them, Scholtz and Trass [3] and Rubell [4,5] considered two- and three-dimensional inviscid, normal and oblique impingements. Their analytical solutions of the surface pressure were, in general, in good agreement with experimental data. In another development which included viscous and turbulence effects, Kotansky and Bower [6] used incompressible Reynolds equations with a one-equation turbulence model to calculate the surface pressure upon a two-dimensional normal impingement. Most recently, Bower [7] extended the problem to three dimensions and used the popular Jones-Lauder two-equation turbulence model [8] for surface pressure and velocity predictions. The results compared reasonably well with measurements. For impingements on a liquid surface, Hunt [9] and Vanden-Broeck [10] treated the problem as a steady and two-dimensional one and used simplified theories to characterize the wave-like hydrodynamic instability occurring at the interface of the two fluids. All of the papers cited above were dealing with steady-state flows and no analyses were given for velocity and pressure distributions when a second fluid was present in the impingement region.

In the present investigation, we have simplified the jet-contaminant flow by treating it as a two-dimensional problem. We have developed a two-fluid flow model and a one-fluid flow model suitable for characterizing the interaction flows developing from two different pre-impingement flow configurations. The unsteady Navier-Stokes equations have been used to describe the flow and the computer code SOLA-VOF [11] has been employed for numerical solutions. Presented are the flow pattern, evolution of the contaminant droplet, effects of variation of flow parameters on the flow, and some typical pressure distributions on the impingement surface.

**II. FLOW MODELS.** Two configurations can be considered to describe the pre-impingement flow situations occurring in the decontamination process. In

the first configuration, as depicted in Figure 1a, a water jet is directed at a contaminant droplet which is at rest on a surface. In the second configuration, Figure 1b, the contaminant droplet is covered by a water layer which is stationary or flowing. In both cases the impingement flow developed is a three-dimensional problem involving two fluids (contaminant and water) interacting in a region open to the ambient. There exist interfaces separating the two fluids and each of them may have free surfaces with the ambient. Methods for solving such a complex problem are not well developed.

In order to simplify the analysis we will develop one-fluid and two-fluid flow models suitable for characterizing the flows developing from the above two configurations and also suitable for utilizing the computer code SOLA-VOF [11] for solutions. Both models describe a two-dimensional viscous flow. It is noted that the computer code is capable of solving flow problems of two fluids separated by interfaces in a region without voids or one fluid having voids (the ambient).

For the two-fluid model, we establish a two-dimensional channel-type flow shown in Figure 2. It is essentially a flow region covering the major part of the flow shown in Figure 1b. The channel contains two fluids, the contaminant and water which fills the rest of the channel. The upper wall of the channel coincides with the upper free surface of the water layer so as to eliminate consideration of the free surfaces. An outflow boundary condition is specified at this wall and at the ends of the channel, allowing the fluids to flow out the region. The contaminant which covers a rectangular region is assumed to wet perfectly the lower wall of the channel. To account for viscous effects, a no-slip condition is used for the lower wall. We adapt a finer mesh near the wall in order to provide better solutions in thin viscous layers. Finally, a steady uniform jet velocity is specified along a section of the upper wall.

For the one-fluid flow model, we establish a flow region shown in Figure 3, in which the contaminant and the water are assumed to have the same physical properties. In addition, the flow model differs from the two-fluid flow model in that the water initially filling in the channel is absent and there is an initial setup for the jet profile inside the channel. After the flow is initiated, the boundary conditions are identical for both flow models. In the one-fluid flow model, there are only free surfaces, but no interfaces, involved. This model is suitable for characterizing the flow developing from the configuration shown in Figure 1a for which the two-fluid flow model is not applicable because of the existence of both interfaces and free surfaces and, thus, beyond the capability of the SOLA-VOF code. The validity of the one-fluid model will be discussed in Section IV of this paper.

III. FLOW EQUATIONS AND METHOD OF SOLUTION. The governing equations for the model flow are:

$$\text{continuity} \quad \frac{1}{\rho c} \frac{\partial p}{\partial t} + \frac{\partial u}{\partial x} + \frac{\partial v}{\partial y} = 0 \quad (1)$$

$$\text{momentum} \quad \frac{\partial u}{\partial t} + u \frac{\partial u}{\partial x} + v \frac{\partial u}{\partial y} = - \frac{1}{\rho} \frac{\partial p}{\partial x} + \nu \left[ \frac{\partial^2 u}{\partial x^2} + \frac{\partial^2 u}{\partial y^2} \right] \quad (2)$$

$$\frac{\partial v}{\partial t} + u \frac{\partial v}{\partial x} + v \frac{\partial v}{\partial y} = - \frac{1}{\rho} \frac{\partial p}{\partial y} + \nu \left[ \frac{\partial^2 v}{\partial x^2} + \frac{\partial^2 v}{\partial y^2} \right] \quad (3)$$

where  $t$  is time variable,  $u$  and  $v$  are the x-component (along the channel) and the y-component (normal to the channel) of the jet velocity  $V_j$ , respectively. The density  $\rho$ , the sound speed  $c$ , and the viscosity  $\nu$ , are constant. In addition, a function  $F$ , called the fractional volume of fluid function, is introduced for tracking the water-contaminant interface. The function is given as

$$\frac{\partial F}{\partial t} + u \frac{\partial F}{\partial x} + v \frac{\partial F}{\partial y} = 0 \quad (4)$$

This equation states that  $F$  moves with the fluid. In a two-fluid flow the value of  $F$  is unity at any point occupied by the first fluid (say, contaminant) and zero elsewhere. When averaged over the cells of a computational mesh, the average value of  $F$  in a cell is equal to the fractional volume of the cell occupied by the first fluid. In particular, a unity value of  $F$  corresponds to a cell full of the first fluid, whereas a zero value indicates that the cell contains only the second fluid (say, water including the jet fluid and the water layer of Figure 2). Cells with  $F$  values between zero and one contain an interface, as illustrated in Figure 4. With this, the interfaces separating the two fluids can be tracked. In the case of one-fluid flow, the second fluid is replaced by the ambient.

The velocity components  $u$  and  $v$  in the momentum Eqs. (2) and (3) have been solved by using the explicit finite difference scheme, while the pressure  $p$  has been computed, coupled with the continuity equation (Eq. (1)) via an implicit finite difference method. The solution of the  $F$  function in Eq. (4) has been obtained by using the Donor-Acceptor flux approximation. Details of the solution method have been given in Reference 11 of this paper. In order to observe the evolution (location and shape) of the region covered by the contaminant droplet, Marker Particles have been embedded in the fluid and move with it, but do not affect the fluid dynamics.

In the current version of the SOLA-VOF, the viscosities of both fluids in a flow are considered the same or simply zero. To adapt this code for solving the present flow which involves two fluids with very different viscosities the following modification is necessary.

$$\nu = \nu_c F + (1 - F) \nu_w \quad (5)$$

where  $\nu$  is the kinematic viscosity of fluid in a cell,  $\nu_c$  the kinematic viscosity of the first fluid (contaminant),  $\nu_w$  the kinematic viscosity of the second fluid (jet fluid), and  $F$  the function defined in Eq. (4). Similarly, if the densities of the fluids are not the same, the density in a cell is approximated to be

$$\rho = \rho_c F + (1 - F) \rho_w \quad (6)$$

From Eqs. (5) and (6), we see that the values of  $v$  and  $\rho$  in a cell are functions of  $F$ .

Finally, it is noted that the Reynolds numbers based on the jet width and the velocities used in our computations are in the range of 20 - 2000. Within this range, Eqs. (2) and (3) are felt to be appropriate for the present flow analysis, even though the equations do not include turbulence considerations.

IV. COMPUTATIONAL RESULTS AND DISCUSSIONS. The following are the input data for the computations:

- $\theta$  = incidence angle of the jet =  $45^\circ$
- $D_j$  = diameter of the jet (width of the jet in the two-dimensional model) = 1.83 mm
- $V_j$  = jet velocity, uniformly across the jet width = 5 - 12.5 m/sec
- $\rho_w$  = density of plain water =  $0.001 \text{ Kg/cm}^3$
- $\rho_c$  = density of the contaminant =  $0.00107 \text{ Kg/cm}^3$
- $\nu_w$  = kinematic viscosity of water =  $0.0098 \text{ cm}^2/\text{sec}$
- $\nu_c$  = kinematic viscosity of the contaminant =  $0.098 - 9.8 \text{ cm}^2/\text{sec}$

Contaminant Droplet With Initial Water Layer Coverage. This refers to the impingement flow developing from the configuration shown in Figure 1b. The two-fluid flow model of Figure 2 applies to this case. The velocities given above correspond to steady dynamic pressures of 2 - 12 psi, which are practical for decontamination. The dimension of the contaminant droplet is taken to be 3 mm x 0.6 mm, representing the average size on a horizontal flat surface. Two assumptions that have been made are that the contaminant droplet wets the wall and that the surface tension between the contaminant and the water can be neglected because it is small.

Before running the computer code SOLA-VOF [11] for the two-fluid flow, test runs of the code have been made to calculate the surface pressure upon an impingement of an incompressible, inviscid, normal jet. The result is in good agreement with Taylor's prediction. The following presents the results we have obtained so far in this research program.

Figure 5 shows the flow patterns following the commencement of the jet impingement. The jet flow comes in along the upper boundary above the left corner of the contaminant droplet. The small arrows in the flow channel represent the direction and the magnitude of fluid velocities at various points. In the left column of the figure, the viscosity of the water (including jet fluid and water layer) is  $\nu_w = 0.0098 \text{ cm}^2/\text{sec}$  (real value), while in the right column,  $\nu_w$  has artificially been raised to the value of  $\nu_c$ , i.e.,  $\nu_w = 0.98 \text{ cm}^2/\text{sec}$ . The reason for raising the viscosity is to examine

the sensitivity of the flow to the variation of the viscosity of the jet fluid. A comparison between these two columns shows that the flow patterns corresponding to these two viscosity values are similar. Figure 6 presents another view of the evolution of the contaminant droplet. In the figure, the dash-line indicates the initial location of the upstream edge of the droplet and the distance  $S$  represents the displacement of the edge. This displacement can explicitly be used to evaluate the performance of a jet impingement flow for removal of contaminant droplets from a surface.

If the initial water layer above the contaminant droplet is reduced from 1 mm in Figure 5 to 0.2 mm presently, similarities also are obtained for the flow pattern and the displacement  $S$  when the two columns in Figure 7 are compared. Table I summarizes the results of the displacement  $S$  and the mean velocities  $\dot{S}$  of the droplet upstream edge for two cases:  $\nu = 0.98 \text{ cm}^2/\text{sec}$  and  $\nu = 9.8 \text{ cm}^2/\text{sec}$ . The mean velocity here is defined as the value obtained by dividing the displacement  $S$  by the time after the commencement of the jet flow. We see that despite a dramatic variation of the jet fluid viscosity from  $\nu = 0.0098 \text{ cm}^2/\text{sec}$  to  $\nu = 9.8 \text{ cm}^2/\text{sec}$ , the difference of the resulting displacements  $S$  is of order of only 10 - 15%. In view of the large initial mean velocities,  $\dot{S} > 3 \text{ m/sec}$ , listed in Table I, this magnitude of difference is considered insignificant since practically the droplet will be displaced almost immediately after application of the jet impingement. Therefore, the one-fluid flow model established in Section II is applicable to characterize the flow field developing from the configuration shown in Figure 1a. Physically, the insensitivity of the flow field to the variation of the jet fluid viscosity has demonstrated the dominance of the inertial force over the shear force. It should be noted, however, if the impingement location is far away from the contaminant droplet or if the initial water layer above the droplet is very thick, then the viscous effects of the jet fluid may not be ignored.

Contaminant Droplet Without Initial Water Layer Coverage. Now consider the flow configuration of Figure 1a for which the one-fluid flow model applies. Figure 8, obtained from the Tektronix Display Terminal, shows a series of flow developments following the initiation of the impingement. The jet stream first spreads out on the wall and then engages the contaminant droplet, and finally is lifted off the wall at some angle. The interface between the fluid and the contaminant is not shown in the figure since the one-fluid flow model is used, in which the two fluids have the same properties. However, using the technique of embedding Marker Particles which follow the fluid particles in the region initially covered by the contaminant droplet, we still are able to track the interface and observe its evolution. The result is shown in the first column of Figure 9. In the other columns of the figure, the results corresponding to higher viscosity values are presented. A comparison of these columns explicitly shows the viscosity dependence of the flow. It is seen that the viscosity smooths out the interface profile and resists the movement of the droplet. The latter effect can be seen in Figure 10. Another interesting result we have found is that even if the fluid viscosity is as small as  $0.098 \text{ cm}^2/\text{sec}$  (i.e., 10 times the viscosity of plain water) the downstream end of the droplet still remains unchanged (shape and location) until a large portion of the droplet on the upstream side has been deformed or broken up.

Figure 11 shows the displacements  $S$  versus time corresponding to various jet velocities  $V_j$ . The origin of the time coordinate in the plot has been chosen to be the moment the droplet upstream edge starts to move. As anticipated, the jet velocity has proven to be an important parameter affecting the jet performance. Figure 12 is a plot of the mean velocity  $\bar{S}$  versus the displacement  $S$ . With the fluid viscosity  $\nu = \nu_w = \nu_c = 0.98 \text{ cm}^2/\text{sec}$ , it shows that as  $V_j > 5 \text{ m/sec}$ , the droplet upstream edge can move with an initial velocity greater than  $4.2 \text{ m/sec}$ . As stated earlier, the velocity is large enough to displace the droplet almost immediately after jet impingement. Another important value we have to determine is the rise of pressure peak on the impingement surface. In some critical areas, such as the optical windows of a vehicle, the impact pressure that the areas can take is limited. Figure 12 presents some typical pressure distributions on the impingement surface as the jet-contaminant interaction flow continues to develop. As a result of transient phenomenon, the instantaneous pressure peak is seen to rise higher than twice the corresponding steady dynamic pressure of the jet velocity,  $1/2\rho V_j^2$ .

**V. SUMMARY AND CONCLUSIONS.** Two flow models have been developed to investigate the flow interaction of a liquid jet with a chemical contaminant droplet on a plane wall. If this situation is considered as a two-dimensional viscous flow, the result from the two-fluid flow model shows that the flow pattern is insensitive to the variation of the jet fluid viscosity. This leads to the feasibility of using the one-fluid flow model for characterizing the flow situation in which the contaminant droplet is not initially covered by a water layer.

The interfaces between fluids in the two-fluid flow and the free surface in the one-fluid flow can be tracked by computer simulations. Results from both models show that the downstream end of the contaminant droplet can remain unchanged (shape and location) until a large portion of the droplet on the upstream side has been deformed or broken up. The jet velocity and the viscosity of the contaminant are important variables affecting the flow field. The displacement and the mean velocity of the droplet upstream edge when subjected to a jet impingement can be calculated and can be used to evaluate the efficiency of the jet impingement for removal of the contaminant. It is found that with a jet velocity  $V_j > 5 \text{ m/sec}$ , the impingement can displace the contaminant droplet almost immediately. The instantaneous pressure on the impingement surface may rise higher than twice the corresponding steady dynamic pressure of the jet velocity,  $1/2\rho V_j^2$ .

Further studies to establish correlations between flow parameters and the efficiency of the jet impingement for decontamination are in progress.

#### REFERENCES

1. G.I. Taylor, "Oblique Impact of a Jet on a Plane Surface," Phil. Trans. R. Soc. A, 260, 1966, pp. 96-100.
2. J.H. Michell, Phil. Trans. A, 181, 1890, pp. 389-431.
3. M.T. Scholtz and O. Trass, "Stagnation Flow-Velocity and Pressure Distribution," AIChE J., 16, No. 1, Jan 1970, pp. 82-96.
4. A. Rubell, "Computations of Jet Impingement on a Flat Surface," AIAA J., 18, No. 2, Feb 1980, pp. 168-175.
5. A. Rubell, "Computations of the Oblique Impingement of Round Jets Upon a Plan Wall," AIAA J., 19, No. 7, Jul 1981, pp. 863-871.
6. D.R. Kotansky and W.W. Bower, "A Basic Study of the VTOL Ground Effect Problem for Planar Flow," J. Aircraft, 15, No. 4, Apr 1978, pp. 214-221.
7. W.W. Bower, "Computations of Three-Dimensional Impinging Jets Based on the Reynolds Equations," AIAA Paper No. 82-1024, presented at the AIAA/ASME 3rd Joint Thermophysics, Fluids, Plasma, and Heat Transfer Conference, St. Louis, MO, 7-11 Jun 1982.
8. W.P. Jones and B.E. Launder, "The Prediction of Laminarization with a Two-Equation Model of Turbulence," Int. J. Heat and Mass Transfer, 15, 1972, pp. 301-313.
9. J.N. Hunt, "Wave Formation in Explosive Welding," 1967.
10. J-M Vanden-Broeck, "Deformation of a Liquid Surface by a Impinging Gas Jet," SIAM J. Appl. Math., 41, No. 2, Oct 1981, pp. 306-309.
11. B.D. Nicholas, C.W. Hurt, and R.S. Hotchkiss, "SOLA-VOF: A Solution Algorithm for Transient Fluid Flow with Multiple Free Boundaries," Los Alamos Scientific Laboratory Report No. LA-8355, 1980.

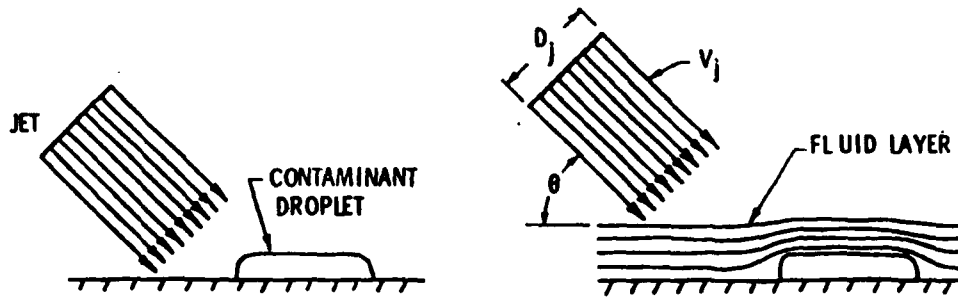
Table I. Displacements and Mean Velocities of Contaminant Droplet Upstream Edge After Initiation of Jet Flow

$\nu_c = 0.98 \text{ cm}^2/\text{sec}$

$V_j$ m/sec	Time MS	$\nu_w = 0.98 \text{ cm}^2/\text{sec}$		$\nu_w = 0.0098 \text{ cm}^2/\text{sec}$		$\frac{S_2 - S_1}{S_2} \%$
		$S_1$ mm	$\xi_1$ m/sec	$S_2$ mm	$\xi_2$ m/sec	
5	0.05	0.207	4.13	0.214	4.28	3.4
	0.10	0.122	4.22	0.436	4.36	3.2
	0.15	0.552	3.68	0.597	3.98	7.5
10	0.05	0.467	9.3	0.52	10.04	10.2
	0.10	0.624	6.24	0.727	7.27	14.1
	0.15	0.642	4.28	0.761	5.07	15.6

$\nu_c = 9.8 \text{ cm}^2/\text{sec}$

$V_j$ m/sec	Time MS	$\nu_w = 9.8 \text{ cm}^2/\text{sec}$		$\nu_w = 0.0098 \text{ cm}^2/\text{sec}$		$\frac{S_2 - S_1}{S_2} \%$
		$S_1$ mm	$\xi_1$ m/sec	$S_2$ mm	$\xi_2$ m/sec	
5	0.05	0.150	3.04	0.17	3.42	11.1
	0.10	0.280	2.80	0.32	3.20	12.5
	0.15	0.409	2.73	0.445	2.97	8.1
10	0.05	0.257	5.14	0.305	6.10	16.0
	0.10	0.510	5.10	0.580	5.80	12.1
	0.15	0.54	3.60	0.620	4.13	13.0



a. Contaminant Droplet Without Initial Fluid Layer Coverage

b. Contaminant Droplet With Initial Fluid Layer Coverage

Figure 1. Pre-impingement Flow Configurations

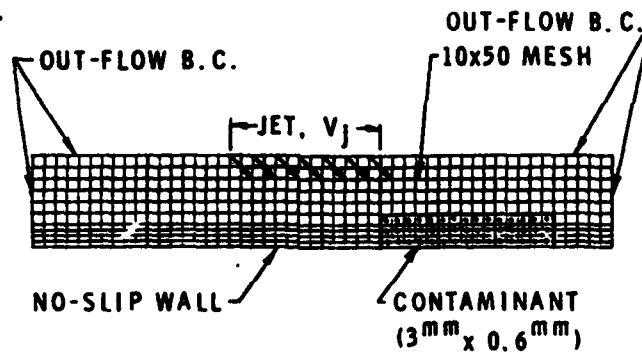


Figure 2. Two-Fluid Flow Model

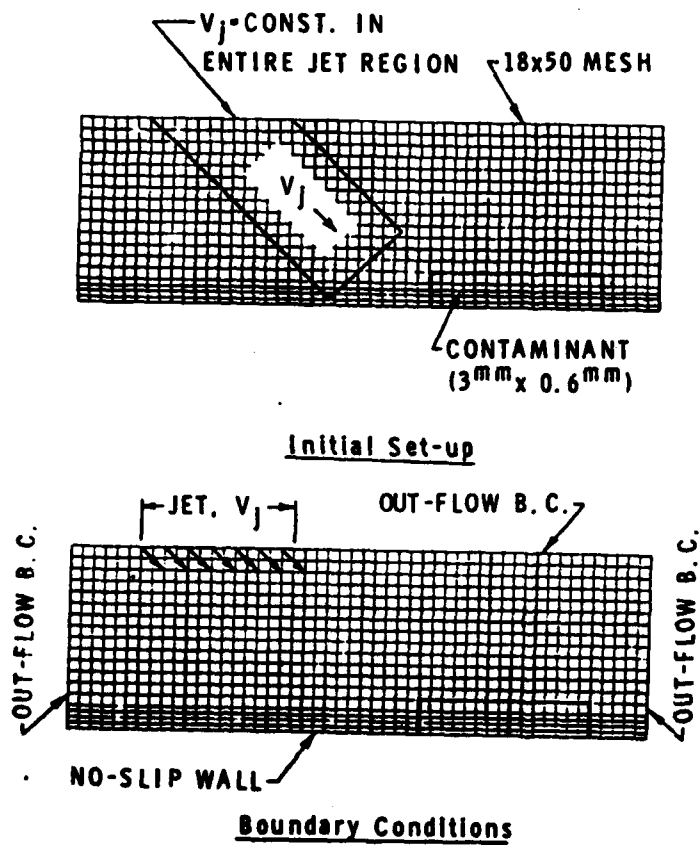


Figure 3. One-Fluid Flow Model

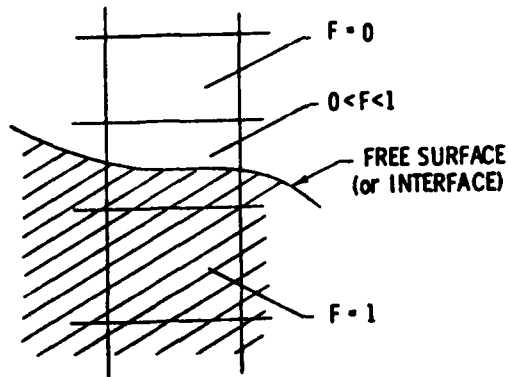


Figure 4. Interface Between Two Fluids  
(or Free Surface of One Fluid)

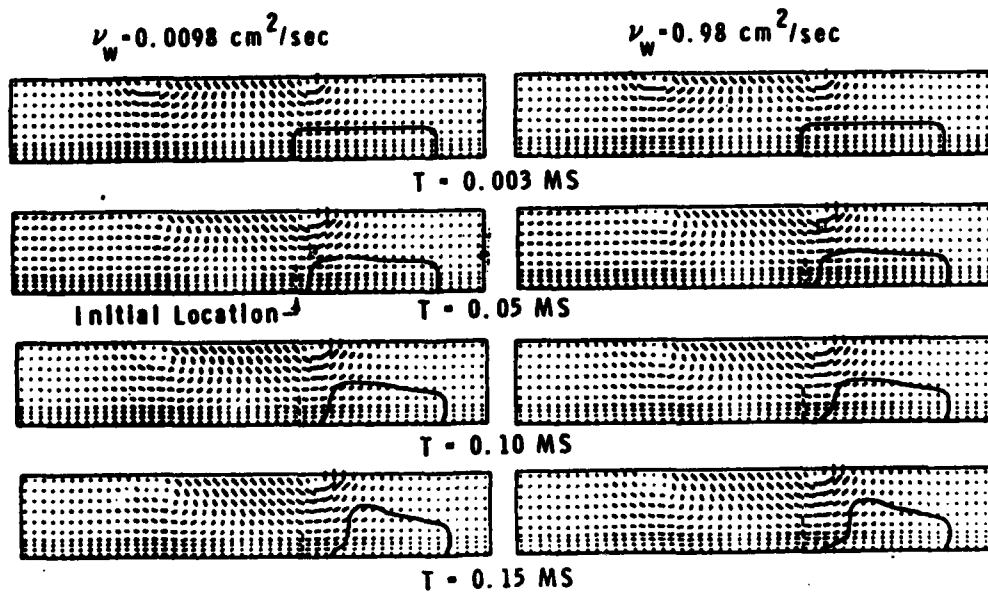


Figure 5. Flow Patterns (Two-Fluid Flow,  $v_c = 0.98 \text{ cm}^2/\text{sec}$ ,  
 $v_j = 10 \text{ m/sec}$ ,  $\theta = 45^\circ$ )

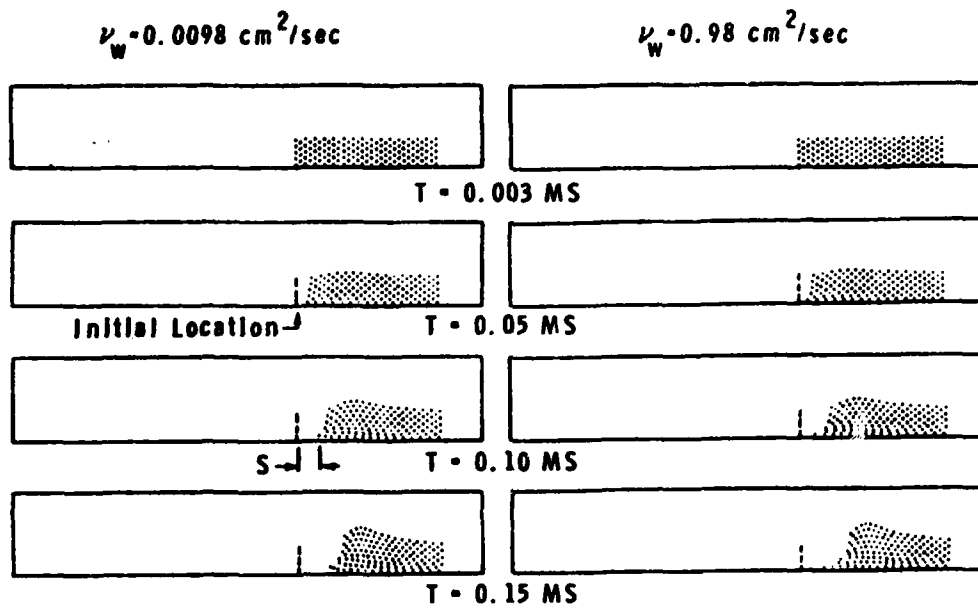


Figure 6. Evolution of  $\text{O}_2$  Contaminant Droplets (Two-Fluid Flow,  $v_c = 0.98 \text{ cm}^2/\text{sec}$ ,  $V_j = 10 \text{ m/sec}$ ,  $\theta = 45^\circ$ )

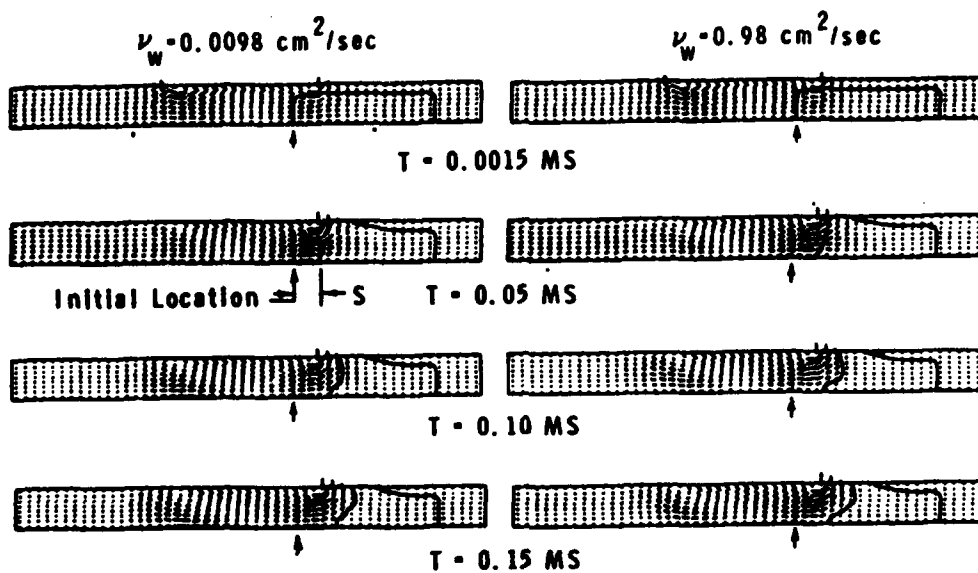


Figure 7. Flow Patterns (Two-Fluid Flow with Reduced Thickness of Initial Fluid Layer Coverage,  $v_c = 0.98 \text{ cm}^2/\text{sec}$ ,  $V_j = 10 \text{ m/sec}$ ,  $\theta = 45^\circ$ )

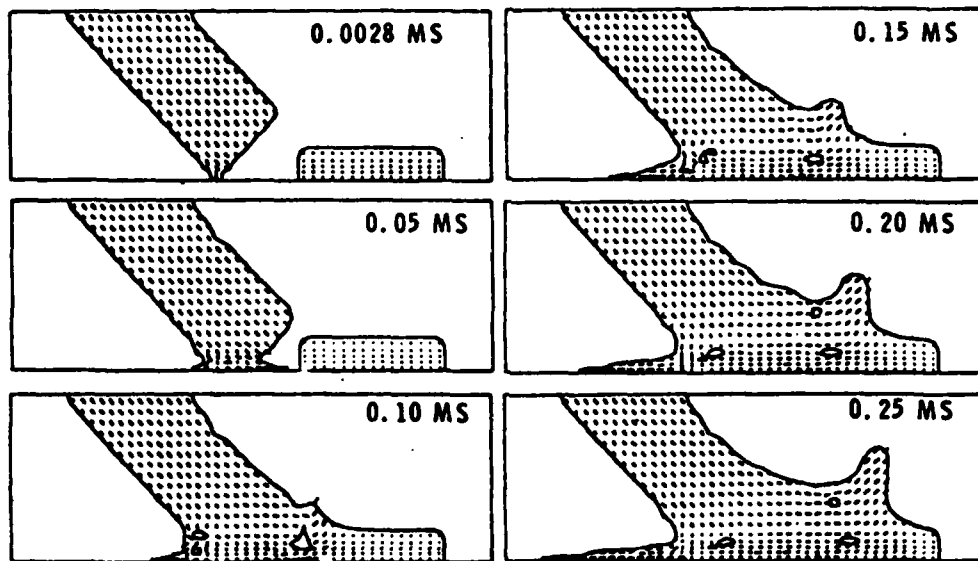


Figure 8. Flow Patterns (One-Fluid Flow,  $\nu_c = \nu_w = \nu = 0.098 \text{ cm}^2/\text{sec}$ ,  $V_j = 10 \text{ m/sec}$ ,  $\theta = 45^\circ$ )

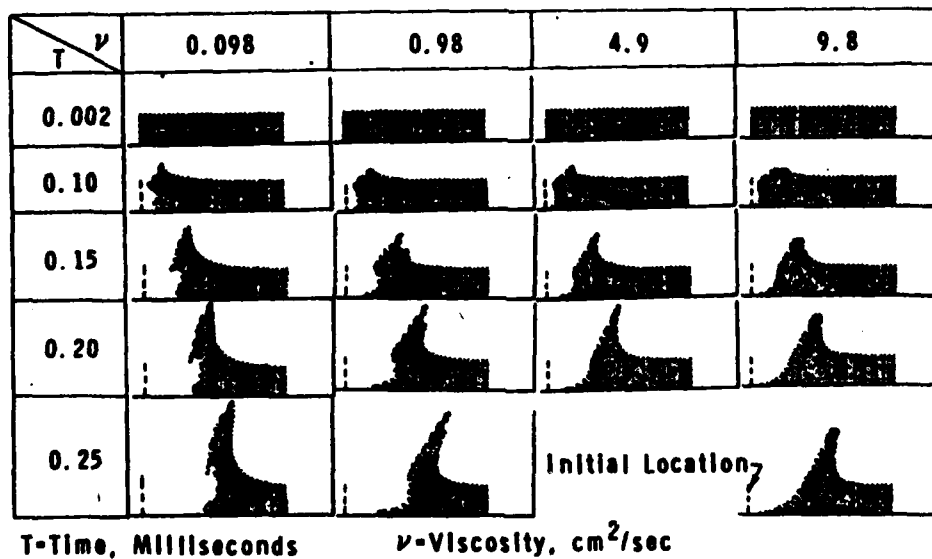


Figure 9. Evolution of Contaminant Droplets Resulting from Various Viscosities (One-Fluid Flow,  $V_j = 10 \text{ m/sec}$ ,  $\theta = 45^\circ$ )

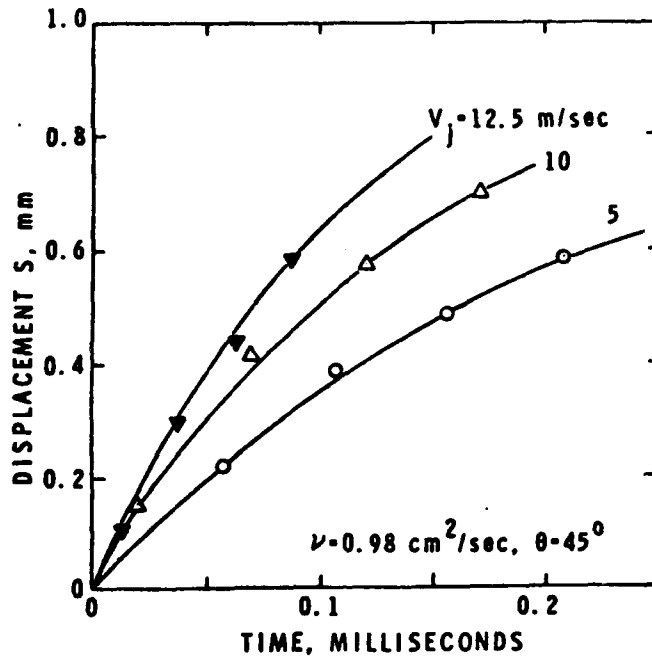


Figure 10. Contaminant Droplet Upstream Edge Displacement Vs. Time after the Edge Starts to Move

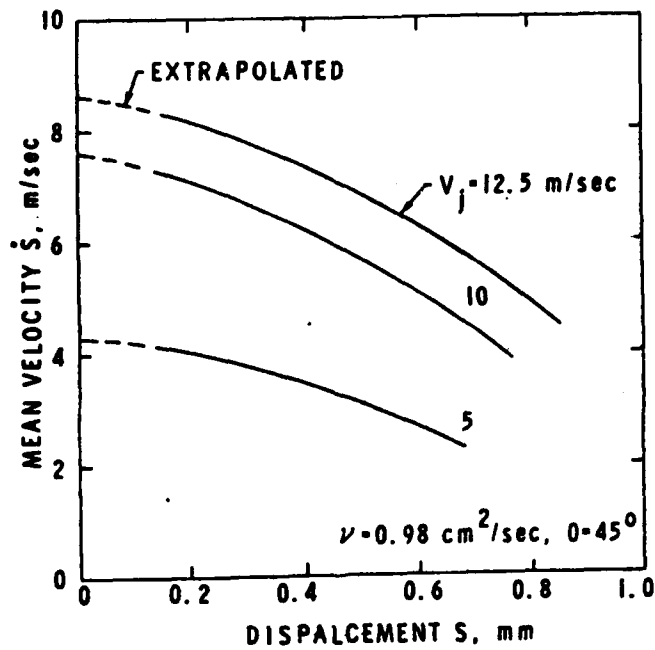


Figure 11. Mean Velocity vs. Displacement of Contaminant Droplet Upstream Edge

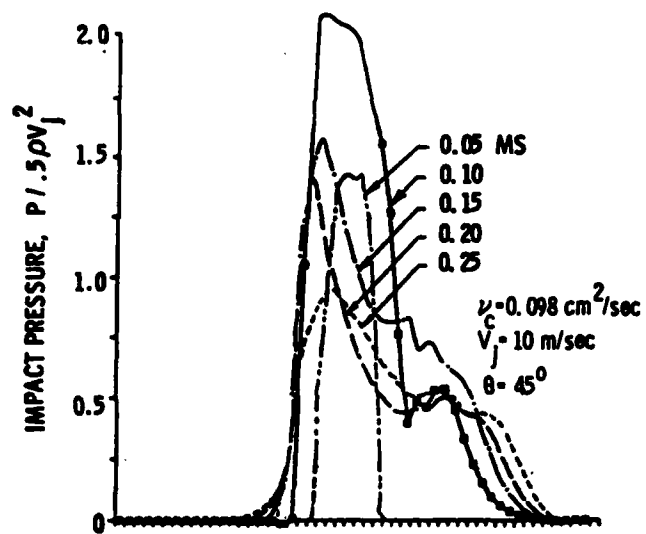
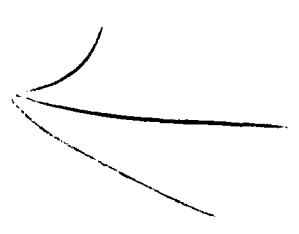


Figure 12. Pressure Distributions on Impingement Surface after Initiation of Jet Flow



AD P 0 1 0 2 3

VISCIOUS FLOW OF A DROPLET ON A FLAT SURFACE

Donald A. Drew  
Department of Mathematical Sciences  
Rensselaer Polytechnic Institute  
Troy, NY 12181

and

Mathematics Research Center  
University of Wisconsin-Madison  
Madison, WI 53706

INTRODUCTION

The author  
finds  
Removal of droplets of a viscous fluid from a surface is important to dishwashing and decontamination. A person familiar with washing dishes knows that the task is impossible without a detergent, but also realizes that some mechanical motion is important. Soaking, even in a good detergent, is not enough. We shall focus our attention on the motion of a viscous drop subject to the forces applied to it by another fluid. This corresponds to the action of the typical mechanical dishwasher, which uses jets of water, as opposed to the use of a hand-held cloth, or sponge. The cleaning is "fluid-mechanical", as opposed to "solid-mechanical" or chemical or thermal.

We consider the motion of a drop of an incompressible viscous fluid on a flat surface subject to the flow of another inviscid fluid around it. The viscous drop is assumed to be so thin that (i) the flow inside the drop is lubrication flow, and (ii) the presence and motion of the drop does not disturb the flow of the outer inviscid fluid. The effects of gravity and surface tension will be assumed to be small compared with the viscous forces.

EQUATIONS OF MOTION

The equations of motion inside the drop are

$$\frac{\partial u}{\partial x} + \frac{\partial v}{\partial y} = 0 \quad (1)$$

$$\rho \left( \frac{\partial u}{\partial t} + u \frac{\partial u}{\partial x} + v \frac{\partial u}{\partial y} \right) = - \frac{\partial p}{\partial x} + \mu \left( \frac{\partial^2 u}{\partial x^2} + \frac{\partial^2 u}{\partial y^2} \right) \quad (2)$$

$$\mu \left( \frac{\partial v}{\partial t} + u \frac{\partial v}{\partial x} + v \frac{\partial v}{\partial y} \right) = - \frac{\partial p}{\partial y} + \mu \left( \frac{\partial^2 v}{\partial x^2} + \frac{\partial^2 v}{\partial y^2} \right) - \rho g \quad (3)$$

where  $t$  is time,  $x$  is the horizontal coordinate,  $y$  is the vertical coordinate,  $u$  is the horizontal velocity,  $v$  is the vertical velocity,  $p$  is the pressure,  $\rho$  is the density,  $\mu$  is the viscosity and  $g$  is the gravitational acceleration.

At the interface  $y = \delta(x,t)$ , the jump condition for the stress becomes

$$p_0(x,y,t)\underline{n} = p\underline{n} + \underline{\mu n} \cdot [\underline{\nabla v} + (\underline{\nabla v})^T] + \sigma \kappa \underline{n} , \quad (4)$$

where  $\underline{n}$  is the unit normal,  $\sigma$  is the surface tension and  $\kappa$  is the curvature of the interface. The kinematic boundary condition is

$$\frac{\partial \delta}{\partial t} + u \frac{\partial \delta}{\partial x} = v , \quad (5)$$

at  $y = \delta(x,t)$ .

We shall assume that the wall is impenetrable, so that

$$v = 0 \quad (6)$$

at  $y = 0$ .

The other boundary condition at the wall has been the subject of much discussion (Dussan V. and Davis 1974, Dussan V. 1976, Hocking 1981).

It is traditional to give conditions on the angle of contact at the contact lines  $x = x_-(t)$  and  $x = x_+(t)$ . Recent discussions (Dussan V. 1976) indicate that if only boundedness of the contact angle is required, there is a difficulty in obtaining a solution. The consensus is that slip must be allowed between the wall and the fluid in the drop. Two candidates for the slip model have been proposed. They are

$$u = U(d) \quad (7a)$$

or

$$u = \lambda \frac{\partial u}{\partial y} \quad (7b)$$

at  $y = 0$ . Here  $U$  is a given function of  $d$ , the distance from the contact line;  $\lambda$  is a parameter which is thought to be proportional to the intermolecular length. Although our discussion will focus on issues which are not strongly affected by the choice of slip model, we shall use (7b).

The pressure outside the drop is obtained by solving the equations of motion for the fluid in the region outside the drop. This involves, presumably, some nozzle, along with some conditions at infinity. We assume that the outer fluid is inviscid and irrotational. The velocity can be

obtained from the solution of Laplace's equation for the stream function  $\psi$ . The pressure can then be obtained from Bernoulli's equation

$$p_0(x,y,t)/\rho_0 + \frac{1}{2} |\nabla\psi|^2 = \text{const.} \quad (8)$$

### APPROXIMATE EQUATIONS

Scaling by

$$\begin{aligned} x &= Lx' \\ y &= \epsilon Ly' \\ u &= Uu' \\ v &= \epsilon Uv' \\ p &= Pp' = \frac{\mu U}{\epsilon^2 L} p' \\ \delta &= \epsilon L\delta' \\ t &= (L/U)t' \end{aligned} \quad (9)$$

gives

$$\frac{\partial u'}{\partial x'} + \frac{\partial v'}{\partial y'} = 0 \quad (10)$$

$$\epsilon^2 \frac{\rho UL}{\mu} \left( \frac{\partial u'}{\partial t'} + u' \frac{\partial u'}{\partial x'} + v' \frac{\partial v'}{\partial y'} \right) = - \frac{\partial p'}{\partial x'} + \left( \frac{\partial^2 u'}{\partial y'^2} + \epsilon^2 \frac{\partial^2 u'}{\partial x'^2} \right) \quad (11)$$

$$\epsilon^4 \frac{\rho UL}{\mu} \left( \frac{\partial v'}{\partial t'} + u' \frac{\partial v'}{\partial x'} + v' \frac{\partial v'}{\partial y'} \right) = - \frac{\partial p'}{\partial y'} + \epsilon^2 \left( \frac{\partial^2 v'}{\partial y'^2} + \epsilon^2 \frac{\partial^2 v'}{\partial x'^2} \right) - F \quad (12)$$

where  $F = \frac{\rho g L^2 \epsilon^3}{\mu U}$ . The kinematic boundary condition becomes

$$\frac{\partial \delta'}{\partial t'} + u' \frac{\partial \delta'}{\partial x'} = v' \quad \text{at } y' = \delta'(x', t') \quad (13)$$

For the jump condition, we have

$$\underline{n} = \frac{j + \frac{\partial \delta'}{\partial x'} \epsilon \underline{i}}{\sqrt{1 + \epsilon^2 \left( \frac{\partial \delta'}{\partial x'} \right)^2}} \quad (14)$$

and

$$\underline{v} = \frac{U}{L} \left[ \underline{j} \frac{1}{\epsilon} \frac{\partial u'}{\partial y'} + \underline{i} \frac{\partial u'}{\partial x'} + \epsilon \underline{i} \frac{\partial v'}{\partial x'} + \underline{j} \frac{\partial v'}{\partial y'} \right]. \quad (15)$$

The pressure outside the droplet is expanded as follows.

$$\begin{aligned} p_0'(x', y', t') &= \frac{\mu U}{\epsilon^2 L} p_0(x, y, t) \\ &= \frac{\mu U}{\epsilon^2 L} p_0(Lx', \epsilon y', (L/U)t') \\ &= \frac{\mu U}{\epsilon^2 L} p_0(Lx', 0, (L/U)t') + o(\epsilon) \\ &= p_0'(x', t') \end{aligned} \quad (16)$$

to order  $\epsilon$ . We shall assume that  $p_0'(x', t')$  is a known function.

The jump condition becomes

$$(p_0' - p' - \sigma' \kappa') \underline{i} - \epsilon \underline{j} \frac{\partial u'}{\partial y'} = o(\epsilon^2) \quad (17)$$

where  $\kappa'$  is the dimensionless curvature, defined by

$$\kappa = \frac{\epsilon}{L} \kappa' \quad (18)$$

so that

$$\kappa' = \frac{\partial^2 \delta' / \partial x'^2}{[1 + \epsilon^2 (\partial \delta' / \partial x')^2]^{3/2}} = \frac{\partial^2 \delta'}{\partial x'^2} + o(\epsilon^2). \quad (19)$$

Also,

$$\sigma' = \frac{\sigma \epsilon^3}{\mu U} \quad (20)$$

is the dimensionless surface tension.

The wall conditions are

$$v' = 0 \quad (21)$$

$$u' = \lambda' \frac{\partial u'}{\partial y'} \quad (22)$$

at  $y = 0$ , where  $\lambda' = \lambda / (\epsilon L)$ .

Let us now let  $\epsilon \rightarrow 0$ , with  $F$ ,  $\sigma'$  and  $\lambda'$  all assumed to be  $O(1)$ .  
We have

$$\frac{\partial u'}{\partial x'} + \frac{\partial v'}{\partial y'} = 0 \quad (23)$$

$$0 = -\frac{\partial p'}{\partial x'} + \frac{\partial^2 u'}{\partial y'^2} \quad (24)$$

$$0 = -\frac{\partial p'}{\partial y'} - F \quad (25)$$

in the drop, and

$$\frac{\partial \delta'}{\partial t'} + u' \frac{\partial \delta'}{\partial x'} = v' \quad (26)$$

$$p' = p_0' - \sigma' \kappa' \quad (27)$$

$$\frac{\partial u'}{\partial y'} = 0 \quad (28)$$

at  $y' = \delta'$ . We shall henceforth drop the primes.

Integrating (25), and using (27) gives

$$p = p_0 - \sigma \kappa - F(y - \delta) . \quad (29)$$

Equation (24) gives

$$\frac{\partial^2 u(x, y, t)}{\partial y^2} = \frac{dp_0}{dx} - \sigma \frac{\partial \kappa}{\partial x} + F \frac{\partial \delta}{\partial x} = A(x, t) . \quad (30)$$

Integrating twice with respect to  $y$ , and applying the boundary condition gives

$$u(x, y, t) = \frac{A}{2} y(y - 2\delta) - A\delta\lambda . \quad (31)$$

The vertical velocity can be found from (23) to be

$$v = - \int_0^y \frac{\partial u}{\partial x} dy' = - \frac{1}{2} \left[ \frac{\partial A}{\partial x} (y^3/3 - y^2\delta) \right] + A \frac{\partial \delta}{\partial x} \frac{y^2}{2} \\ + \left( \frac{\partial A}{\partial x} \lambda \delta + A \frac{\partial \delta}{\partial x} \lambda \right) y . \quad (32)$$

After some manipulations the equation for  $\delta$  becomes

$$\frac{\partial \delta}{\partial t} = \frac{\partial A(\delta^3/3 + \lambda \delta^2)}{\partial x} \quad (33a)$$

or

$$\frac{\partial \delta}{\partial t} = \frac{\partial}{\partial x} \left[ \left( \frac{dp_0}{dx} - \sigma \frac{\partial^3 \delta}{\partial x^3} + F \frac{\partial \delta}{\partial x} \right) (\frac{\delta^3}{3} + \lambda \delta^2) \right]. \quad (33b)$$

We assume that  $\lambda$  is small for reasonable droplets. If the dimensional value of  $\lambda$  is on the order of the intermolecular distance, this merely requires that the droplet is more than a few molecules thick.

We shall also assume that  $F$  and  $\sigma$  are small. If  $\epsilon$  is sufficiently small, it is reasonable to assume  $F$  and  $\sigma$  are small also, since  $F$  and  $\sigma$  are proportional to  $\epsilon^3$ .

With these assumptions,

$$A(x) = \frac{dp_0}{dx}$$

and equation (33) becomes

$$\frac{\partial \delta}{\partial t} + A \delta^2 \frac{\partial \delta}{\partial x} = - \frac{\delta^3}{3} \frac{dA}{dx}. \quad (34)$$

The problem can then be solved by the method of characteristics, where

$$\frac{d\delta}{dt} = \frac{\delta^3}{3} \frac{dp_0}{dx^2} \quad (35)$$

$$\frac{dx}{dt} = - \frac{dp_0}{dx} \delta^2 \quad (36)$$

define the propagation along the characteristics.

Let us now examine various flow possibilities using equations (35) and (36). There are three qualitatively different possibilities, corresponding to "streaming" flow along the surface, separating or detaching flow, and impinging or attaching flow. Both separating and impinging flow are stagnation line flows.

#### STREAMING FLOWS

"Streaming" flow is one with no pressure maxima or minima. We model this situation by assuming  $dp_0/dx = \alpha = \text{constant}$ . Equation (33) becomes

$$\frac{\partial \delta}{\partial t} - \alpha \delta^2 \frac{\partial \delta}{\partial x} = 0 . \quad (37)$$

The characteristics are given by

$$\frac{d\delta}{dt} = 0 \quad (38)$$

$$\frac{dx}{dt} = -\alpha \delta^2 . \quad (39)$$

Thus

$$x = -\alpha \delta^2 t + x_0 \quad (40)$$

on each characteristic. If  $\alpha < 0$ , the characteristics move toward increasing  $x$ . We also note that those carrying larger values of  $\delta$  move faster. Thus, waves can break. If a drop has the shape at  $t = 0$  shown in Figure 1a, it will move to the right, with the leading edge becoming steeper, while the trailing edge becomes shallower. Eventually, in finite time, the slope will become infinite, and after that, the solution predicted by the method of characteristics will be multivalued. While a multivalued solution  $y = \delta(x,t)$  is not ruled out on physical grounds, it is clear that the assumption that the vertical length scale is much smaller than the horizontal length scale is invalid even before the multivalued solution occurs.

As far as the previous approximation is concerned, the steepening leading edge can be treated as leading to a discontinuity in  $\delta$ , which we shall call a shock. At such a discontinuity, the Rankine-Hugonist jump conditions become

$$-U = \frac{\left[ \frac{\delta^3}{3} \left( \frac{dp_0}{dx} \right) \right]}{[\delta]} , \quad (41)$$

where  $U$  is the speed at which the discontinuity propagates. If the discontinuity occurs at the leading edge, then  $[\delta] = \delta_L$ , and

$$-U = \frac{\delta_L^2}{3} \frac{dp_0}{dx} . \quad (42)$$

At the trailing edge, no such jump occurs. Indeed, at the trailing edge,  $\frac{dx}{dt} = 0$  on characteristics. Thus, the trailing edge does not move.

The evolution of a drop which initially has the shape

$$\delta(x,0) = \begin{cases} \delta_0, & 0 < x < L \\ 0, & \text{elsewhere} \end{cases}$$

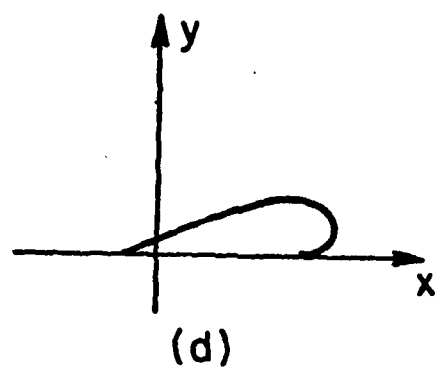
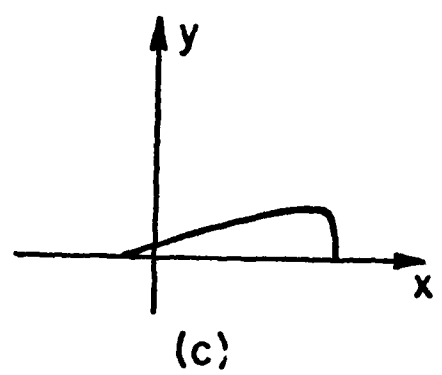
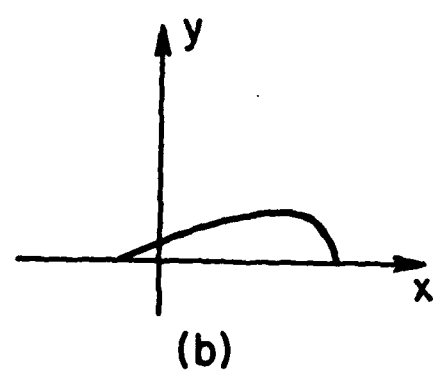
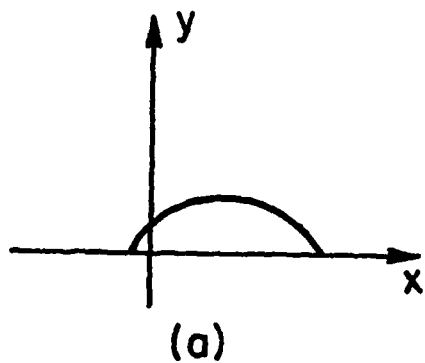


Figure 1. A sequence of drop shapes in streaming flow.

can be found by the method of characteristics. The solution is shown in Figure 2. The scale for the time axis depends on the value of  $\alpha$ . Note that the left end smooths out and does not move. The right end remains a jump. Note that the right end moves more slowly after the arrival of the first characteristic from the left end.

#### STAGNATION LINE FLOW

Suppose the external flow is a stagnation line flow, with  $p_0(x) = \frac{\beta}{2} x^2 + p_{00}$ . Then  $\frac{dp_0}{dx} = \beta x$ , and  $d^2 p_0/dx^2 = \beta$ . The equations valid on characteristics are

$$\frac{d\delta}{dt} = \beta \frac{\delta^3}{3} \quad (43)$$

$$\frac{dx}{dt} = -\beta x \delta^2 \quad (44)$$

Solving (43) gives

$$\delta = \frac{1}{\sqrt{a - \frac{2\beta}{3} t}} \quad (45)$$

as long as  $a - \frac{3\beta}{2} t > 0$ . Solving (44) gives

$$x = c \left( a - \frac{2\beta}{3} t \right)^{3/2} \quad (46)$$

At  $t = 0$ , the characteristics are at  $x_0$ , with  $\delta = \delta(x_0, 0)$ . Therefore

$$a = \frac{1}{\delta^2(x_0, 0)}$$

$$c = x_0 \delta^3(x_0, 0)$$

$$x = \left( x_0^{2/3} - x_0^{2/3} \delta^2(x_0, 0) \frac{2\beta}{3} t \right)^{3/2} \quad (47)$$

$$\delta = \frac{1}{\sqrt{\frac{1}{\delta^2(x_0, 0)} - \frac{2\beta}{3} t}} \quad (48)$$

Note that if  $\beta < 0$ ,  $\delta$  decreases and  $x$  on each characteristic spreads out. If  $\beta > 0$ ,  $\delta$  becomes infinite in finite time, that time being determined by the maximum value of  $\delta(x_0, 0)$ . This violates the assumptions made on the solution, but suggests that impinging stagnation points flatten

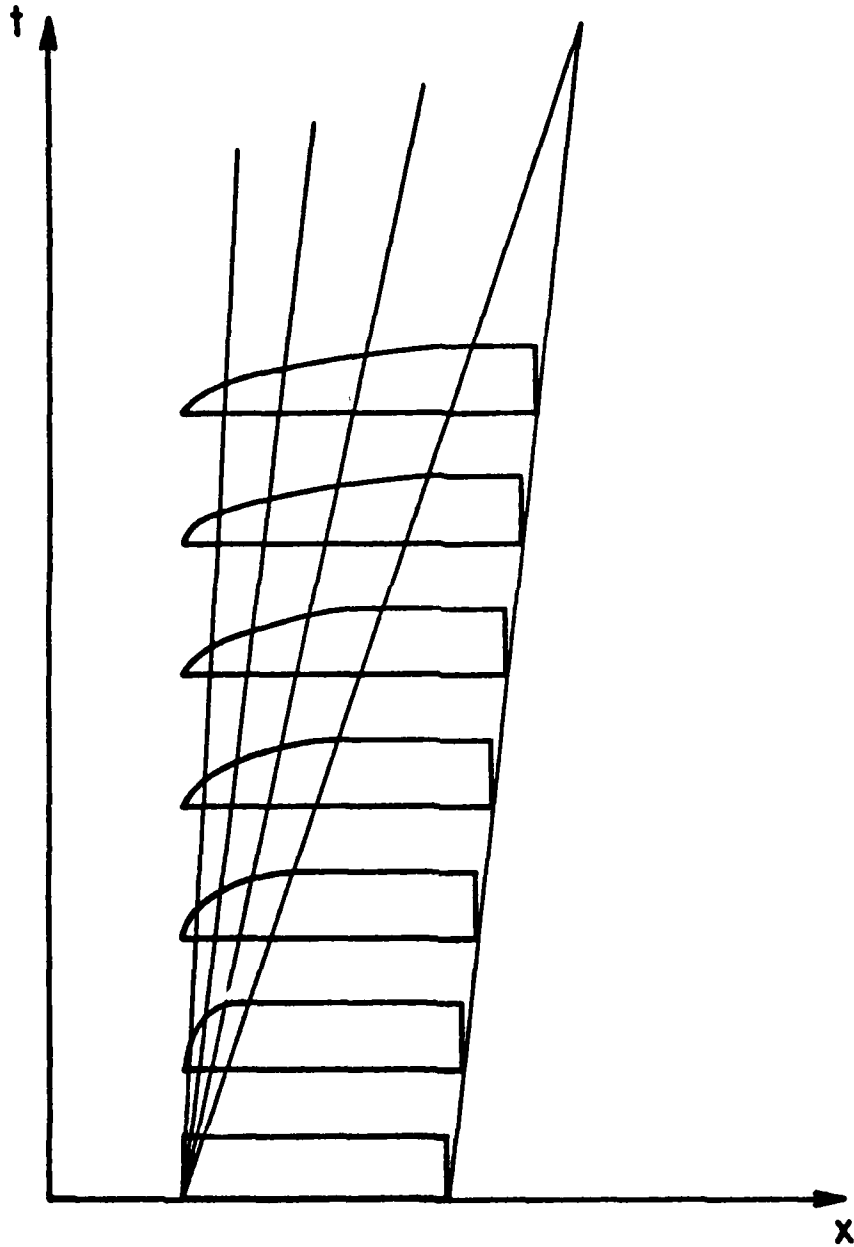


Figure 2. The evolution of a rectangular droplet.

and spread droplets, but separation stagnation points accumulate droplets and can remove them from the wall in finite time. Both surface tension and gravity resist this process.

### THE LEADING EDGE

The equations in the drop near the leading edge require a scaling different from that given by Eq. (9). Both  $x$  and  $y$  change in a short distance, which can be taken to be  $\epsilon L$ . The velocity scale is forced to be  $U$  by the outer solution. In addition, the pressure scale in the outer solution forces us to consider two terms in the pressure expansion. Thus, we assume

$$\begin{aligned}x - x_+ &= \epsilon L x'' \\y &= \epsilon L y'' \\u - \frac{dx_+}{dt} &= U u'' \\v &= U v'' \\p &= \frac{\mu U}{\epsilon^2 L} (p_1'' + \epsilon p_2'') \\ \delta &= \epsilon L \delta' \\t &= (\epsilon L / U) t'' .\end{aligned}\tag{49}$$

The equations become

$$\frac{\partial u''}{\partial x''} + \frac{\partial v''}{\partial y''} = 0\tag{50}$$

$$\epsilon \frac{\rho U L}{\mu} \left( \frac{\partial u''}{\partial t''} + u'' \frac{\partial u''}{\partial x''} + v'' \frac{\partial u''}{\partial y''} \right) = - \frac{1}{\epsilon} \frac{\partial p_1''}{\partial x''} - \frac{\partial p_2''}{\partial x''} + \left( \frac{\partial^2 u''}{\partial x''^2} + \frac{\partial^2 u''}{\partial y''^2} \right)\tag{51}$$

$$\epsilon \frac{\rho U L}{\mu} \left( \frac{\partial v''}{\partial t''} + u'' \frac{\partial v''}{\partial x''} + v'' \frac{\partial v''}{\partial y''} \right) = - \frac{1}{\epsilon} \frac{\partial p_1''}{\partial y''} - \frac{\partial p_2''}{\partial y''} + \left( \frac{\partial^2 v''}{\partial x''^2} + \frac{\partial^2 v''}{\partial y''^2} \right) - F_+\tag{52}$$

where  $F_+ = \frac{\rho g L^2 \epsilon^2}{\mu U} = F / \epsilon$ .

The kinematic boundary condition is

$$\frac{\partial \delta''}{\partial t''} + u'' \frac{\partial \delta''}{\partial x''} = v''\tag{53}$$

at  $y'' = \delta''$ .

Thus, to lowest order in  $\epsilon$ ,

$$p_1^n = \text{const} , \quad (54)$$

$$0 = -\frac{\partial p_2^n}{\partial x^n} + \frac{\partial^2 u^n}{\partial x^{n2}} + \frac{\partial^2 u^n}{\partial y^{n2}} \quad (55)$$

$$0 = -\frac{\partial p_2^n}{\partial y^n} + \frac{\partial^2 v^n}{\partial x^{n2}} + \frac{\partial^2 v^n}{\partial y^{n2}} . \quad (56)$$

These are the equations of Stokes' flow.

The boundary condition (4) is satisfied to order  $\epsilon$  by requiring

$$p_1^n = p(x_+(t), 0) \quad (57)$$

and

$$0 = p_2^n \underline{n} + \underline{n} \cdot [\nabla^n \underline{v}^n + (\nabla^n \underline{v}^n)^T] + \sigma^n \kappa^n \underline{n} \quad (58)$$

where

$$\sigma^n = \frac{\sigma}{\mu U} \quad (59)$$

and

$$\kappa^n = \frac{\partial^2 \delta^n / \partial x^{n2}}{(1 + (\partial \delta^n / \partial x^n)^2)^{3/2}} . \quad (60)$$

The boundary conditions at the wall are

$$v^n = 0 \quad (61)$$

and

$$u^n - \lambda^n \frac{\partial u^n}{\partial y^n} = -U^n \quad (62)$$

at  $y^n = 0$ . Here  $\lambda^n = \lambda/(\epsilon L)$ . The speed  $U^n$  is the speed of the discontinuity in the outer solution, which depends on the outer time, but is independent of the inner time  $t^n$ .

The inner problem is thus a steady Stokes' flow problem. Existence of a stable solution of this problem allows matching to the outer solution.

### CONCLUSION

Equation (33) describes the evolution of a thin droplet on a flat surface when viscosity is dominant. The analysis suggests that thin droplets are not removed from the surface unless the fluid outside the drop separates from the surface. The analysis gives the rate of spread of a droplet in streaming flow. The (dimensional) velocity of the fluid at the top of the droplet is proportional to

$$- \frac{1}{\mu} \frac{dp_0}{dx} \cdot \delta^2 .$$

This velocity scale can be used to obtain a rate of increase of exposed area of the drop. If the drop can be hydrolyzed or reacted with some additive in the outside fluid, the rate of increase of the area can give an estimate of the time needed for the non-mechanical cleaning of the surface.

### REFERENCES

- Dussan V., E. B. and Davis, S. H. 1974 On the motion of a fluid-fluid interface along a solid surface, *J. Fluid Mech.* 65, 71.
- Dussan V., E. B. 1976 The moving contact line: the slip boundary condition, *J. Fluid Mech.* 77, 665.
- Hocking, L. M. 1981 The motion of a drop on a rigid surface, *Proceedings of the Symposium on Bubbles and Drops, Stanford University*, p. 315.



AD P 0 0 1 0 2 4

CAVITATING FLOW WITH SURFACE TENSION

Jean-Marc Vanden-Broeck  
Department of Mathematics and  
Mathematics Research Center  
University of Wisconsin-Madison  
Madison, WI 53706

ABSTRACT. The problem of cavitating flow past a two dimensional curved obstacle is considered. Surface tension is included in the dynamic boundary condition. A perturbation solution for small values of the surface tension is presented. It is found that for most positions of the separation point, the slope is not continuous at the separation point. The velocity is infinite or equal to zero there. However, for a given value of the surface tension there exists a particular position of the separation points for which the slope is continuous. This solution tends to the classical solution satisfying the Brillouin-Villat condition as the surface tension tends to zero. Graphs of the results for the cavitating flow past a circular cylinder are presented. In addition a numerical scheme based on an integro-differential equation formulation is derived to solve the problem in the fully nonlinear case.

I. INTRODUCTION. The classical Helmholtz-Kirchhoff solution for cavitating flow past a flat plate yields infinite curvature of the free surface at the edges of the plate. Ackerberg [1] attempted to remove this singularity in the curvature by including surface tension. He constructed an asymptotic solution for small values of the surface tension in which the slope and the curvature of the free surface at the edges are both equal to those of the plate. However his solution contains capillary waves downstream. Cumberbatch and Norbury [2] observed that these waves are not physically acceptable because they require a supply of energy from infinity. They suggested that solutions without waves could be obtained by forcing the slope of the free surface at the edges to be equal to the slope of the plate and allowing the curvature to be different from zero at the edges. Although they obtained a local solution, they did not match it with any outer solution. Thus they did not obtain a solution with continuous slope at the separation points.

The problem was solved by Vanden-Broeck [3] who provided conclusive analytical and numerical evidence that the slope is not continuous at the separation points. Both velocity and curvature are infinite there. Thus, the inclusion of surface tension in the Helmholtz-Kirchhoff solution does not remove the infinite curvature at the separation points. On the contrary it makes the problem more singular by introducing a discontinuity in slope and therefore an infinite velocity at these points.

Sponsored by the United States Army under Contract No. DAAG29-80-C-0041. This material is based upon work supported by the National Science Foundation under Grant No. MCS-7927062, Mod. 1 and No. MCS800-1960.

These results were generalized by Vanden-Broeck [4] to the cavitating flow past a curved obstacle (see Figure 1). The position of the separation point may be either fixed if it is a pointed corner of the body, or free if it is at a certain location of a smoothly curved obstacle. An example of fixed detachment is provided by the cavitating flow past a flat plate in which the flow leaves the plate at the edges. Similarly the flow sketched in Figure 1 corresponds to fixed detachment if the obstacle is cut along the straight line AB. In the case of free detachment the classical solution leaves the position of the separation points A and B undetermined. This degeneracy is usually resolved by imposing the Brillouin-Villat condition which requires the curvature of the free surface to be finite at the separation points (Birkhoff and Zarantonello [5]). Vanden-Broeck [4] showed that for most positions of the separation points, the slope is not continuous at A and B. The velocity is infinite or equal to zero there. However, for a given value of the surface tension there exists a particular position of the separation points A and B for which the slope is continuous at A and B. This solution tends to the classical solution satisfying the Brillouin-Villat condition as the surface tension tends to zero.

The problem is formulated in Section II and the classical solution without surface tension is computed numerically in Section III. The scheme is similar in philosophy if not in details to the scheme derived by Brodetsky [6] and later extended by Birkhoff et al. [7,8]. Explicit results are presented for the cavitating flow past a circular cylinder.

The perturbation calculation derived by Vanden-Broeck [4] is described in Section IV. In Section V the problem is reformulated as a nonlinear singular integro-differential equation for the unknown shape of the cavity. This equation was solved numerically by Vanden-Broeck [3] for the cavitating flow past a flat plate. A discussion of his results is presented in Section VI.

II. FORMULATION AS A BOUNDARY VALUE PROBLEM. We consider the cavitating flow past a curved obstacle (see Figure 1). We denote by  $L$  a typical dimension of the obstacle. At infinity we have a flow with constant velocity  $U$ . The fluid is assumed to be inviscid and incompressible. We restrict our attention to obstacles which are symmetrical with respect to the direction of the velocity at infinity. Flows past nonsymmetrical obstacles can be treated similarly. It is convenient to introduce dimensionless variables by choosing  $L$  as the unit length and  $U$  as the unit velocity.

We introduce the dimensionless potential  $\phi$  and stream function  $\psi$ . The constant  $b$  is chosen such that  $\phi = 1$  at the separation points. Without loss of generality we choose  $\phi = 0$  at  $x = y = 0$ . The free surface, the obstacle and the negative  $x$ -axis are portions of the streamline  $\psi = 0$ .

We denote the complex velocity by  $u - iv$  and we define the function  $\tau - i\theta$  by the relation

$$u - iv = e^{\tau - i\theta} . \quad (2.1)$$

We shall seek  $\tau - i\theta$  as an analytic function of  $f = \phi + i\psi$  in the half plane  $\psi < 0$ . The complex potential plane is sketched in Figure 2. At

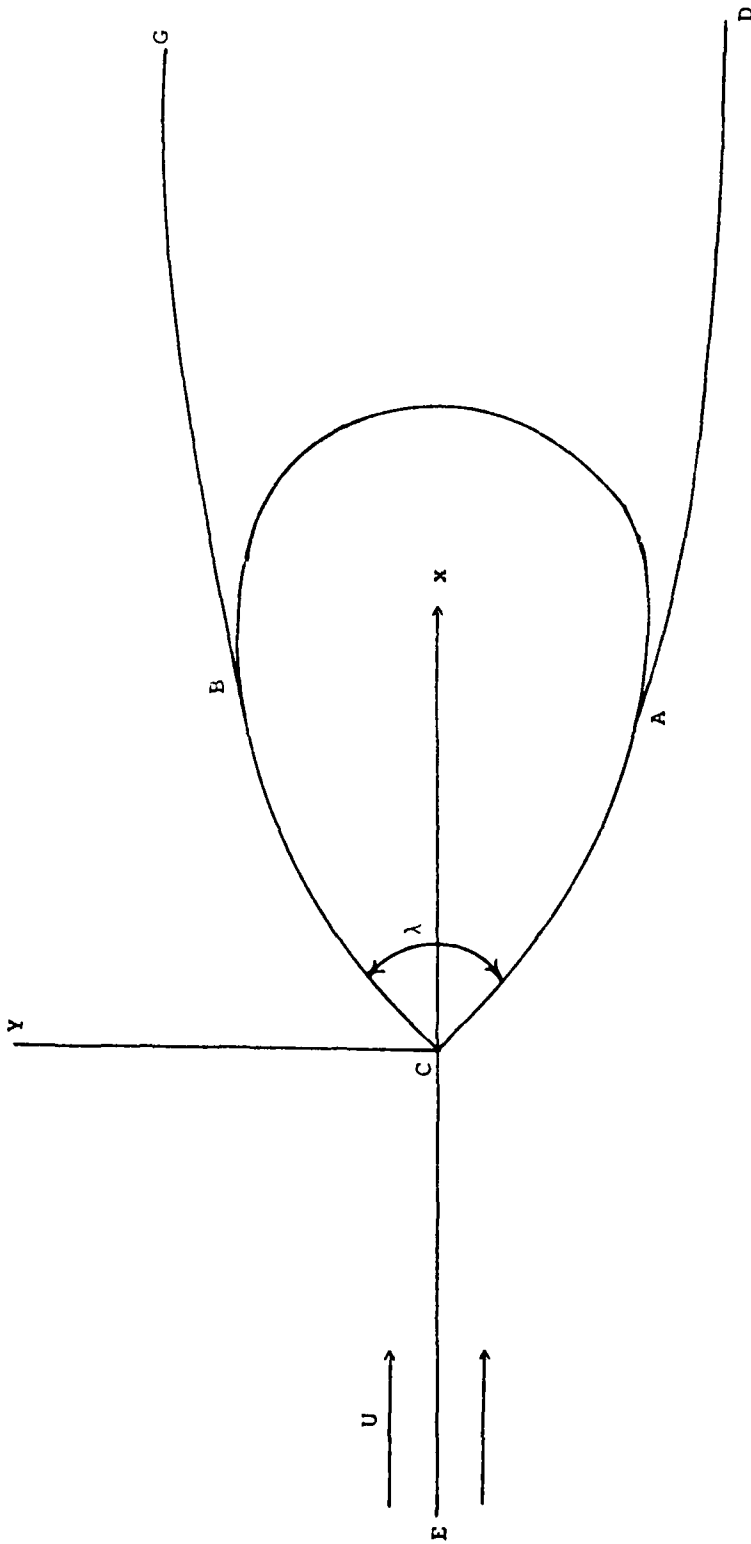


Figure 1  
Sketch of the flow and the coordinates.

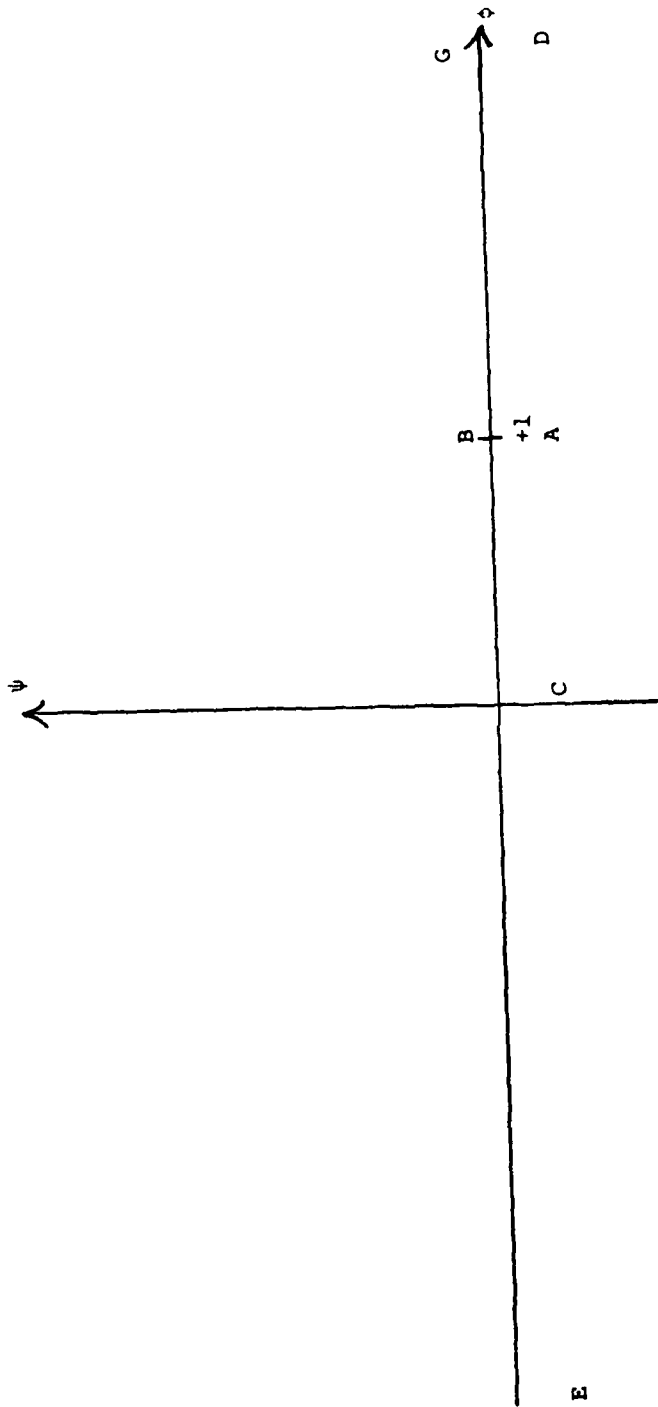


Figure 2  
The image of the flow in the plane of the complex potential  $f = \phi + i\psi$

infinity we require the velocity to be unity in the x-direction so that the function  $\tau - i\theta$  vanishes at infinity in view of (2.1).

On the surface of the cavity the Bernoulli equation and the pressure jump due to surface tension yield

$$\frac{1}{2} q^2 - \frac{T}{\rho} K = \frac{1}{2} U^2 . \quad (2.2)$$

Here  $q$  is the flow speed,  $K$  the curvature of the cavity surface counted positive when the center of curvature lies inside the fluid region,  $T$  the surface tension and  $\rho$  the density. In dimensionless variables this becomes (see Aclerberg [1] for details)

$$\frac{e^\tau}{b} \frac{\partial \theta}{\partial \phi} = \frac{\alpha}{2} (e^{2\tau} - 1), \quad 1 < \phi < \infty . \quad (2.3)$$

Here  $\alpha$  is the Weber number defined by

$$\alpha = \frac{\rho U^2 L}{T} . \quad (2.4)$$

The symmetry of the problem and the kinematic condition on the obstacle yield

$$\theta(\phi) = 0, \quad \psi = 0, \quad \phi < 0 \quad (2.5)$$

$$F[x(\phi), y(\phi)] = 0, \quad \psi = 0, \quad 0 < \phi < 1 . \quad (2.6)$$

Here  $F(x, y) = 0$  is the equation of the shape of the obstacle and the functions  $\theta(\phi)$ ,  $x(\phi)$  and  $y(\phi)$  denote respectively  $\theta(\phi, 0^-)$ ,  $x(\phi, 0^-)$  and  $y(\phi, 0^-)$ .

This completes the formulation of the problem of determining the function  $\tau - i\theta$  and the constant  $b$ . For each value of  $\alpha$ ,  $\tau - i\theta$  must be analytic in the half plane  $\psi < 0$  and satisfy the boundary conditions (2.3), (2.5) and (2.6).

**III. SOLUTION WITHOUT SURFACE TENSION.** When surface tension is neglected, the Weber number is infinite and the condition (2.3) reduces to the free-streamline condition  $\tau = 0$ .

We define the new variable  $t$  by the transformation

$$\sqrt{z} = \left(t - \frac{1}{t}\right) \frac{1}{2i} . \quad (3.1)$$

The problem in the complex plane  $t$  is illustrated in Figure 3. Following Brodetsky [6] we introduce the function  $\Omega'(t)$  by the relation

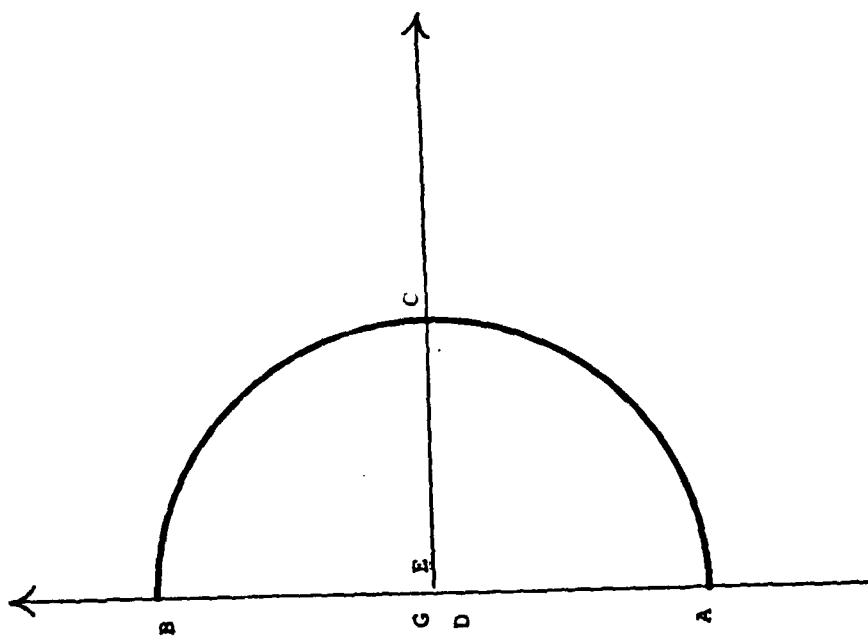


Figure 3  
The t-plane

$$\tau - i\theta = -\frac{\lambda}{\pi} \log \frac{1+t}{1-t} - \Omega'(t) \quad (3.2)$$

where the angle  $\lambda$  is defined in Figure 1. The conditions (2.3) and (2.5) show that  $\Omega'(t)$  can be expressed in the form of a Taylor expansion in odd powers of  $t$ . Hence

$$\tau - i\theta = -\frac{\lambda}{\pi} \log \frac{1+t}{1-t} - \sum_{n=1}^{\infty} A_n t^{2n-1}. \quad (3.3)$$

The function (3.3) satisfies the conditions (2.3) and (2.5). The coefficients  $A_n$  have to be determined to satisfy the condition (2.6) on the surface  $A C B$  of the obstacle. We use the notation  $t = r e^{i\sigma}$  so that points on  $A C B$  are given by  $r = 1$ ,  $-\frac{\pi}{2} < \sigma < \frac{\pi}{2}$ . Using (3.1) and (2.1) we have

$$\frac{\partial x}{\partial \sigma} = b \sin 2\sigma e^{-\tau} \cos \theta, \quad \rho = 1, \quad -\frac{\pi}{2} < \sigma < \frac{\pi}{2} \quad (3.4)$$

$$\frac{\partial y}{\partial \sigma} = b \sin 2\sigma e^{-\tau} \sin \theta, \quad \rho = 1, \quad -\frac{\pi}{2} < \sigma < \frac{\pi}{2}. \quad (3.5)$$

We solve the problem approximately by truncating the infinite series in (3.3) after  $N$  terms. We find the  $N$  coefficients  $A_n$  and the constant  $b$  by a hybrid method involving collocation and finite differences. Substituting  $t = e^{i\sigma}$  into (3.3) we have

$$\theta(\sigma) = \frac{\lambda}{2} + \sum_{n=1}^N A_n \sin[(2n-1)\sigma] \quad (3.6)$$

$$\tau(\sigma) = -\frac{\lambda}{\pi} \log \frac{\sin \sigma}{1 - \cos \sigma} - \sum_{n=1}^N A_n \cos[(2n-1)\sigma]. \quad (3.7)$$

We now introduce the  $N$  mesh points

$$\sigma_I = -\frac{\pi}{2N} I, \quad I = 1, \dots, N \quad (3.8)$$

and the  $N$  intermediate mesh points

$$\sigma_I^M = -\frac{\pi}{2N} \left(I - \frac{1}{2}\right), \quad I = 1, \dots, N. \quad (3.9)$$

Using (3.4)-(3.7) and (3.9) we obtain  $\left(\frac{\partial x}{\partial \sigma}\right)_{\sigma=\sigma_I^M}$  and  $\left(\frac{\partial y}{\partial \sigma}\right)_{\sigma=\sigma_I^M}$  in terms of

the coefficients  $A_n$  and the constant  $b$ . These expressions enable us to evaluate  $x(\sigma_I)$  and  $y(\sigma_I)$  by the trapezoidal rule. Then (2.6) provides  $N$  algebraic equations for the  $N+1$  unknowns  $A_n$  and  $b$ , namely

$$F[x(\sigma_I), y(\sigma_I)] = 0, \quad I = 1, \dots, N. \quad (3.10)$$

The last equation is obtained by specifying the abscissa  $w$  of the separation point A. Thus

$$x\left(-\frac{\pi}{2}\right) = w. \quad (3.11)$$

The system (3.10)-(3.11) is easily solved by Newton's method. Explicit computations were performed for the cavitating flow past a circular cylinder. The unit length  $L$  was chosen as the radius of the cylinder. The scheme converges rapidly and the solutions obtained were found to agree with the numerical results given by Birkhoff and Zarantonello [5].

Profiles of the cavity for various values of the angular position  $\gamma$  of the separation points are presented in Figure 4. For  $\gamma < \gamma^* = 55^\circ$  the free surface enters the body. These solutions are acceptable if the body is cut along the straight line AB. For  $\gamma > \gamma^{**} = 124^\circ$ , the free surfaces cross over and the corresponding solutions are not physically acceptable.

Physically acceptable solutions for  $\gamma > \gamma^{**}$  can be obtained by using the method presented by Vanden-Broeck and Keller [9] to prevent overlapping in capillary waves of large amplitude. These solutions are found to be the cusped cavities considered before by Southwell and Vaisey [10], Lighthill [11] and others (see Figure 4). The pressure in the cavity is found as part of the solution. Similarly in the work of Vanden-Broeck and Keller [9] the pressure in the trapped bubble was found as part of the solution. As  $\gamma$  tends to  $\gamma^{**}$  the pressure in the cavity tends to zero. As  $\gamma$  tends to  $180^\circ$  the cavity shrinks to a point, and the solution reduces to the classical potential flow past a circle. Thus the family of cusped cavities is the physical continuation for  $\gamma > \gamma^{**}$  of the family of open cavities.

The curvature of the free surface in the neighborhood of the separation point A is given by the formula (Brodetsky [6])

$$\frac{1}{b} \frac{\partial \theta}{\partial \phi} \sim -\frac{1}{2} C(\phi - 1)^{-1/2} \quad \text{as } \phi \rightarrow 1 \quad (3.12)$$

where

$$C = -\frac{\lambda b^{-1/2}}{\pi} - b^{-1/2} \sum_{n=1}^N (-1)^{n+1} (2n-1) A_n. \quad (3.13)$$

These formula are true for the cavitating flow past any curved obstacle.

A graph of  $C$  versus the angular position of  $\gamma$  of the separation points for the flow past a circular cylinder is shown in Figure 5. The constant  $C$  vanishes for  $\gamma = \gamma^*$ . Thus (3.12) shows that the curvature at the separation points is infinite unless  $\gamma = \gamma^*$ . If we impose the Brillouin-Villat condition, the problem with free detachment has a unique solution corresponding to  $\gamma = \gamma^*$ .

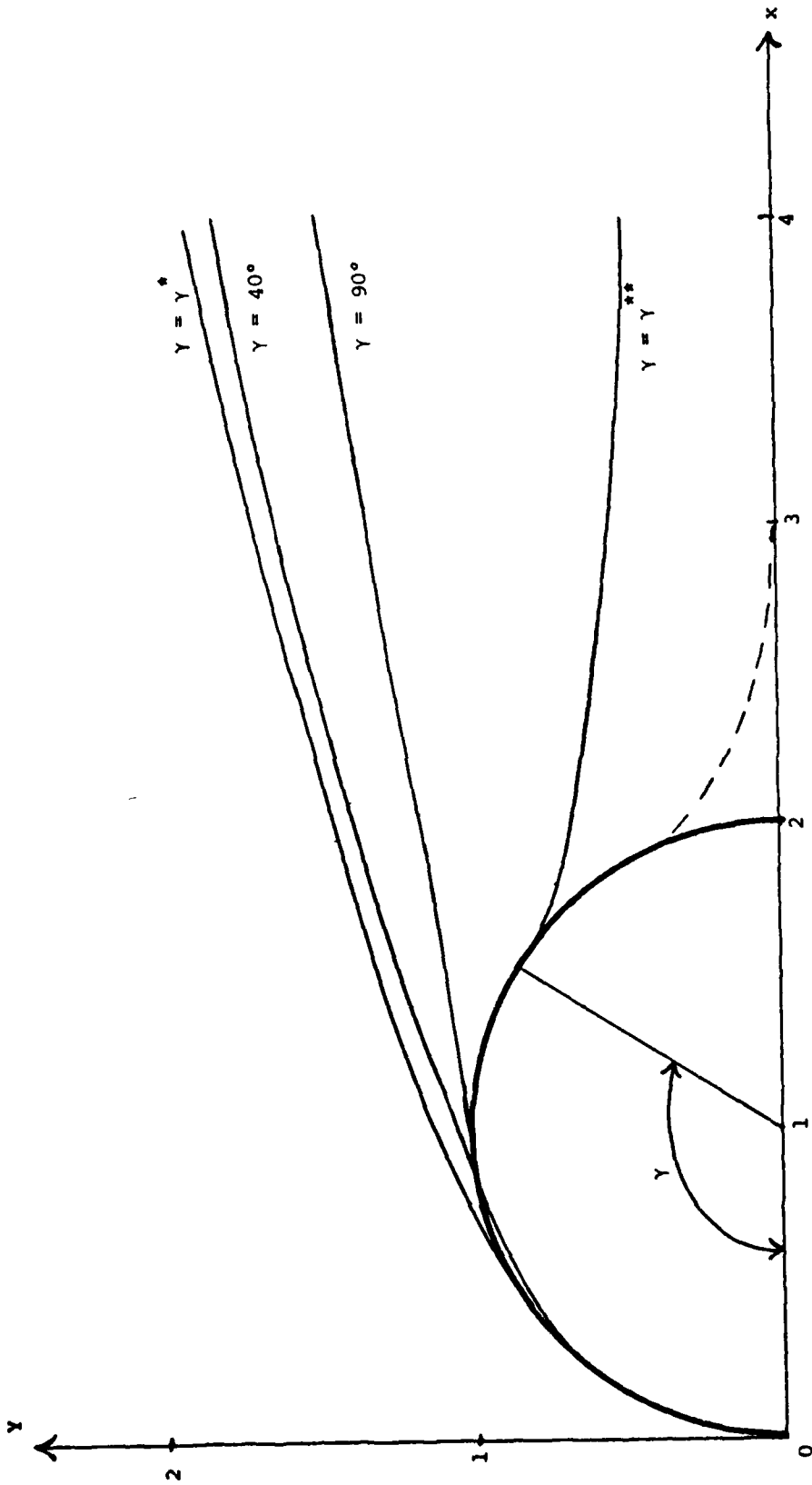


Figure 4

Cavities without surface tension in steady two dimensional flow past a circular cylinder for  $\gamma = 40^\circ$ ,  $\gamma = \gamma^* \sim 55^\circ$ ,  $\gamma = 90^\circ$  and  $\gamma = \gamma^{**} \sim 124^\circ$ . The broken line represents a cusped cavity computed numerically by Southwell and Vaisey (1946). The velocity on the free-streamlines of the cusped cavity is equal to  $0.6 U$ . The corresponding cavitation number is equal to  $-0.64$ .

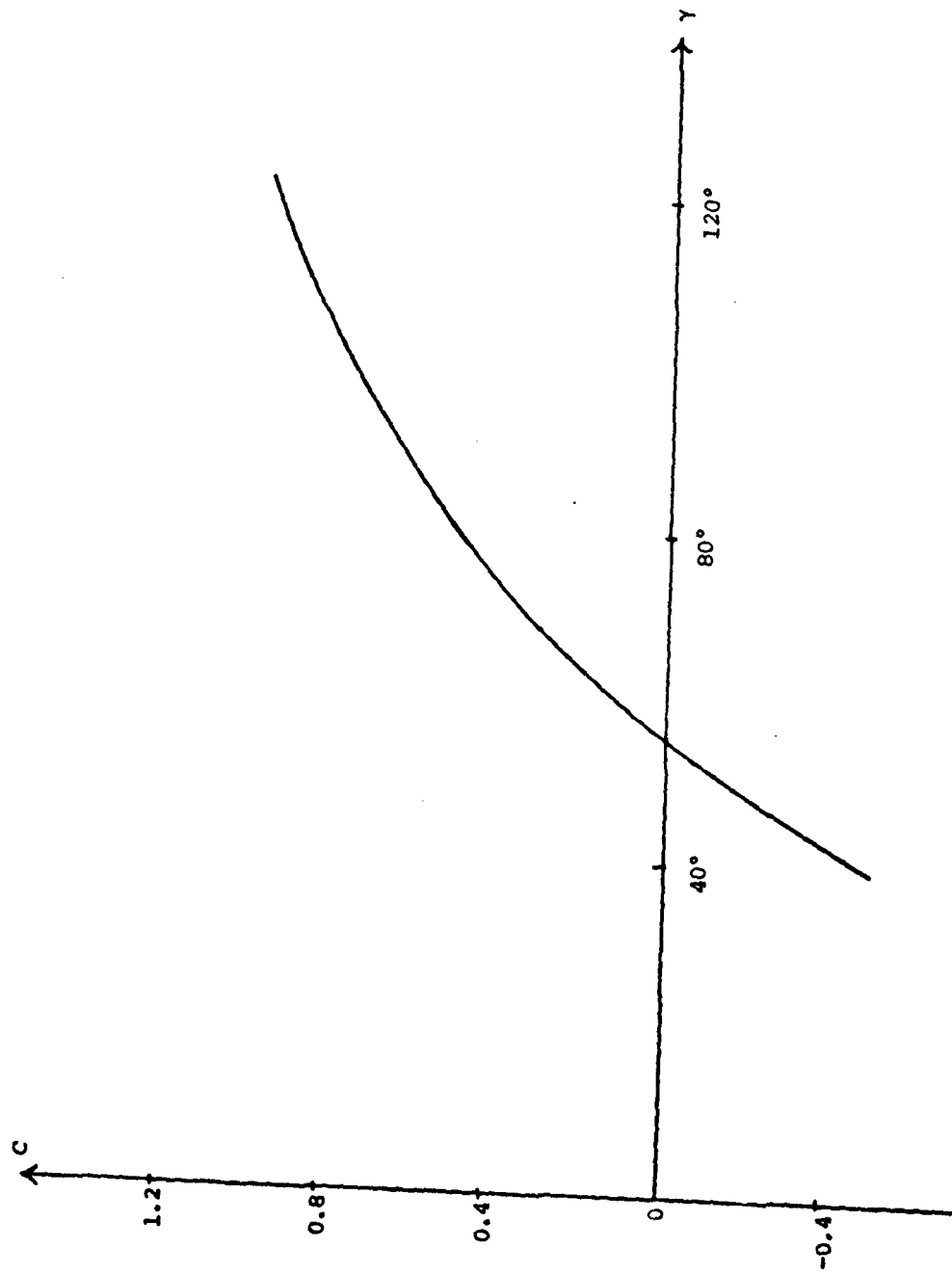


Figure 5  
Computed values of the parameter  $C$  as a function of the angle  $\gamma$

IV. PERTURBATION SOLUTION FOR SMALL VALUES OF THE SURFACE TENSION. We seek a solution in the vicinity of the separation point A. Following Ackerberg [1] we introduce the following scaling of the variables

$$f^* = \alpha(bf - b) \quad (4.1)$$

$$\tau^* - i\theta^* = \alpha^{1/2} (\tau - i\theta - i \frac{\pi}{2} + i\gamma) . \quad (4.2)$$

The function  $\tau^*$  satisfies Laplace's equation in the lower half plane  $\psi^* < 0$ . Thus

$$\frac{\partial^2 \tau^*}{\partial \phi^{*2}} + \frac{\partial^2 \tau^*}{\partial \psi^{*2}} = 0 \quad \text{in} \quad \psi^* < 0 . \quad (4.3)$$

The boundary conditions (2.3) and (2.6) linearize in the limit  $\alpha \rightarrow \infty$  so that the boundary conditions on  $\psi^* = 0$  are (see Ackerberg [1] for details)

$$\frac{\partial \tau^*}{\partial \psi^*} = 0 \quad \text{on} \quad \psi^* = 0 \quad \text{for} \quad \phi^* < 0 \quad (4.4)$$

$$\frac{\partial \tau^*}{\partial \psi^*} = \tau^* \quad \text{on} \quad \psi^* = 0 \quad \text{for} \quad \phi^* > 0 . \quad (4.5)$$

Relation (3.12) gives the behavior

$$\tau^* \sim \text{Im} C(f^*)^{1/2} \quad \text{as} \quad |f^*| \rightarrow \infty . \quad (4.6)$$

Cumberbatch and Norbury [2] noticed that the problem (4.3)-(4.5) had been treated by Friedrichs and Levy [12]. The solution of (4.3)-(4.6) not containing waves and having the weakest singularity at A is given on the free surface by

$$\theta^*(\phi^*) = -\frac{C}{2} \left(\frac{\pi}{\alpha}\right)^{1/2} - \frac{C}{2(\pi)^{1/2}} (\phi^* \ln \phi^* - \phi^*) \quad (4.7)$$

$$\tau^*(\phi^*) = \frac{1}{2\sqrt{\pi}} C \ln \phi^* . \quad (4.8)$$

The leading order terms in (4.7) and (4.8) correspond to flow past a corner of angle

$$\delta = \pi - \frac{C}{2} \left(\frac{\pi}{\alpha}\right)^{1/2} . \quad (4.9)$$

However, the solution (4.7), (4.8) is not valid near  $\phi = 1$  because  $\tau^*$  is unbounded at  $\phi = 1$ . Following Vanden-Broeck [3] we seek a local solution which corresponds to a flow past a corner of angle  $\delta$ . Thus we write

$$e^\tau \sim E(\phi - 1)^{\pi/(2\pi - \delta) - 1} . \quad (4.10)$$

Here E is a constant to be determined as part of the solution. Substituting

(4.10) into (2.3) we have

$$\frac{\partial \theta}{\partial \phi} \sim \frac{\alpha b}{2} \{E(\phi - 1)^{\pi/(2\pi - \delta) - 1} - E^{-1}(\phi - 1)^{1 - \pi/(2\pi - \delta)}\}. \quad (4.11)$$

Matching (4.11) and (4.7) we find

$$E = 1. \quad (4.12)$$

Thus we have succeeded in matching the solution (4.7), (4.8) with a local solution corresponding to the flow past a corner of angle  $\delta$ . In particular these results imply that

$$\theta(1) = -\frac{\pi}{2} + \gamma - \frac{C}{2} \left(\frac{\pi}{\alpha}\right)^{1/2}. \quad (4.13)$$

Relation (4.9) shows that  $\delta > \pi$  for  $C < 0$  and  $\delta < \pi$  for  $C > 0$ . Therefore the velocity at the separation points is infinite for  $C < 0$  and equal to zero for  $C > 0$ .

Graphs of  $\theta(1)$  versus  $\alpha^{-1/2}$  for the circular cylinder are shown in Figure 6. The velocity at the separation points is infinite for  $\gamma < \gamma^*$  and equal to zero for  $\gamma > \gamma^*$ .

Although we did only compute an asymptotic solution for  $\alpha$  large, we have every reason to believe that a solution exists for all values of  $\alpha$ . As  $\alpha$  tends to zero, the free surfaces must approach two horizontal straight lines. Therefore

$$\lim_{\alpha \rightarrow 0} \theta(1) = 0. \quad (4.14)$$

Providing  $\theta(1)$  is a continuous function of  $\alpha$ , Figure 6 and (4.14) imply the existence for each value of  $\gamma^* < \gamma < 90^\circ$  of one value of  $0 < \alpha < \infty$  for which  $\theta_1 = -\frac{\pi}{2} + \gamma$ . We describe this relation between  $\alpha$  and  $\gamma$  by the function

$$\gamma = g(\alpha). \quad (4.15)$$

This result can be reformulated as follows. For each value of the Weber number  $\alpha$  there exists an angular position  $\gamma = g(\alpha)$  of the separation points for which the flow leaves the obstacle tangentially.

As  $\alpha$  tends to zero the free surfaces tend to two horizontal straight lines. This solution leaves the cylinder tangentially only if  $\gamma = 90^\circ$ . Therefore

$$\lim_{\alpha \rightarrow 0} g(\alpha) = 90^\circ. \quad (4.16)$$

As  $\alpha$  tends to infinity, the solution is described by the asymptotic solution (4.7) and (4.8). This solution leaves the obstacle tangentially only

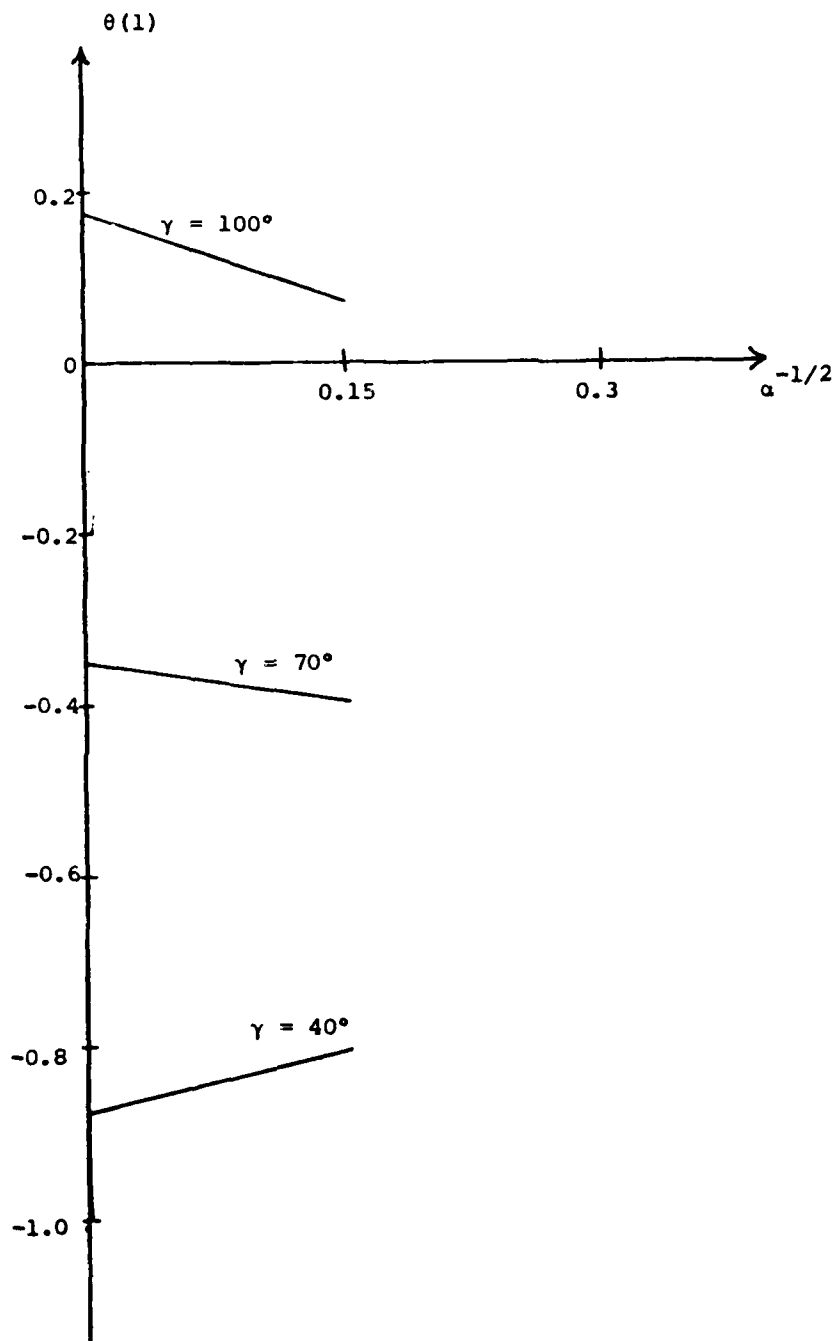


Figure 6  
 Computed values of  $\theta(1)$  as a function of  $\alpha^{-1/2}$  for  
 $\gamma = 40^\circ, 70^\circ$  and  $100^\circ$ .

if  $C = 0$  (see formula (4.9)). Therefore Figure 6 implies

$$\lim_{\alpha \rightarrow 0} g(\alpha) = \gamma^* . \quad (4.17)$$

Relation (4.17) shows that the family of solution defined by (4.15) tends to the classical solution satisfying the Brillouin-Villat condition, as  $\alpha \rightarrow \infty$ .

**V. REFORMULATION AS AN INTEGRO-DIFFERENTIAL EQUATION.** It is convenient to reformulate the boundary value problem as an integro-differential equation by considering  $\tau - i\theta$ . This function is analytic in the half plane  $\psi < 0$  and vanishes at infinity. Therefore on  $\psi = 0$  its real part is the Hilbert transform of its imaginary part. Thus we have

$$\tau(\phi) = \frac{1}{\pi} \int_{-\infty}^{+\infty} \frac{\theta(\phi')}{\phi' - \phi} d\phi' . \quad (5.1)$$

Here  $\tau(\phi)$  and  $\theta(\phi)$  denote respectively  $\tau(\phi, 0^-)$  and  $\theta(\phi, 0^-)$ . The integral in (5.1) is to be interpreted in the Cauchy principal value sense.

Substituting (2.5) into (5.1) we obtain

$$\tau(\phi) = \frac{1}{\pi} \int_0^{\infty} \frac{\theta(\phi')}{\phi' - \phi} d\phi' . \quad (5.2)$$

Using (2.1) we have

$$x(\phi) = b \int_0^{\phi} e^{-\tau} \cos \theta d\phi , \quad (5.3)$$

$$y(\phi) = b \int_0^{\phi} e^{-\tau} \sin \theta d\phi . \quad (5.4)$$

Substituting (5.3) and (5.4) into (2.6) yields

$$F \left[ b \int_0^{\phi} e^{-\tau} \cos \theta d\phi , b \int_0^{\phi} e^{-\tau} \sin \theta d\phi \right] = 0 . \quad (5.5)$$

This completes the formulation of the problem of determining  $\tau(\phi)$ ,  $\theta(\phi)$  and  $b$ . For each value of  $\alpha$ , the functions  $\tau(\phi)$  and  $\theta(\phi)$  and the constant  $b$  must satisfy the integro-differential equation defined by (2.3), (5.2) and (5.5).

**VI. NUMERICAL RESULTS FOR CAVITATING FLOW PAST A FLAT PLATE.** Vanden-Broeck [3] derived a numerical scheme to solve the integro-differential equation defined by (2.3), (5.2) and (5.5). Explicit computations were

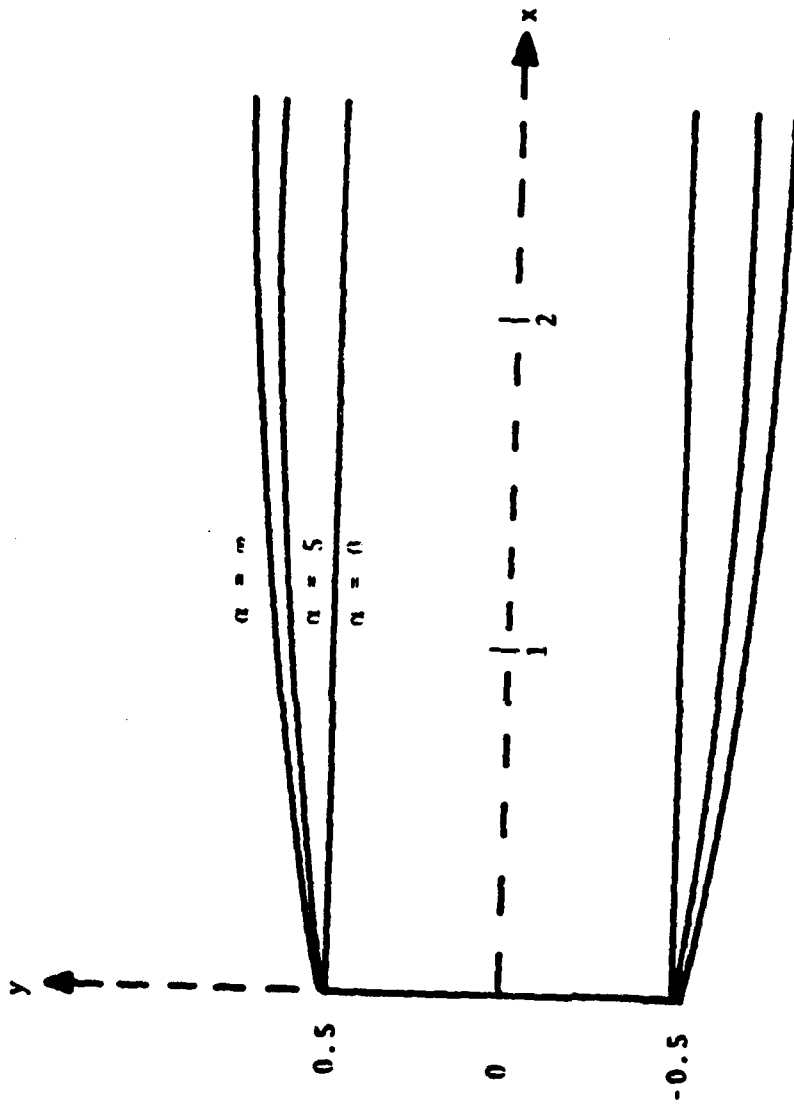


Figure 7  
 Computed profiles for  $\alpha = 0, 5, \infty$ .

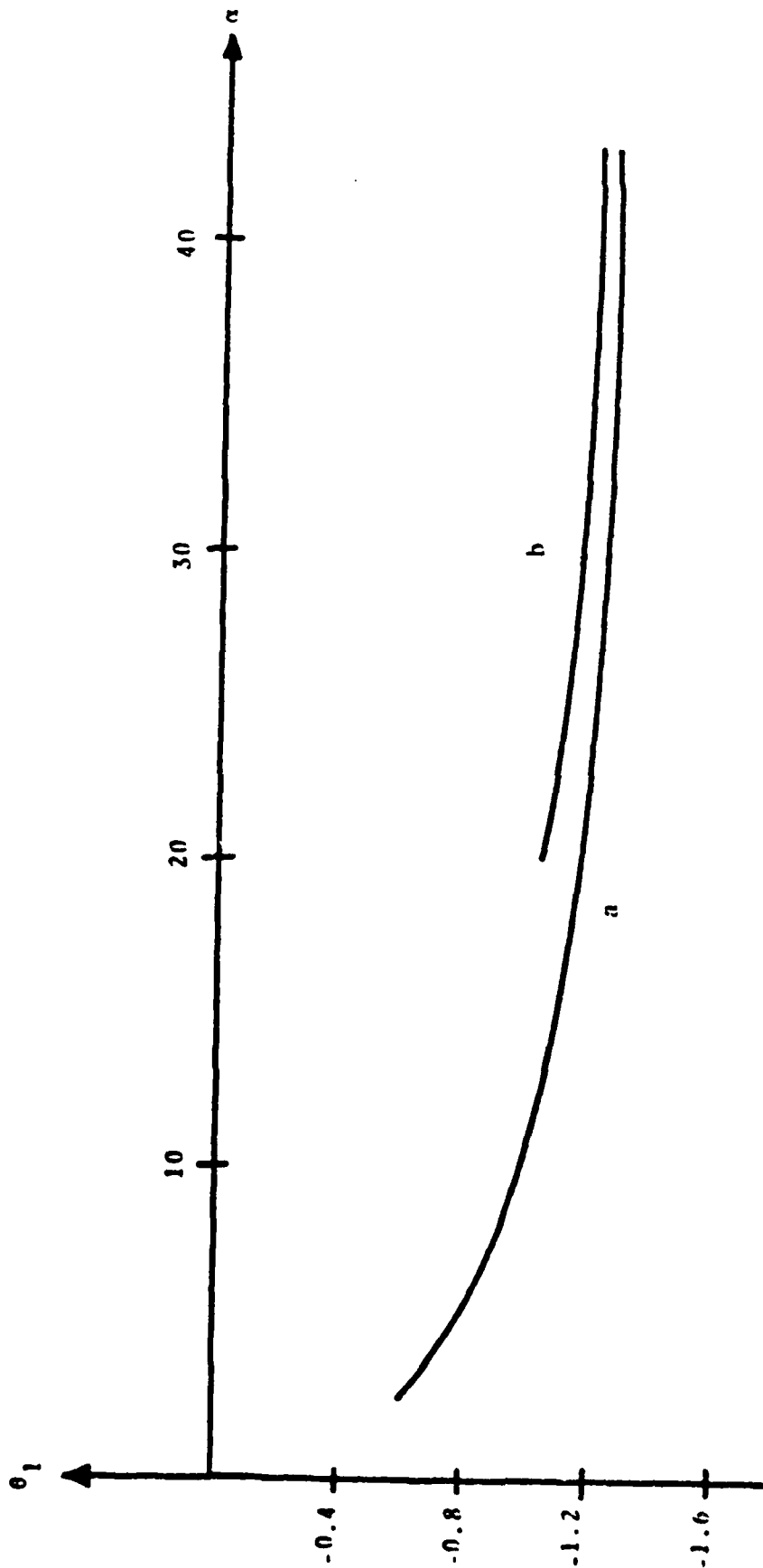


Figure 8  
 The slope  $\theta_1$  of the free surface at the separation points as a function of the Weber number  $\alpha$  as given by the numerical scheme (curve a) and formula (6.1) (curve b).

performed for the cavitating flow past a flat plate. The unit length  $L$  was chosen as the length of the plate.

Typical profiles are shown in Figure 7. We shall denote by  $\theta_1$  the slope of the free surface at the separation point. The numerical values of  $\theta_1$  versus  $\alpha$  are shown in Figure 8. The perturbation solution (4.7) yields

$$\theta_1 \sim -\frac{\pi}{2} + \frac{1}{2} C \left(\frac{\pi}{2}\right)^{1/2}. \quad (6.1)$$

The constant  $C$  in (6.1) can be evaluated from the classical Helmholtz-Kirchhoff solution for cavitating flow past a flat plate. Thus we obtain

$$C = (\pi + 4)^{1/2}. \quad (6.2)$$

The asymptotic solution (6.1), (6.2) is shown in Figure 8. The asymptotic results and the numerical solution are in good agreement for  $\alpha$  large. For  $\alpha = 130$  the value of  $\theta_1$  predicted by (6.1), (6.2) agrees with the numerical results within one percent. This constitutes an important check on the validity of the numerical scheme.

#### REFERENCES

1. Ackerberg, R. C. 1975 *J. Fluid Mech.* 70, 333.
2. Cumberbatch, E. and Norbury, J. 1979 *Q. J. Mech. Appl. Math.* 32, 303.
3. Vanden-Broeck, J.-M. 1981 *Q. J. Mech. Appl. Math.* 34, 465.
4. Vanden-Broeck, J.-M. 1982 MRC Technical Summary Report No. 2356, Mathematics Research Center, University of Wisconsin-Madison.
5. Birkhoff, G. and Zarantonello, E. 1957 *Jets, Wakes and Cavities*. Academic Press, New York.
6. Brodetsky, S. 1923 *Proc. Roy. Soc. London A*, 102, 542.
7. Birkhoff, G., Goldstine, H. and Zarantonello, E. 1954 *Rend. Seminar. Mat. Univ. Politec. Torino* 13, 205.
8. Birkhoff, G., Young, D and Zarantonello, E. 1953 *Proc. Symp. Appl. Math.* 4, 117.
9. Vanden-Broeck, J.-M. and Keller, J. B. 1980 *J. Fluid Mech.* 98, 161.
10. Southwell, R. V. and Vaisey, G. 1946 *Phil. Trans.* 240, 117.
11. Lighthill, M. J. 1949 *Aero. Res. Coun., Rep. and Mem.* no 2328.
12. Friedrichs, K. O. and Lewy, H. 1948 *Communs Pure Appl. Math.* 1, 135.

AD P001025

STRESS SOLUTIONS AT BONDLINE-BOUNDARY INTERSECTIONS  
IN COMPOSITE MATERIALS

Oscar L. Bowie, Colin E. Freese, and Dennis M. Tracey

Mechanics of Materials Division  
Army Materials and Mechanics Research Center  
Watertown, Massachusetts 02172

*r sub lambda-1, lambda*

ABSTRACT. Various analytical studies in planar elasticity have shown that the stress state can be singular at bondline-boundary intersections in composite materials. The singularity has the form  $r^{\lambda-1}$  with  $\lambda$  in the range  $(0, 1)$  and dependent upon the elastic properties of the composite. Here ~~we~~ <sup>we</sup> present an asymptotic analysis for the case of a bondline which is perpendicular to a traction free boundary. The analysis applies to any composite consisting of perfectly bonded dissimilar isotropic materials. Whereas previous analyses have limited attention to the characteristic equation for  $\lambda$ , ~~we~~ <sup>we</sup> present in addition the equations for the angular form of the singular field. *lambda*

The practical problem of a bimaterial tension strip which has a singular elasticity solution was analyzed using the finite element method. Results show that the free surface singularity strongly influences the global solution and that very accurate solutions can be obtained by using singularity elements.

ASYMPTOTIC ANALYSIS. Here we investigate the form of the stress and displacement fields in the immediate vicinity of a bimaterial free boundary-bondline intersection. The problem is illustrated in Fig. (1) where the x-axis is traction free and the materials 1 and 2 are bonded along the positive y-axis. In the first quadrant,  $0 < \theta < \pi/2$ , the shear modulus and Poisson's ratio are denoted  $\mu_1$  and  $\nu_1$ , respectively, while in the second quadrant,  $\pi/2 < \theta < \pi$ , they are denoted  $\mu_2$  and  $\nu_2$ .

Bogy [1968] treated this problem using the Mellin transform method. Actually, he considered the more general problem having arbitrary specified traction acting on the boundary  $y = 0$ . He found that for certain bimaterials the displacement components  $u_x$  and  $u_y$  vary as  $r^\lambda$  and the stress components  $\sigma_{xx}$ ,  $\sigma_{yy}$ ,  $\sigma_{xy}$  vary as  $r^{\lambda-1}$  near the bond-boundary intersection. The exponent  $\lambda$  which defines the strength of singularity depends upon the elastic properties of the composite.

In Bogy's work, the transformed field quantities are shown to depend in common upon a certain function of his transform parameter  $s$ . A zero of this function in a specific range implies that the  $r^\lambda$ ,  $r^{\lambda-1}$  singularity holds for the primary (untransformed) field variables. Converting notation, if there is a root to the following function of  $\lambda$  in the range  $(0, 1)$ , then the power singularity results:

$$[(k_1 - k_2) \sin^2(\lambda \pi/2) - k_1 \lambda^2]^2 + k_3^2 \sin^2(\lambda \pi)/4 - k_2^2 \lambda^2 = \Delta(\lambda) \quad (1)$$

$$k_1 = 2(\mu_1/\mu_2 - 1)$$

$$k_2 = (\mu_1/\mu_2)m_2 - m_1$$

$$k_3 = (\mu_1/\mu_2)m_2 + m_1$$

$$m_j = 4(1 - \nu_j) \quad \text{plane strain}$$

$$m_j = 4/(1 + \nu_j) \quad \text{plane stress}$$

This characteristic equation was derived using the convention that  $\mu_1 \leq \mu_2$ . Bogy found that the most severe singularity in plane stress occurs when  $\mu_1/\mu_2 = 0$  and  $\nu_1 = 0.5$ . This is the case of a rigid material bonded to an incompressible flexible material and then  $\lambda = 0.689$ . In the next section we discuss a plane strain problem for a bimaterial having  $\mu_1/\mu_2 = 1/10$  and  $\nu_1 = \nu_2 = 0.3$ . For this composite, eqn. (1) suggests that  $\lambda = 0.801$ .

We have found that the complex variable formulation, Muskhelishvili [1953], offers a relatively straightforward solution to the intersection problem. We have been able to verify Bogy's characteristic equation and, importantly, have found the angular form of the singular solution. This result does not appear to have been previously discussed in the literature.

Using the complex variable formulation, the basic problem is to find the two analytic stress functions  $\phi(z)$  and  $\psi(z)$ ,  $z = x + iy$ , which represent the Airy biharmonic stress function over the domain of interest. Each constituent of the bimaterial must be considered separately, so that in the first quadrant  $\phi_1$  and  $\psi_1$  govern, while in the second quadrant  $\phi_2$  and  $\psi_2$  govern. The problem is defined by the traction free condition on  $y = 0$  and the continuity conditions on  $x = 0$ . If there is in fact a singularity with displacement varying as  $r^\lambda$ , then in each

constituent the stress functions will have the functional form  $z^\lambda$  near  $r = 0$ . Hence, we will assume that there is a singularity and examine the consequences of this choice. Introducing the complex constants  $A_1, A_2, B_1,$  and  $B_2$ , the stress functions are taken as

$$\begin{aligned}\phi_1 &= A_1 z^\lambda & \phi_2 &= A_2 z^\lambda \\ \psi_1 &= B_1 z^\lambda & \psi_2 &= B_2 z^\lambda\end{aligned}\tag{2}$$

The integrated traction  $f = f_x + i f_y$ , which acts on material to the left of a bounding arc  $\overline{oz}$  is given by the expression

$$f = (\phi + z \overline{\phi'} + \overline{\psi}) \Big|_0^z\tag{3}$$

With point  $o$  at the origin and  $z$  generic position  $re^{i\theta}$ , the assumed stress functions (2) imply that over an arc in material  $j$ ,  $j = 1, 2$ :

$$f = r^\lambda (A_j e^{i\lambda\theta} + \overline{A}_j \lambda e^{i(2-\lambda)\theta} + \overline{B}_j e^{-i\lambda\theta})\tag{4}$$

The traction free condition implies that  $f = 0$  on both  $\theta = 0$  and  $\theta = \pi$ . Furthermore, equilibrium demands that  $f(\pi/2^-) = f(\pi/2^+)$ . Hence, eqn. (4) provides the following three equations, linear and homogeneous in the constants  $A_j, B_j, \overline{A}_j, \overline{B}_j$ :

$$\begin{aligned}A_1 + \overline{A}_1 \lambda + \overline{B}_1 &= 0 \\ A_2 e^{i2\lambda\pi} + \overline{A}_2 \lambda + \overline{B}_2 &= 0\end{aligned}\tag{5}$$

$$(A_1 - A_2) e^{i\lambda\pi} + (\overline{A}_2 - \overline{A}_1) \lambda + \overline{B}_1 - \overline{B}_2 = 0$$

The condition of displacement continuity across the bondline provides an additional equation. If  $U = u_x + i u_y$  is the displacement vector at position  $z$ , then

$$2\mu U = \kappa \phi - z \overline{\phi'} - \overline{\psi}\tag{6}$$

where  $\kappa = 3 - 4\nu$  for plane strain and  $(3 - \nu)/(1 + \nu)$  for plane stress problems. Since  $U(\pi/2^-) = U(\pi/2^+)$ , it follows from eqn. (6) that

$$\mu_2(\kappa_1 A_1 e^{i\lambda\pi} + \overline{A}_1 \lambda - \overline{B}_1) - \mu_1(\kappa_2 A_2 e^{i\lambda\pi} + \overline{A}_2 \lambda - \overline{B}_2) = 0\tag{7}$$

Equations (5) and (7) represent a system of eight linear, homogeneous equations in the eight undetermined real constants  $\text{Re } A_j, \text{Re } B_j, \text{Im } A_j,$  and  $\text{Im } B_j$ . The solution is the trivial one except when the determinant of the system vanishes. Hence our choice of the singular forms (2) is valid only when the determinant, a function of the parameter  $\lambda$ , has a zero in the range  $(0, 1)$ . The expression for

the determinant therefore serves to define the characteristic equation for  $\lambda$ . With a bit of algebra it can be shown that the determinant is exactly Bogy's [1968] expression  $\Delta(\lambda)$  given above as eqn. (1).

Bogy [1968] and Dundurs [1969] discuss the conditions involving the elastic constants which result in the  $r^\lambda$  singularity, i.e., a root of  $\Delta(\lambda)$  in the range (0, 1). One case for plane strain which does not have this singular possibility is when  $\mu_1/\mu_2 = \nu_1/\nu_2$ . We have not pursued this issue beyond what they have discussed. Next we consider the angular form of the solution when the  $r^\lambda$  singularity does in fact apply.

The root of  $\Delta(\lambda)$  defines the coefficients in the 8 x 8 system of linear equations. Being a homogeneous system, the solution takes the form of an eigenvector with undetermined magnitude. This eigenvector defines "eigenfunctions" for  $\phi_j$ ,  $\psi_j$  in eqn. (2). Substituting these results into the expression for the displacement field  $U$ , eqn. (6), and the following expressions defining the stress field gives the angular form of the singularity solution. The general stress equations in terms of  $\phi$  and  $\psi$  are given by

$$\sigma_{xx} + \sigma_{yy} = 4 \operatorname{Re} \phi' \quad (8)$$

$$\sigma_{yy} - \sigma_{xx} + 2i \sigma_{xy} = 2(\bar{z} \phi'' + \psi')$$

Substituting the stress functions (2), these stress equations become

$$(\sigma_{xx} + \sigma_{yy})_j = 4 r^{\lambda-1} \operatorname{Re}(A_j \lambda e^{i(\lambda-1)\theta}) \quad (9)$$

$$(\sigma_{yy} - \sigma_{xx} + 2i \sigma_{xy})_j = 2 r^{\lambda-1} (A_j \lambda(\lambda - 1) e^{i(\lambda-3)\theta} + B_j \lambda e^{i(\lambda-1)\theta})$$

where the subscript  $j$  indicates either material 1 or 2. To within an undetermined scaling factor, eqns. (9) represent the complete asymptotic stress solution.

Results for the case  $\mu_1/\mu_2 = 1/10$ ,  $\nu_1 = \nu_2 = 0.3$  will be discussed below in conjunction with finite element predictions.

ANALYSIS OF COMPOSITE TENSION STRIP. A simple, practical problem for which the above asymptotic analysis has relevance is the bimaterial tension strip shown in Fig. (2). Near the ends of the strip the stress field will be essentially uniaxial tension corresponding to the uniform applied stress  $T$ . In the vicinity of the bondline, however, a complicated stress pattern can result from the material property mismatch. The asymptotic analysis suggests the form of stress distribution near the free boundary, but, of course, it provides no information about the

distribution away from the singularity nor about the relationship between the loading parameter  $T$  and the magnitude of stress within the singular zone. We used the finite element method to determine the plane strain stress field in the rectangular strip with  $\mu_1/\mu_2 = 1/10$  and  $\nu_1 = \nu_2 = 0.3$ . The asymptotic characteristic equation (1) suggests an  $r^{-0.1986}$  stress variation near the bondline-boundary intersection for this case.

The mesh that was used is displayed in Fig. (3). Refinements were made near the bondline and as the intersection point is approached element size decreases in a polar grid. In total, 19 elements are placed along the bondline. Both quadrilateral and triangular quadratic isoparametric elements were used in the mesh. Triangular elements encircle the intersection point. Two analyses were undertaken. One had isoparametric triangles at the intersection. The other had special singularity elements there with the expected  $r^{0.8014}$  displacement mode.

The analysis with conventional elements at the intersection served as an independent check on the asymptotic prediction. Nodal displacement data in the semicircular region  $r \leq 0.06 h$  centered at the intersection were analyzed for conformity with a power singularity. Each of the 29 rays of data were treated separately, and data were converted to polar components  $u_r, u_\theta$ . The  $u_\theta$  component was found to be strongly influenced by rotational distortion so that curve fitting was restricted to  $u_r$  data. A nonlinear least squares algorithm was used to fit the form

$$u_r = a + b r^\lambda$$

The exponent fell in the range  $.780 < \lambda < .814$  in this analysis. This is considered to be a verification of the existence of the intersection singularity for our problem. The results for the stress distribution will be presented below during the discussion of the solution using singularity elements.

The above analysis indicated that the singularity dominates the solution over a significant distance from the intersection and, furthermore, that the material mismatch-free boundary produce significant distortion near the intersection. Accordingly, we implemented the six node singularity element suggested by Stern [1979]. This element has the  $r^\lambda$  mode and also a linear displacement mode. It is an improvement over the power singularity element suggested by Tracey and Cook [1977] which does not have the linear mode necessary to model constant strain and rotation effects. In terms of triangular polar coordinates  $\xi, \eta$  with  $\xi$  a measure of distance from the singularity and  $\eta$  the angular

orientation the displacement assumption is

$$u = (a + b \xi + c \xi \eta) + (d + e \eta + f \eta^2) \xi^\lambda$$

The differences in the two finite element solutions were confined to the two rings of elements nearest the bond-boundary intersection. Nodal stress results at the mid-sides of the triangles ( $r = 0.0027 h$ ) are plotted in Figs. (4) and (5) for both solutions. These results are compared with the asymptotic solution (9) which is scaled to match the singularity element solution for  $\sigma_{xx}$  at  $\theta = \pi$ . As can be seen, the asymptotic and singularity element solutions are in excellent agreement. The conventional element solution shows deviations of up to 10% in  $\sigma_{xx}$  and higher for the other components.

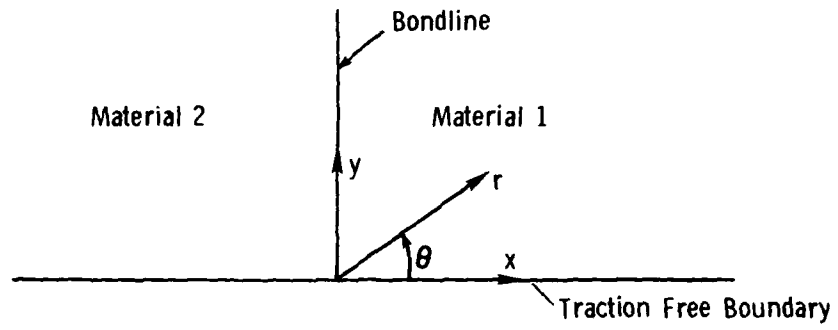
The stress distribution along the bondline is quite complicated and far from predictable, as can be seen in Fig. (6). The  $\sigma_{xx}$  component is reasonably uniform with value approximately equal to  $T$  in the strip interior, but at approximately  $0.2 h$  from the boundary it begins to rise to attain the singular gradient. The shear stress is zero at the center, rises to a value  $0.25 T$  around  $0.2 h$  and thereupon begins its singular increase as the boundary is approached. The normal stress  $\sigma_{yy}$  is discontinuous across the bondline. In material 1, which has the low shear modulus,  $\sigma_{yy}$  equals approximately  $0.4 T$  while in material 2 it equals approximately  $-0.5 T$  in the interior of the strip. As the boundary is approached, the singular forms are attained and the sign difference is maintained.

CONCLUSIONS. Debonding is a serious problem in structural applications of composites. The solutions in this work suggest that methods of design analysis might be significantly improved by accounting for free surface singularities. Linear elastic fracture mechanics suggests an approach. If debonding were correlated on the basis of the singularity amplitude in laboratory tests, then safe working loads in applications could possibly be established on this basis. Of course, much remains to be done. Important questions remain concerning the free edge effects in 3D composites and anisotropic materials.

ACKNOWLEDGMENT. The authors wish to acknowledge valuable discussions with Dr. Thomas S. Cook concerning the nature of the free surface problem and the status of the literature in this area.

REFERENCES

- Bogy, D. B. (1968), "Edge-Bonded Dissimilar Orthogonal Elastic Wedges Under Normal and Shear Loading," J. Appl. Mech., 35, pp. 460-466.
- Dundurs, J. (1969), discussion of Bogy (1968), J. Appl. Mech., 36, pp. 650-652.
- Muskhelishvili, N. I. (1953), Some Basic Problems of the Mathematical Theory of Elasticity, Noordhoff, Groningen, (J. R. M. Radok, trans.).
- Stern, M. (1979), "Families of Consistent Conforming Elements With Singular Derivative Fields," Int'l. J. Num. Mtds. Engng. 14, pp. 409-421.
- Tracey, D. M. and Cook, T. S. (1977), "Analysis of Power Type Singularities Using Finite Elements," Int'l. J. Num. Mtds. Engng. 11, pp. 1225-1233.



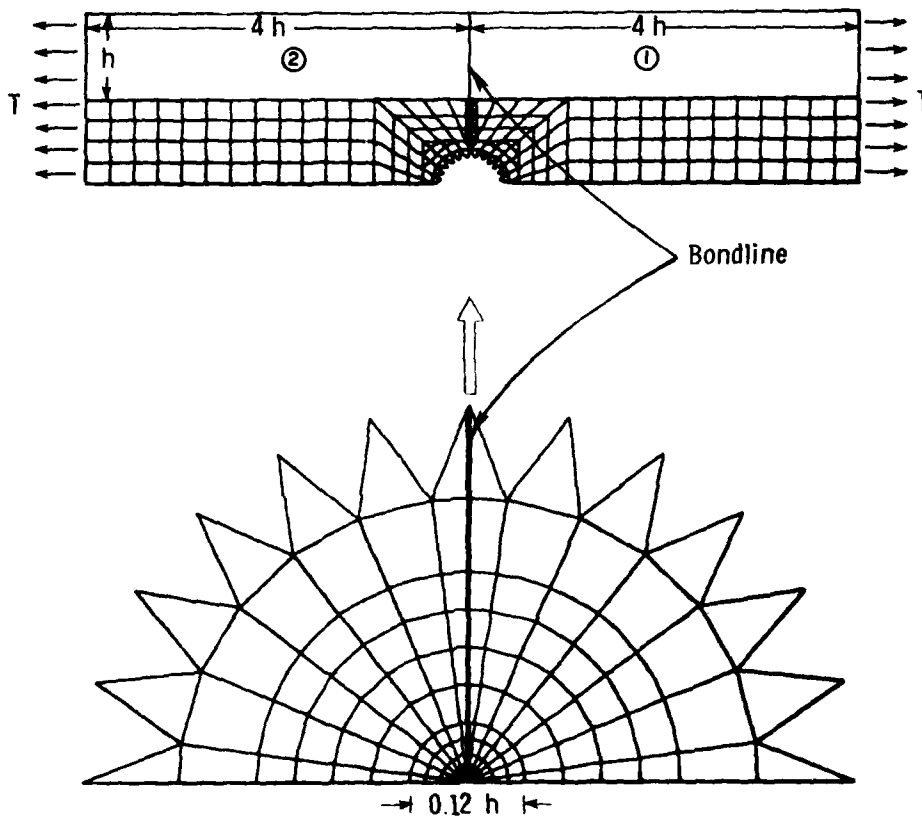
THE BONDLINE-BOUNDARY INTERSECTION PROBLEM

Figure 1



BIMATERIAL TENSION STRIP

Figure 2



FINITE ELEMENT MESH FOR BIMATERIAL TENSION STRIP PROBLEM

Figure 3

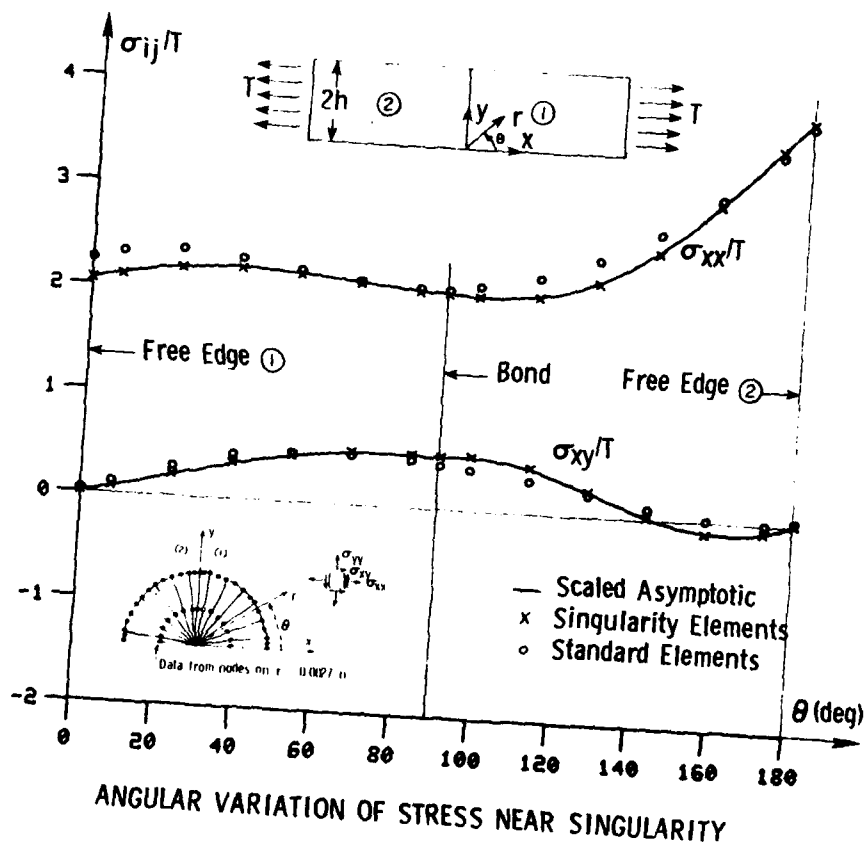


Figure 4

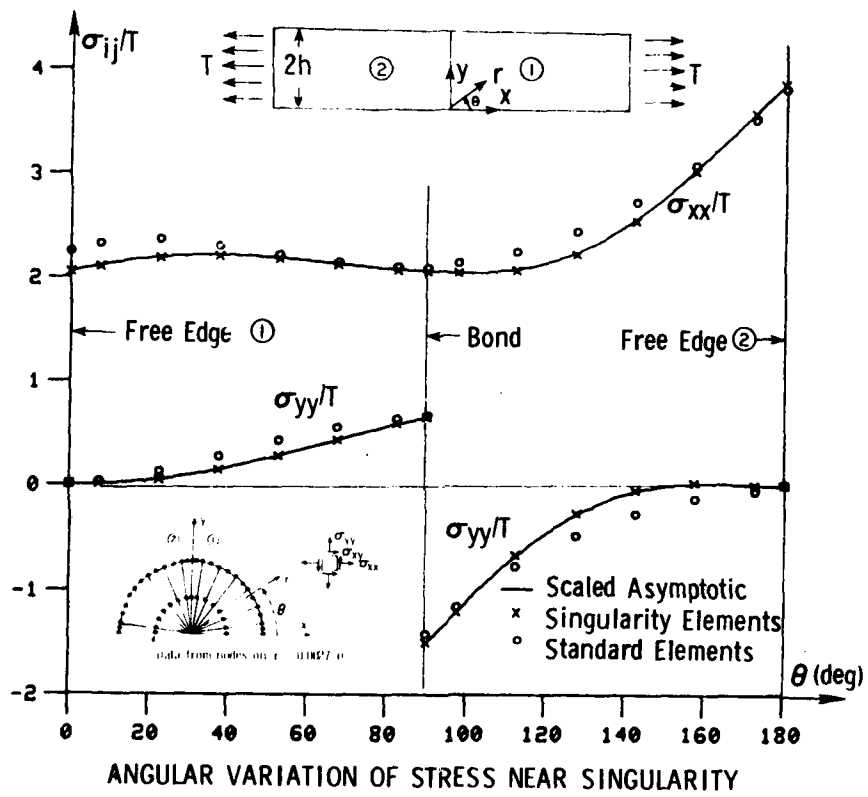
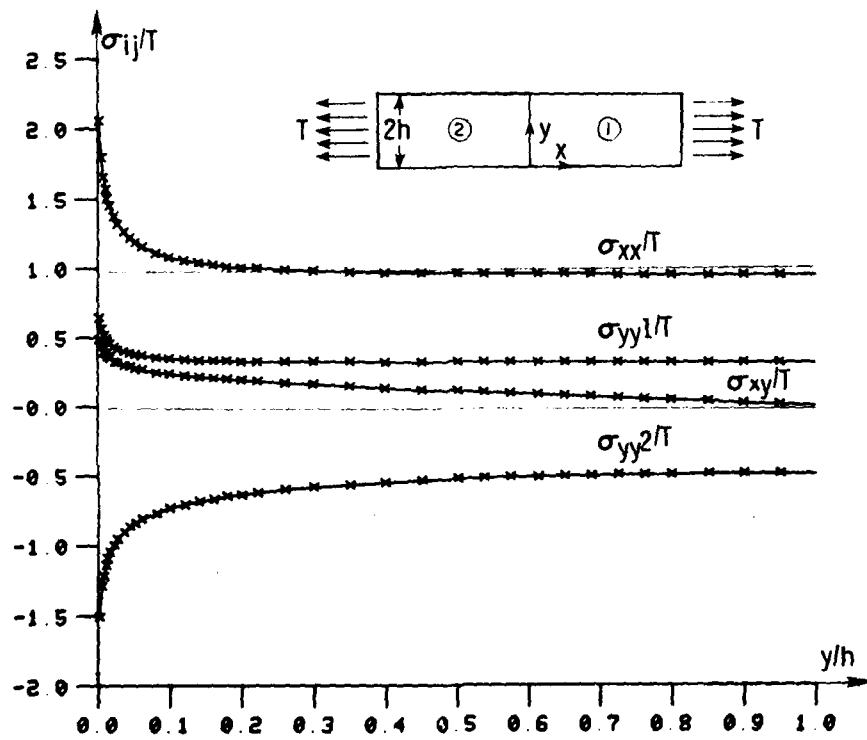


Figure 5



STRESS VARIATION ALONG BONDLINE

Figure 6



dup e

THERMO-ELASTIC-PLASTIC ANALYSIS OF A THICK-WALLED  
CYLINDER WITH TEMPERATURE-DEPENDENT YIELD STRESS

P. C. T. Chen  
US Army Armament Research and Development Command  
Large Caliber Weapon Systems Laboratory  
Benet Weapons Laboratory  
Watervliet, NY 12189

**ABSTRACT.** A numerical approach based on the finite difference method and incremental solution procedure has been developed for analyzing the thermo-elastic-plastic problem of a thick-walled cylinder with temperature-dependent yield stress. The cylinder is subjected to a combination of internal pressure and temperature variation. The material is assumed to obey the von Mises' yield criterion, the associated flow theory, and the isotropic hardening rule. Some numerical results for the displacements and stresses are presented.

**I. INTRODUCTION.** The isothermal elastic-plastic problems of thick-walled cylinders subjected to mechanical and/or thermal loadings have been solved by many investigators based on different theories or methods [1-4]. The yield stress in all isothermal theories is assumed to be temperature-independent. Although good progress has been made recently in developing constitutive relations for thermo-elastic-plastic and time-dependent inelastic theories [5,6], the research effort in this area has not reached a state of completion. In addition, the general solution of thermo-elastic-plastic problems is still very difficult and frequently very costly [6-8]. As a result, our research has been directed towards the development of a special purpose computer program for solving thick-walled cylinder problems of potential importance to the Army.

This paper shows a numerical approach for analyzing the thermo-elastic-plastic problems of thick-walled cylinders with temperature-dependent yield stress. The cylinder is subjected to a combination of internal pressure and temperature variation. The material is assumed to obey the von Mises' yield criterion, the associated flow theory, and the isotropic hardening rule. Some numerical results for the displacements and stresses are presented.

**II. THERMO-ELASTIC-PLASTIC THEORY.** For small displacement analysis, the total strain-rate tensor  $\dot{\epsilon}_{ij}$  is composed of corresponding elastic, plastic, and thermal components as follows

$$\dot{\epsilon}_{ij} = \dot{\epsilon}_{ij}^e + \dot{\epsilon}_{ij}^p + \dot{\epsilon}_{ij}^T \quad (1)$$

The sum of elastic and thermal strain-rates is assumed to be determined by the Duhamel-Neumann law,

$$\dot{\epsilon}_{ij}^e + \dot{\epsilon}_{ij}^T = E^{-1} [(1+\nu) \dot{\sigma}_{ij} - \nu \delta_{ij} \dot{\sigma}_{kk}] + \alpha \dot{T} \delta_{ij} \quad (2)$$

in which  $E$  is Young's modulus,  $\nu$  is Poisson's ratio,  $\alpha$  is the thermal expansion coefficient,  $\dot{T}$  is the rate of temperature change,  $\delta_{ij}$  is the Kroneker delta, and  $\sigma_{ij}$  is the stress tensor.

The plastic strain-rate  $\dot{\epsilon}_{ij}^P$  is derivable from the plastic potential  $g(\sigma_{ij})$  by the normality condition

$$\dot{\epsilon}_{ij}^P = \dot{\lambda} \frac{\partial g}{\partial \sigma_{ij}} \quad (3)$$

where  $\dot{\lambda}$  is a positive scalar variable.

The yield function for non-isothermal isotropic strain-hardening material can be written as

$$F = f(\sigma_{ij}) - \sigma(\epsilon^P, T) \quad (4)$$

where

$$\epsilon^P = \int \dot{\epsilon}^P dt \quad (5)$$

$$\dot{\epsilon}^P = \left( \frac{3}{2} \dot{\epsilon}_{ij}^P \dot{\epsilon}_{ij}^P \right)^{1/2} \quad (6)$$

and  $\sigma(\epsilon^P, T)$  represents the dependence of yield stress on the accumulated increments of effective plastic-strain and temperature. When the von Mises' yield condition and associated flow rule are adopted,

$$f = g = \left( \frac{3}{2} s_{ij} s_{ij} \right)^{1/2} \quad (7)$$

and

$$s_{ij} = \sigma_{ij} - \frac{1}{3} \sigma_{kk} \delta_{ij} \quad (8)$$

On the basis of the above assumptions, we can readily find that

$$\dot{\epsilon}_{ij}^P = \frac{3}{2} (\dot{\epsilon}^P / \sigma) s_{ij} \quad (9)$$

and

$$\dot{\lambda} = \dot{\epsilon}^P = \left[ \frac{3}{2} \frac{s_{ij}}{\sigma} \sigma_{ij} - \frac{\partial \sigma}{\partial T} \dot{T} \right] / H' \quad (10)$$

where

$$H' = \frac{\partial \sigma}{\partial \epsilon^P} = \frac{\omega E}{1-\omega}, \quad \omega E' = \partial \sigma / \partial \epsilon \quad (11)$$

$$\partial \sigma / \partial T = \partial \sigma_0 / \partial T + \epsilon^P (\partial H' / \partial T) \quad (12)$$

and  $\sigma_0$  is the initial yield stress.

Substituting Eqs. (2) and (9) into Eq. (1), one obtains the general constitutive equations relating  $\dot{\epsilon}_{ij}$  to  $\dot{\sigma}_{ij}$  and  $\dot{T}$ . For numerical solutions by the finite-element method or the finite-difference method, it is desirable to find the inverse form which relates  $\dot{\sigma}_{ij}$  to  $\dot{\epsilon}_{ij}$  and  $\dot{T}$ . For the isotropic-hardening, thermo-elastic-plastic theory, the explicit inverse relationships can be derived and a form slightly different from [7] is given below:

$$\dot{\sigma}_{ij} = \frac{E}{1+\nu} [\delta_{ik}\delta_{jl} + \frac{\nu}{1-2\nu} \delta_{ij}\delta_{kl} - \frac{1}{s} s_{ij}s_{kl}] \dot{\epsilon}_{kl} - [\frac{E}{1-2\nu} \alpha \delta_{ij} - \frac{(\partial\sigma/\partial T) s_{ij}}{1+H'/3G} \frac{1}{\sigma}] \dot{T} \quad (13)$$

where

$$s = \frac{2}{3} \sigma^2 (1 + \frac{1}{3} \frac{H'}{G}) \quad (14)$$

III. EQUATIONS FOR THICK-WALLED CYLINDER. For the isotropic-hardening, thermo-elastic-plastic thick-walled cylinders, the incremental form of Eq. (13) reduces to

$$\Delta\sigma_i = d_{ij} \Delta\epsilon_j - \Delta\sigma_i^{\circ} \quad , \quad i = r, \theta, z \quad (15)$$

where

$$d_{ij} = \frac{E}{1+\nu} (\frac{\nu}{1-2\nu} + \delta_{ij} - \frac{1}{s} \sigma_i' \sigma_j') \quad (16)$$

$$\Delta\sigma_i^{\circ} = [\frac{E\alpha}{1-2\nu} - \frac{(\partial\sigma/\partial T) \sigma_i'}{1+H'/3G} \frac{1}{\sigma}] \Delta T$$

$$\sigma_i' = \sigma_i - \sigma_m \quad , \quad \sigma_m = (\sigma_r + \sigma_{\theta} + \sigma_z)/3$$

In the quasi-static with no body forces, the radial and tangential stresses must satisfy the equilibrium equation,

$$r(\partial\sigma_r/\partial r) = \sigma_{\theta} - \sigma_r \quad (17)$$

and the corresponding strains must satisfy the compatibility equation

$$r(\partial\epsilon_{\theta}/\partial r) = \epsilon_r - \epsilon_{\theta} \quad (18)$$

Consider a thick-walled cylinder of inner radius  $a$  and external radius  $b$ . The cylinder is subjected to inner pressure and temperature ( $p$  and  $T_a$ ), external pressure and temperature ( $q$  and  $T_b$ ) and end force ( $f$ ). The boundary conditions for the generalized plane-strain conditions are

$$\sigma_r(a,t) = -p \quad , \quad T(a,t) = T_a \quad (19)$$

$$\sigma_r(b,t) = -q \quad , \quad T(b,t) = T_b \quad (20)$$

$$2\pi \int_a^b r \sigma_z dr = \mu \pi a^2 p + f \quad (21)$$

where  $\mu$  is 0 or 1 for open-end or closed end conditions, respectively. The temperature distribution must satisfy the heat conduction equation subjected to boundary conditions (19) and (20),

$$\frac{1}{r} \frac{\partial}{\partial r} \left( r \frac{\partial T}{\partial r} \right) = \frac{1}{k} \frac{\partial T}{\partial t} \quad (22)$$

where  $k$  denotes thermal diffusivity. For the special case of steady state distribution, the temperature is given by

$$T = T_a + (T_b - T_a) \log(r/a) / \log(b/a) \quad (23)$$

**IV. INCREMENTAL FINITE-DIFFERENCE FORMULATIONS.** For loading beyond the elastic limit, an incremental approach of the finite-difference formulation is used. The cross section of the tube is divided into  $n$  rings with  $r_1=a, r_2, \dots, r_k=\rho, \dots, r_{n+1}=b$ , where  $\rho$  is the radius of the elastic-plastic interface. At the beginning of each increment of loading, the distribution of temperature, displacements, strains, and stresses is assumed to be known and we want to determine  $\Delta u, \Delta \epsilon_r, \Delta \epsilon_\theta, \Delta \epsilon_z, \Delta \sigma_r, \Delta \sigma_\theta, \Delta \sigma_z$  at all grid points for the applied incremental loading,  $\Delta p, \Delta q, \Delta f, \Delta T_1$  ( $i = 1$  to  $n+1$ ). Since the incremental stresses are related to the incremental strains by the incremental form (Eq. (15)) and  $\Delta u = r \Delta \epsilon_\theta$ , there exists only three unknowns at each station that have to be determined for each increment of loading. Accounting for the fact that the axial strain  $\epsilon_z$  is independent of  $r$ , the unknown variables in the present formulation are  $(\Delta \epsilon_\theta)_i, (\Delta \epsilon_r)_i$ , for  $i = 1, 2, \dots, n, n+1$ , and  $\Delta \epsilon_z$ .

The equation of equilibrium (17) and the equation of compatibility (18) are valid for both the elastic and the plastic regions of a thick-walled tube. The finite-difference forms of these two equations at  $i = 1, \dots, n$  are given by

$$c_1(\Delta \sigma_r)_i + c_2(\Delta \sigma_\theta)_i + c_3(\Delta \sigma_r)_{i+1} = c_5 \quad (24)$$

and

$$c_1(\Delta \epsilon_\theta)_i + c_2(\Delta \epsilon_r)_i + c_3(\Delta \epsilon_\theta)_{i+1} = c_4 \quad (25)$$

where

$$\begin{aligned} c_1 &= r_{i+1} - 2r_i, \quad c_2 = -r_{i+1} + r_i, \quad c_3 = r_i \\ c_4 &= (r_{i+1} - r_i)(\epsilon_r - \epsilon_\theta)_i - r_i[(\epsilon_\theta)_{i+1} - (\epsilon_\theta)_i] \\ c_5 &= (r_{i+1} - r_i)(\sigma_\theta - \sigma_r)_i - r_i[(\sigma_r)_{i+1} - (\sigma_r)_i] \end{aligned} \quad (26)$$

Substitution of the incremental stress-strain relations (15) into Eq. (24) leads to

$$c_6(\Delta \epsilon_\theta)_i + c_7(\Delta \epsilon_r)_i + c_8(\Delta \epsilon_\theta)_{i+1} + c_9(\Delta \epsilon_r)_{i+1} + c_{10} \Delta \epsilon_z = c_{11} \quad (27)$$

where

$$\begin{aligned}
 c_6 &= c_1(d_{12})_1 + c_2(d_{22})_1, & c_8 &= c_3(d_{12})_{i+1} \\
 c_7 &= c_1(d_{11})_1 + c_2(d_{21})_1, & c_9 &= c_3(d_{11})_{i+1} \\
 c_{10} &= c_1(d_{13})_1 + c_2(d_{23})_1 + c_3(d_{13})_{i+1} \\
 c_{11} &= c_1(\Delta\sigma_r)_1 + c_2(\Delta\sigma_\theta)_1 + c_3(\Delta\sigma_r)_{i+1} \\
 &+ c_2(\sigma_r - \sigma_\theta)_1 + c_3[(\sigma_r)_1 - (\sigma_r)_{i+1}]
 \end{aligned} \tag{28}$$

The finite-difference forms of the boundary conditions (19), (20), and (21) are

$$(d_{12})_1(\Delta\epsilon_\theta)_1 + (d_{11})_1(\Delta\epsilon_r)_1 + (d_{13})_1 \Delta\epsilon_z = -\Delta p + (\Delta\sigma_r)_1 \tag{29}$$

$$(d_{12})_{n+1}(\Delta\epsilon_\theta)_{n+1} + (d_{11})_{n+1}(\Delta\epsilon_r)_{n+1} + (d_{13})_{n+1} \Delta\epsilon_z = -\Delta q + (\Delta\sigma_r)_{n+1} \tag{30}$$

and

$$\begin{aligned}
 \sum_{i=1}^n [c_{12}^i(\Delta\epsilon_\theta)_i + c_{13}^i(\Delta\epsilon_r)_i + c_{14}^i(\Delta\epsilon_\theta)_{i+1} + c_{15}^i(\Delta\epsilon_r)_{i+1}] \\
 + \left( \sum_{i=1}^n c_{16}^i \right) \Delta\epsilon_z = \mu a^2 \Delta p + \Delta f / \pi + \sum_{i=1}^n c_{17}^i
 \end{aligned} \tag{31}$$

where

$$\begin{aligned}
 \Delta r_i &= r_{i+1} - r_i, & c_{12}^i &= (\Delta r_i) r_i (d_{23})_i \\
 c_{13}^i &= (\Delta r_i) r_i (d_{13})_i, & c_{14}^i &= (\Delta r_{i+1}) r_{i+1} (d_{23})_{i+1} \\
 c_{15}^i &= (\Delta r_i) r_{i+1} (d_{13})_i \\
 c_{16}^i &= (\Delta r_i) [r_i (d_{33})_i + r_{i+1} (d_{33})_{i+1}] \\
 c_{17}^i &= (\Delta r_i) [r_i (\Delta\sigma_z)_i + r_{i+1} (\Delta\sigma_z)_{i+1}]
 \end{aligned} \tag{32}$$

Now we can form a system of  $2n+3$  equations for solving  $2n+3$  unknowns,  $(\Delta\epsilon_\theta)_1$ ,  $(\Delta\epsilon_r)_1$ , at  $i = 1, 2, \dots, n, n+1$  and  $\Delta\epsilon_z$ . Equations (29), (30), and (31) are taken as first and last two equations, respectively, and the other  $2n$  equations are set up at  $i = 1, 2, \dots, n$  using equations (25) and (27). The final system is an unsymmetric matrix of arrow type with the nonzero terms appearing in the last row and column and others clustered about the main diagonal, two below and one above.

**V. NUMERICAL RESULTS AND DISCUSSIONS.** The numerical results for two particular problems are reported in this paper. The first problem is a closed-end thick-walled cylinder subjected to varying internal pressure  $p$  and temperature  $T$  as shown in Figure 1. The heating is uniform throughout the thickness but the initial yield stress is temperature-dependent as shown in Figure 1. The other material constants are  $E = 86,666$  psi,  $\nu = 0.3$ ,  $\omega = 0.0$ ,

$\alpha = 0.0$ . The numerical results for the radial displacements ( $u_a$  and  $u_b$ ) at the inside and outside surface are shown in Figure 2. The percentage of plastic zone is also shown in the figure by the dotted line. The entire cylinder is elastic during the time interval 10 to 12. The results for the three stress components at selected time  $t = 4, 8, 10$ , and 13 are shown in Figures 3 through 5. The differences for the displacements and stresses at  $t = 4$  and 8 clearly demonstrate the effect of temperature-dependence of the yield stress. The same problem with plane-strain condition has been solved by ADINA program [8]. For the purpose of comparison, the ADINA results for the radial displacement at the outside and the residual stress distribution through the wall at time  $\tau = 10$  are also shown in Figures 2 and 4. The agreement is excellent for the stresses and good for the displacement. The small differences in the displacement response may be due to the end conditions and the methods of approaches. The numerical results reported here are based on the finite difference formulations with  $n = 100$ .

As a second example let us consider a closed-end tube subjected to inner temperature  $T_a$  only. The numerical results were based on the following parameters:  $b = 2"$ ,  $a = 1"$ ,  $n = 100$ ,  $\nu = 0.3$ ,  $E = 30 \times 10^6$  psi,  $\omega = 0.0$ ,  $\alpha = 7.75 \times 10^{-6}$  in./in./°F,  $\sigma_0 = 30 \times 10^3$  psi,  $\sigma/\sigma_0 = 1.0 - T/2 \times 10^{-3}/°F$ . When the temperature gradient is of sufficient magnitude, yielding will first expand from the inside. At larger temperature gradient, the plastic zone will expand from both the inside and outside surface toward the interior. The relation between the inside temperature and elastic-plastic interface is shown in Figure 6. The stresses in a closed-end cylinder subjected to temperature gradient of 400°F are shown in Figure 7. The special case when the yield stress is assumed to be temperature-independent has been considered in an earlier paper [4]. For the purpose of comparison, the earlier results are also shown in Figures 6 and 7 by the dotted lines. A comparison of the results between the solid and dotted lines shows the effects of temperature-dependence of the yield stress.

This paper presents the numerical results for a closed-end cylinder subjected to varying internal pressure and/or temperature. The thermal problem is due to uniform heating or thermal gradient. If the temperature distribution is solved by a transit analysis, the corresponding thermal stresses can be calculated. The result of this transit thermal problem is to be reported.

#### REFERENCES

1. D. R. Bland, "Elastoplastic Thick-Walled Tubes of Work-Hardening Material Subject to Internal and External Pressures and to Temperature Gradients," *Journal of the Mechanics and Physics of Solids*, 1956, Vol. 4, pp. 209-229.
2. S. C. Chu, "A Numerical Thermo-Elastic-Plastic Solution of a Thick-Walled Tube," *AIAA Journal*, Vol. 12, No. 3, February 1974, pp. 176-179.
3. J. D. Vasilakis and P. C. T. Chen, "Thermo-Elastic-Plastic Stresses in Hollow Cylinders Due to Quenching," *Transactions of the Twenty-Fifth Conference of Army Mathematicians*, pp. 661-674, January 1980.

4. P. C. T. Chen, "Elastic-Plastic Thick-Walled Tubes Subjected to Internal Pressure and Temperature Gradient," Transactions of the Twenty-Seventh Conference of Army Mathematicians, pp. 113-126, January 1982.
5. A. S. Argon (Editor), "Constitutive Equations in Plasticity," The MIT Press, Cambridge, MA, 1975.
6. D. H. Allen and W. E. Haisler, "A Theory for Analysis of Thermoplastic Materials," Computers & Structures, Vol. 13, 1981, pp. 129-135.
7. S. Utku, M. S. M. Rao, and G. J. Dvorak, "ELAS 65 Computer Program for Equilibrium Problems of Elastic-Thermoplastic Solids and Structures," Duke University Structural Mechanics Series No. 15a, November 1973.
8. K. J. Bathe, "ADINA - A Finite Element Program for Automatic Dynamic Incremental Analysis," Report 82448-1, Acoustics and Vibration Lab., MIT, September 1975, (revised May 1976).

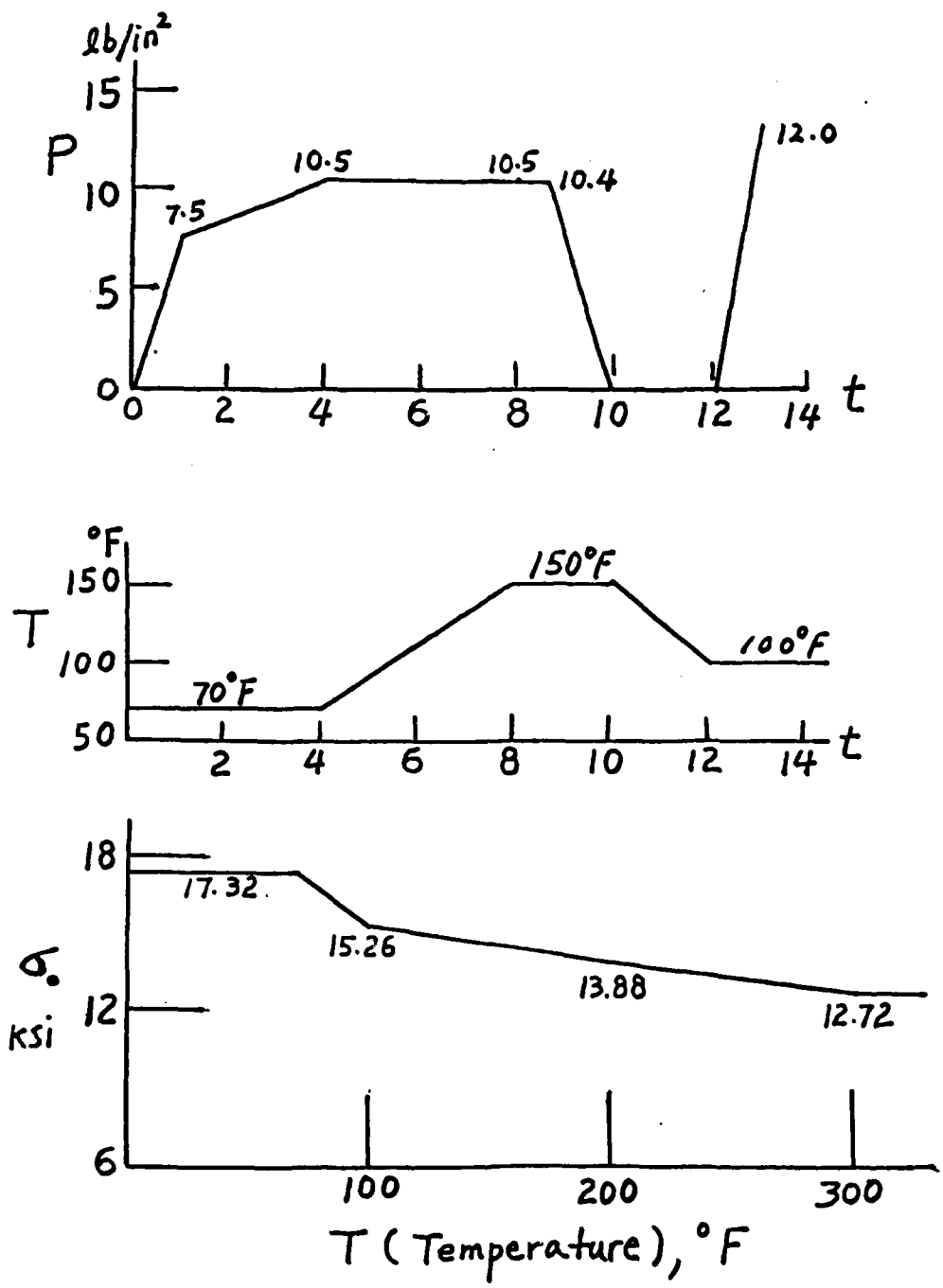


Figure 1. Pressure Temperature History, Temperature-Dependent Yield Stress.

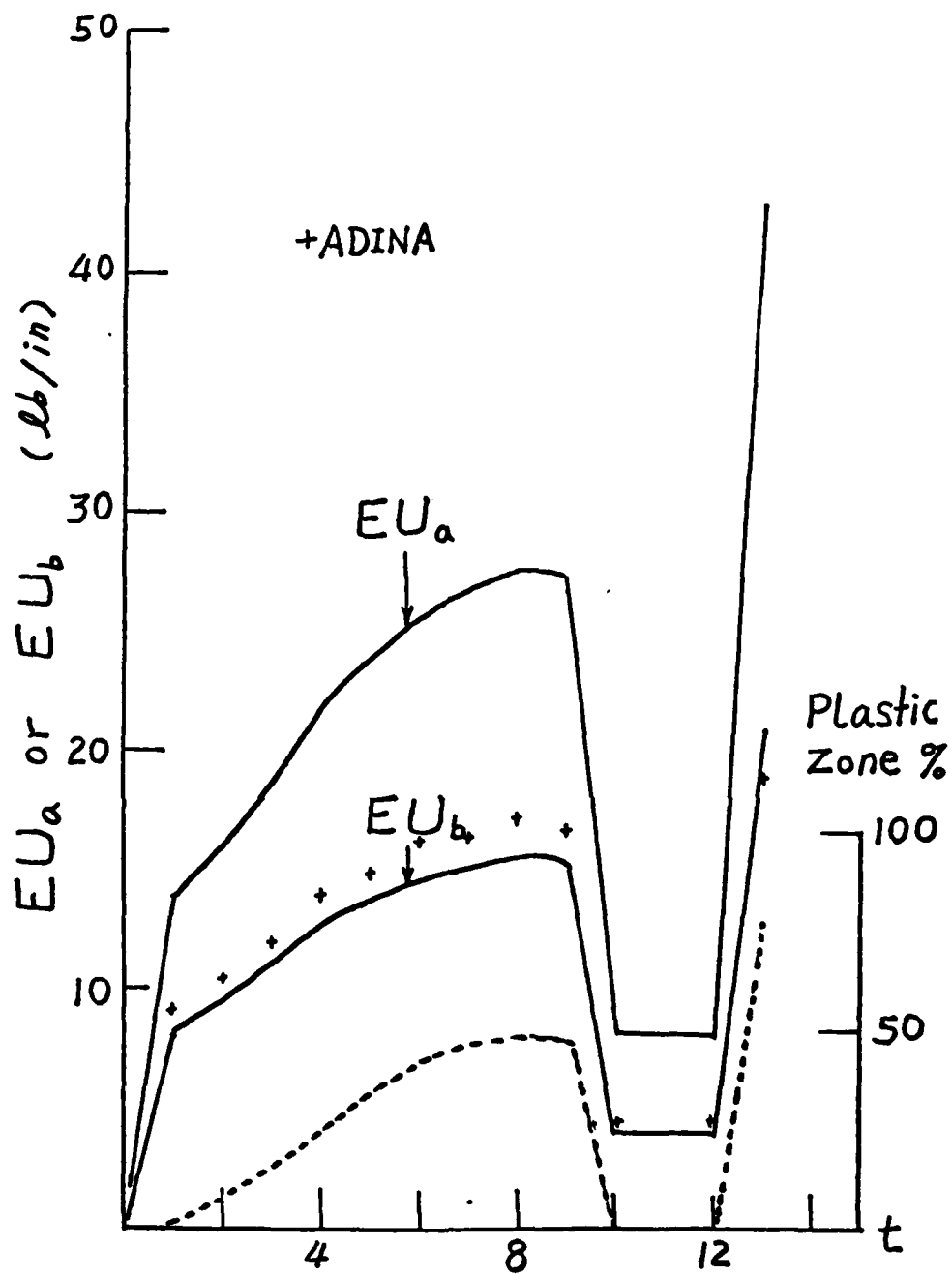


Figure 2. Radial Displacements and Plastic Zone.

$$P/a = 1.23 \rightarrow 1.47$$

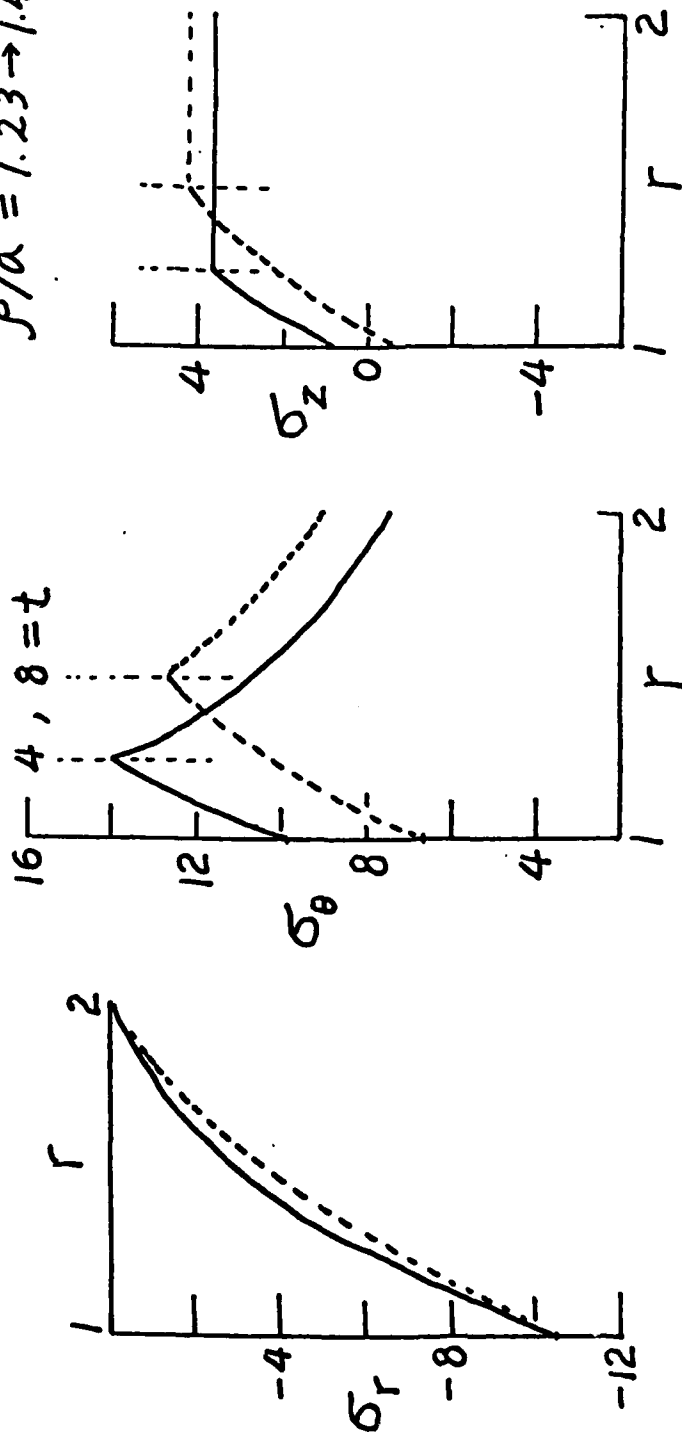


Figure 3. Distribution of Stresses at Time  $t = 4, 8$ .

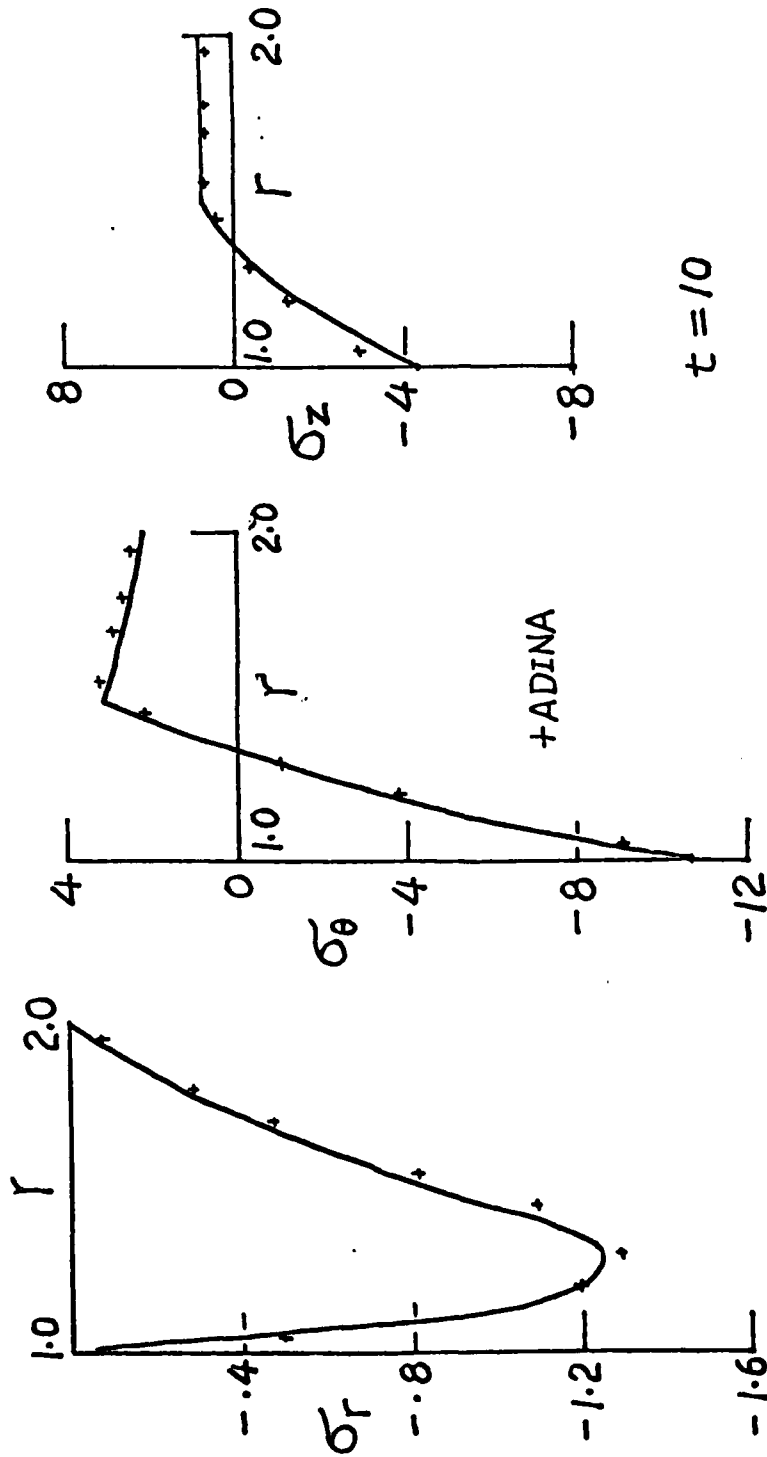


Figure 4. Distribution of (Residual) Stresses at Time  $t = 10$ .

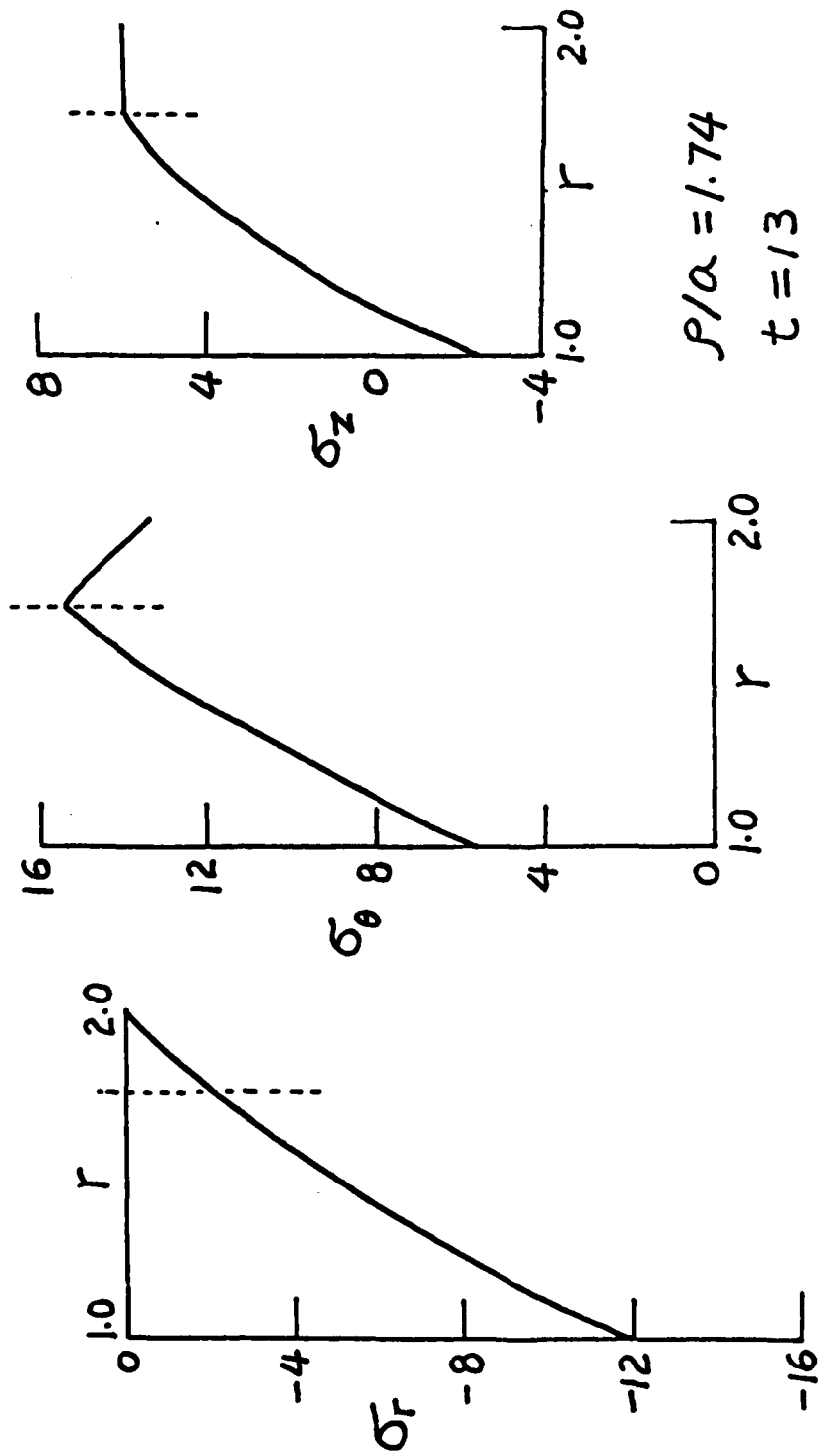


Figure 5. Distribution of Stresses at Time  $t = 13$ .

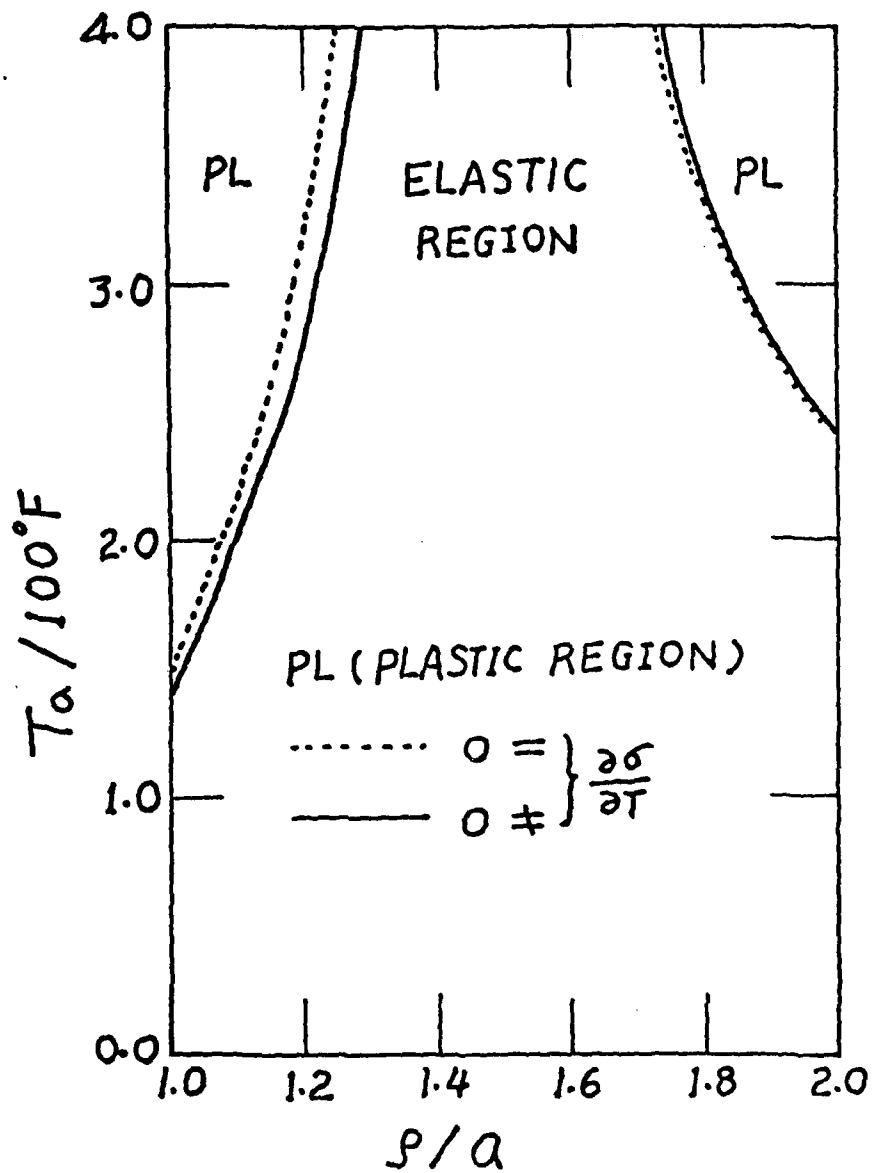


Figure 6. Elastic-Plastic Interface vs. Temperature Gradient.

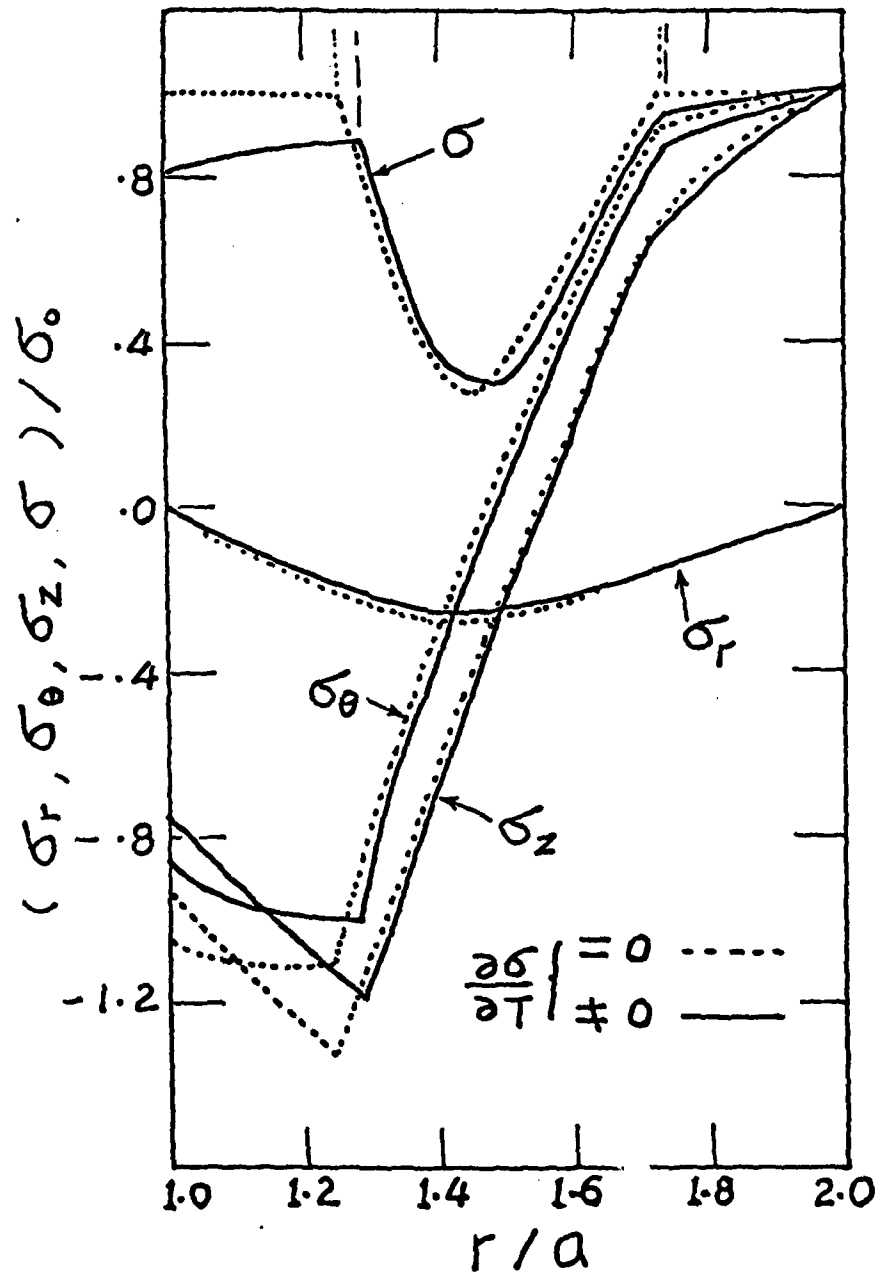


Figure 7. Distribution of Stresses ( $T_a = 400^\circ\text{F}$ ,  $T_b = 0$ ).

AD P001026

A FUNCTIONAL STRESS INTENSITY APPROACH TO MULTIPLY CRACKED,  
PARTIALLY AUTOFRETTAGED CYLINDERS

S. L. Pu

U.S. Army Armament Research & Development Command  
Large Caliber Weapon Systems Laboratory  
Benet Weapons Laboratory  
Watervliet, NY 12189

**ABSTRACT.** The functional stress intensity approach for a partially autofrettaged, thick-walled cylinder is presented. This approach is a combination of a series of methods developed for the computation of stress intensity factors for multiple radial cracks emanating from the inner or the outer surface of a hollow cylinder. The numerical method is mainly based on the finite element method using 12-node quadrilateral, isoparametric elements with singular elements around a crack tip. The difficulty due to the presence of initial stresses in the finite element method is obviated by the method of thermal simulation which replaces the residual stresses existed in an autofrettaged cylinder by an active thermal load. The weight function method is incorporated to reduce the repeated computations of stress intensity factors of the same geometrical configuration subjected to various external loads and residual stresses. The functional stress intensity factor is introduced to overcome the difficulty in seeking the weight function itself.

Numerical results of functional stress intensity factors are given for multiple cracks radiating from the bore or from the outer surface of a cylinder having an external diameter twice that of an internal diameter. A linear superposition of these results gives the resultant stress intensity factor of a cracked geometry subjected to combined external loads and initial stresses. It is highly possible to extend the method for elastic perfectly-plastic materials assumed in this paper to strain hardening materials.

**I. INTRODUCTION.** An analytic method is not available for the computation of stress intensity factors for multiple-radial cracks in a thick-walled cylinder. The computation must depend on various numerical methods [1-5]. Due to increasingly successful applications of finite element technique in structural analysis, the author decided to use higher order finite elements with the aid of special crack-tip elements to study the multiply cracked cylinders. Similar to the quarter-point element in an 8-node quadrilateral element [6,7], a special crack-tip element was developed [8] for a 12-node quadrilateral isoparametric element. Both the 8-node and 12-node quadrilaterals have been implemented in the popular finite element computer code NASTRAN [8,9]. The dummy user element facility of NASTRAN is used for the implementation. Another finite element computer code APES [10], which was written specifically for the use of 12-node quadrilateral, isoparametric elements, has also been used for fracture analysis of cracked hollow cylinders. Quite accurate results of stress intensity factors have been obtained using either NASTRAN or APES for multiple-radial cracks emanating from the bore of a tube [11]. These results are in good agreement with results reported by Tracy [12] using the method of modified mapping collocation.

To increase the maximum internal pressure a cylinder can contain elastically and retard the growth of radial cracks near the bore, it is a common practice to introduce compressive residual stresses near the bore by an autofrettage process. The residual stress in the cylinder has increased difficulties in the estimation of stress intensity factors. One of the difficulties is the disagreement among results for the residual stress distribution obtained by different investigators based on different assumptions. The other is the lack of an initial stress analysis capability in NASTRAN and APES. A method is developed in [13] so that NASTRAN or APES can be used for the computation of stress intensity factors for cracked cylinders with residual stress distribution given in the closed form expressions [14]. The finite element results [15] are in close agreement with Parker's results [16] using modified mapping collocation.

While the autofrettage process produces favorable compressive residual stress near the bore, it also yields a tensile residual stress near the outer cylindrical surface. The sum of this stress and the tensile stress due to a bore pressure may be high enough to cause crack initiation and propagation from the outer surface of the cylinder. This requires the computation of stress intensity factors for externally cracked cylinders. Several investigators have reported their results on this subject [12,17-19].

In order to reduce repeated finite element computations, the weight function method [20] is used together with the finite element method. In this paper the functional stress intensity factor approach is summarized for both internally cracked and externally cracked, partially autofrettaged, pressurized thick-walled cylinders.

**II. RESIDUAL STRESSES AND THERMAL SIMULATION.** The residual stress distribution in an autofrettaged thick-walled cylinder has been studied by a large number of investigators. There is considerable disagreement in their results due to different assumptions which must be made in order to make the problem mathematically tractable. Detailed discussions of the results and the associated assumptions are given in [14,21]. Under the combination of assumptions that the material is incompressible, elastic-perfectly plastic and obeys the Mises' yield criterion and that the cylinder is under the condition of plane strain, the following closed form solution for residual stresses is obtained for an elastically unloaded cylinder after partial autofrettage:

$$\sigma_r(r) = \begin{cases} \frac{\sigma_0}{\sqrt{3}} \left\{ 2 \log \frac{r}{\rho} - 1 + \frac{\rho^2}{b^2} - P_1 \left( \frac{1}{b^2} - \frac{1}{r^2} \right) \right\} & l < r < \rho & (1) \\ \frac{\sigma_0}{\sqrt{3}} (\rho^2 - P_1) \left( \frac{1}{b^2} - \frac{1}{r^2} \right) & \rho < r < b & (2) \end{cases}$$

$$\sigma_{\theta}(r) = \begin{cases} \frac{\sigma_0}{\sqrt{3}} \left\{ 2 \log \frac{r}{\rho} + 1 + \frac{\rho^2}{b^2} - P_1 \left( \frac{1}{b^2} + \frac{1}{r^2} \right) \right\} & 1 < r < \rho & (3) \\ \frac{\sigma_0}{\sqrt{3}} (\rho^2 - P_1) \left( \frac{1}{b^2} + \frac{1}{r^2} \right) & \rho < r < b & (4) \end{cases}$$

where bore radius is taken as unit length,  $b$  is the outer radius of the hollow cylinder,  $\rho$  is the radius of the elastic-plastic interface during pressurization,  $\sigma_0$  is the uniaxial yield stress in tension and compression, and

$$P_1 = P_1(\rho) = \frac{b^2}{b^2 - 1} \left( 1 - \frac{\rho^2}{b^2} + 2 \log \rho \right) \quad (5)$$

This residual stress distribution will be used in this paper as a basis to develop a method to compute stress intensity factors for cracks in such a stress field. It has been shown in [13] that the thermal stresses in the cylinder subjected to a thermal load

$$T(r) = \begin{cases} T_0 - \frac{(T_0 - T_\rho)}{\log \rho} \log r & 1 < r < \rho & (6) \\ T_\rho & \rho < r < b \end{cases}$$

are equivalent to the residual stresses (1) - (4) if the temperature gradient and the yield stress satisfy

$$\frac{E\alpha(T_0 - T_\rho)}{2(1-\nu)\log \rho} = \frac{2\sigma_0}{\sqrt{3}} \quad (7)$$

where  $T_0$  and  $T_\rho$  are the temperatures at the bore, and  $r = \rho$  respectively,  $E$  is Young's modulus, and  $\alpha$  is the coefficient of linear thermal expansion. This thermal simulation provides an effective method to compute stress intensity factors due to initial stresses given by Eqs. (1) through (4) using NASTRAN or APES. The initial stress is replaced by a temperature input of Eq. (6) at all nodes. The stress intensity factors obtained from NASTRAN or APES corresponding to the thermal loads are equivalent to stress intensity factors due to autofrettage residual stresses [22].

**III. WEIGHT FUNCTION AND FUNCTIONAL STRESS INTENSITY.** A weight function is a universal function which depends only on geometry and not on loadings [20]. If the mode I stress intensity factor  $K^{(1)}$  and displacement field  $y^{(1)}$  associated with the symmetric load system 1 are known, the weight function for the cracked geometry is

$$\underline{h} = \frac{H}{2K(1)(c)} \frac{\partial \underline{y}^{(1)}(c)}{\partial c} \quad (8)$$

where  $H = E$  for plane stress and  $H = E/(1-\nu^2)$  for plane strain,  $c$  is the crack depth. Once  $\underline{h}$  is determined, the mode I stress intensity factor induced by any other symmetric load system  $\underline{t}$  and  $\underline{f}$  is given by

$$K = \int_{\Gamma} (\underline{t} \cdot \underline{h}) d\Gamma + \int_A (\underline{f} \cdot \underline{h}) dA$$

where  $\underline{t}$  is the stress vector acting on boundary  $\Gamma$  around the crack tip and  $\underline{f}$  is the body force in region A defined by  $\Gamma$ . This equation can be reduced to

$$K = \frac{H}{K(1)} \int_0^c p_c(x) \frac{\partial v^{(1)}}{\partial c} dx \quad (9)$$

for radially cracked rings with  $x$  being a distance measured along the crack from the base toward the tip. The relation between  $r$  and  $x$  is

$$r(x) = \begin{cases} 1 + x & , \text{ for interior cracks} \\ b - x & , \text{ for exterior cracks} \end{cases} \quad (10)$$

The crack pressure  $p_c(x)$  can be found from the hoop stress (at the site of radial cracks) in an uncracked ring subjected to the loading of interest. Even though the numerical values of  $K(1)$  and  $v(1)$ , the normal component of displacement, are known, the partial derivative  $\partial v^{(1)}/\partial c$  is usually unknown. A technique of computing  $\partial v/\partial c$  was devised in [3] by assuming the crack face displacement  $v$  be a conic section given by Orange [23]. Another method developed in [15] made no assumptions on  $v$  or  $\partial v/\partial c$  but utilized finite element method to compute several stress intensity factors each associated with a simple loading system. For a new load, the new  $K$  is expressed in terms of known values of  $K$ .

The hoop stress in an uncracked cylinder subjected to an internal pressure  $p_1$  is

$$\frac{\sigma_{\theta}(r)}{p_1} = \frac{1}{b^2-1} \left( 1 + \frac{b^2}{r^2} \right) \quad (11)$$

Substituting  $\sigma_{\theta}$  from Eq. (11) as  $p_c$  in Eq. (9) we have

$$\frac{K(p_1)}{p_1} = \frac{1}{b^2-1} K_c(1) + \frac{b^2}{b^2-1} K_c(r^{-2}) \quad (12)$$

where

$$K_C(1) = \frac{H}{K(1)} \int_0^c \frac{\partial v(1)}{\partial c} dx \quad (13)$$

$$K_C(r^{-2}) = \frac{H}{K(1)} \int_0^c [r(x)]^{-2} \frac{\partial v(1)}{\partial c} dx \quad (14)$$

are called functional stress intensity factors.

Similarly we get

$$\frac{K(p_0)}{p_0} = \frac{b^2}{b^2-1} K_C(1) + \frac{b^2}{b^2-1} K_C(r^{-2}) \quad (15)$$

$$\frac{K(\rho=b)}{\sigma_0} = \frac{1}{\sqrt{3}} \{ [2 - P_1(b)] K_C(1) - P_1(b) K_C(r^{-2}) + 2K_C(\log r) \} \quad (16)$$

for the same cylinder subjected to uniform tension  $p_0$  on outer cylindrical surface and fully autofrettaged residual stress respectively. In Eq. (16) the new functional stress intensity factor is

$$K_C(\log r) = \frac{H}{K(1)} \int_0^c \log(r(x)) \frac{\partial v(1)}{\partial x} dx \quad (17)$$

The finite element results of  $K(p_1)/p_1$ ,  $K(p_0)/p_0$  and  $K(\rho=b)/\sigma_0$  enable us to compute the functional stress intensity factors  $K_C(1)$ ,  $K_C(r^{-2})$ , and  $K_C(\log r)$ . For the same flawed cylinder with different degree of autofrettage, the stresses can be computed from one of the following algebraic equations. For an inner crack with the crack tip  $r_c$  in the range  $1 < r_c < \rho$ , the equation is

$$\frac{K(\rho)}{\sigma_0} = \frac{1}{\sqrt{3}} \{ [2 - P_1(\rho)] K_C(1) - P_1(\rho) K_C(r^{-2}) + 2K_C(\log r) \} \quad (18)$$

For an outer crack with  $r_c$  in the range  $\rho < r_c < b$ , the equation is

$$\frac{K(\rho)}{\sigma_0} = \frac{1}{\sqrt{3}} [\rho^2 - P_1(\rho)] [b^{-2} K_C(1) + K_C(r^{-2})] \quad (19)$$

**IV. MODIFICATION FORMULAS.** For a partially autofrettaged cylinder, let  $\epsilon$  be the degree of autofrettage, then  $\epsilon = (\rho-1)/t$  where  $t = b - 1$  is the wall thickness of the cylinder. When a crack crosses the elastic-plastic interface  $r = \rho$ , the hoop stress along the crack face must be represented by both Eqs. (3) and (4). Hence Eqs. (18) and (19) are not valid in such a situation. For inner cracks, we may use Eq. (18) to compute an approximate value which is based on the crack face loading of Eq. (3). The error introduced by Eq. (18) may be corrected by adding the following crack face loading

0,

 $l < r < \rho$ 

$$P_c(r) = \frac{\sigma_0}{\sqrt{3}} (\rho^2 - P_1) \left( \frac{1}{b^2} + \frac{1}{r^2} \right) - \frac{\sigma_0}{\sqrt{3}} \left\{ 2 \log \frac{r}{\rho} + 1 + \frac{\rho^2}{b^2} - P_1 \left( \frac{1}{b^2} + \frac{1}{r^2} \right) \right\}, \rho < r < r_c \quad (20)$$

where  $r_c$  is the radius of the crack tip. Substituting from the above into Eq. (9), we should be able to obtain a correction stress intensity factor  $K_\delta$  if  $\partial v / \partial c$  is known. Assume the crack tip crosses the elastic-plastic interface only slightly, the Westergaard near field solution for  $v$  in terms of crack-tip stress intensity factor  $K^{(1)}$  can be approximately used to find  $\partial v / \partial c$ . Let  $\xi$  be a length measured from the crack tip and be defined by

$$\xi = -(x-c) \quad (21)$$

then

$$v(\xi) = \frac{2K^{(1)}}{H} \left( \frac{2}{\pi} \right)^{1/2} \sqrt{\xi} \quad (22)$$

and

$$\frac{\partial v}{\partial c} = \frac{K^{(1)}}{H} \left( \frac{2}{\pi} \right)^{1/2} \left( \frac{1}{\sqrt{\xi}} + \frac{1}{c} \sqrt{\xi} \right) \quad (23)$$

The approximate correction factor  $K_\delta$  obtained by termwise integration of Eq. (9) using Eqs. (20) and (23) is given by

$$\frac{K_\delta}{\sigma_0} = \frac{1}{\sqrt{3}} \sqrt{2/\pi} \{-1 + 2 \log \rho\} (I_1 + I_1') + \rho^2 (I_2 + I_2') - 2(I_3 + I_3') \quad (24)$$

Using  $\delta t = |r_c - \rho|$ , the abbreviations in Eq. (24) are:

$$I_1 = 2\sqrt{\delta t}, \quad I_1' = \frac{2}{3c} (\delta t)^{3/2} \quad (25)$$

$$I_2 = \frac{1}{1+c} \left[ \frac{\sqrt{\delta t}}{\rho} - \frac{(1+c)^{-1/2}}{2} \log D(\rho) \right] \quad (26)$$

$$I_2' = \frac{1}{c} \left[ \frac{\sqrt{\delta t}}{\rho} + \frac{(1+c)^{-1/2}}{2} \log D(\rho) \right]$$

$$I_3 = -2[(2-\log \rho)\sqrt{\delta t} + (1+c)^{1/2} \log \frac{\sqrt{1+c} - \sqrt{\delta t}}{\sqrt{1+c} + \sqrt{\delta t}}] \quad (27)$$

$$I_3' = \frac{2}{3c} [\sqrt{\delta t} \{\delta t \log \rho - 2(1+c) - 2\delta t/3\} - (1+c)^{3/2} \log D(\rho)]$$

with

$$D(\rho) = [2(1+c) - \rho - 2\sqrt{\delta t(1+c)}]/\rho \quad (28)$$

The sum of  $K_\delta/\sigma_0$  from Eq. (24) and  $K(\rho)/\sigma_0$  from Eq. (18) usually gives a better approximation of crack-tip stress intensity factors when  $\delta = |r_c - \rho|/t$  is small. Since the correction formula  $K_\delta/\sigma_0$  is not a function of  $N$ , the number of cracks, it works for small  $N$  and  $\delta$ . But when  $N$  is large, the crack interaction is strong,  $\delta$  must be small.

A similar formula can be found for exterior cracks crossing the elastic-plastic interface from elastic into plastic region.

$$\frac{K_\delta}{\sigma_0} = \left(\frac{2}{3\pi}\right)^{1/2} \{ (1-2 \log \rho)(J_1+J_1') - \rho^2(J_2+J_2') + 2(J_3+J_3') \} \quad (29)$$

where

$$J_1 = 2\sqrt{\delta t} \quad , \quad J_1' = \frac{2}{3c} (\delta t)^{3/2} \quad (30)$$

$$J_2 = \frac{1}{r_c} \left[ -\frac{\sqrt{\delta t}}{\rho} + r_c^{-1/2} \tan^{-1} \sqrt{\delta t/r_c} \right] \quad (31)$$

$$J_2' = \frac{1}{c} \left[ -\frac{\sqrt{\delta t}}{\rho} + r_c^{-1/2} \tan^{-1} \sqrt{\delta t/r_c} \right] \quad (32)$$

$$J_3 = 2[(-2+\log \rho)\sqrt{\delta t} + 2\sqrt{r_c} \tan^{-1} \sqrt{\delta t/r_c}] \quad (33)$$

$$J_3' = \frac{2}{3c} [(\delta t)^{3/2} \log \rho + \frac{2}{3} (3r_c - \delta t)\sqrt{\delta t} - 2r_c^{3/2} \tan^{-1} \sqrt{\delta t/r_c}] \quad (34)$$

Adding  $K_\delta/\sigma_0$  of Eq. (29) to  $K(\rho)$  of Eq. (19), the result is the corrected crack-tip stress intensity factors for exterior cracks.

V. NUMERICAL RESULTS AND CONCLUSIONS. Extensive numerical results are obtained for a cylinder of  $b = 2$  which is a commonly used value in cannon design. A typical finite element idealization is shown in Figure 1 for inner radial cracks. Slight modifications in element meshes are needed for exterior cracks. In Figure 1 the elements surrounding the crack-tip are enriched elements [10]. If collapsed singular elements are to be used, we can simply replace the enriched quadrilaterals by collapsed quadrilateral elements (triangular elements) with proper shifting of side nodes to new locations. Similar accuracy is achieved using either enriched or collapsed quadrilaterals. Stress intensity factors for internal cracks are given in Table 1 of reference [15] for three different types of loadings. Using these results and using Eqs. (12), (15), and (16), we obtain functional stress intensity factors for internal cracks. Figure 2 shows stress intensity factors as a function of  $c/t$  for various numbers of internal cracks in a fully autofrettaged cylinder. Figures 3, 4, and 5 are similar graphs of functional stress intensity factors. Corresponding graphs for external cracks are shown in Figures 6 through 9.

Readings taken from Figures 3, 4, and 5 are enough for an estimate of stress intensity factor for internally cracked cylinders with any assigned values of  $N$  and  $c/t$  for any combination of  $p_1$  and residual stresses corresponding to a given  $\epsilon$ . If crack tips cross the elastic-plastic interface, then correction formula (24) should be used. As an example, if the stress intensity factor is desired for  $N = 2$ ,  $c/t = 0.3$  in a 25 percent autofrettaged cylinder, we first take readings:  $K_C(1)/\sqrt{\pi c} = 1.41$  from Figure 3;  $K_C(r^{-2})/\sqrt{\pi c} = 1.05$  from Figure 4;  $K_C(\log r)/\sqrt{\pi c} = 0.22$  from Figure 5, then  $K_C(\epsilon=0.25)/\sigma_0\sqrt{\pi c} = -0.12$  is computed from Eq. (18). Since  $r_c = 1.3$  is greater than  $\rho = 1.25$ , the correction stress intensity factor  $K_\delta/\sigma_0\sqrt{\pi c} = -0.023$  is obtained from Eq. (24). The sum of Eqs. (18) and (24) gives  $K/\sigma_0\sqrt{\pi c} = -0.143$ . To check this result, a finite element computation of this case is performed. The result is also  $-0.143$ . For externally cracked cylinders, Eq. (19) involves only two functional stress intensity factors. Therefore, only Figures 7 and 8 are needed. For example, given  $N = 4$ , readings taken from Figure 7 are  $K_C(1)/\sqrt{\pi c} = 1.12$  and  $1.18$  for  $c/t = 0.2$  and  $0.3$  respectively. Readings are  $K_C(r^{-2})/\sqrt{\pi c} = 0.32$  for  $c/t = 0.2$  and  $0.36$  for  $c/t = 0.3$  from Figure 8. Stress intensity factors for  $\epsilon = 0.8$  can be computed from Eq. (19). It gives  $K(\epsilon=0.8)/\sigma_0\sqrt{\pi c} = 0.492$  and  $0.537$  for  $c/t = 0.2$  and  $0.3$  respectively. For  $c/t = 0.3$ , the correction formula (29) must be used. The result is  $K_\delta/\sigma_0\sqrt{\pi c} = -0.05$ . The final result for  $c/t = 0.3$  is  $K(\epsilon=0.8)/\sigma_0 = 0.487$  which is close to the result of  $0.486$  obtained directly from a finite element computation.

For a combination of residual stresses and internal pressure, the stress intensity factor is simply an algebraic sum. Stress intensity factors normalized by  $\sigma_0\sqrt{\pi c}$  are shown in Figure 10 as a function of  $N$  for internal cracks subjected to several selected values of  $p_1$  and  $\epsilon$ . Figure 11 is a similar graph for external cracks.

The functional stress intensity factors are used to obviate the difficulty in finding the weight function itself. The approach is the result of a series of methods developed for multiply cracked cylinders. The extension of the method to residual stress distribution other than that given

by Eqs. (1) through (4) is highly possible.

From numerical results, the stress intensity factor is largest for  $N = 2$  for various combinations of residual stresses and internal pressures for both interior and exterior cracks. The stress intensity factor is monotonically decreasing as the number of cracks increases from  $N = 2$ .

#### REFERENCES

1. Bowie, O. L. and Freese, C. E., "Elastic Analysis for a Radial Crack in a Circular Ring," *Engineering Fracture Mechanics*, Vol. 4, 1972, pp. 315-321.
2. Shannon, R. W. E., "Stress Intensity Factors For Thick-Walled Cylinders," *International Journal of Pressure Vessels and Piping*, Vol. 2, 1974, pp. 19-29.
3. Grandt, A. F., "Two Dimensional Stress Intensity Factor Solutions For Radially Cracked Rings," Technical Report AFML-TR-75-121, Air Force Materials Laboratory, 1975.
4. Goldthorpe, B. D., "Fatigue and Fracture of Thick-Walled Cylinders and Gun Barrels," *Case Studies in Fracture Mechanics*, Technical Report AMMRC-MS 77-5, Army Mechanics and Materials Research Center, 1977.
5. Baratta, F. I., "Stress Intensity Factors for Internal Multiple Cracks in Thick-Walled Cylinders Stressed by Internal Pressure Using Load Relief Factors," *Engineering Fracture Mechanics*, Vol. 10, 1978, pp. 691-697.
6. Henshell, R. D. and Shaw, K. G., "Crack Tip Finite Elements are Unnecessary," *Int. J. for Numerical Methods in Engineering*, Vol. 9, 1975, pp. 495-507.
7. Barsoum, R. S., "On the Use of Isoparametric Finite Elements in Linear Fracture Mechanics," *Int. J. for Numerical Methods in Engineering*, Vol. 10, 1976, pp. 25-37.
8. Pu, S. L., Hussain, M. A., and Lorensen, W. E., "The Collapsed Cubic Isoparametric Element as a Singular Element for Crack Problems," *Int. J. for Numerical Methods in Engineering*, Vol. 12, 1978, pp. 1727-1742.
9. Hussain, M. A., Lorensen, W. E., and Pflagl, G., "The Quarter-Point Quadratic Isoparametric Element as a Singular Element For Crack Problems," NASA TM-X-3428, 1976, p. 419.
10. Gifford, L. N. Jr., "APES - Second Generation Two-Dimensional Fracture Mechanics and Stress Analysis By Finite Elements," Report 4799, David Taylor Naval Ship Research and Development Center, 1975.
11. Pu, S. L. and Hussain, M. A., "Stress Intensity Factors For a Circular Ring With Uniform Array of Radial Cracks Using Cubic Isoparametric Singular Elements," *Fracture Mechanics*, ASTM STP 677, 1979, pp. 685-699.

12. Tracy, P. G., "Elastic Analysis of Radial Cracks Emanating From the Outer and Inner Surfaces of a Circular Ring," *Engineering Fracture Mechanics*, Vol. 11, 1979, pp. 291-300.
13. Hussain, M. A., Pu, S. L., Vasilakis, J. D., and O'Hara, P., "Simulation of Partial Autofrettage By Thermal Loads," *Journal of Pressure Vessel Technology*, Vol. 102, No. 3, 1980, pp. 314-318.
14. Hill, R., The Mathematical Theory of Plasticity, Oxford at the Clarendon Press, 1950.
15. Pu, S. L. and Hussain, M. A., "Stress Intensity Factors For Radial Cracks in a Partially Autofrettaged Thick-Wall Cylinder," *Proceedings of 14th National Symposium on Fracture Mechanics*, 1981.
16. Parker, A. P. and Andrasic, C. P., "Stress Intensity Prediction For a Multiply-Cracked, Pressurized Gun Tube With Residual and Thermal Stresses," *Army Symposium on Solid Mechanics*, AMMRC MS 80-5, 1980, pp. 35-39.
17. Kapp, J. A. and Eisenstadt, R., "Crack Growth in Externally Flawed, Autofrettaged Thick-Walled Cylinders and Rings," Fracture Mechanics, ASTM STP 677, 1979, pp. 746-756.
18. Parker, A. P., "Stress Intensity and Fatigue Crack Growth in Multiply-Cracked, Pressurized, Partially Autofrettaged Thick Cylinders," AMMRC TR 81-37, 1981.
19. Pu, S. L., "Stress Intensity Factors For Radial Cracks at Outer Surface of a Partially Autofrettaged Cylinder Subjected to Internal Pressure," USA ARRADCOM Technical Report ARLCB-TR-82003, Benet Weapons Laboratory, Watervliet, NY, 1982.
20. Rice, J. R., "Some Remarks on Elastic Crack-Tip Stress Fields," *Int. Journal of Solids and Structures*, Vol. 8, 1972, pp. 751-758.
21. Davidson, T. E. and Kendall, D. F., "The Design of Pressure Vessels For Very High Pressure Operation," *Mechanical Behavior of Materials Under Pressure*, Edited by H. L. P. Pugh, Elsevier Co., 1970.
22. Pu, S. L. and Hussain, M. A., "Residual Stress Redistribution Caused by Notches and Cracks in a Partially Autofrettaged Tube," *Journal of Pressure Vessel Technology*, Vol. 103, No. 4, 1981, pp. 302-306.
23. Orange, T. W., "Crack Shapes and Stress Intensity Factors For Edge-Cracked Specimens," ASTM STP 513, 1972, pp. 71-78.

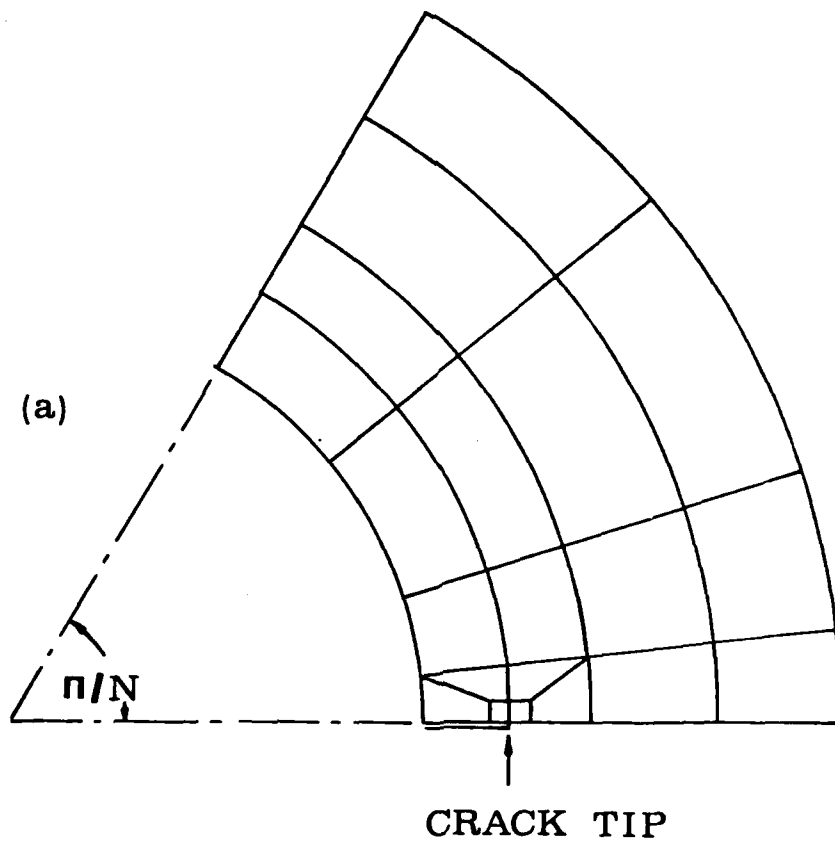


Figure 1(a). A typical finite element idealization.

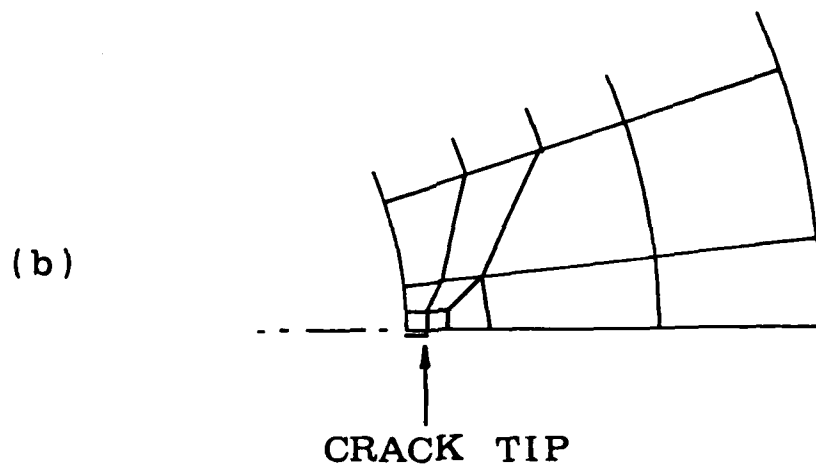


Figure 1(b). Idealization for very shallow cracks.

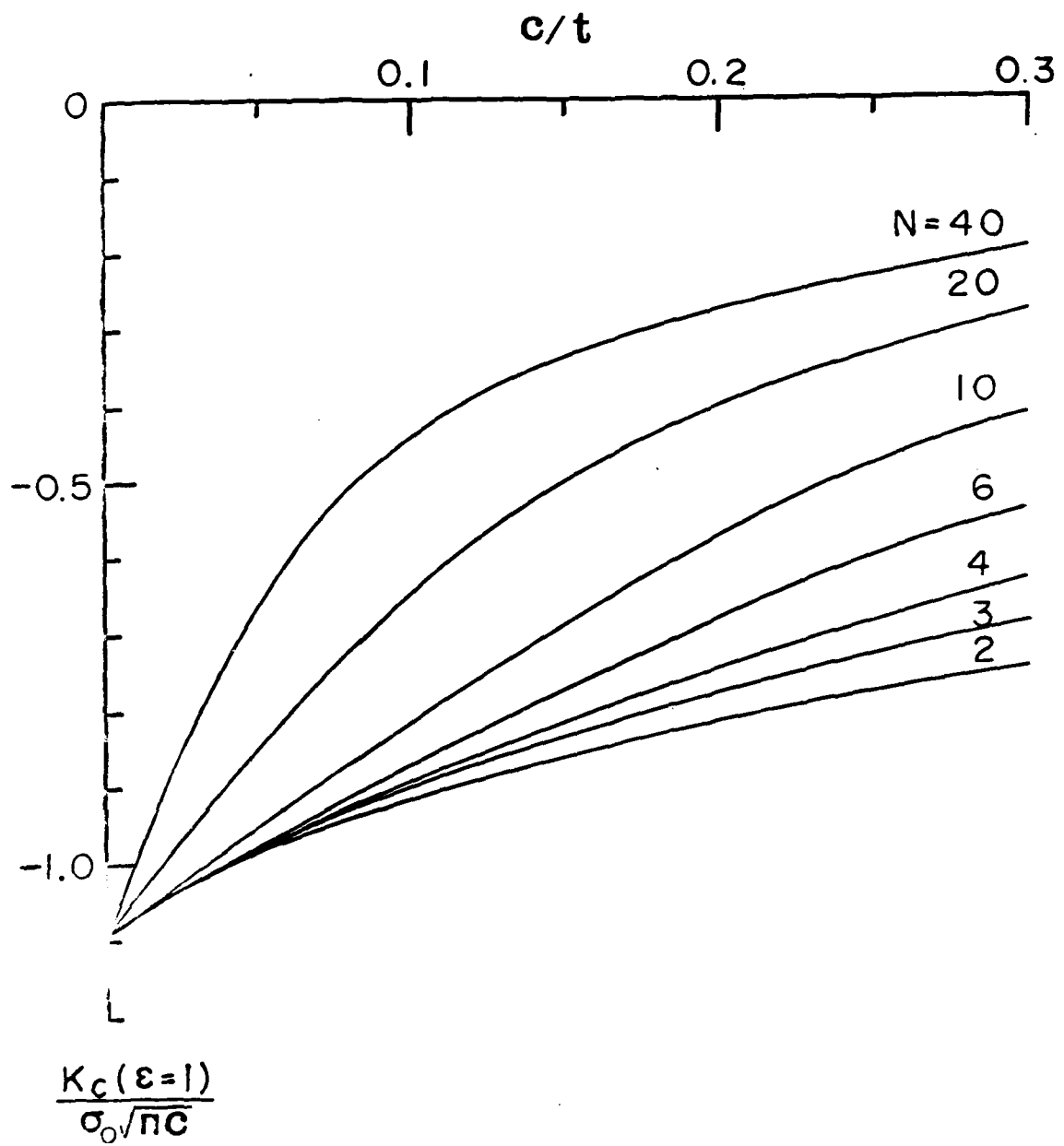


Figure 2. Stress intensity factor as a function of  $c/t$  for  $N$  ID cracks in a fully autofrettaged cylinder of  $b/a = 2$ .

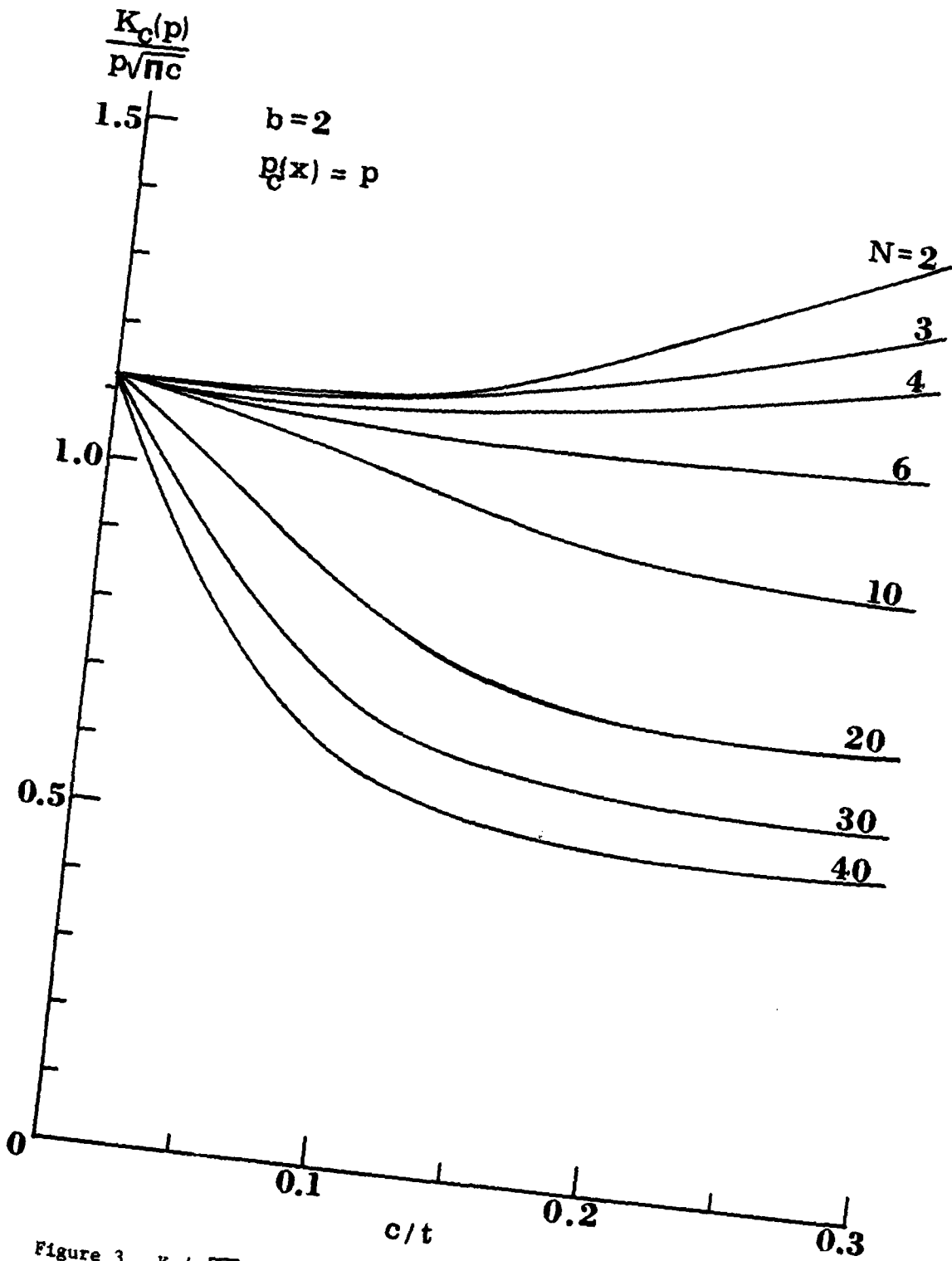


Figure 3.  $K_c/p\sqrt{\pi c}$  as a function of  $c/t$  for  $N$  internal radial cracks with constant crack face loading.

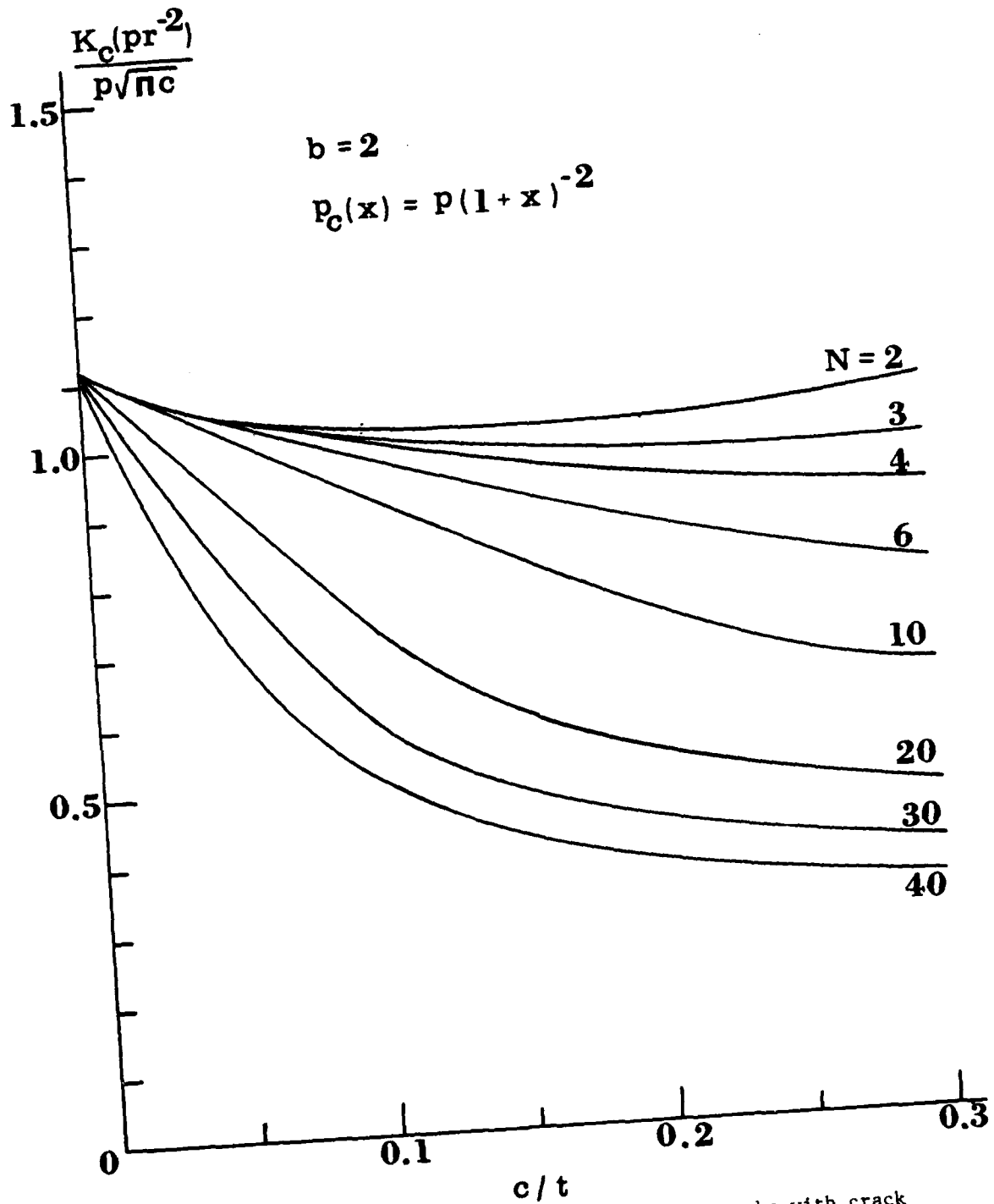


Figure 4.  $K_c/p\sqrt{\pi c}$  vs.  $c/t$  for  $N$  internal radial cracks with crack face loading  $P_c(x) = p(1+x)^{-2}$ .

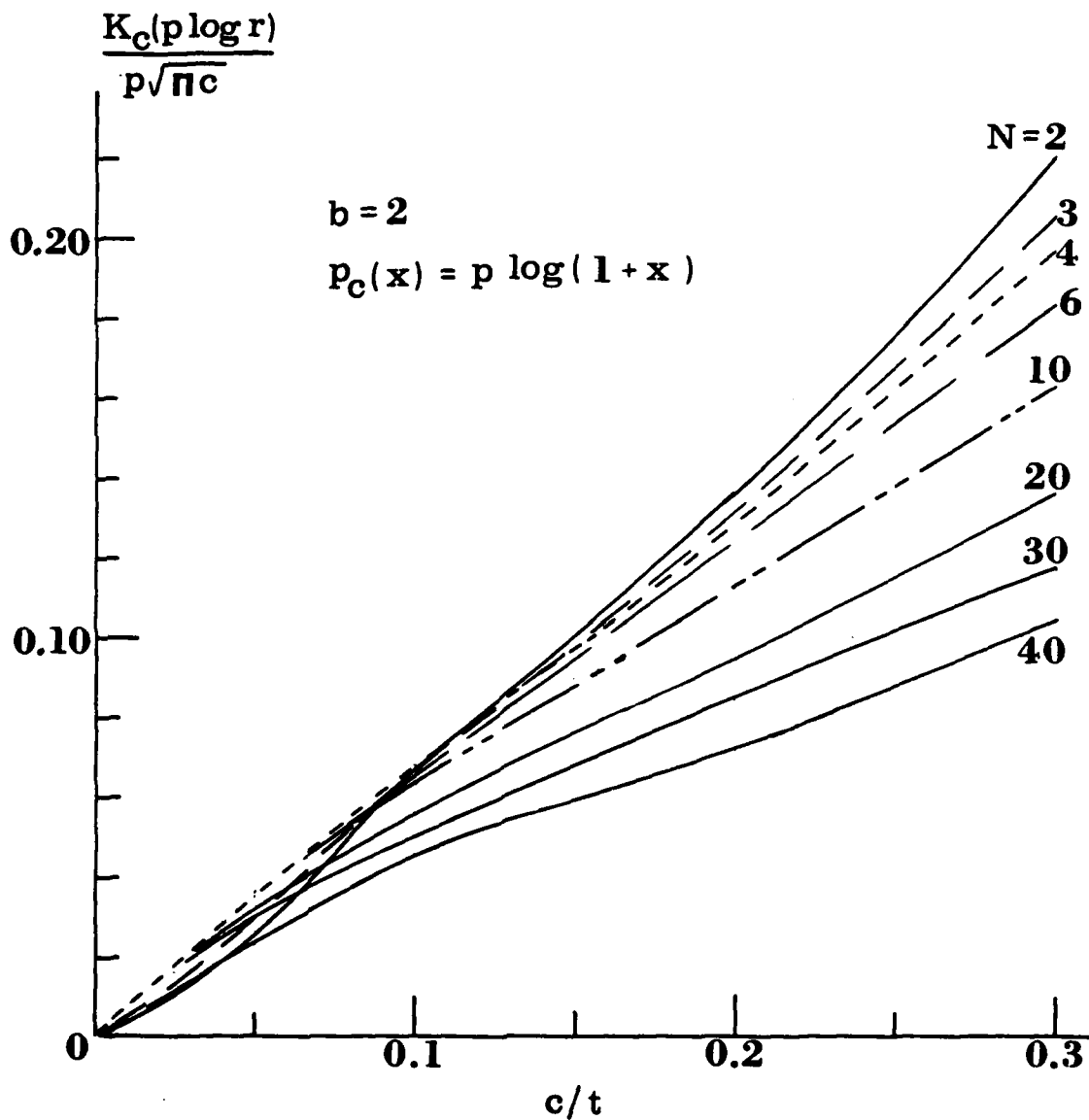


Figure 5.  $K_c/p\sqrt{\pi c}$  vs.  $c/t$  for  $N$  internal radial cracks with crack face loading  $p_c(x) = p \log(1+x)$ .

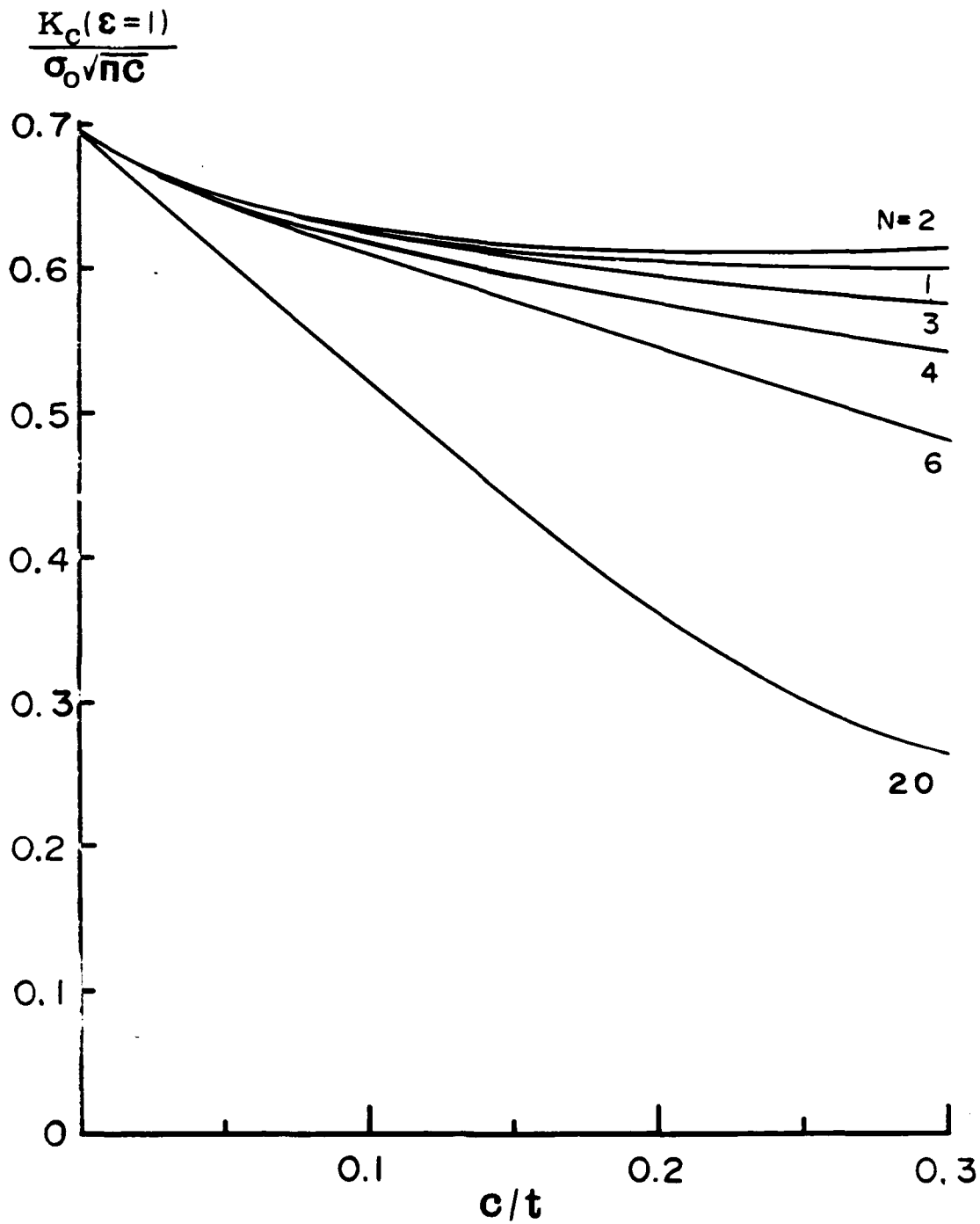


Figure 6.  $K/\sigma_0\sqrt{\pi c}$  as a function of  $c/t$  for  $N$  radial cracks at outer surface of a fully autofrettaged cylinder of  $b/a = 2$ .

AD-A128 683

TRANSACTIONS OF THE CONFERENCE OF ARMY MATHEMATICIANS  
(28TH) HELD AT BETHESDA MARYLAND ON 28-30 JUNE 1982(U)  
ARMY RESEARCH OFFICE RESEARCH TRIANGLE PARK NC FEB 83

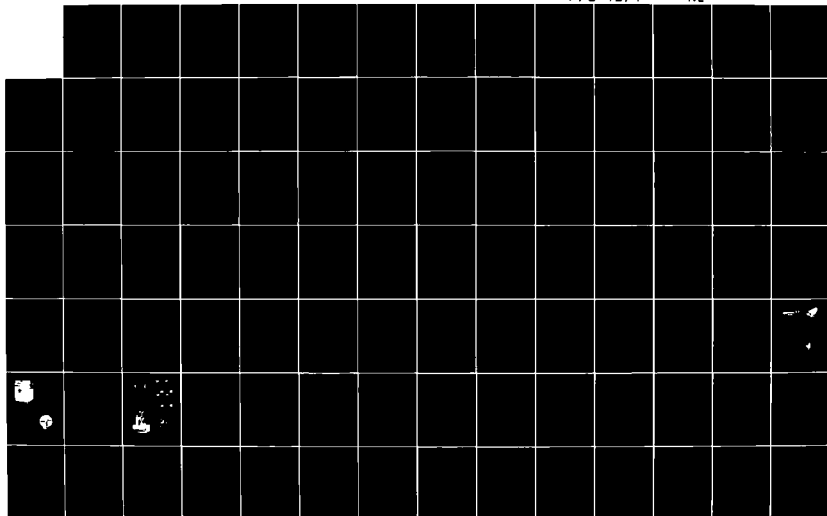
4/6

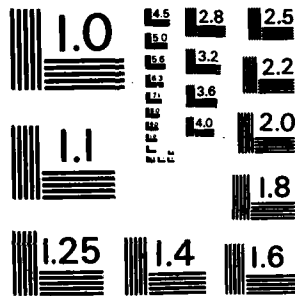
UNCLASSIFIED

ARO-83-1

F/G 12/1

NL





MICROCOPY RESOLUTION TEST CHART  
NATIONAL BUREAU OF STANDARDS-1963-A

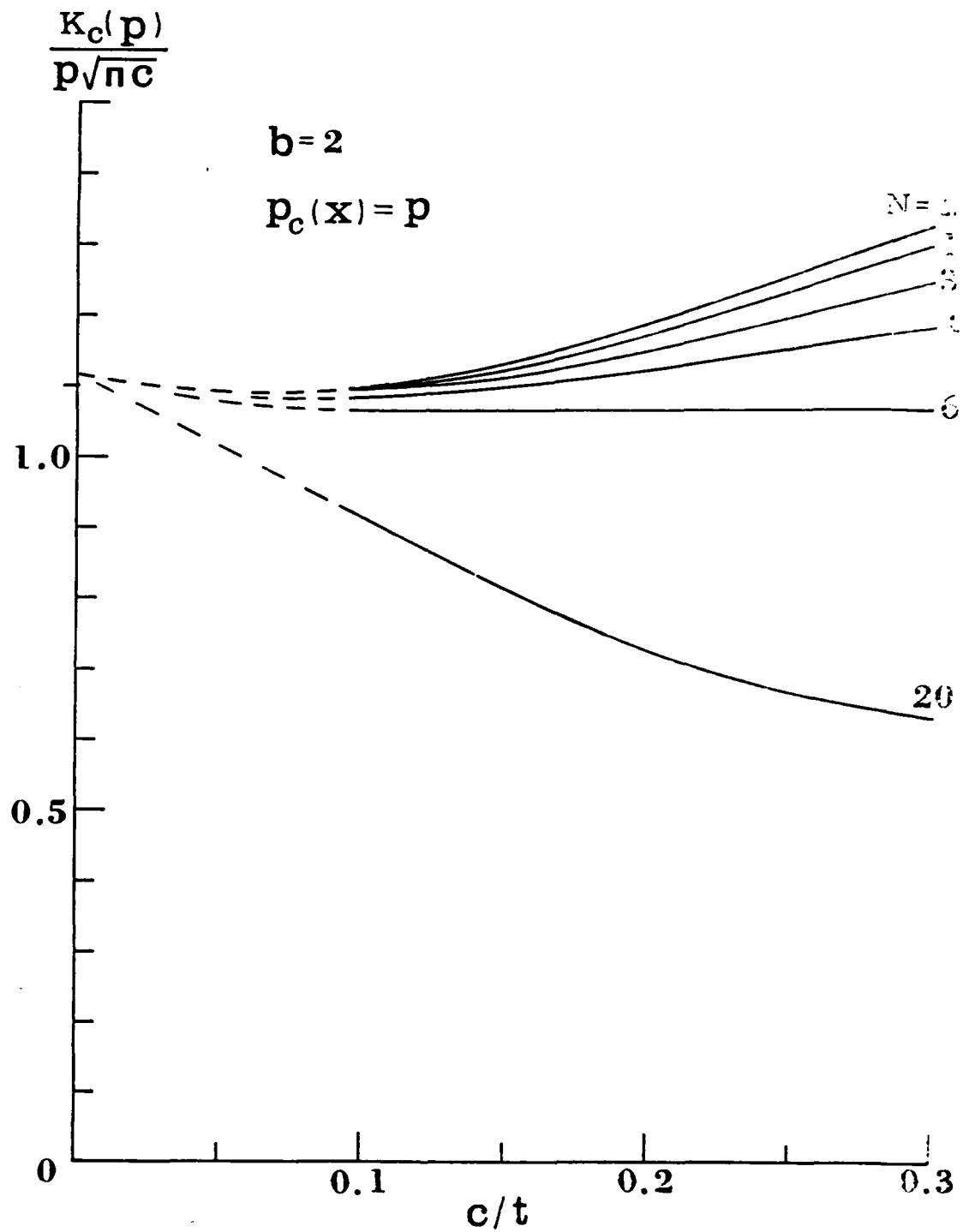


Figure 7.  $K_c(p)/p\sqrt{\pi c}$  as a function of  $c/t$  for  $N$  external radial cracks with constant crack face loading.

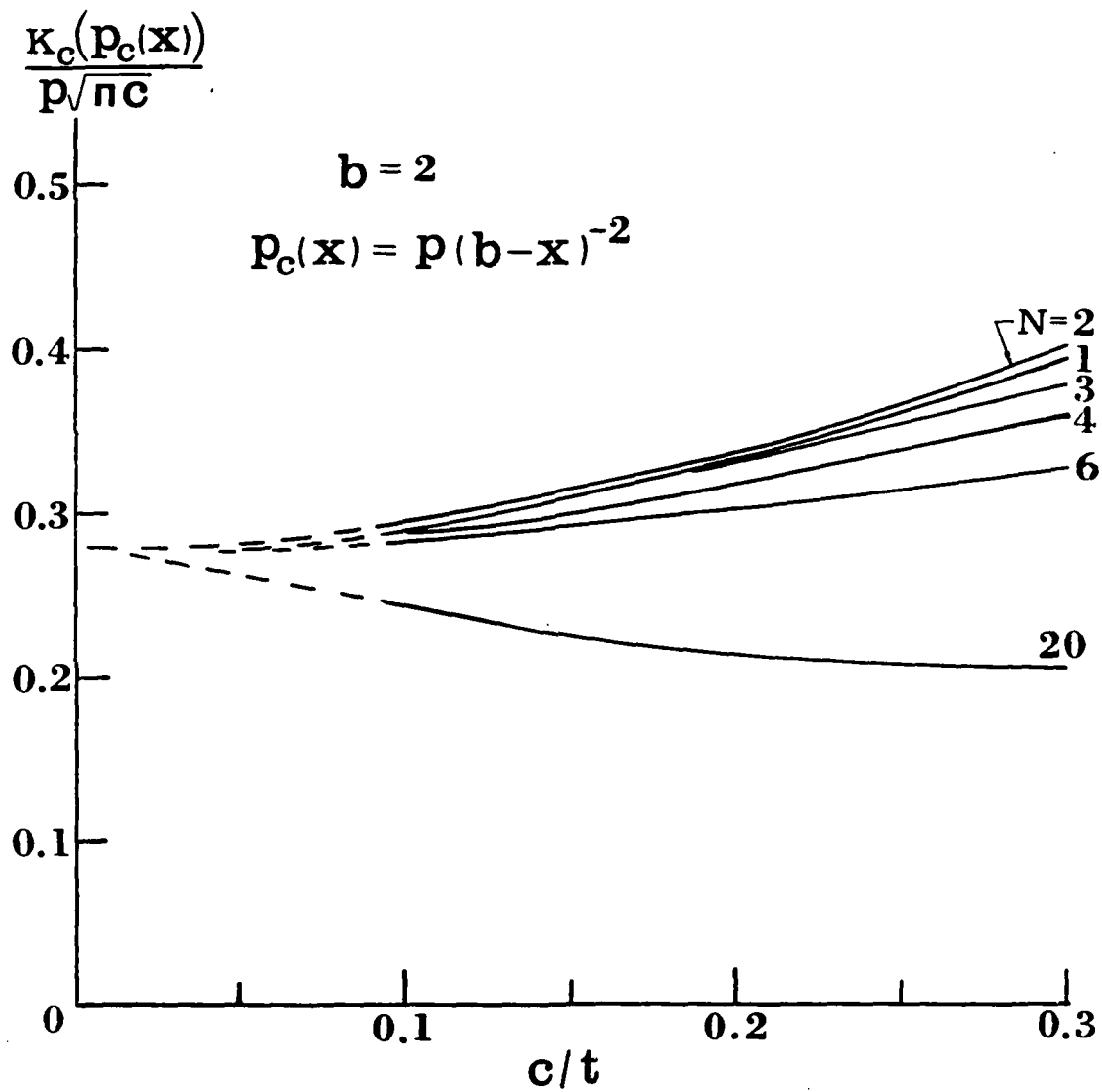


Figure 8.  $K_c/p\sqrt{\pi c}$  vs.  $c/t$  for  $N$  external radial cracks with crack face loading  $p_c(x) = p(b-x)^{-2}$ .

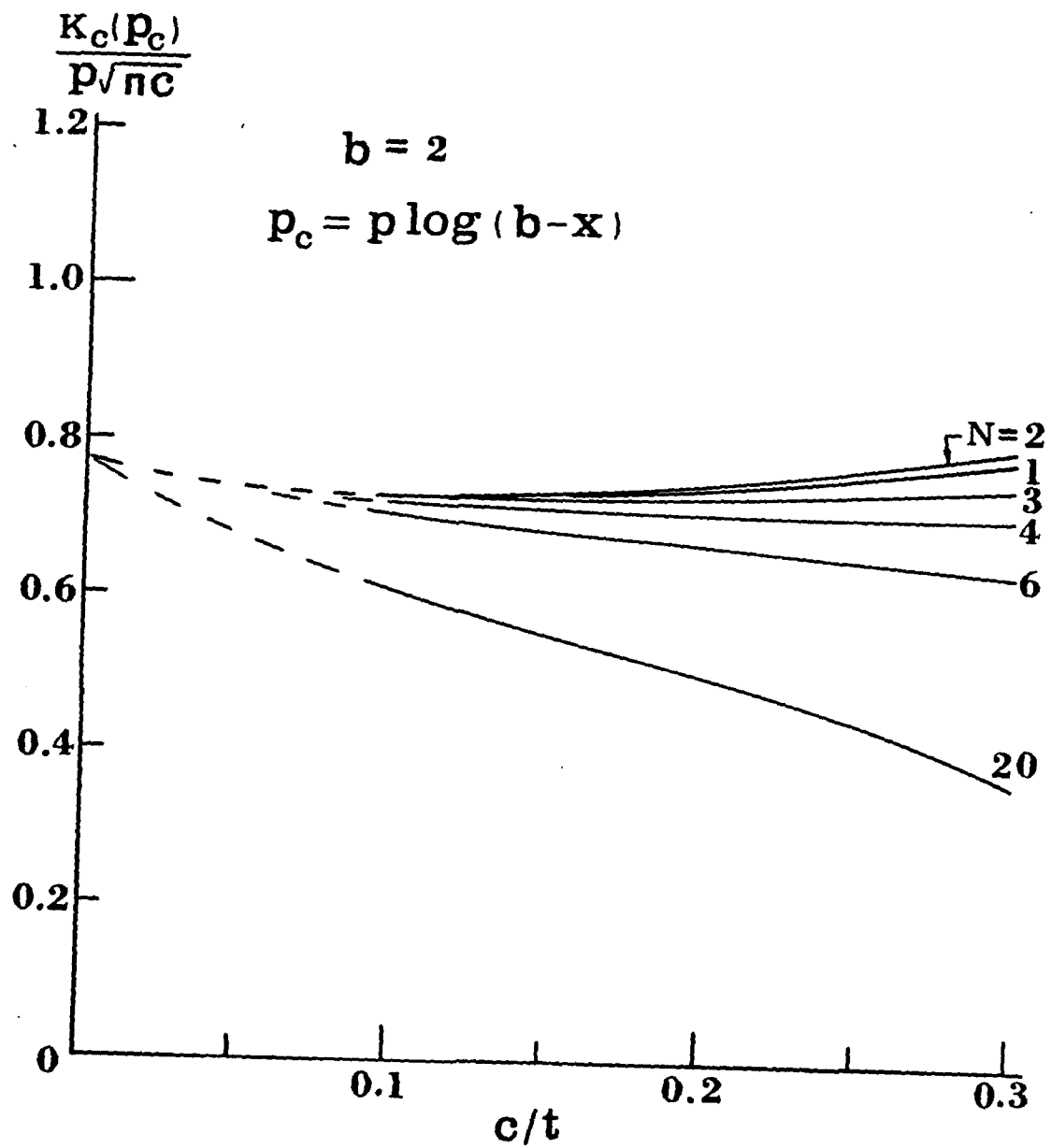


Figure 9.  $K_c/p\sqrt{\pi c}$  vs.  $c/t$  for  $N$  external radial cracks with crack face loading  $p_c(x) = p \log(b-x)$ .

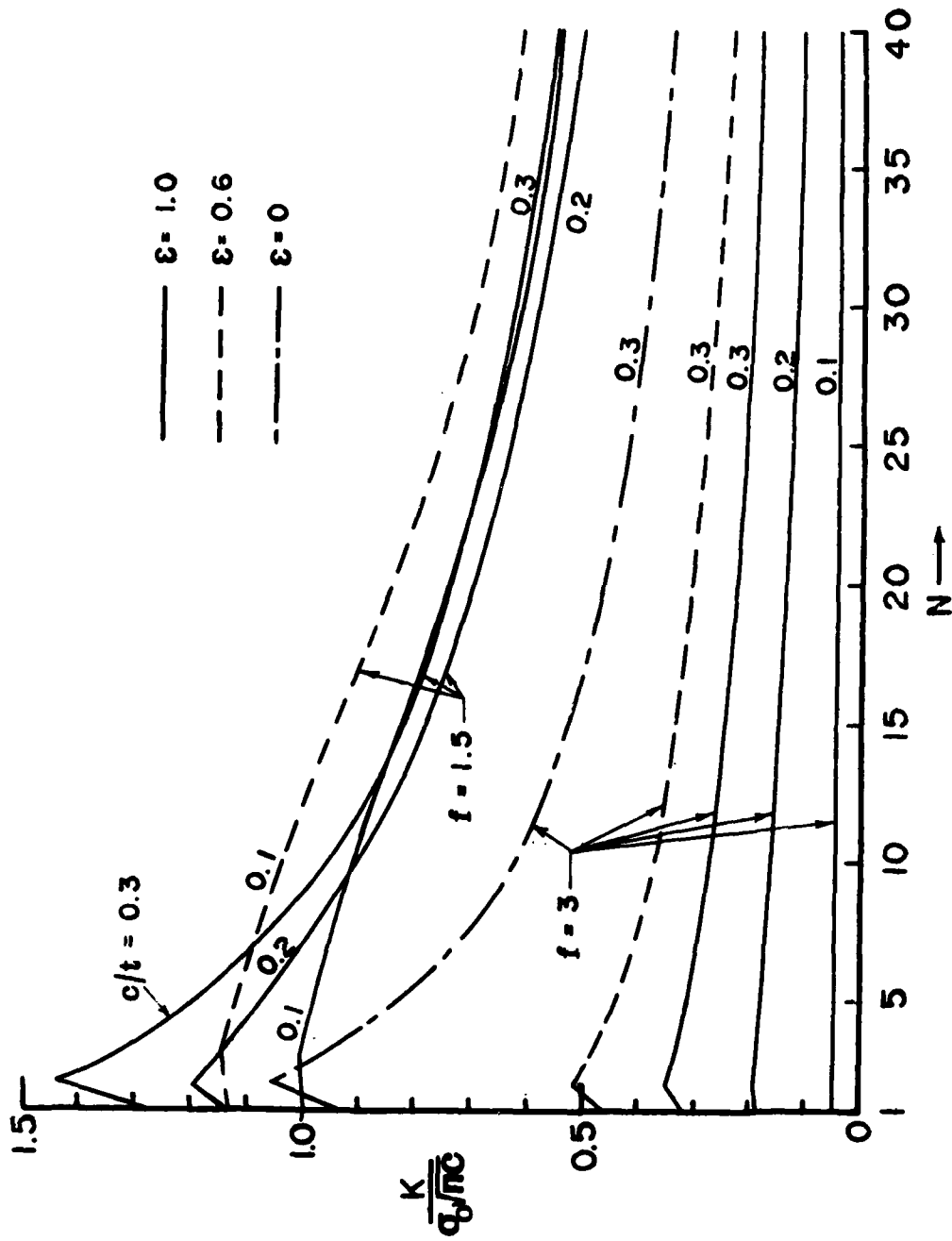


Figure 10.  $K/\sigma_0\sqrt{\pi c}$  for  $N$  radial cracks at inner surface of a cylinder of  $b/a = 2$  subjected to combined internal pressure  $p_i = \sigma_0/f$  and residual stresses corresponding to given degrees of autofrettage,  $\epsilon$ .

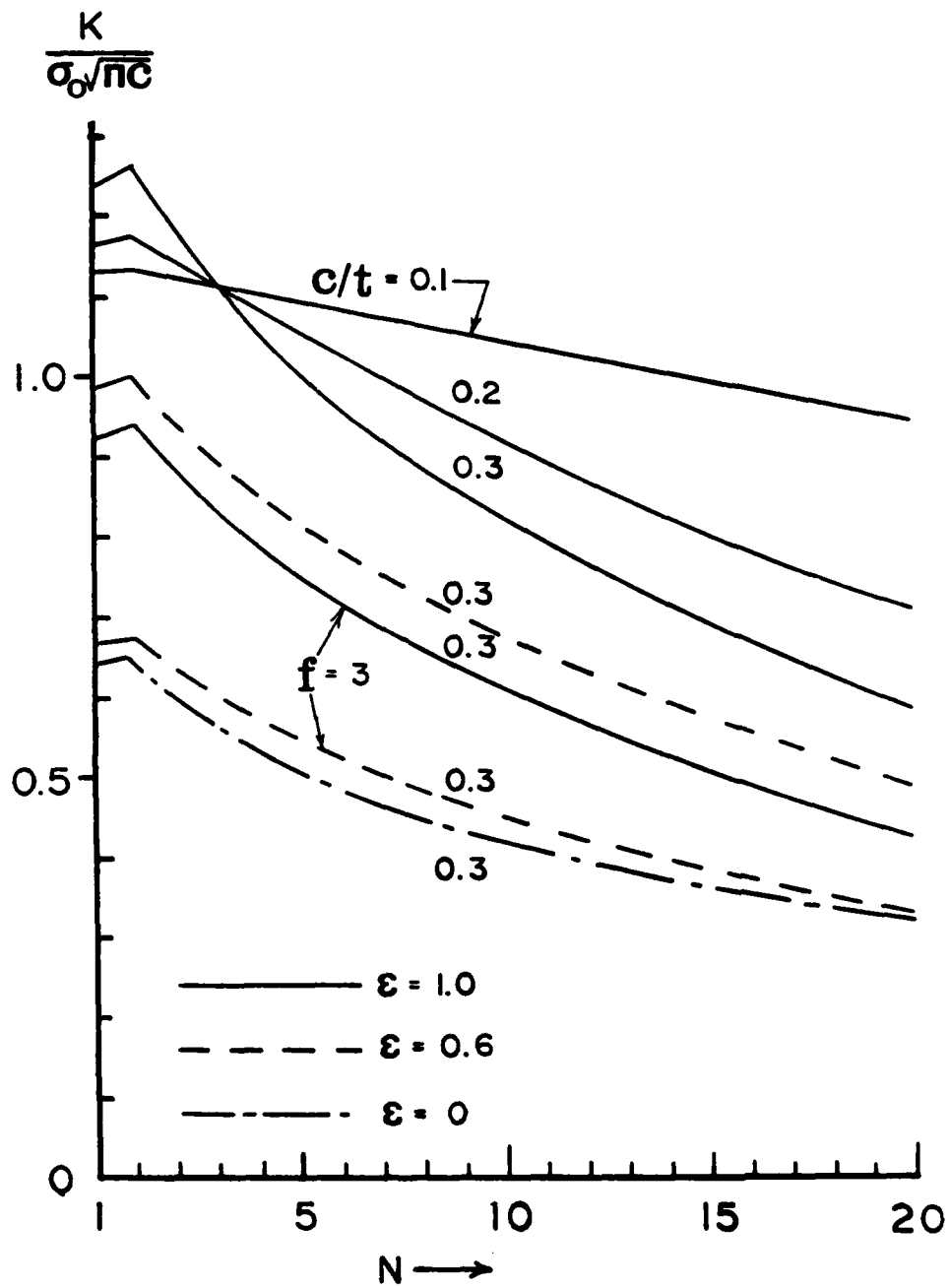


Figure 11.  $K/\sigma_0\sqrt{\pi c}$  for  $N$  radial cracks at outer surface of a cylinder of  $b/a = 2$  subjected to combined internal pressure  $p_i = \sigma_0/f$ , where  $f = 1.5$  except otherwise indicated, and residual stresses corresponding to given degrees of autofrettage  $\epsilon$ .

AD P001027

TWO-PHASE FLOW OF LIQUID PROPELLANT GUNS BY SPACE MEAN APPROACH

R. J. Yalamanchili  
Armament Division  
Fire Control & Small Caliber Weapon Systems Laboratory  
ARRADCOM, Dover, NJ 07801

ABSTRACT

Liquid propellants have many potential advantages over solid propellants for use in guns, including elimination of cartridge cases, reduced gun tube erosion, and higher muzzle velocities. However, in the past, nonreproducibility of ballistics was the main obstacle. An accurate mathematical model is essential to characterize and predict the interior ballistics of a liquid propellant gun in order to overcome this obstacle. A regenerative injection model is considered where the force derived from the combustion of a small portion of the propellant and differential-area piston is utilized to inject the main charge into the chamber. The model involves a compressible liquid, injection fluid mechanics and the burning rate of propellant in addition to an imperfect gas law. The continuity, momentum and energy equations are utilized in addition to two moving boundary conditions which are formulated by Newton's law. These are solved by numerical integration and digital computers. Model capability includes not only conventional interior ballistics results but also the rate of propellant injection, the rate of propellant combustion as well as propellant distribution inside the chamber.

I. INTRODUCTION.

Basically, there are three types of liquid propellant guns. Most of the attention, so far, was placed on the bulk loaded gun. Very little literature exists on regenerative liquid propellant gun systems. At present, work is in progress on all systems, theoretically and experimentally. However, this paper is restricted to the regenerative liquid propellant gun. Undoubtedly, there are some disadvantages over solid propellant guns. However, the advantages such as elimination of the cartridge case and higher performance outweigh the disadvantages and deserves extensive efforts to develop a successful weapon system.

## II. PHYSICAL MODEL.

The schematic of a regenerative liquid propellant system is shown in Figure 1. A monopropellant which contains both fuel and oxidant is considered because of simplicity. A differential piston is used, i.e., the area of a piston facing the projectile is much larger than the area of a piston facing the propellant. Therefore, there is a net force acting in a rearward direction even if the pressure is the same on both sides. A small amount of monopropellant is injected into the region between the bolt and the piston head and the inlet and orifices which are located in the piston head are sealed off. An electric primer is introduced into the combustion chamber between the piston head and the projectile. The primer gases push the piston rearward. The liquid propellant is compressed and higher liquid pressures are generated. This high pressure liquid propellant is injected into the combustion chamber through the injectors. Some of the injected propellant, which is in the form of a spray, is burned and high pressures are generated.

## III. MATHEMATICAL MODEL.

The physical phenomena in a regenerative liquid propellant system is quite complex. The problem is an unsteady, two-phase and three-dimensional flow in a highly reactive environment. This is further complicated by the unknown moving boundary conditions. The kinetics of the propellant decomposition is currently unknown. The regenerative liquid propellant problem is complex due to unsteady environment and interaction between numerous complex droplets of varying sizes and shapes. Therefore, a practical minded approach is considered as a first cut. There is plenty of scope for future improvement in the modeling process. A transient one-dimensional approach fits this category. The governing equations are a system of nonlinear partial differential equations due to the use of space ( $x$ ) and time ( $t$ ) as independent variables. Such a model is under development. The method of characteristics is chosen to reduce, by one, the number of independent variables. The model will be validated and modified as more experimental data becomes available.

The dependent variables change drastically with respect to time when compared to the space coordinate. Moreover, a one-dimensional approach is utilized as a starting point. One may be able to obtain meaningful results by utilization of space mean quantities. There is no loss of accuracy in calculation of space mean quantities rather than a transient one-dimensional approach. The only loss is that their variation with respect to the space coordinate is unknown. However, one may be able to obtain the same, approximately in conjunction with semi-empirical theories. Therefore, the space mean approach is chosen for this paper.

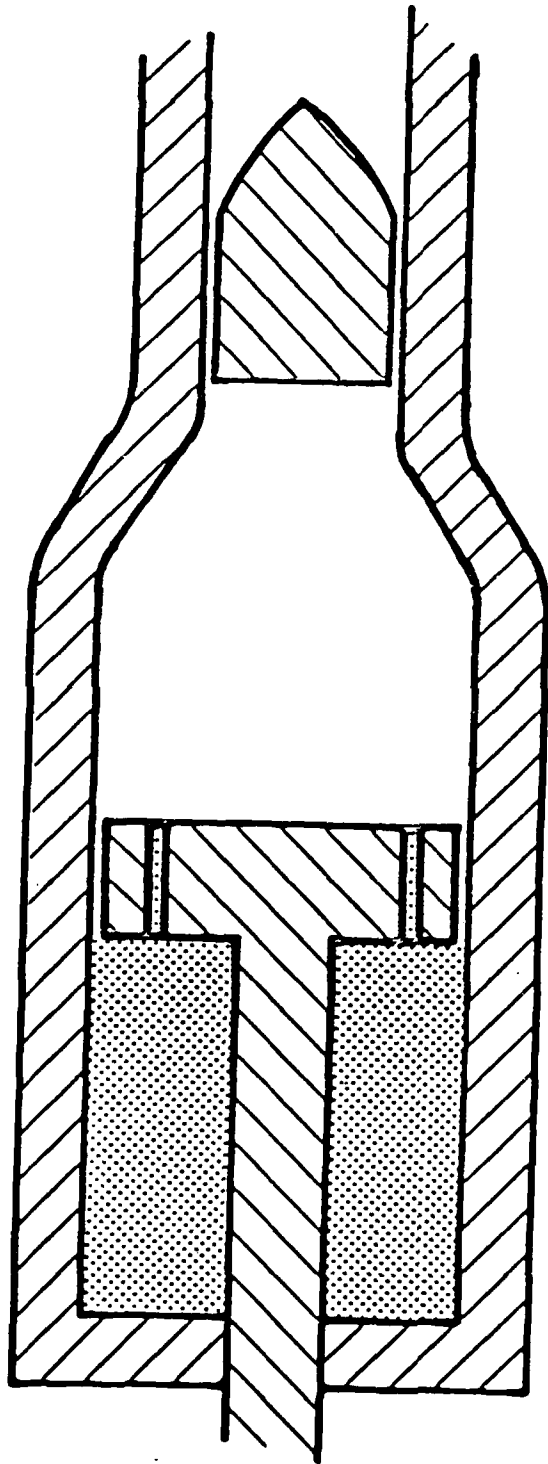


Fig. 1. Schematic of Regenerative Liquid Propellant System

In the model it is assumed that a primer of known charge ( $C_i$ ), force ( $F_i$ ), and adiabatic flame temperature ( $T_i$ ) is present in the combustion chamber, between the piston head and the projectile base. On electric ignition, the primer produces pressure which moves the piston to the propellant reservoir. The liquid monopropellant inside the reservoir chamber (between the bolt and the piston head) is compressed which in turn generates higher pressures. The pressure difference across the piston head causes an injection of liquid propellant into the combustion chamber (hot gas combustion zone) through injectors/orifices. If an incompressible assumption for liquid monopropellant is invoked, the rate of propellant discharge ( $M$ ) can be represented by:

$$\frac{dM}{dt} = \rho_l (A_z - A_R) \frac{dz}{dt} \quad (1)$$

where

- $\rho_l$  = density of liquid propellant
- $A_z$  = cross sectional area of piston head
- $A_R$  = cross sectional area of piston rod
- $z$  = position of piston
- $t$  = time

This equation is based on the condition that the volume displaced by the piston must be equal to the volume of propellant discharged into the combustion chamber.

It is assumed that the pressures inside the liquid propellant is similar to those observed in a conventional gun. An incompressible liquid assumption may not be a good idea at higher pressures. The following equations may be derived for a compressible fluid:

$$\frac{dM}{dt} = C_d \rho_l A_h V_l \quad (2)$$

$$V_l = \sqrt{\frac{2g(P_l - P_z)}{\rho_l}} \quad (3)$$

where

- $C_d$  = discharge coefficient
- $A_h$  = area of the injector/orifice
- $P_l$  = liquid pressure inside the reservoir

- $P_z$  = pressure in the combustion chamber at piston base  
 $g$  = gravitational constant  
 $V_z$  = velocity of fluid at piston base

The coefficient of discharge is a ratio between actual flow and theoretical flow. This value varies between 0 and 1 and is determined empirically. For example, one can introduce the discharge coefficient as a function of Reynold's number.

The piston motion may be described as Newton's second law of motion. The forces acting on the piston in the axial direction are pressure forces and the thrust produced by the action of a jet/spray. The resulting equation for piston motion becomes:

$$\frac{W_p}{g} \frac{dV_z}{dt} = P_z A_z - P_\ell (A_z - A_R) + \rho_\ell A_h V_\ell^2 / g \quad (4)$$

$$\frac{dz}{dt} = V_z \quad (5)$$

- where  $W_p$  = weight of piston  
 $V_z$  = velocity of piston

The liquid propellant pressure variation with respect to chamber pressure may be expressed mathematically by the use of the definition of bulk modulus ( $\beta$ ) and control volume concepts:

$$\frac{dP_\ell}{dt} = \frac{\beta}{U_\ell} [(A_z - A_R) V_z - C_d A_h V_\ell] \quad (6)$$

The rate of change of volume of liquid propellant ( $U_\ell$ ) inside the reservoir can be expressed as

$$\frac{dU_\ell}{dt} = (A_z - A_R) V_z \quad (7)$$

The mathematical definition of bulk modulus of a liquid may be stated as

$$\beta = -U_\ell \frac{\partial P_\ell}{\partial U_\ell} \quad (8)$$

In general, the bulk modulus of a liquid varies with respect to pressure and temperature.

The temperature of a liquid does not vary much during the firing of a single round. However, the pressure of liquid propellant in the reservoir varies drastically as gas pressure in the chamber is increased. Therefore, at least first order corrections are taken into account by using the bulk modulus of a liquid as expressed in the following expression:

$$\beta = a + bP_{\ell} \quad (9)$$

Where  $a$  and  $b$  are constants determined experimentally. though, the temperature of a liquid may not change much during firing of any one shot, the liquid propellant density varies, contrary to the general notion that liquids are incompressible this variation is due to the extremes of chamber pressure. The rate of change of liquid propellant density, based on the definition of density, is formulated as

$$\frac{d\rho_{\ell}}{dt} = \frac{(M_0 - M)(A_z - A_R)}{[U_0 - (A_z - A_R)V_z]^2} V_z - \frac{\rho_{\ell} C_d A_h V_{\ell}}{U_0 - (A_z - A_R)z} \quad (10)$$

Where  $M_0$  = initial amount of liquid propellant in the reservoir.  
and  $U_0$  = initial volume of liquid propellant reservoir.

The derivation of the governing equations for the parameters associated with the liquid propellant reservoir is complete. Now, consider the dynamics inside the combustion chamber. The amount of propellant injected is expressed by equations (1) or (2) and (3). These equations do not consider the injection form (spray etc.) The injection of a jet or spray depends upon the design of the nozzle, properties of liquid propellant, properties of the surrounding gaseous medium, discharge velocity, and so forth. Usually, based on the present injectors, different sizes of droplets are possible. In this case, statistical distribution of droplets is useful. However, a mean droplet size has been chosen for the present study. There is no satisfactory theory for droplet size prediction. Therefore, an empirical derivation, based on Adelberg, is utilized in the initial portion of firing cycle.

$$D_{\ell} = CD_h \quad (11)$$

where  $D_{\ell}$  = mean diameter of liquid propellant droplet  
 $C$  = empirical constant, function of injector and propellant properties  
 $D_h$  = diameter of injector-tip/orifice

It is not uncommon to utilize the Weber number criteria for droplet size prediction. The Weber number (We) is defined as

$$We = \frac{\rho (\Delta V)^2 D_l}{2\sigma} \quad (12)$$

where  $\rho$  = density of hot propellant gas  
 $\Delta V$  = relative velocity between the gas and liquid droplets  
 $\sigma$  = surface tension of liquid propellant

The number of droplets is determined from the mass of liquid propellant injected and the mass of a single droplet based on the previous equations. Further, droplets may break up to smaller sizes. In the model, droplets are allowed to break-up based on Weber number criteria. The Weber number criteria is 6 for low viscosity fluid and 10 for a high viscosity fluid. If the Weber number, at any time, exceeds these values then they are allowed to split-up. The spherical shapes are assumed and maintained during the combustion phase. The solid propellant type of burning rate is assumed, similar to BRL, but with different coefficients and exponents. The resulting equations for the Weber number less than the critical Weber number are as follows:

$$\frac{dm}{dt} = \rho_l S \frac{d\delta}{dt} \quad (13)$$

$$\frac{d\delta}{dt} = BP^n \quad (14)$$

where  $m$  = mass of propellant converted to gas  
 $S$  = total surface area of all droplets  
 $\delta$  = distance burned normal to the surface  
 $P$  = mean chamber pressure  
 $B$  = coefficient in linear burning law  
 $n$  = exponent in pressure dependent burning law

If the Weber number is greater than the critical Weber number, then the number and size of existing are modified and the newly injected droplets are allowed to be smaller in size:

$$\frac{dm}{dt} = C_d \rho_l A_h V_l \quad (15)$$

The free volume available in the chamber for gas molecules can be calculated based on control volume concepts. The free volume (U) is defined by equation (16).

$$U = U_0 + A_z z + Ay - \frac{M - n}{\rho_l} - \eta m \quad (16)$$

$$\frac{dU}{dt} = A \frac{dz}{dt} + A \frac{dy}{dt} + \frac{M - m}{\rho_l^2} \frac{d\rho_l}{dt} - \frac{1}{\rho_l} \left( \frac{dM}{dt} - \frac{dm}{dt} \right) - \eta \frac{dm}{dt} \quad (17)$$

where A = cross sectional area at the projectile base

y = location of projectile

$\eta$  = covolume

The relation for propellant gas density ( $\rho$ ) can be developed based on the definition of density. That is

$$\frac{d\rho}{dt} = \frac{1}{U} \frac{dm}{dt} - \frac{m}{U^2} \frac{dU}{dt} \quad (18)$$

The equation of state can be used to determine the mean pressure (P) in the combustion chamber.

$$P = \frac{mF}{U} \frac{T}{T_0} + \frac{C_i F_i}{U} \frac{T}{T_i} \quad (19)$$

where F = force of the liquid propellant

T<sub>0</sub> = adiabatic flame temperature

T = mean propellant gas temperature in the combustion chamber.

The rate of change of mean combustion chamber pressure can be given as

$$\frac{dP}{dt} = \frac{F}{T_0 V^2} \left[ UT \frac{dm}{dt} + Um \frac{dT}{dt} - mT \frac{dU}{dt} \right] + \frac{F_i C_i}{T_i} \left[ \frac{1}{U} \frac{dT}{dt} - \frac{T}{U^2} \frac{dU}{dt} \right] \quad (20)$$

The propellant gas (mean) temperature (T) can be determined from the conservation of energy equation which states as follows:

Energy released by the burning fuel (Q) equals the sum of the following quantities: interval energy of propellant gases, kinetic energy of propellant gases, kinetic energy of projectile, work done on piston, heat lost to gun tube and energy loss due to projectile friction.

$$Q = m \int_0^{T_0} C_v dT = m \int_0^T C_v dT + KE_{gas} + \frac{W_B}{2g} v_B^2 \quad (21)$$

$$+ \left( P_z A_z + \frac{\rho_l A_z v_z^2}{g} \right) dz + \epsilon m \int_0^{T_0} C_v dT + \theta \frac{W_B}{2g} v_B^2$$

Here, some empirical information based on existing practices and experience is utilized. For example, the heat lost to the gun tube is approximated as a fraction ( $\epsilon$ ) of the energy released by the burned propellant. Similarly, the energy lost due to projectile friction is estimated as fraction ( $\theta$ ) of the kinetic energy of the projectile. The KE gas represents the kinetic energy of propellant gases and  $W_B$  is the weight of the projectile. Therefore, the propellant gas (mean) temperature (T) can be written as:

$$T = \frac{\frac{1-\epsilon}{\gamma-1} (mF + C_i F_i) - \int F_z dz - KE_{gas} - (1+\theta) \frac{W_B v_B^2}{2g}}{\frac{mF}{(\gamma-1)T_0} + \frac{C_i F_i}{(\gamma-1)T_i}} \quad (22)$$

$$\frac{dT}{dt} = \left\{ \frac{\epsilon-1}{\gamma-1} (mF + C_i F_i) + \int F_z dz + KE_{gas} + (1+\theta) \frac{W_B}{2g} v_B^2 \right\} \cdot$$

$$\frac{F dm/dt}{(\gamma-1)T_0 \left[ \frac{mF}{(\gamma-1)T_0} + \frac{C_i F_i}{(\gamma-1)T_i} \right]^2} + \left\{ \frac{1-\epsilon}{\gamma-1} \frac{dm}{dt} - \frac{d}{dt} \int F_z dz \right\} \quad (23)$$

$$- \frac{d}{dt} (KE_{gas}) - (1+\theta) \frac{W_B}{g} v_B \frac{dv_B}{dt} / \left[ \frac{mF}{(\gamma-1)T_0} + \frac{C_i F_i}{(\gamma-1)T_i} \right]$$

$$F_z = P_z A_z + \frac{\rho_l A_z V_l^2}{g}, \quad (24)$$

where

$\gamma$  = ratio of specific heats of propellant gases.

Finally, the projectile motion can be represented based on Newton's second law of motion:

$$\frac{dV_B}{dt} = \frac{A_g}{W_B} (P_S - P_r) \quad (25)$$

$$\frac{dy}{dt} = V_B \quad (26)$$

where  $V_B$  = velocity of projectile

$P_S$  = propellant gas pressure at the base of the projectile

$P_r$  = resistive pressure due to friction between projectile and gun tube and also due to air resistance ahead of projectile.

#### IV. CONCLUSIONS.

In closure, the coefficients and exponents in the burning rate equations are approximated as

$$\begin{aligned} B = 0.04, n = 0.75 & : 3.5\text{MP} < P < 17.2\text{MP} \\ B = 0.011, n = 1.27 & : 52\text{MP} < P < 207\text{MP} \end{aligned}$$

It is assumed that there is a linear gas velocity gradient between the piston and the projectile. This has been shown to be a good approximation. As a matter of fact, it is much better than the uniform density approximation used by others.

The gas density is allowed to vary linearly between the piston and the projectile. The (transient one-dimensional) partial differential equation of motion is integrated with appropriate boundary conditions, to yield the pressures at the base of the projectile and also at the piston head. The liquid propellant droplets locations ( $X_D$ ) are determined by utilizing standard aerodynamic laws based on spherical shapes and the relative velocity between droplet and surrounding gases. In all, there are 15 coupled ordinary differential equations solved by numerical integration techniques. The unknown's are  $M, m, \rho_g, P_g, V_g,$

$V_z, z, P, T, \rho, V_B, y, P_z, P_S, X_D, S,$  and  $U.$  The pre-

liminary results indicate that there is a difference between theoretical results and experimental results. These differences can be eliminated by altering the model. This can be easily done because both the experimental results and the analytical results have similar trends.



AD P 0 0 1 0 2 8

→

Calculation of Legendre Functions on the Cut for Integral Order  
and Complex Degree by Means of Gauss Continued Fractions

Alexander S. Elder  
James N. Walbert  
Eric C. Benck  
Ballistic Research Laboratory, USAARRADCOM  
Aberdeen Proving Ground, MD 21005

ABSTRACT These functions are required for the calculation of biorthogonal functions for the hollow cone as required for solving problems in elasticity and rheology. One form of the biorthogonal function is

$$\chi = [AP_v^\mu(\cos \theta) + BQ_v^\mu(\cos \theta) + CP_{v-2}^\mu(\cos \theta) + DQ_{v-2}^\mu(\cos \theta)] R^v \sin m\phi.$$

The function is obtained by calculating  $F(-v, v+1; 1+m+l; (1-x)/2)$  and  $F(-v, v+1; 2+m+l; (1-x)/2)$  where  $l$  is a sufficiently large integer and  $x = \cos \theta$ . The hypergeometric functions  $F(-v, v+1; 1+m; (1-x)/2)$  and  $F(-v, v+1; 2+m; (1-x)/2)$  are obtained by recursion.

The Legendre functions  $P_v^{-\mu}(\cos \theta)$  and  $P_{v-1}^{-\mu}(\cos \theta)$ , are obtained from standard series taking  $\mu \gg |v|^{3/2}$  to reduce round-off error. Legendre functions for smaller values of  $\mu$  are obtained by recursion. We use the recursion formulas for the hypergeometric function rather than the formulas for the Legendre functions to reduce the exponent range of the calculations. Finally,  $P_v^\mu(\cos \theta)$  is calculated from standard formulas.

The quotient  $Q_v^\mu(\cos \theta + i0)/Q_{v-1}^\mu(\cos \theta + i0)$  can be obtained from the Gauss continued fraction for

$$F(1/2 + \mu, 1+v + \mu; v + 3/2; e^{-2i\theta}) / F(1/2 + \mu, v + \mu; v + 1/2; e^{-2i\theta}).$$

The individual functions  $Q_v^\mu(\cos \theta + i0)$  and  $Q_{v-1}^\mu(\cos \theta + i0)$  are obtained from a Wronskian relation and the functions of the first kind previously calculated. Then  $Q_v^\mu(\cos \theta)$  and  $Q_{v-1}^\mu(\cos \theta)$  can be obtained from standard formulas. Use of complex variables is essential to obtain a rapidly convergent Gauss continued fraction. This algorithm has been programmed in CDC double precision arithmetic. This program is intended only for moderate

values of  $\mu$  and  $|\nu|$ . The logarithmic solution has also been programmed.

I. INTRODUCTION: The associated Legendre functions on the cut for integral order and complex degree are required for several important mechanical applications. One area of particular interest is in the calculation of biharmonic functions for the hollow cone. Such functions appropriate for the cone satisfy

$$\nabla^4 \chi = 0$$

and come in the form

$$\chi = [AP_{\nu}^m(\cos\theta) + BQ_{\nu}^m(\cos\theta) + CP_{\nu-2}^m(\cos\theta) + DQ_{\nu-2}^m(\cos\theta)] R^{\nu} \sin m\phi.$$

These functions are required for stress analysis in the mini-hat gage, which is a strain-type pressure transducer, and in cone-plate rheometers.

We have developed a subroutine for computing

$$P_{\nu}^m(\cos\theta) \text{ and } Q_{\nu}^m(\cos\theta)$$

for

$$0 < \theta < 90^{\circ}$$

integer  $m$  such that  $0 \leq m \leq 12$

and  $\nu$  such that  $\text{Re}(\nu) > -1/2$ .

For moderate values of  $|\nu|$ , we calculate  $P_{\nu}^m(\cos\theta)$  by series and recurrence formulas. On the other hand,  $Q_{\nu}^m(\cos\theta)$  is computed through the use of a Gauss continued fraction and Wronskian relations. For small angles, the logarithmic solution is used to calculate  $Q_{\nu}^m(\cos\theta)$ . Additional analysis will be

necessary for the programming of  $\frac{\partial Q_{\nu}^m(\cos\theta)}{\partial \nu}$  and  $\frac{\partial P_{\nu}^m(\cos\theta)}{\partial \nu}$ . Asymptotic expansions are required when  $|\nu|$  is large.

Programming was done on a CDC 7600 computer in FORTRAN V. CDC double

precision arithmetic was used to get the greatest accuracy possible. Special multiple precision algorithms were avoided so that the programs would be more compatible for use by an engineering laboratory.

II. ASSOCIATED LEGENDRE FUNCTIONS OF THE FIRST KIND. The Legendre functions of the first kind can be accurately calculated for moderate  $|v|$  by

$$P_v^{-m}(\cos\theta) = \frac{1}{m!} (\tan \theta/2)^m {}_2F_1(-v, v+1; 1+m; (\sin\theta/2)^2) \quad (1)$$

and the reflection formula

$$P_v^m(\cos\theta) = (-1)^m \frac{\Gamma(v+m+1)}{\Gamma(v-m+1)} P_v^{-m}(\cos\theta) \quad (2)$$

where

$$\frac{\Gamma(v+m+1)}{\Gamma(v-m+1)} = (v+1-m)(v+2-m)\dots(v+m). \quad (2a)$$

The hypergeometric series, for small  $|v|$  ( $|v| < 2$ ), can be calculated directly from the series

$${}_2F_1(a, b; c; z) = 1 + \frac{ab}{c} \frac{z}{1!} + \frac{a(a+1)b(b+1)}{c(c+1)} \frac{z^2}{2!} + \dots \quad (3)$$

For larger values of  $|v|$ , the series becomes slowly convergent with serious round-off error. In this case, one can alter the parameters and then use a recurrence formula to obtain the desired results.

One possible method to improve the convergence of the hypergeometric series would be to increase  $m$  to a high value and then use a Legendre recurrence formula to obtain the desired answer. Unfortunately, either serious underflow or overflow problems would begin to occur in the calculation of the initial values for the Legendre recurrence formula, as found by Smith, Olver, and Lozier.<sup>4</sup> Occasionally both underflow and overflow occur in the same sequence of calculations. The necessary recurrence formula,

\*Series and Recurrence relations are obtained from references [1],[2],[3].

$$P_{\nu}^{m+1}(\cos\theta) + 2m\cot\theta P_{\nu}^m(\cos\theta) + (\nu+m)(\nu-m+1)P_{\nu}^{m-1}(\cos\theta) = 0, \quad (4)$$

also contains both linear and quadratic coefficients which would lead to rapid variations of the Legendre functions in a recurrence chain.

In order to avoid the difficulties in dealing with the Legendre function, we deal directly with the hypergeometric series using the Gauss contiguous formulas. In the required Gauss contiguous formula,

$$c(c-1)(z-1)F(a,b;c-1;z) + c[c-1-(2c-a-b-1)z]F(a,b;c;z) + (c-a)(c-b)z F(a,b;c+1;z) = 0, \quad (5)$$

the coefficients of the hypergeometric functions are of the same degree in the parameter  $c$ . Therefore, the values of the hypergeometric functions vary slowly as the parameters change in the recurrence chain. Also, the stability criterion for the Gauss contiguous formulas can be verified by elementary methods. Finally, through the use of the hypergeometric functions as the basis of our analysis, we gain an additional parameter leading to greater flexibility in deriving algorithms.

Since the Gauss contiguous formula appears to be superior for the intended work, it is used in the program. We increase  $c$  to a sufficiently large value and then increment downwards with the Gauss contiguous formula to the desired result. Using this technique has produced excellent results, provided that  $|\nu|$  is not too large.

III. ASSOCIATED LEGENDRE FUNCTIONS OF THE SECOND KIND; GAUSS CONTINUED FRACTION METHOD In attempting to calculate  $Q_{\nu}^m(\cos\theta)$ , no series was found which converges well for small  $\nu$  and  $\theta$ . Instead, an approach previously used to calculate Bessel functions of the second kind was used.<sup>5</sup> This approach utilizes the Gauss continued fraction and Wronskian relations. It was found to be highly advantageous to leave the cut for the initial calculations and work in the complex plane. However,  $Q_{\nu}^m(\cos\theta)$ , as defined on the cut  $-1 < x < +1$ , is not analytic when  $x=z$ , a complex number. We have the formula

$$Q_v^m(x) = \frac{1}{2} e^{-im\pi} [e^{-\frac{1}{2}i\pi} Q_v^m(x+i0) + e^{\frac{1}{2}i\pi} Q_v^m(x-i0)] \quad (6)$$

where  $x+i0$ ,  $x-i0$  indicate limits as the complex variable  $z$  approaches the cut. If  $v = \alpha+i\beta$ , and  $\beta$  is large

$$Q_v^m(\cos\theta+i0) \text{ is } O(e^{-\beta\theta})$$

and

$$Q_v^m(\cos\theta-i0) \text{ is } O(e^{+\beta\theta}), \text{ where } x = \cos\theta.$$

This behavior corresponds to that of Hankel functions in the theory of Bessel functions.

In the complex plane, we have

$$e^{-im\pi} Q_v^m(\cos\theta+i0) \Gamma(v+3/2) = \pi^{1/2} \Gamma(v+m+1) e^{\frac{1}{2}m\pi} (2\sin\theta)^m \times e^{-i\theta(1+v+m)} F\left(\frac{1}{2}+m, 1+v+m; v+3/2; e^{-2i\theta}\right). \quad (7)$$

Replacing  $v$  by  $v-1$  and then dividing the result into the previous equation,

$$R_v^m(\cos\theta+i0) = \frac{Q_v^m(\cos\theta+i0)}{Q_{v-1}^m(\cos\theta+i0)} = \frac{(v+m)}{(v+1/2)} e^{-i\theta} \frac{F\left(\frac{1}{2}+m, 1+v+m; v+3/2; e^{-2i\theta}\right)}{F\left(\frac{1}{2}+m, v+m; v+1/2; e^{-2i\theta}\right)} \quad (8)$$

Letting  $a = \frac{1}{2}+m, b = v+m, c = v+1/2, z = e^{-2i\theta}$ ,

$$R_v^m(\cos\theta+i0) = \frac{b e^{-i\theta}}{c} \frac{F(a, b+1; c+1; z)}{F(a, b; c; z)} \quad (9)$$

This can be calculated by using the Gauss continued fraction<sup>6</sup>

$$\frac{F(a, b+1; c+1; z)}{F(a, b; c; z)} = \frac{1}{1 - \frac{a(c-b)z}{c(c+1)} \frac{1 - (b+1)(c-a+1)z}{(c+1)(c+2)} \frac{1 - (a+1)(c-b+1)z}{(c+2)(c+3)} \frac{1 - (b+2)(c-a+2)z}{(c+3)(c+4)} \dots}$$

The Gauss continued fraction converges everywhere in the complex plane, except on the real axis from +1 to  $+\infty$ . and at isolated zeros of  $F(a, b; c; z)$ .

In order to obtain  $Q_v^m(\cos\theta+i0)$  from its continued fraction, we utilize the following Wronskian relations:

$$W\{P_v^{-m}(z), Q_v^m(z)\} = P_v^{-m}(z) \frac{dQ_v^m(z)}{dz} - Q_v^m(z) \frac{dP_v^{-m}(z)}{dz} \quad (11)$$

and

$$W\{P_v^{-m}(z), Q_v^m(z)\} = \frac{e^{i\pi m}}{(1-z^2)}.$$

Equating these, we have

$$P_v^{-m}(z) \frac{dQ_v^m(z)}{dz} - Q_v^m(z) \frac{dP_v^{-m}(z)}{dz} = \frac{e^{i\pi m}}{(1-z^2)}. \quad (12)$$

Now using the derivative relations

$$(z^2-1) \frac{dP_v^{-m}(z)}{dz} = v z P_v^{-m}(z) - (v-m) P_{v-1}^{-m}(z) \quad (13)$$

and

$$(z^2-1) \frac{dQ_v^m(z)}{dz} = v z Q_v^m(z) - (v+m) Q_{v-1}^m(z),$$

we find

$$(\nu+m) P_{\nu}^{-m}(z) Q_{\nu-1}^m(z) - (\nu-m) P_{\nu-1}^{-m}(z) Q_{\nu}^m(z) = e^{i\pi m}. \quad (14)$$

Dividing both sides by  $Q_{\nu-1}^m(z)$  and replacing  $z$  by  $\cos\theta+i0$ , we get

$$(\nu+m) P_{\nu}^{-m}(\cos\theta+i0) - (\nu-m) P_{\nu-1}^{-m}(\cos\theta+i0) R_{\nu}^m(\cos\theta+i0) = \frac{e^{i\pi m}}{Q_{\nu-1}^m(\cos\theta+i0)}. \quad (15)$$

Replacing  $\nu$  by  $\nu+1$  and then solving for  $Q_{\nu}^m(\cos\theta+i0)$ ,

$$Q_{\nu}^m(\cos\theta+i0) = \frac{e^{i\pi m}}{[(\nu+m+1)P_{\nu+1}^{-m}(\cos\theta+i0) - (\nu-m+1)P_{\nu}^{-m}(\cos\theta+i0)R_{\nu+1}^m(\cos\theta+i0)]}. \quad (16)$$

Since

$$P_{\nu}^{-m}(\cos\theta+i0) = e^{1/2 i\pi m} P_{\nu}^{-m}(\cos\theta), \quad (17)$$

$$Q_{\nu}^m(\cos\theta+i0) = \frac{e^{1/2 i\pi m}}{[(\nu+m+1)P_{\nu+1}^{-m}(\cos\theta) - (\nu-m+1)P_{\nu}^{-m}(\cos\theta)R_{\nu+1}^m(\cos\theta+i0)]}. \quad (18)$$

Now we can use the relation

$$Q_{\nu}^m(\cos\theta) = e^{3/2 i\pi m} Q_{\nu}^m(\cos\theta+i0) + i\pi/2 P_{\nu}^m(\cos\theta) \quad (19)$$

to finally get

$$Q_v^m(\cos\theta) = \frac{(-1)^m}{[(v+m+1)P_{v+1}^{-m}(\cos\theta) - (v-m+1)P_v^{-m}(\cos\theta)R_{v+1}^m(\cos\theta+i0)]} + i\pi/2 P_v^m(\cos\theta). \quad (20)$$

Results from programming the above method indicate that it works exceptionally well. Unfortunately, this method will likely run into difficulties for large  $|v|$ . Even though the Gauss continued fraction seems to converge more rapidly with increasing  $|v|$ , difficulties may be encountered because of losses in accuracy with  $P_v^m(\cos\theta)$ . For large  $|v|$ , it will be necessary to use asymptotic expansions to calculate  $Q_v^m(\cos\theta)$  and  $P_v^m(\cos\theta)$ .

Another region where trouble occurs is at small angles ( $\theta < 1^\circ$ ). The complex Gauss continued fraction algorithm is still very accurate at small angles, but the continued fraction converges at a very slow rate. Sometimes several thousand terms are required for convergence, which in turn uses an inordinate amount of computer time. This problem occurs because the argument approaches the cut of the Gauss continued fraction at  $+1$ . To avoid this problem, we use the logarithmic solution to calculate  $Q_v^m(\cos\theta)$  for small angles.

A similar method for computing  $Q_v^m(\cos\theta)$  has also been developed using real analysis only. Since no simple series formula for  $Q_v^m(\cos\theta)$  could be found, we concentrated on  $P_v^m(-\cos\theta)$  instead.  $P_v^m(-\cos\theta)$  is related to  $Q_v^m(\cos\theta)$  and  $P_v^m(\cos\theta)$  by

$$Q_v^m(\cos\theta) = \frac{\pi}{2\sin[\pi(v+m)]} \{ \cos[\pi(v+m)] P_v^m(\cos\theta) - P_v^m(-\cos\theta) \}, \quad 0 < \theta < \pi/2. \quad (21)$$

Similar computational difficulties exist for the computation of  $P_v^m(-\cos\theta)$  as  $Q_v^m(\cos\theta)$ . Using the same equations as in calculating  $P_v^m(\cos\theta)$ , we can derive the following continued fraction

$$\frac{P_v^m(-\cos\theta)}{P_{v-1}^m(-\cos\theta)} = \frac{(v+m)}{(v-m)} \frac{F(-v, v+1; 1+m; (\cos\theta/2)^2)}{F(-v+1, v; 1+m; (\cos\theta/2)^2)}. \quad (22)$$

Letting  $a=-v$ ,  $b=v$ ,  $c=m$ ,  $z=(\cos\theta/2)^2$ , then

$$S_v^m(z) = \frac{F(a,b+1;c+1;z)}{F(a+1,b;c+1;z)} = \frac{F(a,b+1;c+1;z)}{F(a,b;c;z)} \frac{F(b,a;c;z)}{F(b,a+1;c+1;z)} \quad (23)$$

This can be calculated by either two Gauss continued fractions or by two continued fractions of Frank<sup>7</sup> which are of the form

$$\frac{F(a,b;c;z)}{F(a,b+1;c+1;z)} = 1 - \frac{a(c-b)z}{c(c+1)} \cfrac{\frac{(a-b)z}{(c+1)} + 1 - \frac{(a+1)(c+1-b)z}{(c+1)(c+2)}}{\frac{(a+1-b)z}{(c+2)} + 1 - \frac{(a+2)(c+2-b)z}{(c+2)(c+3)}} \cfrac{\frac{(a+2-b)z}{(c+3)} + 1 - \dots}{\dots}$$

The continued fraction of Frank has its cut on the unit circle. It has proved to be of little value here because of its much slower convergence rate as compared to the Gauss continued fraction. This is especially true for small angles, which effectively limit the use of the Frank continued fraction to angles greater than  $30^\circ$ .

Utilizing similar Wronskian relations as in the complex analysis, we proceeded in a similar manner, with the exception of replacing  $Q_v^m(\cos\theta)$  by Eq. (21). The final result of the real analysis is then

$$Q_v^m(\cos\theta) = \frac{\pi}{2} P_v^m(\cos\theta) \cot[\pi(v+m)] + \frac{(-1)^m}{(v+1+m)[P_{v+1}^{-m}(\cos\theta) + P_v^{-m}(\cos\theta)S_{v+1}^m(z)]} \quad (25)$$

This result can easily be seen to be inferior to the complex analysis since it is undefined for integral  $\nu$ . Also, it is necessary to calculate two continued fractions which have relatively slow convergence rates which worsen with increasing  $|\nu|$ . Therefore, only the complex algorithm is used in the final programming. The real method will be useful in helping to check and compare the accuracy of the complex method for calculating  $Q_\nu^m(\cos\theta)$ .

IV. ASSOCIATED LEGENDRE FUNCTIONS OF THE SECOND KIND; THE LOGARITHMIC SOLUTION As mentioned previously, the logarithmic solution is used for the calculation of  $Q_\nu^m(\cos\theta)$  at small angles ( $\theta < 1^0$ ). From references [1] and [2], the following formulas can be derived

$$\begin{aligned}
 Q_\nu^m(\cos\theta) = & \frac{1}{2} P_\nu^m(\cos\theta) \left[ \log(1/\tan^2(\theta/2)) - 2\gamma - 2\psi(\nu+1) + \sum_{s=1}^m \frac{2s-1}{(\nu+s)(\nu+1-s)} \right] \\
 & + \frac{(-1)^m}{2\nu} \left( \frac{1}{\tan\theta/2} \right)^m \sum_{r=0}^m (-v^2)(1-v^2)(4-v^2)\dots((r-1)^2-v^2)(\nu+r) \frac{(m-r-1)!}{r!} \\
 & (-1)^r (\sin\theta/2)^{2r} \\
 & + \frac{(\sin\theta/2)^m}{2\nu} \sum_{\ell=1}^{\infty} \frac{(-v^2)(1-v^2)\dots((m+\ell-1)^2-v^2)(m+\nu+\ell)}{\ell!(m+\ell)!} \\
 & \left( 1 + \frac{1}{2} + \frac{1}{3} + \dots + \frac{1}{\ell} \right) (\sin\theta/2)^{2\ell} \\
 & + \frac{(-1)^m}{2\nu} (\nu-m+1)(\nu-m+2)\dots(\nu+m) (\tan\theta/2)^m \\
 & \sum_{r=0}^{\infty} \frac{(-v)^2(1-v^2)\dots((r-1)^2-v^2)(\nu+r)}{v! (r+m)!} \left( 1 + \frac{1}{2} + \frac{1}{3} + \dots + \frac{1}{m+r} \right) (\sin\theta/2)^{2r}
 \end{aligned} \tag{26}$$

For  $m=0$ , but  $v$  not an integer,

$$Q_v^0(\cos\theta) = \frac{1}{2} P_v^0(\cos\theta) [\log(\cot^2(\theta/2)) - 2\gamma - 2\psi(v+1)] \\ + \frac{1}{v} \sum_{\ell=1}^{\infty} \frac{(-v^2)(1-v^2)\dots((\ell-1)^2-v^2)(\ell+v)}{(\ell!)^2} \left(1 + \frac{1}{2} + \frac{1}{3} + \dots + \frac{1}{\ell}\right) (\sin\theta/2)^{2\ell} . \quad (26a)$$

For  $m=0$  and  $v=n$ , an integer,

$$Q_n^0(\cos\theta) = \frac{1}{2} P_n^0(\cos\theta) [\log(\cot^2(\theta/2)) - 2(1 + \frac{1}{2} + \frac{1}{3} + \dots + 1/n)] \\ + \sum_{\ell=1}^n \frac{(-1)^\ell (n+\ell)! (1 + \frac{1}{2} + \frac{1}{3} + \dots + \frac{1}{\ell})}{(\ell!)^2 (n-\ell)!} (\sin\theta/2)^{2\ell} . \quad (26b)$$

Comparing this method with alternate methods of calculating  $Q_v^m(\cos\theta)$ , shows a significant loss of accuracy in calculating the logarithmic solution in the range  $|v| < 10$ . The loss of accuracy stems from the psi function subroutine. The asymptotic series used in the calculation of  $\psi(v+1)$  for small  $v$  does not obtain the desired accuracy. At its worst, only 12 significant figures can be obtained. Outside this range, the logarithmic solution is as accurate as the rest of the programming. Even though this method can have some losses of accuracy, it requires a much more reasonable amount of computer time to execute for small angles than the Gauss continued fraction.

**RESULTS** The tables given in Appendix A are examples of the results of our programming. Throughout most of the intended range at least 25 significant figures can be obtained. The only significant loss occurs for  $Q_v^H(\cos\theta)$  in the range  $\theta < 1^\circ$  and  $|v| < 10$  where the logarithmic solution is utilized. For certain values in this range, accuracies of only 12 significant figures can be obtained.

In the certain cases  $P_{-1/2+1\lambda}^m(\cos\theta)$  and  $Q_\nu^m(\cos\theta)$  for real  $\nu$ , the imaginary parts can be analytically shown to equal zero. Therefore, the remaining imaginary parts from our programming in these cases provide a quick check on the accuracy of the programming.

VI. CONCLUSION We have developed an accurate and efficient method of calculating the associated Legendre functions for integral order and complex degree. The programming for this paper was done in double precision FORTRAN V.

In general, the accuracy of  $P_\nu^m(\cos\theta)$  and  $Q_\nu^m(\cos\theta)$  was approximately equal to the maximum accuracy attainable with double precision arithmetic. By comparing with special cases and alternate means of calculating the associated Legendre functions (Gaussian quadratures, alternate series of formulas), the modulus of the results appeared to be accurate to at least 25 significant figures. The upper limit of  $|\nu|$  at which this programming is still highly accurate has not yet been determined. It is expected that the cutoff range will probably lie somewhere in the region  $60 < \nu < 100$ .

The logarithmic solution, used in calculating  $Q_\nu^m(\cos\theta)$  for  $\theta < 1^\circ$ , is not as accurate as the rest of the programming in the range  $|\nu| < 10$ . In this range the modulus can be accurate to as few as 12 significant figures. Work is continuing to improve the accuracy of the logarithmic solution. The logarithmic solution is used to reduce the excessive computer time which the complex Gauss continued fraction method requires for small angles.

In routines still under development at BRL, special series and nonhomogeneous recurrence formulas are being used to calculate  $\frac{\partial P_\nu^m}{\partial \nu}(\cos\theta)$  and  $\frac{\partial Q_\nu^m}{\partial \nu}(\cos\theta)$ . Also being programmed are asymptotic expansions to extend the range of  $|\nu|$  to very large values. For small angles ( $\theta < 30^\circ$ ), Bessel function expansions will be used<sup>8</sup>. Special hypergeometric series along with sines and cosines will be used for larger angles.

---

Note added in proof

The error in the program for the psi function was discovered and corrected late in August. Calculations for  $Q_\nu^m(\cos\theta)$  obtained from the logarithmic

APPENDIX A  
NUMERICAL CALCULATIONS

solution and by means of the Gauss continued fraction now agree to 25 significant figures when  $|v| < 10$ . These corrections will be incorporated in the BRL Report.

#### REFERENCES

1. A. Erdelyi, et. al., Higher Trancendental Functions, Vol. 1, Bateman Manuscript Project, McGraw Hill Book Co., Inc., New York, 1953.
2. W. Magnus and F. Oberhettinger, Formulas and Theorems for the Special Functions of Mathematical Physics, Chelsea publishing Co., New York, 1949.
3. M. Abramowitz and J.A. Stegun, Handbook of Mathematical Functions with Formulas, Graphs, and Mathematical Tables, National Bureau of Standards, Washington, D.C., No. 55, Applied Mathematics Series, June 1964.
4. J.M. Smith, F.V.J. Olver and D.W. Lozier, "Legendre Polynomials," ACM Transactions on Mathematical Software, 7, 94-95, (1981).
5. A.S. Elder, "Formulas for Calculating Bessel Functions of Integral Order and Complex Argument," USA Ballistic Research Laboratory, Report No. 1423, (1968).
6. H.S. Wall, Analytic Theory of Continued Fractions, d. Van Nostrand Company, Inc., New York, 1948.
7. E. Frank, "A New Class of Continued Fraction Expansions for the Ratios of Hypergeometric Functions," Transactions of the American Mathematical Society 81, 454, (1956).
8. N.K. Chu Khrukidze, "Asymptotic Formulae for Legendre Functions," USSR Computational Mathematics and Mathematical Physics, 6, (1966).

LEGENDRE FUNCTION OF THE FIRST KIND  
 COMPLEX DEGREE  
 OF ORDER M=1

$P'_{\frac{1}{2}M}$  (.5)

$T^{\circ}$	RE(P)	IM(P)	PI
0.0	.19283D+01	0.	.1928259688113789174434852D+01
5.0	.21508D+01	-.17831D+00	.2158176100171473440761966D+01
10.0	.28542D+01	-.23317D+00	.2863659780970458842277890D+01
15.0	.41267D+01	.46458D-01	.4126977466186821020326076D+01
20.0	.60389D+01	.10514D+01	.6129724822597131899761240D+01
25.0	.84842D+01	.34262D+01	.9149912295777483731255082D+01
30.0	.10900D+02	.80476D+01	.1354901172068409761426361D+02
35.0	.11902D+02	.15759D+02	.1974864446399352141754244D+02
40.0	.90258D+01	.26701D+02	.2818511588552356896644090D+02
45.0	-.99719D+00	.39221D+02	.3923325343547951799172666D+02
50.0	-.20927D+02	.48802D+02	.5309943506798511542732713D+02
55.0	-.50514D+02	.48020D+02	.6969627297539731201857550D+02
60.0	-.83715D+02	.28787D+02	.8852620143781054579469150D+02
65.0	-.10786D+03	-.12808D+02	.1086130544687463880522555D+03
70.0	-.10714D+03	-.70980D+02	.1285224122384756340016543D+03
75.0	-.70810D+02	-.12825D+03	.1464971456516190779006579D+03
80.0	-.14646D+01	-.16069D+03	.1607039134070375039410322D+03
85.0	.79443D+02	-.14978D+03	.1695474850140847489642333D+03
90.0	.14394D+03	-.94119D+02	.1719777613030166201808234D+03

LEGENDRE FUNCTION OF THE FIRST KIND  
 COMPLEX DEGREE  
 OF ORDER M=10

$P_{10}^m(x)$  (.5)

T	RE(P)	IM(P)	IPI
0.0	-.175670-23	0.	.17567406452001785565315590-23
5.0	-.457180+04	.865330+04	.97867218322653841041196340+04
10.0	-.314130+05	.176430+05	.36028196115072803808138740+05
15.0	-.112830+06	-.170590+05	.11411378337902771629119110+06
20.0	-.208830+06	-.253910+06	.32876048346744076803377290+06
25.0	.875990+05	-.862090+06	.86653132185731852923980780+06
30.0	.169110+07	-.124020+07	.20970662619339281734298520+07
35.0	.453820+07	.112870+07	.46764644832455623253170960+07
40.0	.390600+07	.881660+07	.96406101840753922149059480+07
45.0	-.921090+07	.159540+08	.18421790515796532619486960+08
50.0	-.325880+08	.265790+07	.32695988141790905195968170+08
55.0	-.332640+08	-.425150+08	.53981465789233646563728960+08
60.0	.279720+08	-.781350+08	.82991034618931210835185680+08
65.0	.116450+09	-.239480+08	.1188920593519715894629010+09
70.0	.106550+09	.117690+09	.15876225186147215154304490+09
75.0	-.608360+08	.188070+09	.19766507335310095814740260+09
80.0	-.224820+09	.459240+08	.22946616538431742736989990+09
85.0	-.162080+09	-.188200+09	.24837460556835351141106830+09
90.0	.864590+08	-.235270+09	.25065147977222993928132580+09

LEGENDRE FUNCTION OF THE SECOND KIND  
 COMPLEX DEGREE  
 OF ORDER M=1

$U_{2,1}^{\nu}(\cdot, 5)$

T°	RE(Q)	IM(Q)	!Q!
57.5	.766970+02	.742800+02	.10677085492860820934246040+03
57.6	.429460+02	.133800+03	.14052254738536134110099030+03
57.7	-.363390+02	.172960+03	.17673481054961012911209420+03
57.8	-.143980+03	.155510+03	.21192600528957554404911840+03
57.9	-.233290+03	.637540+02	.24184806515241059912142830+03
58.0	-.250400+03	-.781720+02	.26232049438736520326844760+03
58.1	-.172370+03	-.208110+03	.27022321733888762321551580+03
58.2	-.299010+02	-.262620+03	.26431475287966178420985210+03
58.3	.109360+03	-.219870+03	.24556770877396376688049970+03
58.4	.185690+03	-.112070+03	.2168909948370819948460040+03
58.5	.182340+03	.168200+01	.18235249649482025331748610+03
58.6	.125230+03	.754460+02	.14619960499263037814845090+03
58.7	.556420+02	.972130+02	.11201023075871074579105440+03
58.8	.330660+01	.821310+02	.8219736250682050309840370+02
58.9	-.228720+02	.532080+02	.57915579570664339019365650+02
59.0	-.285920+02	.269220+02	.39272587759803798006009100+02
59.1	-.238170+02	.961980+01	.25686135076695285203435320+02
59.2	-.162260+02	.766550+00	.16243738983723713501527600+02
59.3	-.962450+01	-.265250+01	.99833653481520635570144100+01
59.4	-.500180+01	-.346520+01	.60848942002130322855059510+01
59.5	-.201890+01	-.351430+01	.40529671016597781477783160+01

LEGENRE FUNCTION OF THE SECOND KIND  
 COMPLEX DEGREE  
 OF ORDER M=10

$Q_{2m}^m (0.5)$

$\gamma$	RE (Q)	IM (Q)	:C:
57.5	-.30838D+08	.80986D+08	.8665892504808939120011191U+08
57.6	-.97126D+08	-.30047D+08	.1016676631684915507256846D+09
57.7	.23620D+08	-.18191D+09	.1834338145301002362238196D+09
57.8	.27473D+09	-.87713D+08	.2883900964858638118524417D+09
57.9	.25152D+09	.25686D+09	.3595011393852248646233413D+09
58.0	-.14957D+09	.34743D+09	.3782595851276043292972753D+09
58.1	-.370C1D+09	-.41902D+08	.3723724995989596125389625D+09
58.2	-.65276D+08	-.36197D+09	.3678087514662628100563560D+09
58.3	.28871D+09	-.18294D+09	.3417854866099812991461015D+09
58.4	.23110D+09	.13795D+09	.2691424684710954185029470D+09
58.5	-.14857D+08	.16760D+09	.1682617546537580692969713D+09
58.6	-.89733D+08	.99449D+07	.9028242752038134450690579D+08
58.7	-.12504D+08	-.71791D+08	.7287193730271655602441233D+08
58.8	.47975D+08	-.50989D+08	.7001021968127669672669953D+08
58.9	.51513D+08	-.21060D+08	.5565216027851491663680815D+08
59.0	.41385D+08	-.17081D+08	.4477153244625372403167582D+06
59.1	.41213D+08	-.23506D+08	.4744486266497728843344702D+08
59.2	.48107D+08	-.27254D+08	.5529036759747865711439618D+08
59.3	.56418D+08	-.26786D+08	.6245407061253059287527080D+08
59.4	.64259D+08	-.21250D+08	.6833541521031097238195973D+08
59.5	.70887D+08	-.17085D+08	.7291725044065368809826759D+08

LEGENDRE FUNCTION OF THE SECOND KIND  
 REAL DEGREE  
 OF ORDER M=1

QY (.5)

V	RE(Q)	IM(Q)	ICI
.1	-.12147D+01	.80148D-27	.1214729831787468904014472D+01
.5	-.13217D+01	.58060D-26	.1321735968318148511510837D+01
1.0	-.10531D+01	.12975D-25	.1053063344637798747398940D+01
1.5	-.31585D+00	.18680D-25	.3158481299074220286859035D+00
2.0	.72981D+00	.19993D-25	.7298060598018049369381857D+00
2.5	.17818D+01	.15752D-25	.1781762440653684814270190D+01
3.0	.24919D+01	.54779D-26	.2491852591708954292271142D+01
5.0	-.93897D+00	-.33422D-25	.9389683027208977621403322D+00
10.0	.30252D+01	-.45438D-25	.3025224135390428165893211D+01
15.0	.51429D+01	.24082D-25	.5142880448081924064676661D+01
20.0	.16408D+01	.12056D-24	.1640757079927005441272228D+01
25.0	-.47689D+01	.11713D-24	.4768885023680780976087511D+01
30.0	-.71988D+01	-.51143D-25	.7198807367671732724696795D+01
40.0	.60285D+01	-.22537D-24	.6028464981382909025653896D+01
50.0	.25168D+01	.42611D-24	.2516786983916781053353678D+01

LEGENDRE FUNCTION OF THE SECOND KIND  
 REAL DEGREE  
 OF ORDER M=10

$Q_0^M$  (.5)

V	RE(Q)	IM(Q)	ICI
.1	.44220D+08	.20802D-20	.4422019441063084063027027D+08
.5	.44992D+08	.84264D-21	.4499152949357942571172878D+08
1.0	.46540D+08	-.11364D-20	.465402311111111111111111D+08
1.5	.48805D+08	.58355D-21	.4880508920090121938912310D+08
2.0	.51896D+08	.26140D-20	.5189632000000000000000D+08
2.5	.55972D+08	.10642D-20	.5597232143658146092088463D+08
3.0	.61249D+08	.26472D-20	.61248853333333333333333D+08
5.0	.10245E+09	.36158D-20	.1024546133333333333333D+09
10.0	.19325D+10	-.33475D-17	.1932505390653060265343828D+10
15.0	-.14338D+12	.76848D-15	.1433781263803476703462301D+12
20.0	-.55354D+12	-.53513D-13	.5535387942959007654405168D+12
25.0	.23167D+14	-.21982D-12	.2316748691686197413966697D+14
30.0	.95826D+14	.28102D-11	.9582603845208352062519367D+14
40.0	-.23100D+16	-.51656D-11	.2309966419476341425267896D+16
50.0	.12973D+17	-.64892D-09	.1297283270469044388418573D+17

CONICAL LEGENDRE FUNCTION OF THE FIRST KIND  
 COMPLEX DEGREE  
 OF ORDER M=1

$P_{\lambda, \nu}^{\mu}$  (.5)

Y	RE(P)	IM(P)	IPI
.1	.155520+00	-.613440-37	.15552007267513654263023250+00
.5	.308900+00	-.788810-47	.30889931143353596441863850+00
1.0	.852490+00	-.717660-47	.85249333434783483823985720+00
1.5	.199730+01	.466350-35	.19973262751681190295872210+01
2.0	.418770+01	0.	.41877084758316896827828910+01
2.5	.824640+01	-.644430-32	.82464104821428748796918980+01
3.0	.156510+02	.380050-33	.15651379836797780973855520+02
5.0	.171430+03	-.732040-30	.17143494782052233848947420+03
10.0	.467810+05	-.823390-27	.46781022940599679876805790+05
15.0	.108530+08	-.126990-25	.10852960776347177009844210+08
20.0	.236410+10	-.263930-21	.23640638837358112648967540+10
25.0	.497810+12	-.208280-19	.49781366889965494786618090+12
30.0	.102630+15	.899050-17	.10262960807376627389172410+15
40.0	.419250+19	.818360-12	.41925103953819107803860260+19
50.0	.165700+24	-.354510-07	.16570401429028412573707120+24

CONICAL LEGENDRE FUNCTION OF THE FIRST KIND  
 COMPLEX DEGREE  
 OF ORDER M=10

$P_{10}^{\nu}(z)$  (.5)

Y	RE(P)	IM(P)	IPI
.1	.489140+03	-.940100-26	.48913585134593560012170610+03
.5	.114780+04	-.293120-43	.11478410243829040410861450+04
1.0	.500700+04	-.421510-43	.50070386186075993238050600+04
1.5	.218580+05	.510360-31	.21857825018393532089200930+05
2.0	.920750+05	0.	.92075211208276866556112640+05
2.5	.373930+06	-.292220-27	.37392953232534501245459720+06
3.0	.146520+07	.355790-28	.14652154098920242714762300+07
5.0	.246960+09	-.105450-23	.24695549286117219972770460+09
10.0	.137230+14	-.241540-18	.13723468018111848115909750+14
15.0	.128830+18	-.150740-15	.12882834633792463793109230+18
20.0	.433690+21	.738980-08	.43369083034979352196541640+21
25.0	.779040+24	-.129130-04	.77904260498089933257409090+24
30.0	.925260+27	.223460-01	.92526360969238511960080180+27
40.0	.590890+33	-.885940+04	.59089366337138470757923660+33
50.0	.193830+39	.112640+10	.19382736426993325063842310+39

CONICAL LEGENDRE FUNCTION OF THE SECOND KIND  
 COMPLEX DEGREE  
 OF ORDER M=1

$$Q_{\frac{1}{2}+iY}^{(1)}(\cdot 5)$$

Y	RE(U)	IM(C)	(CI)
.1	-.77264D+00	-.74317D-01	.7762014449479514948190226D+00
.5	-.70177D+C0	-.44502D+00	.8309762935091629828831826D+00
1.0	-.54069D+00	-.13341D+01	.1439505070071872545380754D+01
1.5	-.38026D+C0	-.31369D+01	.3159850133794794020391434D+01
2.0	-.25513D+00	-.65780D+01	.6582936937967470642573545D+01
2.5	-.16671D+C0	-.12953D+02	.1295450011993121097935867D+02
3.0	-.10712D+00	-.24585D+02	.2458536300852372259696280D+02
5.0	-.16662D-01	-.26929D+03	.2692843868362017280961636D+03
10.0	-.12310D-03	-.73483D+05	.7348345849880177044514794D+05
15.0	-.61543D-07	-.17048D+08	.1704779692233492042226242D+08
20.0	.52328D+01	-.37135D+10	.3713462862599816990964776D+10
25.0	.44549D+C8	-.78194D+12	.7819418950269444511616637D+12
30.0	.86531D+14	.64910D+14	.1081704865803723968194729D+15
40.0	.49804D+10	.65856D+19	.6585574926816694581238248D+19
50.0	.84420D+05	.26029D+24	.2602872569823473629081995D+24

CONICAL LEGENDRE FUNCTION OF THE SECOND KIND  
 COMPLEX DEGREE  
 OF ORDER M=10

$Q_{10}^m(x) (0.5)$

Y	RE(C)	IM(C)	ICI
.1	.437820+08	-.233740+03	.43781989399457307721149980+08
.5	.435000+08	-.165360+04	.43499831939445316981130020+08
1.0	.426310+08	-.763570+04	.42630825762273961890454350+08
1.5	.412240+08	-.343290+05	.412243355237761774941548300+08
2.0	.393400+08	-.144630+06	.39339978251706168803719860+08
2.5	.370540+08	-.567370+06	.37058171837997440309511730+08
3.0	.344540+08	-.230160+07	.34530799179481372592288350+08
5.0	.227690+08	-.367920+09	.3885844270555205139822480+09
10.0	.384040+07	-.215570+14	.21556773153737672893928180+14
15.0	.292870+06	-.202360+18	.20236309321467289828164950+18
20.0	-.700740+11	-.681240+21	.68123996330234816908619560+21
25.0	-.694020+19	-.122370+25	.12237197265179322867840160+25
30.0	-.996560+27	-.155210+28	.18444759122757150914669060+28
40.0	-.270780+25	.928170+33	.92817359724582902151311800+33
50.0	-.315580+21	.304460+39	.30446331182754753912411440+39

LEGENDRE FUNCTION OF THE SECOND KIND  
 REAL DEGREE  
 OF ORDER M=0

$Q_2^0(\cos T)$

T°	COMPLEX GAUSS CONTINUED FRACTION METHOD	SPECIAL CASE (FOR ACCURACY CHECK) $Q_2^0(\cos T) = \text{LOG}(\cot^2(T/2))$ $+(3\cos^2(T)-1)/4 - 3/2\cos(T)$
.01	.7846543924828646523610051D+01	.7846543924828646523610051D+01
.10	.5543929083720490521528767D+01	.5543929083720490521528767D+01
.50	.3933951318124424740236797D+01	.3933951318124424740236797D+01
1.00	.3239410991461712058234597D+01	.3239410991461712058234597D+01
10.00	.8488417132323570536433152D+00	.8488417132323570536433152D+00
20.00	.21368715885539562955563D-01	.21368715885539562955563D-01
30.00	-.4759394200986475272549308D+00	-.4759394200986475272549308D+00
40.00	-.7647683970726550081259554D+00	-.7647683970726550081259554D+00
50.00	-.8728124046175654413013493D+00	-.8728124046175654413013493D+00
60.00	-.8186632680417568557122028D+00	-.8186632680417568557122028D+00
70.00	-.6286869187008021321194748D+00	-.6286869187008021321194748D+00
80.00	-.3402505773017355382714222D+00	-.3402505773017355382714222D+00

LEGENRE FUNCTION OF THE SECOND KIND  
 REAL DEGREE  
 OF ORDER M=0

$Q_2^2(\cos T)$

LOGARITHMIC  
 SOLUTION

SPECIAL CASE  
 (FOR ACCURACY CHECK)  
 $Q_2^2(\cos T) = \text{LOG}[\cos^2(T/2)]$   
 $*(3\cos^2(T)-1)/4 - 3/2*\cos(T)$

$T^\circ$	LOGARITHMIC SOLUTION	SPECIAL CASE (FOR ACCURACY CHECK) $Q_2^2(\cos T) = \text{LOG}[\cos^2(T/2)]$ $*(3\cos^2(T)-1)/4 - 3/2*\cos(T)$
.001	.10149129419463179221840000+02	.10149129419463179221840000+02
.005	.85396914025408148341674130+01	.85396914025408148341674130+01
.010	.78465439248286465236097320+01	.78465439248286465236097320+01
.050	.62370980886374955708579670+01	.62370980886374955708579670+01
.100	.55439290837204905215284480+01	.55439290837204905215284480+01
.250	.46275062070036467500059950+01	.46275062070036467500059950+01
.500	.39339513181244247402364790+01	.39339513181244247402364790+01
.750	.35278779523052303898696420+01	.35278779523052303898696420+01
1.000	.32394109914617120582342780+01	.32394109914617120582342780+01
5.000	.16013306569183374630464030+01	.16013306569183374630464030+01
10.000	.84884171323235705364295480+00	.84884171323235705364295480+00

LEGENDRE FUNCTION OF THE SECOND KIND  
 OF DEGREE  $\nu=0.1$   
 OF ORDER  $m=0$

$Q_{\nu}^m(\cos t)$

$t^{\circ}$	LOGARITHMIC SOLUTION	COMPLEX GAUSS CONTINUED FRACTION METHOD
.005	.94862307847470407285922310+01	.90862307847438733186655740+01
.010	.91930835960243609350807400+01	.91930835960211875257560770+01
.050	.75836454514429439328132290+01	.75836454514397705227523670+01
.100	.68904975992741527472418780+01	.68904975992709793375803930+01
.250	.59742025442558357907450050+01	.59742025442526623824797590+01
.500	.52810411013397401964307430+01	.52810411013365667931493360+01
.750	.48755535282315919467464240+01	.48755535282284185517724610+01
1.000	.4587841225609607500059560+01	.45878412256064341760925050+01
5.000	.29770072346883877190183830+01	.29770072346851949738569520+01
10.000	.2250030914101047133259370+01	.22800309141578763845408060+01

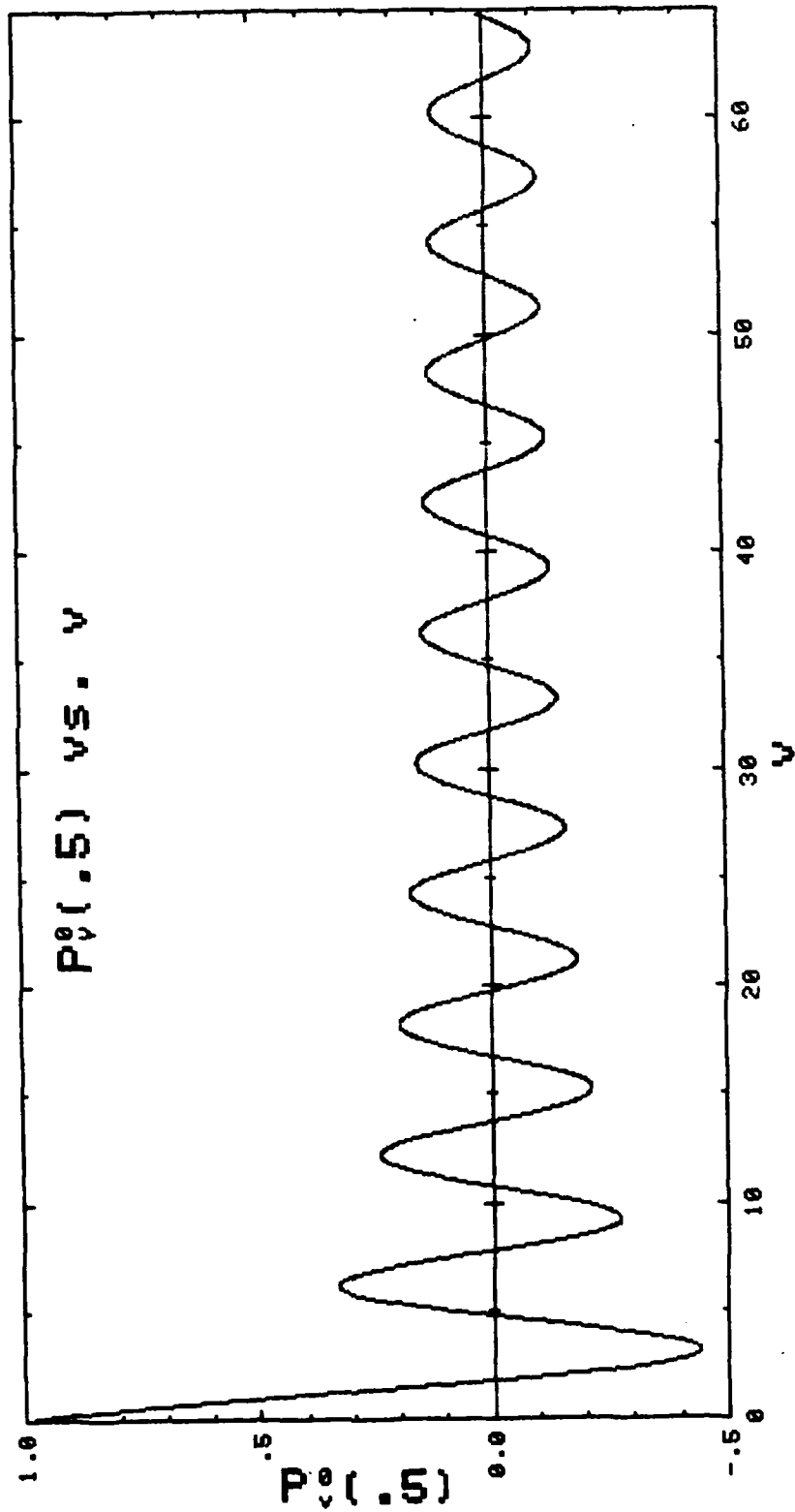
LEGENDRE FUNCTION OF THE SECOND KIND  
 OF DEGREE  $\nu=10.5$   
 OF ORDER  $M=1$

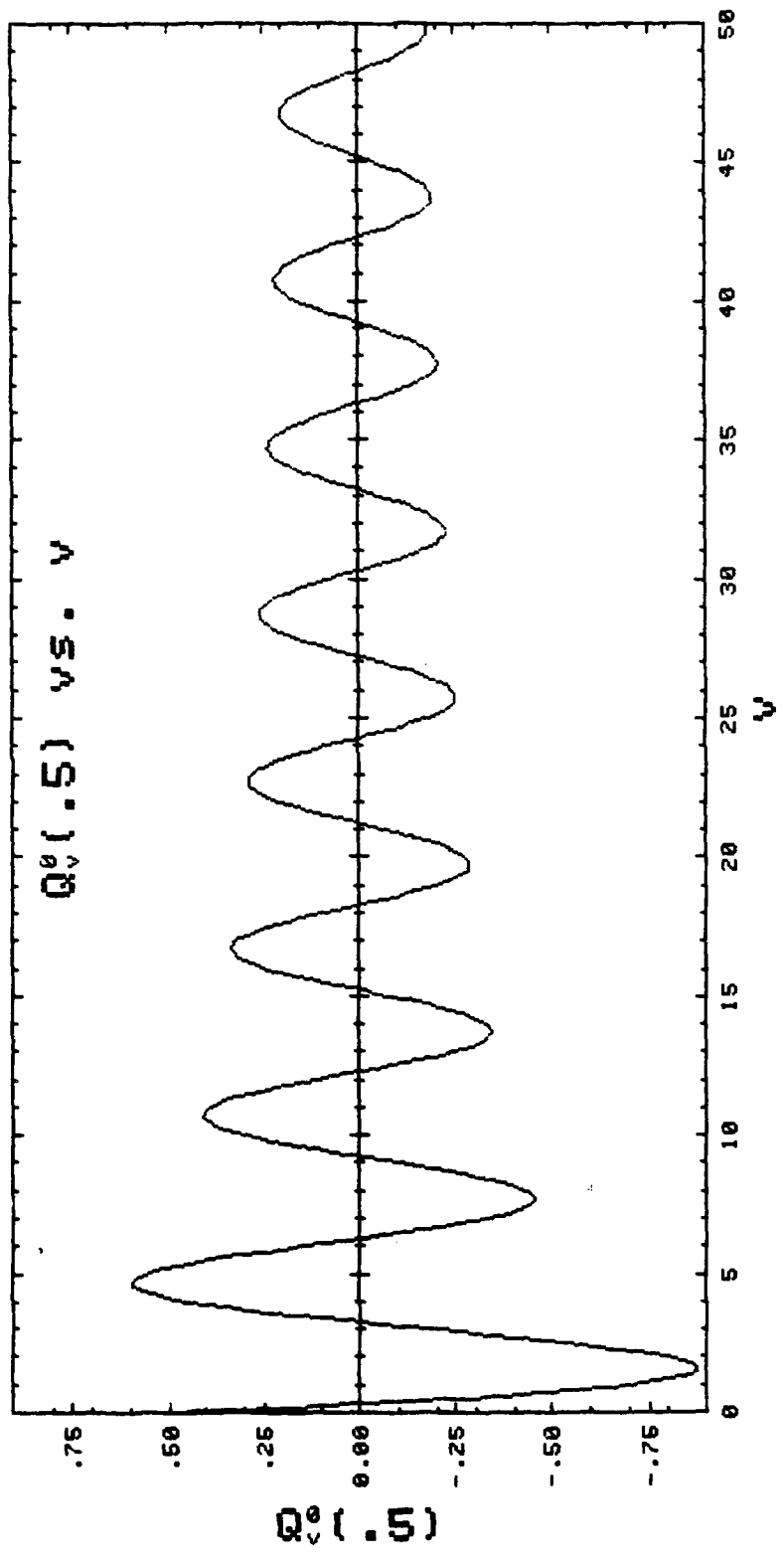
$$Q_{10.5}^{(1)}(\cos \theta)$$

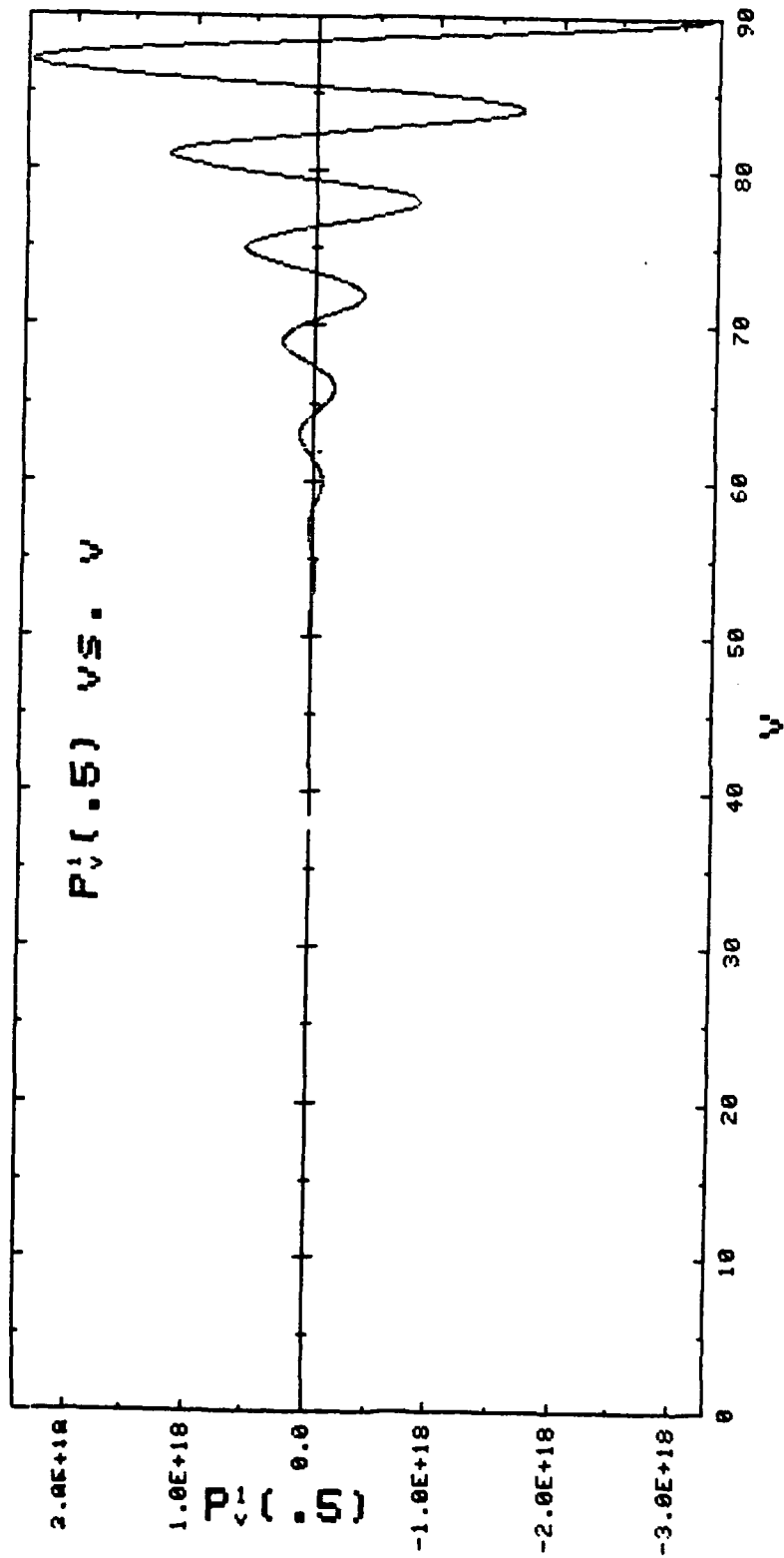
T	LOGARITHMIC SOLUTION	COMPLEX GAUSS CONTINUED FRACTION METHOD
.005	-.11459195770945768881171870+05	-.11459195770945768881171870+05
.010	-.57296503839534367514029990+04	-.57296503839534367814029990+04
.050	-.11461929533880912255798930+04	-.11461929533880912255798930+04
.100	-.57343946311317633105893220+03	-.57343946311317633105893220+03
.250	-.23014563676988900106772980+03	-.23014563676988900106772980+03
.500	-.11614982435180295584522110+03	-.11614982435180295584522110+03
.750	-.78407963278666147798055460+02	-.78407963278666147796055460+02
1.000	-.59671851253427786672521210+02	-.59671851253427766672521210+02
5.000	-.14122993109806857135954470+02	-.14122993109806857135954470+02
10.000	-.26651079459708560980737880+01	-.26651079459708560980737880+01

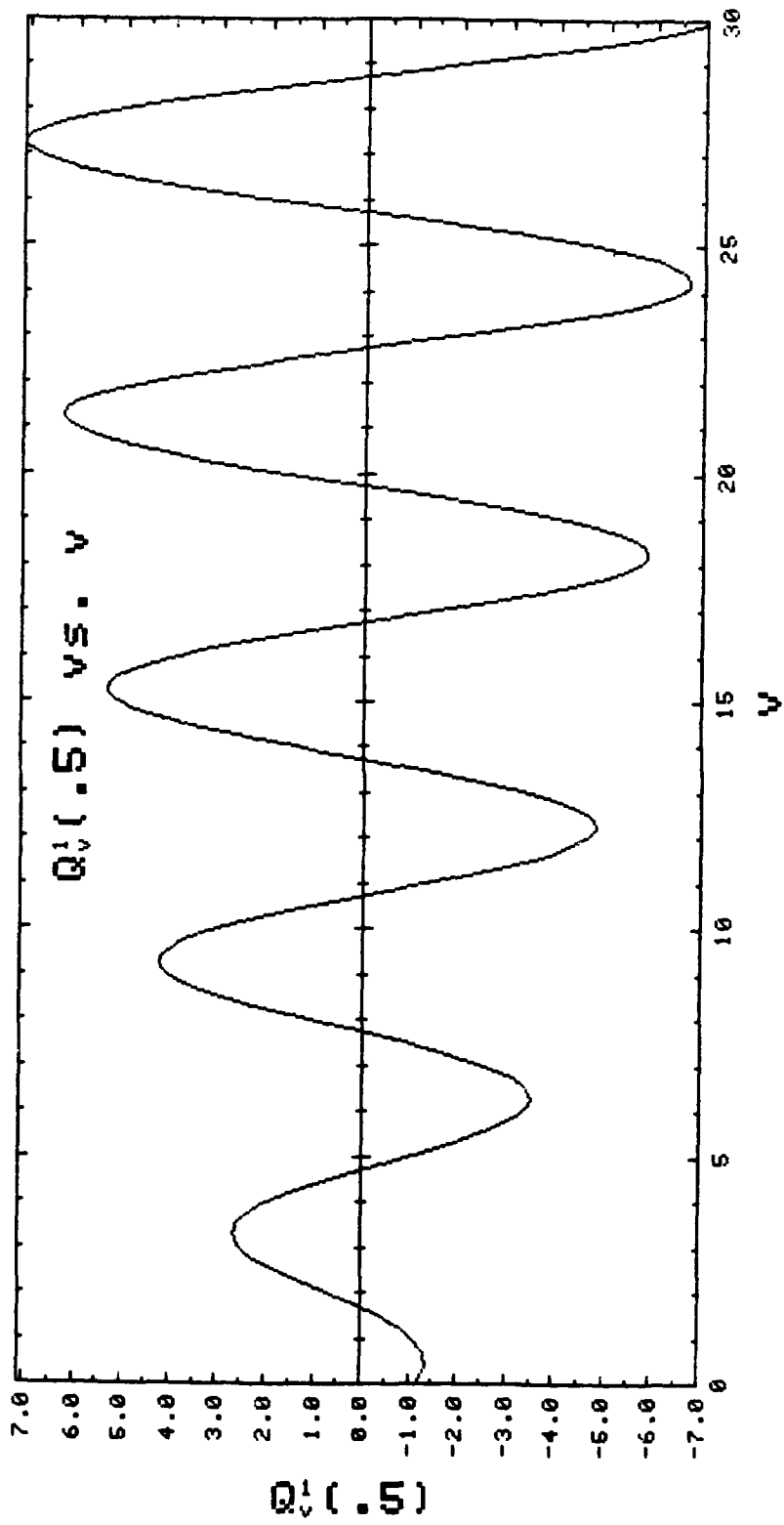
APPENDIX B

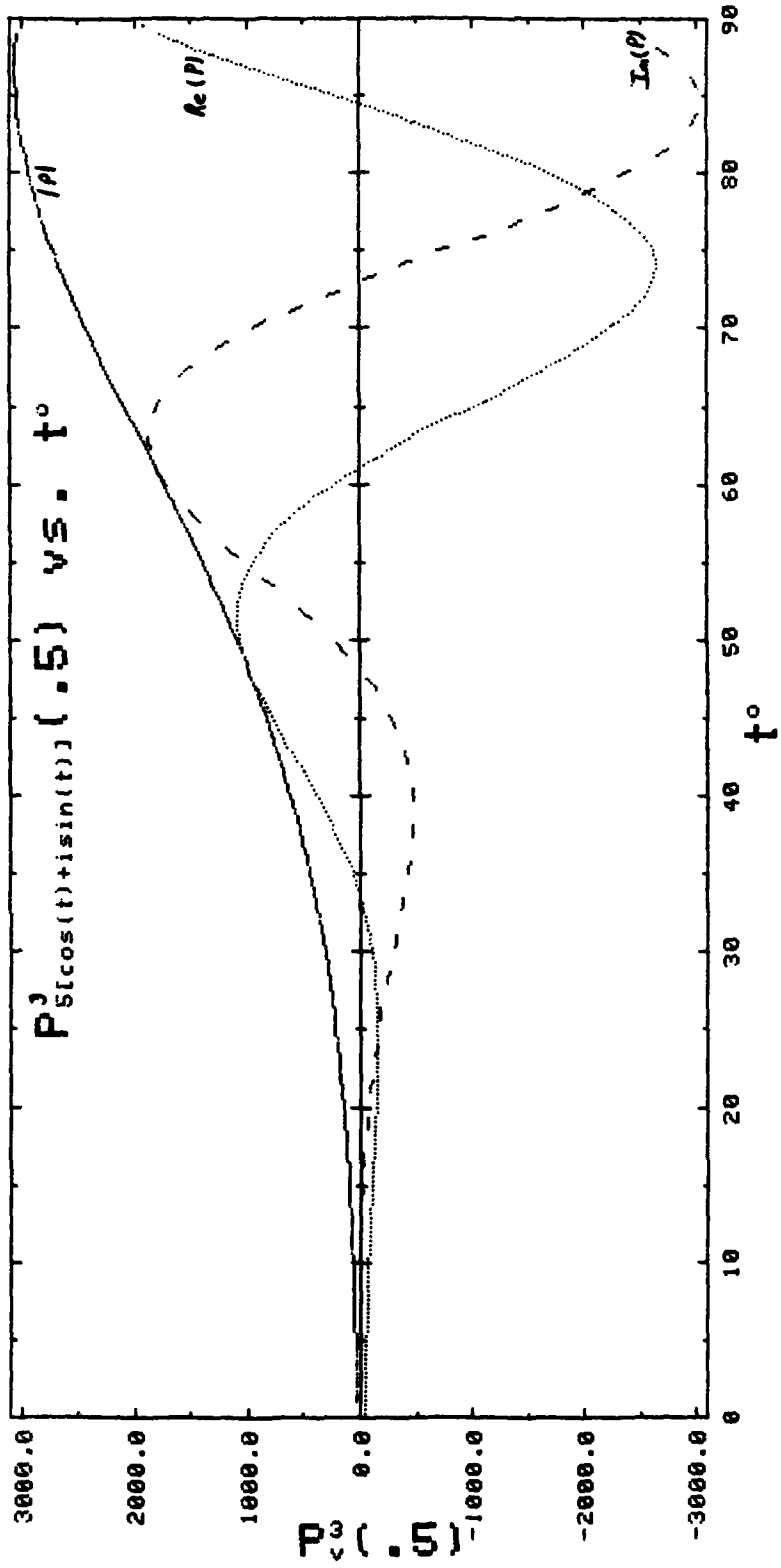
GRAPHS

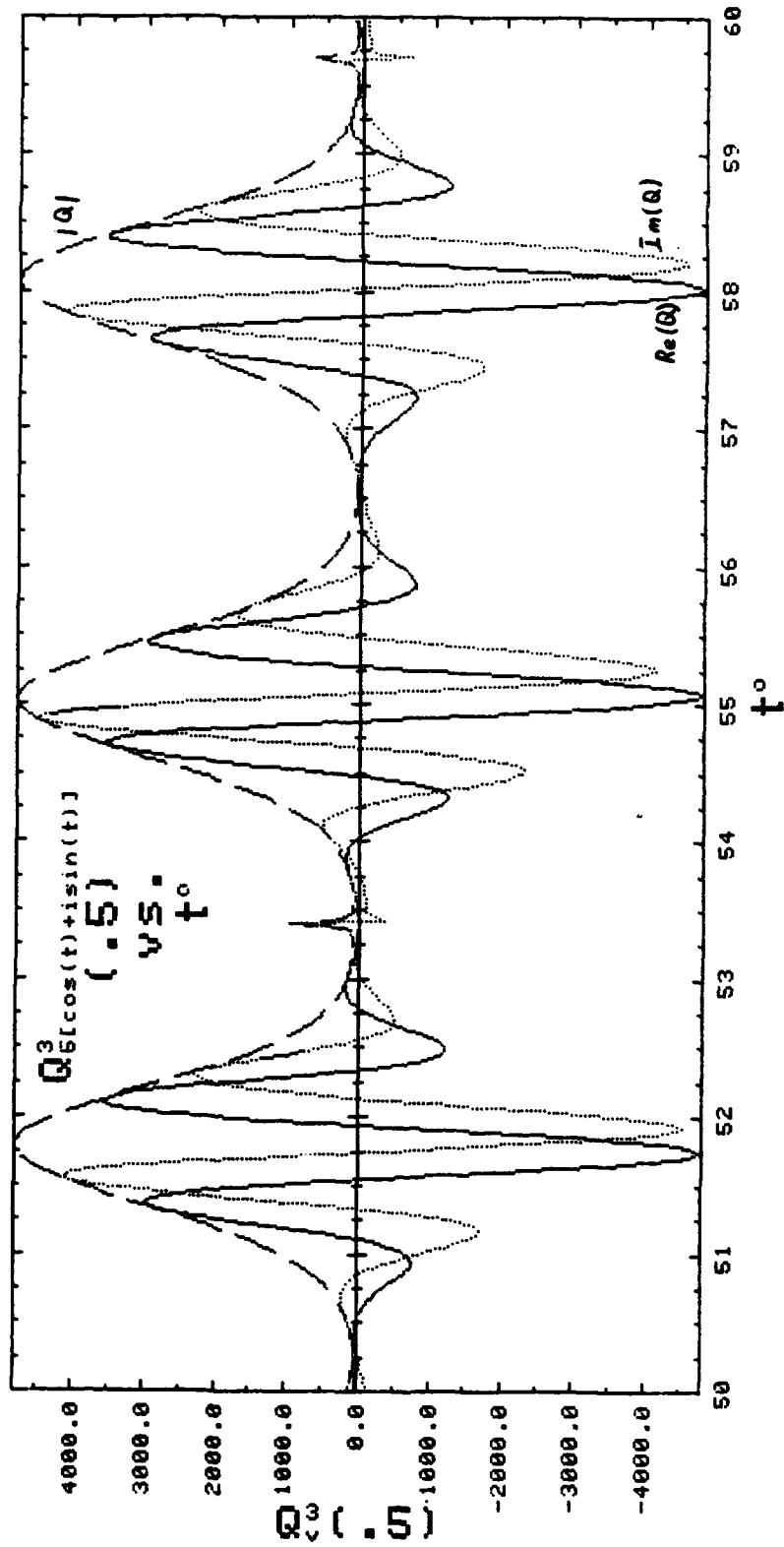


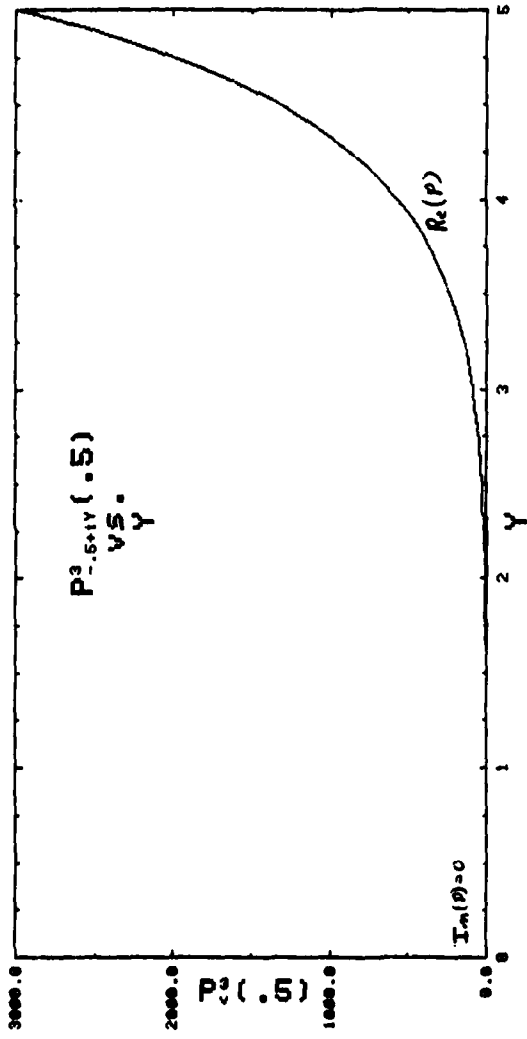


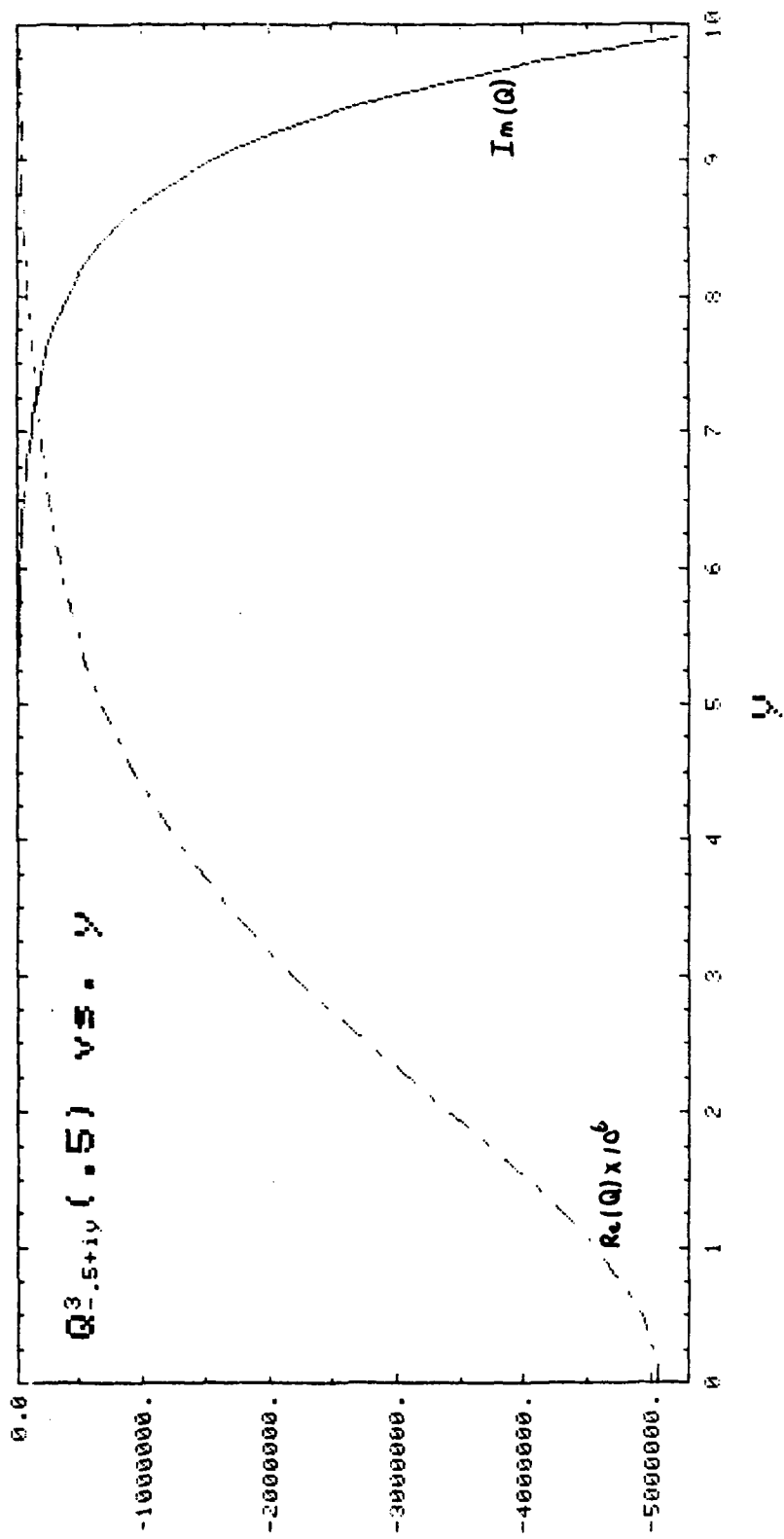












$Q^3(.5)$



AD P 0 0 1 0 2 9



THE BEST POSSIBLE CLASS OF INITIAL VALUES  
FOR THE POROUS MEDIUM EQUATION IN  $\mathbb{R}^N$

Michael G. Crandall  
Mathematics Research Center  
University of Wisconsin-Madison  
610 Walnut Street  
Madison, WI 53706

**ABSTRACT.** Some of the main results of the paper [4] by the author, Ph. Bénilan and M. Pierre are briefly described. These results concern the initial-value problem for the porous medium equation, that is

$$\begin{cases} u_t - \Delta(|u|^{m-1}u) = 0 & \text{for } 0 < t < T, x \in \mathbb{R}^N, \\ u(x,0) = \phi(x) \end{cases}, \quad (\text{IVP})_m$$

where  $m > 1$  is given. The questions treated are concerned with identifying the most general class of initial functions  $\phi$  for which  $(\text{IVP})_m$  has a solution on some time strip  $0 < t < T, x \in \mathbb{R}^N$ . The existence time  $T$  may depend on  $\phi$ . The main results show, among other things, that  $(\text{IVP})_m$  has a solution if and only if

$$\sup_{R>1} \left( \frac{1}{N + \frac{2}{m-1}} \int_{B_R} |\phi(x)| dx \right) < \infty \quad (1)$$

where  $B_R$  is the  $R$ -ball centered at  $0$ ; establish estimates on the solution of  $(\text{IVP})_m$ ; and then show the uniqueness of solutions obeying these estimates.

**I. INTRODUCTION.** If  $m = 1$ , then  $(\text{IVP})_1$  is the Cauchy problem for the linear heat equation. It may prove helpful to the reader if we review this case first. If  $m = 1$ , one expects  $(\text{IVP})_1$  to be uniquely solved by

$$u(x,t) = \frac{1}{(4\pi t)^{N/2}} \int e^{-|x-y|^2/4t} \phi(y) dy \quad (2)$$

but this hope is rather naive. For example, A. N. Tychonov wrote down a  $C^\infty$  function  $u$  (see, e.g., [5, pg. 50]) satisfying  $u(x,t) = 0$  for  $t < 0$ ,  $u(\cdot, t) \neq 0$  for  $t > 0$  and  $u_t - \Delta u = 0$  for all  $x, t$ . In particular,  $u(x,t)$  is not given by (2) for  $t > 0$  with  $\phi = u(\cdot, 0) = 0$ , and one must consider restrictions on solutions  $u$  of  $(\text{IVP})_1$  in order to have uniqueness.

A natural restriction was considered by Widder [7]. The results of this line of research show that if  $u > 0$  is a solution of  $u_t - \Delta u = 0$  for  $0 < t < T, x \in \mathbb{R}^N$ , then

$$\lim_{t \rightarrow 0} u(\cdot, t) = \phi \quad (3)$$

exists and (2) holds. (However,  $\phi$  may be a measure and " $\phi(y)dy$ " then stands for this measure in (2)). In particular, if  $\phi > 0$  then there is at most one solution  $u > 0$  of (IVP)<sub>1</sub>, and there is such a solution only if the integral in (2) defines one. This will be the case (given  $\phi > 0$ ) exactly when

$$\int e^{-c(y)^2} \phi(y) dy < \infty \text{ for some } c > 0, \quad (4)$$

and then (2) provides a solution for  $0 < t < 1/4c$ . Hence (IVP)<sub>1</sub> is solvable in this sense exactly when (4) holds. For (IVP)<sub>m</sub> we do not have formulas to guide us, but we do have a few explicit solutions. The solution

$$\begin{cases} \Gamma(x, t) = \frac{1}{t^\lambda} g\left(\frac{|x|}{t^{\lambda/N}}\right), \\ g(s) = ((a - bs^2)^+)^{\frac{1}{m-1}} \end{cases} \quad (5)$$

where  $r^+ = \max(r, 0)$  and

$$\begin{cases} \lambda = N/(N(m-1) + 2), \\ b = \lambda(m-1)/2mN, \\ \text{and } a > 0 \text{ is given by } \int g(|x|) dx = 1. \end{cases} \quad (6)$$

is called the Barenblatt-Pattle solution.  $\Gamma$  assumes the initial-value  $\delta_0$ , the Dirac mass at the origin. The equation  $u_t - \Delta(|u|^{m-1}u) = 0$  is formally invariant under the change of variables  $t \rightarrow T-t$ ,  $x \rightarrow ix$ , so

$$G(x, t) = \Gamma(ix, T-t) = \frac{1}{(T-t)^\lambda} \left( a + b \frac{|x|^2}{(T-t)^{1/(N(m-1)+2)}} \right)^{\frac{1}{m-1}} \quad (7)$$

is a solution together with  $\Gamma$ . The solution  $G$  has an initial-value behaving like  $c|x|^{2/(m-1)}$  near  $\infty$  and  $G$  "blows up in finite time". We expect from these examples that we need to accommodate initial-values  $\phi$  which could be any finite measure or grow like  $|x|^{2/(m-1)}$ . Moreover, solutions both "get better", as in the case of  $\Gamma$  which has a rough initial datum, and blow up as in the case of  $G$ . This already occurs in the linear case. The solution of (IVP)<sub>1</sub> for  $\phi = \delta_0 + (4\pi)^{-N/2} \exp(|x|^2/4)$  is

$$u = \frac{1}{(4\pi t)^{N/2}} e^{-\frac{|x|^2}{4t}} + \frac{1}{(4\pi(1-t))^{N/2}} e^{\frac{|x|^2}{4(1-t)}}$$

which first improves and then blows up.

The appropriate set of initial values for  $(IVP)_m$  turns out to be the set of functions (or, more generally, measures) satisfying (1). It is clear that if  $\phi$  is integrable then it satisfies (1), while if  $|\phi(x)| < K(1+|x|^2)^{1/(m-1)}$  it also satisfies (1). The necessity that (1) hold was proved by Aronson and Caffarelli [2] who showed that if  $u > 0$  is a solution of  $u_t - \Delta(u^m) = 0$  on  $0 < t < T, x \in \mathbb{R}^N$ , then

$$\int_{B_R} u(x,0) dx < C \left( \frac{R^{N+\frac{2}{m-1}}}{T^{\frac{1}{m-1}}} + T^{N/2} (u(0,T))^{(N(m-1)+2)/2} \right) \quad (8)$$

where  $C$  depends only on  $m > 1$  and  $N$ . These authors also proved that if  $u$  is a nonnegative solution on the strip  $0 < t < T$ , then the limit of  $u(\cdot, t)$  as  $t \rightarrow 0$  exists uniquely in the class of measures satisfying (1). Some of the results obtained in [4] concerning existence and uniqueness are outlined in the next section.

## II. EXISTENCE AND UNIQUENESS

For each number  $r > 0$  let

$$|\phi|_r = \sup_{R > r} \frac{1}{R^{N+\frac{2}{m-1}}} \int_{\{|x| < R\}} |\phi(x)| dx \quad (9)$$

We also put

$$|\phi|_\infty = \lim_{r \rightarrow \infty} |\phi|_r \quad (10)$$

and

$$X = \{\text{measurable } \phi : \mathbb{R}^N \rightarrow \mathbb{R} \text{ such that } |\phi|_1 < \infty\}.$$

Another space we will need is the weighted  $L^1$  space

$$L^1(\rho_\alpha) = \{f \in L^1_{loc}(\mathbb{R}^N) : \rho_\alpha f \in L^1(\mathbb{R}^N)\},$$

where  $\rho_\alpha(x) = (1+|x|^2)^{-\alpha}$ , which is equipped with the obvious norm. The spaces  $X, L^1(\rho_\alpha)$  are related by:

Lemma 1.

(i)  $X \subset L^1(\rho_\alpha)$  for  $\alpha > \frac{N}{2} + \frac{1}{m-1}$

and

(ii)  $X \supset L^1(\rho_\alpha)$  for  $\alpha > \frac{N}{2} + \frac{1}{m-1}$ .

Combining various results of [4], we formulate a version of the basic existence theorem:

Theorem 1. Let  $\phi \in X$ . Then there is a number  $T(\phi), 0 < T(\phi) < \infty$ , such that  $(IVP)_m$  has a solution  $u$  on  $\mathbb{R}^N \times [0, T(\phi))$  which satisfies

(i)  $\sup_{x \in \mathbb{R}^N} (\rho_{1/(m-1)}(x) |u(x,t)|)$  is locally bounded on  $(0, T(\phi))$ .

- (ii)  $u_t = \Delta(|u|^{m-1}u)$  in the sense of distributions on  $0 < t < T(\phi)$ ,  $x \in \mathbb{R}^N$
- (iii) For  $2(m-1)\alpha > N(m-1) + 2$ ,  $t \rightarrow u(\cdot, t) \in C([0, T(\phi)) : L^1(\rho_\alpha))$  and  $u(\cdot, 0) = \phi$ .
- (iv) Either  $T(\phi) = \infty$  or  $\liminf_{t \rightarrow T(\phi)} \|u(\cdot, t)\|_1 = \infty$ .

The content of Theorem 1 is that  $(IVP)_m$  has a solution on a maximal (by (iv)) interval  $(0, T(\phi))$  in the sense described by (i), (ii), (iii). Note that (i) guarantees that (ii) is meaningful. The natural expectation that  $u(\cdot, t)$  should assume its initial-value in the sense of the space  $X$  does not hold. This can be seen from (i), since  $\{v \in X : \rho_{1/(m-1)} v \in L^\infty(\mathbb{R}^N)\}$  is not dense in  $X$  ([4], Appendix). However, (iii) is adequate in the sense that it is strong enough to imply uniqueness. Theorem U of [5] implies:

**Theorem 2.** Let  $T > 0$  and  $u, v \in C([0, T] : L^1(\rho_\alpha))$  for some  $\alpha$ . Assume  $\rho_{1/(m-1)}(|u| + |v|)$  is bounded in  $L^\infty(\mathbb{R}^N)$  uniformly on compact subsets of  $[0, T]$ , and  $u_t - \Delta(|u|^{m-1}u) = v_t - \Delta(|v|^{m-1}v)$  in  $\mathcal{D}'(\mathbb{R}^N \times (0, T))$ . If  $u(\cdot, 0) = v(\cdot, 0)$ , then  $u = v$ .

According to Theorems 1 and 2, to each  $\phi \in X$  we can associate an existence time  $T(\phi) > 0$  and a unique solution  $u(x, t)$  of (IVP). We write  $u(\cdot, t) = U(t)\phi$ , that is  $U(t)$  is the associated "time- $t$ " map.  $U(t)\phi$  is defined for  $0 < t < T(\phi)$ . We next give some more quantitative information than that provided by Theorem 1. However, proofs of some of these facts are part of the proof of Theorem 1.

(A) There is a constant  $c_1 > 0$  such that for  $r > 1$  we have

$$T(\phi) > T_r(\phi) = c_1 / \|\phi\|_r^{m-1}.$$

If  $\phi > 0$ , then  $T(\phi) = \infty$  exactly when  $\|\phi\|_\infty = 0$ .

(B) There is a constant  $c_2 > 0$  such that for  $\phi \in X$

$$\rho_1(x) |U(t)\phi(x)| < c_2 \|\phi\|_1^{2\lambda/N} t^{-\lambda} \text{ for } 0 < t < T_1(\phi),$$

where  $T_1(\phi)$  is defined in (A).

(C) For  $M > 0$ ,  $\phi \rightarrow U(t)\phi$  is Lipschitz continuous from  $L^1(\rho_\alpha) \cap C_M$  into  $L^1(\rho_\alpha)$  and from  $C_M$  into  $X$  where

$$C_M = \{\phi \in X : \|\phi\|_1 < M \text{ and } 0 < t < \min(T_1(\phi), M)\}.$$

(D)  $\phi > \psi$  implies  $U(t)\phi > U(t)\psi$ .

(E) There is a constant  $c > 0$  such that

$$\|U(t)\phi\|_{L^1(\mathbb{R}^N)} < c \left( \frac{1}{t^\lambda} \|\phi\|_0^{2\lambda/N} + \|\phi\|_0 \right) \text{ for } t > 0$$

where

$$\|\phi\|_0 = \sup_{z \in \mathbb{R}^N} \int_{\{|x-z| < 1\}} |\phi(x)| dx .$$

Either explicit solutions or scaling arguments may be used to show that if  $T(\phi)$  is to be estimated by a function of  $\|\phi\|_\infty$ , it must behave like  $c/\|\phi\|_\infty^{m-1}$ , so (A) is sharp in this respect. Similarly, the Aronson-Caffarelli result [8] shows that  $\|\phi\|_\infty = 0$  is necessary for  $T(\phi) = \infty$  if  $\phi > 0$ . Note that  $L^1(\mathbb{R}^N) \subset \{\phi \in X : \|\phi\|_\infty = 0\}$ . Other inclusions are explained in [4]. (B) is a "regularizing effect" showing that arbitrary initial data  $\phi \in X$  yields a solution  $U(t)\phi$  bounded by multiples of  $(1 + |x|^2)^{1/(m-1)}$  for  $0 < t < T(\phi)$ . The estimate may, of course, "blow up" as  $t \uparrow T(\phi)$  or  $t \downarrow 0$  in a way consistent with (7) and (B). (C) states continuous dependence results with respect to initial data, while (D) is the order preservation with respect to initial data one expects from the maximum principle. Finally, (E) (in conjunction with (8)) essentially characterizes those initial data for which  $U(t)\phi \in L^\infty(\mathbb{R}^N)$  for  $t > 0$ , generalizing results of Véron [6] and Bénilan [3].

There is much more we could say, but the above suffices to introduce the results. The proofs are interesting, but we will not attempt to describe them except very briefly. Roughly speaking, the Aronson-Bénilan inequality [1]  $-\Delta(u^{m-1}) \leq c/t$ , which holds for certain nonnegative solutions of  $u_t = \Delta(u^m)$  is used to estimate  $\rho_{1/(m-1)} u$  in  $L^\infty(\mathbb{R}^N)$  in terms of  $\|u\|_1$  for nonnegative solutions of  $(IVP)_m$ . This is then used in the evolution equation to estimate  $\|\rho_{1/(m-1)} u\|$  in  $L^\infty(\mathbb{R}^N)$  in terms of  $\|\phi\|_1$  for solutions of  $(IVP)_m$ , yielding (B) above. These estimates are used to prove (C), which in turn allows one to pass from  $\phi$ 's for which existence is known (e.g.,  $\phi \in L^1(\mathbb{R}^N)$ ) to the general case  $\phi \in X$ .

Other information in the paper concerns addition regularity assertions, the case of measures  $\phi$ , etc. .

#### REFERENCES

- [1] Aronson, D. G. and Ph. Bénilan, Régularité des solutions de l'équation des milieux poreux dans  $\mathbb{R}^N$ , C. R. Acad. Sci. Paris Série A 288 (1979), 103-105.
- [2] Aronson, D. G. and L. Caffarelli, The initial trace of a solution of the porous medium equation, to appear.
- [3] Bénilan, Ph., Opérateurs accréatifs et semi-groupes dans les espaces  $L^p$  ( $1 < p < \infty$ ), Functional Analysis and Numerical Analysis, Japan-France Seminar, Tokyo and Kyoto, 1976; H. Fujita (Ed.): Japan Society for the Promotion of Science, 1978.

- [4] Bénilan, Ph., Crandall, M. G. and M. Pierre, Solutions of the porous medium equation in  $\mathbb{R}^N$  under optimal conditions on initial values, Mathematics Research Center TSR #2387, University of Wisconsin-Madison (1982) and to appear in Indiana U. Math. J. .
- [5] Hellwig, Günter, Partial Differential Equations, Blaisdell, New York, 1964.
- [6] Véron, L., Coercivité et propriétés régularisantes des semi-groupes nonlinéaires dans les espaces de Banach, Publ. Math. Fac. Sci. Besançon 3 (1977).
- [7] Widder, D. V., Positive temperatures in an infinite rod, Trans. Amer. Math. Soc. 55 (1944), 85-95.



AD P 01030

A NEW FLIGHT INSTABILITY AFFECTING SPINNING PROJECTILES  
HAVING NON-RIGID PAYLOADS

Miles C. Miller  
Chemical Systems Laboratory  
US Army Armament Research and Development Command  
Aberdeen Proving Ground, Maryland 21010

ABSTRACT

Severe flight instabilities were experienced by an Army spin stabilized projectile which had a partial solid/partial liquid payload. Characteristic of this flight instability was a sharp increase in projectile yaw angle accompanied by an abrupt loss in projectile spin rate. Although it was known that this instability was due to movement of the non-rigid payload, the exact mechanism causing the effect was not understood. A special laboratory test fixture was used to force a full-scale projectile payload to simulate the combined spin and simple coning motion of the projectile in flight. The fixture was used to determine critical factors influencing the payload induced despin moment, and from this the associated flight stability was inferred. Candidate payload configurations intended to eliminate the instability were evaluated on the fixture culminating in a payload design which provided the desired functional and flight performance. Subsequent fixture tests with homogeneous, viscous liquid fills produced similar despin characteristics to those obtained with the partial solid/partial liquid payloads. The despin data indicated increasing instability with increasing liquid viscosity with a maximum effect at a kinematic viscosity of about  $10^5$  CS whereupon the instability decreases with increasing viscosity. Instrumented flight tests of projectiles having identical fills to those tested on the fixture showed good correlation with fixture results. This payload induced flight instability appears to be fundamentally different from the Stewartson type phenomena associated with liquid filled projectiles. The similarity in the instability characteristics due to the simple homogeneous, viscous liquids and the more complex non-rigid payloads could aid in the development of a general theory describing the source of the instability and the establishment of design criteria for future spinning projectile systems.

## INTRODUCTION

The XM761, 155mm Improved Smoke Screening artillery projectile contained a preloaded payload canister assembly illustrated in Figure 1. A total of 48 cotton wicks were contained in the canister in three tiers with 16 wicks per tier. Each wick measured 16.5 cm in length and weighed 17-grams. An aluminum cruciform baffle divided the interior into four quadrants as illustrated in Figure 2. The canister also contained white phosphorus (WP) having the specific mass density of 1.7, a melting temperature of 44°C, and a subsequent kinematic viscosity of 1.5 CS. The loaded canister had a mass of 12.25 kg including 5.8 kg of WP, giving a total projectile weight of about 46.27 kg. Upon expulsion from the projectile over the target, the WP saturated wicks were dispersed onto a relatively large area of ground. Each wick would spontaneously ignite providing a series of point sources of smoke resulting in a rapidly formed, dense smoke screen of relatively long duration. Although the XM761 produced the desired smoke screening performance, flight tests revealed a serious flight stability problem.<sup>1,2,3</sup>

When fired at low ambient temperatures where the WP was in a solid state, the projectile had stable flight under all flight conditions. Figure 3 contains yaw sonde data for a typical stable flight. The peak-to-peak amplitude of the SIGMA N trace denotes the total angle of yaw possessed by the projectile, the reduction of yaw with time indicates a stable projectile flight.

At elevated temperatures where the WP was in a liquid state, the projectile experienced a severe flight instability. The unique feature of this instability was that both a large increase in yaw angle and severe loss in spin rate were suffered by the projectile, causing the round to fall short of its intended range. This problem was particularly critical at the Zone 4 (transonic muzzle velocity) firing condition where the projectile possesses minimum aeroballistic stability and experienced relatively large initial yaw angles. Figure 4 presents yaw sonde data from a typical unstable flight depicting the increase in yaw angle and simultaneous spin loss.

The payload induced coupled yaw and roll effect of the XM761 appeared to be similar to a projectile instability problem analyzed by Murphy<sup>4</sup> which involved an inertial effect created by internal moving rigid parts. This particular analysis did not directly apply to the XM761 situation because of the non-rigid i.e., partial solid/partial liquid) composition of the XM761 payload. However, as in the case of the instability produced by the moving rigid internal parts, it was assumed that both the yawing moment and the despin moment observed for the XM761 instability were components of a single payload induced moment.

A special ground test fixture was built by the Chemical Systems Laboratory (CSL) which caused an actual, full-scale projectile payload assembly to undergo the basic spin and nutational motion of the projectile in flight.<sup>5</sup> The internal payload motion was thereby created, the resulting despin moment measured, and the data used to evaluate the potential flight stability of the projectile carrying the payload configuration tested.

This paper describes the use of this test fixture to determine the critical performance characteristics of the despin resulting from the relative motion of the XM761-type non-rigid payload and the subsequent use of the fixture to evolve a stable WP smoke round payload configuration. The results of studies with simple homogeneous, viscous liquid fills which demonstrated their similarity to the more complex partial solid/partial liquid non-rigid payloads in producing this type of flight instability are also presented. Other investigation associated with this phenomena are noted along with comments regarding current and future experimental efforts.

#### SYMBOLS

M	despin moment due to non-rigid payload
P	spin rate of projectile
SIGMA N	angle of projectile centerline relative to sun direction
t	time
$\gamma$	specific mass density
$\theta$	canister coning angle
$\nu$	kinematic viscosity
$\Omega$	canister coning rate
$\omega$	canister spin rate
WP	white phosphorus

#### LABORATORY TEST FIXTURE

Figure 5 contains a photograph of the laboratory test fixture. A full-scale canister and inclosed payload assembly was mounted between two clevis type bearing housings. The clevises were mounted to the test fixture frame so that the canister longitudinal axis could be oriented at an angle to the vertical, representing the fixed nutational coning angle. The canister could be set at angles from 0 to 20 degrees in 5 degree increments. The upper clevis contained a nozzle/air turbine arrangement providing spin torque to the canister. The frame, and attached canister were rotated about a vertical axis by means of an electric motor located on the lower section of the test fixture. The canister spin rate was measured by means of a magnetic tachometer located on the lower clevis, and the coning rate indicated by a photo tachometer located beneath the table.

With the canister mounted at a particular angle ( $\theta$ ), the air turbine spun the canister up to the spin rate of the projectile for the specific conditions being tested. When the desired canister spin rate ( $\omega$ ) has been achieved, the electric motor spun the frame with the attached spinning canister at the desired nutational coning frequency. With the canister at a constant coning rate ( $\Omega$ ), the air turbine was cut-off allowing the canister to spin down due to the combined effects of bearing friction and the payload induced despin moment. The canister spin rate was recorded as a function of time. The despin moment due to friction was known from previous calibration, therefore, any additional despin moment was due to a payload induced effect. Tests were conducted over a range of constant coning rates at each fixed coning angle, thus encompassing nutation rates corresponding to various flight velocities and yaw angles.

#### EVALUATION OF THE XM761 PAYLOAD

A series of test was conducted on the test fixture using an actual XM761 canister assembly containing 48 patio torch wicks, the baffle and calcium nitrate as simulant for WP. Calcium nitrate has the same mass density and melting temperature as WP and the payload could be evaluated with the WP simulant in both a solid (cool) or liquid (hot) state.

Figure 6 shows the payload induced despin moment as a function of coning rate and coning angle for the WP simulant in a liquid state. The despin moment was not a function of canister spin rate, provided a sufficient canister spin rate was present ( $> 1,000$  rpm). The data indicate that the despin moment is a non-linear function of the coning rate. Figure 7 contains the despin moment as function of canister coning angle and coning rate indicating that the despin moment is also a non-linear function of the coning angle.

Tests with the WP simulant in solid state produced no payload induced despin moment. The fixture results revealed that the payload induced despin moment is not dependent on longitudinal acceleration at launch and could also be reproduced after a liquid/solid/liquid WP state cycle.

#### EVOLUTION OF XM825 CONFIGURATION

The test fixture was used to evaluate several candidate payload canister configurations intended to eliminate the XM761 stability problem. It was known that the instability was due to payload movement and, if the payload were constrained, the instability would be eliminated. However, because of the liquid nature of WP, it was impossible to completely constrain this type of payload and the degree of constraint required to minimize the instability effect was not known.

Fixture tests were conducted with the nominal XM761 payload configuration, using a blended Freon WP simulant which matched the physical properties of liquid WP, including the specific density and specific viscosity without requiring elevated temperatures.

A payload configuration was evolved composed of 120 3/4-inch thick felt wedges stacked between the longitudinal baffle as illustrated in Figure 8. The felt wedges served the same function as the cotton wicks, but the denser material and tighter packing of the felt wedges restricted their movement inside the canister. Test fixture results for this payload configuration are shown in Figure 9 and indicate a despin moment considerably lower than that measured for the nominal XM761. Data are shown for a coning rate of 500 rpm which is the projectile nutational frequency for the critical Zone 4 (transonic launch) condition. Subsequent flight tests of the felt wedge configuration using actual liquid WP resulted in stable flights under firing conditions which cause the nominal XM761 WP/wick configuration to be unstable.<sup>6</sup> This configuration was subsequently entered into development as the XM825 projectile.

#### HOMOGENEOUS, VISCOUS LIQUID FILLS

Although an improved smoke screening projectile configuration was achieved, the exact mechanism behind the payload induced instability was not understood. Vaughn<sup>7</sup> suggested that the combined solid/liquid XM761 payload acts as a homogeneous, highly viscous liquid. An extensive series of controlled experiments were conducted with the laboratory test fixture using liquid fills of various viscosities and densities.<sup>8,9</sup> These tests indicated that a cylindrical canister, completely filled (i.e., no void) with a homogeneous viscous liquid produces a measurable payload induced despin moment under combined spinning and coning motion. Figure 10 contains representative test results for corn syrup having a specific mass density of 1.4 and a kinematic viscosity of 200,000 CS. The despin moment was found to be independent of canister spin rate and was a non-linear function of both the coning rate and coning angle; results similar to those for the XM761 type payload.

Figure 11 shows the despin moment as a function of the liquid fill kinematic viscosity for a 20 degree coning angle, with the moment normalized to the mass density of water. These data show that the despin increases with the liquid fill viscosity, achieving a maximum value in the  $10^5$  CS range, thereupon diminishing to zero at very large values of viscosity. Instrumented flight tests of full-scale 155mm projectiles having identical viscous liquid payloads to those evaluated on the test fixture were conducted by Ballistics Research Laboratory (BRL)<sup>10,11</sup> and showed good qualitative correlation to the fixture results. The similarity between the unstable flight motion of a corn syrup filled projectile and that of the XM761 is apparent from Figure 12.

These results are significant in that if the instabilities are due to a common mechanism, theoretical analysis based on a well defined homogeneous viscous liquid fill would be more tractable than for the more difficult to quantify partial liquid/partial solid type non-rigid payloads.

#### OTHER EXPERIMENTAL RESULTS

Additional fixture studies were conducted with homogeneous viscous liquids contained in a transparent canister.<sup>13</sup> These investigations provided an insight into the internal flow characteristics by indicating the distortion of the air void (i.e., center of liquid rotation) due to the combined spinning and coning motion of the canister. The studies revealed that the characteristic sinusoidal void distortion is restricted to the plane of the coning angle. Further, this distortion increases with coning rate and coning angle, but decreases with increasing liquid viscosity as shown in Figure 13.

D'Amico and Rogers<sup>14</sup> at the Ballistics Research Laboratory (BRL), used a spinning/coning free yaw laboratory gyroscope to obtain measurements of the yawing effect induced by the highly viscous liquid fills. This work indicated conditions of fluid properties and canister motion which defined a demarcation between the inertial wave, Stewartson type instability and that associated with the highly viscous liquids.

A concerted research effort is underway at the Chemical Systems Laboratory (CSL) to investigate the basic phenomena associated with this new instability. The laboratory test fixture shown in Figure 14 has been substantially modified to provide the operational characteristics and performance capabilities required to support these studies. The rectangular frame allows unobstructed viewing of the canister from three orthogonal directions including along the canister longitudinal axis. The canister spin turbine has been located at the lower end of the canister to permit the mounting of cameras and other instrumentation on the fixture frame. The canister bearing housings have been designed to accept a variety of canister sizes and geometries and to facilitate coning angle changes. The new air turbine configuration includes higher supply pressures and increased air flow volume providing greatly increased canister spin torque; canister spin rates of 15,000 rev/min being possible. The larger torque available will also act to sustain high canister spin rates in the presence of large payload induced despin moments. The larger coning motor can produce coning rates up to 1,200 rev/min.

It is conjectured that shear stress created by the non-rigid payload on the inner surface of the canister could be the fundamental mechanism responsible for the despin and destabilizing moment. In the case of the homogeneous, viscous liquid fills, this shear stress is basically a product of the velocity gradient and the liquid viscosity. In the case of the low viscosity liquids, the action of the spinning and coning canister produces high shear rates, but the small

values of viscosity result in low shear stresses and low payload induced moments. For the extremely high viscosity liquids the relative motion and associated shear rates are very low, in effect approaching a rigid body condition. Consequently, even with their large viscosity only small shear stresses and moments are produced. The intermediate viscosity liquids possess both large shear rates and viscosity values to produce substantial shear stresses and moments. The maximum effect for the motion conditions of the spin stabilized projectile considered here, being  $10^5$  CS. This shear stress dependence would differentiate this type of instability from a Stewartson<sup>12</sup> type instability which is produced by normal stresses (i.e., pressures).

Experiments are planned for the modified laboratory test fixture to specifically investigate the relation of the shear stress to this instability. This will include the determination of the detailed internal flow field of a viscous liquid undergoing simultaneous spinning and coning motion as well as direct measurement of the resulting internal wall shear stress. It is hoped that these data will provide additional insight into the basic phenomena associated with this new and critical flight instability.

#### CONCLUSIONS

1. Certain non-rigid payloads can create both a destabilizing yawing motion and a despin effect in spinning projectiles.
2. The payload induced despin moment can be produced and measured on a laboratory test fixture which simulates the simultaneous spinning and coning motion of a projectile in flight.
3. The payload induced despin moment increases non-linearly with coning frequency and coning angle and is independent of the spinning frequency provided a minimum spin rate is present.
4. Similar instability characteristics are produced by partial solid/partial liquid payload arrangements as well as homogeneous, highly viscous liquid fills.
5. Experimental and analytical studies for the homogeneous, viscous liquid case could establish a general theory describing the common mechanism for this instability.

#### REFERENCES

1. D'Amico, W. P.; "Early Flight Experiences With the XM761," BRL-MR-2791, Sep 77.
2. D'Amico, W. P.; "Field Tests of the XM761: First Diagnostic Test," BRL-MR-2792, Sep 77.
3. D'Amico, W. P.; "Field Tests of XM761: Second Diagnostic Test," MR-02806, Jan 78.
4. Murphy, C. H.; "Influence of Moving Internal Parts on Angular Motion of Spinning Projectiles," Journal of Spacecraft and Rockets, VOL 1, Mar-Apr 78, PP 117-122.
5. Miller, M. C.; "Flight Instability Test Fixture for Non-Rigid Payloads," US Army Research and Development Command, ARRADCOM-SP-79005, Jan 79.
6. D'Amico, W. P. and Oskay, V.; "Aeroballistic Testing of the XM825 Projectile - Phase II," BRL-MR-679, Mar 80.
7. Vaughn, H. R.; "Flight Dynamic Instabilities of Fluid Filled Projectiles," Sandia Laboratories, Albuquerque, NM, SAND 78-0999, Jun 78.
8. "In-House Laboratory Independent Research (ILIR) Program - Annual Review FY78," US Army Chemical Systems Laboratory Special Report 79003, PP3, I-9, Oct 78.
9. Miller, M. C.; "Flight Instabilities of Spinning Projectiles Having Non-Rigid Projectiles," Journal of Guidance, Control and Dynamics, VOL 5, Mar-Apr 82, PP 151-157.
10. D'Amico, W. P. and Miller, M. C.; "Flight Instabilities Produced by a Rapidly Spinning, Highly Viscous Liquid," Journal of Spacecraft and Rockets, VOL 16, Jan-Feb 79, PP 62-64.
11. D'Amico, W. P. and Clay, W. H., "High Viscosity Liquid Payload Yawsonde Data for Small Launch Yaws," BRL-MR-03029, Jun 80.
12. Stewartson, K.; "On the Stability of a Spinning Top Containing Liquid," Journal of Fluid Mechanics, VOL 5, Part 4, Jun 59, PP 577-792.
13. Miller, M. C.; "Void Characteristics of a Liquid-Filled Cylinder Undergoing Spinning and Coning Motion," Journal of Spacecraft and Rockets, VOL 18, No. 3, May-Jun 81, PP 286-288.
14. D'Amico, W. P., Jr. and Rogers, T. H.; "Yaw Instabilities Produced by Rapidly Rotating, Highly Viscous Liquids," AIAA-81-0224, 19th Aerospace Sciences Meeting, 12-15 Jan 81.

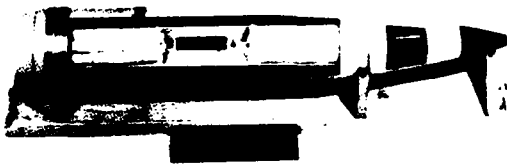


FIG. 1. XM761 PROJECTILE AND  
PAYLOAD ARRANGEMENT

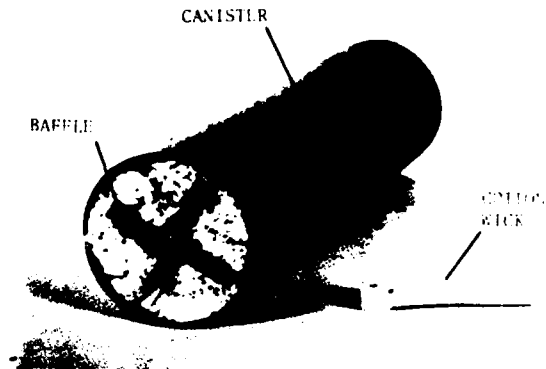


FIG. 2. XM761 PAYLOAD CANISTER  
AND WICK

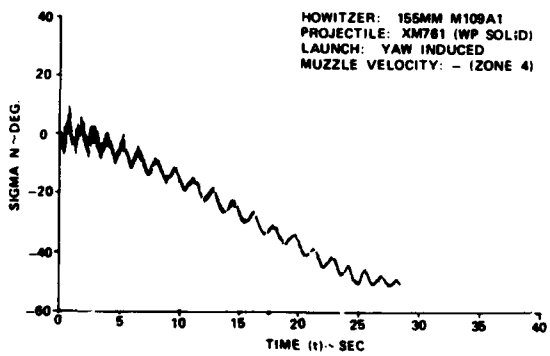
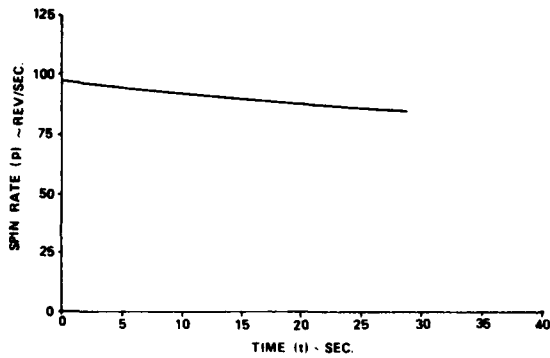


FIG. 3. YAWSONDE DATA FOR XM761  
STABLE FLIGHT (WP SOLID)

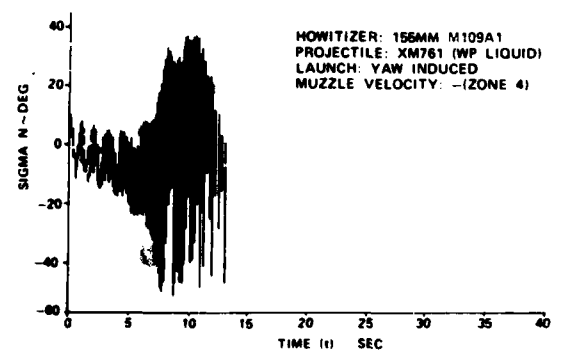
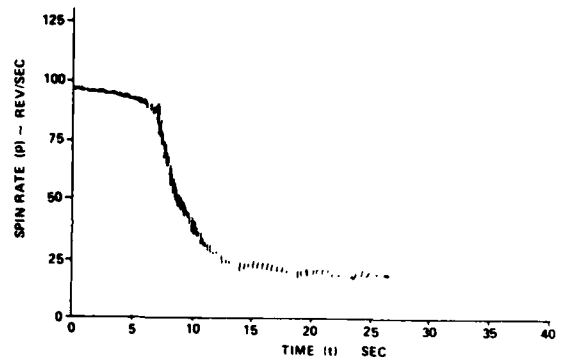


FIG. 4. YAWSONDE DATA FOR XM761  
UNSTABLE FLIGHT (WP LIQUID)

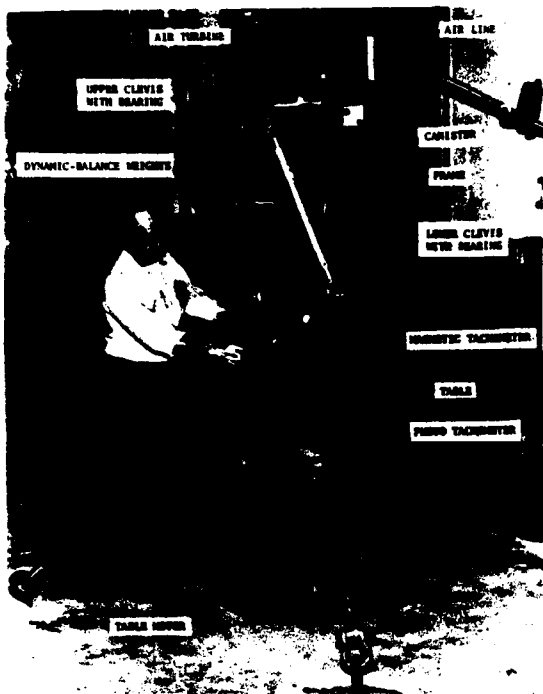


FIG. 5. LABORATORY TEST FIXTURE

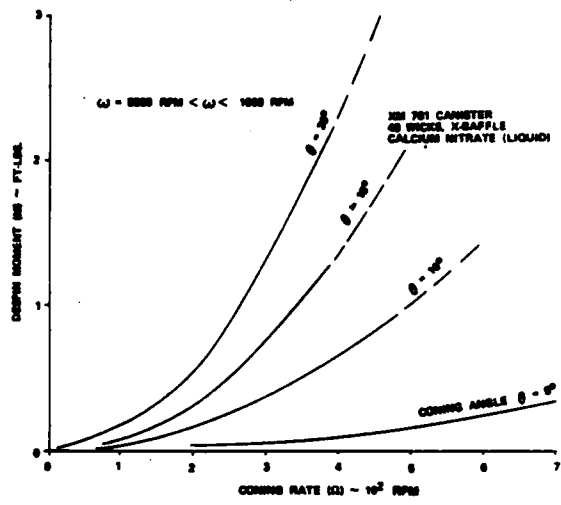


FIG. 6. DESPIN MOMENT FOR THE XM761 PAYLOAD VS CONING RATE AND CONING ANGLE

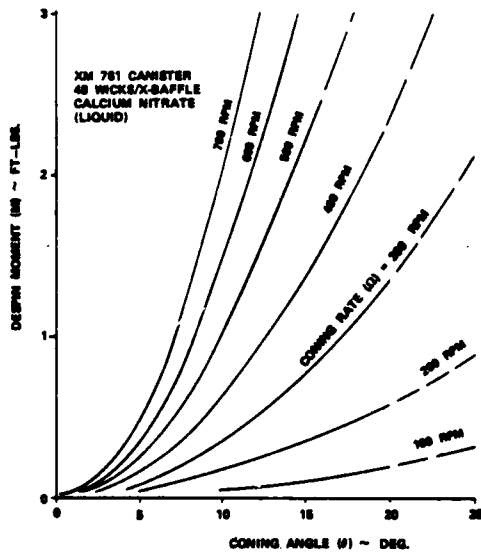


FIG. 7. DESPIN MOMENT FOR THE XM761 PAYLOAD VS CONING ANGLE AND CONING RATE

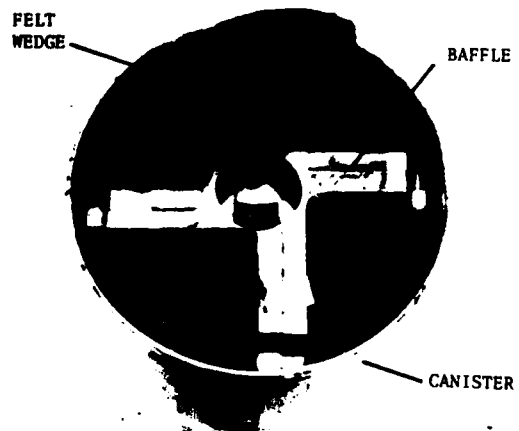


FIG. 8. XM825 FELT WEDGE PAYLOAD CONFIGURATION

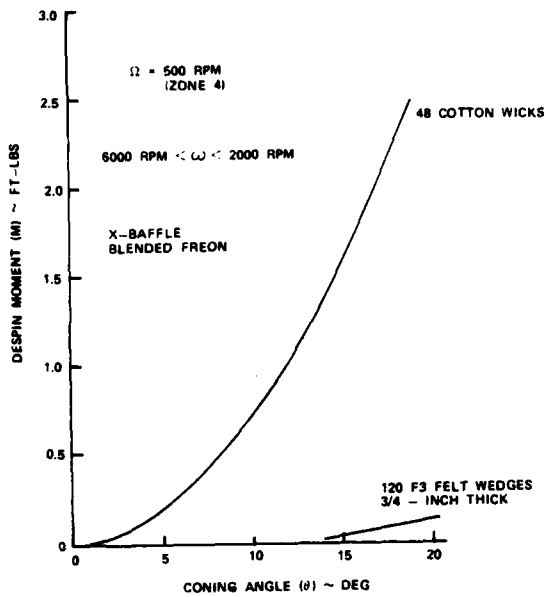


FIG. 9. DESPIN MOMENT FOR COTTON WICK (XM761) AND FELT WEDGE (XM825) PAYLOAD

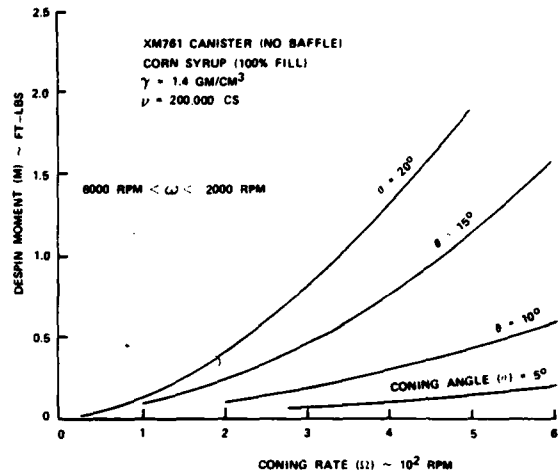


FIG. 10. DESPIN MOMENT FOR HOMOGENEOUS HIGH VISCOSITY LIQUID VS CONING RATE AND CONING ANGLE

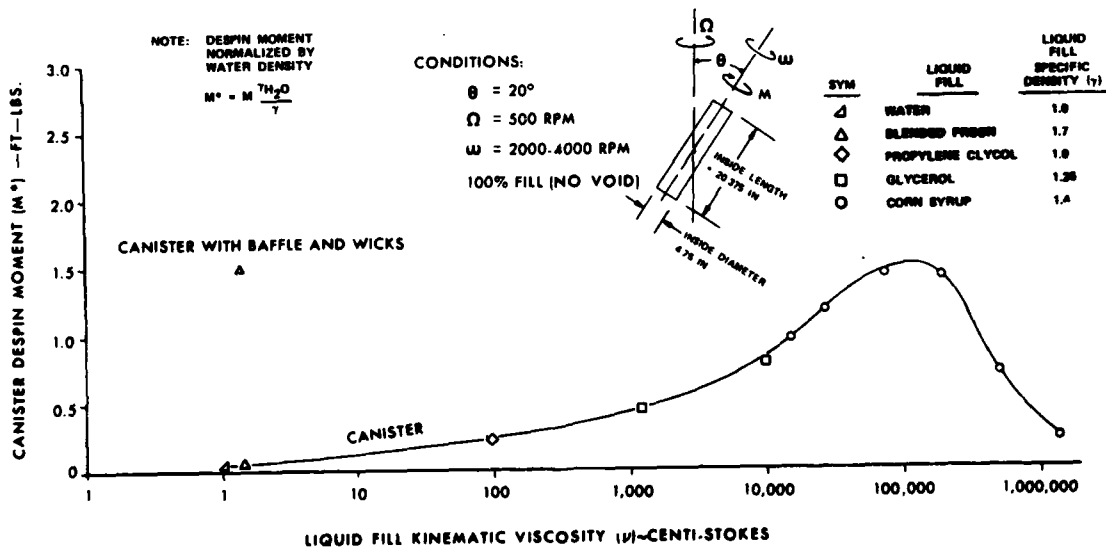


FIG. 11. DESPIN MOMENT AS A FUNCTION OF LIQUID FILL VISCOSITY FOR A  $20^\circ$  CONING ANGLE

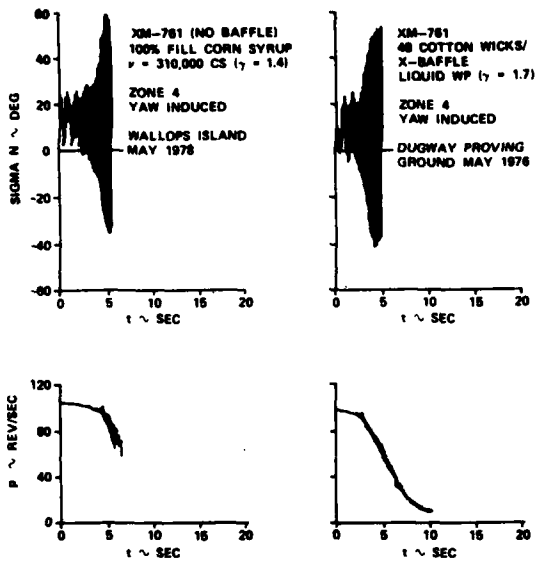


FIG. 12. UNSTABLE FLIGHT MOTION DUE TO A HOMOGENEOUS, VISCOUS LIQUID FILL AND PARTIAL LIQUID/PARTIAL SOLID PAYLOAD

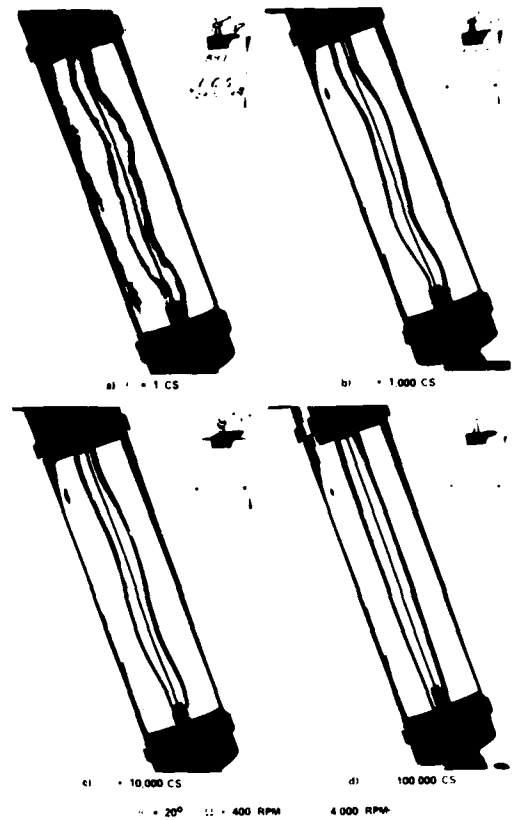


FIG. 13. EFFECT OF VISCOSITY ON VOID DISTORTION

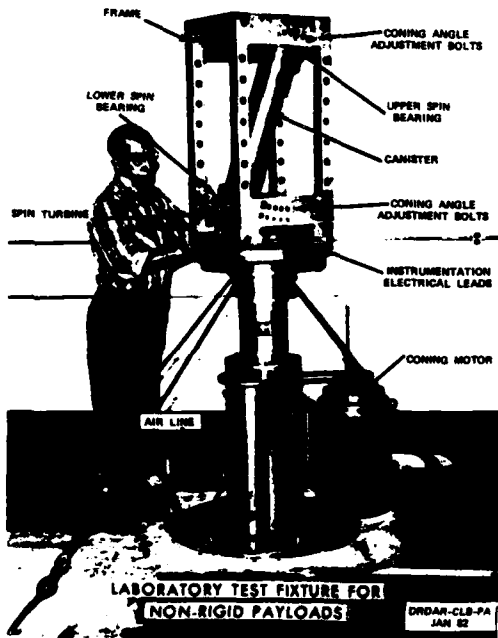


FIG. 14. MODIFIED LABORATORY TEST FIXTURE



"We should have changed to winter grade!"

FIG. 15. LIQUID VISCOSITY IS NOT A NEW ORDNANCE PROBLEM

AD P001031

TERRAIN MESOROUGHNESS DESCRIPTION AND  
ITS APPLICATION TO MOBILITY AND COVER

Richard A. Weiss  
Mobility Systems Division  
U. S. Army Engineer Waterways Experiment Station  
Vicksburg, Mississippi 39180

**ABSTRACT.** The mobility of vehicles traveling off the road has always been of interest to military planners. In fact, the survivability of military vehicles on a battlefield depends to a large extent on the degree of mobility and cover afforded by the terrain. In order to develop accurate measures of the mobility and cover characteristics of terrain, a study was made of the statistical description of terrain elevation variations on a scale smaller than shown on a topographic map. This study shows that a useful set of terrain descriptors are the standard deviations of the detrended elevation and its derivatives. The probabilities of a vehicle encountering specified values of slope or finding cover in a specified interval are calculated in terms of the terrain roughness descriptors. These probabilities can be used to quantify terrain areas of a battlefield and develop map overlays showing patches which indicate the degree of slopes expected to be encountered and the amount of cover that should be available. Numerical values of the probabilities are calculated for several terrain areas.

**1. INTRODUCTION.** A significant part of the determination of the survivability of military vehicles on a battlefield is an estimation of their mobility on the battlefield terrain and an estimation of the degree of cover afforded by the terrain. The detection of a target and the subsequent fire-power accuracy, including hit and kill probabilities, depend on the percent of a target that is exposed to fire and on the speed at which a vehicle can move across the battlefield terrain. This paper presents a method of estimating the mobility characteristics and available cover of battlefield terrain and specifies the terrain parameters required to accomplish this.

This is the second of a two-part study of the methods used for a quantitative description of terrain roughness. The first part considered the description of terrain microroughness with applications to the prediction of the dynamic response of military vehicles operating on rough terrain.<sup>1,2</sup> An analytical description of microroughness is necessary for the design of track and wheel suspension systems and also for the design of optical observation and sighting devices, gun stabilization systems, and many other complex weapons systems that are part of modern military vehicles. Many of the analytical procedures introduced for the description of microroughness can be used to describe large-scale variations of terrain elevation.

The second part of the terrain roughness study deals with large-scale elevation variations on a scale appropriate for the description of the mobility, cover, and concealment properties of a terrain area.<sup>3</sup> For the purposes of this paper the large-scale terrain elevations can be separated into two classes: mesoroughness which describes the terrain elevation variations on a scale between

microroughness and the elevations described by a topographic map, and macro-roughness which is essentially the terrain elevations given by contours on a topographic map. The mesorroughness is not obtainable from a standard topographic map, and the terrain elevation variations of the mesorroughness may afford cover for vehicles on a battlefield.

Aside from vegetation, the cover, concealment, and mobility characteristics of a mesorroughness elevation profile, as seen from a point on a contour of a topographic map, are determined by the magnitude and character of its elevation variations. Therefore, an analytical description of terrain mesorroughness is required for the prediction of cover and mobility, and the U. S. Army Engineer Waterways Experiment Station (WES) was requested to develop improved analytical representations of terrain mesorroughness and to incorporate this development into cover and mobility indices for military mapping purposes.

Measurement of Terrain Elevation Profiles. A study of terrain roughness begins with the measurement of an elevation profile. A simple and very accurate method of obtaining a profile uses the theodolite and surveyor's staff, but this method is very time-consuming. The measuring wheel method is quicker but has the disadvantages of disturbing the terrain and not being useful in very rough terrain. Terrain elevation measurements done by WES utilize the theodolite and surveyor's staff.

Photogrammetric methods of measuring terrain elevation profiles are simpler and faster because extended areas can be measured by areal surveys.<sup>4,5</sup> They have the further advantages of not affecting terrain conditions, and measuring all terrain features such as vegetation, roads, rivers, ditches, etc., as well as elevations. Photogrammetry has several disadvantages including the facts that vegetation often impairs terrain elevation measurements, evaluating photographs is time-consuming and expensive, and the resolution of elevations is limited especially for high altitude photographs.<sup>6</sup>

Terrain profiles determined by any method are presented as measurements of elevation at discrete points along some predetermined line. The effect of this discrete scanning is to remove from the actual elevation profile frequencies higher than  $(\Delta L)^{-1}$  where  $\Delta L$  = scanning length, so that scanning can be represented as a low pass filter. The spatial frequency  $(\Delta L)^{-1}$  is essentially the Nyquist frequency associated with the measurement of the elevation profile and enters the calculation of power spectra through the spectral window functions for the slope and curvature. Photogrammetric methods tend to underestimate the values of the standard deviations of elevation, slope, and curvature and their associated power spectra especially in the high frequency regions.

Macroterrain Roughness. A battlefield area can be divided into a grid of square areas at whose vertices the terrain elevations are specified. These elevations are recorded on a topographic map at uniform spacings of generally about 10 or 100 m. These terrain elevations form a three-dimensional surface called the macroterrain roughness. The macroroughness describes the large-scale trend of elevation variations, and is suitable for the descriptions of cover and vehicle mobility over large areas.<sup>7</sup> Terrain elevation variations on a scale less than the 100-m grid length are not obtainable from a topographic map.

Mesoterrain Roughness. Superimposed on the macroterrain (the trend given by the elevations specified at the 100-m intervals of a topographic map) are the elevation variations on a scale less than the 100-m interval--the terrain mesoroughness. Troops and equipment may possibly be concealed and covered with the terrain elevation variations of the 100-m interval connecting two elevation contours of a topographic map, whereas a straight line or other extrapolation of elevation between these two points would not suggest this.

The slopes occurring within the mesoroughness may differ considerably from that obtained from a topographic map, and therefore the actual vehicle mobility in a battlefield area may be considerably different from the predicted by the slopes obtained from a topographic map. Knowledge of the mesoroughness terrain elevations will be critical for estimating transit time of vehicles across a battlefield. Obstacles of various sizes and shapes are also expected to occur within the mesoroughness and these will affect the degree of mobility in a given area. The mesoroughness description is necessary for the prediction of cover, concealment, and mobility over small distance scales and small time scales.

The mesoroughness elevation varies throughout a battlefield area, and, accordingly, the amount of cover for a target and the mobility of a vehicle can vary rapidly over small distances (~10 m). Therefore, it will be of advantage for military purposes to be able to estimate the mesoroughness for the areas of a battlefield. A number of mesoroughness descriptors need to be developed in order to do this. The battlefield is divided into areas within which the mesoroughness descriptors have essentially the same values. The mesoroughness descriptors can be estimated for a given area by sampling a number of mesoterrain elevation profiles in the area.

A reduction of the size of the grid spacing of the macroterrain roughness descriptions would adequately incorporate the mesoroughness, but this would require large computer storage capacity. A more reasonable procedure is to describe the mesoroughness by a set of stochastic variables.

The determination of the descriptors of the random mesoroughness component requires the removal of the trend of the terrain elevation data. A detrending procedure is described in Part II of this paper. With a properly selected filter constant the detrended elevation profile gives the mesoroughness elevations between two points on a topographic map. The detrending is accomplished by a computer program RFNWUD.<sup>3</sup> It is assumed that the mesoroughness irregularities can be described by a zero mean stationary Gaussian (normal) random process.<sup>8,9</sup> The mesoroughness displacement and its derivatives will be represented by zero-mean Gaussian processes which are described by the standard deviations of displacement, slope, curvature, etc. The standard deviations of the mesoroughness displacement and its derivatives to any order are calculated from a detrended elevation program by the computer program RFNWUD.

Cover and Mobility Characteristics. Cover refers to protection from direct weapons fire, while the term concealment refers to features that would interrupt the line of sight. For instance, vegetation may afford concealment but not necessarily cover. Vegetation is not considered in this report, and only cover (concealment) due to terrain elevation variations is treated. The

degree of available cover afforded a target is measured by the fraction of target height that is covered, i.e. the depth of the hole in which the vehicle sits compared to the vehicle's height.

The mobility of vehicles depends on a large number of terrain features including: vegetation, soil strength, terrain slopes, etc. However, the primary terrain roughness variable that enters mobility calculations is the slope expected to be encountered along some path.<sup>10</sup> Each vehicle is associated with a critical slope which it cannot negotiate.

Because the mesoterrain roughness is represented by stochastic variables, the average mesoroughness displacement and the fraction of target height that is covered can only be described by a probability theory. This is also true of the slopes expected to be encountered on a battlefield area. With the assumption of zero mean Gaussian distributions to describe the mesoroughness, the calculation of average values and probabilities of encountering specified terrain characteristics is relatively simple and is done in Part III. These average values and probabilities are expressed in terms of the mesoroughness descriptors (standard deviations of terrain displacement and its derivatives) and can serve as indices to delineate patches on a map that have similar cover and mobility characteristics.

The basic objective of this paper is the development of new mesoroughness terrain descriptors. The objectives and scope of this paper are shown in Figures 1a and 1b.

2. STATISTICAL DESCRIPTION OF MESOTERRAIN ROUGHNESS. This section develops the parameters necessary for the description of terrain mesoroughness. It is assumed that the mesoroughness can be described by a zero-mean stationary Gaussian random process which is obtained from a measured elevation profile by a suitable detrending process. The frequency content of a stationary random process is described by the power spectrum or alternatively by the autocorrelation or autocovariance functions.<sup>11</sup> It is shown that that autocovariance functions are completely determined by the standard deviations of the mesoterrain elevation and all its derivatives. Therefore, the basic mesoroughness descriptors are the standard deviations of the mesoterrain elevation and its derivatives.

The standard deviations of mesoroughness displacement and its derivatives are calculated from detrended terrain elevation data. The accuracy of the values of the numerical derivatives obtained from the elevation data decreases for the higher derivatives. But many terms (higher derivatives) are required for a useful power series expansion of the autocorrelation function for large argument. Therefore, the power series method of calculating the autocorrelation function and the power spectrum is more formal than practical, and for numerical calculations it is more useful to represent the power spectrum as a polynomial whose coefficients are determined by using only the standard deviations of displacement, slope, and curvature.<sup>1</sup>

Although the power series representations for the autocorrelations functions are only of formal value for determining the power spectra, they can be

used to calculate the probabilities of finding specified mesoterrain displacements and slopes in a small spatial interval of the terrain. These probabilities are important for the description of cover and mobility characteristics.

Detrending. Except for relatively flat areas, a macroterrain elevation profile cannot be represented as a stationary random process because it has a trend, i.e. a variation of the statistical parameters along the length of the profile. In general the nonstationary character of the measured elevation profile has to be removed by a detrending procedure in order to obtain the standard deviations of the resulting mesoroughness. In the cases where no trend exists the measured elevation data can be processed directly.<sup>1</sup> The nonstationary property of an elevation profile can be removed by a detrending procedure which removes the long wavelength (the trend) components as shown in Figure 2a.

The mesoroughness will be treated as a stationary random process. The mesoroughness is extracted from the measured elevation profile by using the following exponentially weighted moving average.<sup>12</sup>

$$\zeta(x) = h(x) - \frac{1}{2\lambda} \int_0^{\infty} [h(x-a) + h(x+a)] e^{-a/\lambda} da \quad (1)$$

where

- $\zeta$  = mesoroughness displacement
- $h$  = terrain elevation
- $\lambda$  = detrending constant (filter constant)
- $x$  = horizontal distance
- $a$  = integration variable

The detrending procedure given in Equation 1 removes all wavelength components of the macroterrain elevations that are greater than  $\lambda$ . A computer program RFNWUD was developed to accomplish the detrending.<sup>3</sup>

Plausibility arguments can be given to select a value for  $\lambda$ . If the measurement interval of the macroroughness is  $L$  the filter constant can be taken to be

$$\lambda \sim L \quad (1a)$$

in order to remove the trend of the macroterrain as shown in Figure 2b. Another possible choice for  $\lambda$  would account for the elevation difference between two points on the macroterrain of a topographic map as follows

$$\lambda \sim \sqrt{L^2 + H^2} \quad (1b)$$

where  $H$  = elevation difference. Equations 1a and 1b represent intuitive possibilities; in fact the values of the parameter  $\lambda$  should be chosen to produce

agreement between the probability calculations of cover and mobility given in Part III and the measured cover and mobility characteristics of an area.

Mesoterrain Roughness Description. Terrain elevation is specified at finite intervals of horizontal distance and is generally a continuous function whose derivatives are discontinuous at the points of measurement. For the purpose of calculating standard deviations the derivatives at each point can be assumed to be the slope of the straight line segment to its right or left as shown in Figure 2c. To simplify notation the n'th derivative of the mesoterrain displacement  $\xi(x_i)$  at the point  $x_i$  will be written as

$$\xi_n(x_i) = \frac{d^n \xi}{dx_i^n} \quad (2)$$

where  $n = 0, 1, 2, \dots$ . As usual the zeroth derivative is just the displacement itself

$$\xi_0(x_i) = \xi(x_i) \quad (3)$$

The root mean square (rms) values of these derivatives are calculated as follows

$$\Sigma_0^2 = \frac{1}{N} \sum_{i=1}^N \xi^2(x_i) = \frac{1}{N} \sum_{i=1}^N [\xi_0(x_i)]^2 \quad (4)$$

$$\Sigma_1^2 = \frac{1}{N} \sum_{i=1}^N \left( \frac{d\xi}{dx_i} \right)^2 = \frac{1}{N} \sum_{i=1}^N [\xi_1(x_i)]^2 \quad (5)$$

$$\Sigma_2^2 = \frac{1}{N} \sum_{i=1}^N \left( \frac{d^2\xi}{dx_i^2} \right)^2 = \frac{1}{N} \sum_{i=1}^N [\xi_2(x_i)]^2 \quad (6)$$

$$\Sigma_3^2 = \frac{1}{N} \sum_{i=1}^N \left( \frac{d^3\xi}{dx_i^3} \right)^2 = \frac{1}{N} \sum_{i=1}^N [\xi_3(x_i)]^2 \quad (7)$$

or in general

$$\Sigma_n^2 = \frac{1}{N} \sum_{i=1}^N \left( \frac{d^n \xi}{dx_i^n} \right)^2 = \frac{1}{N} \sum_{i=1}^N [\xi_n(x_i)]^2 \quad (8)$$

where

- $\Sigma_0$  = rms value of displacement
- $\Sigma_1$  = rms value of slope
- $\Sigma_2$  = rms value of second derivative (curvature)
- $\Sigma_3$  = rms value of third derivative of displacement
- $\Sigma_n$  = rms value of n'th derivative of displacement
- N = number of points where elevations are measured

The number N is generally large being of the order of hundreds or thousands.

The mean values of the macroterrain displacement and its derivatives are calculated as follows

$$\xi_n^M = \frac{1}{N} \sum_{i=1}^N \frac{d^n \xi}{dx_i^n} = \frac{1}{N} \sum_{i=1}^N \xi_n(x_i) \quad (9)$$

The standard deviations of macroroughness displacement and derivatives are given by<sup>11</sup>

$$\sigma_n^2 = \Sigma_n^2 - (\xi_n^M)^2 \quad (10)$$

The standard deviations can also be written as

$$\sigma_n^2 = \frac{1}{N} \sum_{i=1}^N \psi_n^2(x_i) \quad (11)$$

where

$$\psi_n(x_i) = \xi_n(x_i) - \xi_n^M \quad (12)$$

are the values of mesoterrain displacement and its derivatives measured from their mean values, i.e. their values for a zero mean process since  $\psi_n^M = 0$ . The computer program RPNWUD calculates the standard deviations of mesoterrain displacement, slope, curvature, etc. from measured elevation data using the formulas 1 through 10.

Autocorrelation and Autocovariance Functions. The autocorrelation and autocovariance functions of the mesoterrain elevation and its derivatives are defined by<sup>11</sup>

$$R_n(\alpha) = \frac{1}{N} \sum_{i=1}^N \xi_n(x_i) \xi_n(x_i + \alpha) \quad (13a)$$

$$C_n(\alpha) = R_n(\alpha) - \left(\xi_n^M\right)^2 \quad (13b)$$

where

$R_n(\alpha)$  = autocorrelation function of  $n$ 'th derivative of elevation

$C_n(\alpha)$  = autocovariance function of  $n$ 'th derivative of elevation

$n = 0, 1, 2, 3, \dots$

The autocovariance functions can also be written as<sup>11</sup>

$$C_n(\alpha) = \frac{1}{N} \sum_{i=1}^N \psi_n(x_i) \psi_n(x_i + \alpha) \quad (14)$$

where  $\psi_n(x_i)$  is given by Equation 12. Because of the stationarity assumption, the parameters  $\Sigma_n$ ,  $\sigma_n$ , and  $\xi_n^M$  are independent of the interval  $\alpha$ . From Equations 8, 11, 13a, and 14 it follows that

$$R_n(0) = \Sigma_n^2 \quad (15a)$$

$$C_n(0) = \sigma_n^2 \quad (15b)$$

Useful quantities that describe the random variables  $\psi_n$  are the correlation coefficients<sup>11</sup>

$$r_n(\alpha) = \frac{C_n(\alpha)}{C_n(0)} \quad (16)$$

where  $n = 0, 1, 2, 3, \dots$ . The correlation coefficients describe the statistical properties of the mesoterrain displacement and all its derivatives. The correlation coefficients will be used in Part III to calculate the probability of encountering specified displacements and slopes in a given spatial interval.

The autocorrelation and autocovariance are even functions and therefore have the following even power Taylor series expansions<sup>13</sup>

$$R_n(\alpha) = R_n(0) + \frac{R_n^{(2)}(0)}{2!} \alpha^2 + \frac{R_n^{(4)}(0)}{4!} \alpha^4 + \dots \quad (17a)$$

$$C_n(\alpha) = C_n(0) + \frac{C_n^{(2)}(0)}{2!} \alpha^2 + \frac{C_n^{(4)}(0)}{4!} \alpha^4 + \dots \quad (17b)$$

where

$$R_n^{(j)}(0) = j\text{'th derivative of } R_n(\alpha) \text{ evaluated at } \alpha = 0$$

$$C_n^{(j)}(0) = j\text{'th derivative of } C_n(\alpha) \text{ evaluated at } \alpha = 0$$

The correlation coefficients are given by Equations 16 and 17b to be

$$r_n(\alpha) = 1 + \frac{1}{2!} \frac{C_n^{(2)}(0)}{C_n(0)} \alpha^2 + \frac{1}{4!} \frac{C_n^{(4)}(0)}{C_n(0)} \alpha^4 + \dots \quad (18)$$

It can be shown that the autocovariance function and its derivatives are related to the standard deviations of the displacement and its derivatives in the following way<sup>3</sup>

$$C_n(0) = \sigma_n^2 \quad (19)$$

$$C_n^{(2)}(0) = -\sigma_{n+1}^2 \quad (20)$$

$$C_n^{(4)}(0) = \sigma_{n+2}^2 \quad (21)$$

$$C_n^{(6)}(0) = -\sigma_{n+3}^2 \quad (22)$$

$$C_n^{(2s)}(0) = (-1)^s \sigma_{n+s}^2 \quad (23)$$

Similar expressions hold for the  $R_n^{(j)}(0)$  coefficients with the  $\sigma$ 's replaced by the  $\Sigma$ 's.

The Taylor series of the autocovariance functions (Equation 17b) and the correlation coefficients (Equation 18) can therefore be written as

$$C_n(\alpha) = \sigma_n^2 - \frac{\sigma_{n+1}^2 \alpha^2}{2!} + \frac{\sigma_{n+2}^2 \alpha^4}{4!} - \dots \quad (24)$$

$$r_n(\alpha) = 1 - \frac{1}{2!} \left( \frac{\sigma_{n+1}}{\sigma_n} \right)^2 \alpha^2 + \frac{1}{4!} \left( \frac{\sigma_{n+2}}{\sigma_n} \right)^2 \alpha^4 - \dots \quad (25)$$

In this way the correlation coefficients can be evaluated in terms of the standard deviations of mesoterrain displacement and its derivatives. The general expressions for these functions are

$$C_n(\alpha) = \sigma_n^2 \sum_{j=0}^{\infty} (-1)^j \frac{S_{nj}}{(2j)!} \alpha^{2j} \quad (26)$$

$$r_n(\alpha) = 1 + \sum_{j=1}^{\infty} (-1)^j \frac{S_{nj}}{(2j)!} \alpha^{2j} \quad (27)$$

where

$$S_{n0} = 1 \quad (28)$$

$$S_{n1} = \left( \frac{\sigma_{n+1}}{\sigma_n} \right)^2 \quad (29)$$

$$S_{n2} = \left( \frac{\sigma_{n+2}}{\sigma_n} \right)^2 \quad (30)$$

$$S_{nj} = \left( \frac{\sigma_{n+j}}{\sigma_n} \right)^2 \quad (31)$$

The coefficients appearing in the power series expansion of the correlation coefficients have a simple physical interpretation if it is noticed that the characteristic wavelengths for the mesoterrain displacement and its derivatives are given as follows

$$\lambda_n = 2\pi \frac{\sigma_n}{\sigma_{n+1}} \quad (32)$$

where

$\lambda_n$  = wavelength of n'th derivative of the mesoroughness displacement. Specifically,

$\lambda_0 = 2\pi\sigma_0/\sigma_1$  = characteristic wavelength of displacement

$\lambda_1 = 2\pi\sigma_1/\sigma_2$  = characteristic wavelength of slope

$\lambda_2 = 2\pi\sigma_2/\sigma_3$  = characteristic wavelength curvature

$\lambda_3 = 2\pi\sigma_3/\sigma_4$  = characteristic wavelength of the third derivative

and so on. Therefore from Equations 31 and 32 it follows that

$$s_{nj} = \left( \frac{2\pi}{\lambda_n} \frac{2\pi}{\lambda_{n+1}} \frac{2\pi}{\lambda_{n+2}} \cdots \frac{2\pi}{\lambda_{n+j-1}} \right)^2 \quad (33)$$

for  $j = 1, 2, 3, \dots \infty$ .

In terms of these wavelengths the correlation coefficients are written as

$$r_n(\alpha) = 1 - \frac{1}{2!} \left( \frac{2\pi\alpha}{\lambda_n} \right)^2 + \frac{1}{4!} \left( \frac{2\pi\alpha}{\lambda_n} \frac{2\pi\alpha}{\lambda_{n+1}} \right)^2 - \frac{1}{6!} \left( \frac{2\pi\alpha}{\lambda_n} \frac{2\pi\alpha}{\lambda_{n+1}} \frac{2\pi\alpha}{\lambda_{n+2}} \right)^2 + \dots \quad (34)$$

If the following set of dimensionless numbers are introduced

$$T_n = \frac{2\pi\alpha}{\lambda_n} \quad (35)$$

the correlation coefficients can be written as

$$r_n(\alpha) = 1 - \frac{1}{2!} T_n^2 + \frac{1}{4!} (T_n T_{n+1})^2 - \frac{1}{6!} (T_n T_{n+1} T_{n+2})^2 + \dots \quad (36)$$

$$= 1 + \sum_{j=1}^{\infty} (-1)^j \frac{1}{(2j)!} (T_n T_{n+1} T_{n+2} \cdots T_{n+j-1})^2 \quad (37)$$

Written out in full the expressions for the correlation coefficients of mesoterrain displacement, slope, and curvature are respectively

$$r_0 = 1 - \frac{1}{2} T_0^2 + \frac{1}{24} (T_0 T_1)^2 - \frac{1}{720} (T_0 T_1 T_2)^2 + \frac{1}{40320} (T_0 T_1 T_2 T_3)^2 - \dots \quad (38)$$

$$r_1 = 1 - \frac{1}{2} T_1^2 + \frac{1}{24} (T_1 T_2)^2 - \frac{1}{720} (T_1 T_2 T_3)^2 + \frac{1}{40320} (T_1 T_2 T_3 T_4)^2 - \dots \quad (39)$$

$$r_2 = 1 - \frac{1}{2} T_2^2 + \frac{1}{24} (T_2 T_3)^2 - \frac{1}{720} (T_2 T_3 T_4)^2 + \frac{1}{40320} (T_2 T_3 T_4 T_5)^2 - \dots \quad (40)$$

with the restriction that  $T_j \ll 1$ . Figure 3 shows typical correlation coefficients calculated using Equations 38 through 40 and the computer program MESO. These curves show how the calculation breaks down for large spatial distance (large  $T_j$ ) because only a finite number of standard deviations are accurately obtained from a measured elevation profile. In other words the use of a truncated series restricts these results to small values of spatial distance  $\alpha$ .

Power Spectra. The power spectrum measures the frequency content of a random process. It is defined as the Fourier transform of the autocorrelation function as follows<sup>11,13</sup>

$$P_n^*(k) = \frac{1}{\pi} \int_{-\infty}^{\infty} R_n(\alpha) e^{-ik\alpha} d\alpha \quad (41)$$

$$R_n(\alpha) = \frac{1}{2} \int_{-\infty}^{\infty} P_n^*(k) e^{ik\alpha} dk \quad (42)$$

where

$$\begin{aligned} k &= 2\pi\Omega \\ \Omega &= \text{spatial frequency} \\ n &= 0, 1, 2, 3, \dots \end{aligned}$$

The definition of the power spectrum is physically valid only if the average values of the random processes have physical significance, because according to Equation 13u, the average values  $\xi_n^M$  appear in the definition of the autocorrelation functions  $R_n(\alpha)$ .

However, for the mesoroughness description the autocovariance functions  $C_n(\alpha)$  are of more physical interest because elevation profiles are measured from an arbitrary baseline and this leads to arbitrary average values  $\xi_n^M$  for the mesoroughness profile. The autocovariance functions, however, describe the mesoterrain roughness relative to the average values, i.e. it takes the average values to be the baseline and therefore describes zero mean random processes. For terrain roughness descriptions the power spectra of physical interest are defined by the following Fourier transform pairs

$$P_n(k) = \frac{1}{\pi} \int_{-\infty}^{\infty} C_n(\alpha) e^{-ik\alpha} d\alpha \quad (41a)$$

$$C_n(\alpha) = \frac{1}{2} \int_{-\infty}^{\infty} P_n(k) e^{ik\alpha} dk \quad (42a)$$

where

$$k = 2\pi\Omega$$

Equation 41a is the formal definition of the power spectra for mesoterrain displacement, slope, curvature, etc. This equation can be used to determine  $P_n(k)$  provided  $C_n(\alpha)$  is completely specified for all  $\alpha$ , and this is never the case for actual terrain elevation data. In particular the integral (Equation 41a) converges only if  $C_n(\alpha) \rightarrow 0$  for large  $\alpha$ , i.e.,  $C_n(\alpha)$  must be known for large  $\alpha$  and must approach zero in this limit. This precludes using the series expansion in Equation 26, which is valid only for small  $\alpha$ , because in this case

$$P_n(k) = \frac{\sigma_n^2}{\pi} \sum_{j=0}^{\infty} (-1)^j S_{nj} \int_{-\infty}^{\infty} \alpha^{2j} e^{-ik\alpha} d\alpha \quad (43)$$

$$= \frac{2\sigma_n^2}{\pi} \sum_{j=0}^{\infty} (-1)^j S_{nj} F_j(k)$$

where

$$F_j(k) = \int_0^{\infty} \alpha^{2j} \cos(k\alpha) d\alpha \quad (44)$$

The integrals  $F_j(k)$  do not converge, so that the power spectrum cannot be obtained from a power series expansion of the autocovariance function.

The use of a finite set of data points precludes the complete determination of  $C_n(\alpha)$  using Equation 14 and therefore  $P_n(k)$  cannot be determined for the full range of frequencies  $0 < \Omega < \infty$  by using Equation 41a. A finite set of data points results from the finite length  $L$  of the elevation profile and from the fact that the elevation profile is measured at intervals  $\Delta L = L/N$ , so that the limits on the domain of definition of  $C_n(\alpha)$  are  $\Delta L < \alpha < L$ . Then the spatial frequencies have the following bounds  $L^{-1} < \Omega < (\Delta L)^{-1}$ , so that the lack of information about  $C_n(\alpha)$  for large  $\alpha$  leads to a lack of information about  $P_n(\Omega)$  for small  $\Omega$ , while the lack of information about  $C_n(\alpha)$  for small  $\alpha$  leads to an uncertainty in the values of  $P_n(\Omega)$  for high frequencies. The upper frequency limit  $(2\Delta L)^{-1}$  often occurs in information theory and is called the Nyquist frequency.<sup>11</sup>

In order to determine the behavior of  $P_n(\Omega)$  for  $\Omega < 1/L$  and for  $\Omega > 1/\Delta L$  a model approach for the mesoterrain roughness power spectrum is adopted. The procedure uses the following mathematical model for the power spectra of mesoterrain displacement, slope, curvature, etc.<sup>1,2</sup>

$$P_0(\Omega) = C\Omega^{-2} + D\Omega^{-3} + E\Omega^{-4} \quad (45)$$

$$P_1(\Omega) = (2\pi)^2 \Omega^2 \left[ \frac{\sin(\pi\Omega\Delta L)}{\pi\Omega\Delta L} \right]^2 P_0(\Omega) \quad (46)$$

$$P_2(\Omega) = (2\pi)^4 \Omega^4 \left[ \frac{\sin(\pi\Omega\Delta L)}{\pi\Omega\Delta L} \right]^4 P_0(\Omega) \quad (47)$$

$$P_n(\Omega) = (2\pi)^{2n} \Omega^{2n} \left[ \frac{\sin(\pi\Omega\Delta L)}{\pi\Omega\Delta L} \right]^{2n} P_0(\Omega) \quad (48)$$

The coefficients C, D, and E of the three-parameter power spectrum model are evaluated from the values of  $\sigma_0$ ,  $\sigma_1$ , and  $\sigma_2$  that are obtained from detrended (and in some cases undertrended) elevation profile data measured at intervals of length  $\Delta L$ .<sup>1,2</sup> This model predicts the five basic types of power spectra that are shown in Figure 4. Spectral types 3 and 4 exhibit no trend, so that for these cases it is possible to use undertrended elevation data to determine the power spectrum.<sup>1,2</sup> The five spectral types can be used to classify mesoterrain areas.

**3. MESOTERRAIN COVER AND MOBILITY PROBABILITIES.** The main objective of this paper is the development of a quantitative method for estimating the effects of a specified mesoterrain roughness on the survivability of a vehicle on a battlefield. Survivability depends in part on the mobility and cover characteristics of the mesoroughness. The mobility characteristics are described by the degree of slopes expected to be encountered, while the cover afforded a vehicle is described by the expected amplitudes and widths (wavelengths) of the hills and holes of the mesoroughness.

This part of the paper uses the terrain descriptors defined in Part II to calculate the probabilities for encountering specified values, and ranges of values, of mesoterrain elevation and slope. For the description of available cover the specified value of the mesoterrain displacement is the depth of a hole, generally equal to the vehicle height or larger, which will afford cover to a vehicle. For mobility considerations a critical slope may be specified which would limit a vehicle's performance.

As described in Part II the mesoroughness elevation variation and its derivatives are described by stochastic variables whose parameters are the standard deviations  $\sigma_0$ ,  $\sigma_1$ ,  $\sigma_2$  ... of the displacement and its derivatives. For the calculation of cover and slope probabilities, a Gaussian distribution is assumed for the random variables of terrain displacement and its derivatives.

Two kinds of probability index are calculated in this paper: (a) the probability of finding a given mesoroughness elevation and slope at a fixed point in the battlefield area, and (b) the probability of encountering a specified mesoroughness elevation and slope in a specified small interval of the

battlefield terrain. The first probability is useful in the case where the vehicle motion (or travel time) is not important; while the second type of probability is used for moving vehicles looking for a covered firing position. The two situations are quite distinct and an area having large probability of cover at a fixed point in the area may exhibit a relatively small probability of finding cover in a specified small distance interval.

For a fixed point in the battlefield the probability of cover can be evaluated if the standard deviation of mesoroughness elevation  $\sigma_0$  is known for the area which contains the point. The probability of a moving vehicle finding cover in a specified interval will also depend on the spatial frequency content of the mesoterrain roughness. Thus a relatively smooth area (of long wavelengths) will afford less cover in a specified interval than an undulating area (of shorter wavelengths) with the same standard deviation of mesoroughness elevation. The calculation of the probability of finding a specified elevation (cover) in a given interval will be shown to depend on  $\sigma_1$  as well as  $\sigma_0$ , so that for the case of a moving vehicle looking for a covered firing position the standard deviation of slope is a critical terrain roughness descriptor.

The probability of encountering a given mesoterrain elevation or range of elevations (cover) in a specified interval of distance corresponds to finding cover in a corresponding specified interval of time given by  $\alpha = \mu t$ , where  $\alpha$  = specified distance,  $\mu$  = vehicle speed, and  $t$  = specified time. If the time interval is taken to be the time interval between successive rounds fired by an enemy gun  $t_f$ , then the vehicle had better be able to find cover in the distance  $\alpha_f = \mu t_f$  else its chances for survival will be small. Therefore it is of practical value to calculate the probability of finding cover in a specified distance in terms of the roughness descriptors and to use these probabilities as an index to delineate areas of a battlefield having different degrees of cover.

In a similar way it will be shown that the probability of encountering a specified slope in a given interval will depend on the standard deviation of the second derivative  $\sigma_2$  as well as on the standard deviation of the slope  $\sigma_1$ . Therefore for mobility problems over short distances in a battlefield the curvature roughness parameter is as important as the slope roughness parameter. This probability is important to assess the possible values of slopes that may be encountered in a dash for cover in the interval  $\alpha_f = \mu t_f$ .

Probability Density Functions for a Point in the Battlefield. The calculation of probabilities of finding specified values of the mesoterrain elevation and its derivatives at a point in the battlefield requires the calculation of probability density functions and probability distribution functions.<sup>11,13</sup> These functions are commonly used in probability theory. Of particular interest to military problems will be the probability of encountering specified values of elevation and slope.

This paper assumes that the mesoterrain elevation, slope, curvature, and all higher derivatives are independent stationary random processes whose distribution about their mean values are given by Gaussian probability density functions defined by

$$p_G^M(\xi_n) = \frac{1}{\sqrt{2\pi}\sigma_n} e^{-\frac{(\xi_n - \xi_n^M)^2}{2\sigma_n^2}} \quad (49)$$

If the stochastic variables are measured from their mean values by  $\psi_n = \xi_n - \xi_n^M$ , the zero mean Gaussian distribution is given by

$$p_G(\psi_n) = \frac{1}{\sqrt{2\pi}\sigma_n} e^{-\frac{\psi_n^2}{2\sigma_n^2}} \quad (50)$$

where as defined in Part II the variables  $\xi_n$  and  $\psi_n$  correspond to the detrended elevation profile assumed to describe the mesoroughness as follows

$\xi_n$  = n'th derivative of mesoterrain roughness elevation measured from arbitrary level

$\psi_n$  = n'th derivative of the mesoterrain elevation measured from its mean value

Only the standard deviations  $\sigma_n$  are required to describe the Gaussian distributions. The probability density functions determine the probability of encountering a specified value of  $\xi_n$ .

The probability density functions have the following properties for  $n = 0, 1, 2, 3, \dots$

$$\int_{-\infty}^{\infty} p_G^M(\xi_n) d\xi_n = 1 \quad (51)$$

$$\langle \xi_n \rangle = \int_{-\infty}^{\infty} \xi_n p_G^M(\xi_n) d\xi_n = \xi_n^M \quad (52)$$

$$\langle \xi_n^2 \rangle = \int_{-\infty}^{\infty} \xi_n^2 p_G^M(\xi_n) d\xi_n = \sigma_n^2 \quad (53)$$

and for the zero mean probability density functions

$$\int_{-\infty}^{\infty} p_G(\psi_n) d\psi_n = 1 \quad (54)$$

$$\langle \psi_n \rangle = \int_{-\infty}^{\infty} \psi_n p_G(\psi_n) d\psi_n = 0 \quad (55)$$

$$\langle \psi_n^2 \rangle = \int_{-\infty}^{\infty} \psi_n^2 p_G(\psi_n) d\psi_n = \sigma_n^2 \quad (56)$$

Typical shapes of the  $p_G^M(\xi_n)$  and  $p_G(\psi_n)$  functions are given in Figure 5a.

A further descriptor of the zero mean Gaussian distribution is the average of positive values only of the stochastic variables

$$\langle \psi_n \rangle^+ = \int_0^{\infty} \psi_n p_G(\psi_n) d\psi_n = \frac{\sigma_n}{\sqrt{2\pi}} \quad (55a)$$

Therefore  $\sigma_n/\sqrt{2\pi}$  is a measure of the average amplitude of the variation of the stochastic variables about its mean value of zero.

If joint probabilities are required it should be remembered that the derivatives  $\xi_n$  are not completely arbitrary in the sense that  $\sigma_0, \sigma_1, \sigma_2, \sigma_3, \dots$  are not completely independent.<sup>1,2</sup> Therefore the joint distribution is not simply the product of two or more probability density functions, but requires the introduction of correlation coefficients between the various derivatives.<sup>11,13</sup> This has not been studied in this paper.

Probability Distribution Function for a Point in the Battlefield. The probability distribution function defined for the zero mean Gaussian distribution is

$$\begin{aligned} P_G(\beta_n) &= \frac{1}{\sqrt{2\pi}\sigma_n} \int_{-\infty}^{\beta_n} e^{-\psi_n^2/(2\sigma_n^2)} d\psi_n \\ &= \int_{-\infty}^{\beta_n} p_G(\psi_n) d\psi_n \end{aligned} \quad (57)$$

where  $\beta_n$  = a specified value of  $\psi_n$  for  $n = 0, 1, 2, 3, \dots$ . This function determines the probability that  $\psi_n \leq \beta_n$ , i.e.,<sup>11,13</sup>

$$\text{Prob}(\psi_n \leq \beta_n) = P_G(\beta_n) \quad (58)$$

The probability that  $\psi_n > \beta_n$  is then given by

$$\text{Prob}(\psi_n > \beta_n) = 1 - P_G(\beta_n) \quad (59)$$

The probability distribution functions for Gaussian distributions are often written as

$$P_G(\beta_n) = \text{erf}\left(\frac{\beta_n}{\sigma_n}\right) + \frac{1}{2} \quad (60)$$

where the error function  $\text{erf}(x)$  is defined as<sup>13</sup>

$$\text{erf}(x) = \frac{1}{\sqrt{2\pi}} \int_0^x e^{-z^2/2} dz \quad (61)$$

A graph of the function  $\text{erf}(x)$  is shown in Figure 5b.

Probability of Cover for a Vehicle at a Point in the Battlefield. The zero mean Gaussian probability distribution representing the mesoterrain elevation variations can be used to estimate the probability of finding cover for a vehicle at some point in a battlefield. The condition for complete cover is assumed to be that the vehicle sits in a depression whose depth is equal or greater than the height of the vehicle  $\psi_0 \leq -H_v$ , where  $H_v$  = vehicle height (see Figure 5c). The probability for finding cover is

$$\begin{aligned} \text{Prob}(\psi_0 \leq -H_v) &= P_G(-H_v) \\ &= \frac{1}{2} + \text{erf}(-H_v/\sigma_0) \\ &= \frac{1}{2} - \text{erf}(H_v/\sigma_0) \end{aligned} \quad (62)$$

A typical graph of the function  $P_G(-H_v)$  is given in Figure 5d. The relevant mesoroughness parameter is the standard deviation of the mesoterrain elevation.

Slope Probability at a Point in the Battlefield. For slope probabilities the situation is somewhat different because both positive and negative values of these parameters must be considered. The probability distribution function for slope is expressed in terms of a critical slope  $\psi_1^C$  such that mobility is possible for  $|\psi_1| < \psi_1^C$ . The probability for slope  $\psi_1$  being outside this range is

$$\begin{aligned}
\text{Prob}(\psi_1 < -\psi_1^c \text{ or } \psi_1 > \psi_1^c) &= \frac{1}{\sqrt{2\pi}\sigma_1} \int_{-\infty}^{-\psi_1^c} e^{-\psi_1^2/(2\sigma_1^2)} d\psi_1 \\
&\quad + \frac{1}{\sqrt{2\pi}\sigma_1} \int_{\psi_1^c}^{\infty} e^{-\psi_1^2/(2\sigma_1^2)} d\psi_1 \\
&= \frac{2}{\sqrt{2\pi}\sigma_1} \int_{-\infty}^{-\psi_1^c} e^{-\psi_1^2/(2\sigma_1^2)} d\psi_1 \\
&= 2P_G(-\psi_1^c) = 1 - 2 \text{erf}(\psi_1^c/\sigma_1)
\end{aligned} \tag{63}$$

Then the probability for  $|\psi_1| < \psi_1^c$  is

$$\text{Prob}(|\psi_1| < \psi_1^c) = 1 - 2P_G(-\psi_1^c) = 2 \text{erf}(\psi_1^c/\sigma_1) \tag{64}$$

and this can be used as a mobility index. This function appears in Figure 5e. A similar analysis can be done for the curvature and higher derivatives. Wheeled vehicles have  $\psi_1^c = 0.3$  and tracked vehicles have  $\psi_1^c = 0.45$ .

The situation of a moving vehicle seeking cover in a specified distance and of encountering a specified range of slopes in this interval can also be quantified by the theory of probability. The probabilities of encountering specified values of mesoterrain elevation and slope in a given interval can be expressed in terms of the autocovariance functions defined in Part II and in terms of the standard deviations of the elevations and its derivatives.

Probability Density Functions in an Interval of Travel. The probability density functions for encountering specified values of the zero mean Gaussian random processes  $\psi_n$ , given by  $\psi_n = \beta_n$ , in a small interval  $\alpha$  are given by<sup>13</sup>

$$P_n(\alpha) = \frac{1}{\pi} \sqrt{\frac{2[C_n(0) - C_n(\alpha)]}{C_n(0)}} \frac{e^{-1/2(\beta_n/\sigma_n)^2}}{\sqrt{2\pi}\sigma_n} \tag{65}$$

where  $n = 0, 1, 2, 3, \dots$  refer to the mesoterrain elevation and its derivatives. These probability density functions can be rewritten in terms of the correlation coefficients defined in Equation 16 as follows<sup>13</sup>

$$\begin{aligned}
p_n(\alpha) &= \frac{1}{\pi} \sqrt{2[1 - r_n(\alpha)]} \frac{e^{-1/2(\beta_n/\sigma_n)^2}}{\sqrt{2\pi}\sigma_n} \\
&= \frac{1}{\pi} \sqrt{2[1 - r_n(\alpha)]} p_G(\beta_n, \sigma_n)
\end{aligned}
\tag{66}$$

The probability density functions can be rewritten in terms of the standard deviations using the power series expansions in Equations 25 and 27 as follows

$$p_n(\alpha) = \frac{\alpha}{\pi} M_n \frac{e^{-1/2(\beta_n/\sigma_n)^2}}{\sqrt{2\pi}\sigma_n} = \frac{\alpha}{\pi} M_n p_G(\beta_n, \sigma_n)
\tag{67}$$

where

$$\begin{aligned}
M_n &= \sqrt{\frac{2}{2!} \left(\frac{\sigma_{n+1}}{\sigma_n}\right)^2 - \frac{2}{4!} \left(\frac{\sigma_{n+2}}{\sigma_n}\right)^2 \alpha^2 + \frac{2}{6!} \left(\frac{\sigma_{n+3}}{\sigma_n}\right)^2 \alpha^4 - \dots} \\
&= \sqrt{2 \sum_{j=1}^{\infty} (-1)^{j+1} \frac{S_{nj}}{(2j)!} \alpha^{2(j-1)}}
\end{aligned}
\tag{68}$$

where  $S_{nj}$  is defined in Equation 31.

The probability density functions can also be written in terms of the dimensionless wavelength parameters  $T_n$  given in Equation 35 as follows

$$p_n(\alpha) = \frac{T_n \phi_n}{\pi} \frac{e^{-1/2(\beta_n/\sigma_n)^2}}{\sqrt{2\pi}\sigma_n}
\tag{69}$$

where

$$\begin{aligned}
\phi_n &= \frac{\alpha}{T_n} M_n = \frac{\lambda_n M_n}{2\pi} = \frac{\sqrt{2(1-r_n)}}{T_n} \\
&= \sqrt{1 - \frac{2}{4!} T_{n+1}^2 + \frac{2}{6!} (T_{n+1} T_{n+2})^2 - \frac{2}{8!} (T_{n+1} T_{n+2} T_{n+3})^2 + \dots} \\
&= \sqrt{1 + \sum_{j=2}^{\infty} (-1)^{j+1} \frac{2}{(2j)!} (T_{n+1} T_{n+2} T_{n+3} \dots T_{n+j-1})^2} \\
&= \sqrt{1 + \sum_{j=2}^{\infty} (-1)^{j+1} \frac{2}{(2j)!} \left(\frac{\lambda_n}{2\pi}\right)^2 S_{nj} \alpha^{2(j-1)}}
\end{aligned} \tag{70}$$

For reference, the first few  $\phi_n$  are

$$\phi_0 = \sqrt{1 - \frac{2}{4!} T_1^2 + \frac{2}{6!} (T_1 T_2)^2 - \frac{2}{8!} (T_1 T_2 T_3)^2 + \dots} \tag{71}$$

$$\phi_1 = \sqrt{1 - \frac{2}{4!} T_2^2 + \frac{2}{6!} (T_2 T_3)^2 - \frac{2}{8!} (T_2 T_3 T_4)^2 + \dots} \tag{72}$$

$$\phi_2 = \sqrt{1 - \frac{2}{4!} T_3^2 + \frac{2}{6!} (T_3 T_4)^2 - \frac{2}{8!} (T_3 T_4 T_5)^2 + \dots} \tag{73}$$

For small values of  $\alpha$  the values of  $\phi_n$  are nearly unity.

The probability density functions (Equation 69) for an interval in the mesoterrain can be written in terms of the Gaussian probability density function as follows

$$p_n(\alpha) = \frac{\alpha \sigma_{n+1}}{\pi \sigma_n} \phi_n p_G(\beta_n, \sigma_n) = \frac{2\alpha}{\lambda_n} \phi_n p_G(\beta_n, \sigma_n) \tag{74}$$

Consider now the special cases of mesoterrain elevation, slope, and curvature

$$p_0(\alpha) = \frac{\alpha \sigma_1}{\pi \sigma_0} \phi_0 p_G(\beta_0, \sigma_0) = \frac{2\alpha}{\lambda_0} \phi_0 p_G(\beta_0, \sigma_0) \tag{75}$$

$$p_1(\alpha) = \frac{\alpha \sigma_2}{\pi \sigma_1} \phi_1 p_G(\beta_1, \sigma_1) = \frac{2\alpha}{\lambda_1} \phi_1 p_G(\beta_1, \sigma_1) \tag{76}$$

$$p_2(\alpha) = \frac{\alpha\sigma_3}{\pi\sigma_2} \phi_2 p_G(\beta_2, \sigma_2) = \frac{2\alpha}{\lambda_2} \phi_2 p_G(\beta_2, \sigma_2) \quad (77)$$

A result similar to Equation 75, but involving the power spectrum, has already appeared in the literature.<sup>14</sup> From Equation 75, it is clear that in addition to the elevation Gaussian probability density function  $p_G(\beta_0, \sigma_0)$ , a spatial frequency term  $\sigma_1/\sigma_0$  appears in the expression for the mesoterrain elevation probability density function. Therefore, to first order the standard deviations  $\sigma_0$  and  $\sigma_1$ , determine the elevation probability density function. The standard deviations of the second and higher order derivatives enter to a lesser degree through the function  $\phi_0$ . Likewise Equation 76 shows that the probability density function for encountering a specified slope in a given interval is proportional to  $\sigma_2/\sigma_1$  in addition to the slope Gaussian probability density function.

Probability Distribution Function in an Interval of Travel. The probability distribution functions associated with the probability density functions given in Equation 74 are

$$\begin{aligned} P(\beta_n) &= \int_{-\infty}^{\beta_n} p_n d\psi_n \\ &= \frac{\alpha\sigma_{n+1}}{\pi\sigma_n} \phi_n \int_{-\infty}^{\beta_n} p_G(\psi_n, \sigma_n) d\psi_n \\ &= \frac{\alpha\sigma_{n+1}\phi_n}{\pi\sigma_n} P_G(\beta_n) = \frac{2\alpha}{\lambda_n} \phi_n P_G(\beta_n) \end{aligned} \quad (78)$$

where  $P_G(\beta_n)$  is related to the error function as in Equation 60.

Cover Available in a Specified Interval of Travel. The probability of finding cover for a vehicle of high  $H_v$  in a specified interval of the mesoroughness is calculated in terms of the probability distribution function (Equation 78) as follows

$$\begin{aligned} \text{Prob}(\psi_0 < -H_v) &= P(-H_v) \\ &= \frac{\alpha\sigma_1\phi_0}{\pi\sigma_0} P_G(-H_v) = \frac{2\alpha}{\lambda_0} \phi_0 P_G(-H_v) \\ &= \frac{\alpha\sigma_1\phi_0}{\pi\sigma_0} \left[ \frac{1}{2} - \text{erf}(H_v/\sigma_0) \right] \end{aligned} \quad (79)$$

The probability for finding cover in a specified mesoterrain interval depends on  $\sigma_1$  as well as  $\sigma_0$  through the ratio  $\sigma_1/\sigma_0 \sim 1/\lambda_0$ . In other words Equation 79 shows that for the same values of  $\sigma_0$  the mesoterrain containing longer elevation wavelengths affords less cover in a specified distance. The standard deviations of the second and higher elevation derivatives also influence the degree of cover through the functions  $\phi_0$  defined in Equation 71.

Degree of Mobility Possible in a Specified Interval of Travel. The problems of determining a mobility probability index for mapping purposes amounts to calculating the probability that  $|\psi_1| < \psi_1^c$  in a specified interval, where  $\psi_1^c$  = critical slope beyond which a vehicle cannot go. This is calculated as follows

$$\begin{aligned} \text{Prob}(\psi_1 < -\psi_1^c \text{ or } \psi_1 > \psi_1^c) &= \int_{-\infty}^{-\psi_1^c} p_1 d\psi_1 + \int_{\psi_1^c}^{\infty} p_1 d\psi_1 \\ &= \frac{2\alpha\sigma_2\phi_1}{\pi\sigma_1} P_G(-\psi_1^c) \\ &= \frac{4\alpha}{\lambda_1} \phi_1 P_G(-\psi_1^c) \\ &= \frac{2\alpha\sigma_2\phi_1}{\pi\sigma_1} \left[ \frac{1}{2} - \text{erf}(\psi_1^c/\sigma_1) \right] \end{aligned} \tag{80}$$

Then the probability of finding slopes less than the critical slope is given by

$$\begin{aligned} \text{Prob}(|\psi_1| < \psi_1^c) &= \frac{2\alpha\sigma_2\phi_1}{\pi\sigma_1} \text{erf}(\psi_1^c/\sigma_1) = \frac{4\alpha}{\lambda_1} \phi_1 \text{erf}(\psi_1^c/\sigma_1) \\ &= \frac{2\alpha\phi_1}{\lambda_1} \left[ 1 - 2P_G(-\psi_1^c) \right] \end{aligned} \tag{81}$$

The probability of encountering a critical slope in a mesoterrain interval depends on  $\sigma_2$  as well as on  $\sigma_1$  through the characteristic slope wavelength  $\sigma_2/\sigma_1 \sim 1/\lambda_1$ . The standard deviations of the third and higher derivatives also affect the calculation, but to a smaller degree, through the function  $\phi_1$  defined in Equation 72.

Average Distance Between Covered Positions and Between Points of Critical Slope. The average distance that a vehicle would have to travel between two

covered positions and between two adjacent points where the critical slope value occurs can be estimated from the values of the characteristic mesoterrain elevation wavelength  $\lambda_0$  and the characteristic mesoterrain slope wavelength  $\lambda_1$  that are given in Equation 32. The simplest assumptions give the following results

$$\alpha_0 \sim \lambda_0 \frac{H_v}{\sigma_0} = 2\pi \frac{H_v}{\sigma_1} \quad (82)$$

$$\alpha_1 \sim \lambda_1 \frac{\psi_1^c}{\sigma_1} = 2\pi \frac{\psi_1^c}{\sigma_2} \quad (83)$$

where

$\alpha_0$  = average distance between two adjacent covered positions for a vehicle of height  $H_v$

$\alpha_1$  = average distance between two slope mobility failures for a vehicle whose critical slope is  $\psi_1^c$ .

Numerical Analysis of Terrain Roughness Probabilities. Macroterrain elevation data were available for only two terrain sites - Freiensteinau and Wetzlar both located in West Germany. A 1-mile section of macroterrain elevation data was selected from each site. Smaller sections of 100-m length within the one mile sections, the mesoterrain elevation profiles, were analyzed and the results compared the descriptors of the full 1-mile section.

The standard deviation of the detrended elevation can be used as a measure of the relative roughness of the Freiensteinau and Wetzlar sites. These standard deviations appear in Figure 6a in terms of the reciprocal of the detrending parameter. In terms of this descriptor the Freiensteinau site is about four times more rough than the Wetzlar site. Nevertheless, as seen in Figures 6b through 6d, the characteristic wavelengths  $\lambda_0$  and  $\lambda_1$  are roughly the same for the two sites.

The power spectra of the terrain displacement were calculated using Equation 45 and the techniques developed in References 1 and 2. The results appear in Figures 7a and 7b from which it is clear that several different types of power spectra can occur for the 100-m sections within a 1-mile terrain elevation profile. Therefore the power spectrum type will vary along a terrain section, and the mesoterrain roughness power spectra is expected to be different from the macroterrain roughness power spectra.

Figure 8a shows the Gaussian cumulative probability for terrain elevations as calculated from Equations 60 and 62. Figure 8b shows the results of using Equation 62 to calculate the Gaussian cumulative probability for finding cover for a vehicle of height  $H_v = 8$  ft in terms of the detrending parameter  $\lambda$ . The detrending parameter enters the probability calculation through the function  $\sigma_0(\lambda)$  given in Figure 6a. Equation 79 is used to calculate the cumulative probability for finding cover in a 1-ft unit interval, and the

results are shown in Figure 8c. A peak occurs in the Freiensteinau probability curve in Figure 8c because the probability varies inversely with  $\lambda_0$  as in Equation 79, and  $\lambda_0$  is a rapidly decreasing function of  $\lambda^{-1}$  as given in Figure 6b.

Figures 8d through 8f give the probability distribution functions for encountering critical slopes using Equations 63, 80, and 81. The critical slopes were taken to be 0.3 for wheeled vehicles and 0.45 for track-laying vehicles. The standard deviation of the slopes at the Wetzlar and Freiensteinau terrain sites are about an order of magnitude smaller than the critical slopes so that the probability of encountering these critical slope values is vanishingly small. No terrain data is available for a site which would exhibit high probabilities for encountering the critical slopes. In order to obtain some numerical results the elevations at the Freiensteinau and Wetzlar sites were arbitrarily magnified by a factor of 10. Figures 8d through 8f give the critical slope probability distribution functions for this artificial situation. However since relative probabilities are of interest, it is clear that Freiensteinau has the higher probability for encountering a critical slope value.

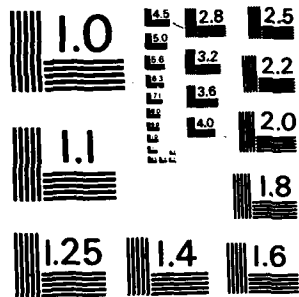
Mobility and Cover Map Overlays. The cover and mobility probabilities can be used to construct military map overlays on which areas having distinct mobility or cover characteristics are isolated to form a patchwork. Each patch of a map overlay for a specified vehicle is associated with a probability index of cover or mobility as calculated from the standard deviations of the elevation and its derivatives. Several elevation profiles are measured for each area to determine a descriptive set of values for  $\sigma_0$ ,  $\sigma_1$ ,  $\sigma_2$ , and so on. In this way map overlays can be produced in a logical fashion from some elevation profiles measured in each area.

4. CONCLUSIONS. This paper develops a formalism for developing cover and mobility map overlays. The formalism is based on a rigorous application of probability theory to the description of random terrain elevation data. Terrain descriptors obtained from elevation profiles measured in a battlefield area are used to develop cover and mobility indices for the purpose of determining patches on a map overlay having distinct cover and mobility characteristics.

The studies of mesoterrain roughness gave the following conclusions:

- a. The mesoterrain roughness can be extracted from a measured elevation profile by a detrending procedure with a proper choice of filter constant (Part II).
- b. The basic set of terrain descriptors required for the complete specification of mesoroughness are the standard deviations of the mesoterrain elevation and its derivatives (Part II).
- c. The probabilities for encountering specified ranges of mesoterrain elevation or slope in a given distance can be determined from the





MICROCOPY RESOLUTION TEST CHART  
NATIONAL BUREAU OF STANDARDS-1963-A

standard deviations of mesoterrain elevation and its derivatives, and these probabilities can be used as indices for determining patches on a map that have distinct cover and mobility characteristics (Part III).

5. ACKNOWLEDGEMENT. I wish to thank N. R. Murphy, Jr., C. J. Nuttall, Jr., and J. H. Robinson for their helpful advice. The computer program RFNWUD was developed by R. B. Ahlvin.

#### REFERENCES

1. Weiss, R. A., "Characterization of Terrain Roughness, Volume I, Micro-roughness Description and Its Application to the Dynamic Response of Vehicles," Draft Report, September 1980, U. S. Army Engineer Waterways Experiment Station, CE, Vicksburg, Miss.
2. Weiss, R. A., "Terrain Microroughness and the Dynamic Response of Vehicles," in Trans. of 27th Conf. of Army Mathematicians, ARO Report 82-1, West Point, N. Y., 1981.
3. Weiss, R. A., "Characterization of Terrain Roughness, Volume II, Meso-roughness Description and Its Application to Mobility and Cover," Draft Report, September 1981, U. S. Army Engineer Waterways Experiment Station, CE, Vicksburg, Miss.
4. Zeller, M., Textbook of Photogrammetry, Lewis, London, 1952.
5. Hallert, B., Photogrammetry, McGraw-Hill, New York, 1960.
6. Raasch, W., "Photometric Measurement of Terrain Roughness," May 1978, IABG, Ottobrunn bei Munchen, Germany.
7. Clark, G. and Lobdell, M., "Terrain and Environment," Chapter 3 in the Tank Weapon System, edited by Howland, D. and Clark, G., Report No. RF-573, AR66-1(V), June 1966, Ohio State University, Columbus, Ohio.
8. Bussman, D. R., "Vibrations of a Multi-Wheeled Vehicle," in Tank Weapon System, edited by Howland, D. and Clark, G., Report No. RF-573, TR 64-1(U), August 1964, Ohio State University, Columbus, Ohio.
9. Kozin, F., Code, L. and Bogdanoff, J., "Statistical Studies of Stable Ground Roughness," Report No. 8391-LL-95, 1963, U. S. Army Tank-Automotive Center, Warren, Mich.
10. Jurkat, M., Nuttall, C., and Haley, P., "The AMC '74 Mobility Model," Technical Report No. 11921 (LL-149), May 1975, U. S. Army Tank-Automotive Command, Warren, Mich.
11. Bendat, J. and Piersol, A., Random Data, Wiley-Interscience, New York, 1971.
12. Van Deusen, R., "A Statistical Technique for the Dynamic Analysis of Vehicles Traversing Rough Yielding and Non-Yielding Surfaces," Contract Report No. NASW-1287, May 1966, Advanced Projects Organization, Chrysler Corp, Detroit, Mich.
13. Papoulis, A., "Probability Random Variables and Stochastic Process," McGraw-Hill, New York, 1965.
14. Stollmack, S., "Environmental Models," Chapter 2.1 of Tank Weapon System, edited by Howland, D. and Clark, G., Report No. RF-573, AR 66-2(U), December 1966, Ohio State University, Columbus, Ohio.

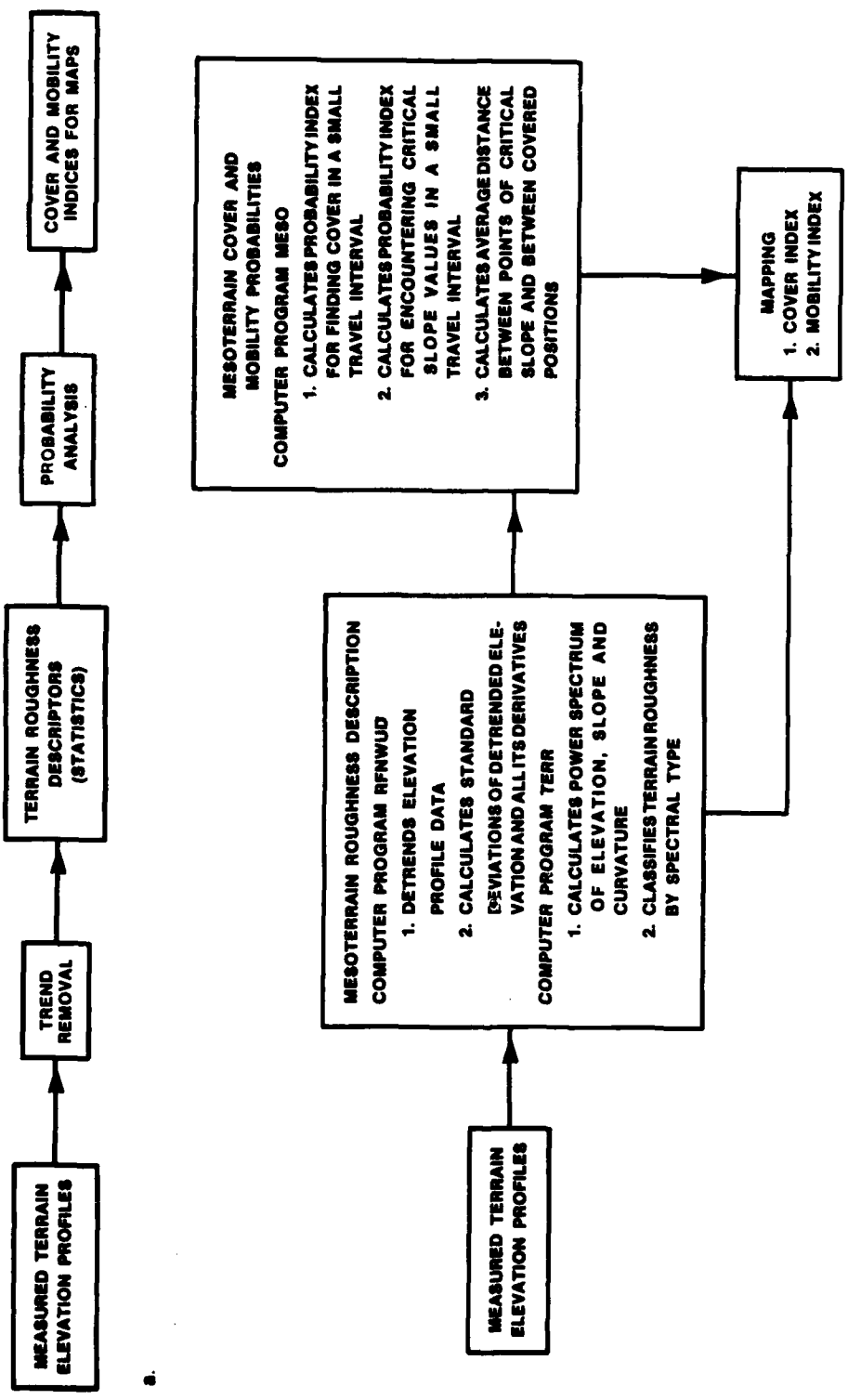


Figure 1

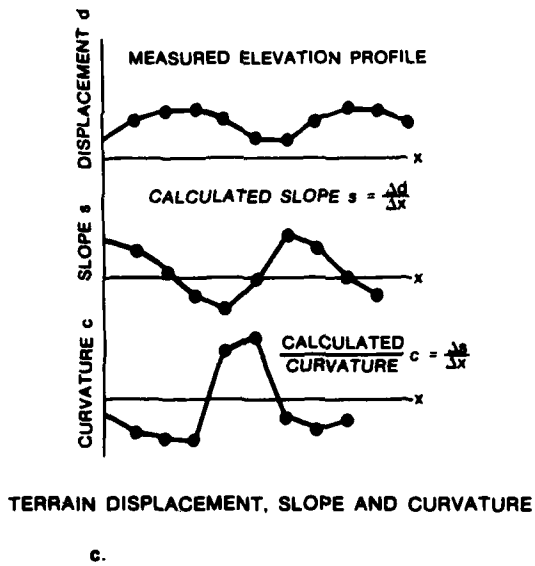
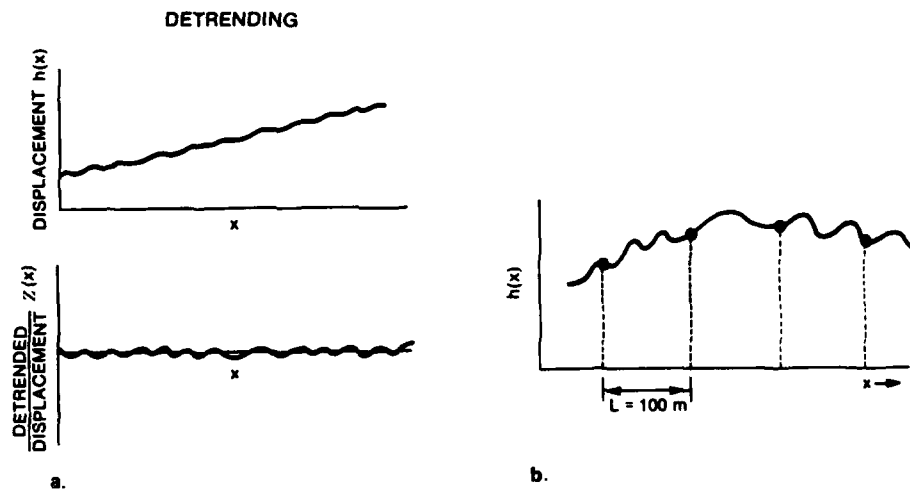


Figure 2

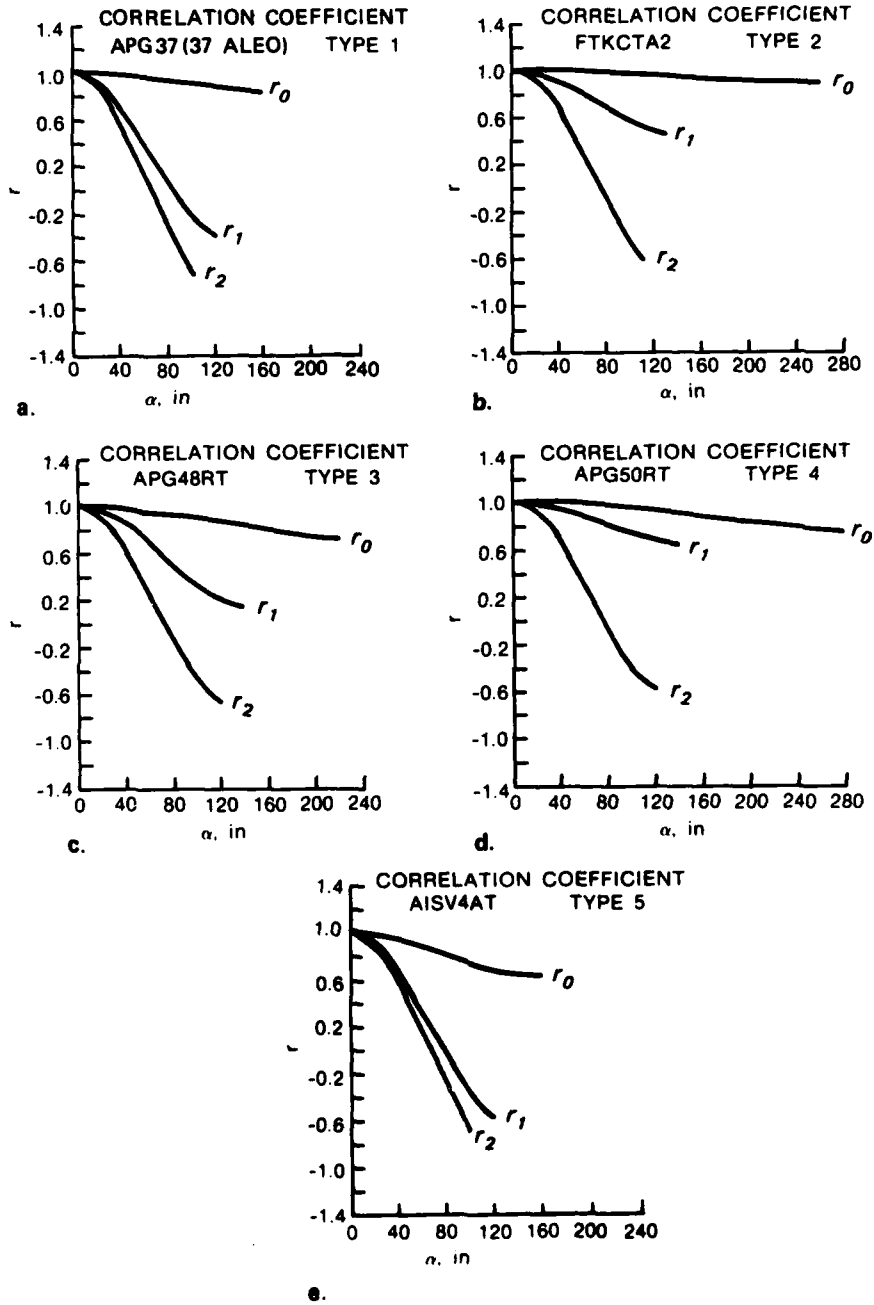


Figure 3

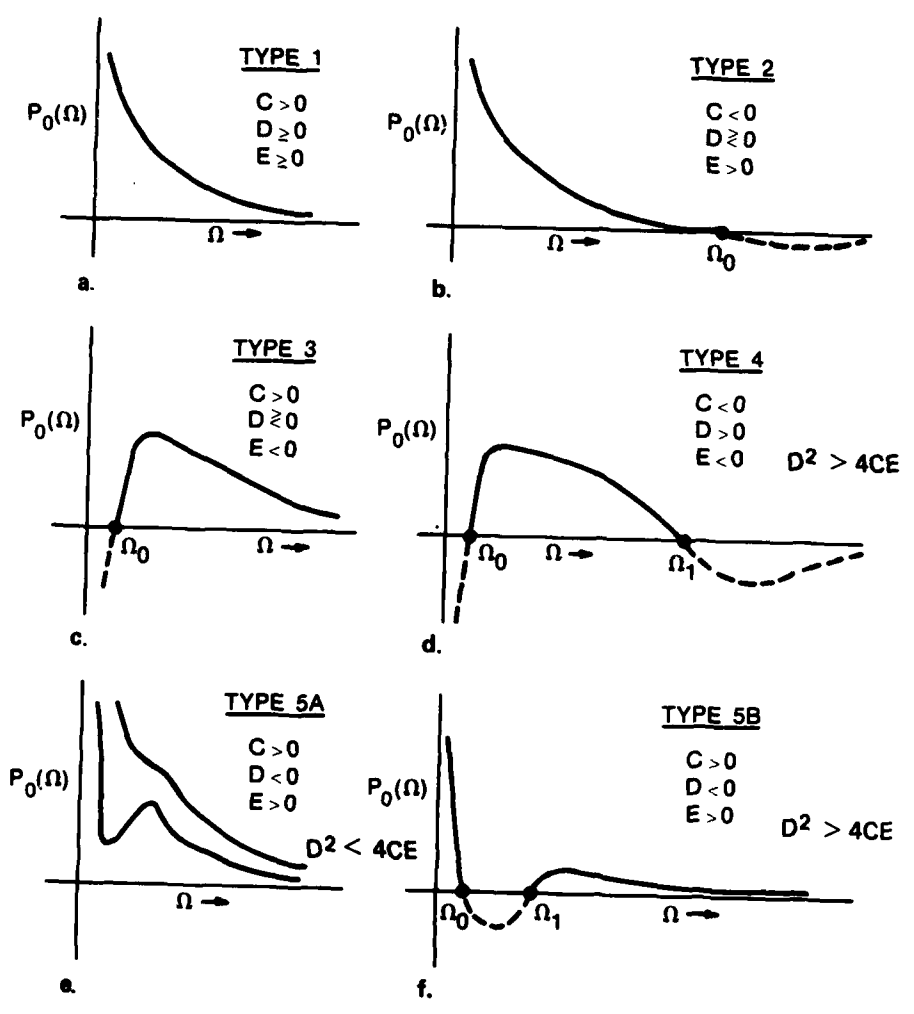
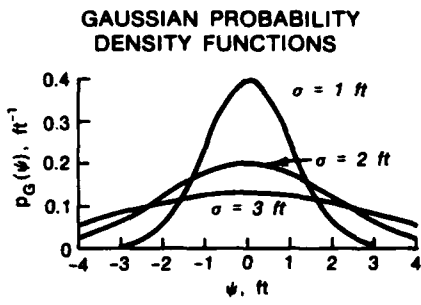
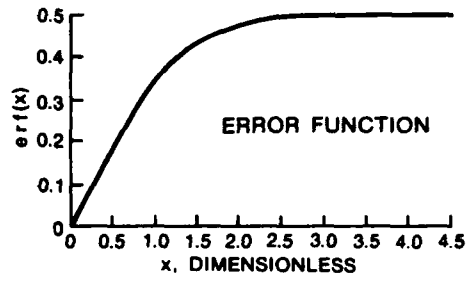


Figure 4

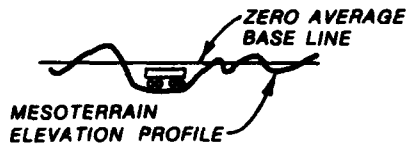


a.

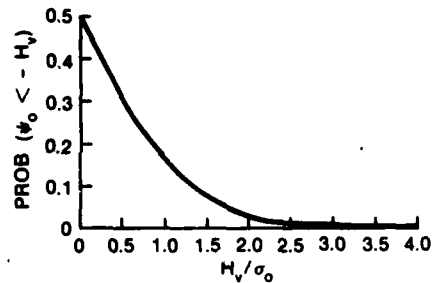


b.

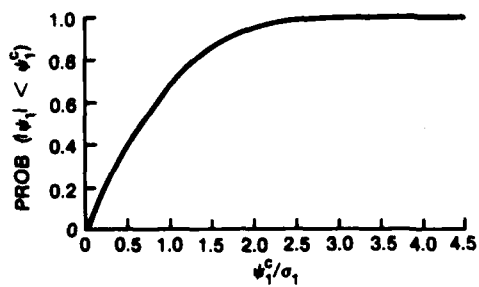
COVER CONDITION,  $\psi_0 < -H_v$   
 $H_v$  = VEHICLE HEIGHT  
 $\psi_0$  = MESOROUGHNESS ELEVATION



c.



d.



e.

Figure 5

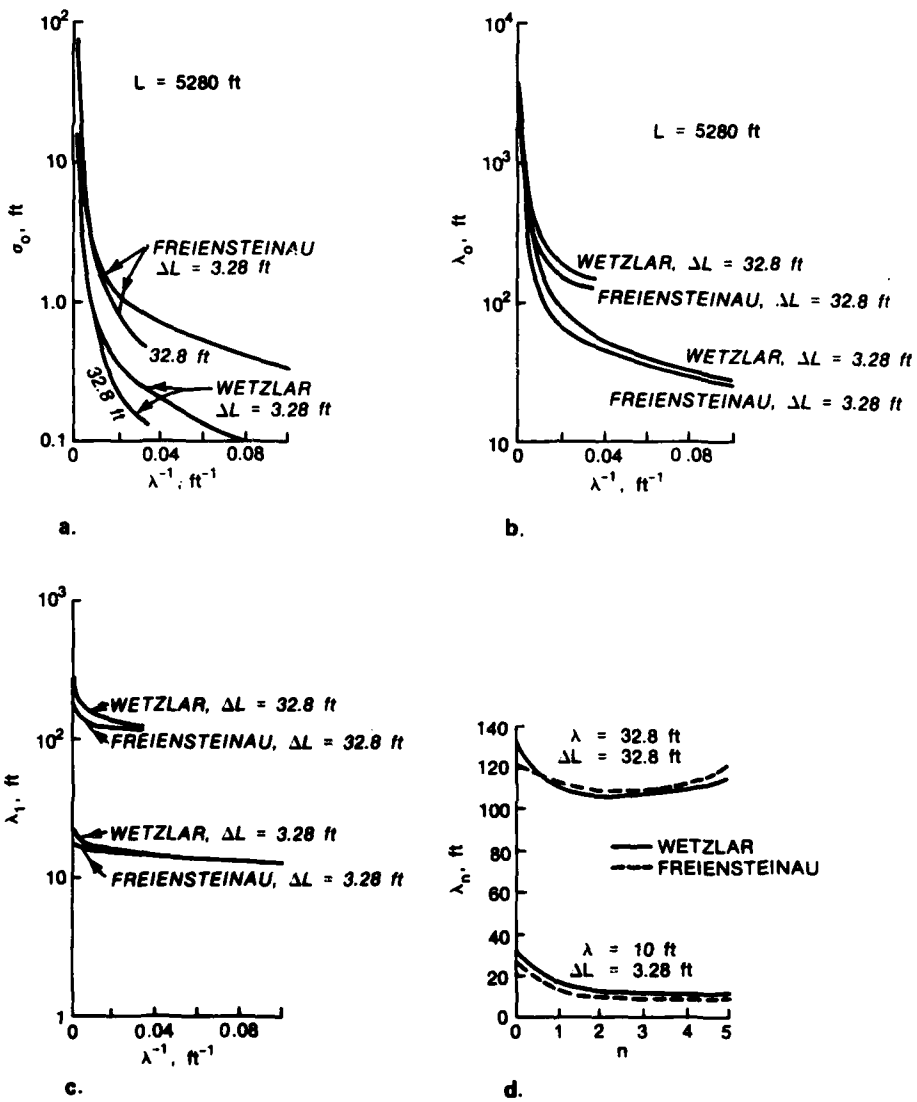


Figure 6

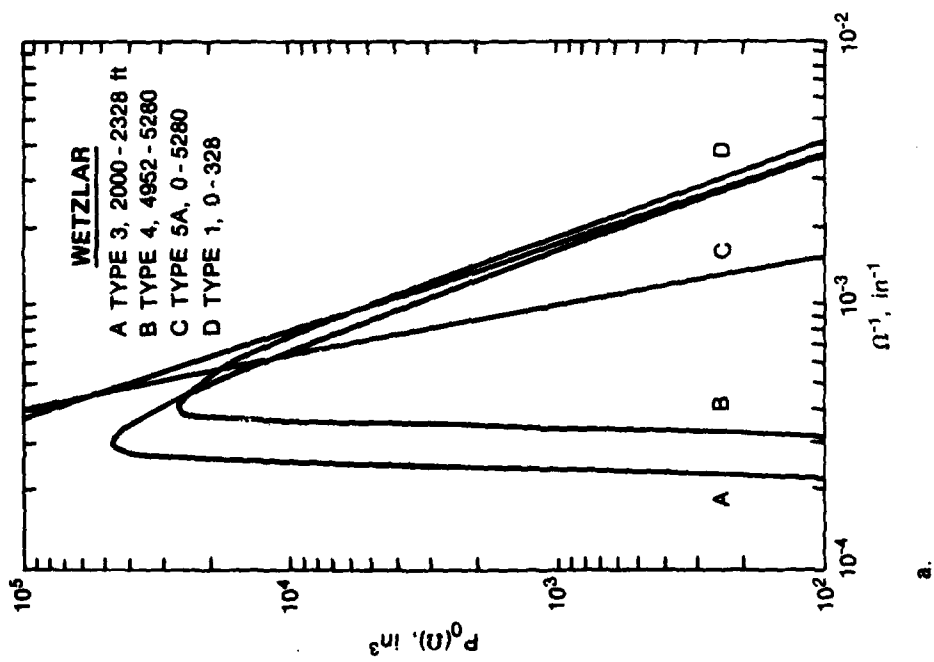
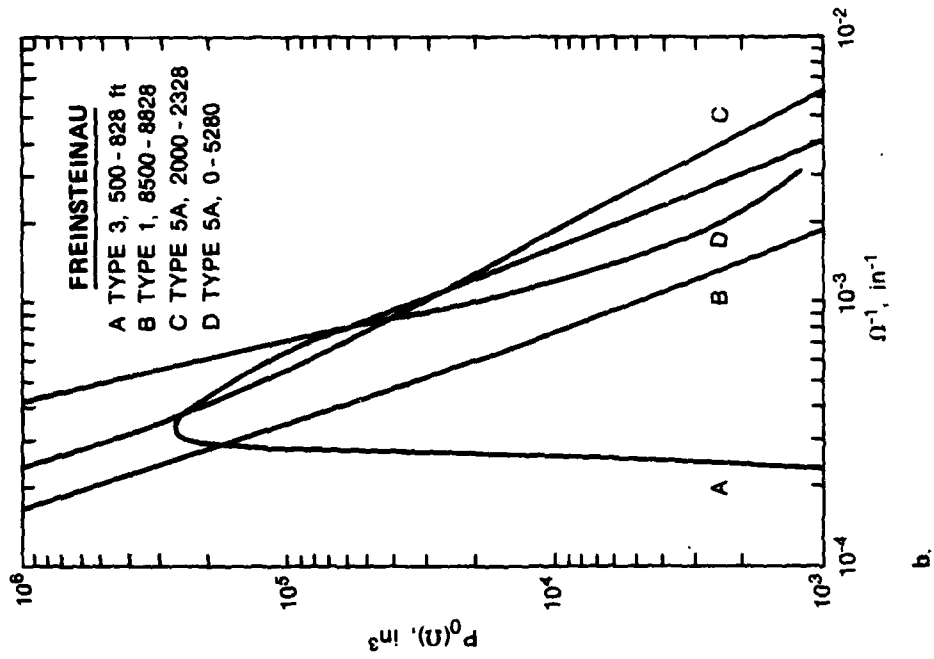


Figure 7

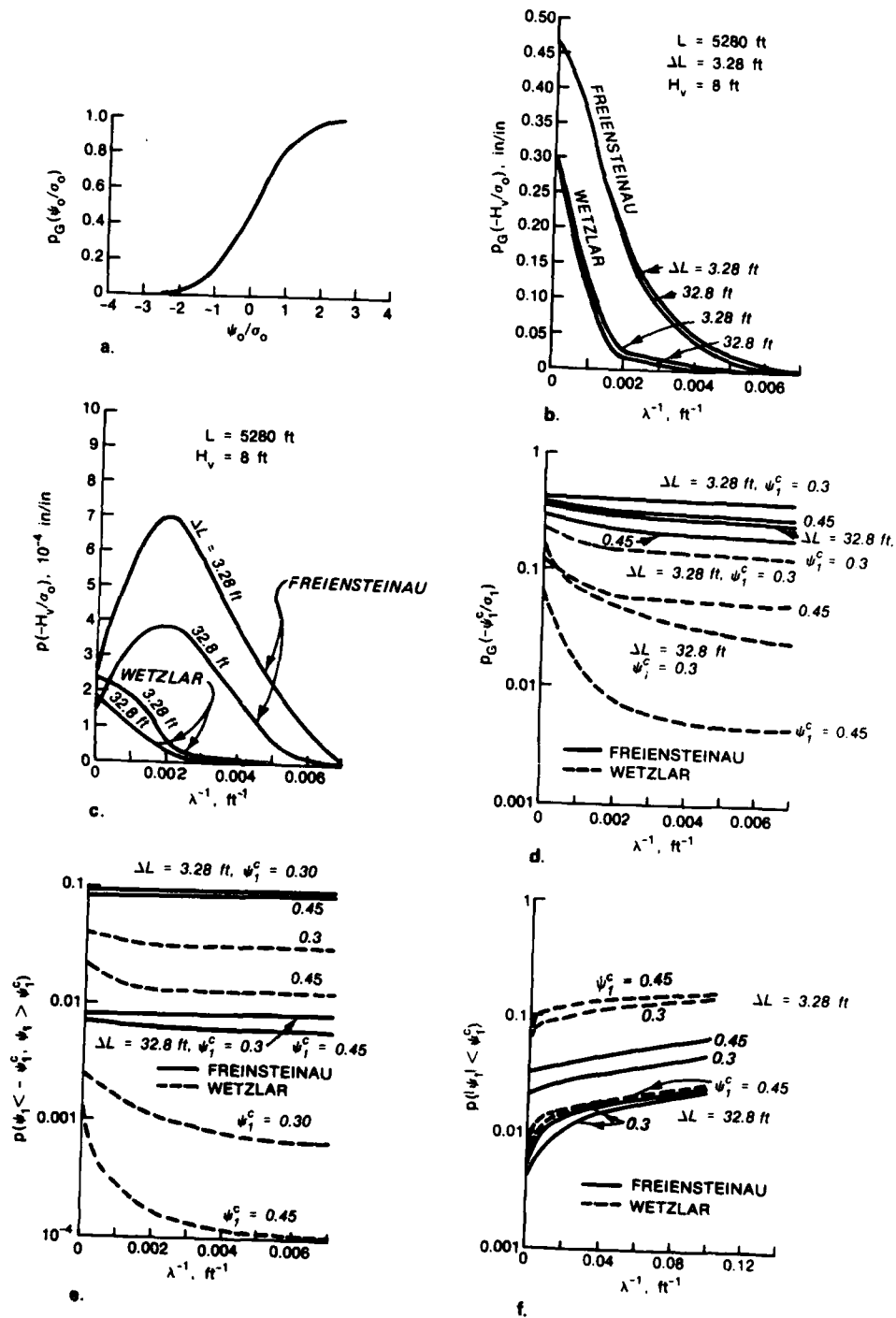


Figure 8

dupe

INTERVAL BOUNDS FOR STATIONARY VALUES OF FUNCTIONALS

L. B. Rall  
Mathematics Research Center  
University of Wisconsin-Madison

**ABSTRACT.** A number of important problems in applied mathematics can be reduced to finding stationary values of functionals (maxima, minima, and critical values). For functionals defined in terms of integrals, the method of interval integration provides a way to obtain interval (two-sided) bounds for the stationary values. As a special case of this method, upper and lower bounds for eigenvalues of linear operators can be obtained. The inclusion of stationary values in intervals is based on the use of interval functions which include the functional for which the functional is stationary, and its derivatives. A simple way to construct such interval functions is given, and examples are presented of a minimum eigenvalue problem. The improvement of initial results by iteration is indicated.

**1. VARIATIONAL PROBLEMS.** A number of important problems in physical mathematics and applied analysis, particularly the calculus of variations and control theory, reduce to finding maxima and minima of functionals

$$(1.1) \quad f = f[y], \quad y \in A,$$

where  $A$  is the class of *admissible functions* for the problem. In addition to the *extremal values*

$$(1.2) \quad \underline{f} = \min_{y \in A} \{f[y]\}, \quad \bar{f} = \max_{y \in A} \{f[y]\},$$

of  $f$ , one may seek its *critical values*

$$(1.3) \quad f^* = f[y^*],$$

where the *critical point*  $y^* \in A$  of  $f$  satisfies the *Euler equation*

$$(1.4) \quad f'[y] = 0,$$

it being assumed in this case that the Gâteaux derivative  $f'$  of  $f$  exists on  $A$  [5]. Under this assumption, *extremal points*  $\underline{y}, \bar{y} \in \text{int}A$  such that  $\underline{f} = f[\underline{y}]$ ,  $\bar{f} = f[\bar{y}]$  will be *critical points* of  $f$  (see [2]). For simplicity, *extremal and critical points and values* of a functional will be called its *stationary points and values*, respectively. A *variational problem* for  $f$  on  $A$  is to find one or more of the pairs  $(\underline{f}, \underline{y})$ ,  $(\bar{f}, \bar{y})$ ,  $(f^*, y^*)$ , if such exist.

An *interval bound* for a stationary value  $f^*$  of a functional  $f$  is simply an interval  $[a, b]$  such that  $f^* \in [a, b]$ , that is

$$(1.5) \quad a < f^* < b.$$

Research sponsored by the United States Army under Contract No. DAAG29-80-C-0041.

RESEARCH AND ANALYSIS DIVISION

For functionals defined in terms of integrals, such as

$$(1.6) \quad f[y] = \int_{x_0}^{x_1} f(x, y, y', y'', \dots, y^{(n)}) dx, \quad y \in A,$$

it will be shown that the method of interval integration [1], [4], provides a way to obtain interval bounds for stationary values of  $f$ . In the variational problem for  $f$  defined by (1.6), the class  $A$  of admissible functions is usually characterized by continuity, differentiability, and boundary conditions on  $y$ .

It should be noted that *one-sided* bounds for extremal values are easy to obtain: For arbitrary  $y \in A$ , one has

$$(1.7) \quad \underline{f} \leq f[y] \leq \bar{f}.$$

Lower bounds for minima and upper bounds for maxima, however, are often not easy to obtain, and in the case of nonextremal stationary values (such as intermediate eigenvalues of a linear operator), one is often completely in the dark. The two-sided bounds (1.5) furnished by interval integration are easy to compute, by contrast, as will be seen below. The methodology will be developed for functionals of the form (1.6) for clarity, and its immediate extension to several independent variables will be presented in the final section.

2. INTERVAL INTEGRATION. Interval analysis [3] is the branch of mathematics which takes real bounded intervals  $[a, b]$  as its basic units, and studies transformations of them. Its relationship to real analysis is somewhat analogous to that of complex analysis, since the reals can be identified with the subset of intervals which have equal endpoints, the so-called *degenerate* intervals  $x = [x, x]$  for real  $x$ . An *interval function*  $Y$  of a real variable  $x$  assigns the interval  $[\underline{y}(x), \bar{y}(x)]$  to each  $x$  in its interval of definition  $X = [x_0, x_1]$ . The *interval integral* of  $Y$  over  $X$  is the interval

$$(2.1) \quad \int_X Y(x) dx = \left[ (LD) \int_{x_0}^{x_1} \underline{y}(x) dx, (UD) \int_{x_0}^{x_1} \bar{y}(x) dx \right],$$

where (LD) and (UD) denote lower and upper Darboux integrals, respectively [1]. Since these Darboux integrals exist for all real functions, it follows that all interval functions are integrable, and hence integration is a universal operation in interval analysis [1].

In the study of interval transformations, the transformation  $T$  of  $X$  into  $T(X)$  is said to be *monotone* if  $X \subset Z \Rightarrow T(X) \subset T(Z)$ , and a transformation  $U$  *includes*  $T$  on  $X$  if  $T(X) \subset U(X)$ , in particular, if  $y$  is a real function, then the interval function  $Y$  includes  $y$  on  $X$  if

$$(2.2) \quad y(X) = \{y(x) \mid x \in X\} \subset Y(X)$$

[3]. In this sense, the interval function  $Y$  is the set of *all* real functions  $y$  such that  $\underline{y}(x) \leq y(x) \leq \bar{y}(x)$  for  $x \in X$ , and one writes  $y \in Y$  in this case. The interval integral (2.1) is a monotone function of its integrand [1], so that

$$(2.3) \quad \int_{x_0}^{x_1} y(x) dx \subset \int_{x_0}^{x_1} Y(x) dx \quad \text{for } y \in Y,$$

whether or not  $y$  has a real (Riemann or Lebesgue) integral. The real integral of a real function, if it exists, is of course contained in its interval integral, which always exists [1], [4]. The calculation of the interval integral of  $Y$  is simplified if the *endpoint functions*  $\underline{y}, \bar{y}$  of  $Y$  are Riemann (R) integrable. Then,

$$(2.4) \quad \int_X Y(x) dx = [ (R) \int_X \underline{y}(x) dx, (R) \int_X \bar{y}(x) dx ],$$

so that inclusions of interval integrals can be computed for integrands  $Z \supset Y$  with Riemann integrable endpoint functions [1].

3. INTERVAL BOUNDS. Considering the integrand of (1.6) to be a function  $f(x, u_0, u_1, \dots, u_n)$  of  $n + 2$  variables, an interval inclusion  $F(X, U_0, U_1, \dots, U_n)$  of it can be constructed by interval arithmetic [3] or otherwise. Then, interval integration provides the following result.

Theorem 3.1. Suppose that  $\hat{y} \in A$  is a stationary point of the functional  $f$  defined by (1.6),  $\lambda = f[\hat{y}]$  is the corresponding stationary value of  $f$ , and the interval functions  $Y_0, Y_1, \dots, Y_n$  on  $X = [x_0, x_1]$  are such that  $\hat{y}^{(i)} \in Y_i, i = 0, 1, \dots, n$ . Then

$$(3.1) \quad \lambda \in [a, b] = \int_{x_0}^{x_1} F(x, Y_0(x), Y_1(x), \dots, Y_n(x)) dx$$

This result provides the two-sided bounds (1.5) for  $\lambda$  immediately. It appears that one must assume a lot about  $\hat{y}$  and its derivatives to use (3.1). In many cases, however, one only has to assume something about  $\hat{y}^{(n)}$  (for example, that it is bounded), and then the interval functions  $Y_{n-1}, \dots, Y_1, Y_0$  can be constructed by the use of interval integration and the boundary conditions. For example, suppose that

$$(3.2) \quad \hat{y}^{(n)} \in Y_n, \hat{y}^{(n-1)}(x_0) \in [\alpha_0, \beta_0], \hat{y}^{(n-1)}(x_1) \in [\alpha_1, \beta_1].$$

Note that *interval* boundary conditions can be prescribed. Thus, interval techniques can be useful in practical problems in which boundary conditions are not known precisely, or in which it is desired to study the behavior of a system over a range of boundary conditions.

Indefinite interval integration of (3.2) gives the functions

$$(3.3) \quad Y_L(x) = [\alpha_0, \beta_0] + \int_{x_0}^x Y_n(t) dt, \quad Y_R(x) = [\alpha_1, \beta_1] + \int_{x_1}^x Y_n(t) dt.$$

Definition 3.1. The interval function  $Y_n$  is said to be *admissible* for the boundary conditions (3.2) if  $[\alpha_1, \beta_1] \subset Y_L(x_1)$ ,  $[\alpha_0, \beta_0] \subset Y_R(x_0)$ , and the intersection  $Y_L(x) \cap Y_R(x)$  is nonempty for  $x \in X$ .

Theorem 3.2. If the interval function  $Y_n$  is admissible for the boundary conditions (3.2) and  $\hat{y}^{(n)} \in Y_n$ , then

$$(3.4) \quad \hat{y}^{(n-1)} \in Y_{n-1} = Y_L \cap Y_R.$$

Proof. By construction, the interval function  $Y_{n-1}$  defined by (3.4) contains all real functions  $g$  such that  $g' \in Y_n$ ,  $g(x_0) \in [\alpha_0, \beta_0]$  and  $g(x_1) \in [\alpha_1, \beta_1]$ , as a consequence of the definition of the indefinite interval integral [1]. QED.

It should be noted that  $Y_{n-1}$  constructed in this way also contains other real functions which satisfy the boundary conditions, but may have no continuity or differentiability properties at all. An example of the actual construction of an interval function of this type is given in the next section.

4. THE SIMPLEST PROBLEM OF THE CALCULUS OF VARIATIONS. This is the case  $n = 1$  of (1.6) [2], and to simplify matters further, the boundary conditions

$$(4.1) \quad y(x_0) = y_0, \quad y(x_1) = y_1$$

will be imposed. The class  $A$  of admissible functions will be restricted to those for which  $y'$  is *bounded*, that is,  $y' \in [\underline{m}, \bar{m}]$ , where  $\underline{m}, \bar{m}$  denote constant interval functions with the corresponding real value. Interval integration gives

$$(4.2) \quad Y_L(x) = y_0 + [\underline{m}, \bar{m}](x - x_0), \quad Y_R(x) = y_1 - [\underline{m}, \bar{m}](x - x_1),$$

and thus  $Y_1 = [\underline{m}, \bar{m}]$  is admissible for (4.1) if

$$(4.3) \quad \underline{m} \leq m \leq \bar{m}, \quad m = \frac{y_1 - y_0}{x_1 - x_0}.$$

The graph of the corresponding interval function  $Y_0$  is thus a parallelogram with vertices  $(x_0, y_0)$  and  $(x_1, y_1)$ , bounded above by the intersecting lines

$$(4.4) \quad \bar{y}_L(x) = y_0 + \bar{m}(x - x_0), \quad \bar{y}_R(x) = y_1 - \underline{m}(x - x_1),$$

and below by

$$(4.5) \quad \underline{y}_L(x) = y_0 + \underline{m}(x - x_0), \quad \underline{y}_R(x) = y_1 - \bar{m}(x - x_1).$$

Using this interval function  $Y_0$ , one has immediately that

$$(4.6) \quad f[y] \in \int_{x_0}^{x_1} F(x, Y_0(x), [\underline{m}, \bar{m}]) dx$$

on the class A of functions satisfying (4.1) for which  $y' \in [\underline{m}, \bar{m}]$ . For example, suppose that

$$(4.7) \quad f[y] = \int_{x_0}^{x_1} \sqrt{1 + (y')^2} dx,$$

and one seeks  $\lambda = \min\{f[y]\}$  on A. Since

$$(4.8) \quad (y')^2 \in [0, \max\{\underline{m}^2, \bar{m}^2\}],$$

one has

$$(4.9) \quad \lambda \in [x_1 - x_0, d], \quad d = \int_{x_0}^{x_1} \sqrt{1 + m^2} dx = \sqrt{(x_1 - x_0)^2 + (y_1 - y_0)^2},$$

since each admissible  $Y_1$  contains  $y' = m$ , and thus each  $Y_0$  contains the degenerate interval (real) function

$$(4.10) \quad y_m(x) = y_0 + m(x - x_0),$$

for which the value  $f[y_m] = d$  is attained. Better lower and upper bounds for this value are obtained as  $Y_0$  encloses  $y_m$  more tightly.

5. EIGENVALUE PROBLEMS. For selfadjoint linear operators A in a Hilbert space H, *eigenvalues* are critical values of the *Rayleigh quotient*

$$(5.1) \quad R(y) = (Ay, y)/(y, y), \quad y \neq 0.$$

An eigenvalue  $\lambda$  satisfies the Euler equation

$$(5.2) \quad Ay - \lambda y = 0, \quad y \neq 0,$$

and the corresponding critical points y in a function space H are called *eigenfunctions* of A belonging to  $\lambda$  [2]. If the inner product  $(, )$  in H is defined in terms of integrals, then interval integration can be applied as above to find lower and upper bounds for eigenvalues of A. If  $Y_0, Y_1$  are interval functions such that  $\varphi \in Y_0, 0 \in Y_0$ , and  $\Lambda\varphi \in Y_1$  for some eigenfunction  $\varphi$  of A, then

$$(5.3) \quad \lambda \in (Y_1, Y_0)/(Y_0, Y_0) = [a, b]$$

for the corresponding eigenvalue  $\lambda$ , thus giving an interval bound. Once again, the interval functions  $Y_0, Y_1$  are to be determined in some way, perhaps on the basis of an approximate solution of (5.2). If A is an integral operator, then one can use interval integration to get  $Y_1 = AY_0$ . On the other hand, if A is a differential operator, it may be possible to obtain  $Y_0$  from  $Y_1$  by use of interval

integration and the boundary conditions, as before. For example, suppose that

$$(5.4) \quad Ay = -y'', \quad y(0) = y(\pi) = 0.$$

Since eigenfunctions are determined by (5.1) and (5.2) only up to a multiplicative constant, it is useful to introduce a normalization condition which excludes  $y = 0$  in particular. In this case, suppose that  $-y''(\pi/2) = 1$ , and take  $Y_1$  defined by

$$(5.5) \quad \bar{y}_1(0) = [0,1], \quad \bar{y}_1(x) = 1, \quad 0 < x < \pi, \quad \bar{y}_1(\pi) = [0,1],$$

( $\bar{y}_1(x)$  is an interval step function [1]), and

$$(5.6) \quad \underline{y}_1(x) = (2/\pi)x, \quad 0 \leq x \leq \pi/2, \quad \underline{y}_1(x) = (2/\pi)(\pi - x), \quad \pi/2 \leq x \leq \pi.$$

By integrating  $Y_1(x)$  twice and using the boundary conditions in (5.4), one gets  $Y_0$  defined by

$$(5.7) \quad \bar{y}_0(x) = \frac{x}{2}(\pi - x), \quad 0 \leq x \leq \pi,$$

and

$$(5.8) \quad \underline{y}_0(x) = \begin{cases} x\left(\frac{\pi}{4} - \frac{x^2}{3\pi}\right), & 0 \leq x \leq \pi/2, \\ (\pi - x)\left(\frac{\pi}{4} - \frac{(\pi - x)^2}{3\pi}\right), & \pi/2 < x \leq \pi. \end{cases}$$

Computation with these interval functions gives

$$(5.9) \quad (Y_1, Y_0) = \frac{\pi^3}{6} \left[ \frac{1}{5}, \frac{1}{2} \right], \quad (Y_0, Y_0) = \frac{\pi^5}{120} \left[ \frac{17}{42}, 1 \right].$$

and thus eigenvalues  $\lambda$  belonging to eigenfunctions  $\varphi \in Y_0$  will be elements of the interval Rayleigh quotient  $(Y_1, Y_0)/(Y_0, Y_0)$ , that is,

$$(5.10) \quad \lambda \in \Lambda_0 = \frac{20}{\pi^2} \left[ \frac{1}{5}, \frac{21}{17} \right] \subset [0.4052, 2.5033].$$

In this case,  $\varphi(x) = \sin x$  is the only eigenfunction of  $\Lambda$  contained in  $Y_0$ , and (5.10) provides lower and upper bounds for the corresponding eigenvalue  $\lambda = 1$ .

The endpoint functions (5.5) are crude approximations to  $\sin x$ , and it can be noted that (5.7) and (5.8) define an interval function which, when normalized, is smaller than  $Y_1$  and bounded by better approximations to the eigenfunction. This suggests an iteration process, the next step being to take  $(2/\pi)^2 Y_0 = Y_1$  as a new interval function containing  $-\varphi''$ , which leads to an improved  $Y_0$  and a corresponding value  $\Lambda_1$  for the interval Rayleigh quotient. Indeed, if  $\Lambda_1 \subset \Lambda_0$ , then the existence

of an eigenvalue  $\lambda \in \Lambda_1$  of  $A$  is guaranteed by the Schauder fixed point theorem [5].

6. VARIATIONAL PROBLEMS IN SEVERAL DIMENSIONS. The extension of Theorem 3.1 to problems in several independent variables follows immediately from the corresponding extension of the interval integral. In  $R^V$ , let  $x = (\xi_1, \xi_2, \dots, \xi_V)$ , and the region of integration be denoted by  $\Omega$ . Following the prescription given in [1], partition  $\Omega$  by elements  $\Omega_1, \Omega_2, \dots, \Omega_m$  with measures (areas or volumes)  $d\Omega_i$ ,  $i = 1, 2, \dots, m$ , and let

$$(6.1) \quad \forall Y_i = \left[ \inf_{x \in \Omega_i} \{Y(x)\}, \sup_{x \in \Omega_i} \{Y(x)\} \right],$$

where  $Y$  is an interval-valued function defined on  $\Omega$ . If  $\mathcal{D}_m$  denotes the set of all partitions of  $\Omega$  into  $m$  subregions, then

$$(6.2) \quad \Sigma_m = \bigcap_{\mathcal{D}_m} \sum_{i=1}^m \forall Y_i \cdot d\Omega_i, \quad m = 1, 2, 3, \dots,$$

form a nested sequence of closed intervals, and thus the interval integral of  $Y$  over  $\Omega$ ,

$$(6.3) \quad \int_{\Omega} Y(x) d\Omega = \bigcap_{m=1}^{\infty} \Sigma_m$$

exists for arbitrary  $Y$ . It is not difficult to show that this interval integral is an inclusion monotone function of its integrand using the same arguments as in [1].

Now, one can let  $D_i$  denote the vector of partial differential operators of order  $i$  in  $R^V$ , for example,  $D_1 = (\partial/\partial\xi_1, \partial/\partial\xi_2, \dots, \partial/\partial\xi_V)$ , and consider the functional

$$(6.4) \quad f[Y] = \int_{\Omega} f(x, Y, D_1 Y, D_2 Y, \dots, D_n Y) d\Omega,$$

which is the analogue of (1.6) in  $R^V$ . If  $F$  is an interval inclusion of the integrand of (6.4), and  $\lambda = f[\hat{y}]$  is a stationary value of  $f$ , then interval integration provides the following result.

**Theorem 6.1.** If  $\hat{y}$  is a stationary point of  $f$  and interval vector functions  $Y_0, Y_1, \dots, Y_n$  exist such that  $D_i \hat{y} \in Y_i$  on  $\Omega$ ,  $i = 1, 2, \dots, n$ , then

$$(6.5) \quad \lambda = f[\hat{y}] \in \int_{\Omega} F(x, Y_0(x), Y_1(x), \dots, Y_n(x)) d\Omega.$$

As an application of this theorem, suppose that in  $R^3$  the values of  $y$  are prescribed on the boundary  $\partial\Omega$  of a region  $\Omega$ , and one wishes interval bounds for

$$(6.6) \quad \lambda = \min \int_{\Omega} (\partial^2 y / \partial t^2 + \partial^2 y / \partial \eta^2 + \partial^2 y / \partial \zeta^2) d\Omega$$

over some class A of admissible functions. A construction similar to the one in §3 can be used, or  $Y_0$  can be constructed on the basis of an approximate solution of the Euler equation for (6.6), which in this case is simply the Laplace equation

$$(6.7) \quad \Delta y = 0, \quad y = y_0 \text{ on } \partial\Omega.$$

#### REFERENCES

1. O. Caprani, K. Madsen, and L. B. Rall. Integration of interval functions, SIAM J. Math. Anal. 12 (1981), 321-341.
2. R. Courant and D. Hilbert. Methods of Mathematical Physics, Vol. 1. Interscience, New York, 1953.
3. R. E. Moore. Methods and Applications of Interval Analysis, SIAM Studies in Applied Mathematics 2, Soc. Ind. Appl. Math., Philadelphia, 1979.
4. L. B. Rall. Integration of interval functions II. The finite case, SIAM J. Math. Anal. 13, no. 4 (1982).
5. J. T. Schwartz. Nonlinear Functional Analysis. Gordon and Breach, New York, 1969.

AD P001032

A SPATIAL DOMAIN WALSH FEATURE SET

Charles R. Giardina  
Electrical Engineering and Computer Science Department  
Stevens Institute of Technology  
Hoboken, N.J. 07030

Frank P. Kuhl  
Fire Control and Small Caliber Weapon Systems Laboratory  
ARRADCOM  
Dover, N.J. 07801

T. A. Grogan and O. Robert Mitchell  
School of Electrical Engineering  
Purdue University  
West Lafayette, IN 47907

*ABSTRACT.* A truncated Walsh Series is utilized as a feature set for chain encoded images. The number of terms used in this series is directly related by an easy to use formula to the number and type of vectors used in the encoded chain and the accuracy desired. The resulting Walsh approximation is shown to form an  $\epsilon$ -net for the figure thereby preserving the information of the figure while smoothing out possible noisy vectors. A normalization scheme is explained and examples given.

*I. INTRODUCTION.* The Walsh Functions are introduced as products of Rademacher Functions and are used to represent projections of Freeman encoded boundary functions. Here the projections are approximated to within a prespecified degree of accuracy  $\epsilon$  by piecewise constants using a Truncated Walsh Series. The heights of these piecewise constant portions are easily found and involve the area under the projections. A Walsh Feature Set is obtained by composing the piecewise constant Walsh Approximations. This Walsh Feature Set by nature of the approximation forms an  $\epsilon$ -net for the original boundary. Normalization algorithms are then specified for both the observable and prototypes in the recognition classes. Subsequently use is made of the  $\epsilon$ -net property and the normalization scheme to describe a possible shape recognition procedure.

II. WALSH SERIES OF X AND Y PROJECTIONS. A Walsh series for the x and y projections can be found exactly the same way a conventional Fourier Series is found. Instead of expressing x or y in terms of faster and faster varying sine waves we will express them in terms of faster and faster varying "square waves" - the Walsh Functions.

The Walsh Functions form a complete orthonormal system of functions among the square integrable functions in the interval [0,1]. They are defined below. The first Walsh Function is  $W_0(t) = 1$ , and the rest are defined by the following formula:

$$W_n(t) = r_{n_1+1}(t) \cdot r_{n_2+1}(t) \cdot \dots \cdot r_{n_p+1}(t)$$

where the integer  $n \geq 1$  is expressed "in binary" as

$$n = 2^{n_1} + 2^{n_2} + \dots + 2^{n_p}$$

where the integers  $n_i$  are determined using

$$n_1 < n_2 < \dots < n_p$$

and the  $r_k(t)$  are the Rademacher Functions as follows:

$$r_0(t) = 1$$

$$r_1(t) = \begin{cases} 1 & [0, \frac{1}{2}) \\ -1 & [\frac{1}{2}, 1) \end{cases}$$

$$r_1(t+1) = r_1(t)$$

$$r_{k+1}(t) = r_1(2^k t) \quad k = 0, 1, 2, \dots$$

In the following we will only discuss the x projection of the boundary because the same calculations can be made for the y projections. The known projection  $x(t)$  can be represented as an infinite series of the form  $x(t) = \alpha_0 W_0(t) + \alpha_1 W_1(t) + \alpha_2 W_2(t) + \dots$  because we have a complete set. Here  $W_i(t)$  is the  $i^{\text{th}}$  Walsh Function and  $\alpha_i$  is intuitively the  $i^{\text{th}}$  harmonic component and is called the  $i^{\text{th}}$  sequency component. It is found by integrating:

$$\alpha_i = \int_0^1 x(t) W_i(t) dt$$

Each  $\alpha_i$  is made up of the area under portions of the projection added and subtracted together. In any practical application only a finite number of terms in a Walsh Series can be employed - say the first  $2^N$ . If only these terms are used, an error is made called the truncation error. This error shall be discussed later. Let us assume that  $N \geq 1$  has

been chosen and let

$$x_{2^N}(t) = \alpha_0 W_0(t) + \alpha_1 W_1(t) + \dots + \alpha_{2^N-1} W_{2^N-1}(t).$$

Then we would expect  $x_{2^N}(t)$  to closely approximate  $x(t)$  in some sense particularly if  $N$  is large since we have a complete set. This in fact is the case, and furthermore  $x_{2^N}(t)$  is easier to work with on a computer than  $x(t)$  since it attains only a finite number of heights and, therefore, will be used in defining a feature set for the image. The rest of this discussion is dedicated to finding  $x_{2^N}(t)$ . A most simple method is given for determining  $x_{2^N}(t)$  at the end of this section. To find the sequency components it is convenient to represent them in vector form. So let  $\vec{\alpha}_x$  be a  $2^N$  by 1 column vector where

$$\vec{\alpha}_x = \begin{pmatrix} \alpha_0 \\ \alpha_1 \\ \alpha_2 \\ \cdot \\ \cdot \\ \alpha_{2^N-1} \end{pmatrix}$$

This vector is termed the sequency vector and since each component of this vector equals the sum and difference of the area under  $x(t)$  on intervals of length  $2^{-N}$  it is desirable to first find what is called the Area Vector  $\vec{A}_x$  whose components are just the area under  $x(t)$  taken on intervals of length  $2^{-N}$ ; i.e.,

$$\vec{A}_x = \begin{pmatrix} A_0 \\ A_1 \\ \cdot \\ \cdot \\ \cdot \\ A_{2^N-1} \end{pmatrix}$$

where each  $A_i$  is found by the expression

$$A_i = \int_{\frac{i}{2^N}}^{\frac{(i+1)}{2^N}} x(t) dt \quad i = 0, 1, 2, \dots, 2^N-1$$

The sequency vector is easily found by pre-multiplying the Area Vector by the Hadamard Matrix  $H$ , which consists of  $2^N$  rows and each row consists of  $2^N$  ones or -1's. The  $i^{\text{th}}$  row of this matrix is a vector representation of the  $i^{\text{th}}$  Walsh Function, i.e., one is used when  $W_i(t)$  equals one and -1 is used where  $W_i(t)$  equals -1 in the intervals of length  $2^{-N}$ .

Specifically, assuming that each  $\gamma_{ij} = \pm 1$  and that the Walsh Function is

$$W_i(t) = \sum_{j=0}^{2^N-1} \gamma_{ij} \chi_{\left(\frac{j}{2^N}, \frac{j+1}{2^N}\right)}(t)$$

then the  $i^{\text{th}}$  row  $i = 0, 1, 2, \dots, 2^N-1$  is

$$(\gamma_{i0} \quad \gamma_{i1} \quad \gamma_{i2} \quad \dots \quad \gamma_{i2^N-1})$$

In any case we have

$$\vec{\alpha}_x = H \vec{A}_x$$

Once  $\vec{\alpha}_x$  has been found we can find the Truncated Walsh Series  $x_{2^N}(t)$ . This series can be obtained much more quickly if we use vector representation. A vector representation will lead to a direct computation of the truncated Walsh Series. Since  $x_{2^N}(t)$  will attain at most  $2^N$  different values and will be constant in each basic interval of length  $2^{-N}$  we can write

$$x_{2^N}(t) = \sum_{i=0}^{2^N-1} c_i \chi_{\left(\frac{i}{2^N}, \frac{i+1}{2^N}\right)}(t).$$

The  $c_i$  are constants that can be found using either the above or by noticing, if we let the vector  $\vec{x}_{2^N}$  be defined as

$$\vec{x}_{2^N} = \begin{pmatrix} c_0 \\ c_1 \\ \cdot \\ \cdot \\ \cdot \\ c_{2^N-1} \end{pmatrix}$$

that

$$\vec{x}_{2^N} = H^T \vec{\alpha}_x,$$

Where  $H^T$  denotes the transpose of the Hadamard Matrix. But, since  $H$  is symmetric we have  $H = H^T$  and

$$\vec{x}_{2^N} = H \vec{\alpha}_x$$

Therefore,

$$\vec{x}_{2^N} = H^2 \vec{A}_x,$$

but using the orthonormality properties of the Walsh Functions we obtain the important conclusion that

$$\bar{x}_{2^N} = 2^N \bar{A}_x.$$

In other words the Truncated Walsh Series gives a staircase type function whose height is proportional to the area under the projection in the corresponding basic interval; i.e.,

$$x_{2^N}(t) = 2^N \sum_{i=0}^{2^N-1} A_i \chi_{\left(\frac{i}{2^N}, \frac{(i+1)}{2^N}\right)}(t)$$

$$\text{or } c_i = 2^N A_i$$

So to find  $x_{2^N}(t)$  partition  $x(t)$  into equal intervals of length  $2^{-N}$  in  $[0,1]$  and find the area under each basic interval and substitute into the last formula for  $x_{2^N}(t)$ .

**III. TRUNCATION ERROR FOR WALSH EXPANSIONS.** In the last section we arrived at formulas that enabled us to find the truncated Walsh Expansion  $x_{2^N}(t)$  for the  $x$  projection  $x(t)$ . If we define the error between  $x(t)$  and  $x_{2^N}(t)$  to be the absolute maximum pointwise difference then we have:

$$\|x(t) - x_{2^N}(t)\|_{\infty} = \sup_{0 \leq t < 1} |x(t) - x_{2^N}(t)| \leq \frac{M}{2^{N+1}}$$

where  $M$  is the maximum slope in the  $x$  projection. This follows from the more general result [1] that if  $x(t)$  satisfies a Holder Condition of order  $\alpha$ ,  $0 < \alpha \leq 1$ , with constant  $M$ , that is if

$$|x(t+h) - x(t)| \leq M|h^\alpha| \quad M \geq 0$$

for all  $t$  and  $h$  real, then

$$\|x(t) - x_{2^N}(t)\| \leq \frac{M 2^{\alpha-1}}{(2^\alpha - 1)(2^\alpha)^{N+1}}$$

And, in particular if  $\alpha = 1$  (which is true if  $x(t)$  is piecewise linear), we have what is commonly called a Lipschitz Condition or Holder 1 Condition for  $x(t)$  giving

$$\|x(t) - x_{2^N}(t)\| \leq \frac{M}{2^{N+1}}$$

**IV.  $\epsilon$ -NET.** An  $\epsilon$ -net ( $\epsilon > 0$ ) for an arbitrary bounded image  $f(x,y)$  in  $[0,1]^{R \times R}$  is another image  $W(x,y)$  in  $[0,1]^{R \times R}$  where

$$W(x,y) = \bigcup_{i=1}^L \{(x_i, y_i) | 1\}.$$

That is,  $W(x,y)$  consists of a "finite number of black dots," and furthermore every point in  $f(x,y)$  must be within  $\epsilon$  away from some point in  $W(x,y)$  in the vertical and

horizontal directions at the same time. In other words, the nonwhite points of  $W(x,y)$  are scattered in such a way that each nonwhite point of  $f(x,y)$  is no more than  $\epsilon$  away from some nonwhite point in  $W(x,y)$ . So given any nonwhite point in  $f(x,y)$  - say  $(x_\alpha, y_\alpha) | U_f(x_\alpha, y_\alpha), U_f(x_\alpha, y_\alpha) > 0$ , there must exist at least one point in  $W(x,y)$  call it  $(x_i, y_i) | 1$  such that  $|x_\alpha - x_i| \leq \epsilon$  and  $|y_\alpha - y_i| \leq \epsilon$ ;

$$\text{i.e., } \max(|x_\alpha - x_i|, |y_\alpha - y_i|) \leq \epsilon$$

Since  $x(t)$  is the projection of a Freeman Encoded boundary  $x(t)$  is a piecewise linear function that as a consequence satisfies a Lipshitz Condition with  $M$  equal to the maximum absolute slope among all linear segments.

The key fact about the Walsh Feature Set  $W$  is that it forms an  $\epsilon$ -net for the original image  $f$ . Let us describe this a little differently from previous sections with the help of the diagram in Figure 1 below.

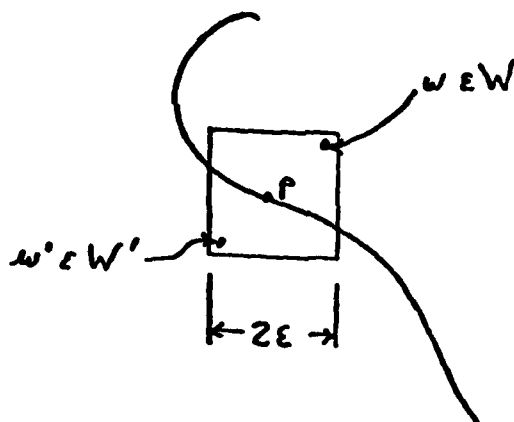


Fig. 1. Sketch of  $\epsilon$  neighborhood.

If we take any point say  $p$  on the original image  $f$  and draw a square as illustrated of sides  $2\epsilon$  centered about it, then since  $W$  is an  $\epsilon$ -Net for  $f$  there must exist a point  $w$  from  $W$  in this square. However if  $W'$  is also an  $\epsilon$ -Net for the same image  $f$  then there must also be a point  $w'$  in this same square. The conclusion to follow is the key to the recognition procedure and it is that the farthest that  $w$  and  $w'$  can be from each other in the Euclidean Sense is  $2\sqrt{2}\epsilon$ .

V. DETERMINING A WALSH FEATURE SET. In this section we shall go thru a step by step procedure for determining a Walsh Feature Set. In order to proceed we must have two things. The first is a boundary say  $f(x,y)$  given in terms of a chain encoding as described in reference [2]. The second is  $\epsilon$  the maximum allowable error in the x and y direction between  $f(x,y)$  and  $W(x,y)$  (The Walsh Feature Set) as explained in section III of this paper.

#### WALSH FEATURE SET ALGORITHM

- 1) For the given image  $f(x,y)$  find the x and y projections by traversing  $f$  at a constant counterclockwise rate such that the traversal time is one unit. This step is described in great depth in reference [2]. The projections are denoted by  $x(t)$  and  $y(t)$ .
- 2) Using the desired accuracy  $\epsilon$  determine the number of Walsh Functions needed for the truncated x and y expansions. Set  $N$  equal to the larger of  $n$  and  $k$  where

$$n = \lceil \log_2 \left( \frac{M}{\epsilon} \right) - 1 \rceil$$

$$\text{and } k = \lceil \log_2 \left( \frac{L}{\epsilon} \right) - 1 \rceil$$

$$\text{where } |x(t) - x_{2^n}(t)| \leq \frac{M}{2^{n+1}}$$

$$\text{and } |y(t) - y_{2^k}(t)| \leq \frac{L}{2^{k+1}}$$

and  $M$  and  $L$  are Lipschitz constants for  $x$  and  $y$  respectively.

- 3) Partition the abscissa of  $x(t)$  and  $y(t)$  into equally spaced intervals of length  $2^{-N}$  in  $[0,1]$  and in each of these intervals find the  $2^N$  by 1 Area Vectors as explained in section II of this paper. So we have

$$\bar{A}_x = \begin{pmatrix} A_{0x} \\ A_{1x} \\ \cdot \\ \cdot \\ A_{2^N-1x} \end{pmatrix} \quad \bar{A}_y = \begin{pmatrix} A_{0y} \\ \cdot \\ \cdot \\ \cdot \\ A_{2^N-1y} \end{pmatrix}$$

where each tuple is given by:

$$A_{ix} = \int_{\frac{i}{2^N}}^{\frac{i+1}{2^N}} x(t) dt \quad i = 0, 1, \dots, 2^N - 1$$

Similar equations apply for  $A_{iy}$ .

Finally

4) Form the Walsh Feature Set

In vector form we have using Matrix Partitioning

$$\bar{W}_{2^N} = 2^N \left( \bar{\Lambda}_x | \bar{\Lambda}_y \right) = \begin{pmatrix} 2^N A_{0x} & 2^N A_{0y} \\ 2^N A_{1x} & 2^N A_{1y} \\ \cdot & \cdot \\ \cdot & \cdot \\ 2^N A_{2^N-1x} & 2^N A_{2^N-1y} \end{pmatrix}$$

or in function form.

$$W_{2^N}(x,y) = \sum_{k=0}^{2^N-1} \chi_{\{(2^N A_{kx}, 2^N A_{ky})\}}(x,y)$$

In any case we see that  $W_{2^N}(x,y)$  "consists of dots" and does indeed approximate the original image of  $f(x,y)$ , and as explained in section IV of this paper it forms an  $\epsilon$ -net for  $f(x,y)$ .

We could have found  $W_{2^N}(x,y)$  by first finding  $x_{2^N}(t)$  and  $y_{2^N}(t)$  and composing the two. Also  $x_{2^N}(t)$  and  $y_{2^N}(t)$  can be found using the sequency vectors  $\bar{\alpha}_x$  and  $\bar{\alpha}_y$  but this is more work than the procedure outlined above.

**VI. NORMALIZATION OF WALSH FEATURES.** To compare the Walsh feature set of an unknown contour to a prototype, normalization with respect to translation, scale, rotation, and shift in starting-point must be accomplished. The following describes such a procedure. This procedure is not sufficiently general for all shapes to have a unique normalization, but will serve as a basis for continued study. Other techniques such as those using moment methods could also be employed [3,4].

While tracing the contour on a grid, the Freeman chain-code links are used to store the contour information. When the shape is to be analyzed (recognized) the chain-code is converted to a complex vector  $\bar{x} + i\bar{y}$  and the arc-length for this piecewise linear representation is calculated. The coefficients for the DC and first fundamental ellipse for the  $\bar{x}$  and  $\bar{y}$  projections are computed from the chain-code using the fast DFT method of Kuhl&Giardina[2]. The DC component,  $dc = (a_0 + ib_0)$  is equal to the area under the complex function  $\bar{x} + i\bar{y}$  divided by the arc-length. The scale factor,  $s = \sqrt{(a_1 + d_1)^2 + (b_1 - c_1)^2}$ , is the radius of the fundamental circle. The rotation angle is  $\psi = \frac{\psi_1 + \psi_2}{2}$ , where  $\psi_1 = \tan^{-1} \left[ \frac{c_1 - b_1}{a_1 + d_1} \right]$ ,  $\psi_2 = \tan^{-1} \left[ \frac{c_1 + b_1}{a_1 - d_1} \right]$ . The shape is

normalized to  $\bar{c}$ , where the  $i^{\text{th}}$  component is

$$c'_i = e^{-j\psi} \times \left( c_i - (a_0 + ic_0) \right) / s.$$

This normalization moves the "center" of the shape to the origin, scales, and rotates the shape so that the major axis of the fundamental ellipse is along the x-axis. There are two possible rotations that will put the major axis of the fundamental ellipse along the x-axis. To resolve this ambiguity, an additional  $180^\circ$  rotation is applied if necessary to place the maximum absolute x value in the right half plane.

After this normalization the Walsh points are computed. Then the starting-point along the shape needs to be moved to some standard position. This is accomplished by shifting the starting-point to that Walsh point having the largest positive x value.

As previously mentioned, there are some notable problems with this procedure. First, shapes exhibiting N-fold symmetry have N possible orientations for which the fundamental ellipse will be along the x-axis. Also, the method for choosing between the two possible orientations of the fundamental ellipse is sensitive to contour noise. It is also possible there is no single maximum absolute x. The starting-point normalization is also sensitive to this situation.

#### Examples:

Shown in Fig. 2 is the original contour of a F104 aircraft generated using a computer graphics program. Also shown are the x and y projections. Also shown in Fig. 2 are the normalized Walsh points corresponding to several powers of 2. The boxes around each Walsh point have width  $2\epsilon$ . So, each point on the original contour will lie inside one of the  $2\epsilon$  neighborhoods of at least one Walsh point. Shown in Figs. 3-6 are the x and y projections corresponding to the Walsh dots.

#### REFERENCES

- [1] C. R. Giardina, "Bounds on the Truncation Error for Walsh Expansions," Notices of American Math Society, Feb. 1978, Volume 25, #2.
- [2] F. Kuhl, C. R. Giardina, "Elliptic Fourier Features of a Closed Contour," Computer Graphics and Image Processing, March 1982, Vol. 18, #3, pp. 238-258.
- [3] M. R. Teague, "Image Analysis via the General Theory of Moments," Journal of the Optical Society of America, Vol. 70, 1980.
- [4] A. P. Reeves and A. Rostampour, "Shape Analysis of Segmented Objects Using Moment," Proceedings IEEE Computer Conference on Pattern Recognition and Image Processing, August 1981.

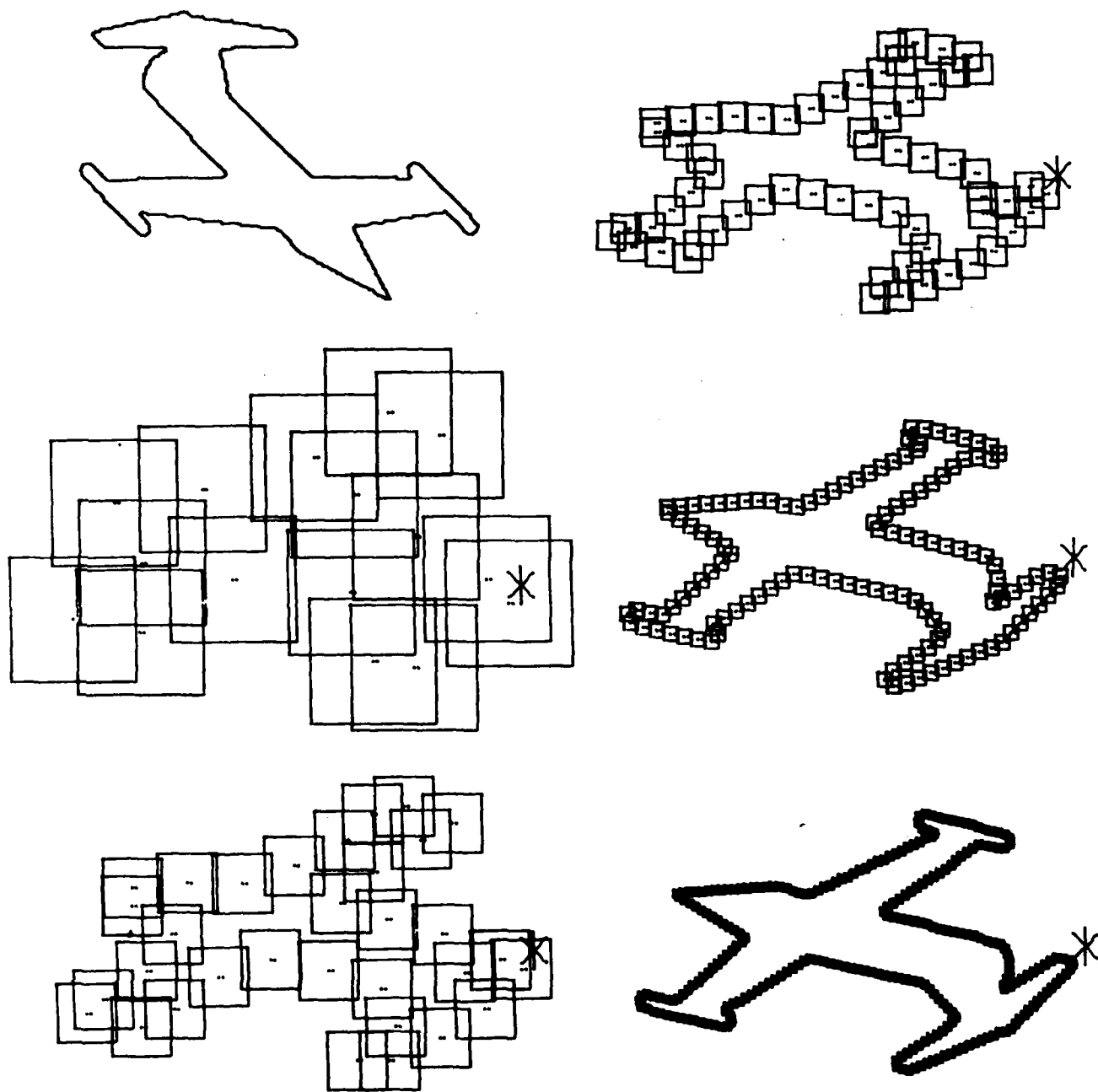


Fig. 2. Original F104 contour and Walsh points with corresponding neighborhoods after normalization for  $2^N = 16, 32, 64, 128, 256$ .

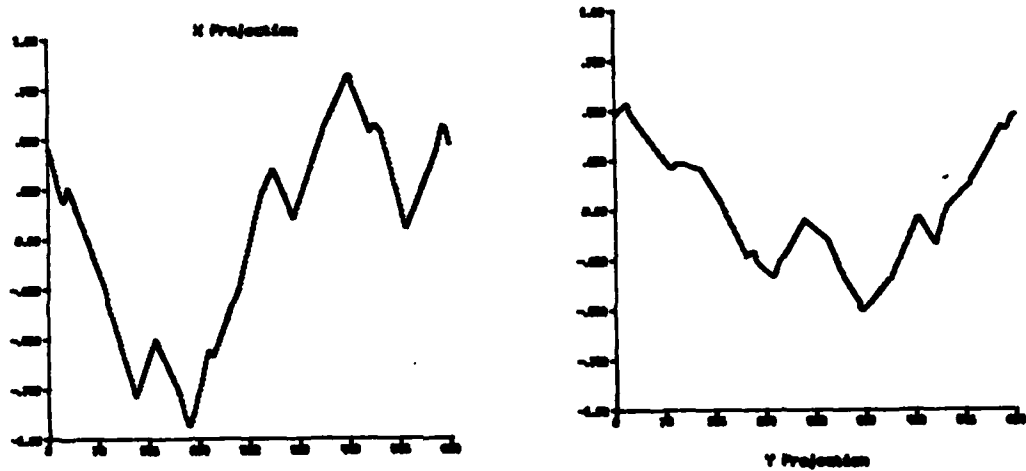


Fig. 3. Original contour projections (624 points).

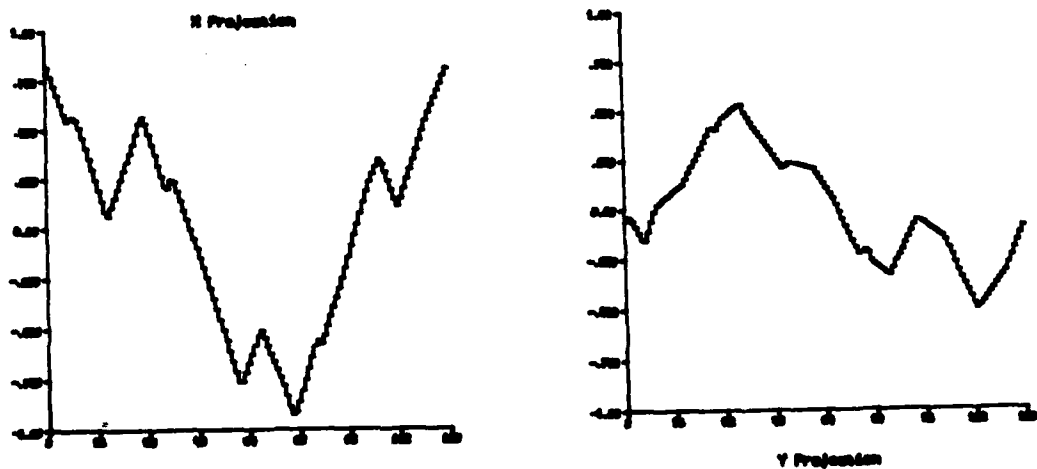


Fig. 4. Normalized Walsh point projections ( $2^N = 128$ ).

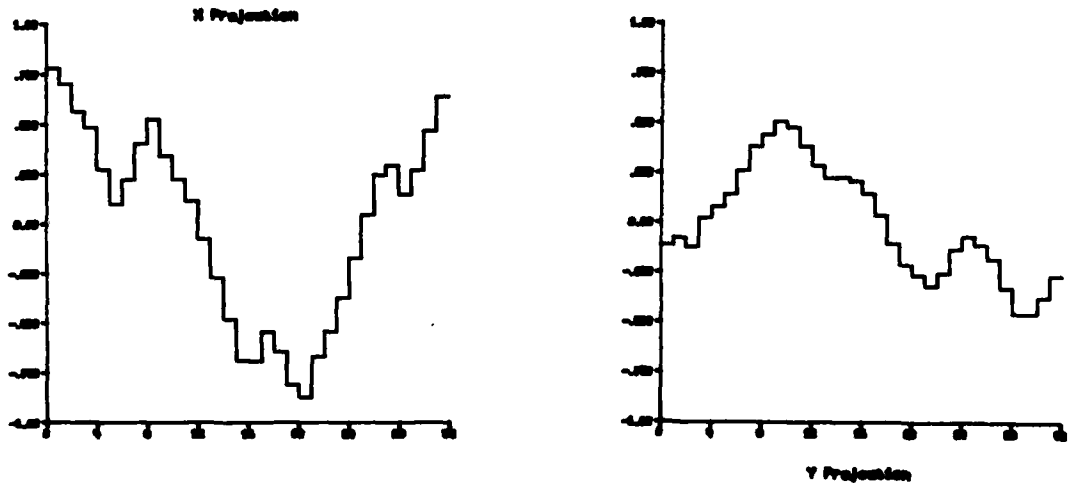


Fig. 5. Normalized Walsh point projections ( $2^N = 32$ ).

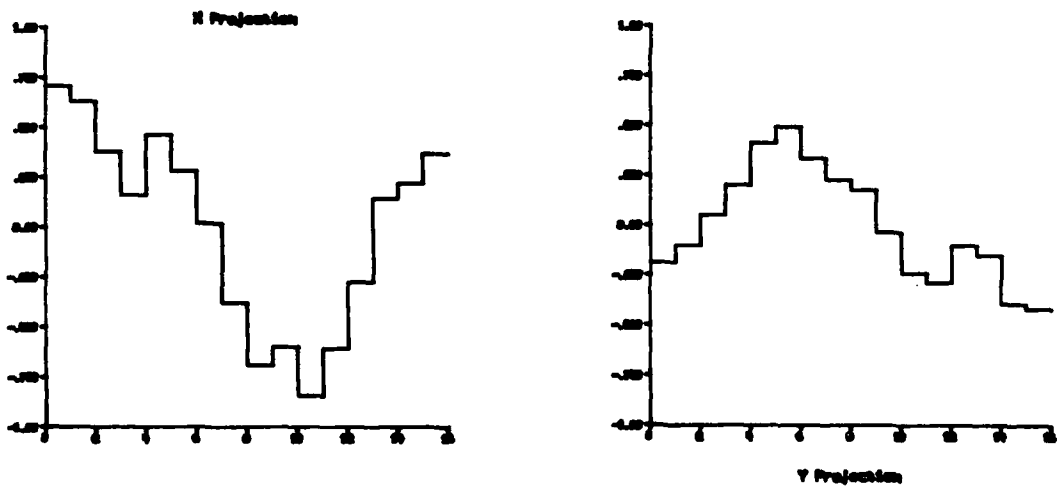


Fig. 6. Normalized Walsh point projections ( $2^N = 16$ ).



AD P 01033

↙

MULTIPLE MODEL ADAPTIVE FILTER FOR TANK FIRE CONTROL  
AND ITS MICROPROCESSOR IMPLEMENTATION

P. T. Yip

U.S. Army Armaments Research & Development Command  
Fire Control & Small Caliber Weapons Systems Laboratory  
Dover, NJ 07801

ABSTRACT This study is to investigate the feasibility and performance of an adaptive fire control filter-predictor system in the microprocessor environment. The filter model used is our previous design which includes a Kalman estimator for tank target state estimation and an UD-factorization scheme to propagate the state error covariance matrix. This method insures computation stability and enhances accuracy of the filter algorithm. Moreover the parallel structure of filter configuration in this model is inherently suitable for microprocessor implementation. Three Intel 386/12a single board computers are used to process the parallel filters simultaneously. One of them is designed to access the other two to gather critical data for adaptive prediction in real time. The computation accuracy of the target state estimates and the processing time are examined.

I. INTRODUCTION This study is to investigate the feasibility of implementing and the performance of an advanced adaptive fire control filter-predictor system in real time and in the microprocessor environment. The filter model used is our previous design which includes a Kalman estimator for tank target state estimation and an UD-factorization scheme to propagate the state error covariance matrix. This method provides excellent computation stability and enhances accuracy of the filter algorithm. In addition, the parallel structure of filters in this model is inherently suitable for microprocessor implementation.

We start our exercise with the UD-factorization of the state error covariance matrix. The system configuration is considered next. Then the interface of microprocessors is described. The requirements of implementation are stated. Lastly, the results and conclusions are addressed.

II. UD-FACTORIZATION OF THE STATE ERROR COVARIANCE MATRIX In the conventional Kalman filter algorithm, the error information propagates through updating the state error covariance matrix. They are

$$\bar{P}_{k/k-1} = \Phi_{k,k-1} \hat{P}_{k-1} \Phi_{k,k-1}^T + G Q_{k-1} G^T \quad (1)$$

$$K_k = \bar{P}_{k/k-1} H_k^T (H_k^T \bar{P}_{k/k-1} H_k + r)^{-1} \quad (2)$$

$$\hat{P}_k = \bar{P}_{k/k-1} - K_k H_k^T \bar{P}_{k/k-1} \quad (3)$$

where  $\hat{P}$  is the a posteriori state error covariance matrix,  $\bar{P}$ , the a priori state error covariance matrix,  $\Phi$ , the state transition matrix,  $H$ , the measurement matrix,  $G$ , the distribution matrix,  $K$ , the Kalman gain matrix,  $Q$ , the plant noise covariance matrix, and  $r$ , the measurement noise variance.

The  $P$  matrix is required to be positive semi-definite in order that the system is stable. As we may see in Equation (3) that the difference of two semi-definite matrices can produce a negative definite  $P$  especially when the accumulated round-off error becomes significant. Hence, the UD-factorization method is adopted for its inherent stability and enhanced accuracy.

The recursive formula of the UD-algorithm for updating the state error covariance matrix in each measurement cycle are

$$W\tilde{D}W^T = \Phi\hat{U}\hat{D}\hat{U}^T\Phi^T + GQG^T \quad (4)$$

$$\bar{U}\bar{D}\bar{U}^T = W\tilde{D}W^T \quad (5)$$

$$\alpha = H^T\bar{U}\bar{D}\bar{U}^TH + r \quad (6)$$

$$K = \bar{U}\bar{D}\bar{U}^TH/\alpha \quad (7)$$

$$\hat{U}\hat{D}\hat{U}^T = \bar{U}\left[\bar{D} - \frac{1}{\alpha}(\bar{D}\bar{U}^TH)(\bar{D}\bar{U}^TH)^T\right]\bar{U}^T \quad (8)$$

where  $\bar{D} = \begin{bmatrix} \hat{D} & \emptyset \\ \emptyset & Q \end{bmatrix}$  is  $N$  by  $N$  and

$$N = n + N_w, \quad W = [\Phi U; G] \quad n \text{ by } N,$$

$$G = \begin{bmatrix} \emptyset \\ 1 & \dots & \emptyset \\ \emptyset & \dots & 1 \end{bmatrix} \quad n \text{ by } N,$$

$$U = \begin{bmatrix} 1 & U_{1,2} & \dots & U_{1,n} \\ & & \dots & \\ & & & U_{n-1,n} \\ \emptyset & & & 1 \end{bmatrix} \quad n \text{ by } n,$$

$$H^T = (h_1 \dots h_n)$$

D, n by n diagonal matrix and  
 $\emptyset$ , zero elements.

with  $\underline{b} = U^T H$ ,  $\underline{y} = \bar{D} U^T H$  and initial conditions  
 $\hat{d}_1 = \bar{d}_1 r / \alpha_1$ ,  $\alpha_1 = r + v_1 b_1$ , and  
 $k_2^T = (v_1 0 \dots 0)$

where  $U_{ij}$  and  $K_{ij}$  are the  $i$ th element of the column vector  $U_j$  and  $K_j$  respectively.

Then, the elements of  $d$ ,  $U$ , and  $K$  are computed recursively as the following:

For  $j=2, \dots, n$  (Equations 9 through 13)

$$\alpha_j = \alpha_{j-1} + v_j b_j \quad (9)$$

$$\hat{d}_j = \bar{d}_j \alpha_{j-1} / \alpha_j \quad (10)$$

$$\lambda_j = -b_j / \alpha_{j-1} \quad (11)$$

For  $i=1, \dots, n$  (Equations 12 through 13)

$$\hat{U}_{ij} = \bar{U}_{ij} + \lambda_j K_{ij} \quad (12)$$

$$K_{i,j+1} = K_{ij} + v_j U_{ij} \quad (13)$$

The Kalman gain  $K$  of this measurement cycle is given by

$$K = K_{n+1} / \alpha_n$$

Since  $r$  is always positive, the positive definite condition of  $D$  is assured by Equation (10). As cancellation type errors that may happen in Equation (3) are avoided in Equation (10), the accuracy of computation is enhanced.

**III. SYSTEM CONFIGURATION** In our previous estimator-predictor design, three types of target models have been incorporated. Type 1 is a constant velocity model. Type 2 is a first order Markov acceleration model and type 3 is a second order acceleration model with one zero and two poles. The parameters of these models have been identified with real test data to account for various target maneuvering levels. Noised corrupted data of range and azimuth angle

of target are measurement inputs to the three parallel extended Kalman filters modified with the UD-factorization scheme. The adaptive prediction comes in when one of the filters with the largest likelihood function is selected to provide estimates for gun lead prediction.

Three microprocessors are used and each processes one filter. The one with the constant velocity model is the master board which also processes the filter selection and gun lead predictions by virtue of its smaller load of computational burden. The communication control and data transfer between the master board and the other two microprocessor boards will be described in the next section.

IV. MICROPROCESSORS AND THEIR INTERFACE Three Intel 86/12a single board computers (SBC) are used to process the parallel filters simultaneously. Each has 32K bytes of random access memory (RAM) and 8K bytes of electronic programmable read only memory (EPROM) which can be extended to 32K bytes. If more memory is needed, extra RAM and EPROM boards can be attached. The memory in own board is accessed by the central processing unit (CPU) of the board through the local bus. Additional memory up to one megabyte can be planned and accessed through the system bus.

The communication between the keyboard or the microprocessor development system and the master board is established through a serial interface cable. Two out of the three programmable peripheral interface input/output ports are used to take care of the communication traffic control between the master board and the other two boards.

The data transfer uses the multibus interface which requires only one bus clock of 9.22 MHz for synchronized communication among the SBC. The local CPU must reside in that part of its own memory which has not been assigned as dual port RAM inside the megabyte addressing plan when another CPU actually accesses the dual port RAM area.

The 86/12a single board computer which has twelve 16-bit registers performs floating point computations with the help of a floating point mathematics library simulating 32-bit operation. The test chip of 8087 coprocessor was made available for development on August 1981. This coprocessor which can be attached to the 86/12a computer board easily has eight 80-bit registers capable of performing 32- and 64-bit floating point multiplication with very high speed such as tens of microseconds.

V. IMPLEMENTATION After the proper interfacing of the microprocessors, some real target paths of various noise statistics are selected. The function of the entire set-up, the prediction estimates and the processing time of the second order algorithm in this system are investigated.

a. A rather linear portion of a target path is used to verify the proper functioning of the entire microprocessor set-up. A similar program is run on an IBM 360 computer to obtain results for comparison.

b. A segment of real target path data with an average maneuvering noise level 1.176 meters per second and an average speed 13 miles per hour is corrupted with random Gaussian noise of 3 meters in range measurement and 0.3 milliradians in angle measurement. These corrupted data is sampled at 10 samples per second as input to the system and the prediction estimates are compared with the results from previous study using a conventional extended Kalman filter without modification.

c. With the same data the system performance is evaluated for processing the data at 5 samples per second instead of 10 samples per second.

d. The processing times for the floating point multiplication, division and square root operation with the 86/12a CPU are compared to that with the 8087 numerical coprocessor.

e. The actual processing time of the second order algorithm with a 8087 coprocessor test unit is examined. The number of measurements processed in 10 seconds is noted.

VI. RESULTS AND CONCLUSIONS Under the implementation conditions in the previous section, results are summarized as follows:

a. Results from IBM 360 and Intel 86/12a SBC show a 1.2 percent or less difference in lead angle estimates and much less in impact range estimates. The proper functioning of the multi-microprocessor set-up is verified.

b. From previous study for the given target path in implementation of b and averaging over seventeen points, the estimated prediction errors in milliradians are 1.29, 1.72 and 0.91 for constant velocity, first order acceleration and second order acceleration filter types respectively. From the multi-microprocessors under the same conditions, the estimated prediction errors in milliradians are 1.2, 1.49 and 0.88 for constant velocity, first order acceleration and second order acceleration filter types respectively.

The accuracy of the estimates from this algorithm are highly competitive or better than that from the conventional extended Kalman filter algorithm.

c. With a sampling rate of 5 samples per second the estimated prediction errors in milliradians are 1.16, 1.54 and 0.9 for constant velocity, first order acceleration and second order acceleration filter types respectively. The change in performance is about 3 percent.

d. Averaging over ten thousand iterations, the floating point operation of the command group LOAD, MUL, STORE and WAIT takes 4 milliseconds with the 86/12a CPU while the same takes 63.9 microseconds with the 3087 coprocessor. It is a 63 times faster in multiplication with the latter.

For the command group LOAD, DIV, STORE and WAIT, the floating point operation takes 5.5 milliseconds with the 86/12a CPU and 35.6 microseconds with the 3087 coprocessor. It is 64 times faster in division with the latter.

For the command group LOAD, SQRT, STORE and WAIT, the 86/12a CPU takes 40 milliseconds to process a square root procedure while the 3087 coprocessor with its micro program for SQRT takes 77.6 microseconds. It is 515 times faster with the latter.

e. With a test unit of 8087 coprocessor planted in the 86/12a board, the second order algorithm is processed for 10 seconds. Only 88 sets of measurements are processed. This indicates that a 12 percent improvement in speed is needed to do 10 samples per second real time processing. Fine tuning the program code or changing the programming language to assembler type may help eliminate this time lag.

In all, the numerical characteristics of the UD-factorization algorithm are impressive. It has been encouraging to know that microprocessor technology has caught up in speed and flexibility to process advance parallel algorithms with heavy load of computation. We see that great many applications of microprocessor to multiple input, multiple output and parallel processing are forthcoming.

#### REFERENCES

1. P. T. Yip, N. P. Coleman, "An Adaptive Lead Prediction Algorithm for Maneuvering Target Engagement", ARO Report 81-1, Trans. of the 26th Conference of Army Mathematicians, pp 141-152, Jan 81.
2. G. J. Bierman, "Factorization Methods for Discrete Sequential Estimation", Academic Press, New York, 1977.

SOLUTION OF A HYPERBOLIC VOLTERRA EQUATION  
BY A FINITE DIFFERENCE SCHEME

Peter Markowich\* and Michael Renardy\*\*,1

**ABSTRACT:** A model equation for viscoelastic solids is investigated. The solutions of this equation have the feature that they remain smooth globally in time for sufficiently small data, whereas "large" solutions may develop shocks. This is verified numerically using a Lax-Wendroff type finite difference scheme.

**1. INTRODUCTION.** Viscoelastic materials are generally modelled by constitutive laws relating the stress to the history of the strain [3], [7], [8]. This leads to partial integrodifferential equations of motion. In this paper, we study the following model equation, for a one-dimensional viscoelastic solid, which was first analyzed by Dafermos and Nohel [1], [2]

$$(1.1) \quad u_{tt} = \phi(u_x)_x - \int_0^t a(t-s)\psi(u_x(x,s))_x ds + f(x,t) .$$

Here  $\phi, \psi$  are smooth functions satisfying  $\phi(0) = \psi(0) = 0, \phi'(0) > 0, \psi'(0) > 0, \phi'(0) - \psi'(0) \cdot \int_0^\infty a(s)ds > 0$ . The kernel  $a$  is assumed to have the form

$$(1.2) \quad a(s) = \sum_{\ell=1}^N K_\ell e^{-\lambda_\ell s}, \quad K_\ell, \lambda_\ell > 0 .$$

Equation (1.1) can be regarded as a perturbation of the quasilinear wave equation  $u_{tt} = \phi(u_x)_x$ . It is well known that this equation generally does not have a global smooth solution even if the initial data are smooth. Also, there is an energy conservation law. On the other hand, Dafermos and Nohel [1], [2] have shown that solutions to (1.1) on a finite  $x$ -interval (with Dirichlet or Neumann boundary conditions) remain smooth and decay to zero as  $t \rightarrow \infty$ , if the initial data  $u(t=0), u_t(t=0)$  and the forcing term  $f$  are small in appropriate Sobolev norms. For large initial data, the analysis of similar models shows [4], [6], [10] that this can not be expected and shocks may develop. One may regard this as the result of a competition between nonlinearity (leading to shocks) and dissipation introduced by the integral term. For small data, dissipation wins, and for large data nonlinearity wins.

Below, we shall sketch a new proof of global existence for small data in the case of periodic boundary conditions. More details are given in a forthcoming publication [5]. Ideas similar to those developed here have also been

---

\* Inst. f. Angew. u. Num. Mathematik, Techn. Univ. Wien, A-1040 Wien, Austria.

\*\* Mathematics Research Center, University of Wisconsin-Madison, Madison, WI 53706. Sponsored by the United States Army under Contract No. DAAG29-80-C-0041.

1

The work of this author was supported by Deutsche Forschungsgemeinschaft.

used to show the stability of the numerical scheme, which is explained in Section 3. We have proved convergence on finite time intervals and globally in time in the case of small solutions [5]. In Section 4, we report computations. They illustrate decay and global smoothness for small initial data and the development of shocks for large data.

ACKNOWLEDGEMENT. This research was motivated by a suggestion of Professor John A. Nohel.

2. ANALYTICAL THEORY. We consider spatially periodic (to be definite, say,  $2\pi$ -periodic) solutions to (1.1) with a given initial condition  $u(0,x) = u_0(x)$ ,  $u_t(0,x) = u_1(x)$ . In our analysis, we make essential use of the fact that (1.1) may be transformed to a symmetric hyperbolic system. For simplicity, let us assume  $\phi = \psi$ . The substitution  $v = u_x$ ,  $w = u_t$ ,  $g_i =$

$$-u_t + \int_0^t e^{-\lambda_i(t-s)} \phi(u_x(x,s))_x ds \text{ leads to the system}$$

$$\dot{v} = w_x$$

$$(2.1) \quad \dot{w} = \phi(v)_x - \sum_{j=1}^N K_j g_j - \left( \sum_{j=1}^N K_j \right) w + f$$

$$\dot{g}_i = -\lambda_i g_i - \lambda_i w + \sum_{j=1}^N K_j (g_j + w) - f$$

The hyperbolic system (2.1) becomes symmetric hyperbolic when we define  $\omega(y) = \int_0^y \sqrt{\phi'(y)} dy$ ,  $\beta(y) = \omega'(\omega^{-1}(y))$  and set  $\tilde{v} = \omega(v)$ . This yields a system of the form

$$(2.2) \quad \begin{aligned} \dot{\tilde{v}} &= \beta(\tilde{v}) w_x \\ \dot{w} &= \beta(\tilde{v}) \tilde{v}_x + \dots \\ &\dots \dots \end{aligned}$$

Our global existence proof for small solutions consists of three steps (for details, see [5]):

- (i) Show that the trivial solution  $\tilde{v} = 0$ ,  $w = 0$ ,  $g_i = 0$  is stable in the linearized sense. This follows from a straightforward Fourier analysis.
- (ii) Show that the linearized stability persists under small perturbations. A problem arises here because the hyperbolic part leads to relatively unbounded perturbations of the linearized operator. Therefore, a more refined argument than standard perturbation theory is needed. We can make use of the fact that the leading operator in a symmetric hyperbolic system is skew-adjoint. With this and the information from step 1, the linearization of (2.2) at a small  $\tilde{v}_0(x,t)$ ,  $w_0(x,t)$  can, after a suitable transformation, be written in the form

$$(2.3) \quad \dot{y} = (A + B + C)y$$

where the operator A is dissipative, B is skew-adjoint and C has small norm. It is immediate that A + B + C is still dissipative.  
 (iii) Use a contraction argument for the nonlinear problem. As a result, we have obtained:

Theorem 2.1: If  $f \in H^n([0, \infty) \times \mathbb{R}/2\pi\mathbb{Z}; \mathbb{R})$  and  $\tilde{v}(0), w(0), g_1(0), \dots, g_N(0) \in H^n(\mathbb{R}/2\pi\mathbb{Z}; \mathbb{R})$  ( $n > 2$ ) have sufficiently small norms, and  $\int_0^{2\pi} f(x, t) dx = 0$  for all t, then (2.2) has a solution  $(\tilde{v}, w, g_1, \dots, g_N) \in H^n([0, \infty) \times \mathbb{R}/2\pi\mathbb{Z}; \mathbb{R}^{2N+2})$  which assumes the prescribed initial values.

3. THE LAX-WENDROFF SCHEME. The Lax-Wendroff scheme approximates an equation of the form  $\dot{y} = F(y, t)$  by a Taylor expansion of second order:

$$\begin{aligned} (3.1) \quad y(t+\Delta t) &= y(t) + \Delta t \cdot \dot{y}(t) + \frac{(\Delta t)^2}{2} \ddot{y}(t) \\ &= y(t) + \Delta t \cdot F(y, t) + \frac{1}{2} (\Delta t)^2 (D_y F \cdot F + D_t F) . \end{aligned}$$

We apply this idea to the system resulting from (1.1) by the substitution  $v = u_x, w = u_t, z_\ell = K_\ell \int_0^t e^{-\lambda_\ell(t-s)} \cdot \psi(v(s))_x ds$ . Choosing a uniform mesh, this leads to a scheme of the form

$$\begin{aligned} (3.2) \quad v_i^{n+1} &= v_i^n + k \Delta w_i^n + \frac{k^2}{2} [\Delta^+ \Delta^- \phi(v_i^n) - \Delta \sum_{\ell=1}^N z_{\ell i}^n + \Delta f_i^n] \\ w_i^{n+1} &= w_i^n + k [\Delta \phi(v_i^n) - \sum_{\ell=1}^N z_{\ell i}^n + f_i^n] \\ &\quad + \frac{k^2}{2} [\Delta^+ (\phi'(\frac{1}{2}(v_i^n + v_{i-1}^n)) \Delta^- w_i^n) - \sum_{\ell} K_\ell \psi(v_i^n) + \sum_{\ell} \lambda_\ell z_{\ell i}^n + (f_t)_i^n] \\ z_{\ell i}^{n+1} &= z_{\ell i}^n + k [K_\ell \Delta \psi(v_i^n) - \lambda_\ell z_{\ell i}^n] \\ &\quad + \frac{k^2}{2} [\Delta^+ (K_\ell \psi'(\frac{1}{2}(v_i^n + v_{i-1}^n)) \Delta^- w_i^n) \\ &\quad - \lambda_\ell (K_\ell \Delta \psi(v_i^n) - \lambda_\ell z_{\ell i}^n)] . \end{aligned}$$

Here i denotes the spatial, and n the temporal index of gridpoints.  $\Delta^+, \Delta^-$  and  $\Delta$  are the righthanded, lefthanded and symmetric difference approximations to  $\frac{\partial}{\partial x}$ . The scheme is formally of second order. In [5] we have given a stability analysis which shows that, provided  $\frac{k}{h}$  ( $k$  = temporal mesh size,  $h$  = spatial mesh size) is less than a certain limit, the scheme

converges with an error  $O(h^2 + k^2)$ . This holds on finite time intervals as long as the exact solution stays smooth. It also holds uniformly for  $t \in [0, \infty)$  for the case of small solutions discussed in Chapter 2. In order to avoid stiffness problems for large  $\lambda_2$ , it is sometimes of advantage to replace  $z_{2i}^n$  in the last term of (3.2) by  $z_{2i}^{n+1}$ .

4. NUMERICAL RESULTS. In the following calculations we have used the initial conditions

$$v(0, x) = u_x(0, x) = (1 - 3x - x^2 + x^3)e^{-x^2/2}/N,$$

$$w(0, x) = u_t(0, x) = (1 - x^2)e^{-x^2/2}/N,$$

the integral kernel

$$a(s) = 0.4e^{-s} + 0.2e^{-2s},$$

and the function  $\phi(u_x) = \psi(u_x) = 2u_x + 5u_x^2 + 25u_x^3$ . The force  $f$  was put equal to 0. Plots 1-3 show the evolution of  $v$  for  $N = 1$ . It can be seen that shocks develop very quickly. In contrast, solutions remain smooth and decay for  $N = 40$  (Figure 4, 5).  $L^2N$  in these figures denotes the  $L^2$ -norm of  $v$ . It can be seen that the asymptotic character of the solution is that of two diverging wave packets with decreasing amplitudes. In contrast, the wave equation (without the integral) shows development of shocks and no decay (Figure 6, 7). Figures 8-11 show one of the shocks (for  $N = 5$ ) in dependence of the mesh size. It can be seen that a boundary layer of thickness  $3h$  develops. The Lax-Wendroff scheme can be viewed as an artificial viscosity method with a viscosity of order  $h$  (see [9]).

#### REFERENCES

- [1] C. M. Dafermos and J. A. Nohel, Energy methods for nonlinear hyperbolic Volterra integrodifferential equations, *Comm. P.D.E.* 4(1978), 219-278.
- [2] C. M. Dafermos and J.A. Nohel, A nonlinear hyperbolic Volterra equation in viscoelasticity, *Amer. J. Math.*, in press.
- [3] A. E. Green and R. S. Rivlin, Non-linear materials with memory, *Arch. Rat. Mech. Anal.* 1 (1957), 1-21.
- [4] H. Hattori, Breakdown of smooth solutions in dissipative nonlinear hyperbolic systems, Ph.D. Thesis, Rensselaer Polytechnic Institute, Troy, NY, 1981.
- [5] P. Markowich and M. Renardy, Lax-Wendroff methods for hyperbolic history value problems, MRC TSR, University of Wisconsin-Madison, to appear.
- [6] J. A. Nohel, A nonlinear conservation law with memory, MRC TSR #2251, University of Wisconsin-Madison, 1981.
- [7] W. Noll, A mathematical theory of the mechanical behavior of continuous media, *Arch. Rat. Mech. Anal.* 2 (1958), 197-226.

- [8] J. G. Oldroyd, On the formulation of rheological equations of state, Proc. Roy. Soc. London A200 (1950), 523-541.
- [9] R. D. Richtmyer and U. W. Morton, Difference Methods for Initial Value Problems, J. Wiley, New York 1967.
- [10] M. Slemrod, Instability of steady shearing flows in a nonlinear viscoelastic fluid, Arch. Rat. Mech. Anal. 68 (1978), 211-225.

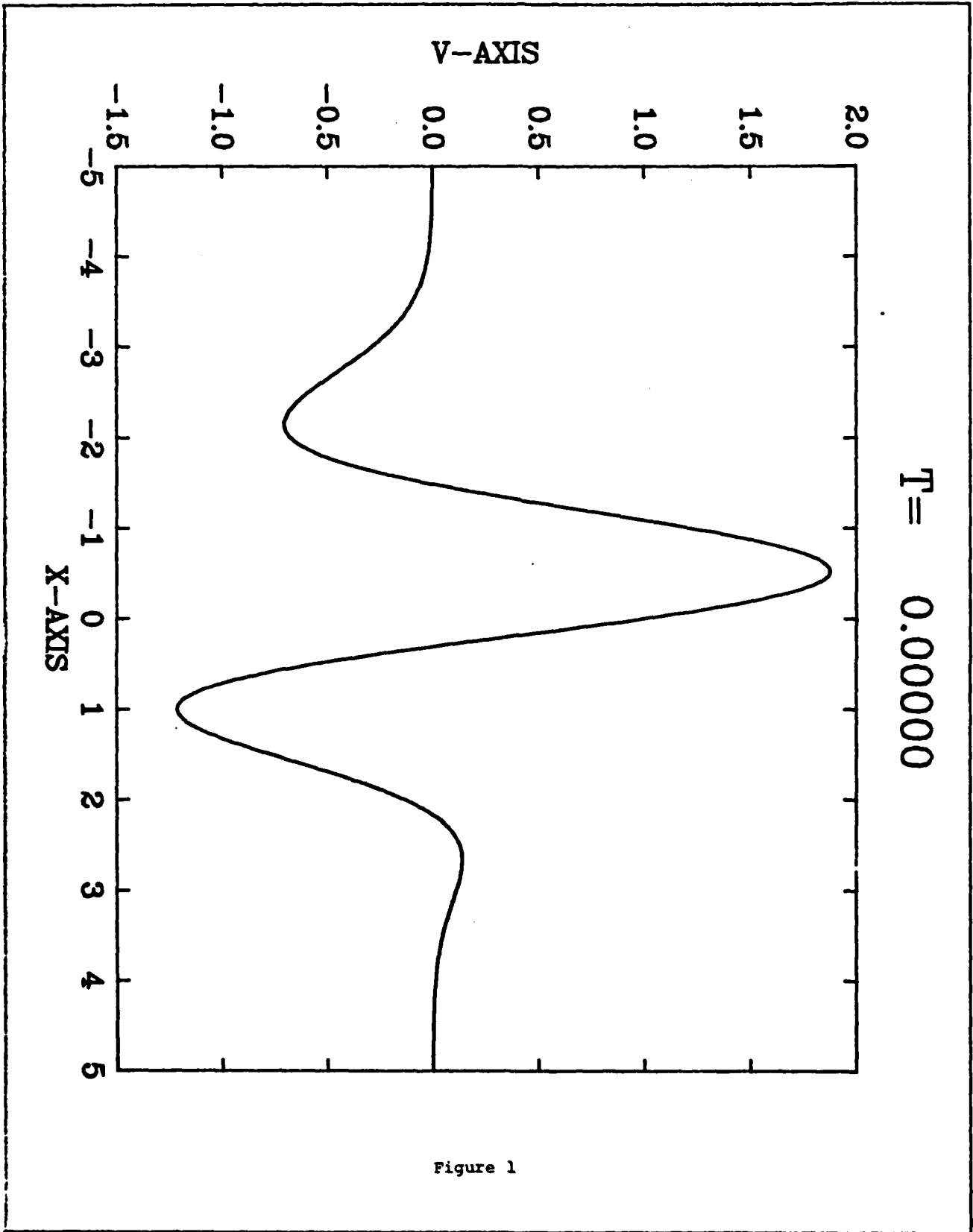


Figure 1

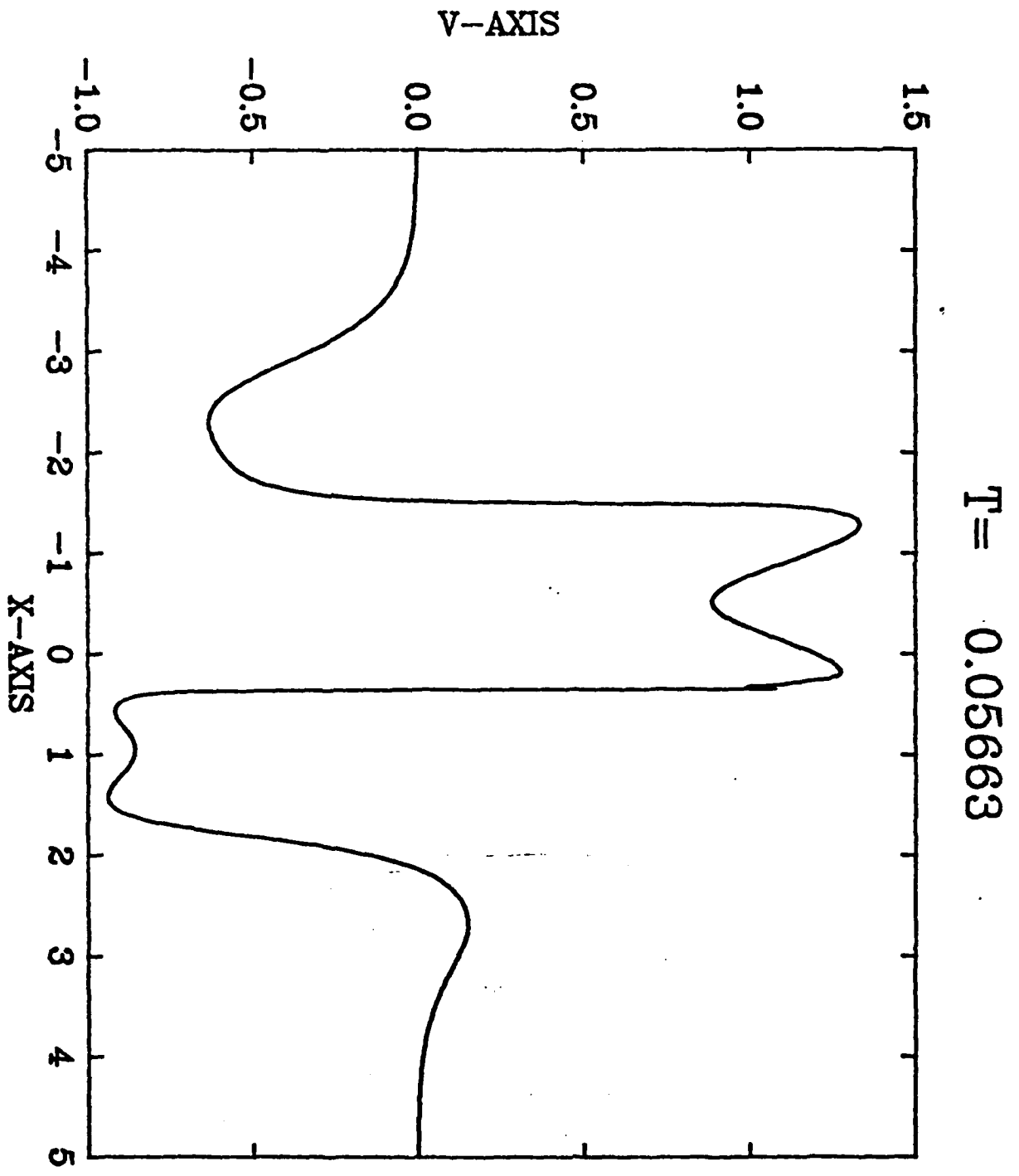


Figure 2

$T = 0.08876$

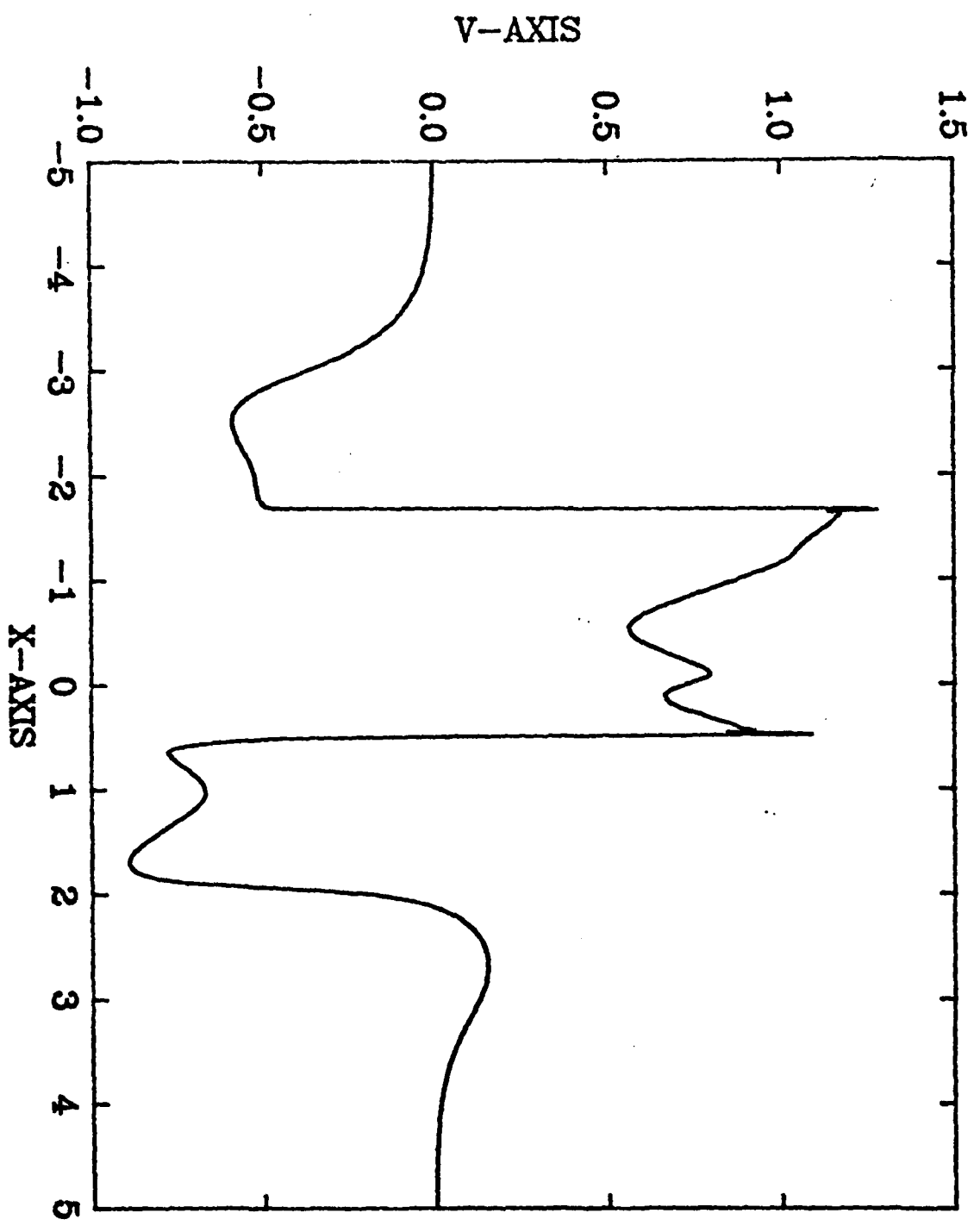


Figure 3

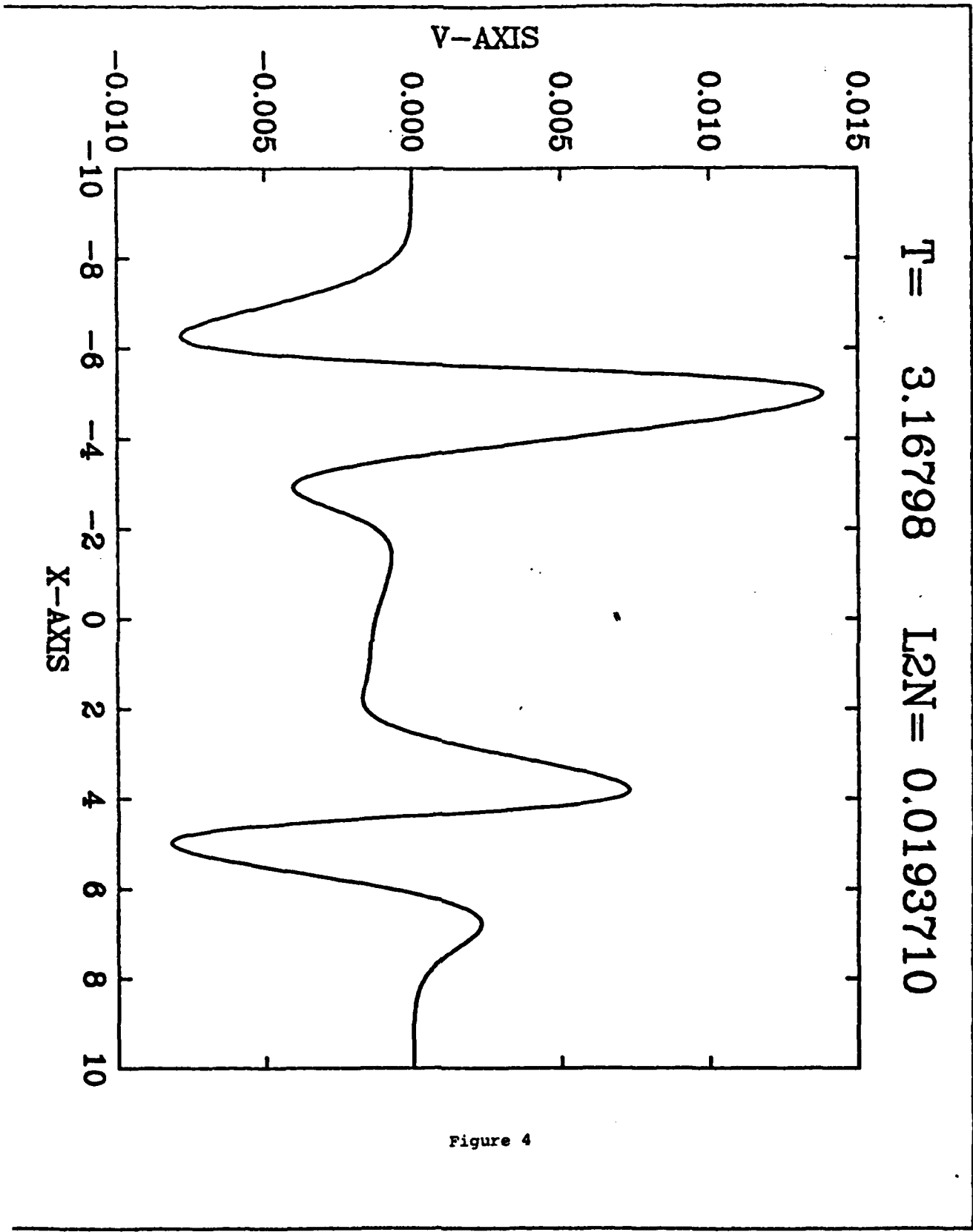


Figure 4

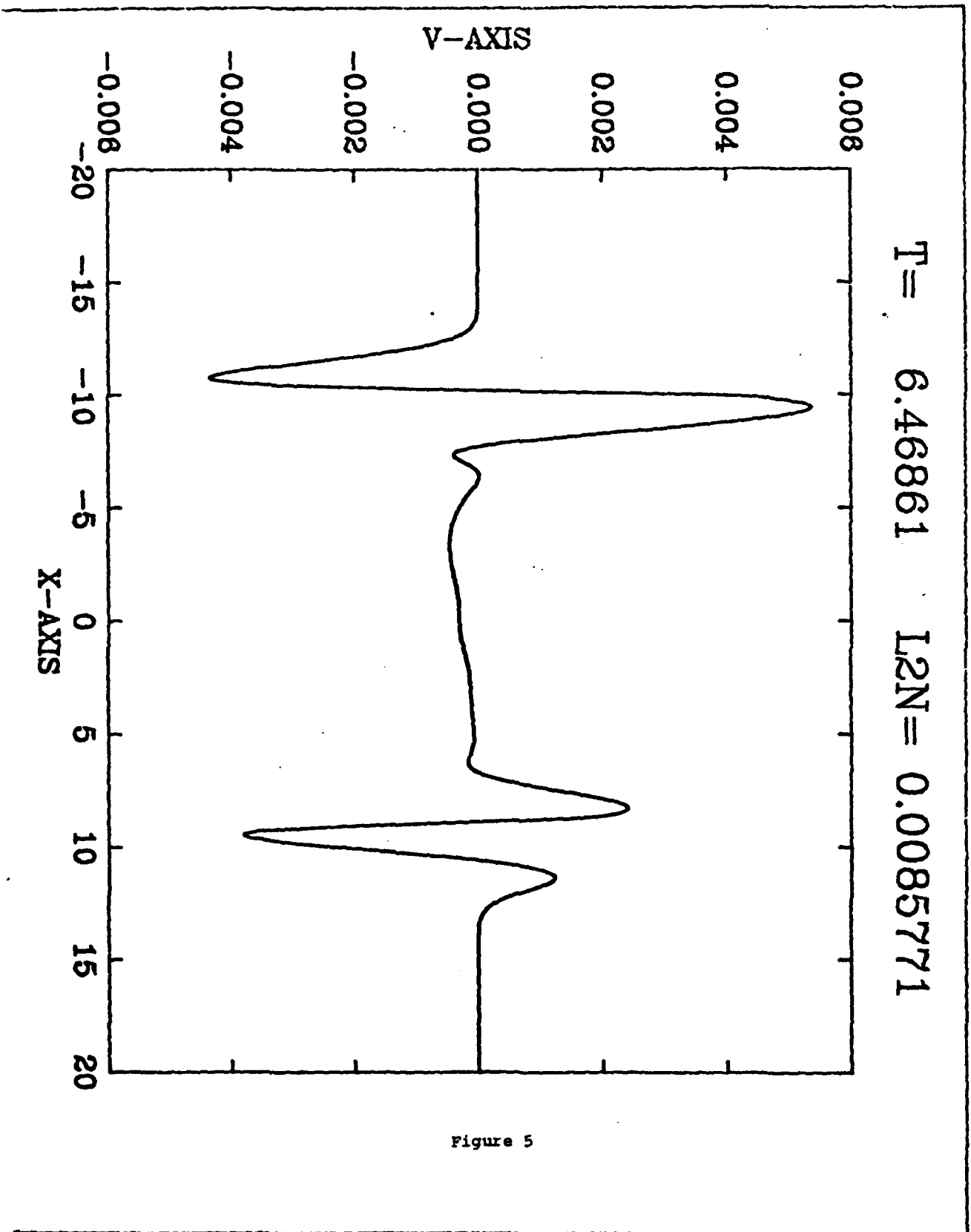


Figure 5

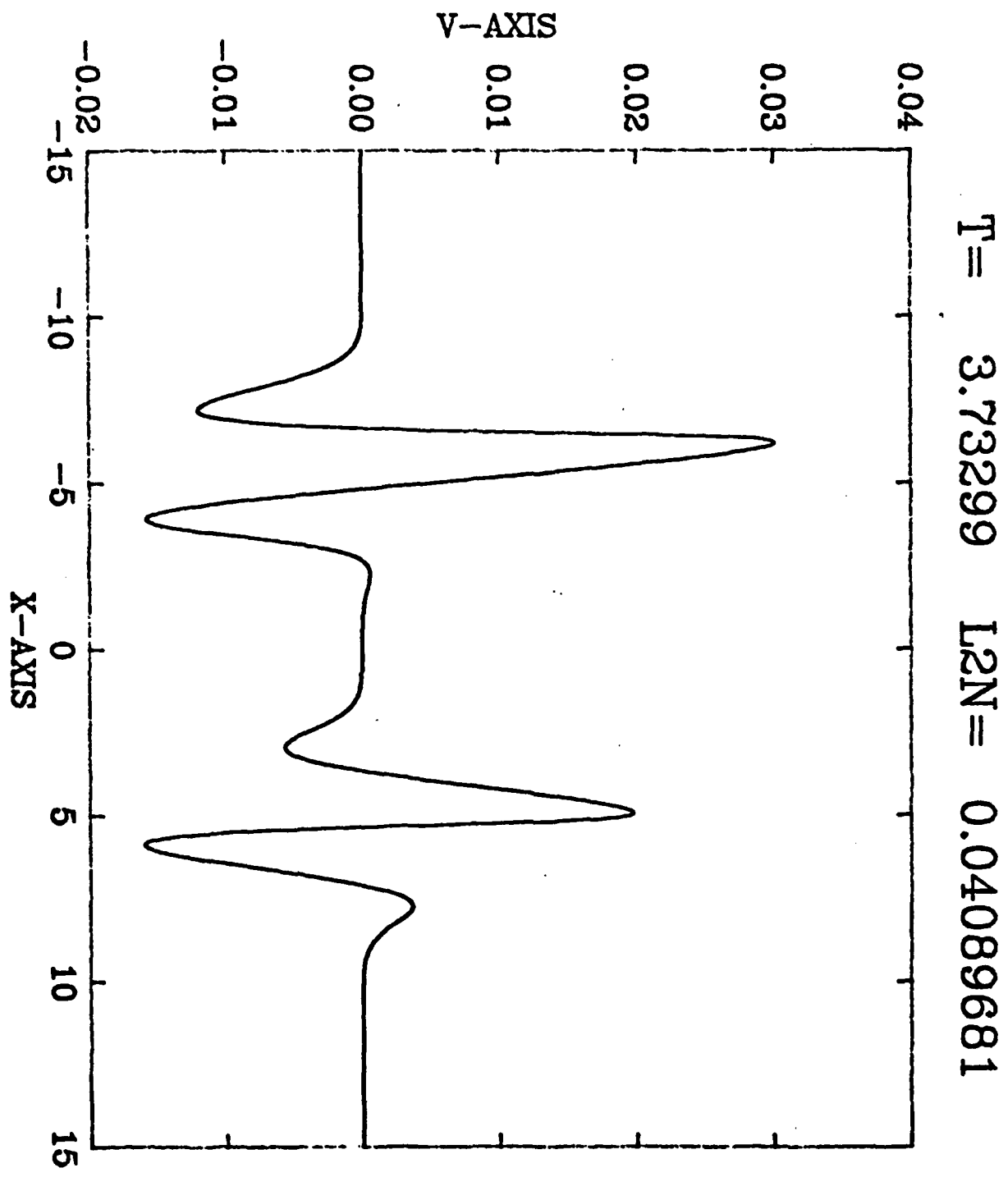


Figure 6

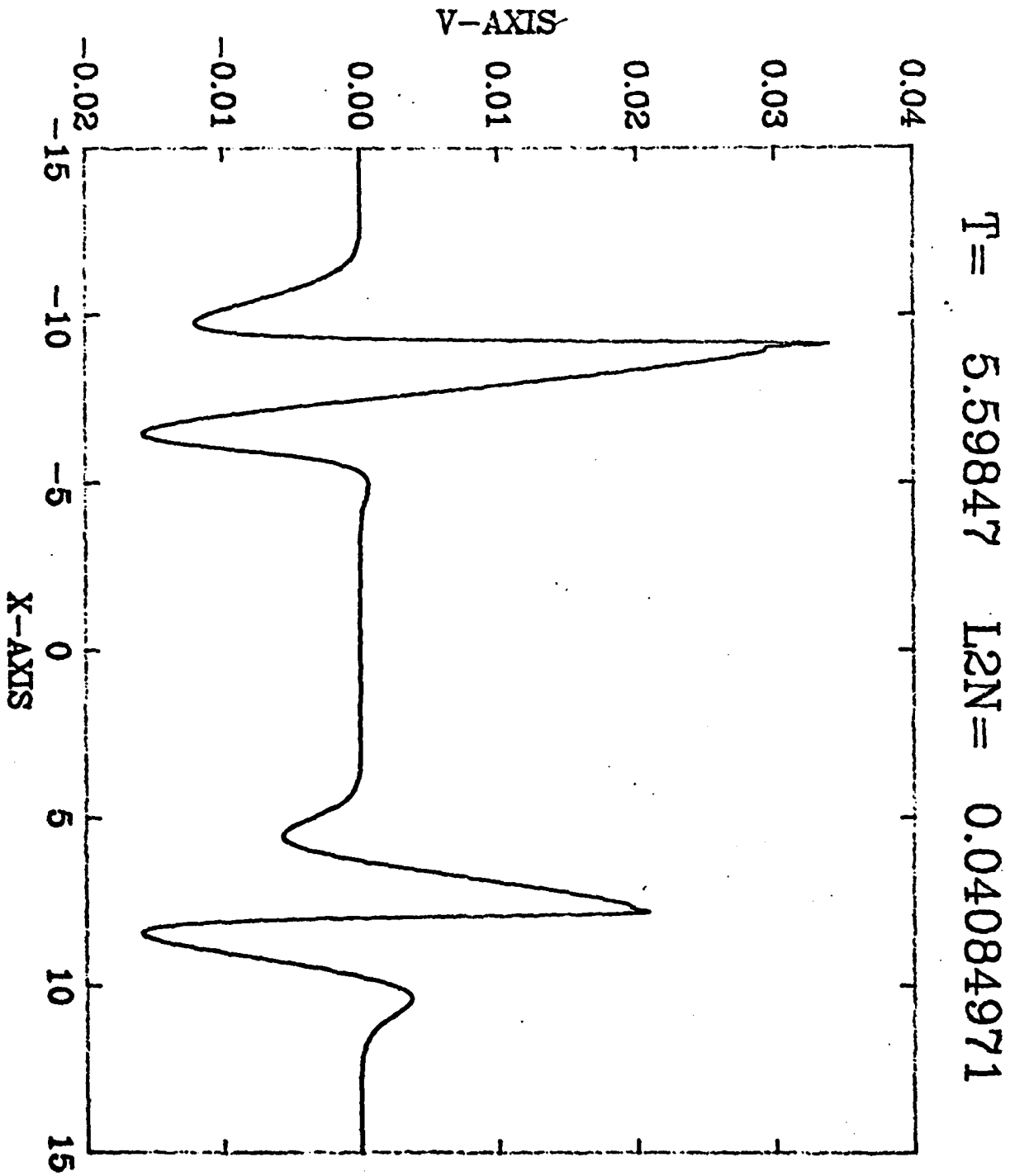


Figure 7

T= 0.62099 LN= 0.25373794

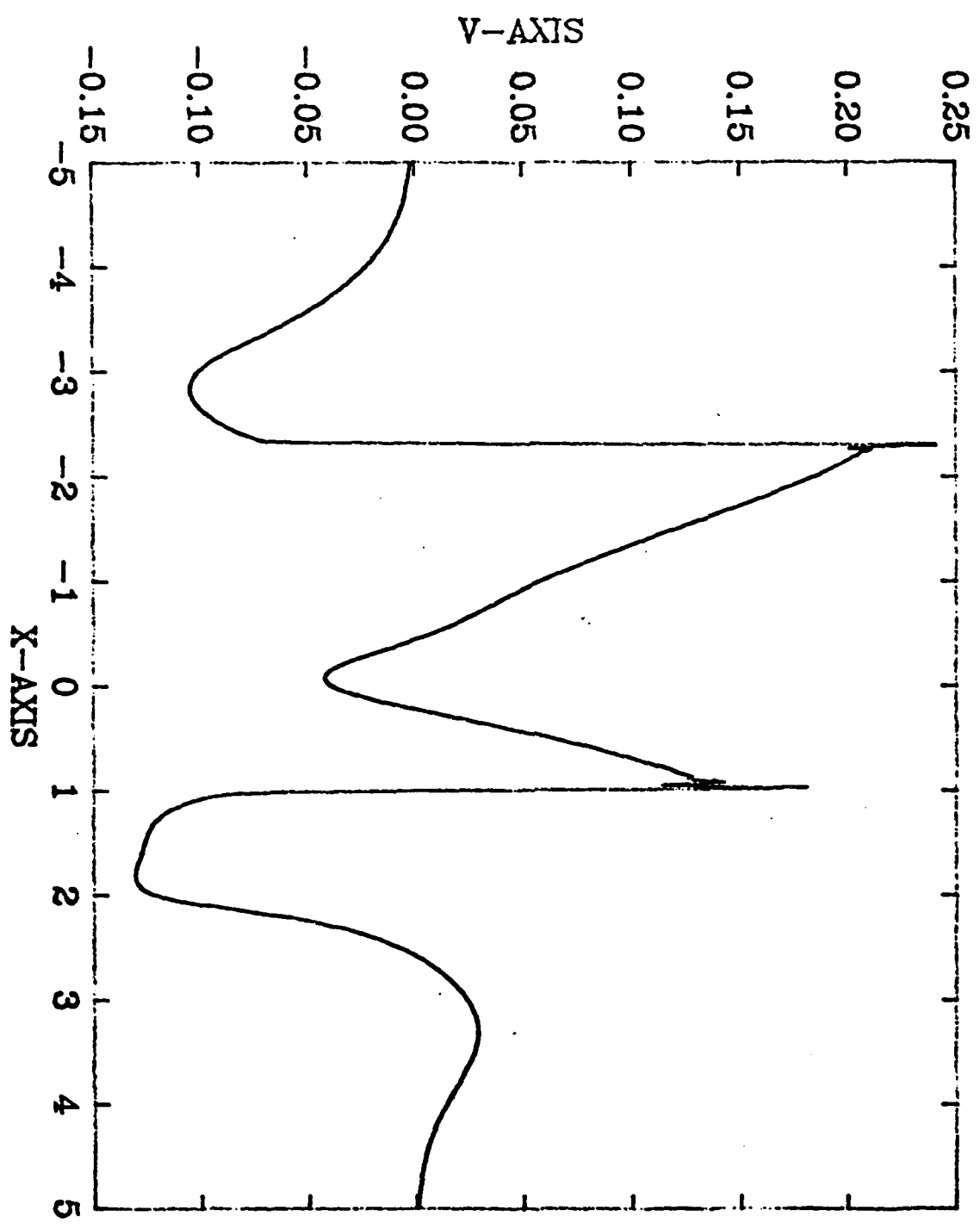


Figure 8

$T = 0.63100$   $H = 0.040000$

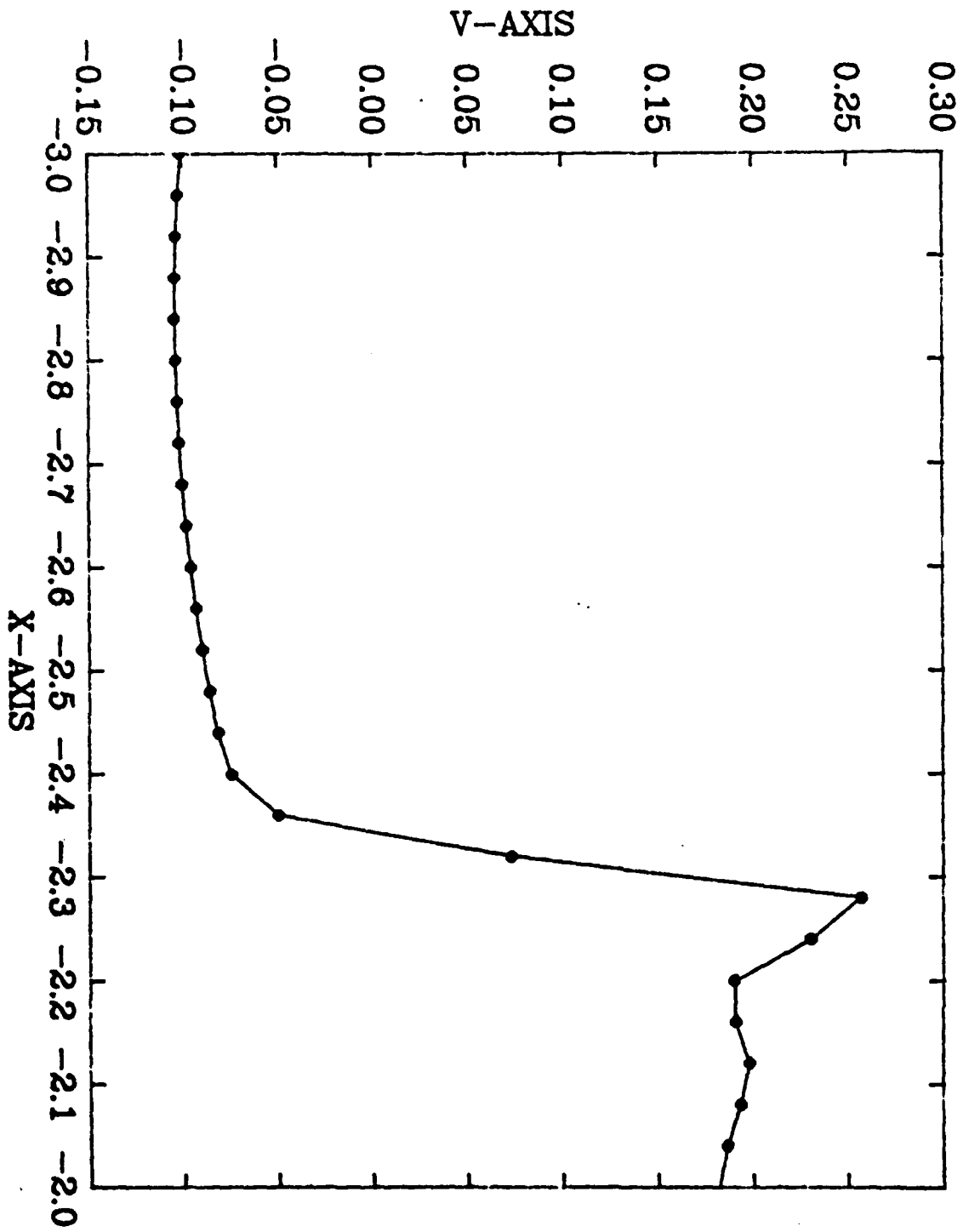


Figure 9

$T = 0.63100$   $H = 0.020000$

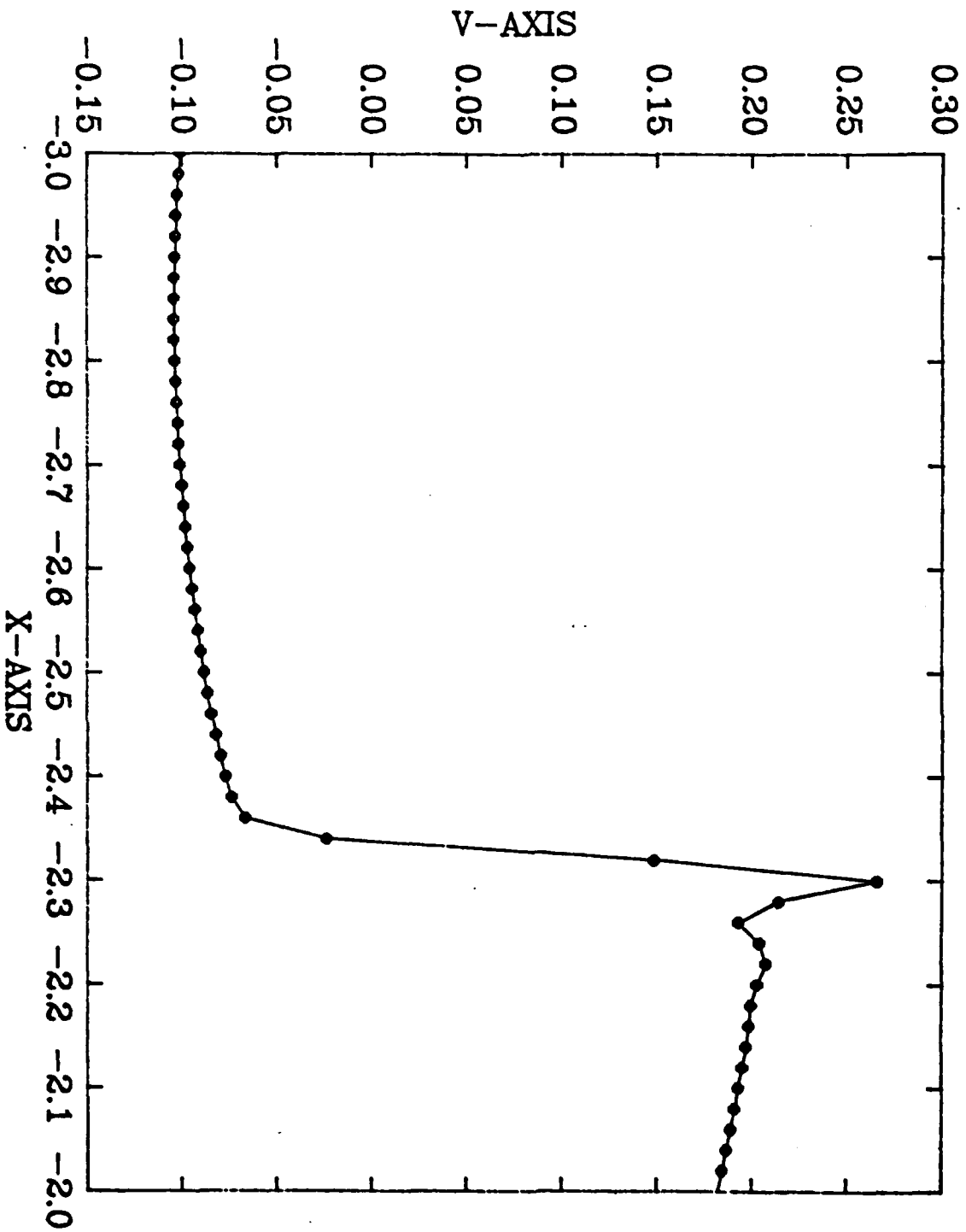


Figure 10



AD P001034

LARGE DEFORMATIONS AND STABILITY OF AXISYMMETRIC  
MOONEY MEMBRANES - FINITE ELEMENT SOLUTIONS

A. R. Johnson

US Army Natick Research and Development Laboratories (DRDNA-UE)  
Natick, MA 01760

**ABSTRACT.** The nonlinear deformations of axisymmetric Mooney membranes are determined using the finite element method. A one-dimensional form of the potential energy is used. Element gradient and tangent stiffness matrices are computed directly from the potential energy and they are expressed as a sum of coefficients, that depend nonlinearly on the finite element interpolation functions, times a set of matrices, that depend on the element interpolation functions. Numerical integration is used to obtain these element matrices which contain rational expressions of the nodal unknowns. Axisymmetric deformations of the inflated initially flat disk, the out-of-plane deformations of a disk with a circular rigid inclusion, the inflation of a torus with both circular and elliptical initial cross sections and the inflation and stretching of a cylinder are all determined. The torus solutions are carried out beyond the limit pressure yielding both stable and unstable solutions for one internal pressure. The effects of the order of numerical integration used to compute the gradient and tangent matrices and the effects of the order of the polynomial elements used on the convergence of the method with respect to mesh reduction are numerically computed using Richardson's method.

**INTRODUCTION.** The design of Army field tentage involves the use of nonlinear mechanics. The nonlinear mechanics problems associated with axisymmetric rubber membranes are useful for testing the application of numerical algorithms intended for use in more general nonlinear design problems. Levinson<sup>1</sup> introduced the use of the principle of stationary potential energy for determining finite deformations of rubber membranes. The use of the stationary potential energy method was pursued with the Ritz method by Tielking and Feng<sup>2</sup> to determine the nonlinear deformations of axisymmetric Mooney (rubber) membranes. Tielking and Feng's formulation determined the stationary points by finding the extreme value of the total potential energy with respect to trial functions which describe the configuration of the membrane instead of functions which represent displacements due to the loading. They solved the nonlinear equations which result from differentiating the potential energy (and are satisfied at the stationary points) by the Newton-Raphson method. This required that they differentiate twice to obtain the tangent matrix (Hessian) of the potential energy. Argyris, et al.<sup>3</sup> elaborated on finite element formulations for nonlinear problems. In particular, techniques which allowed the element tangent stiffness matrix to be determined by direct differentiation of the element's potential energy were discussed. Fried<sup>4,5</sup> expressed gradient and tangent element matrices for the potential energy in nonlinear problems as a sum of terms which depend nonlinearly on the shape functions times a set of matrices which also depend on the shape functions and demonstrated that numerical integration could be used to approximate these gradient and tangent matrices.

Johnson<sup>6</sup> applied this method to determine the nonlinear deformations of axisymmetric rubber membranes. Here, the calculations of the element gradient and tangent stiffness matrices for determining the nonlinear deformations of axisymmetric Mooney membranes (as presented in reference 6) are given and the results for the deformation of a torus are extended to include unstable configurations. Solutions for several other axisymmetric membrane problems are presented in the form of deformed body plots. The inflation of a toroidal membrane with an initially circular cross section is determined for pressure above what would be considered physically practical to show how this finite element formulation can be used to determine the limit point of a nonlinear deformation.

The calculation of the element gradient and tangent stiffness matrices involves integration of expressions which contain the interpolation functions rationally. Gauss-Legendre integration is attractive but not exact in this case. To evaluate the effects of using different orders of Gauss-Legendre integration, convergence data was obtained, using Richardson's extrapolation to the limit, by mesh refinement for each of several orders of numerical integration. The predicted limiting values of displacements were compared and used to compute the accuracy obtained at a given mesh size.

THE POTENTIAL ENERGY FOR AXISYMMETRIC MOONEY MEMBRANES. The form of the potential energy used here is the same as that given by Tielking and Feng<sup>2</sup>. It is included here for completeness. An infinitesimal portion of an axisymmetric membrane both before and after deformation is shown in Figure 1. The undeformed and deformed membrane configurations are described as follows. The undeformed membrane configuration is expressed as a function of the radius (distance from the axis of symmetry) by the relationship.

$$s = s(r) \quad (1)$$

The coordinates of a point with an initial radial position,  $r$ , are  $x_1(r)$  in the radial direction and  $x_2(r)$  in the vertical direction after deformation. That is,

$$x_i = x_i(r) \quad i = 1, 2 \quad (2)$$

The stretch ratios  $\lambda_1$  and  $\lambda_2$  become (see Figure 1)

$$\lambda_1 = \frac{A'C'}{AC} = \left[ \frac{x_{1,r}^2 + x_{2,r}^2}{1 + s_{,r}^2} \right]^{1/2} \quad (3)$$

and

$$\lambda_2 = \frac{A'B'}{AB} = \frac{x_1}{r} \quad (4)$$

The potential energy for axisymmetric Mooney membrane is

$$\Pi = 2\pi \int_{r_1}^{r_2} C_1 [(I_1 - 3) + \alpha(I_2 - 3)] r (1 + s_r^2)^{\frac{1}{2}} dr - W \quad (5)$$

where  $C_1$ ,  $\alpha$  = material constants (1.0 and 0.1 here)

$W$  = the work done by the applied forces

$(r_1, r_2)$  = the domain in  $r$  over which the undeformed membrane is defined.

$$I_1 = \lambda_1^2 + \lambda_2^2 + \frac{1}{\lambda_1 \lambda_2} \quad (6)$$

$$I_2 = \lambda_1^2 \lambda_2^2 + \frac{1}{\lambda_1} + \frac{1}{\lambda_2} \quad (7)$$

Then, the following form of the potential energy will be used with equations (3) and (4) for the finite element analysis.

$$\begin{aligned} \Pi = 2\pi C_1 \int_{r_1}^{r_2} & \left[ \left( \lambda_1^2 + \lambda_2^2 + \frac{1}{\lambda_1 \lambda_2} - 3 \right) + \alpha \left( \lambda_1^2 \lambda_2^2 + \frac{1}{\lambda_1} + \frac{1}{\lambda_2} - 3 \right) \right] \\ & \times r (1 + s_r^2)^{\frac{1}{2}} dr - W \quad (8) \end{aligned}$$

COMPUTATION OF THE ELEMENT GRADIENT AND TANGENT MATRICES. We discretize by the finite element method and construct mapping functions  $r = f_e(\xi)$  which take the  $e$ 'th element to the interval  $\xi \in (-1, 1)$ . We then use Gauss-Legendre numerical integration at "j" points to approximate the integration ( $w_j$  = the weight factor at point j). The potential energy for an element then becomes

$$\begin{aligned} \Pi_e = 2\pi C_1 \sum_{j=1}^L w_j & \left[ \left( \lambda_1^2 + \lambda_2^2 + \frac{1}{\lambda_1 \lambda_2} - 3 \right) \right. \\ & \left. + \alpha \left( \lambda_1^2 \lambda_2^2 + \frac{1}{\lambda_1} + \frac{1}{\lambda_2} - 3 \right) \right]_{\xi = \xi_j} Q_j f_{ej} \dot{f}_{ej} - W \quad (9) \end{aligned}$$

where

$$\dot{f}_{ej} = \left. \frac{df_e}{d\xi} \right|_{\xi=\xi_j} \quad (10)$$

and

$$Q_j = (1+s_r^2)^{1/2} \Big|_{\xi=\xi_j} \quad (11)$$

Next, the following finite element approximations to the functions  $x_1(r)$  and  $x_2(r)$  are made.

$$x_m = M_m^T u_e = u_e^T M_m \quad m = 1, 2 \quad (12)$$

where  $M_m$  = a vector of interpolation functions

and  $u_e$  = a vector of element nodal unknowns

These approximations are used in equations (3) and (4) which are in turn used in (9). The element gradient then becomes

$$g_e = 2\pi C_1 \sum_{j=1}^L w_j Q_j \dot{f}_{ej} \dot{f}_{ej} \left[ \left[ \left(1 - \frac{1}{\lambda_1^4 \lambda_2^2}\right) + \alpha \left(\lambda_2^2 - \frac{1}{\lambda_1^4}\right) \right] \right] \quad (13)$$

$$\times (M_{1,r}^T a + M_{2,r}^T b)$$

$$+ \left[ \left(1 - \frac{1}{\lambda_1^2 \lambda_2^4}\right) + \alpha \left(\lambda_1^2 - \frac{1}{\lambda_2^4}\right) \right] M_{1,c} \Big|_{\xi=\xi_j} - \frac{\partial W_e}{\partial u_e^T}$$

$$\text{where } a = \frac{M_{1,r}^T u_e}{2Q} \quad (14)$$

$$b = \frac{M_{2,r}^T u_e}{2Q} \quad (15)$$

$$\text{and } c = \frac{M_{1,c}^T u_e}{2r} \quad (16)$$

$$\lambda_1^2 = \frac{u_e^T (M_{1,r} M_{1,r}^T + M_{2,r} M_{2,r}^T) u_e}{1 + s_r^2} \quad (17)$$

and

$$\lambda_2^2 = \frac{u_e^T M_{1,1} M_{1,1}^T u_e}{r^2} \quad (18)$$

Similarly, the element tangent stiffness matrix becomes

$$K_e = 2\pi C_1 \frac{L}{\Sigma} w_j Q_j f_{ej} \dot{f}_{ej} \left[ A_1 M_{1,r} M_{1,r}^T + A_2 M_{2,r} M_{2,r}^T \right. \quad (19)$$

$$+ A_3 M_{1,1} M_{1,1}^T + A_4 (M_{1,r} M_{2,r}^T + M_{2,r} M_{1,r}^T)$$

$$+ A_5 (M_{1,1} M_{1,r}^T + M_{1,r} M_{1,1}^T)$$

$$\left. + A_6 (M_{1,2,r} M_{2,r}^T + M_{2,r} M_{1,1}^T) \right]_{\xi=\xi_j} - \frac{\partial^2 W_e}{\partial u_e \partial u_e^T}$$

where

$$A_1 = 2a^2 \left[ \frac{1}{\lambda_1 \lambda_2} + \frac{\alpha}{\lambda_1} \right] + \frac{1}{Q} \left[ \left[ 1 - \frac{1}{\lambda_1 \lambda_2} \right] + \alpha \left[ \lambda_2^2 - \frac{1}{\lambda_1} \right] \right] \quad (20)$$

$$A_2 = 2b^2 \left[ \frac{1}{\lambda_1 \lambda_2} + \frac{\alpha}{\lambda_1} \right] + \frac{1}{Q} \left[ \left[ 1 - \frac{1}{\lambda_1 \lambda_2} \right] + \alpha \left[ \lambda_2^2 - \frac{1}{\lambda_1} \right] \right] \quad (21)$$

$$A_3 = 2c^2 \left[ \frac{1}{\lambda_1 \lambda_2} + \frac{\alpha}{\lambda_2} \right] + \frac{1}{r} \left[ \left[ 1 - \frac{1}{\lambda_1 \lambda_2} \right] + \alpha \left[ \lambda_1^2 - \frac{1}{\lambda_2} \right] \right] \quad (22)$$

$$A_4 = 2ab \left[ \frac{1}{\lambda_1 \lambda_2} + \frac{a}{\lambda_1} \right] \quad (23)$$

$$A_5 = ac \left[ \frac{1}{\lambda_1^4 \lambda_2^4} + a \right] \quad (24)$$

and

$$A_6 = bc \left[ \frac{1}{\lambda_1^4 \lambda_2^4} + a \right] \quad (25)$$

Both quadratic,  $C^0$ , and cubic,  $C^1$ , interpolation is used here. The detail of the interpolation of the coordinate displacement functions  $x_1(r)$  and  $x_2(r)$  are given as follows.

$$x_{ij} = x_i(r) \text{ at node } j \quad (i, j = 1, 2)$$

$\xi$  = element coordinates,  $\xi \in (-1, 1)$   
 $r$  = global coordinates

For quadratic elements we have

$$M_1^T = (\frac{1}{2}\xi(\xi-1), 0, 1-\xi^2, 0, \frac{1}{2}\xi(1+\xi), 0) \quad (26)$$

$$M_2^T = (0, \frac{1}{2}\xi(\xi-1), 0, 1-\xi^2, 0, \frac{1}{2}\xi(1+\xi))$$

$$u_e^T = (x_{11}, x_{21}, x_{12}, x_{22}, x_{13}, x_{23})$$

and for cubic elements we have

$$M_1^T = (\phi_1, \phi_2, 0, 0, \phi_3, \phi_4, 0, 0) \quad (27)$$

$$M_2^T = (0, 0, \phi_1, \phi_2, 0, 0, \phi_3, \phi_4)$$

$$u_e^T = \left[ x_{11}, \frac{dx_{11}}{dr}, x_{21}, \frac{dx_{21}}{dr}, x_{12}, \frac{dx_{12}}{dr}, x_{22}, \frac{dx_{22}}{dr} \right]$$

where  $\phi_1 = \frac{1}{4} (2 - 3\xi + \xi^3)$  (28)

$$\phi_2 = \Delta/4 (1 - \xi)^2 (1 + \xi)$$

$$\phi_3 = \frac{1}{4} (1 + \xi)^2 (2 - \xi)$$

and  $\phi_4 = \Delta/4 (\xi - 1) (1 + \xi)^2$

$\Delta = \frac{1}{2}$  the length of the element in the global system.

DETERMINING STATIONARY POINTS AND STABILITY. The total potential energy is the sum of the element potential energies. Thus, global gradient and tangent stiffness matrices can be determined by the standard procedures of assembling load and stiffness matrices in the finite element method. After application of the boundary conditions, the global nodal displacement vector, gradient vector, and tangent stiffness matrix ( $u$ ,  $g$ , and  $K$  respectively) can be used to write the following Taylor expansion of the potential energy near a stationary point.

$$\Pi(u+\Delta u) = \Pi(u) + \Delta u^T g + \frac{1}{2} \Delta u^T K \Delta u + O(\|\Delta u\|^3) \quad (29)$$

Thus, to have the stable solutions to  $g = 0$  (minimal points of the potential energy)  $K$  must be positive definite. The matrix  $K$  must then have all positive eigenvalues at a stable point. When a stationary point is found, its stability is determined by evaluating the eigenvalues of  $K$  at that point. To obtain the stationary points we assume we can start near one. Then, the Newton-Raphson method can be used to locate the stationary point. That is, successive updates to the global vector of nodal unknowns,  $u$ , are determined using

$$u_{n+1} = u_n - K_n^{-1} g_n \quad (30)$$

OUT OF PLANE DEFORMATIONS OF A DISK. The undeformed and deformed geometry of the circular disk are shown in Figure 2. The meridional stretch ratio,  $\lambda_1$ , and the circumferential stretch ratio,  $\lambda_2$ , are given as follows.

$$\lambda_1 = \left[ \left( \frac{dx_1}{dr} \right)^2 + \left( \frac{dx_2}{dr} \right)^2 \right]^{1/2} \quad (31)$$

and

$$\lambda_2 = \frac{x_1}{r} \quad (32)$$

The work term,  $W_e$ , associated with element  $e$  is

$$W_e = \int P \pi x_1^2 dx_2 \quad (33)$$

or

$$W_e = -\pi P \int_e x_1^2 \frac{dx_2}{d\xi} d\xi \quad (34)$$

The contribution to the element gradient and tangent stiffness expressions are

$$\frac{\partial W_e}{\partial u_e^T} = -\pi P \sum_{j=1}^L w_j \left[ 2 \left[ \frac{dM_2^T}{d\xi} u_e \right] (M_1^T u_e) M_1 + (M_1^T u_e) \frac{dM_2}{d\xi} \right]_{\xi=\xi_j} \quad (35)$$

and

$$\frac{\partial^2 W_e}{\partial u_e \partial u_e^T} = -2\pi P \sum_{j=1}^L w_j \left[ (M_1^T u_e) \left[ M_1 \frac{dM_2^T}{d\xi} + \frac{dM_2}{d\xi} M_1^T \right] + \left[ \frac{dM_2^T}{d\xi} u_e \right] (M_1 M_1^T) \right]_{\xi=\xi_j} \quad (36)$$

After application of boundary conditions the Newton-Raphson method was used with the incremental pressure method to determine the configurations shown in Figure 3. By changing only the range of integration in  $r$ , the boundary conditions, and dropping the work term the deformations of a circular disk with a rigid inclusion pulled axisymmetrically out of the plane can be determined. The deformations for one inclusion are shown in Figure 4.

**INFLATION OF A TORUS.** Using parametric coordinates  $\eta$  and  $\xi$  to measure arc length of the undeformed and deformed meridional curves respectively, the meridional stretch ratio,  $\lambda_1$ , and the circumferential stretch ratio,  $\lambda_2$ , are given as follows for the torus with a circular undeformed cross section, see Figure 5.

$$\lambda_1 = \frac{d\xi}{d\eta} \quad (37)$$

and

$$\lambda_2 = \frac{x_1}{R + a \cos(\omega)} \quad (38)$$

If we let  $\frac{d(\cdot)}{d\omega} = (\cdot)'$  the expressions for  $\lambda_1^2$  and  $\lambda_2^2$  in terms of  $x_1$ ,  $x_2$ , and  $\omega$  become

$$\lambda_1^2 = \frac{(x_1')^2 + (x_2')^2}{a^2} \quad (39)$$

and

$$\lambda_2^2 = \frac{x_1^2}{(R + a \cos(\omega))^2} \quad (40)$$

The work,  $W$ , done by the pressure,  $P$ , during a deformation is

$$W = \int P dV = 4\pi P \int_{\omega=\pi}^0 x_1 x_2 \frac{dx}{d\omega} d\omega - PV_0 \quad (41)$$

Dropping the constant term, integrating by parts, and using the boundary conditions, we obtain

$$W = 2\pi P \int_{\omega=0}^{\pi} x_1^2 \frac{dx}{d\omega} d\omega \quad (42)$$

The element contributions to the gradient and tangent matrices become

$$\frac{\partial W}{\partial u_e^T} = 2\pi P \sum_{j=1}^L w_j \left[ 2x_1 \frac{dx_2}{d\Omega} M_1 + x_1^2 \frac{dM_2}{d\Omega} \right]_{\Omega=\Omega_j} \quad (43)$$

and

$$\frac{\partial^2 W}{\partial u_e \partial u_e^T} = 4\pi P \sum_{j=1}^L w_j \left[ x_1 \left[ M_1 \frac{dM_1^T}{d\Omega} + \frac{dM_1}{d\Omega} M_1^T \right] + \frac{dx_2}{d\Omega} M_1 M_1^T \right]_{\Omega=\Omega_j} \quad (44)$$

where  $\Omega \in (-1, 1)$

$$f_e(\Omega) = \omega_{ce} + \Delta\Omega$$

$\omega_{ce}$  =  $\omega$  at the center of the undeformed element

and  $2\Delta$  = the angular size of the element

With several modifications the inflation of a torus with an elliptical cross section can be analyzed. Setting  $a$  = the semimajor axis length in the  $x_1$  direction and  $b$  = the semiminor axis length in the  $x_2$  direction then the expressions for  $\lambda_1^2$  and  $\lambda_2^2$  become

$$\lambda_1^2 = \frac{(x_1')^2 + (x_2')^2}{\left[ \rho^2 + \frac{\rho^6(a^2 - b^2) \sin^2(\omega) \cos^2(\omega)}{a^4 b^4} \right]} \quad (45)$$

and

$$\lambda_2^2 = \frac{x_1^2}{(R + \rho \cos(\omega))^2} \quad (46)$$

where

$$\rho^2 = \frac{1}{\frac{\cos^2(\omega)}{a^2} + \frac{\sin^2(\omega)}{b^2}} \quad (47)$$

After an additional modification to represent integration over a torus with an elliptical cross section instead of a circular cross section, the deformations of either a circular or an elliptical torus can be computed, see Figures 6 and 7.

**INFLATION AND STRETCHING OF A CIRCULAR CYLINDER.** The geometry used here for the analysis of the inflation and stretching of a circular cylinder is shown in Figure 8. The ends of the cylinder are attached to rigid unit radii disk inclusions. The axial stretch is specified by prescribing the distance between the end inclusions. The stretch ratios take the following form.

$$\lambda_1 = \left( (x_1')^2 + (x_2')^2 \right)^{\frac{1}{2}} \quad (48)$$

and

$$\lambda_2 = \frac{x_1}{\rho} \quad (49)$$

The work done by the forces stretching and inflating the cylinder can be expressed as follows

$$W = \int_{\eta=0}^{\eta=x_2^p-1} 2p^{-1} F(\eta) d\eta + \int_{r=0}^{r=1} P\pi x_1^2 \frac{dx_2}{dr} dr - PV_0 \quad (50)$$

where the cylinder is stretched from  $\eta = 0$  to  $\eta = x_2^p - 1$ , the force required to stretch the cylinder is  $F(\eta)$  and  $V_0 =$  the internal volume of the cylinder. Dropping the terms which do not depend on the nodal variables we have

$$W = P\pi \int_{r=0}^1 x_1^2 \frac{dx_2}{dr} dr \quad (51)$$

This work term is of the same general form as that given in equation (34) so the element contributions to the gradient and tangent matrix are similar to those of equations (35) and (36). A partial profile of the inflation of a cylinder stretched to five times its original length is shown in Figure 9.

UNSTABLE STATIONARY POINTS (DEFORMATIONS) FOR THE CIRCULAR TORUS. The inflation of a torus with  $R = 1.0$  and  $a = 0.25$  (see Figures 5 and 10) was determined for a pressure range which included both stable and unstable configurations (stationary points). The profiles of the undeformed and three deformed configurations for a pressure of 6.0 are shown in Figure 10. Two of the deformed configurations are stable and one is unstable. The unstable configuration, in this case, is near the first stable solution and indicates that a check for stability is important. Other indications of stability are the so-called "limit points" (a point where the rate of change of a variable with respect to a change in the loading reverses sign). Figures 11 and 12 contain plots of the inner and outer torus radii vs pressure. These calculations were carried out for two values of  $\alpha$  ( $\alpha =$  the material constant in the internal energy density expression  $(I_1 - 3) + \alpha(I_2 - 3)$ ). It is interesting to note that when  $\alpha = 0.1$ , two limit points are found, but when  $\alpha = 0.0$ , only one was found.

COMMENTS ON ACCURACY. Two sources of error are considered here. The first is the error due to modeling a continuous variable over an interval by the finite element interpolation and the second is that due to the use of Gauss-Legendre numerical integration to integrate the rational expressions in the formulas for the element gradient and tangent matrices. If the mesh is fine enough, then we can use Richardson's extrapolation method to estimate the convergence rates and the accuracy of the calculations. The finite element solution,  $\tilde{u}(h)$ , for a given order of numerical integration and for a given uniform element size  $h$  is assumed to be of the following form.

$$\tilde{u}(h) = \tilde{u}(0) + a_1 h^{r_1} + O(h^{r_2}) \quad (52)$$

where  $\bar{u}(0)$  = the solution when  $h = 0$

$r_2 > r_1 > 0$  are positive real numbers

and  $a_1$  = a constant that does not depend on  $h$ .

Using the first two terms on the right side of equation (52) and obtaining  $\bar{u}(h)$  for three different values of  $h$  (element size) the values of  $a$ ,  $r$  and  $\bar{u}(0)$  can be determined. Estimates of the accuracy at a given mesh size and the rate of convergence are then available.

Numerical results for convergence of the outer radius and the strain energy (internal energy) are presented in Tables 1 and 2 for the inflation of the circular torus shown in Figure 6 ( $R = 1.0$ ,  $a = 0.5$ , and  $\alpha = 0.1$ ). Table 1 contains the results for the case of quadratic interpolation and Table 2 for the case of cubic interpolation. The numerical predictions agree well. The convergence graphs shown in Figures 13 and 14 suggest that the higher order interpolation results in an order of magnitude increase in accuracy for a given number of elements. Also, higher order numerical integration schemes do not appear to be computationally advantageous since the accuracy is not as sensitive to the integration scheme as it was to the element size (mesh size).

#### REFERENCES.

1. M. Levinson, "The application of the principle of stationary potential energy to some problems in finite elasticity", J. Appl. Mech. 87 (1965), 656-660.
2. J. T. Tielking and W. W. Feng, "The application of the minimum potential energy principle to nonlinear axisymmetric membrane problems", J. Appl. Mech. (1974), 491-496.
3. J. H. Argyris, H. Balmer, J. Doltsinis, P. Dunne, M. Haase, M. Muller, and D. Scharpf, "Finite element method - the natural approach", Comp. Meths. Appl. Mech. Eng. 17/18 (1979), 1-106.
4. I. Fried, "Discrete integration in nonlinear finite element analysis", unpublished, Dept. of Math., Boston University (1979).
5. I. Fried, "Nonlinear finite element computation of the equilibrium and stability of the circular plate", Int. J. Num. Meth. Eng. (1981), 1436-1440.
6. A. Johnson, "Finite element analysis of axisymmetric rubber membranes", Dissertation, Boston University (1981).



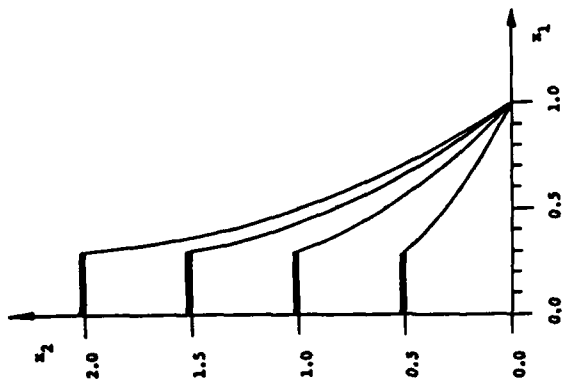


Figure 4. Cross section profiles for disk with inclusion, inclusion radius = 0.3

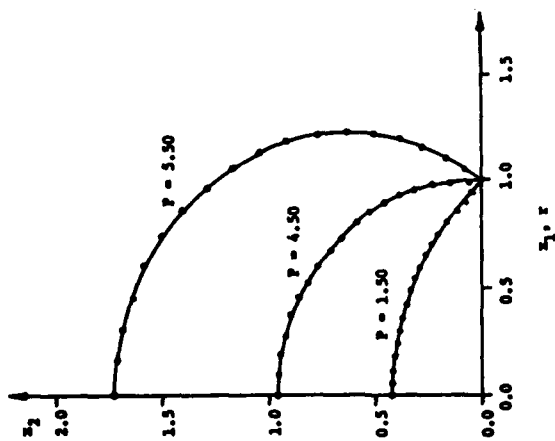


Figure 3. Profiles of inflated disk

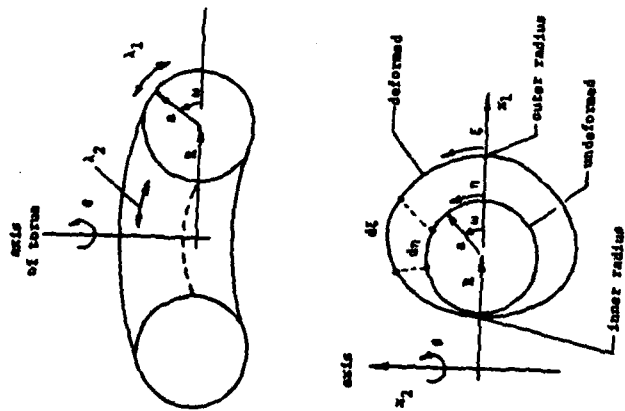


Figure 5. Torus with circular cross section

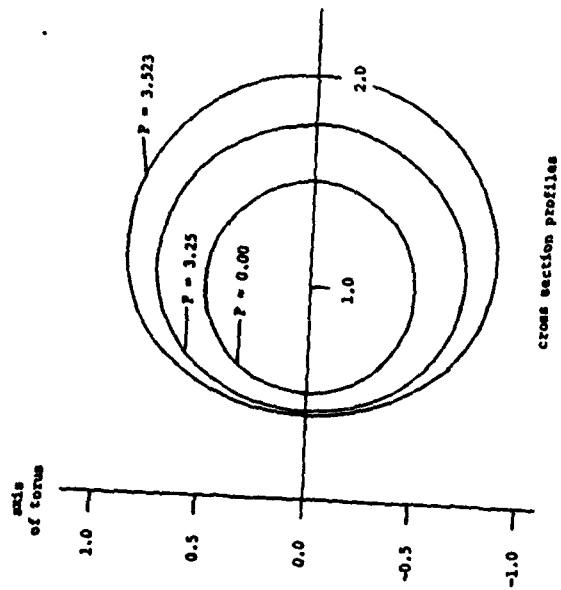


Figure 6. Inflation of torus

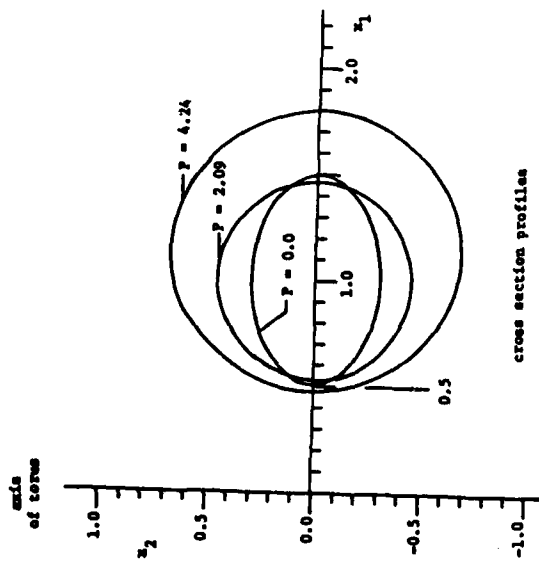


Figure 7. Inflation of a torus with an elliptical cross section

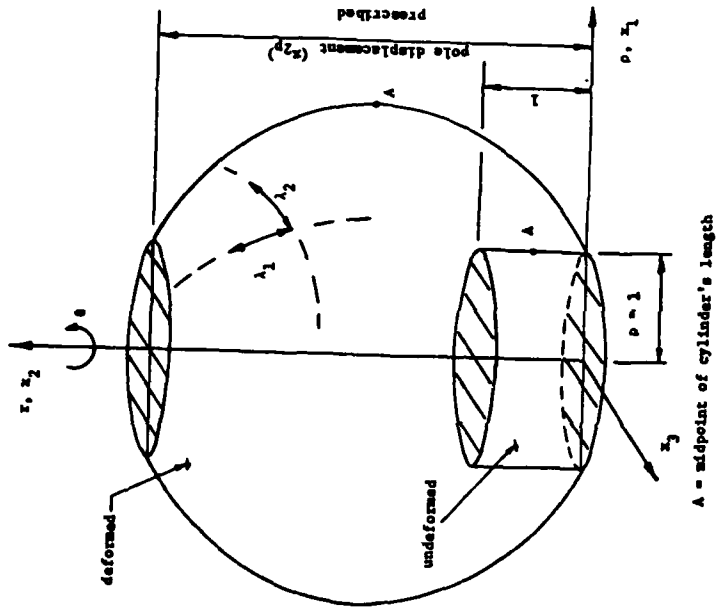


Figure 8. Inflation and stretching of cylinder

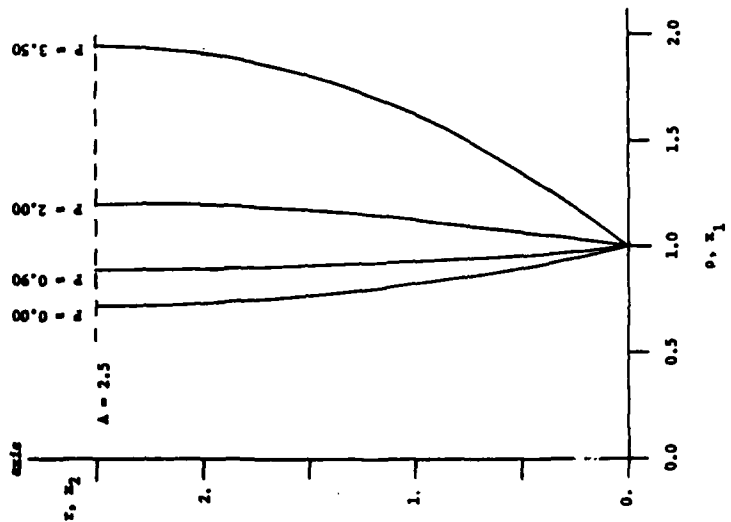


Figure 9. Profiles of the inflation of a stretched cylinder

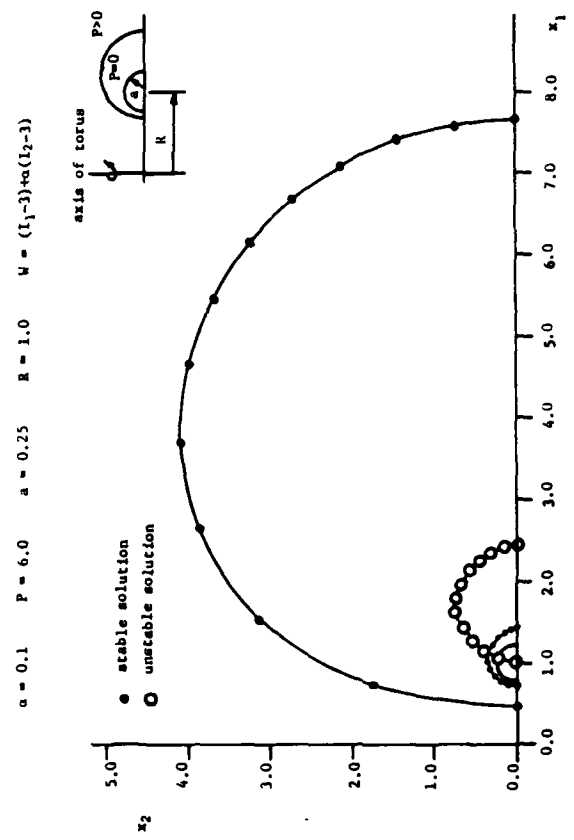


Figure 10. Profiles of torus inflated to  $P = 6.0$ , two stable solutions and one unstable solution,  $\alpha = 0.1$

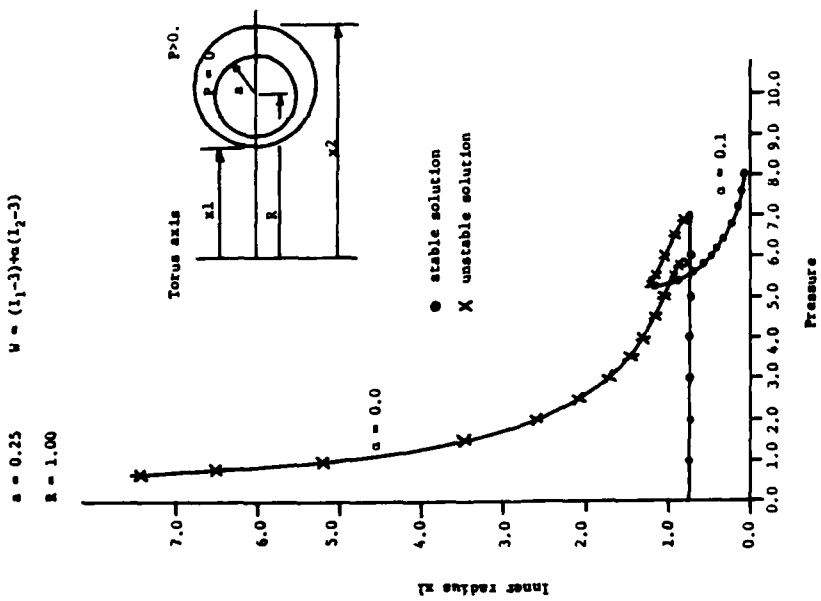
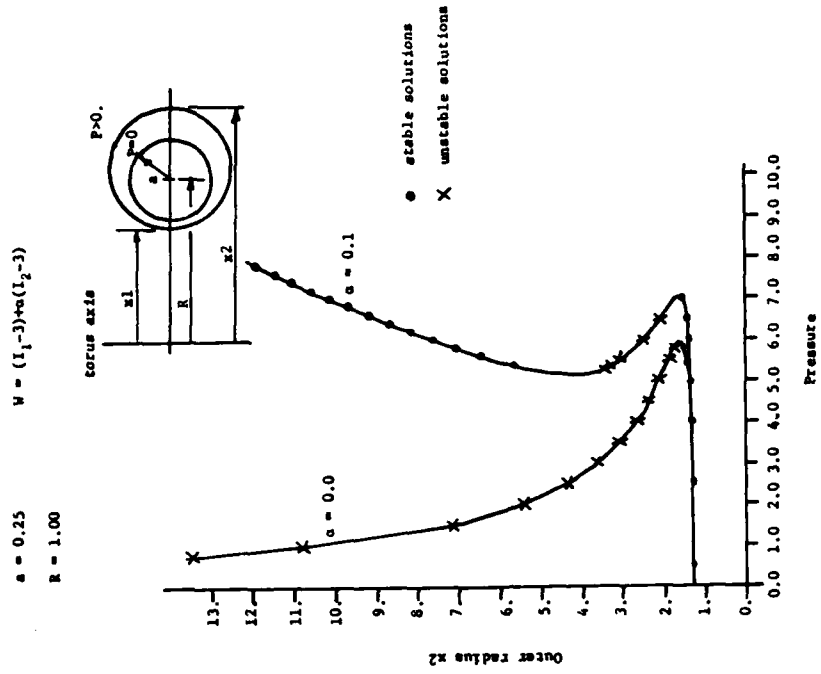
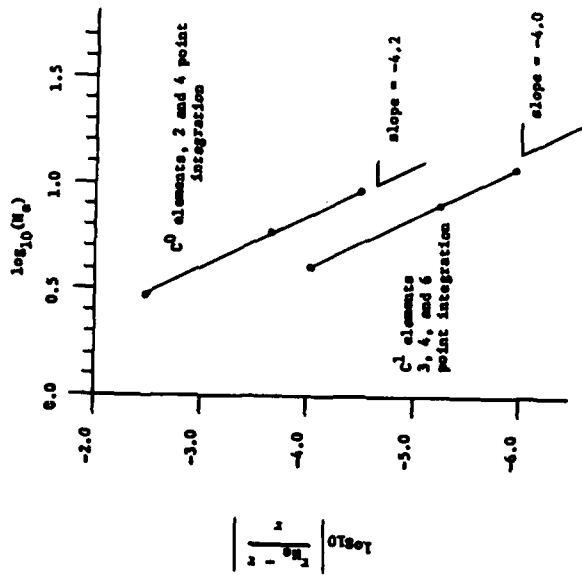
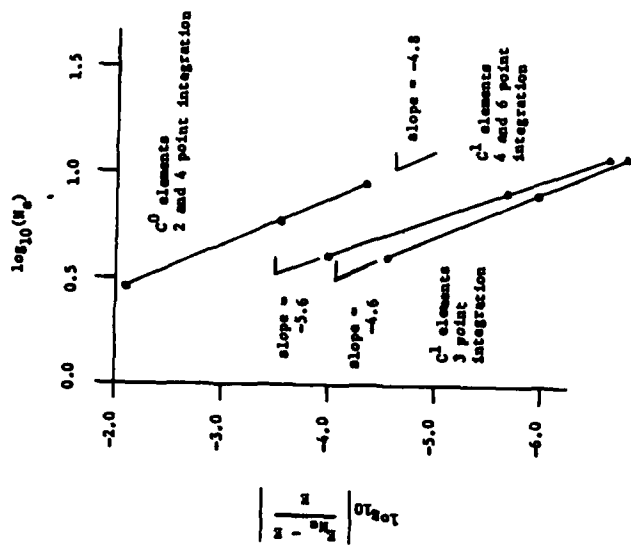


Figure 12. Outer torus radius vs pressure

Figure 11. Inner torus radius vs pressure



$r$  = computed outer radius of torus when  $N_e$  elements are used  
 $r$  = converged value of outer radius of torus



$E$  = strain energy computed using  $N_e$  elements  
 $E$  = converged value of strain energy

Figure 13. Convergence of outer radius, inflation of torus

Figure 14. Convergence of strain energy, inflation of torus

TABLE 1

CONVERGENCE DATA FOR INFLATION OF TORUS,  
QUADRATIC ELEMENTS

Outer Radius (P = 3.25)

No. of Integration Points	3 Elements	6 Elements	9 Elements	Converged
2	1.7530039	1.7591435	1.7593895	1.7594454
4	1.7541697	1.7591665	1.7593966	1.7594489

Strain Energy (P = 3.25)

No. of Integration Points	3 Elements	6 Elements	9 Elements	Converged
2	12.5898661	12.689202	12.692323	12.692851
4	12.687924	12.693023	12.693598	----

TABLE 2

CONVERGENCE DATA FOR INFLATION OF TORUS,  
CUBIC ELEMENTS

Outer Radius (P = 3.25)

No. of Integration Points	4 Elements	8 Elements	12 Elements	Converged
3	1.7596120	1.7594601	1.7594520	1.7594500
4	1.7596131	1.7594602	1.7594520	1.7594500
6	1.7596131	1.7594602	1.7594520	1.7594500

Strain Energy (P = 3.25)

No. of Integration Points	4 Elements	8 Elements	12 Elements	Converged
3	12.692719	12.693058	12.693070	12.693072
4	12.691811	12.693046	12.693069	12.693072
6	12.691827	12.693046	12.693069	12.693072



AD P 001035



## STRUCTURAL ANALYSIS OF A MINE WITH TWO VISCOELASTIC EXPLOSIVE FILLS

Aaron D. Gupta  
Mechanical Engineer

U.S. Army Ballistic Research Laboratory  
U.S. Army Armament Research and Development Command  
Aberdeen Proving Ground, Maryland 21005

**ABSTRACT.** The structural response of a Soviet TM-46 land mine with two viscoelastic explosive fills subjected to an externally applied pressure wave has been analyzed with the ADINA finite element code. The main charge consists of 5.72 kg TNT while the booster charge in the fuze contains .04 kg Tetryl in the fuze well. The finite element model of the mine uses the axisymmetric two-dimensional mesh configuration with a rigid base support boundary condition. Both implicit and explicit time integration schemes have been used for this analysis.

The viscoelastic explosive filler materials exhibit marked nonlinear behavior. It was therefore decided that the tension cut-off curve description material models were the appropriate models to use. Relationships between the volume strains and the bulk moduli were obtained from the Mie-Grüneisen equations of state. These models include failure criteria which allow tension cut-off planes to form in a direction normal to the principal tensile stress whenever the strain initially exceeds 0.1% in tension. The materials for the steel casing were modeled with bilinear stress-strain curves, von Mises yield condition, and kinematic hardening rule. Trapped air inside the mine body was modeled as an assembly of inviscid linear compressible fluid elements.

The finite element model was initially verified for mode shapes at a few low order eigenfrequencies and a failure criterion for the casing was incorporated based on a comparison of the value of the three-dimensional second invariant of plastic strain with that of the one-dimensional value obtained from the tensile tests. Solution of the problem in terms of stresses and displacements out to .75 ms of real time indicates high stress concentration and large displacements of the top cover plate in the stepped region and minimal response of the interior structure until the cover plate is in contact with the intermediate partition of the mine body.

**1. INTRODUCTION.** This paper describes the response of the Soviet TM-46 Antitank mine with a unique double walled construction of the top pressure plate designed to resist a transient blast load. The rationale for this analysis is the need to develop a remote, expeditious means of clearing a path through an enemy mine field. A method of imparting a relatively large transient pressure and impulse to the surface of the earth by means of explosives is under development. The current study is a part of a general investigation to determine the extent of structural damage sustained by the mine body from a given level of blast wave amplitude and shape. The principal kill mechanism is to be a serious distortion or rupture of the mine casing rather than fuze initiation or removal of pressure plate since the damage mechanisms could be easily changed from a particular type of mine to another and a surekill could not be ensured based on a particular mode of actuation.

The mine investigated represents a typical Soviet antitank mine, which consists basically of a round thin metal body filled with an explosive. The unique feature of this mine is a double walled construction of the top wall resulting from joining of the top pressure plate with the intermediate wall along the circular edge through a crimped joint which tends to increase the blast resistance behavior of the mine. The other distinctive feature is the fuze mechanism. However a variety of radically different fuzes, different both in mechanical designs and method of activation could be substituted for the currently used ball-spring mechanism. Therefore the numerical model in the present study does not include a model of the fuze.

The paper has four major areas as follows: (a) problem definition, (b) determination of material properties and selection of failure criteria of the casing as well as numerical characterization of the viscoelastic explosive fills, (c) finite element model description and calculations, and (d) dynamic response prediction of the structural assembly.

## 2. PROBLEM DEFINITION.

A. Antitank Mine Description. The TM-46 land mine has a cylindrical steel body with a primary fuze well in the center of the top and one at the bottom, presumably for antilift or booby trapping purposes. In addition, it has a secondary fuze well in the sidewall underneath the carrying handle. A sectional drawing of the mine is shown in Figure 1. The mine has a nominal diameter of 29.7 cm, height of 7.3 cm and weighs 8.7 kg with a main charge of 5.7 kg TNT.

The mine body is made of three pieces of sheet steel which are joined at the upper periphery by a 360° crimp. The top cover of the mine body is only 0.635 mm thick and has three steps. This cover connects to a central circular plate formed by spot-welding of a thick plate to the thin cover section. The intermediate wall is formed from 0.94 mm thick steel sheet to which a hollow cylindrical piece 0.56 mm thick is attached to form the centrally located top fuze well. The fuze well contains a 40 g tetryl booster charge for fuze activation.

The lower part of the mine body is formed by a deep drawing operation which results in very inhomogenous material properties. The central cavity in the main body of the mine is filled with a charge of 5.7 kg TNT explosive. The cavity between the top and intermediate walls is unfilled. However compression of air in this region can contribute to alteration of the response behavior of the mine and subsequent uncrimping of the joint.

The normal method of activation of the fuze is by means of force applied to the pressure cap depressing the fuze and releasing the striker to strike the booster charge in the fuze well. This activates the tetryl booster which in turn detonates the primary TNT charge. The secondary fuze well on the TM-46 mine gives it anti-disturbance capability.

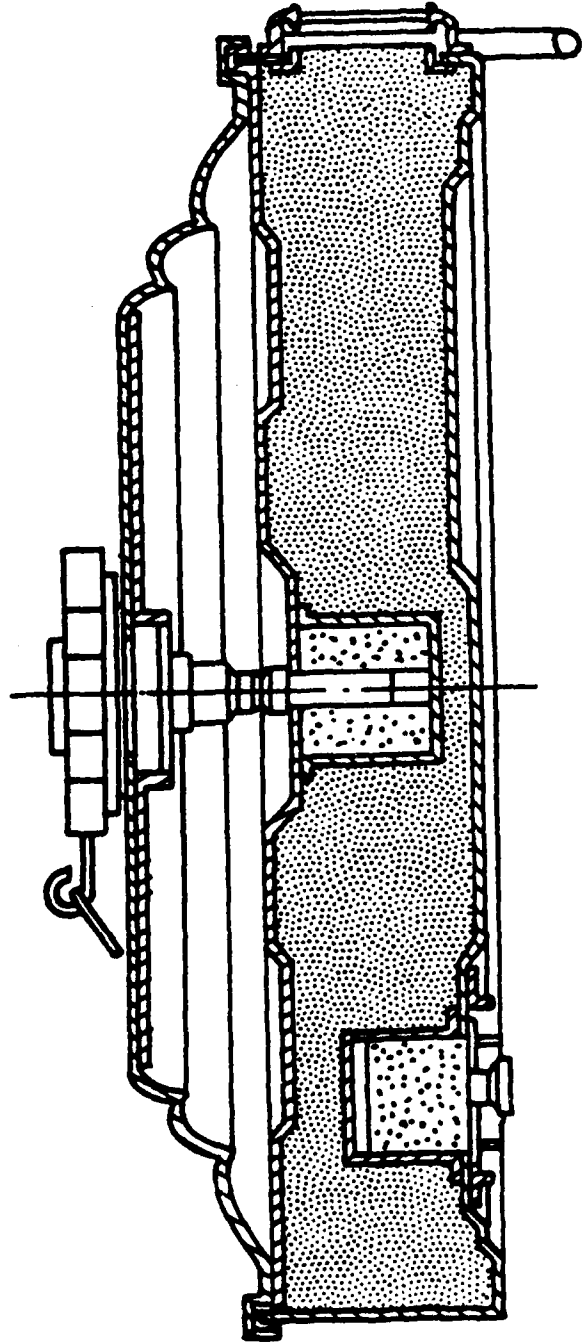


Figure 1. Soviet Anti-tank Mine Model TII-46

B. Guidelines for the Numerical Model. In keeping with the objective of identifying a general failure mechanism independent of some specific design feature, all fuzes and springs were omitted from the finite element model of the mine. This was done in accordance with the previously stated guideline of not identifying failure of the fuze components. The model considered for this study does not include secondary fuzes and filling holes. However the secondary tetryl booster charge is included to facilitate assessment of the influence of trapped air in the unfilled space below the top wall on structural response of the mine.

The auxillary fuze wells were not considered in the current investigation since they increase susceptibility of the mine to damage due to stress concentration near the junction between the body and the fuze. Thus, the simplified model is conservative in terms of blast load requirements for mine deactivation. Also, inclusion of these unsymmetrically loaded structures would require the use of a three-dimensional (3-D) finite element model resulting in significant increase in computing time and costs. The dimples at the base of the mine were eliminated for the same reasons. Because of these simplifications the 2-D axisymmetric model was cost-effective and conservative for dynamic response evaluation.

C. Base Support and Surface Loading. During field emplacement, the mines may be placed on the surface and covered with grass or other materials for concealment. In other cases, the mine may be shallow buried. In both cases, the mine will experience transient pressure loading on the top surface due to detonation of a countermine explosive in the vicinity. It is expected that typical field boundary support conditions would be bracketed by two extreme situations. In one case, the mine could be simulated as being buried in soil up to its top surface while the base is supported on nonlinear springs as described in Reference 1. The other support condition allows the mine to be supported on a rigid roller base which closely models the experimental conditions described in Reference 2. In the current study only the second support condition was simulated in the numerical model but inclusion of the soil medium implicitly through nonlinear spring node-tie boundary elements or explicitly through dynamic property characterization of the soil could be made without significant change in the basic model. A roller support condition was used allowing lateral, but no vertical, motion. In this rigid support condition, the input shock load is applied to the top and sides of the mine.

For structural loading the pressure pulse used in this paper simulated peak pressure and impulse measured from experiments conducted with mine clearance types of explosives in Reference 2. The peak pressure was 13.8 MPa and the impulse delivered was 6.5 kPa-sec. A decaying exponential function was fitted to these parameters resulting in the following equation

$$P(t) = 13.76e^{-2117t} \quad (1)$$

A curve of this function varying in time is shown in Figure 2.

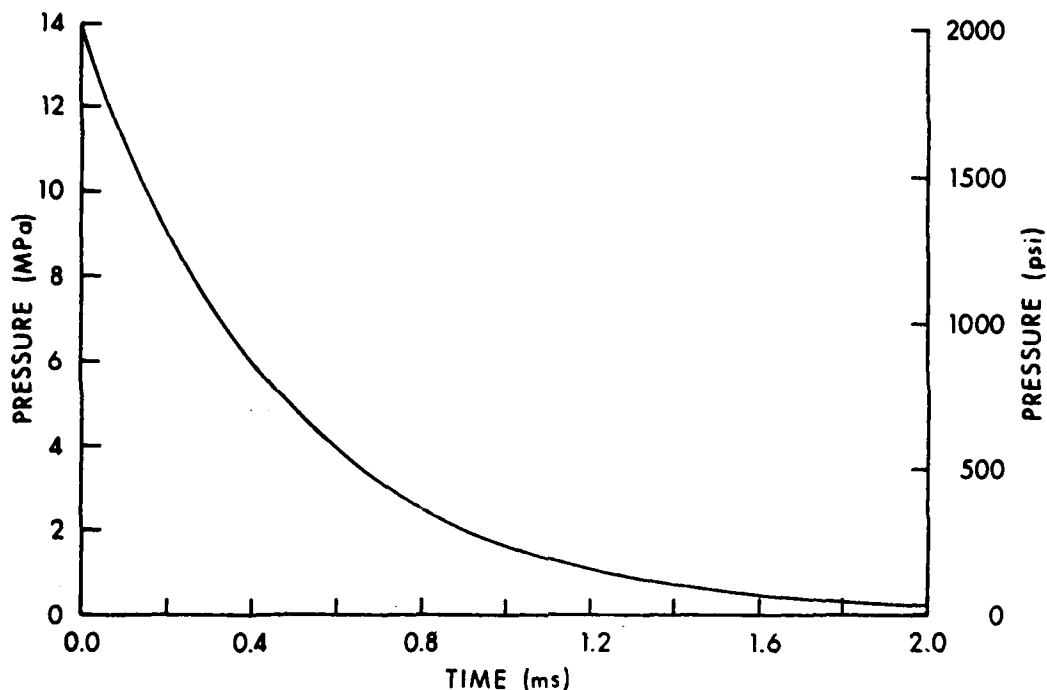
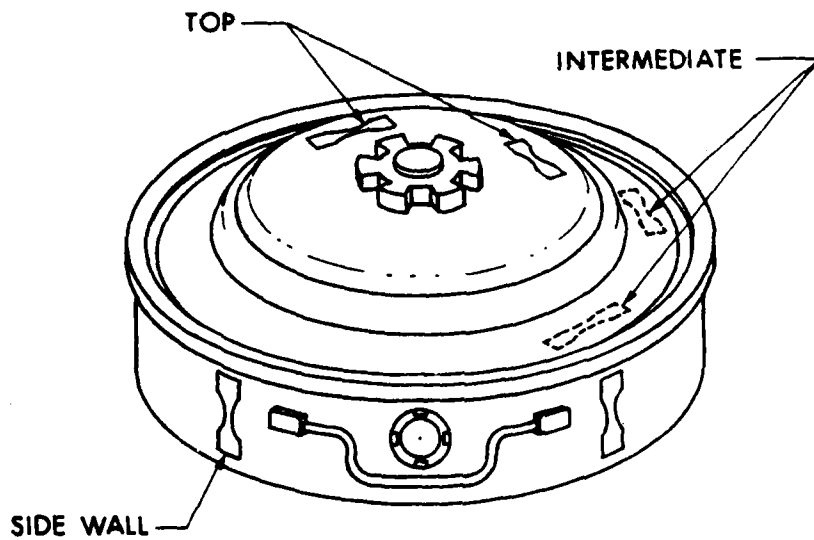


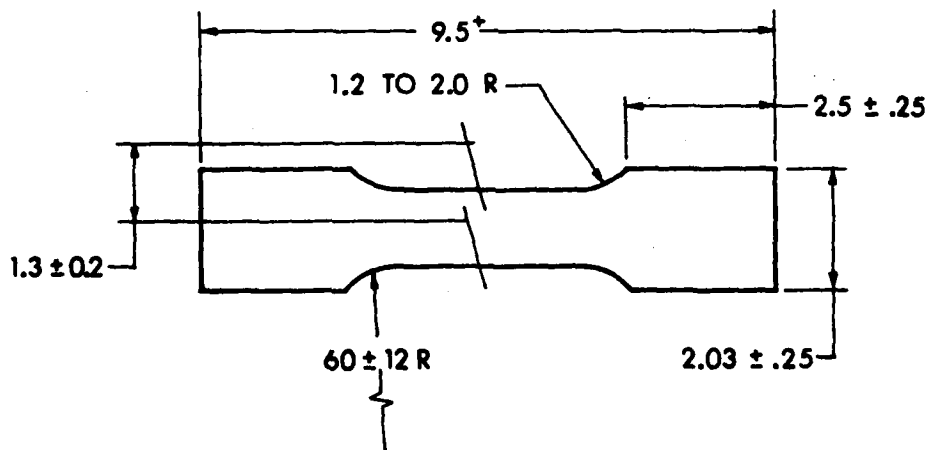
Figure 2. Shock Loading in Antitank Mines

**3. MATERIAL PROPERTIES CHARACTERIZATION AND FAILURE CRITERIA.** Material properties were required for the steel jackets, the explosive filler materials and the trapped air before numerical simulation could be carried out. Mechanical properties were measured for the steel jackets by employing uniaxial tensile tests. The high pressure equation of state data for explosives were obtained from available publications. Failure criteria used for the steel jackets and the filler materials were similar to the formulations in Reference 3.

**A. Steel Casing.** The TM-46 jacket is made of a low carbon soft magnetic steel equivalent to mild steel. The lower part of the casing was deep drawn, but it retained an equiaxed grain microstructure with isotropic properties. Two tensile specimens were cut from each of the significant surfaces of the mine body. Locations of these specimens are shown in Figure 3(a). The specimens were machined with a large radius on the test section as shown in Figure 3(b). An extensometer and a biaxial strain gage were attached at the location of the minimum width and the specimens were tested in an Instron Testing Machine at a relatively slow rate of strain. Typical quasi-static stress-strain curves for the Soviet mine body are shown in Figure 4. Evidence of work hardening and residual stress was significant in the casing material due to the forming operation and operating field conditions.



(a) LOCATION OF SPECIMENS, TM-46 MINE



(b) PREPARATION OF SPECIMEN DIMENSIONS (cm)

Figure 3. Details of Tensile Specimen Sampling and Preparation

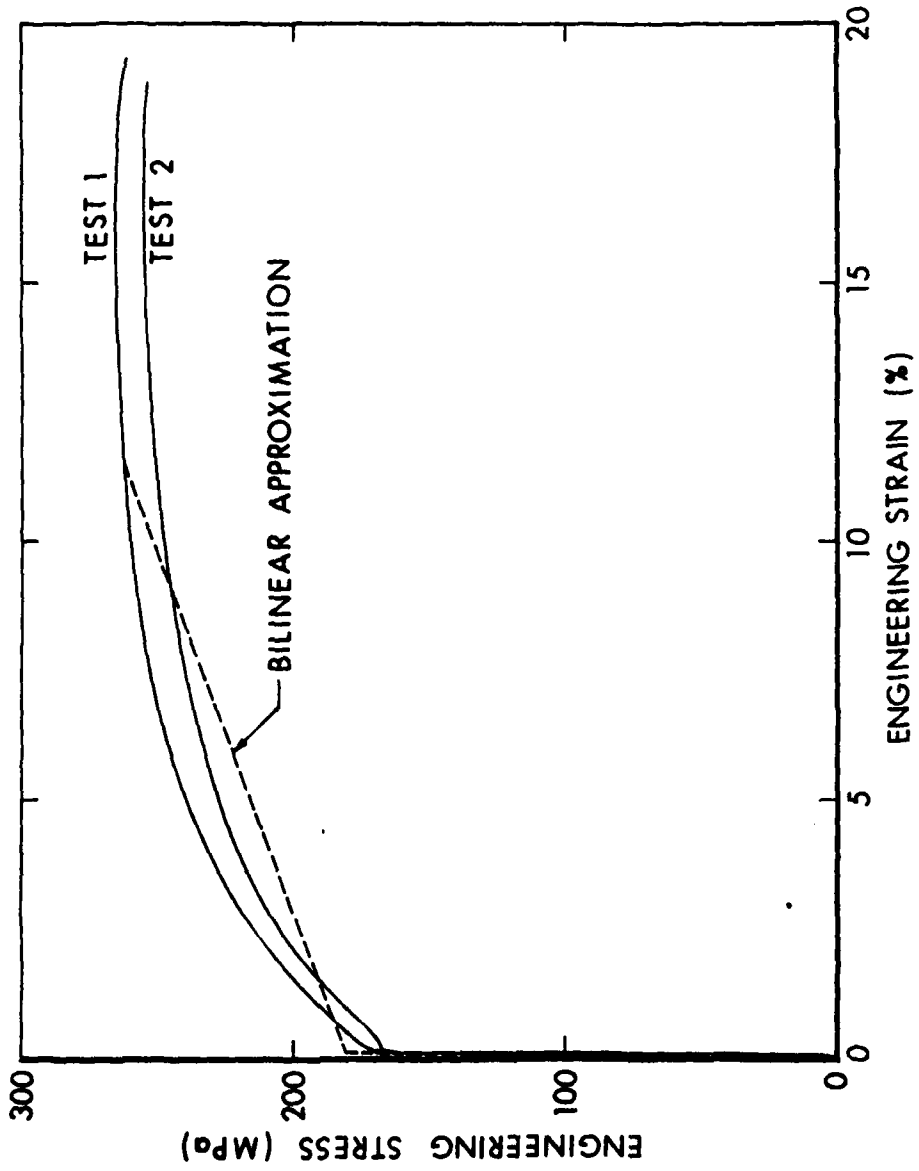


Figure 4. Stress-Strain Curves for the Top Cover Plate Specimens from the TM-46 Mine

Bilinear approximations to the stress-strain curves obtained by averaging the data for the individual specimens are shown superimposed in Figure 4. The ADINA (4, 5) finite element code used in this analysis has a bilinear, elastic-plastic, von Mises yield condition, kinematic hardening, axisymmetric 2-D element for the steel jacket.

The criterion selected to predict failure of the steel casing material was described in Reference 3 as the value of the second invariant of plastic deviatoric strain at failure,  $I_{2f} \epsilon^P$ , defined as

$$I_{2f}(\epsilon^P) = \frac{1}{2} \epsilon_{ij}^P \epsilon_{ij}^P \quad (2)$$

where  $\epsilon_{ij}^P$  are the plastic component of strains at failure. In the uniaxial tension test where the load is applied in the axial Z-direction we have,

$$I_{2f}(\epsilon_{1-D}^P) = \frac{3}{4} (\epsilon_{zz}^P)^2 \quad (3)$$

**B. Characterization of Explosive Fills.** There are two types of explosive filler materials employed in the TM-46 mine, i.e., TNT as the main charge and tetryl as the fuzewell booster charge.

After surveying the available material properties of explosives and the various 2-D axisymmetric materials models in the ADINA code, the curve description material model (Section XII, pp 17-22, Reference 4) was found to be the appropriate model to use. This model requires tables of loading and unloading bulk moduli and shear moduli versus volumetric strain.

A relationship between the volumetric strain and the bulk modulus obtained from the Mie-Grüneisen equation of state (Reference 1, 6) for shock propagation in solids is given as

$$P(\nu, E) = A\nu + B\nu^2 + C\nu^3 + \Gamma E/V \quad (4)$$

where A, B, and C are material constants determined experimentally from Hugoniot-pressure volume states obtained in shock transitions. The above equation characterizes the P, V, and E state variables which are attainable by the solid. In this case the solid is either TNT or tetryl explosive.

The adiabatic loading bulk modulus is defined by

$$\kappa_\ell = -V \left( \frac{\partial P}{\partial V} \right)_s \quad (5)$$

Assuming that the state of the system is defined by the variables s, E, and V, we have corresponding to the expressions  $P = P(V, E)$  and  $E = E(V, s)$ , respectively,

$$dP = \left(\frac{\partial P}{\partial V}\right)_E dV + \left(\frac{\partial P}{\partial E}\right)_V dE \quad (6)$$

$$dE = \left(\frac{\partial E}{\partial V}\right)_S dV + \left(\frac{\partial E}{\partial S}\right)_V ds \quad (7)$$

Substituting dE from (7) into (6), we find

$$dP = \left[ \left(\frac{\partial P}{\partial V}\right)_E + \left(\frac{\partial P}{\partial E}\right)_V \left(\frac{\partial E}{\partial V}\right)_S \right] dV + \left(\frac{\partial P}{\partial E}\right)_V \left(\frac{\partial E}{\partial S}\right)_S ds \quad (8)$$

But from  $P = P(V, s)$  we know that

$$dP = \left(\frac{\partial P}{\partial V}\right)_S dV + \left(\frac{\partial P}{\partial S}\right)_V ds \quad (9)$$

Comparing Equations (8) and (9), we have the following expression,

$$\left(\frac{\partial P}{\partial V}\right)_S = \left(\frac{\partial P}{\partial V}\right)_E + \left(\frac{\partial P}{\partial E}\right)_V \left(\frac{\partial E}{\partial V}\right)_S \quad (10)$$

Defining the pressure by the relation

$$P = - \left(\frac{\partial E}{\partial V}\right)_S \quad (11)$$

and substituting this in Equation (9), we have

$$\left(\frac{\partial P}{\partial V}\right)_S = \left(\frac{\partial P}{\partial V}\right)_E - P \left(\frac{\partial P}{\partial E}\right)_V \quad (12)$$

Performing the required differentiation of (4), and using,

$$\left(\frac{\partial P}{\partial V}\right)_E = \left(\frac{\partial P}{\partial \mu}\right)_E \frac{d\mu}{dV} \quad (13)$$

we obtain, after some manipulation

$$\kappa_\ell = P\Gamma + \Gamma E/V + (1 + \mu)(A + 2B\mu + 3C\mu^2) \quad (14)$$

Using  $P = P(E, V)$  from (4) the relationship between bulk modulus and volumetric strain is given as

$$\kappa_\ell = \Gamma(\Gamma + 1) E\rho + A + A'\mu + B'\mu^2 + C'\mu^3 \quad (15)$$

\*We define volumetric strain ratio,  $\mu = (V_0 - V)/V$  and  $V_0 = 1/\rho_0$ .

where

$$A' = A(\Gamma + 1) + 2B$$

$$B' = B(\Gamma + 2) + 3C$$

$$C' = C(\Gamma + 3)$$

In order to transform Equation (15) to a form  $\kappa = \kappa(V)$  the assumptions of unidimensional shock equations and conservation laws of mass, momentum and energy are invoked. The three conservation equations in a frame moving at the shock velocity,  $U_s$ , are:

$$\rho V = \rho_0 V_0 \quad (16)$$

$$P + \rho V^2 = P_0 + \rho_0 V_0^2 \quad (17)$$

$$\rho V E + \frac{1}{2}(\rho V)V^2 + PV = \rho_0 V_0 E_0 + \frac{1}{2}(\rho_0 V_0)V_0^2 + P_0 V_0 \quad (18)$$

where  $V$  and  $U$  are particles velocities,  $E$  is the specific internal energy and the quantities with zero subscript are undisturbed values while the quantities without subscripts are applicable behind the shock. In a stationary frame assuming  $U_0 = 0$ , the following relations between frames of references could be used

$$V = U - U_s \quad \text{and} \quad V_0 = -U_s \quad (19)$$

Substituting above in (16), (17) and (18) the corresponding stationary conservation equations reduce to

$$\rho_0 U_s = \rho(U_s - U) \quad (20)$$

$$P - P_0 = \rho_0 U_s U \quad (21)$$

$$E - E_0 = \frac{(P + P_0)(\rho - \rho_0)}{2\rho\rho_0} = \frac{1}{2}(P + P_0)(V_0 - V) \quad (22)$$

Assuming  $P_0 = E_0 = 0$ , and substituting  $E$  from above into (4), we obtain:

$$P = (A\mu + B\mu^2 + C\mu^3)/(1 - \mu\Gamma/2) \quad (23)$$

Similarly, substituting  $E$  from (22) into (15):

$$\kappa_E = \rho P \Gamma (\Gamma + 1) (V_0 - V) / 2 + A + A'\mu + B'\mu^2 + C'\mu^3 \quad (24)$$

Finally, substituting P from (23) into (24) the final form is obtained as

$$\kappa_{\ell} = \frac{\Gamma(\Gamma + 1)(A\mu^2 + B\mu^3 + C\mu^4)}{2 - \mu\Gamma} + A + A'\mu + B'\mu^2 + C'\mu^3 \quad (25)$$

where

$\kappa_{\ell}$  = the loading bulk modulus

$\Gamma$  = the Grüneisen coefficient

$A' = A(\Gamma + 1) + 2B$

$B' = B(\Gamma + 2) + 3C$

$C' = C(\Gamma + 3)$

$\mu = \epsilon_V / (1 - \epsilon_V)$

$\epsilon_V = (V_0 - V)/V_0$ , volume strain taken positive in compression

$V_0 = 1/\rho_0$  = specific volume at normal conditions.

For the particular case when  $\epsilon_V = 0$  which implies  $\mu = 0$  and  $V = V_0$  it can be easily seen from Equation (25) that  $\kappa_0 = A$ . Also in the Grüneisen equation of state, at  $\epsilon_V = 0$ , we take both the pressure and internal energy to be zero. The values for the material constants of the explosives used are shown in Table 1.

TABLE 1. MATERIAL CONSTANTS FOR EXPLOSIVES AND SOIL

Type	$\rho_0$ (g/cm <sup>3</sup> )	$\Gamma$	A (Gpa)	B (Gpa)	C (Gpa)	$\nu$
TNT	1.614	.737	10.367	9.101	138.33	.3
TETRYL	1.70	1.6	10.498	17.8	20.6	.3
WET TUFF	2.0	1.5	21.77	32.5	18.33	—

Since data to relate the unloading bulk modulus to the volumetric strain were unavailable, the bulk moduli for unloading were assumed to be identical to the moduli for loading for all explosives. The loading shear modulus,  $G_{\ell}$ , was obtained from the loading bulk modulus,  $\kappa_{\ell}$ , by use of the relationship,

$$G_{\ell} = \frac{3\kappa_{\ell}(1 - 2\nu)}{2(1 + \nu)} \quad (26)$$

\*Here we define specific volume,  $V = 1/\rho$  or  $\rho V = 1$ .

Figures 5, 6 show the dependence of bulk and shear moduli of the two explosives represented by Equations (25) and (26) on volumetric strain. Table 2 gives the values of the two moduli as they were used in the ADINA program. ADINA uses linear interpolation between discrete points.

The tensile volumetric strain at failure of -0.1 per cent as given in Reference 7 was used in calculations for all explosives in this investigation. The method of application of this failure criterion in the ADINA code is through the technique of superimposing on the load-induced strains, a localized gravitational pressure sufficient to cause a hydrostatic compression equal in magnitude to the tensile failure. When the total strain becomes tensile or negative (as per convention used in the material model in the code), a tension cut-off plane is assumed to form normal to the principal strain direction. The normal and shear stiffnesses across this plane are reduced by a factor determined by an input value. One or two additional planes orthogonal to existing cut-off plane (s) are allowed to form if the strain criterion is met. The planes become inactive if compression again develops in the normal direction to the planes.

The pseudo-hydrostatic prestrain is applied by positioning the vertical Z-coordinate at an appropriate negative value. The hydrostatic pressure applied at an element integration point is given for an element, j, by

$$P_j = -\rho_e g \sum_{i=1}^N h_{ij} Z_{ij} \quad (27)$$

where

- g is the acceleration due to gravity.
- $\rho_e$  is the density of the overburden.
- $h_{ij}$  is the shape function for node i of element j.
- $Z_{ij}$  is the vertical coordinate for node i in element j.
- N is the total number of nodes in the element.

The depth of the overburden in terms of the system vertical coordinate position can be obtained from the equation,

$$Z_{ave} = \frac{\kappa_0 \epsilon^f v}{g \rho_e} \quad (28)$$

where

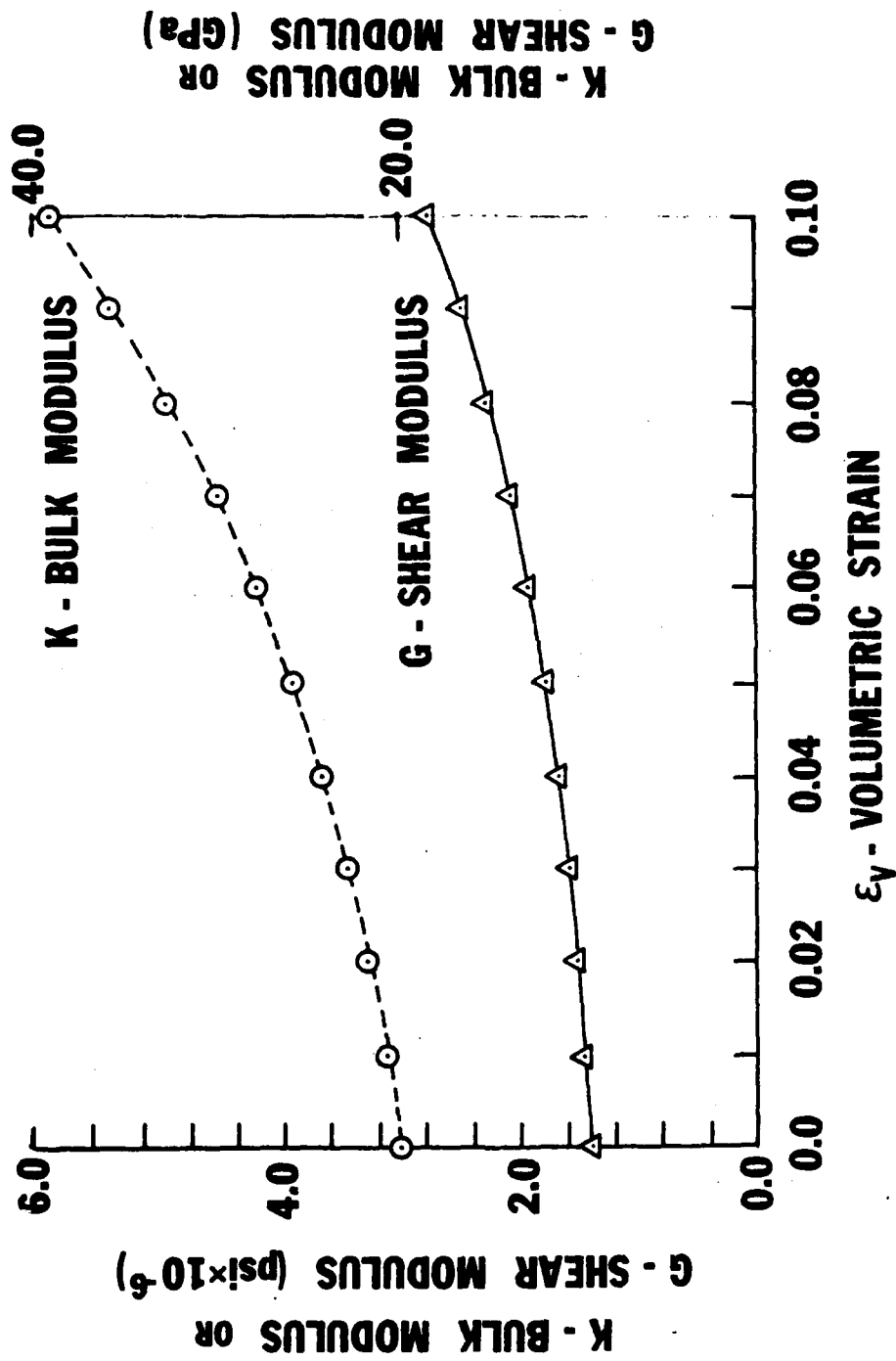


Figure 5. Bulk and Shear Moduli vs Volume Strain for TNT Explosive Used in the TM-46 Mine.

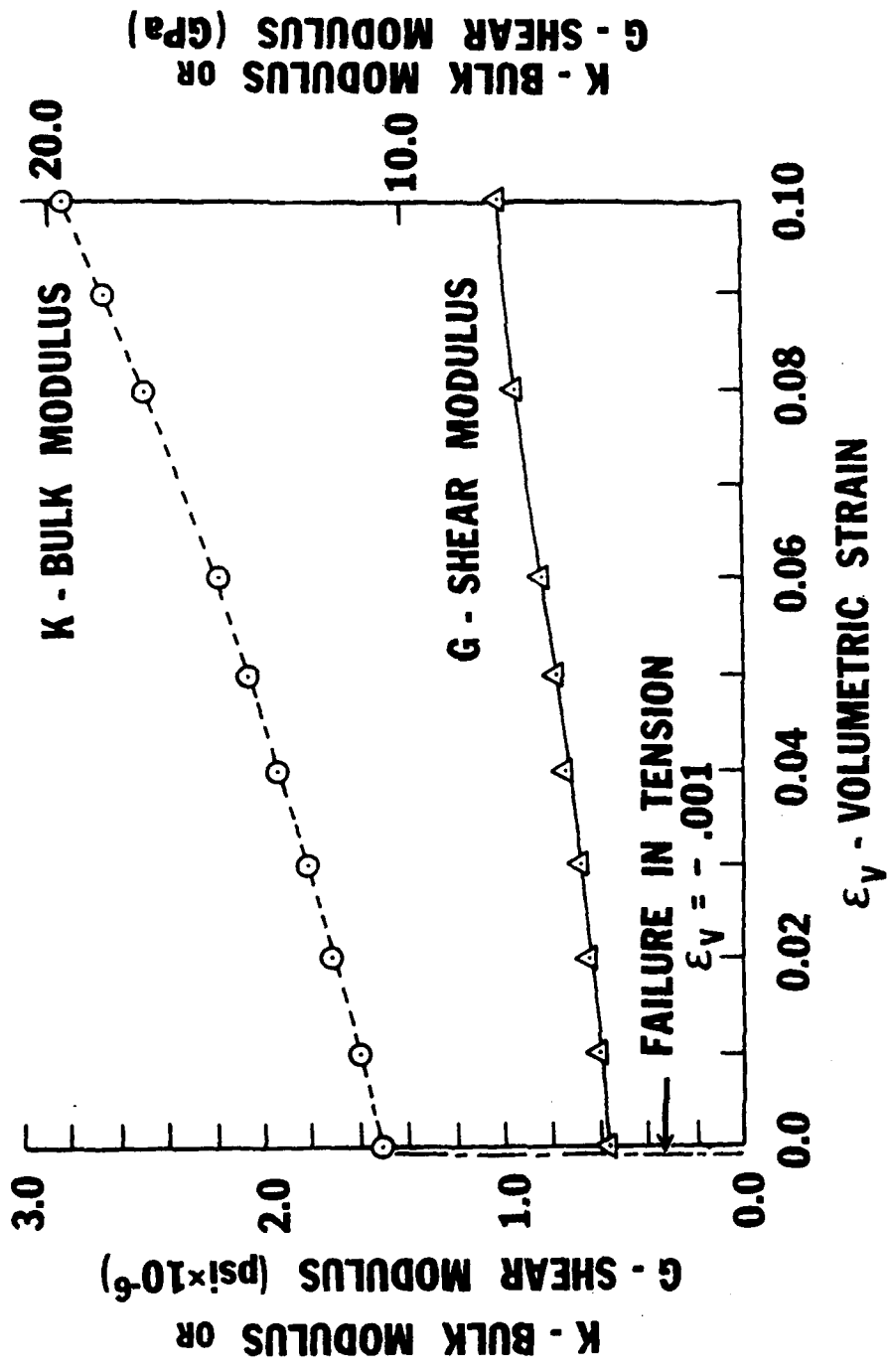


Figure 6. Bulk and Shear Moduli vs Volume Strain for Tetryl Fuze Well Charge of the TM-46 Mine

TABLE 2. ADINA INPUT VALUES FOR BULK AND SHEAR MODULI FOR FILLER MATERIALS

<u>TNT EXPLOSIVE</u>				
Point No.	$\epsilon_V$ (%)	$\kappa_\ell$ (GPa)	$\kappa_U$ (GPa)	$G_\ell$ (GPa)
1	0	21.72	21.72	10.62
2	1.0	23.03	23.03	11.24
3	3.0	25.65	25.65	12.55
4	5.0	28.68	28.68	14.01
5	9.0	35.85	35.85	17.51
6	11.0	40.20	40.20	19.65
<u>TETRYL FILLER</u>				
1	0	10.5	10.5	4.03
2	1.0	11.15	11.15	4.27
3	3.0	12.59	12.59	4.83
4	5.0	14.24	14.24	5.46
5	8.0	17.2	17.2	6.60
6	10.0	19.56	19.56	7.50
<u>WET TUFF</u>				
1	0	10.37	10.37	4.79
2	1.0	10.78	10.78	4.98
3	3.0	11.93	11.93	5.505
4	6.0	14.62	14.62	6.75
5	8.0	17.24	17.24	7.96
6	10.0	20.64	20.64	9.51

$\kappa_0$  is the initial bulk loading modulus,

$\epsilon_V^f$  is the volumetric failure strain, negative in tension, and

$Z_{ave}$  is the negative of the distance from the ground surface to the mid-plane of the mine.

C. Soil Simulation. For the structural response calculations of the shallow buried mine, only the top of the mine was exposed to blast pressure while the remainder was assumed to be embedded in soil. In the M-15 mine in Reference 1 an implicit modeling technique was employed whereby nodal tie elements were used to model the base support.

However for the TM-46 mine it is proposed to use an explicit modeling technique whereby initially two compressible layers of soil surrounding the mine body could be included through finite element discretization. Although separation of the mine from the soil medium subsequent to the initial response and sliding phenomenon could not be accounted for, the technique would be a considerable improvement over previous methods due to realistic simulation of the response which includes blast attenuation effects. No simulation of the soil was necessary for the rigid support calculations.

Due to the large variety of soils in which mines would be emplaced, it is possible only to select a soil simulation model which would be representative of some subclass of soils. Thus, a typical shock Hugoniot curve for wet tuff from Reference 8, 9 was selected to define the soil element properties. The data were reduced to a high pressure equation of state and subsequently to a dependent formulation of the bulk moduli on volumetric strain in order to be compatible with the requirements for the tension cut-off curve description model in the ADINA code. For a fully buried mine the soil modeling could be extended in the region above the top of the mine casing and only the top layer of the soil medium could be pressurized by the blast load. The detailed ADINA input values for the soil are shown in Table 2.

D. Simulation of Void in TM-46 Mine. The TM-46 mine has a cavity between the top pressure plate and the middle plate covering the primary charge. This cavity is filled with air which transfers some load to the middle plate as the volume of the cavity is decreased sufficiently. Further uncrimping of the crimped joint connecting the side, top and intermediate walls, due to air compression and angular deflection of the casing near the joint could conceivably occur resulting in loss of some primary explosive charge and consequent deactivation of the mine. Although it is difficult to predict uncrimping using the finite element method, the code could be used profitably to yield moments generated and angular deflection of the casing at critical sections. A separate analysis based on classical theory could then be applied to predict occurrence of uncrimping.

The airgap inside the mine cavity was represented in the finite element model as a set of 2-D axisymmetric fluid elements composed of an inviscid linear compressible material. A constant bulk modulus was used in lieu of a

pressure dependent bulk modulus due to a lack of available data for air. However, the primary difficulty with this model was that there was nothing in the model to prevent the upper plate from penetrating the middle plate as the deformation progressed.

Since the air was judged to apply only a minimal restraint on the motion of the upper plate and due to the need to prevent the two plates passing through one another, a different model has been adopted to simulate contact and avoid interpenetration.

E. Simulation of Contact in TM-46 Mine. Due to lack of contact elements in the code along the interface between the top and intermediate plates substantial interpenetration occurs without any transfer of loading. As a result a major part of deformation is confined to the upper plate, particularly in the stair-cased region, which is clearly unrealistic.

Pending modification of the code to include contact capability, other alternatives were considered to overcome the problem without significantly altering the response behavior in an unrealistic manner. A few alternatives were eliminated due, either to a lack of initial stress input capability, or inability to vary the contact element stiffness as a step function with axial compression at or near the time of contact to prevent overflow at the interface. The model finally selected consists of fictitious axial truss elements connecting the two circular plates. The material model for the trusses is nonlinear and develops only a small force up until the axial strain in trusses approaches -1. At this strain, a large stiffness is specified to simulate contact between the two plates. Constraints are applied to the upper end of the trusses to insure that its radial coordinate is the same as the radial coordinate at the lower end. Also, the axial coordinate of upper end is constrained to translate with the upper plate. These constraints are necessary to prevent element rotation. The model allows movement only in the axial direction and relaxation upon initial contact but it excludes sliding surface capability which could conceivably be introduced through transverse or radial trusses but would make the model unnecessarily complicated. However, for initial simulation only areas with high probability of contact have been considered for contact simulation.

#### 4. FINITE ELEMENT MODEL DESCRIPTION AND CALCULATIONS.

A. Mesh Generation. The finite element mesh for the mine was generated with the aid of the GEN3D mesh generator program. The mine was modeled as an assembly of axisymmetric 2-D structures using the ADINA finite element code. A six node QUAD element with quadratic displacement interpolation functions in the direction parallel to the surface was used for the steel casing. This type of element models the bending of the thin metal casing better than a four node QUAD. The explosive components were modeled with four-node QUAD elements except where they interfaced the steel jacket, in which case a mid-side node was included on the interface edge.  $2 \times 2$  Gaussian integration points were used at each element for computational purpose. A total of 304 nodes and 157 elements were used to represent the axisymmetric model.

In ADINA, each material having a distinct material formulation must be modeled as a separate element group. In general four major groups of elements were represented: (1) nonlinear 2-D elements for the steel case, (2) nonlinear curve description 2-D elements for the primary charge, (3) nonlinear 2-D elements for the fuzewell booster charge, and (4) nonlinear truss elements. For the steel case, four material subtypes were used to model the steel properties in different regions of the inhomogeneous mine body. The material model for the casing was a bilinear, von Mises yield condition, kinematic hardening, 2-D axisymmetric element model.

B. Time Step Solution. In ADINA, one has the choice of marching the dynamic solution forward in time via explicit or implicit finite-difference techniques. The implicit schemes are unconditionally stable and can tolerate larger time step size resulting in reduction of computational times. However, equilibrium iteration and stiffness reformation at regular intervals are necessary to obtain meaningful results. In general, it is difficult to make absolute statements as to which is best for a given application. For highly transient shock loads such as shown in Figure 2, it has been our experience that the explicit method gives the higher quality solution for a given amount of central processor computer time. The subject problem was run for a relatively large number of cycles using both explicit and implicit (with equilibrium iterations included) time integration solutions. After a selected amount of problem solution time, the results were compared for solution quality. The explicit solution appeared to have a smoother variation in both displacements and stresses. For this reason, we selected the explicit solution method.

The time step used for the calculations was determined from the Courant stability condition

$$\Delta t = \frac{\Delta t_{\text{crit}}}{n} = \frac{\Delta L_{\text{min}}}{n \sqrt{E_{\text{max}}/\rho}}$$

where

$\Delta t_{\text{crit}}$  is the minimum Courant stability step size.

$\Delta L_{\text{min}}$  is the distance between the two closest nodes in the system.

$E_{\text{max}}$  is the Young's modulus for the stiffest material.

$\rho$  is the density of the material,

and  $n$  is the number of time steps which we wish to represent the shock wave in passing through the distance  $\Delta L$ .

The value of  $\Delta t_{\text{crit}}$  was approximately 200 nanoseconds and a value of  $n$  of four was used, so that the time step for the central difference explicit time integration method was 50 nanoseconds.

C. TM-46 Mine Calculations. The ADINA calculations for the TM-46 mine are in progress. However, some of the salient features of the model have been developed from progress made in studies of the mine thus far. A drawing of the current mesh configuration is shown in Figure 7.

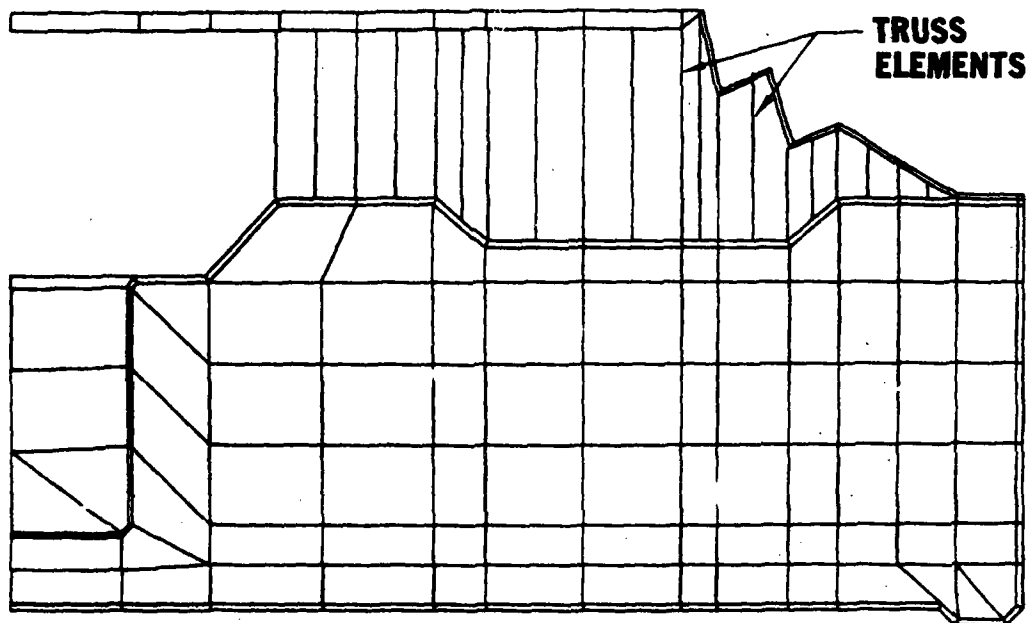


Figure 7. Finite Element Mesh for the TM-46 Mine

Since experimental data indicated significantly varying material properties in different regions of the outer steel jacket of the TM-46 mine several different sets of materials properties were used to model the various steel components of the mine.

At the outset two particular difficulties were expected to be encountered in modeling the TM-46 mine. First, the difference in stiffness between the steel plates and the air filled region leads to numerical problems. The collapse of the air filled region leads to the impact of the upper plate on the middle plate. This phenomenon needs to be modeled rather carefully. Secondly, the thin stepped region of the top cover shown in the upper right part of Figure 7 leads to a very inefficient mechanism for load transfer from the top cover to the main mine body. On the other hand, failure of the top cover may not indicate deactivation of the mine and a viable failure mechanism must inevitably involve a failure of the main mine body.

Since the ADINA code does not currently have a contact element to sense when the top cover plate impacts the intermediate plate, an approach described in Section 3E involving nonlinear truss elements has been used to approximate the interaction of the two plates.

Eigenfrequencies and mode shapes were also obtained for the TM-46 mine in order to ascertain if the model has been formulated correctly and also as an aid in estimating an appropriate time step for the explicit integration scheme. The eigenfrequencies and associated periods for the lower modes are given in Table 3.

TABLE 3. EIGENFREQUENCIES AND PERIODS FOR THE TM-46 MINE

Frequency (cps)	Period (sec)
3041	$3.288 \times 10^{-4}$
10466	$9.555 \times 10^{-5}$
17068	$5.859 \times 10^{-5}$
31071	$3.218 \times 10^{-5}$

All calculations described herein used the total Lagrangian formulation with a lumped mass matrix with the exception of the nodal tie and truss elements. The formulations used for these were material nonlinearity only and updated Lagrangian analysis procedure, respectively.

**5. DYNAMIC RESPONSE PREDICTIONS.** Several modifications to the ADINA program were made to assist us in interpreting the response predictions. These are described fully in Reference 1. Due to the very large amount of data available from the ADINA results, search routines were incorporated to identify the extreme (maximum/minimum) stresses and strains in the steel components. Additionally for stresses in the plastic regime a quadratic correction was applied to bring the stress tensor back to the von Mises yield surface and allow calculations to proceed without premature interruptions. The details of these modifications are also described in Reference 10.

From the complex structural construction of the mine, particularly near the stair-cased region in the top plate which appeared to be susceptible to blast induced damage and failure, it was decided to model this region very accurately using shadowgraph measurements. The elements and nodes in the top plate were configured to line up in the axial direction with those in the intermediate plate to facilitate inclusion of contact elements and minimize element rotation.

The initial calculations for the mine on a rigid base support were run without the contact elements to approximately 4000 cycles corresponding to an elapsed time of 0.2 milliseconds. The purpose of the initial runs were to determine the regions and the time of initial contact between the two plates. The results indicated occurrence of initial contact at .06 milliseconds near the crimped region of the mine body and the stair cased region of the top cover.

Failures were predicted in several elements in the stepped regions accompanied by considerable plastic flow. Stresses were significantly high particularly near sharp corners due to acute stress concentration effects. A major part of the response was evident in the top plate while the rest of the mine body did not exhibit any appreciable deformation. The deformation of the mine confined mainly in the area of the top cover plate may not be very realistic since the mine supported on a rigid roller base has unrestrained sidewalls where appreciable deformation is expected but unrealized due to inefficient load transfer mechanism between the top and intermediate walls. One of the chief difficulties encountered has been in trying to provide the appropriate model for the interaction of the top cover plate on the middle plate. We have used the improvisation of nonlinear truss elements (see Figure 7) to simulate the impact of these two components. Since a sudden stiffening of the trusses near the time of contact generated spurious transients and was insufficient to arrest penetration of the intermediate plate due to inertia effects, earlier stiffening of the trusses in a gradual manner initially and at an accelerated rate subsequently as shown in Figure 8 was resorted to. The trusses developed significantly high stresses and internal forces in the region where contact first occurred. Subsequently upon impact the separation of plates caused the stresses in the affected trusses to be released while the next set of trusses in the neighboring region approached impact conditions and developed high stresses which were then released as plates separated and the traveling wave propagated radially inward until the initial contact process was completed. Although the response of the trusses appeared to be realistic, some overflow occurred in the corner region and further stiffening was deemed to be necessary to prevent interpenetration and obtain meaningful results.

A typical response of the system at an early time is shown in Figure 9. In this figure the dotted lines represent the undeformed or original configuration before imposition of the blast load. The vertical lines between the top cover plate and the middle plate represent the nonlinear truss elements. Currently, the calculation has not proceeded to the point where any failure of the main mine body can occur. However, failure of some casing elements in the stepped region has been observed at several time periods beginning at .02 ms and continuing beyond .1 ms when formation of a zone of rupture was indicated in the top cover. However, the main mine body did not show any evidence of failure due to the inefficient load transfer mechanism between the top and intermediate plates. The model of this mine is still evolving and is undergoing modifications to improve accuracy and reliability of prediction.

**6. CONCLUSIONS.** The soviet TM-46 mine because of its complex stair-cased, double-walled construction was somewhat difficult to model accurately, to analyse and to deactivate. Failure of a particular region of the mine casing itself might not be sufficient to indicate overall failure of the mine. A conservative approach was therefore taken to model the mine by eliminating nonessential details and by requiring defeat of the main mine body through case rupture.

The explicit time integration method appeared to be advantageous for the shock loaded mines due to smoothness of stresses and strains as a function of time. However, second order corrections were necessary to assure that the stress state remained on the yield surface during plastic flow.

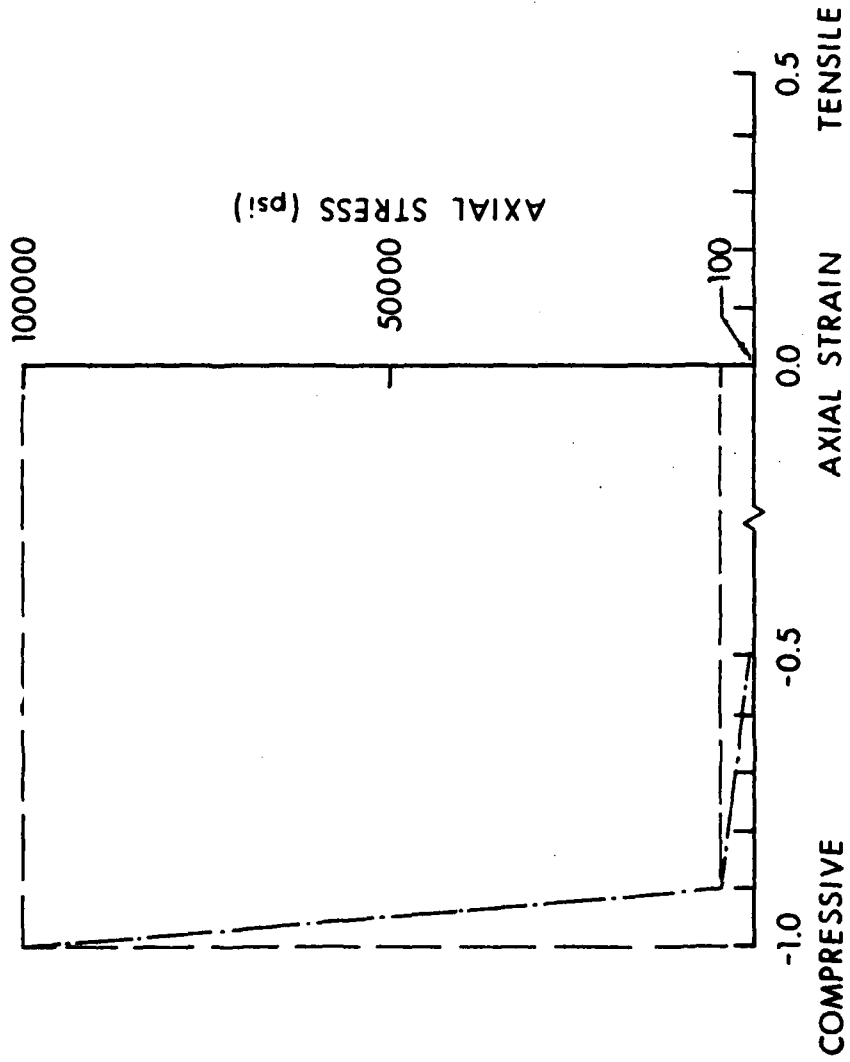


Figure 8. Input Values for Stiffness Variation of Truss Elements Used in the ADINA Code

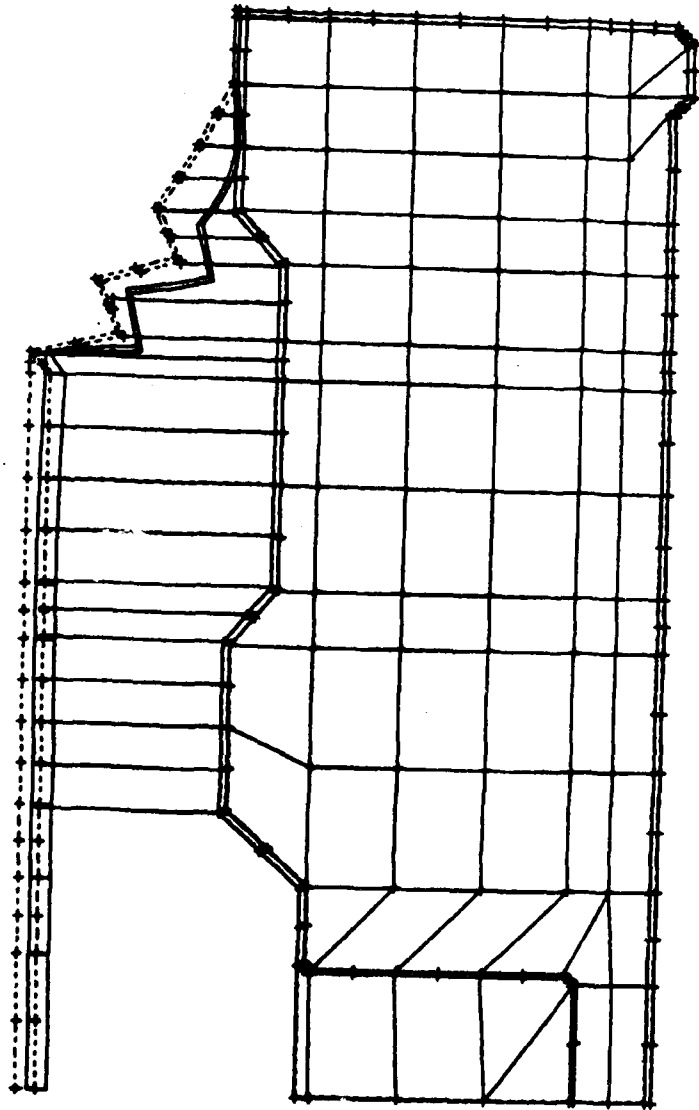


Figure 9. Deformed Shape of the TM-46 Mine on Rigid Support at 75 Microseconds

The parts of the outer steel jacket of the TM-46 mine which are work hardened in the deep drawing metal forming operation have significantly varying materials properties. These variations in stress-strain relations must be measured and modeled carefully since they directly affect mine failure under blast loads.

The contact problem arising from interpenetration of plates results in inefficient load transfer mechanism between the cover and the intermediate plate. Truss contact elements may be used profitably to overcome this shortcoming provided nodal constraints are used to avoid truss rotations.

Linear fluid elements can be used successfully to represent interaction of air in voids with structural response. However, in TM-46 mine it's effect on frequencies and mode shapes is very minimal.

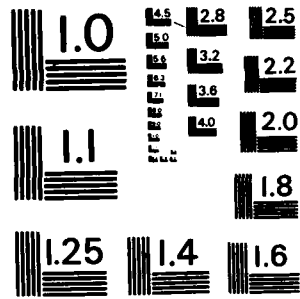
The initial deformation of the TM-46 mine was limited to the response of the top cover plate. The finite element modeling with the ADINA program has presented some difficulty in describing accurately the impact of the top plate on the intermediate plate which contains the primary TNT charge. From past experience main body failure is expected to occur at later times near the corners of the fuze well due to a change of thickness and a sharp radius resulting in significantly high stress concentration and case rupture. This study is still in progress.

ACKNOWLEDGEMENTS. This investigation was a part of a project on mine neutralization research sponsored by the Countermine Laboratory, MERADCOM, Fort Belvoir, VA. Valuable assistance of Messrs Frederick H. Gregory, Charles N. Kingery, Dr. Joseph M. Santiago (BRL) and Dr. John Crawford (Aerospace Corporation) is gratefully acknowledged. Finally, I wish to thank Messrs Robert Franz and Dominic Diberardo for their expert work in measuring the stress-strain properties of the TM-46 mine casing.

#### REFERENCES.

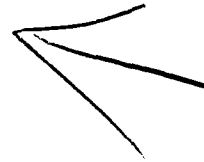
1. Frederick H. Gregory, "Failure of the M-15 Antitank Mine Due to Blast Loads", BRL Report No. ARBRL-TR-02420, Sep. 1982.
2. Allen J. Tulis et al (IIT Research Institute) and David C. Heberlein et al (MERADCOM), "Improved Fuel Air Explosives", (U) U.S. Army Mobility and Equipment R&D Command Report 2222, Sep. 1977 (S).
3. Frederick H. Gregory, "Finite Element Modeling of the Vulnerability of an M-15 Land Mine Using an Explicit Integration Scheme", Proceedings of the 1981 Army Numerical Analysis and Computers Conference, ARO Report 81-3, Aug. 1981
4. "ADINA, A Finite Element Program for Automatic Dynamic Incremental Nonlinear Analysis", ADINA Engineering, Inc., Watertown, MA, Report AE 81-1, Sep. 1981.
5. K. J. Bathe, "Static and Dynamic Geometric and Material Nonlinear Analysis Using ADINA", MIT-82448-2, May 1977.



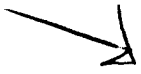


MICROCOPY RESOLUTION TEST CHART  
NATIONAL BUREAU OF STANDARDS-1963-A

6. Brigitta M. Dobratz, "Properties of Chemical Explosives and Explosive Simulants", UCRL-51319 (Rev 1), July 1974.
7. M. S. Chawla and R. B. Frey, "A Numerical Study of Projectile Impact on Explosives", BRL-MR-2741, Apr. 1977.
8. W. E. Johnson and L. R. Hill, "Energy Partitioning During Hypervelocity Impact on Rocks", Rep. No. SC-R-70-4402, Sandia Laboratories, Albuquerque, New Mexico, Dec. 1970.
9. C. A. Hogentogler, Engineering Properties of Soil, First Edition, McGraw-Hill Book Co., 1937, p. 223.
10. Joseph M. Santiago, "On the Accuracy of Flow Rule Approximations Used in Structural and Solid Response Computer Programs", Proceedings of the 1981 Army Numerical Analysis and Computers Conference, Huntsville, Alabama, 26-27 Feb. 1981.



AD P001036



FORMATION OF SINGULARITIES FOR A CONSERVATION LAW WITH MEMORY

Reza Malek-Madani<sup>1</sup>  
 Department of Mathematics  
 Virginia Polytechnic Institute and State University  
 Blacksburg, VA 24061

and

John A. Nohel<sup>2</sup>  
 Mathematics Research Center  
 University of Wisconsin-Madison  
 Madison, WI 53706

**ABSTRACT.** The formation of singularities in smooth solutions of the model Cauchy problem

$$u_t + \phi(u)_x + a' * \psi(u)_x = 0, \quad x \in \mathbb{R}, \quad t \in [0, \infty) \quad (*)$$

$$u(x, 0) = u_0(x)$$

is studied. In (\*)  $\phi, \psi : \mathbb{R} \rightarrow \mathbb{R}$  are given smooth constitutive functions,  $a : \mathbb{R}^+ \rightarrow \mathbb{R}$  is a given memory kernel, subscripts denote partial derivatives,  $' = d/dt$  and  $*$  denotes the convolution on  $[0, t]$ . Under physically reasonable assumptions concerning the functions  $\phi, \psi$  and  $a$  it is shown that a smooth solution  $u$  develops a singularity in finite time, whenever the smooth data  $u_0$  become "sufficiently large" in a precise sense<sup>3</sup>.

**I. INTRODUCTION.** In this paper <sup>the authors</sup> we study the formation of singularities for ~~the~~ initial value problem.

$$u_t + \phi(u)_x + a' * \psi(u)_x = 0$$

$$u(x, 0) = u_0(x), \quad x \in (\mathbb{R}), \quad t \in [0, \infty) \quad (1.1)$$

where  $\phi, \psi : \mathbb{R} \rightarrow \mathbb{R}$  are given smooth constitutive functions,  $a : \mathbb{R}^+ \rightarrow \mathbb{R}$  is a given kernel, subscripts denote partial derivative,  $' = d/dt$ , and where  $*$  denotes the usual convolution operator

$$(f * g)(t) = \int_0^t f(t - \tau)g(\tau)d\tau.$$

The motivation for studying equation (1.1) is provided by the more complex problem of the motion of a one-dimensional homogeneous viscoelastic body governed by the equation

<sup>1</sup>Partially supported by the Mathematics Research Center.  
<sup>1,2</sup>Sponsored by the United States Army under Contract No. DAAG29-80-C-0041.  
<sup>3</sup>See the note labeled SIGNIFICANCE AND EXPLANATION directly following this article.

REMOVED FROM BLACK-AND-WHITE

$$u_{tt} - \sigma_x = 0, \quad (1.2)$$

together with appropriate initial and homogeneous boundary conditions; in (1.2) the stress  $\sigma$  is related to the strain  $u_x$  by the constitutive relation

$$\sigma(u_x) = \phi(u_x) + \int_0^t a'(t - \tau) \psi(u_x(x, \tau)) d\tau \quad (1.3)$$

Under appropriate physical assumptions concerning  $\phi, \psi$  and  $a$ , the "memory" term in (1.3) generally induces a weak dissipation mechanism into the structure of the solutions of (1.2). It has been shown (cf. Dafermos and Nohel [1]) that under proper assumptions on  $a, \phi, \psi$  and on the initial data  $u_0$  and  $u_1$ , the initial-boundary value problem (1.2) has a unique global  $C^2$  solution if the initial data are sufficiently "small" in an appropriate sense. A similar result is shown to hold for (1.1) (cf. Nohel [2]). These two results are of special interest since when  $a'(t) \equiv 0$ , (1.1) reduces to the Burgers equation, while (1.2), (1.3) reduce to the quasilinear wave equation  $u_{tt} = \phi(u_x)$ , and it is well known (cf. Lax [3]) that under proper convexity assumptions on  $\phi$  and on the initial data there are smooth solutions of (1.1) and (1.2) which develop a singularity in finite time, no matter how smooth and small one chooses the initial data. Thus,  $a'(t) \not\equiv 0$  induces a dissipation mechanism which prohibits the breaking of waves when the initial amplitude of these waves is small.

This paper considers the natural question of how large one must choose the initial data in order that the shock forming structure of (1.1) overcomes this dissipation. Analytically, equation (1.1) has a simpler structure than (1.2) due to the fact that (1.1) has only one family of "genuinely nonlinear" characteristics due to the convolution term. We are then able to study the variation of the solution of (1.1) along the characteristics with the aid of Riemann invariants. A similar approach (under active study) appears promising for the more complicated higher order problem (1.2); this equation has three families of characteristics and thus, in general, does not have Riemann invariants. With the introduction of the generalized Riemann invariants (cf. John [4]) there is reason to expect that much of the analysis outlined in this paper will be applicable to (1.2). Some experimental evidence for the breakdown of smooth solutions of model equations governing viscoelastic materials can be found in the work of Tordella [5]. In addition some results in the loss of regularity of solutions in the equations for viscoelastic fluids for sufficiently large data have been obtained by Slemrod [6] and for dissipative hyperbolic problems by Hattori [7]; these are special cases of (1.2), (1.3) when  $\psi \equiv \phi$ . Their methods are different from ours, and in particular, do not appear capable of generalization to the more natural situation in which  $\psi \neq \phi$ .

II. NOTATIONS AND ASSUMPTIONS. We begin by transforming (1.1) to an equivalent system by introducing the dependent variable  $z$  by

$$z(x, t) = \int_0^t a'(t - \tau) \psi(u(x, \tau)) d\tau. \quad (2.1)$$

Equation (1.1) then takes the form

$$\begin{aligned} u_t + \phi(u)_x + z_x &= 0 \\ z_t &= a'(0)\psi(u) + a''\psi, \end{aligned} \quad (2.2)$$

together with the initial data  $u(x,0) = u_0(x)$ ,  $z(x,0) = 0$ . In matrix notation (2.2) can be written as  $\underline{U}_t + A(\underline{U})\underline{U}_x + \underline{B}(\underline{U},t) = 0$  where  $\underline{U} = [u,z]^T$  and

$$A(\underline{U}) = \begin{bmatrix} \phi'(u) & 1 \\ 0 & 0 \end{bmatrix}, \quad \underline{B}(\underline{U},t) = \begin{bmatrix} 0 \\ -a'(0)\psi(u) - a''\psi \end{bmatrix}.$$

Since  $A(\underline{U})$  is a  $2 \times 2$  matrix having distinct eigenvalues  $\phi'(u)$  and 0 if  $\phi'(\cdot) \neq 0$ , it is well-known (cf. Lax [8]) that (2.2) has a pair of linearly independent Riemann invariants  $r(u,z)$  and  $s(u,z)$ . By definition

$$\begin{aligned} \underline{x}_1 \cdot \nabla r &= 0 \\ \underline{x}_2 \cdot \nabla s &= 0 \end{aligned} \quad (2.3)$$

where  $\underline{x}_1$  and  $\underline{x}_2$  are the right eigenvectors of  $A(\underline{U})$ . A simple calculation shows that  $\underline{x}_1 = \begin{bmatrix} 1 \\ -\phi(u) \end{bmatrix}$  and  $\underline{x}_2 = \begin{bmatrix} 1 \\ 0 \end{bmatrix}$ . Equations (2.3) then yield

$$\begin{aligned} r(u,z) &= z + \phi(u) \\ s(u,z) &= z; \end{aligned} \quad (2.4)$$

Moreover,  $\frac{\partial(r,s)}{\partial(u,z)} = \phi'(u) \neq 0$  if  $\phi'(\cdot) \neq 0$ .

Let  $x(t,\xi)$  denote the characteristic curve through  $\xi$  associated with (1.1) and defined by the initial value problem

$$\frac{dx}{dt} = \phi'(u(x,t)) \quad x(0,\xi) = \xi. \quad (2.5)$$

Proceeding formally, the derivative of  $r$  along this characteristic is

$$\begin{aligned} \frac{dr}{dt} &\equiv r_t + \phi'(u)r_x = z_t + \phi'(u)u_t + \phi'(u)[z_x + \phi'(u)u_x] \\ &= z_t + \phi'(u)[- \phi'(u)u_x - z_x] + \phi'(u)[z_x + \phi'(u)u_x] \\ &= z_t = s_t. \end{aligned}$$

Thus, we may replace (2.2) by the equivalent system

$$\frac{dr}{dt} = s_t \tag{2.6}$$

$$s_t = a'(0)\psi(u) + a''\psi(u) ,$$

together with the initial data  $r(u,z)(x,0) = \phi(u_0(x))$ ,  $s(u,z)(x,0) \equiv 0$ .

The basic constitutive assumption concerning  $\phi$  is

Assumption 2.1:  $\phi \in C^2(-\infty, \infty)$  and  $k > \phi'(\cdot) > \alpha_1 > 0$ ,  $\phi''(\cdot) > \beta_1 > 0$ .

Since by this assumption  $\phi$  is invertible, (2.4), in turn, implies that  $u = \phi^{-1}(r - s)$ ,  $z = s$ , so that (2.6) can be thought of as a system with dependent variables  $r$  and  $s$ .

Let  $v(t, \xi) \equiv x_\xi(t, \xi)$ . This variable, which measures the amount of variation of two nearby characteristics at time  $t$  with respect to their initial positions, plays the key role in our analysis. Note that  $v(0, \xi) = 1$ . We will subsequently show that, for large enough initial data,  $v(t, \xi)$  approaches zero in finite time. Thus the distance between two characteristics with initial positions near  $\xi$  must tend to zero in finite time, and it will be shown that a singularity is formed. Also

$$u_x(x(t, \xi), t) = \frac{u_\xi(x(t, \xi), t)}{x_\xi(t, \xi)} ,$$

and our analysis will show that  $u_x$  becomes unbounded in finite time, once we are able to bound  $u_\xi(x(t, \xi), t)$  away from zero.

In order to establish the formation of singularities in finite time we require the following constitutive restrictions concerning  $\psi$ .

Assumption 2.2:  $\psi \in C^1(-\infty, \infty)$  with  $\psi'(\cdot) > 0$  and there exist  $\alpha_2$  and  $\beta_2$  such that  $0 < \alpha_2 < \frac{\psi'(\cdot)}{\phi'(\cdot)} < \beta_2$ .

We note that when  $\psi'(\cdot) \equiv \phi'(\cdot)$  then the above assumption is a consequence of Assumptin 2.1. Finally, we require that the memory kernel  $a$  be positive, decreasing, and convex in the sense of

Assumption 2.3:  $a(\cdot) \in C^2[0, \infty)$  and

$$(-1)^i a^{(i)}(t) < 0 \quad i = 0, 1, 2$$

with strict inequality to hold at  $t = 0$ .

III. FORMATION OF SINGULARITIES. Before stating our main result we begin with the following local result for (1.1); the reader is referred to [2; Proposition 4.1 and Remark 4.2] for the proof.

Proposition 3.1. Let  $a', a'' \in L^1(0, \infty)$ ,  $\phi, \psi \in C^2(\mathbb{R})$ ,  $\phi(0) = \psi(0) = 0$ ,  $\psi'(0) > 0$ , and there exists a constant  $\kappa > 0$  such that

$\phi'(\xi) > \kappa > 0$  ( $\xi \in \mathbb{R}$ ); let  $u_0 \in H^2(\mathbb{R})$ . There exists a  $T_0 > 0$  and a  
unique solution  $u \in C^1(\mathbb{R} \times [0, T_0])$  of (1.1). Moreover,

$u_{tt}, u_{tx}, u_{xx} \in C([0, T]; L^2(\mathbb{R}))$  for every  $T < T_0$ , and if  $T_0 < \infty$

$$\limsup_{t \rightarrow T_0} \int_{\mathbb{R}} [u^2(x, t) + u_t^2(x, t) + u_x^2(x, t) + u_{xx}^2(x, t) + u_{xt}^2(x, t) + u_{tt}^2(x, t)] dx = +\infty.$$

The reader should observe that the assumptions of Proposition 3.1, while somewhat different are considerably less restrictive than Assumptions 2.1-2.3 above; no restriction on the "size" of the initial data  $u_0$  is imposed here. It should also be observed that Proposition 3.1 (or similar existence results) forms the basis for further study of the nature solutions of (1.1). Standard ODE theory applied to (2.5) justifies all the formal calculations of Section 2 establishing the equivalence between (1.1), (2.2), and (2.6), under the present hypotheses, for as long as a smooth solution of (1.1) is known to exist.

Our main result on the development of singularities in a smooth solution of (1.1) in finite time is:

Theorem 3.1. Let Assumptions 2.1-2.3 hold. Let  $u$  be a  $C^1$  solution of  
(1.1) with  $u_0 \in C^1(-\infty, \infty)$ . Assume further that there exists  $\xi$  such that  
 $u_0'(\xi) < 0$ . If  $|u_0'(\xi)|$  is sufficiently large then there exists  $T < \infty$  such  
that  $x_\xi(T, \xi) = 0$  and  $|u_x(x(T^-, \xi), \xi)| = \infty$ .

Proof. Assume that  $u$  is a  $C^1$  solution of (1.1) on  $\mathbb{R} \times [0, \infty)$  and consider the initial value problem (2.5). Assumption 2.1 coupled with standard ODE theory allows us to obtain the differential equation for  $v(t, \xi) \equiv x_\xi(t, \xi)$ . Differentiating (2.5) yields

$$\frac{dv}{dt} = \phi''(u(x(t, \xi), t)) u_\xi(x(t, \xi), t), \quad v(0, \xi) = 1.$$

Since  $\phi(u) = r - s$ , we have

$$\phi'(u) u_\xi = r_\xi - s_\xi = r_\xi - s_x x_\xi, \quad (2.8)$$

thus

$$u_\xi = \frac{1}{\phi'(u)} r_\xi - \frac{1}{\phi'(u)} s_x v.$$

From (2.2a), (2.4) we have

$$\frac{du}{dt} = -r_x = -s_x v,$$

so that

$$u_{\xi} = \frac{1}{\phi'(u)} r_{\xi} + \frac{1}{\phi'(u)} \frac{du}{dt} v$$

and (2.7) takes the form

$$\frac{dv}{dt} = \frac{\phi''(u)}{\phi'(u)} r_{\xi} + \frac{\phi''(u)}{\phi'(u)} \frac{du}{dt} v, \quad v(0, \xi) = 1.$$

Equation (2.9) is an ODE for  $v$  along characteristics having  $[\phi'(u)]^{-1}$  as an integrating factor. Thus

$$\frac{1}{\phi'(u)} v(t, \xi) - \frac{1}{\phi'(u_0(\xi))} = \int_0^t \frac{\phi''(u)}{\phi'^2(u)} r_{\xi} d\tau.$$

or equivalently

$$v(t, \xi) = \frac{\phi'(u(x(t, \xi), t))}{\phi'(u_0(\xi))} \tag{2.10}$$

$$\left[ 1 + \phi'(u_0(\xi)) \int_0^t \frac{\phi''(u(x(\tau, \xi), \tau))}{[\phi'(u(x(\tau, \xi), \tau))]^2} r_{\xi}(x(\tau, \xi), \tau) d\tau \right].$$

We invoke Assumption 2.1 again. Since  $r_{\xi}(x(\tau, \xi), \tau)|_{\tau=0} = \phi'(u_0(\xi))u_0'(\xi)$  is negative, it will remain negative for  $t \in [0, T_1]$  for some  $T_1$ .

The remainder of the proof of the theorem hinges on estimating  $T_1$  in terms of  $\alpha_1, \beta_1$  and  $a$ . Let  $C$  be defined by  $\phi'(u_0(\xi))u_0'(\xi) = -C$  and note that  $C$  is positive. Then there is a  $T_1$  such that

$$-C < r_{\xi}(x(t, \xi), t) < -\frac{C}{2} \quad \text{for } t \in [0, T_1]. \tag{2.11}$$

Since  $\phi''(u) > \beta_1$ ,  $0 < \alpha_1 < \phi'(u) < k$ , then  $\frac{\phi''(u)}{\phi'^2(u)} > \frac{\beta_1}{k^2}$  and

$$\int_0^t \frac{\phi''(u(x(\tau, \xi), \tau))}{[\phi'(u(x(\tau, \xi), \tau))]^2} r_{\xi}(x(\tau, \xi), \tau) d\tau < -\frac{C}{2} \frac{\beta_1}{k^2} t.$$

Therefore, one has

$$v(t, \xi) < \frac{\phi'(u(x(t, \xi), t))}{\phi'(u_0(\xi))} \left[ 1 - \frac{C}{2} \frac{\beta_1 \alpha_1}{k^2} t \right]. \tag{2.12}$$

The right hand side of (2.12) becomes zero at  $t = \frac{2k^2}{\alpha_1 \beta_1 C}$ , since  $v(0, \xi) = 1$ ,

$v(t, \xi)$  must vanish at a time  $T < \frac{2k^2}{\alpha_1 \beta_1 C}$ . By taking  $C$  large enough we insure that  $\frac{2k^2}{\alpha_1 \beta_1 C} < T_1$ .

The next task is to show that  $T_1$  is independent of  $C$ . Equations (2.6) combine to yield.

$$\frac{dr}{dt} = a'(0)\psi(u(x(t, \xi), t)) + \int_0^t a''(t - \tau)\psi(u(x(t, \xi), \tau))d\tau. \quad (2.13)$$

Differentiating (2.13) with respect to  $\xi$  (justified by Assumptions 2.1 and standard theory) gives

$$\begin{aligned} \frac{dr_\xi}{dt} &= a'(0)\psi'(u(x(t, \xi), t))u_\xi(x(t, \xi), t) \\ &+ \int_0^t a''(t - \tau)\psi'(u(x(t, \xi), \tau))u_\xi(x(t, \xi), \tau)d\tau. \end{aligned} \quad (2.14)$$

We evaluate (2.8) at  $(x(t, \xi), \tau)$

$$\phi'(u(x(t, \xi), \tau))u_\xi(x(t, \xi), \tau) = r_\xi(x(t, \xi), \tau) - s_\xi(x(t, \xi), \tau) \quad (2.15)$$

and combine (2.14) with (2.15) to obtain

$$\begin{aligned} \frac{dr_\xi}{dt} &= a'(0) \frac{\psi'(u)}{\phi'(u)} (r_\xi - s_\xi) \Big|_{(x(t, \xi), t)} \\ &+ \int_0^t a''(t - \tau) \frac{\psi'(u)}{\phi'(u)} (r_\xi - s_\xi) \Big|_{(x(t, \xi), \tau)} d\tau. \end{aligned} \quad (2.16)$$

Since  $r_\xi(x(t, \xi), \tau) \Big|_{\substack{t=0 \\ \tau=0}} = \phi'(u_0(\xi))u_0'(\xi) = -C$  and  $s_\xi(x(t, \xi), \tau) \Big|_{\substack{t=0 \\ \tau=0}} = 0$ ,

there exists  $T_1$  such that

$$-C < r_\xi(x(t, \xi), \tau) - s_\xi(x(t, \xi), \tau) < \frac{C}{2} \quad (2.17)$$

and

$$-C < r_\xi(x(t, \xi), \tau) < -\frac{C}{2} \quad (2.18)$$

for  $0 < \tau < t < T_1$ . Recall Assumptions 2.2 and 2.3. These and inequality (2.17) imply that for  $0 < \tau < t < T_1$  we can estimate the integral in (2.16)

by

$$\int_0^t a''(t-\tau) \frac{\psi'(u)}{\phi'(u)} (r_\xi - s_\xi) d\tau > -C \int_0^t a''(t-\tau) \frac{\psi'(u)}{\phi'(u)} d\tau$$

$$> -C\beta_2 \int_0^t a''(t-\tau) d\tau > -C\beta_2(a'(t) - a'(0)).$$

Therefore, from (2.16) using  $a'(0) < 0$ ,  $r_\xi(x(t, \xi), t) - s_\xi(x(t, \xi), t) < 0$  we obtain

$$\frac{dr_\xi}{dt} > a'(0) \frac{\psi'(u)}{\phi'(u)} (r_\xi - s_\xi) - C\beta_2(a'(t) - a'(0))$$

$$> \alpha_2 a'(0)(r_\xi - s_\xi) - C\beta_2(a'(t) - a'(0)),$$

or

$$\frac{d}{dt} (e^{-\alpha_2 a'(0)t} r_\xi) > -\alpha_2 a'(0) e^{-\alpha_2 a'(0)t} s_\xi$$

$$- C\beta_2 e^{-\alpha_2 a'(0)t} (a'(t) - a'(0)), \quad 0 < t < T_1.$$

Integrating the above inequality yields

$$e^{-\alpha_2 a'(0)t} r_\xi(x(t, \xi), t) + C > -\alpha_2 a'(0) \int_0^t e^{-\alpha_2 a'(0)\tau} s_\xi(x(\tau, \xi), \tau) d\tau$$

$$- C\beta_2 \int_0^t e^{-\alpha_2 a'(0)\tau} (a'(\tau) - a'(0)) d\tau, \quad 0 < t < T_1. \quad (2.19)$$

Inequality (2.19) reduces to

$$r_\xi(x(t, \xi), t) > -C e^{\alpha_2 a'(0)t} - \alpha_2 a'(0) \int_0^t e^{\alpha_2 a'(0)(t-\tau)} s_\xi(x(\tau, \xi), \tau) d\tau$$

$$- C\beta_2 \int_0^t e^{\alpha_2 a'(0)(t-\tau)} a'(\tau) d\tau - \frac{\beta_2}{\alpha_2} C + \frac{\beta_2}{\alpha_2} C e^{\alpha_2 a'(0)t}, \quad 0 < t < T_1. \quad (2.20)$$

Next, Recall that

$$s_\xi(x(t, \xi), t) = \int_0^t a'(t-\tau) \frac{\psi''(u)}{\phi'(u)} (r_\xi - s_\xi) |_{(x(t, \xi), \tau)} d\tau.$$

Assumptions 2.2, 2.3 and inequality (2.17) imply that

$$0 < \alpha_2 \int_0^t a'(t-\tau) |r_\xi - s_\xi|_{(x(t,\xi),\tau)} d\tau < s_\xi(x(t,\xi),t) < \\ < \beta_2 \int_0^t a'(t-\tau) |r_\xi - s_\xi|_{(x(t,\xi),\tau)} d\tau, \quad 0 < t < T_1.$$

Thus the second term on the right hand side of (2.20) can be estimated as follows:

$$-\alpha_2 a'(0) \int_0^t e^{\alpha_2 a'(0)(t-\tau)} s_\xi(x(\tau,\xi),\tau) d\tau > \tag{2.22}$$

$$-\alpha_2^2 a'(0) \int_0^t e^{\alpha_2 a'(0)(t-\tau)} \int_0^\tau a'(\tau-\eta) |r_\xi - s_\xi|_{(x(\tau,\xi),\eta)} d\eta d\tau, \quad 0 < t < T_1.$$

The integral on the right hand side of (2.22) is bounded below by (cf. (2.17))

$$\alpha^2 \frac{C}{2} a'(0) \int_0^t e^{\alpha_2 a'(0)(t-\tau)} (a(\tau) - a(0)) d\tau, \quad 0 < t < T_1.$$

We next obtain a uniform estimate for  $T_1$  (independent of  $C$ ). Combining (2.18), (2.20) and (2.22) yields

$$-\frac{C}{2} > -C e^{-\alpha_2 a'(0)t} + \frac{\alpha_2}{2} C a'(0) \int_0^t e^{\alpha_2 a'(0)(t-\tau)} (a(\tau) - a(0)) d\tau \tag{2.23}$$

$$-C \beta_2 \int_0^t e^{\alpha_2 a'(0)(t-\tau)} a'(\tau) d\tau - \frac{\beta_2}{\alpha_2} C + \frac{\beta_2}{\alpha_2} C e^{\alpha_2 a'(0)t}, \quad 0 < t < T_1,$$

in which  $C > 0$  is a factor of every term. Thus letting

$$F(t) = 1/2 - e^{\alpha_2 a'(0)t} + \frac{\alpha_2}{2} a'(0) \int_0^t e^{\alpha_2 a'(0)(t-\tau)} (a(\tau) - a(0)) d\tau \\ - \beta_2 \int_0^t e^{\alpha_2 a'(0)(t-\tau)} a'(\tau) d\tau - \frac{\beta_2}{\alpha_2} + \frac{\beta_2}{\alpha_2} e^{\alpha_2 a'(0)t},$$

inequality (2.23) is equivalent to  $F(t) < 0$  for  $t \in [0, T_1]$ . But  $F(0) = -1/2$ , so that there exists  $T_1 = T_1(a(\cdot), \alpha_1, \beta_1)$ , independent of  $C$ , such that  $F(t) < 0$  for  $0 < t < T_1$ .

The proof is now easily completed as follows. We have

$$u_x(x(t, \xi), t) = \frac{u_\xi(x(t, \xi), t)}{x_\xi(t, \xi)} = \frac{u_\xi(x(t, \xi), t)}{v(t, \xi)}.$$

Assumption 2.1, together with (2.8) and (2.17) imply that  $u_\xi(x(t, \xi), t)$  remains bounded away from zero for  $t \in [0, T_1]$ . But as we have shown above  $v(t, \xi) = x_\xi(t, \xi)$  vanishes at a time  $T$ ,  $0 < T < T_1$ , for  $C$  sufficiently large, where  $T_1$  depends only on  $\alpha_1, \beta_1$  and  $a$ , but not on  $C$ . Therefore,  $u_x(x(t, \xi), t)$  becomes unbounded at  $T$  which contradicts the assumption that  $u$  is a smooth solution of (1.1) on  $R \times [0, \infty)$  and completes the proof of Theorem 3.1.

Remark 3.1. Assumption 2.1 may be replaced by  $\frac{\phi''(\cdot)}{[\phi'(\cdot)]^2} > \beta_3 > 0$  for some  $\beta_3$  and the proof of the above theorem remains unchanged. Of course Assumption 2.1 can be weakened further if one knows that solutions of (1.1) satisfy the a priori estimate  $\sup_{x,t} |u(x,t)| < \text{const.}$

Remark 3.2. While Theorem 3.1 establishes breakdown of smooth solutions of (1.1) for sufficiently large data, it does not prove the development of a shock front. Numerical evidence for this more complex phenomenon has been found by Markowich and Renardy [9] for the Cauchy problem associated with (1.2), (1.3) in the special case  $\psi \equiv \phi$  when the smooth data becomes sufficiently large. This analytical problem is under active study.

#### REFERENCES

- [1] C. M. Dafermos and J. A. Nohel, A nonlinear hyperbolic Volterra equation in viscoelasticity, *American J. Math.*, Supplement (1981), 81-116.
- [2] J. A. Nohel, A nonlinear conservation law with memory, *Mathematics Research Center Technical Summary Report #2251*, August 1981.
- [3] P. D. Lax, Development of singularities of solutions of nonlinear hyperbolic differential equations, *J. Math. Phys.* 5 (1964), 611-613.
- [4] F. John, Formation of singularities in one-dimensional nonlinear wave propagation, *Comm. Pure Appl. Math.* Vol. 27 (1974), 377-405.
- [5] J. P. Tordella, Unstable flow of molten polymers, *Rheology Theory and Applications*, 5 (1969), 57-92.
- [6] M. Slemrod, Instability of steady shearing flows in a nonlinear viscoelastic fluid, *Arch. Rational Mech. Anal.* 68 [1978], 211-225.
- [7] H. Hattori, Breakdown of smooth solutions in dissipative nonlinear hyperbolic equations, *Ph.D. Thesis, R.P.I.*, 1981.
- [8] P. D. Lax, Hyperbolic systems of conservation laws, II, *Comm. Pure Appl. Math.*, 10 (1957), pp. 227-241.
- [9] P. Markowich and M. Renardy, Lax-Wendroff methods for hyperbolic history value problems, *MRC Technical Summary Report to appear.*

## SIGNIFICANCE AND EXPLANATION

Problems arising in continuum mechanics can often be modeled by quasilinear hyperbolic systems in which the characteristic speeds are not constant. Such systems have the property that waves may be amplified and solutions that were initially smooth may develop discontinuities ("shocks") in finite time. Of particular interest are situations in which the destabilizing mechanism arising from nonlinear effects can coexist and compete with dissipative effects. An interesting situation arises when the amplification and dissipative mechanisms are nearly balanced and the outcome of their confrontation cannot be predicted at the outset. Examples are provided by quasilinear second order wave equations with first order frictional damping; it has been shown that when the initial data are sufficiently smooth and "small" in suitable norms, classical solutions exist globally in time. However, if the smooth initial data become sufficiently "large" in a precise sense, the smooth solution develops a singularity in finite time, no matter how smooth one takes the data. Thus the dissipative mechanism is not sufficiently powerful to prevent the breaking of waves for large enough data.

A considerably subtler dissipative mechanism is induced by memory effects of elastico-viscous materials. Using energy methods Dafermos and Nohel [1] have studied the motion of a one-dimensional homogeneous viscoelastic body (governed by equations (1.2), (1.3) below). They show that the memory term in (1.3) induces a weak dissipative mechanism under physically reasonable constitutive assumptions, which, for sufficiently "small" and smooth data, prevents the breaking of waves; indeed, a unique classical solution exists globally in time, and the solution decays as  $t \rightarrow \infty$ . A natural and open question (except in very special cases) is whether this weak dissipative mechanism can also prevent the breaking of waves for large enough smooth data; experimental evidence suggests that it cannot.

In order to gain a deeper understanding of this complex phenomenon we study the simpler model problem stated in the abstract, under comparable constitutive assumptions concerning the functions  $\phi, \psi$  and  $a$ . Here the weak dissipative mechanism which is induced by the memory term acts exactly as the one for the viscoelastic problem for sufficiently smooth and small data (see [2]). In this paper we show, under physically reasonable constitutive assumptions, that this weak dissipative mechanism cannot overcome the shock forming tendency of the nonlinear Burgers operator  $\frac{\partial u}{\partial t} + \phi(u)$ , when  $\phi$  is convex; indeed, a singularity develops in the smooth solution in finite time, whenever the smooth initial data  $u_0(x)$  have  $u_0'(x) < 0$  and  $(-u_0'(x))$  is sufficiently large.

It is possible to gain some insight into the problem under study by considering the following simple example without memory terms:

$$u_t + uu_x + au = 0$$
$$u(x,0) = u_0(x) \quad (x \in \mathbb{R});$$

---

The responsibility for the wording and views expressed in this descriptive summary lies with MRC, and not with the author of this report.

in (0.1) the memory term is replaced by  $\alpha u$  where  $\alpha > 0$  is a constant, and  $\phi(y) = u^2/2$ , is a strictly convex function on  $R$ . If  $u_0$  is smooth ( $C_0^1(R)$ ), (0.1) has a unique classical solution  $u$  valid on a maximal interval  $R \times [0, T_0)$ ,  $0 < T_0 < \infty$ . Suppose the solution  $u$  of (0.1) exists globally in  $t$ . Differentiate (0.1) with respect to  $x$  obtaining

$$u_{tx} + uu_{xx} + u_x^2 + \alpha u_x = 0.$$

Putting  $w = u_x$  and noting that  $w_t + uw_x$  is the derivative of  $w$  along the characteristic curves  $x(t, \xi)$  of (0.1) defined by the ODE

$$\frac{dx}{dt} = u(x(t, \xi), t), \quad x(0, \xi) = \xi,$$

we see that  $w$  satisfies the ODE

$$(0.2) \quad \frac{dw}{dt} + w^2 + \alpha w = 0, \quad w(x, 0) = u_0'(x),$$

along the characteristics, where  $\frac{d}{dt} = \frac{\partial}{\partial t} + u \frac{\partial}{\partial x}$ . Integration of (0.2) shows that if  $u_0'(x) > -\alpha$  ( $x \in R$ ),  $w = u_x$  remains bounded for all  $t > 0$  and the smooth solution  $u$  of (0.1) exists globally; if, however,  $u_0'(x) < -\alpha$  for

some  $x$ , then  $w = u_x \rightarrow -\infty$  as  $t \rightarrow \frac{1}{\alpha} \log \frac{u_0'(x)}{\alpha + u_0'(x)}$ ; i.e., the classical

solution  $u$  of (0.1) develops a singularity in the first derivatives in finite time, no matter how smooth the initial data  $u_0$  is taken. This elementary method does not, unfortunately, extend to the problem with memory terms under study, and for this reason our analysis is different and necessarily considerably more technical.



AD P001037

THEORIES FOR CONTROL OF NEUROTRANSMITTER RELEASE  
AND FOR TWO PROBLEMS IN PHYSICAL CHEMISTRY

Lee A. Segel

Department of Applied Mathematics  
Weizmann Institute, Rehovot 76100, Israel

and

Department of Mathematical Sciences  
Rensselaer Polytechnic Institute, Troy NY 12181

ABSTRACT. Three problems are surveyed: (1) The control by calcium entry of neurotransmitter release; (2) The spatially inhomogeneous polymerization reaction when a layer of initiator is placed next to a reservoir of monomer; (3) A spinodal decomposition type of phase change modelled by the nonlinear fourth order Cahn-Hilliard equation.

I. INTRODUCTION. This report treats three aspects of the author's recent research, respectively in collaboration with H. Parnas, M. Falkovitz, and A. Novick-Cohen. First, in a kinetic study of neurotransmitter release we sought experiments with striking qualitative behavior and attempted to explain them by phenomenological modelling that was in accord with broadly accepted biological principles. It turned out that saturation was important in all the processes involved, so that nonlinear effects turned out to be vital. The greater understanding of release can be useful in better comprehension of the effects of drugs and toxins.

The second problem concerns spatially inhomogeneous polymerization. At the outset, we were faced with an infinite set of equations of reaction-diffusion type, with diffusivities that depend on the extent of polymerization. Considerable thought was given to appropriate simplification. In the end it was possible to achieve a better understanding of a process that may be of industrial importance.

The original motivation for the third problem came from experiments by our colleague G. Tanny wherein phase changes were manipulated to "cast" membranes for desalination and other applications. A generalization of the diffusion concept is required, that takes into account the free energy cost of spatial inhomogeneity. Appropriate to our purposes was the Cahn-Hilliard equation, a nonlinear parabolic equation that is fourth order in spatial differentiations. The analysis concentrated on elucidating some effects of the nonlinearities.

In this survey, we sketch some of the broad features of the problems and the results we have obtained. The cited references may be consulted for further detail.

II. NEUROTRANSMITTER RELEASE. Nerve cells generally communicate with each other or with muscles by means of transmitter substances that are released from the nerve terminals after the arrival of an electrical impulse. *Facilitation* occurs if, after one or a few impulses, a test impulse is given and the amount of transmitter released for this

impulse is greater than for an initial control impulse. That is  $F = L_1/L_2$  where  $L_1(L_2)$  is the amount of release after the control (test) impulse.

We shall describe a phenomenological theory of transmitter release based on a description of the three processes of *entry* of Ca into the terminal, *removal* of the internal Ca, and *release* of transmitter as a function of the internal Ca concentration at the time of the triggering impulse. Our model is based on observations (Dodge & Rahamimoff, 1967; Rahamimoff, 1968; Cooke, Okamoto & Quastel, (1973) that

- (a) Transmitter release is a saturating function of external Ca concentration  $C_e$ .
- (b) For short intervals between impulses (e.g. 5 ms) the facilitation  $F$  is a decreasing function of the external Ca concentration but for longer intervals  $F$  increases as the external Ca concentration increases.
- (c) Log - plots of release as a function of  $\log C_e$  rise monotonically from an asymptote as  $\log C_e \rightarrow -\infty$  to another asymptote as  $\log C_e \rightarrow +\infty$ .

Let us suppose for the moment that entry is some unspecified increasing function of the extracellular Ca concentration  $C_e$ :

$$E = E(C_e), \quad \partial E / \partial C_e > 0. \quad (2.1)$$

Experimental result (a) suggests that release  $L$  is a saturating function of intracellular concentration  $C$  at the time of an impulse. If this is the case, Parnas and Segel (1980) argue that result (b) requires the assumption that removal saturates at high Ca concentrations. The simplest saturating removal equation is

$$dC/dt = -\mu C / (K_\mu + C), \quad \mu \text{ and } K_\mu \text{ constants.} \quad (2.2)$$

At the first impulse, the intracellular concentration is raised by the entry  $E(C_e)$ . Assuming that this very fast process is instantaneous, and neglecting the generally small "residual" amount of Ca already present, this gives  $C(0) = E$  as an initial condition for (2.2), so that

$$K_\mu \ln C + C = -\mu t + K_\mu \ln E + E. \quad (2.3)$$

As a simple example of the sort of reasoning involved in this type of analysis, we will show that result (b) cannot be explained with a linear release hypothesis if saturation in release is neglected. Suppose that release is indeed linear, and consider the facilitation at time  $t$ , i.e.  $t$  units after the control impulse. We have

$$F(t) = \frac{E + C(t)}{E}, \quad \frac{\partial F}{\partial E} = \frac{1}{E} \left( \frac{\partial C}{\partial E} - \frac{C}{E} \right). \quad (2.4)$$

But by implicit differentiation of (2.3)

$$\frac{\partial C}{\partial E} = \frac{C}{E} \frac{K_{\mu} + E}{K_{\mu} + C}$$

so that

$$\frac{\partial F}{\partial E} = \frac{C}{E^2} \frac{E - C}{K_{\mu} + C} > 0 .$$

Thus, contrary to (b),  $F$  is always larger at larger values of  $E$  (or of  $C_e$ ). A similar analysis shows that  $\partial F/\partial E$  remains positive even if (2.2) is replaced by a removal law that is both saturating and "cooperative"

$$dC/dt = -\mu C^n / (K_{\mu} + C^n), \quad C(0) = E .$$

Based on considerations of the type just discussed, we arrive at the following hypothesis for the dependence of release  $L$  on the intracellular calcium concentration  $C$ :

$$L(C) = \lambda C^n / (K_{\lambda} + C^n), \quad (2.5)$$

where the exponent  $n$  allows for the possibility of cooperativity in the underlying chemical reactions. Study of experimental results (c) (Parnas & Segel 1981) leads to the postulation of the entry equation

$$E(C_e) = \epsilon C_e^r / (K_e + C_e^r) . \quad (2.6)$$

The final governing equations thus consist of (2.2), (2.5) and (2.6) with the initial condition for (2.2)

$$C(0) = E + C_r, \quad (2.7)$$

where the residual calcium concentration  $C_r$  has been included to afford further flexibility in the model.

Parnas and Segel (1982) discussed how the theory could be used to try to make a more accurate assessment of the effects on release of drugs and toxins. For example they examined findings of Oberg & Kelly (1976) that  $\beta$ -bungarotoxin increased release but that the slope of the curve of  $\log$  release vs  $\log C_e$  appeared unchanged. From the fact that no increase in release was observed when  $C_e \approx 0$ , they deduced that an effect on removal is unlikely. The theory indicates that the observations are due to changes in the maximum entry parameter  $\epsilon$  or in the entry saturation parameter  $K_e$ , and suggests that more extensive measurements of release as a function of  $C_e$  would be informative.

See Parnas et al (1981) for experiments confirming saturation.

**III. UNSTIRRED BULK POLYMERIZATION.** A second project treated experiments by Ozari and Jagur (1975), in which a layer of pure styrene was poured above a solution of sodium naphthalem in TPPA. The container was kept at rest for a few days. At the initiation of the process a strip of low molecular weight dead polymer was established. Above this strip, a relatively thick layer of gel, consisting of high molecular weight living polymer was formed. The gel-liquid boundary was observed to elevate slowly with time, starting from the bottom of the initiator-monomer interface. Particularly noteworthy is the fact that the polymer obtained by this process was characterized by a narrow molecular weight distribution.

In a first attempt at formulation, equations were written for concentrations of initiator (I), monomer (M), activated monomer ( $P_1$ ), n-unit polymer ( $P_n$ ), unreactive polymer ( $P_n^*$ ), impurity (K), and inactive solvent (S). With J's denoting ordinary diffusive fluxes (proportional to concentration gradients) and k's the various rate constants (with reactions assumed irreversible), these equations were taken to be

$$\begin{aligned} DI/Dt &= -k_i IM - V \cdot (J_I + I v^B) \\ DP_1/Dt &= k_i IM - k_p P_1 M - k_t P_1 K - V \cdot (J_1 + P_1 v^B) \\ DP_n/Dt &= k_p (P_{n-1} P_m K - V \cdot (J_n + P_n v^B)) \\ DP_n^*/Dt &= k_i P_n K - V \cdot (J_n^* + P_n^* v^B) \\ DM/Dt &= -k_i IM - k_p AM - V \cdot (J_M + M v^B) \\ DK/Dt &= -k_t A K - V \cdot (J_K + K v^B) \\ DS/Dt &= -V \cdot (J_S + S v^B) . \end{aligned}$$

where A is the concentration of actively polymerizing centers

$$A(\underline{r}, t) = \sum_n P_n(\underline{r}, t) ,$$

and  $v^B$  is the bulk velocity (Crank 1975)

$$v^B = -[\sum_n (nm_M + m_I) J_n + \sum_n (nm_M + m_K) J_n^* + m_M J_M + m_S J_S + m_K J_K] / \rho$$

$$\rho = m_I (I+A) + m_M (N+M) + m_K K + m_S S .$$

$m_I, m_M, m_K, m_S$  are the molecular weights of initiator, monomer, impurities and solvent respectively.

After suitable scaling and consideration of the various parameter values, the problem was essentially reduced to a consideration of just two dimensionless equations, for concentrations of monomer and active

centers in the domain above the original initiator layer:

$$M_t = -AM + \lambda [(1-M)DM_z]_z$$

$$A_t = -\lambda (ADM_z)_z$$

Here the dimensionless parameter  $\lambda^{1/2}$  can be regarded as the reciprocal of a Thiele modulus, giving the relative importance of reaction and diffusion. Initial and boundary conditions are

$$M(z,0)=1, A(z,0)=\phi, z \geq 0; M_z(0,t)=0, t \geq 0.$$

Choice of the function  $\phi$  that gives the initial extent of polymerization depends on the mechanism that is assumed to dominate in the first few moments of the process. At first this mechanism was assumed to be purely diffusive, but this produced results at variance with the observations. Account was then taken of the exothermic nature of the initiation reaction; a calculation showed that considerable convection would result. A fairly elaborate numerical analysis then produced results for various assumptions concerning the nature of the dependence of the monomer diffusivity  $D$  on the local extent of polymerization as reflected by the monomer concentration  $M$ . The following physical picture emerged.

The initiation step of the process lasts for a short time - about a minute. During this step, changes in the monomer concentration are negligible. The initiation is divided into two sub-steps. At first initiator molecules penetrate into the domain occupied by the monomer, with which they react to form active centers capable of further polymerizing. During this sub-step, active centers are noticeable in a strip whose thickness grows at a rate of order  $\sqrt{Dt}$ . During the second sub-step, the above process is accompanied by convective mixing in a layer near the interface between the original two phases. The active centers, formed out of the initiator which penetrates into the monomer-rich domain, are dispersed in a layer with thickness proportional to  $\sqrt{\kappa t}$  (where  $\kappa$  is thermal diffusivity), which is much wider than the previously mentioned strip. During the initial step a small amount of monomer penetrates into the initiator-rich domain, where its effect is noticeable in a very thin strip, with width of order  $\sqrt{D_s t} \ll \sqrt{Dt}$ . Here  $D_s$  is the diffusivity of monomer in the rather viscous solvent for the initiator.

The main part of the reaction, which lasts for days, is characterized by three physical processes. Active centers combine with neighboring monomer molecules. Fresh monomer molecules, from the domain which is void of active centers, diffuse into the domain which contains active centers, to replace those molecules which were consumed by the polymerization. The penetration of monomer molecules into the "polymerization zone" results in a swelling of this layer. The initial monomer domain, which was originally homogeneous, is separated into two phases - gel, in which most of the active centers are located, and liquid, which contains small amounts of active centers. The gel-liquid front propagates at rate proportional to  $\sqrt{Dt}$ .

As a result of the penetration of monomer into initiator during the initial step, a barrier is formed which prevents supply of additional initiator molecules to the original monomer domain. During the main step of the process the active centers, which are located not too close to the barrier, react in a neighborhood very rich in monomer. This fact results in the very narrow molecular weight distribution which is the salient observed feature of this polymerization procedure.

For further details, see Falkovitz and Segel (1982).

IV. NONLINEAR PROPERTIES OF THE CAHN-HILLIARD EQUATION. Numerous attempts have recently been made to explain the dynamics of pattern formation via phase transition. Sufficient cooling of a binary solution may lead to phase separation which will proceed in one of two main ways: either by nucleation in which sufficiently large nuclei of the second phase appear randomly and grow, or by so-called spinodal decomposition in which the whole solution appears to nucleate at once, and periodic or semi-periodic structure is seen.

In the work reported here a continuum model due originally to Cahn and Hilliard (1958) was analyzed. Early linear treatments of the Cahn-Hilliard equation gave unphysical results, and the Cahn-Hilliard equation to a great extent fell out of favor and was deemed incapable of describing phase transition. The non-linear Cahn-Hilliard equation was for the most part discarded as untreatable. In its place many more involved formulations have developed in which statistical fluctuations are included. Here we have reverted to the original equation and attempted to ascertain to what extent the deterministic nonlinear continuum model is capable of describing the intricacies of phase separation which have been observed experimentally and theoretically.

Study of the Cahn-Hilliard equation can be regarded as a useful supplement to the classical pattern-formation stability theory of the Bénard and Taylor problems. The "negative viscosity" destabilizing mechanism occurs in other physical contexts (Kuramoto & Yamada 1976) and as has been indicated, pattern formation via phase transition is of interest for important technological applications. On general grounds perhaps the most interesting feature of the Cahn-Hilliard equation is its close connection with a "free-energy" or Liapunov functional. A long range research goal is to understand what role the existence of such a functional plays in determining qualitative behavior of nonlinear partial differential equations in the vicinity of bifurcation points.

The Cahn-Hilliard equation is

$$\frac{\partial c}{\partial t} = \nabla \cdot \left[ M(c) \nabla \left( \frac{\partial f}{\partial c}(c) - K \nabla^2 c \right) \right],$$

where in our analysis  $f$  will be taken to be a fourth order polynomial with three relative extrema. In the absence of accurate information about its behavior as a function of the concentration,  $K$  will be assumed to be a constant. On the other hand,  $M(c)$  which is known to

be highly concentration dependent, will initially be restricted only by the condition  $M(c) > 0$ .

The one-dimensional version of the rescaled Cahn-Hilliard equation for the composition perturbation  $c$  around a uniform concentration  $c_0$  is

$$c_t = [M(c) (\pm c + Bc^2 + c^3 - c_{xx})]_{xx}$$

where the plus (minus) sign is used if the uniform solution is linearly unstable (stable). We have found a class of solutions to this equation in terms of  $\tau \equiv (c-\alpha)/(c-\beta)$  (Cayley's method of reduction):

$$x = \int^{\phi} \frac{d\tau}{(A_1 \tau^2 - B_1)^{1/2} (A_2 \tau^2 - B_2)^{1/2} (\alpha - \beta)}, \quad \phi \equiv \frac{c-\alpha}{c-\beta}$$

Here  $\phi$  is a Jacobian elliptic function. There are, however, twelve different such functions. The permissible forms are determined by locating those parameter regions  $\{A_1, A_2, B_1, B_2\}$  that will allow real bounded periodic solutions for  $c(x; A_1, A_2, B_1, B_2)$ , and imposing the condition that total mass is conserved. The nature of the solutions is discussed in the paper of Novick and Segel (1982).

In classical thermodynamics a homogeneous solution  $c(x) \equiv c_0$  is considered to be stable if there does not exist a two-phase configuration whose total free energy is lower than the total free energy of the homogeneous solution. If such a two phase configuration with lower free energy does exist, the original homogeneous solution is considered to be metastable or unstable depending on whether a finite or infinitesimal concentration change is necessary to provide a lower free energy.

Classical thermodynamics can only deal with situations that are infinitesimally close to spatial and temporal uniformity. To break free somewhat from these limitations and to put the study of stability into a strictly defined context, Novick and Segel (1982) applied to the Cahn-Hilliard equation the idea of the limit of monotonic global stability as studied by Joseph (1976) in the context of fluid dynamics.

Closed finite regions are considered, i.e. we will require

$$J|_{\text{boundary}} = 0.$$

Natural boundary conditions will also be enforced:

$$\frac{\partial c}{\partial n}|_{\text{boundary}} = 0.$$

The mobility function will be assumed to be a positive non-increasing function of  $|c|$  such that

$$\frac{1}{M^2(c)} \left( \frac{dM}{dc} \right)^2 < 12 ,$$

i.e.,  $M(c)$  will be non-increasing and  $M(c) \geq M(0) \exp(-\sqrt{12} |c|)$ . Enhanced generality will be obtained by considering the parameter  $B$  to be time dependent.

**THEOREM.** Consider material confined to a cube of side  $L$ . If  $c + c_0$  ( $c_0$  a constant) is a solution of the Cahn-Hilliard equation we define  $\bar{B}(L)$  by

$$\frac{1}{\bar{B}(L)} = \sup_{t > 0} \sup_{c \in H(L)} \left[ \frac{-\text{sgn } B \int_{R_L} 2cM(c) (\nabla c)^2 dv}{\int_{R_L} M(c) [(1+3c^2) (\nabla c)^2 + (\nabla^2 c)^2] dv} \right]$$

For  $B^2 < \bar{B}^2(L)$  in the parameter region where  $c_0$  is stable to infinitesimal perturbations, consider the "energy" of all perturbations  $c(x,t)$

$$\epsilon(t) = \int_{R_L} \frac{1}{2} c^2 dv .$$

This energy decays, since

$$\epsilon(t) \leq \epsilon(0) \exp\left\{-\frac{2\hat{\Lambda}}{L^2} \int_0^t \left(1 - \frac{|B(\tau)|}{\bar{B}}\right) M(\bar{c}(\tau)) d\tau\right\} ,$$

for some  $\hat{\Lambda} \geq 2/3$ , where  $M(\bar{c}(t))$  is the mobility evaluated at some  $c(x(t),t)$ . Furthermore if  $B^2(0) > \bar{B}^2(L)$ , then there exists an admissible initial perturbation  $c(x,t)$  such that  $d\epsilon/dt > 0$  at  $t=0$ . Here the class  $H(L)$  of admissible  $c(x,t)$  will be all smooth functions that satisfy the composition conservation constraint and the boundary conditions. See Novick and Segel (1982) for an outline of a proof of this theorem.

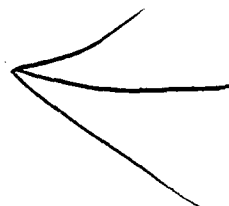
Beyond the limit of monotonic global stability, all perturbations to the uniform state decay monotonically, whereas within this limit there exist initial conditions which will cause the "energy" to grow initially. Knowledge of the existence of the one-dimensional equilibrium solutions turns out to be crucial in determining where the limit of monotonic global stability lies. The possibility that this limit

does not coincide with the coexistence (neutral stability) curve but rather lies beyond it gives rise to the possibility of a narrow "excitable" region just outside the coexistence curve where an enhancement of the fluctuation level without the appearance of phase separation would signal the proximity of the two phase region. The actual existence of such a postulated excitable zone could be tested experimentally, or perhaps theoretically by further determination of the location of the limit of monotonic global stability.

ACKNOWLEDGEMENTS. This work was partially supported by the Army Research Office and the National Science Foundation.

#### REFERENCES

- Cahn, J.W. & Hilliard, J.E. (1958). J. Chem. Phys. 28, 258.
- Cooke, J.D., Okamoto, K. & Quastel, D.M.J. (1973). J. Physiol. 228, 459.
- Crank, J. (1975). The Mathematics of Diffusion. Oxford: Clarendon Press.
- Dodge, F.A. Jr. & Rahamimoff, R. (1967). J. Physiol. 193, 419.
- Falkovitz, M. & Segel, L.A. (1982). "Spatially inhomogeneous polymerization in unstirred bulk", SIAM J. Appl. Math., in press.
- Joseph, D.D. (1976). "Stability of Fluid Motions I", Springer Verlag, Berlin, Chapter 1.
- Novick-Cohen, A. & Segel, L.A. (1982). "Nonlinear aspects of the Cahn-Hilliard equation", Physica D Nonlinear Phenomena, in press.
- Oberg, S. & Kelly, R. (1976). J. Neurobiol. 7, 129.
- Ozari, Y., Jagur-Grodzinski J. (1975). "Interfacial initiation of anionic polymerization", Proc. of 43rd Annual Meeting, Israel Chem. Soc., 124.
- Parnas, H., Dudel, J. & Parnas, I. (1982). Pflügers Arch. 393, 1.
- Parnas, H. & Segel, L.A. (1980). J. theor. Biol. 84, 3.
- Parnas, H. & Segel, L.A. (1981). J. theor. Biol. 91, 125.
- Parnas, H. & Segel, L.A. (1982). J. theor. Biol. 94, 923.
- Rahamimoff, R. (1968). J. Physiol. 195, 471.



AD P 0 1 0 3 8

LINEARIZED DYNAMICS OF SHEARING DEFORMATION  
PERTURBING REST IN VISCOELASTIC MATERIALS

A. Narain and D. D. Joseph  
Dept. of Aerospace Engineering and Mechanics  
University of Minnesota  
Minneapolis, MN 55455

This paper extends <sup>the author's</sup> ~~our~~ earlier work [6, 7] on the propagation of jumps in velocity and displacement for shearing deformations imposed impulsively at the boundary of viscoelastic fluids and solids obeying constitutive equations in integral form with arbitrary kernels of fading memory type. The earlier work is briefly reviewed in §1 and we give new results. In §2 we relate old results to experiments. The limiting velocity distribution for start-up of Couette flow between parallel plates is a linear shear. It is common practice to assume that the real motion is close to linear shear long before the stress approaches its asymptotic steady state value. When the simplified kinematics are assumed, the evolution of the wall shear stress is determined by material functions, independent of deformation. These material functions are then determined by experimental measurements. We argue that in some cases only very special features of the material functions can be determined by this method because (in all cases) the early time behavior of the motion is incorrectly given by the kinematic assumption. The assumption that the early part of the stress response can be ignored is at best an approximation when the dynamics shows the presence of a delta function singularity in the wall shear stress at time  $t=0$  and at subsequent discrete times of reflection off bounding walls. This delta function contribution cannot be ignored even if the steady state is achieved rapidly. In fact the early time behavior of the material functions can be obtained from experiments only by using a correct theory based on dynamics rather than kinematical assumptions. When this is done it is possible to interpret data showing stress jumps with linear theories based on commonly used constitutive equations and to interpret early oscillations in the observed values of material functions in terms of repeated reflections off bounding walls. The foregoing remarks apply equally to the interpretation of stress relaxation experiments and other experiments involving impulsive changes in velocity and displacement. In §3 we derive formulas for the amplitude of jumps and reflections for fluids sheared between concentric cylinders. In §4 we develop integral methods of solution analogous to Duhamel integrals for inverting start up problems with arbitrary data perturbing rest. In §5 we apply our analysis to start up for viscoelastic solids and show how creep depends on the kernel of the integral equation.

§1. A Summary of Previous Work on Step Jumps of Velocity and Displacement.

In our earlier work [6], we treated the problems of step increase in velocity and displacement using a constitutive expression of the type:

$$(1.1) \quad \underline{T} = -p\underline{1} + \mu A_{\underline{1}} + \int_0^{\infty} \tilde{\mu}(s) \underline{G}(s) ds$$

where,  $\tilde{\mu}(s) \equiv \frac{dG}{ds}$  and  $G: [0, \infty) \rightarrow \mathbb{R}^+ = \{x \in \mathbb{R} | x > 0\}$

is assumed to be (i) strictly monotonically decreasing, (ii) continuous and piecewise continuously differentiable, (iii) of  $O(e^{-\lambda s})$  as  $s \rightarrow \infty$  for some  $\lambda > 0$  and, whenever needed, we may assume (iv)  $G'(s) < 0$  is strictly monotonically increasing to  $\lim_{s \rightarrow \infty} G'(s) = 0$ .

Constitutive equations such as (1.1) may be justified in various ways (see Saut and Joseph [11] and Renardy [9]). We considered two singular problems in which the velocity is assumed to be in the form  $\underline{v} = \hat{e}_y v(x, t)$  in the semi-infinite space above a flat plate and

$$\Omega = [x, y, z; 0 < x < \infty, -\infty < y < \infty, -\infty < z < \infty].$$

At  $x=0$  we imagine either a step-jump in velocity or displacement, satisfying

$$(1.2) \quad \mu \frac{\partial^2 v}{\partial x^2}(x, t) + \int_0^t G(s) \frac{\partial^2 v}{\partial x^2}(x, t-s) ds = \rho \frac{\partial v}{\partial t}(x, t).$$

$$v(x, 0) = 0,$$

$$v(x, t) \text{ is bounded as } x, t \rightarrow \infty.$$

And for step-increase in velocity at  $x=0$

$$(1.3) \quad v(0, t) = H(t-0) .$$

For the step-increase in displacement of the bottom plate we have

$$(1.4) \quad v(0, t) = \delta(t).$$

§1.1 Linearized Simple Fluids of Maxwell Type ( $\mu=0$ ).

The solution of problem (1.2) and (1.3) is given in §4-6 of [6] as:

$$v(x, t) = f(x, t) H(t-\alpha x)$$

tives at  $s=0$  are unbounded; that is the contact between the vertical axis and the curve  $G(s)$  at  $s=0$  is  $C^\infty$  smooth. Some form of continuity of solution on kernels possessing nearly identical features globally might be expected. For example we may construct kernels with  $G'(0) = -\infty$ , and even with  $C^\infty$  contact at the vertical axis whose graphs are indistinguishable from kernels for which  $G'(0)$  is finite in all neighborhoods bounded away from  $s=0$ . This may lead to smooth, shock like solution (see Fig. 1.1). Such problems are in some sense like the ones which are perturbed with a small viscosity  $\mu$ . We shall remark in §1.3, that the small viscosity leads to a transition layer of size  $\mu$  which collapses onto a shock as  $\mu \rightarrow 0$ . For small  $\mu$  the solution is smooth, but shock like (see Figs. 1.1, 1.3). The heuristic argument for the equivalence of problems for kernels of type (i) with those perturbed by a small viscosity is as follows. We are given  $G(s)$ ,  $s > 0$  such that  $G(0)$  is finite,  $G'(s) < 0$ ,  $s > 0$ , and  $G'(0) = -\infty$ . Now we implement the construction of a comparison kernel of Maxwell type. First choose a small time  $\epsilon$ . Then, at  $G(\epsilon)$  draw the tangent  $G'(\epsilon)$ . This tangent pierces  $s=0$  at the value  $G_M(0)$ . Define  $G_M(s)$

$$G_M(s) = \begin{cases} G'(\epsilon)s + G_M(0), & s \leq \epsilon \\ G(s), & s > \epsilon \end{cases}$$

We may write

$$\int_0^t G(s) \frac{\partial^2 v}{\partial x^2}(x, t-s) ds = \int_0^t G_M(s) \frac{\partial^2 v}{\partial x^2}(x, t-s) ds + \int_0^\epsilon (G(s) - G_M(s)) \frac{\partial^2 v}{\partial x^2}(x, t-s) ds$$

Using the mean value theorem the last integral may be written as

$$\epsilon [G(\bar{s}) - G_M(\bar{s})] \frac{\partial^2 v}{\partial x^2}(x, t-s), \quad 0 < \bar{s} < \epsilon.$$

Then with  $\epsilon \rightarrow 0$  we get  $\bar{s}(\epsilon) \rightarrow 0$  and we approximate the perturbing term with

$$\epsilon [G(0) - G_M(0)] \frac{\partial^2 v}{\partial x^2}(x, t).$$

The approximating problem is like one perturbed by a small viscosity  $\mu = \epsilon [G(0) - G_M(0)]$ .

The reader may notice that the heuristic argument just given applies

to any two kernels which coincide for  $s > \epsilon$ . The implication is that an approximation to the solution corresponding to one kernel may be obtained by solving a problem with the other kernel, perturbed by a viscous term with a suitably selected viscosity coefficient.

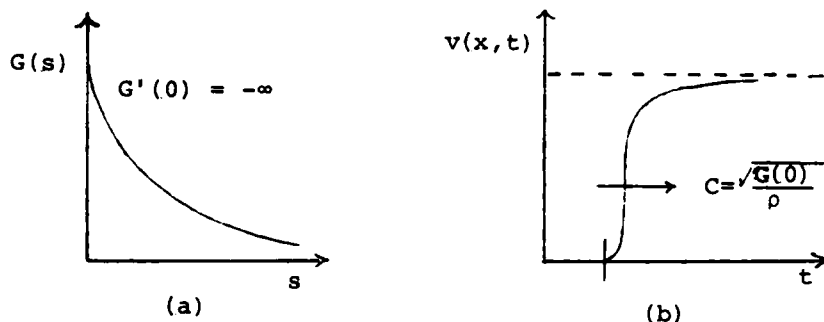


Fig. 1.1.: Propagating smooth solutions (b) occur when  $G(s)$ , satisfying (i), is as sketched in (a).

To establish the above heuristic argument, we let  $f(x,t) = f_1(x,t)$  in (5.10) of [6] be the solution for the kernel with  $G'(0) = -\infty$  and let  $f(x,t) = f_2(x,t)$  be the solution for the comparison kernel  $G(s)$ ,  $G(0) = \tilde{G}(0)$ ,  $\tilde{G}'(s)$  is finite for  $0 \leq s < \epsilon$  and  $\tilde{G}(s) = G(s)$  for  $s \geq \epsilon$ . Then by choosing small  $\epsilon$  we reduce the value of  $|G(iy) - \tilde{G}(iy)|$ . Now invoking the continuity of (5.10) with  $r(y)$  and  $p(y)$ , we find that  $|f_1(x,t) - f_2(x,t)|$  is small.

In the second special case we have

$$(ii) \quad G'(0) = 0.$$

In this case,  $a(x) = 1$ , and

$$\frac{\partial f}{\partial t}(x, \alpha x^+) = \alpha x \left[ \frac{G''(0)}{G(0)} \right].$$

It is necessary that  $G''(0) \geq 0$  if  $G$  is to be strictly monotonically decreasing in  $[0, \infty)$ . For the case in which  $G'(0) > 0$  there will be a velocity over-shoot in the neighborhood of  $t = \alpha x$  at all  $x$ .

where

$$c = \frac{1}{\alpha} = \sqrt{G(0)/\rho}$$

and  $f(x,t)$  is defined in (5.10) of [6]. Here it will suffice to note that (see [10], [6], and [2])

$$a(x) \stackrel{\text{def}}{=} f(x, \alpha x^+) = \exp(\alpha x G'(0)/2G(0)).$$

$$(1.5) \quad \frac{\partial f}{\partial t}(x, \alpha x^+) = -\alpha x \exp\left(\frac{\alpha x G'(0)}{2G(0)}\right) \left[ \frac{3}{8} \left(\frac{G'(0)}{G(0)}\right)^2 - \frac{1}{2} \frac{G''(0)}{G(0)} \right].$$

$$\frac{\partial f}{\partial x}(x, \alpha x^+) = \alpha f(x, \alpha x^+) \left[ \frac{G'(0)}{2G(0)} + \alpha x \left\{ \frac{3}{8} \left(\frac{G'(0)}{G(0)}\right)^2 - \frac{1}{2} \frac{G''(0)}{G(0)} \right\} \right].$$

$$\text{If } G(s) = ke^{-\mu s}, \text{ then } \frac{3}{8} \left(\frac{G'(0)}{G(0)}\right)^2 - \frac{1}{2} \frac{G''(0)}{G(0)} = -\frac{1}{2} \mu^2 < 0.$$

The solution of step-displacement problem (1.2) and (1.4) is given as (see in (10.7) of [6]).

$$(1.6) \quad v(x, t) = \frac{\partial f}{\partial t}(x, t) H(t-\alpha x) + f(x, \alpha x^+) \delta(t-\alpha x)$$

where  $f(x, t)$  is the same as in (1.5).

### §1.2 Special Kernels for Fluids of the Maxwell Type ( $\mu=0$ ).

There are two special cases ( $G'(0) = -\infty$ ,  $G'(0)=0$ ):

$$(i) \quad G'(0) = -\infty \text{ and } 0 < G(0) < \infty$$

In this case the amplitude  $a(x)$  of the shock (given in (1.5)) is zero. Thus the discontinuity of the data is removed but the support of the solution propagates with the speed  $c = \frac{1}{\alpha}$ .

In fact Renardy [8] has shown that for a kernel (used in certain molecular models)

$$G'(s) = -\sum_{n=1}^{\infty} \exp(-n\alpha s), \quad \alpha > 1,$$

$$G'(0) = -\infty,$$

$$G(0) = \sum_{n=1}^{\infty} \frac{1}{n\alpha}$$

the solution is  $C^\infty$  smooth at the support (see Fig. 1.1). It may be noted that the special kernel used by Renardy is such that all of its deriva-

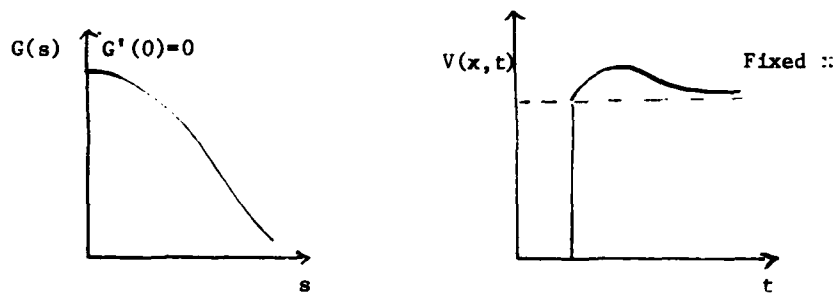


Fig. 1.2: Shock profile for the case  $G'(0) = 0$ .

### §1.3 Viscosity and Transition Layers

Consider the problem of a step increase of velocity for Newtonian fluids ( $\mu > 0$ ,  $\tilde{u}(s) \equiv 0$  in (1.1)). The classical solution of this problem ((1.2), (1.3)) is given by:

$$(1.7) \quad v(x, t) = \operatorname{erfc}(x/\sqrt{4\nu t})$$

where  $\nu = \frac{\mu}{\rho}$ , and  $\operatorname{erfc}$  is the complementary error function.

If  $\mu > 0$  is small and  $G$  has the assumed properties, it can be shown (see §18 of [6]) that there is a transition layer around the shock solution with  $\mu = 0$ . This smooth transition layer exists in a bounded domain of  $\{(x, t) \mid x > 0 \text{ and } t > 0\}$  and its thickness scales with  $\mu$ . Thus:

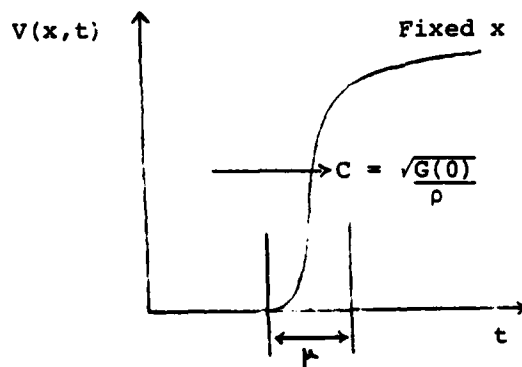


Fig. 1.3.: Transition layers when  $\mu > 0$  is small.

52 Remarks on the Experimental Determination of Relaxation Functions.

Many experimental measurements of relaxation functions are based on the incorrect assumption that a linear velocity profile (which is the asymptotic state for the problem of step change in velocity) can be achieved impulsively (see Fig. 2.1-2.3)

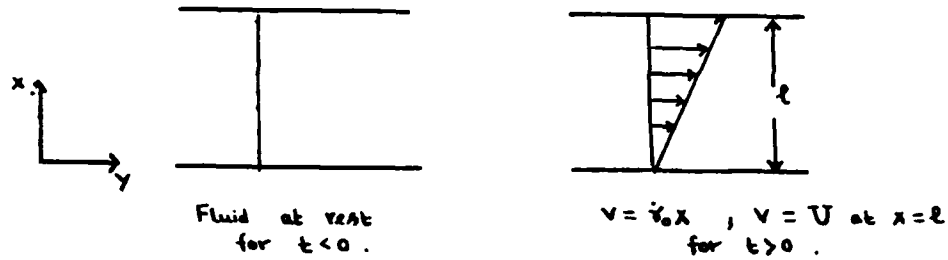


Fig. 2.1: Assumed "solution" for the step increase in velocity. The stress is measured after times  $t > 0$ . The relaxation function is determined from the constitutive equation on the assumed, dynamically inadmissible, velocity field.

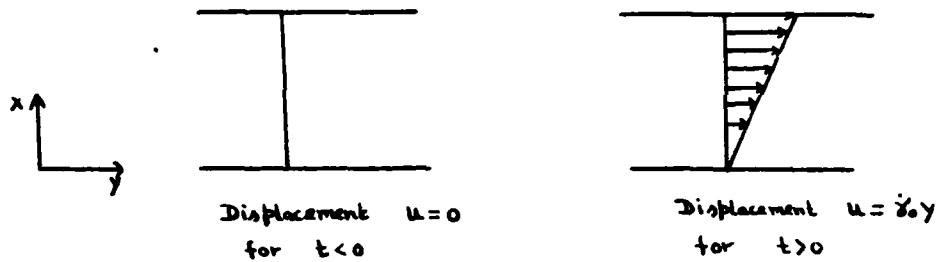


Fig. 2.2: Assumed "solution" for the step increase in displacement. The stress is measured at times  $t > 0$ . The relaxation function is determined from evaluating the constitutive equation on the assumed dynamically inadmissible, deformation field.

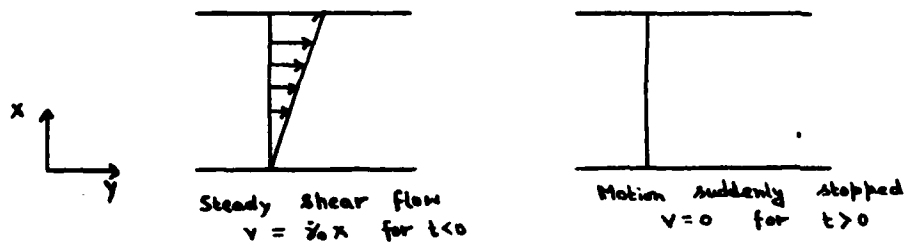


Fig. 2.3: Assumed "solution" for sudden cessation of motion. The stress is measured at times  $t > 0$ . The relaxation function is determined

from evaluating the constitutive equation on the assumed dynamically inadmissible deformation field.

However we have shown that the deformation assumed in Figs. 2.1 - 2.3 cannot be achieved at finite times on solutions of the initial-boundary value problem in the realm of linear viscoelasticity. The deformations assumed are in fact limiting cases for  $t \rightarrow \infty$ . It is therefore necessary to explain how and in what sense the customary methods of determining relaxation functions have validity. The following observations are important:

(1) The customary methods can always be used to measure "viscosity" ( $\mu + \int_0^{\infty} G(s) ds$ ) by measurement at large times. But the test is inadequate to determine separately  $\mu$  and  $\int_0^{\infty} G(s) ds$ .

(2) Suppose  $\mu=0$ , then the customary methods measure the stress on the stationary plate as a function of time. We are here concerned with the question whether the experimental measurement is going to be close to the relaxation function as indicated by the assumed kinematics of Fig. 1.4. In the context of linear viscoelasticity, we will show that this experimental measurement will never give the integral  $\int_0^t G(s) ds$  for small time  $t$  near zero. However, this integral can be close to measured values for large times provided that the half life time of discontinuities is small. For simple Maxwell models with non-zero values of  $|G'(0)|$ , this time can be estimated as  $-G(0)/G'(0)$ .

To obtain expressions for the shear stress at the wall we consider the dynamics solution given in §8 of [6] for the step increase in velocity (see Fig. 2.1). In that solution the moving plate is at  $x=0$  and the stationary plate is at  $x=l$ . For the case in which the moving plate is at  $x=l$  we ultimately have simple shear  $U(1-\frac{x}{l})$  as  $t \rightarrow \infty$  with shear rate  $\frac{\partial v}{\partial x} \stackrel{\text{def}}{=} -\dot{\gamma}_0 = -\frac{U}{l}$ . The solution of this problem is:

$$(2.1) \quad v(x,t) = U[f(x,t)H(t-\alpha x) + \{f(x+2l,t)H(t-\alpha(x+2l)) - f(2l-x,t)H(t-\alpha(2l-x))\} + \{\dots\} + \dots].$$

The stress at the wall  $x=0$  and  $x=l$  is given by:

$$(2.2) \quad T^{<xy>}(0,t) = \int_0^t G(s) \frac{\partial v}{\partial x}(0,t-s) ds$$

and

$$(2.3) \quad T^{<xy>}(l,t) = \int_0^t G(s) \frac{\partial v}{\partial x}(l,t-s) ds. \quad 506$$

If we assume an instantaneous deformation as in Fig. 2.1, then (1.5) implies that

$$(2.4) \quad T^{<xy>}(x, t) = -\frac{U}{l} \int_0^t G(s) da, \quad x \in [0, l].$$

However (2.1) implies that

$$(2.6) \quad \frac{\partial v}{\partial x}(0, t) = U \left\{ \frac{\partial f}{\partial x}(0, t) H(t-0) - \alpha f(0, t) \delta(t-0) \right\} \\ + 2 \left\{ \frac{\partial f}{\partial x}(2l, t) H(t-(2\alpha l)) - \alpha f(2l, t) \delta(t-(2\alpha l)) \right\} \\ + 2 \{ \dots \} + \dots,$$

and

$$(2.7) \quad \frac{\partial v}{\partial x}(l, t) = 2U \left\{ \frac{\partial f}{\partial x}(l, t) H(t-\alpha l) - \alpha f(l, t) \delta(t-\alpha l) \right\} \\ + \left\{ \frac{\partial f}{\partial x}(3l, t) H(t-\alpha(3\alpha l)) - \alpha f(3l, t) \delta(t-(3\alpha l)) \right\} \\ + \{ \dots \} + \dots.$$

Combining (2.6) and (2.2), we find that in the time interval  $0 < t < \alpha(2l)$ , the stress at the driving plate is

$$(2.8) \quad T^{<xy>}(0, t) = U \int_0^t G(t-s) \frac{\partial f}{\partial x}(0, s) ds - U \alpha G(t) f(0, 0^+)$$

but equation (1.5) implies that

$$U f(0, 0^+) = v(0, 0^+) = U.$$

Hence,

$$(2.9) \quad -T^{<xy>}(0, 0^+) = U \sqrt{\rho G(0)}.$$

Combining (1.13) and (1.10) we get

$$(2.10) \quad T^{<xy>}(l, t) = 0 \text{ for } 0 < t < \alpha l \text{ and}$$

$$(2.11) \quad -T^{<xy>}(l, \alpha l^+) = 2U \sqrt{\rho G(0)} \exp\left(\frac{\alpha l G'(0)}{2G(0)}\right).$$

In general, for  $t > (2n\alpha l)$ ;  $n=1, 2, \dots$  we find by combining

(2.6) and (2.7) with (2.2) and (2.3) that

$$(2.12) \quad -T^{<xy>}(0, t) = \left[ -\int_0^t G(t-s) \frac{\partial f}{\partial x}(0, s) ds + \alpha G(t) \right] \\ + 2 \left[ -\int_0^t G(t-s) \frac{\partial f}{\partial x}(2\ell, s) ds + G(t-(2\alpha\ell)) \exp\left(\frac{G'(0)}{2G(0)} 2\alpha\ell\right) \right] \\ (2\alpha\ell) \\ + 2[\dots] + \dots$$

and

$$(2.13) \quad -T^{<xy>}(\ell, t) = 2U[\alpha G(t-\alpha\ell) f(\ell, \alpha\ell^+) - \int_{\alpha\ell}^t G(t-s) \frac{\partial f}{\partial x}(\ell, s) ds] \\ + 2U[\alpha G(t-(3\alpha\ell)) f(3\ell, (3\alpha\ell)^+) - \int_{3\alpha\ell}^t G(t-s) \frac{\partial f}{\partial x}(3\ell, s) ds] \\ (3\alpha\ell) \\ + 2[\dots] + \dots$$

In order to understand (2.12) and (2.13), we need to know some features of the function  $\frac{\partial f}{\partial x}(2n\ell, t)$  for  $n=0, 1, 2, \dots$ . For a Maxwell fluid  $G(s) = Ke^{-\mu s}$  and (see (7.3) of [6]):

$$(2.14) \quad -\frac{\partial f}{\partial x}(x, t) = -U \sqrt{\frac{\rho\mu^2}{K}} \frac{\partial \hat{f}}{\partial \hat{x}}(\hat{x}, \hat{t}) \quad \text{where } \hat{x} = \sqrt{\frac{K}{\rho\mu^2}} \hat{x}, \quad t = \frac{1}{\mu} \hat{t} \\ \frac{\partial \hat{f}}{\partial \hat{x}}(\hat{x}, \hat{t}) = -\frac{1}{2} e^{-\frac{\hat{x}}{2}} - \frac{\hat{x}}{8} e^{-\frac{\hat{x}}{2}} + \frac{1}{2} \int_{\hat{x}}^{\hat{t}} \frac{e^{-\frac{\sigma}{2}}}{\sqrt{\sigma^2 - \hat{x}^2}} I_1\left(\frac{1}{2}\sqrt{\sigma^2 - \hat{x}^2}\right) d\sigma \\ + \frac{\hat{x}^2}{2} \int_{\hat{x}}^{\hat{t}} \frac{e^{-\frac{\sigma}{2}}}{(\sigma^2 - \hat{x}^2)} \left\{ \frac{I_1\left(\frac{1}{2}\sqrt{\sigma^2 - \hat{x}^2}\right)}{\sqrt{\sigma^2 - \hat{x}^2}} - \frac{1}{2} I_1'\left(\frac{1}{2}\sqrt{\sigma^2 - \hat{x}^2}\right) \right\} d\sigma$$

We also recall that when a steady state  $v(x, \infty) = \frac{U(\ell-x)}{\ell}$  is approached we have

$$(2.15) \quad \lim_{t \rightarrow \infty} T(x, t) = -\frac{U}{\ell} \int_0^\infty G(s) ds, \quad x \in [0, \ell].$$

There are two cases to consider: (i)  $\sqrt{G(0)\rho} > \ell^{-1} \int_0^\infty G(s) ds$  and (ii)  $G(0)\rho < \ell^{-1} \int_0^\infty G(s) ds$ . In the first case the initial value of the stress is larger than the final value (overshoot). A typical graph is sketched in Fig. 2.4(i). In the second case there is a jump of stress less than the steady state value. This case is sketched in Fig. 2.4(ii).

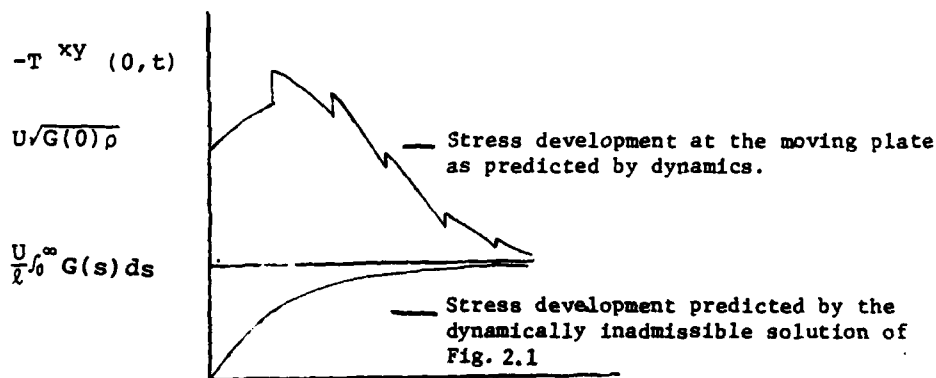


Fig. 2.4 (i)

Stress development at the lower wall of a channel filled with a viscoelastic fluid of Maxwell type under a step change of shear.

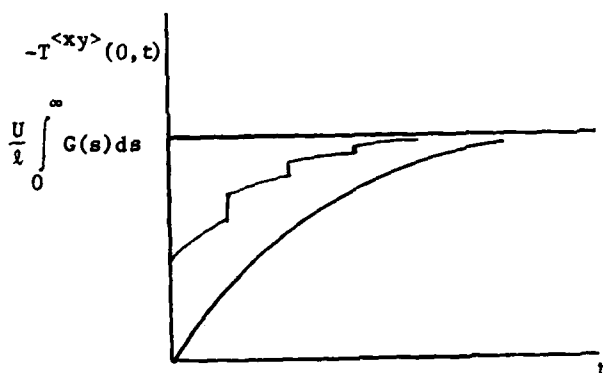


Fig. 2.4 (ii)

Stress development at the lower wall of a viscoelastic fluid of Maxwell type under a step change of shear.

Of course the amplitude of jumps in Fig. 2.4 (i), (ii) ultimately tend to steady state value. Moreover in the two special cases  $G'(0) = -\infty$  or  $\mu > 0$  and small we will have essentially the same response as in Figs. 2.4 with smooth bumps replacing jumps. In any experiment the jumps (for  $\mu = 0$ ) would not be vertical because step changes at the boundary are discontinuous idealizations of smooth rapid changes and if  $v(0,t)$  is a continuous function close to  $UH(t-0)$ , then  $T^{<xy>}(0,0^+) = 0$  but  $T^{<xy>}(0, \epsilon_1) \approx U\sqrt{G(0)\rho}$  and  $T^{<xy>}(l, \epsilon_2) \approx 2U\sqrt{G(0)\rho} \exp(\frac{\alpha l G'(0)}{2G(0)})$  for some  $\epsilon_1, \epsilon_2 > 0$  and small. This observation follows as a consequence of the continuous dependence of the solution on the data [6] and our solution for arbitrary initial data.

The aforementioned results may be applied to the interpretation of experiments by Meissner [5], Huppler et al [3], among others. They plot

$$\frac{T^{<xy>}(0,t)}{T^{<xy>}(0,\infty)} \stackrel{\text{def}}{=} \frac{\eta^+(t)}{\eta_0}$$

where

$$\begin{aligned} T^{<xy>}(0,t) &\stackrel{\text{def}}{=} -\dot{\gamma}_0 \eta^+(t) \\ &= -\frac{U}{l} \eta^+(t), \\ \eta_0 &= \int_0^\infty G(s) ds \end{aligned}$$

Our analysis shows that at the driving plate

$$\frac{\eta^+(0^+)}{\eta_0} = \frac{l\sqrt{G(0)\rho}}{\int_0^\infty G(s) ds}$$

Where  $\frac{\eta^+(\infty)}{\eta_0} = 1.$

The stress response at the stationary wall is given by

$$\frac{T^{<xy>}(l, \alpha l^+)}{T^{<xy>}(l, \infty)} = \frac{\eta^+(\alpha l^+)}{\eta_0} = \frac{2l\sqrt{\rho G(0)}}{\int_0^\infty G(s) ds} \exp\left(\frac{\alpha l G'(0)}{2G(0)}\right)$$

Where,  $\frac{\eta^+(\infty)}{\eta_0} = 1$

Typical representations of experimental results of various authors are represented schematically in Fig. 2.5 (cf. Bird, Armstrong and Hassager, [1] Fig. A.4-9).

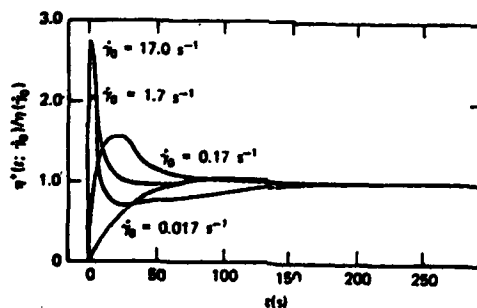


Fig. 2.5

Representations of stress development in a parallel plate channel under a step change of velocity. These representations are supposed to represent the results of experiments.

The experimental results represented in Fig. 2.5 do not exhibit the stress jumps, at small rates of shear, which are required by linearized dynamics. It is possible that the conditions of the experiments were such as to make the initial jumps in stress small relative to asymptotic ( $t \rightarrow \infty$ ) levels of stress. However, stress overshoot could possibly occur even in the realm of linear theory. We cannot know whether or not overshoots do occur without reliable estimates of  $G(0)$ . The methods which are presently used to determine  $G(0)$  are inadequate because they do not apply at small times. Some micro-molecular models like those of Kee and Carreau [4], have tried to explain this overshoot by allowing for such features in a "non-linear stress-strain history model" when evaluated at a kinematic assumption of Fig. 1.4. We believe it is now apparent that any such modeling on the above experimental data is meaningless if the dynamics are going to be neglected.

It is perhaps also possible to explain the oscillations at small times in the stress observed by Meissner [5] in terms of larger amplitudes of stress which are generated by reflections off bounding walls for fluids of the type which support shocks or near shocks (fluids with  $G(0) < \infty$ ,  $-G'(0) \leq \infty$  with or without a small viscosity.) Nonlinearity also participates in the results observed at high shears. For example, the narrowing of the width of peak region in the graphs shown in Fig. 2.5 may not be entirely explained by linear theory.

### §2.1 The stress response for the step displacement problem

This problem is associated with Fig. 2.2. The kinematic assumption mentioned in the caption of that figure leads to a direct formula

$$(2.16) \quad \frac{U}{l} G(t) = -T^{<xy>}(0, t) .$$

The dynamic solution for the linearized problem associated with that experiment is given in §12 of Eq. [6]. Following procedures used to obtain (2.9), (2.11) and (2.15) we find

$$(2.17) \quad -T^{<xy>}(0, 0^+) = \frac{U}{2} G'(0) \sqrt{\frac{\rho}{G(0)}} < 0$$

and

$$(2.18) \quad T^{<xy>}(0, \infty) = 0 .$$

At the stationary plate we have

$$(2.19) \quad -T^{<xy>}(\ell, \alpha\ell^+) = 2U[-G(0)\frac{\partial f}{\partial x}(\ell, \alpha\ell^+) + \alpha G'(0) f(\ell, \alpha\ell^+)]$$

and

$$T^{<xy>}(\ell, \infty) = 0$$

Eq. (2.16) may be a correct representation of linearized dynamics for large  $t$  but it is a false representation of linearized dynamics for small  $t$ .

## §2.2 Summary

The asymptotic values of  $G(t)$  for large  $t$  can be obtained in the usual way using the kinematic assumptions exhibited in Figs. 1.5 and 1.6. The early time behavior of  $G(t)$  is not well represented by the asymptotic solution and at least should be correlated with the results of dynamic analysis. In the context of linearized dynamics which should be valid at least for small shears, we find that

$$-T^{<xy>}(0, 0^+) = U\sqrt{G(0)\rho}$$

$$-T^{<xy>}(\ell, \alpha\ell^+) = 2U\sqrt{\rho G(0)} \exp(\alpha\ell G'(0)/2G(0))$$

for the step change in velocity. Here  $\ell$  is the distance from the driving plate at  $x=0$  to the stationary plate and  $\alpha\ell$  is the time of first reflection. In the problem of the step change in displacement, we find that

$$-T^{<xy>}(0, 0^+) = \frac{U}{2} G'(0) \sqrt{\frac{\rho}{G(0)}} < 0$$

$$-T^{xy}(\ell, \alpha\ell^+) = 2U[-G(0)\frac{\partial f}{\partial x}(\ell, \alpha\ell^+) + \alpha G'(0) f(\ell, \alpha\ell^+)]$$

It may be useful to reinterpret existing experimental results in terms of the dynamic theory. For example, the constants  $\kappa_i$  and  $\mu_i$  appearing in the Maxwell model with finitely many relaxation times

$$G(s) = \sum_{i=1}^N \kappa_i e^{-\mu_i s} \quad 512$$

could, in principle, be determined by comparing experimental results with formulas which could be obtained from the analysis of the type of Kazakia and Rivlin [10].

It may be true that conclusions similar to the ones which we have considered here for experiments with viscoelastic fluids apply in the theory of viscoelastic solids [7].

§3 Cylindrical vortex sheets generated by sudden spin up of a cylinder in a fluid

The problem of spin up was considered in §14 of [6]. In this case the velocity of shearing motion is in circles

$$\underline{v}(\underline{x}, t) = w(r, t) \underline{e}_\theta$$

and  $w(r, t)$  is defined in

$$D = \{r \geq a, 0 \leq \theta \leq 2\pi, -\infty < z\}$$

The boundary value problem for sudden spin up is given (see (14.8) of [6]) by

$$\rho \frac{\partial w}{\partial t}(r, t) = \int_0^t G(s) \left[ \frac{\partial^2 w}{\partial r^2}(r, t-s) + \frac{1}{r} \frac{\partial w}{\partial r}(r, t-s) - \frac{w(r, t-s)}{r^2} \right] ds, \quad (3.1)$$

$$w(a, t) = \begin{cases} a \Omega = 1 & \text{for } t > 0 \\ 0 & \text{for } t < 0 \end{cases}$$

$$w(r, 0) = 0, \quad r \geq a > 0,$$

$$w(r, t) \text{ is bounded as } r, t \rightarrow \infty$$

We showed in [6] that the solution of (3.1) is given by

$$(3.2) \quad w(r, t) = g(r, t) H(t - (r-a)\alpha).$$

where  $g(r, t)$  is defined in (14.16) of [6]. Here we derive a simpler form for  $g(r, \alpha(r-a)^+)$  than the one given by (14.19) of [6]. This derivation follows along lines leading to the formulas (5.21), (5.23) in [6].

We know from (14.11) of [6] that

$$(3.3) \quad w(r, t) = \frac{1}{2\pi i} \int_{\gamma-i\infty}^{\gamma+i\infty} \frac{e^{ut}}{u} \frac{K_1\left(r\sqrt{\frac{\rho u}{G(u)}}\right)}{K_1\left(a\sqrt{\frac{\rho u}{G(u)}}\right)} du; \quad u \quad \text{Re } u > 0$$

where  $K_1$  is a modified Bessel function whose asymptotic form is given by

$$(3.4) \quad K_1(z) = \sqrt{\frac{\pi}{2z}} \exp(-z) + o\left(\frac{1}{z}\right)$$

The asymptotic expansion

$$(3.5) \quad \bar{G}(u) = \frac{G(0)}{u} + \frac{G'(0)}{u^2} + o\left(\frac{1}{u^3}\right)$$

was established as (5.16) of [6].

It is easy to verify that:

$$(3.6) \quad \sqrt{\frac{\rho u}{G(u)}} = \sqrt{\frac{\rho}{G(0)}} u - \sqrt{\frac{\rho}{G(0)}} \frac{G'(0)}{2G(0)} + o\left(\frac{1}{u}\right) \\ = \alpha u - \frac{\alpha G'(0)}{2G(0)} + o\left(\frac{1}{u}\right).$$

Equation (3.4) and (3.6) imply that

$$(3.7) \quad \frac{K_1\left(r \sqrt{\frac{\rho u}{G(u)}}\right)}{K_1\left(a \sqrt{\frac{\rho u}{G(u)}}\right)} = \sqrt{\frac{a}{r}} \exp\left[(r-a) \frac{\alpha G'(0)}{2G(0)}\right] \exp\left[-\alpha u(r-a)\right] + o\left(\frac{1}{u}\right) \\ = \sqrt{\frac{a}{r}} \exp\left[(r-a) \frac{\alpha G'(0)}{2G(0)}\right] \exp\left[-\alpha u(r-a)\right] + o\left(\frac{1}{u}\right)$$

Substituting (3.7) into (3.3), we get:

$$(3.8) \quad w(r,t) = \frac{1}{2\pi i} \exp\left[\frac{(r-a)\alpha G'(0)}{2G(0)}\right] \int_{\gamma-i\infty}^{\gamma+i\infty} \sqrt{\frac{a}{r}} \frac{e^{u\{t-\alpha(r-a)\}}}{u} du \\ + \frac{1}{2\pi i} \int_{\gamma-i\infty}^{\gamma+i\infty} e^{ut} o\left(\frac{1}{u^2}\right) du \\ = \sqrt{\frac{a}{r}} \exp\left[\frac{(r-a)\alpha G'(0)}{2G(0)}\right] H(t-\alpha(r-a)) \\ + \frac{1}{2\pi i} \int_{\gamma-i\infty}^{\gamma+i\infty} e^{ut} o\left(\frac{1}{u^2}\right) du.$$

The last term in (3.8) is continuous  $r \geq a$  and  $t \geq 0$  because the integral is uniformly convergent for any fixed  $r, t$ . Comparing (3.8) with (3.2) while using the continuity of the second term in (3.8) we get

$$(3.9) \quad g(r, \alpha(r-a)^+) = \sqrt{\frac{a}{r}} \exp\left[\frac{(r-a)\alpha G'(0)}{2G(0)}\right]. \quad 515$$

The decay with  $r$  of cylindrical vortex sheets is more rapid than plane sheets which damp according to (1.5) without the factor  $r^{-1/2}$ .

We next consider the problem of reflections off the walls of concentric cylinders which bound a fluid occupying the region

$$\hat{D} = \{a < r \leq b, 0 \leq \theta < 2\pi, -\infty < z < \infty\}$$

The spin up problem may be stated as follows

$$\begin{aligned} \rho \frac{\partial w}{\partial t} &= \int_0^t G(s) \frac{\partial^2 w}{\partial r^2}(r, t-s) + \frac{1}{r} \frac{\partial w}{\partial r}(r, t-s) - \frac{w(r, t-s)}{r^2} ds, \\ w(a, t) &= \begin{cases} a\Omega = 1 & \text{for } t > 0 \\ 0 & \text{for } t \leq 0 \end{cases} \\ (3.10) \quad w(b, t) &= 0 \quad t \quad , \\ w(r, 0) &= 0 \quad r \quad [a, b] \quad , \\ w(r, t) &\text{ is bounded as } r, t \rightarrow \infty. \end{aligned}$$

We now utilize the method of Laplace transforms, following arguments given in §6 of [6] and find that

$$(3.11) \quad w(r, t) = \frac{1}{2\pi i} \int_{\gamma-i\infty}^{\gamma+i\infty} e^{ut} \bar{w}(r, u) du$$

where

$$(3.12) \quad \bar{w}(r, u) = \frac{1}{u} \frac{I_1(bn(u))K_1(rn(u)) - K_1(bn(u))I_1(rn(u))}{K_1(an(u))I_1(bn(u)) - K_1(bn(u))I_1(an(u))} ,$$

$$n(u) = \sqrt{\frac{\rho u}{G(u)}} .$$

An asymptotic form for (3.11) follows from combining the asymptotic expressions for  $|z| \rightarrow \infty$

$$(3.13) \quad \begin{aligned} I_1(z) &= \frac{e^z}{\sqrt{2\pi z}} + o\left(\frac{1}{z}\right) \\ K_1(z) &= \frac{\pi}{\sqrt{2z}} e^{-z} + o\left(\frac{1}{z}\right) \end{aligned}$$

with (3.12). Thus

$$\bar{w}(r, u) = \sqrt{\frac{a}{r}} \frac{e^{(b-r)\eta(u)} - e^{-(b-r)\eta(u)}}{e^{(b-a)\eta(u)} - e^{-(b-a)\eta(u)}} + o\left(\frac{1}{u}\right).$$

Hence

$$(3.14) \quad w(r, t) = \sqrt{\frac{a}{r}} \frac{1}{2\pi i} \int_{\gamma-i\infty}^{\gamma+i\infty} \frac{e^{ut}}{u} \frac{e^{(b-r)\eta(u)} - e^{-(b-r)\eta(u)}}{e^{(b-a)\eta(u)} - e^{-(b-a)\eta(u)}} du$$

$$+ \frac{1}{2\pi i} \int_{\gamma-i\infty}^{\gamma+i\infty} e^{ut} o\left(\frac{1}{u}\right) du$$

We next note that the first term in (3.14) is the same as in (8.3)-(8.7) of §8 of [6] if we set  $r-a = x$ , and  $b-a = \ell$ . The second term in (3.14), being uniformly convergent for any  $r$  and  $t$ , in a continuous function of  $r$  and  $t$ . Thus

$$(3.15) \quad w(r, t) = \sqrt{\frac{a}{r}} \left[ f(x, t) H(t-\alpha x) + \{ f(x+2\ell, t) H(t-\alpha(x+2\ell)) - f(2\ell-x, t) H(t-\alpha(2\ell-x)) \} + \dots \right] + h(x, t)$$

The function  $f$  in (3.15) is the same  $f$  appearing in (1.5) while  $h(x, t)$  is continuous for  $x = r-a \in [0, \ell]$  and  $t \geq 0$ . It follows from (3.15) that discontinuities are reflected along the characteristic lines shown in Fig. 3.1.

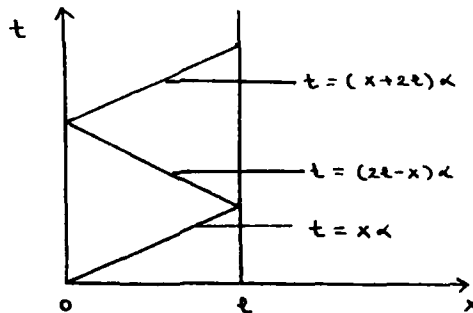


Fig. 3.1. Characteristic lines for reflection from the walls of concentric cylinders,  $x = r-a$ ,  $\ell = b-a$

The asymptotic steady state in case of flow governed by (1.20) is given by:

$$\lim_{t \rightarrow \infty} w(r, t) = \lim_{u \rightarrow 0} u \bar{w}(r, u)$$

Using (1.22) and

$$\left. \begin{aligned} I_1(z) &\sim \frac{2}{4} \\ K_1(z) &\sim \frac{1}{z} \end{aligned} \right\} \text{ as } z \rightarrow 0 \text{ and } \operatorname{Re} z > 0$$

we get

$$\begin{aligned} (3.16) \quad \lim_{t \rightarrow \infty} w(r, t) &= \frac{\frac{b}{r} - \frac{r}{b}}{\frac{b}{a} - \frac{a}{b}} \\ &= \frac{a}{r} \frac{b^2 - r^2}{b^2 - a^2}, \quad \text{for } a\Omega = 1. \end{aligned}$$

§4 Solutions of start up problems with arbitrary boundary data by integrals of Duhamel's type

A shearing motion is initiated at  $x=0$  by data of the form

$$v(0,t) = \begin{cases} g(t) & , t > 0 \\ 0 & , t < 0 \end{cases}$$

where  $g(t)$  is an arbitrary function (possessing a Laplace transform). The velocity  $V(x,t)$  then satisfies

$$(4.1) \quad \int_0^t G(s) \frac{\partial^2 v}{\partial x^2}(x,t-s) ds = \rho \frac{\partial v}{\partial t}(x,t)$$

$$v(0,t) = g(t), \text{ where } g(t) \equiv 0 \quad t < 0$$

$$v(x,0) = 0 \quad x \geq 0$$

$v(x,t)$  is bounded

We shall solve (4.1) by superposition using the solution of the following singular problem:

$$\int_0^t G(s) \frac{\partial^2 u}{\partial x^2}(x,t-s) ds = \rho \frac{\partial u}{\partial t}(x,t)$$

$$u(0,t) = \delta(t-\tau), \quad \tau(0,t)$$

$$u(x,0) = 0 \quad x \geq 0$$

$u(x,t)$  is bounded for  $x, t \rightarrow \infty$ .

It is easy to see and not hard to prove that the solution of (4.2) is the time-derivation of the solution of (3.1) where

$$v(0,t) = \begin{cases} 1 & \text{for } t > \tau \\ 0 & \text{for } t \leq \tau. \end{cases}$$

It then follows that the solution of (4.2) is

$$(4.3) \quad u(x,t) = \frac{\partial f}{\partial t}(x, t-T) H(t-T-ax) \\ + f(x, ax^+) (t-T-ax)$$

Of course (4.3) can be obtained directly as the inverse of the Laplace

transform of (4.2). (The details of the type of calculation are given in §10 of [6]). We note that  $t$  in the upper limit of integration in the integral on the left of (4.2), may be replaced with  $t+\delta$ ,  $\delta>0$  because  $u(x,-\delta) = 0$  for  $\delta>0$ . The interpretation of the  $\delta$  function which this implies may be expressed as follows: for any  $h(s)$  such that  $h(s) = 0$ ,  $s<0$  we have

$$\int_{-\infty}^{\infty} h(s) \delta(s) ds = \int_0^{\infty} h(s) \delta(s) ds = h(0)$$

We now assert that the solution of problem (4.1) in a linear superposition (integration) of the function  $g(\tau) u(x,t)$ . This is true because

$$\begin{aligned} (4.4) \quad v(0,t) &= g(t) = \int_0^{\infty} g(t-\eta) \delta(\eta) d\eta = \int_0^t g(t-\eta) \delta(\eta) d\eta \\ &= \int_0^t g(\tau) \delta(t-\tau) d\tau \end{aligned}$$

Using (4.3) and (4.4), we find that the solution of (4.1) is

$$\begin{aligned} (4.5) \quad v(x,t) &= \int_0^t g(\tau) u(x,t) d\tau \\ &= \int_0^t g(\tau) \left[ \frac{\partial f}{\partial t} (x, t-\tau) H(t-\tau-ax) + f(x, ax^+) \delta(t-\tau-ax) \right] d\tau \end{aligned}$$

It follows from (2.5) that if

$$(4.6) \quad t-ax < 0 \text{ then } v(x,t) = 0$$

This implies that the information of rest prior to start-up is always preserved. On the other hand, when  $t-ax > 0$ , (4.5) gives

$$\begin{aligned} (4.7) \quad v(x,t) &= \int_0^{t-ax} g(\tau) \frac{\partial f}{\partial t} (x, t-\tau) d\tau + f(x, ax^+) \int_0^{t-ax} g(t-ax-\eta) \delta(\eta) d\eta \\ &= \int_0^{t-ax} g(\tau) \frac{\partial f}{\partial t} (x, t-\tau) d\tau + f(x, ax^+) g(t-ax) \\ &= \int_0^{t-ax} g(\tau) \frac{\partial f}{\partial t} (x, t-\tau) d\tau + \exp\left(\frac{\alpha x G'(0)}{2G(0)}\right) g(t-ax) \end{aligned}$$

It is easy to verify that (4.7) reduces to (1.5) for  $g(\tau) = H(\tau)$  and (1.6) for  $g(\tau) = \delta(\tau)$ . Eqs. (4.6) and (4.7) together constitute the solution of the problem posed in (4.1). Thus we conclude that discontinuities in the boundary values of  $g$  or its derivatives propagate into the interior with speed  $C=1/\alpha$ . Hence (4.7) also proves that any discontinuity in a start-up problem of linear viscoelasticity can come only through the boundary data. It is also clear from (4.7), that this propagating discontinuity is exponentially damped.

We turn next to the construction of the solution of start-up problems between parallel plates. The problem to be solved may be expressed as:

$$(4.8) \quad \int_0^t G(s) \frac{\partial^2 v}{\partial x^2}(x, t-s) ds = \rho \frac{\partial v}{\partial t}$$

$$v(0, t) = g(t) \quad ; \quad \text{when } g(t) \equiv 0 \quad t < 0$$

$$v(l, t) = 0$$

$$v(x, 0) = 0$$

$$v(x, t) \text{ is bounded as } t \rightarrow \infty.$$

Proceeding as in the previous problem we first consider the case in which  $g(t) = \delta(t-\tau)$ . The  $\hat{v}(x, t)$  for this singular problem is given by

$$\hat{v}(x, t) = [\psi(x, t-\tau) + \{\psi(x+2l, t-\tau) - \psi(2l-x, t-\tau)\} \\ + \dots]$$

where

$$(4.9) \quad \psi(x, t) = \frac{\partial f}{\partial t}(x, t) H(t-\alpha x) + f(x, \alpha x^+) \delta(t-\alpha x)$$

The function  $f(x, t)$  in (4.9) is defined by (1.5). We now use the principle of superposition to compose the solution of (4.8) in Duhamel form

$$(4.10) \quad v(x, t) = \int_0^t g(\tau) \hat{v}(x, t) d\tau$$

$$\begin{aligned}
&= \int_0^t g(\tau) \left[ \frac{\partial f}{\partial t}(x, t-\tau) + \left\{ \frac{\partial f}{\partial t}(x+2l, t-\tau) - \frac{\partial f}{\partial t}(2l-x, t-\tau) \right\} \right. \\
&\quad + \dots \left. \right] H(t-\tau-\alpha x) \\
&\quad + \{ f(x, \alpha x^+) g(t-\alpha x) + \{ f(2l+x, \alpha(2l+x)^+) g(t-\alpha x) \\
&\quad - f(2l-x, \alpha(2l-x)) g(t-\alpha x) \} + \dots \} d\tau
\end{aligned}$$

The dots in (4.10) represent similar terms arising out of repeated reflection between the walls at  $x=0$  and  $x=l$  of the original characteristic  $t-\alpha x = \text{const.}$  It also follows from (4.10) that  $v(x,t)=0$  when  $t-\alpha x < 0$  and, when  $t-\alpha x > 0$  we find that:

$$\begin{aligned}
(4.11) \quad v(x,t) &= \int_0^{t-\alpha x} g(\tau) \left[ \frac{\partial f}{\partial t}(x, t-\tau) + \left\{ \frac{\partial f}{\partial t}(x+2l, t-\tau) - \frac{\partial f}{\partial t}(2l-x, t-\tau) \right\} \right. \\
&\quad + \dots \left. \right] d\tau + \left[ f(x, \alpha x^+) g(t-\alpha x) + \{ f(2l+x, \alpha(2l+x)^+) \right. \\
&\quad \left. g(t-\alpha x) - f(2l-x, \alpha(2l-x)^+) g(t-\alpha x) \} + \dots \right]
\end{aligned}$$

We may use (4.11) to study the interactions of multiple shocks generated by multiple discontinuities in the boundary data  $g(t)$ . For example, consider

$$(4.12) \quad g(t) = \begin{cases} 0 & \text{for } t < 0 \\ 1 & \text{for } 0 \leq t \leq 1 \\ 0 & \text{for } t > 1 \end{cases}$$

It follows from (4.11) that the discontinuities of  $g(t)$  propagate along the characteristic lines  $t-\alpha x=0$  and  $t-\alpha x=1$  and their repeated reflections, as in Fig. 4.1

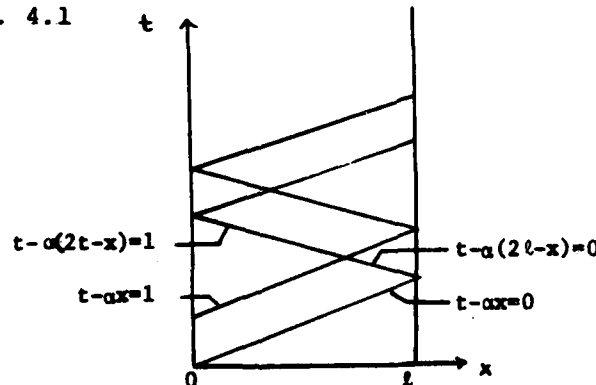


Fig. 4.1. Propagation of the singular data given by (4.12)

Similar solutions can be obtained for spin-up problems between cylinders.

## §5. Linear viscoelastic solids

In [7] we used Laplace transforms to study problems of singular boundary data in viscoelastic solids. If  $G(0) > 0$  and  $G'(0) < 0$  are finite, steps in displacement initiated at the boundary will propagate into the interior of the solid. We interpreted this to mean that the material fails in shear. Stress relaxation experiments in solids are in some sense modeled by steps in displacement. As in fluids, it is necessary to understand the underlying dynamics of such problems. To pursue such an understanding we study the following initial-boundary value problem with smooth, but otherwise arbitrary boundary data  $g(t)$ ,  $t \geq 0$ :

$$\rho \frac{\partial^2 v}{\partial t^2} = (\mu + G(0)) \frac{\partial^2 v}{\partial x^2} + \int_0^t \frac{dG}{ds}(s) \frac{\partial^2 v}{\partial x^2}(x, t-s) ds,$$

$$(5.1) \quad v(0, t) = g(t); \quad g(t) = 0 \quad t < 0,$$

$$v(x, 0) = \frac{\partial v}{\partial t}(x, 0) = 0,$$

$$v(x, t) \text{ is bounded as } x, t \rightarrow \infty.$$

We can solve (5.1) using the methods which led to the Duhamel type of integrals displayed in equations (4.1-4.7). Thus

$$(5.2) \quad v(x, t) = \int_0^t g(\tau) \frac{\partial \hat{f}}{\partial t}(x, t-\tau) d\tau + \hat{f}(x, \alpha x^+) g(t-\alpha x)$$

where

$$\alpha = \sqrt{\frac{\rho}{\mu + G(0)}}$$

and  $\hat{f}(x, t) = f(x, t)$  where  $f(x, t)$  is defined by equation (3.10,11) of [7] and  $f(x, t)$  has the properties specified in §1 of this paper.

The implications of this type of solution for the rheometry of viscoelastic solids should resemble those discussed in §2 for fluids. We defer a detailed comparison of theory and experiment in solids to a later paper. For now it will suffice to note that in theory of solids the notion of homogeneous strain and stress is frequently used, especially in the study of the creep of viscoelastic solids. Such homogeneous strains and stresses are undoubtedly incompatible with exact analysis of the underlying dynamics. Following the usual path, assuming a homogeneous state of stress, we prove the following intuitive result: If the homogeneous stress in a linear viscoelastic solid relaxes mono-

tonically in step-strain tests, then the longitudinal strain in the same solid increases monotonically in creep tests (see Fig. 5.1). To prove this we note that the stress  $T$  in a linear viscoelastic solid undergoing uni-axial strain  $\epsilon(x,t) = \frac{\partial u}{\partial x}(x,t)$  is given by  $T = (\mu + G(0)) \epsilon(t) + \int_0^{\infty} \frac{dG}{ds} \epsilon(t-s) ds$ . A monotonically decreasing stress relaxation for a homogeneous step-strain implies that  $G$  satisfies assumptions (i)-(ii) listed under (1.1). We have assumed either that  $G'(0) \neq 0$  or  $G''(0) \neq 0$ . The strain  $\epsilon$  defining creep is governed by

$$(5.3) \quad T = (\mu + G(0)) \epsilon(t) + \int_0^t \frac{dG}{ds}(s) \epsilon(t-s) ds$$

$$= \begin{cases} 1 & \text{for } t > 0 \\ 0 & \text{for } t < 0. \end{cases}$$

By taking various limits of (5.3) and its derivative we can show that

$$\epsilon(0^+) = \frac{1}{\mu + G(0)}$$

$$\epsilon'(0^+) = \frac{-G'(0)}{\{\mu + G(0)\}^2} > 0, \text{ if } G'(0) \neq 0$$

$$\epsilon''(0^+) = -G''(0)/\{\mu + G(0)\}^2 \text{ if } G'(0) = 0 \text{ and } G''(0) \neq 0$$

$$\lim_{t \rightarrow \infty} \epsilon(t) = \epsilon^* = \frac{1}{\mu} \left. \right\}$$

It is easy to verify, using (5.3) that  $\epsilon(t)$  is continuous and  $\epsilon'(t)$  exists for any  $t > 0$ . We want to prove that

$$(5.5) \quad \epsilon'(t) > 0 \quad t > 0$$

If (5.5) is not true, then (using (5.4)) there exists a  $t > 0$  such that

$$(5.6) \quad \epsilon'(\bar{t}) = 0 \text{ and } \epsilon'(t) > 0 \quad t \in [0, \bar{t}]$$

By differentiating (5.3) once with respect to  $t$ , we find that

$$(5.7) \quad (\mu + G(0)) \epsilon'(t) + G'(t) \epsilon(0) + \int_0^t G'(s) \epsilon'(t-s) ds$$

$$= 0 \quad t > 0$$

After evaluating (5.7) at  $t = \bar{t}$ , using (5.6), we get:

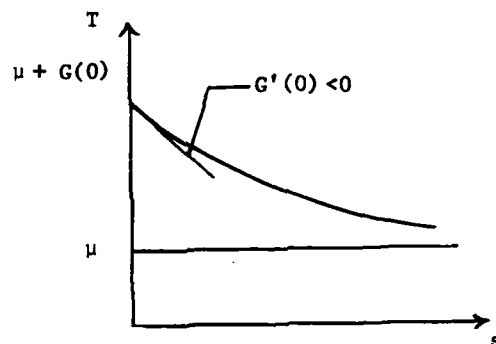
$$(5.8) \quad G'(t) \varepsilon(0) + \int_0^{\bar{t}} G'(s) \varepsilon'(\bar{t}-s) ds = 0$$

But (5.8) then leads to a contradiction because the assumptions about  $G(s)$  make the left side of (5.8) strictly negative. It follows that  $\varepsilon'(\bar{t}) > 0$  and not  $\leq 0$ . It is not hard to demonstrate that  $\varepsilon'(t) > 0$  when

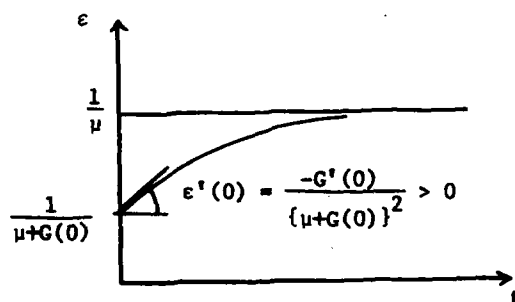
$$(5.9) \quad G(s) = a \delta(s) + h(s)$$

where  $a > 0$ ,  $h(s)$  satisfies the assumptions under (1.1) and  $\delta(s)$  is a Dirac measure at the origin.

Graphical representations of the monotonicity result are exhibited in Fig. 5.1 below:



(a): Homogeneous step-strain relaxation



(b) Creep response to a homogeneous step in stress

Fig. 5.1: Relation between stress relaxation and creep.

When  $a > 0$  in (5.9), the response to a step increase in stress is monotonic as in Fig. 5.1 (b), but it passes through the origin as in Fig. 5.2.

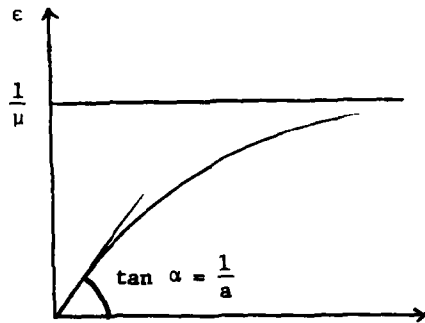


Fig. 5.2: Creep response for kernels of the type (5.9)

We close by reminding the reader that the type of response which we have described above depends tacitly on the unfounded and actually incorrect assumption that homogeneous step-strain (relaxation) and step-stress (creep) tests are admissible deformations compatible with dynamics.

**Acknowledgement:** The results of this paper are taken from the Ph.D. thesis of A. Narain. This work was supported by the U.S. Army.

CORRIGENDUM

Linearized Dynamics for Step Jumps of Velocity and Displacement of Shearing Flows of A Simple Fluid, by A. Marain and D. D. Joseph (Rheol. Acta 21, 228-250 (1982)).

- 1) The quantities  $G(s)$ ,  $C_t(t)$  and  $A_1(t)$  are tensors and should be in boldface.
- 2) The equations under (3.4) should read

$$\lambda^t(x,s) = 0 \quad \text{for } t \leq 0$$

and

$$\frac{d\lambda^t}{ds}(x,s) = - \frac{\partial v}{\partial x}(x,t-s).$$

- 3) The first sentence under Fig. 5.1 should read "Now for  $t-\alpha x < 0 \dots$ "
- 4) Eqn (6.8) should be replaced by:

$$\begin{aligned} Mv_n + Mv &\equiv \int_{\alpha x}^t G(t-s) f_{xx}(x,s) ds - 2\alpha G(t-\alpha x) f_x(x, \alpha x^+) \\ &\quad + \alpha^2 G'(t-\alpha x) f(x, \alpha x^+) - \alpha^2 G(t-\alpha x) \frac{\partial f}{\partial t}(x, \alpha x^+) \\ &\quad - \rho \frac{\partial f}{\partial t}(x,t). \end{aligned}$$

- 5) Eqn. (6.11) should be replaced by:

$$2 \frac{\partial f}{\partial t}(x, \alpha x^+) + \frac{2}{\alpha} \frac{\partial f}{\partial x}(x, \alpha x^+) = \frac{G'(0)}{G(0)} f(x, \alpha x^+)$$

- 6) The left side of (14.11) should be replaced by

$$\frac{\omega(r,t)}{a\Omega}$$

- 7) Eqn. (14.12) (ii) is:

$$K_1(z) \sim \sqrt{\frac{\pi}{2z}} \exp(-z) \quad \text{as } |z| \rightarrow \infty.$$

- 8) Eqn. (16.5) can be ignored.
- 9) The sentence under Eqn. (4.5) should read "Eqs. (4.3, 4.5) imply  $\dots \dots$  half-plane  $\text{Re } u > -\lambda$ ."
- 10) The equations between (14.3) and (14.6) should be numbered (14.4) and (14.5).
- 11) The left side of the equation above (14.6) should read  $\langle r\theta \rangle(t)$  in place of  $\langle \pi\theta \rangle(t)$ .
- 12) The left side of Eqn (6.7) should read:

$$\frac{\partial^2 v_n}{\partial x^2}$$

13) The definition of  $\eta(u)$  underneath (10.4) is

$$\eta(u) = \sqrt{\frac{\rho u}{G(u)}}$$

14) The eqn. (5.17) should read

$$\left[ 1 + \frac{G'(0)}{G(0)u} + \frac{G''(0)}{G(0)u^2} + o\left(\frac{1}{u^3}\right) \right]^{-\frac{1}{2}}$$
$$= 1 - \frac{\bar{\gamma}'}{2u} + \frac{3}{8} \frac{\bar{\gamma}''}{u^2} + \frac{\bar{\gamma}'''}{u^2} + o\left(\frac{1}{u^3}\right).$$

where  $\bar{\gamma}' \stackrel{\text{def}}{=} \frac{G'(0)}{G(0)}$

$$\bar{\gamma}'' \stackrel{\text{def}}{=} -\frac{1}{2} \frac{G''(0)}{G(0)}$$

15) The right side of (12.5) should read:

$$v(x,t) = U[g(x,t) + \{g(x+2l, t) - g(2l-x,t)\}$$
$$+ \{\dots\} + \dots\dots]$$

### References

1. Bird, R.B., R.C. Armstrong, O. Hassager: Dynamics of Polymeric Liquids, Vol. I, John Wiley, New York, 1977.
2. Coleman, B.D. and M.E. Gurtin: Waves in Materials with Memory II. On the Growth and Decay of one dimensional Acceleration Waves, Arch. Rational Mech. Anal. 19, 239-265 (1965).
3. Huppler, J.D., I.F. MacDonald, E. Ashare, T.W. Spriggs, R.B. Bird and L.A. Holmes: Rheological Properties of three solutions. Part II. Relaxation and growth of shear and normal stresses. Trans. Soc. of Rheology, 11, 181-204 (1967).
4. Kee, D.D. and P.J. Carreau: A constitutive equation derived from Lodge's Network Theory. J. of Non-Newtonian Fluid Mechanics, 6, 127-143 (1979).
5. Meissner, J: Modifications of the Weissenberg Rheogonimeter for Measurement of Transient Rheological Properties of Molten Polyethylene under shear. Comparison with tensile data. J. of Appl. Polym. Sci., Vol. 16, pp. 2877-2899 (1972).
6. Narain, A. and D.D. Joseph: Linearized dynamics for step jumps of velocity and displacement of shearing flows of a simple fluid. Rheologica Acta 21, 228-250 (1982).
7. Narain, A. and D.D. Joseph: Classification of linear viscoelastic solids based on a failure criterion. Accepted and to appear in Journal of Elasticity (1982).
8. Renardy, M.: Some remarks on the propagation and non-propagation of discontinuities in linearly viscoelastic fluids. Rheol. Acta. 21, 251-254 (1982).
9. Renardy, M.: On the domain space for constitutive laws in linear viscoelasticity, (to appear).
10. Kazakia, J.Y. and Rivlin, R.S.: Run-up and spin-up in a viscoelastic fluid I. Rheol. Acta 20, 111-127 (1981).
11. Saut, J.C. and D.D. Joseph: Fading Memory, to appear in Arch. Rational Mech. and Anal. (1982).

ATTENDANCE LIST  
for the  
28th CONFERENCE OF ARMY MATHEMATICIANS  
28-30 June 1982  
Uniformed Services University of Health Sciences  
Bethesda, Maryland

Alexander S. Elder	Ballistic Research Laboratory
San-Li Pu	Benet Weapons Laboratory
Arthur Hausner	Harry Diamond Laboratories
Ashwani Kapila	Rensselaer Polytechnic Institute
C. Daly	U. S. Army CRREL
J. Nohel	Mathematics Research Center
Arthur Johnson	U. S. Army Natick R&D Laboratories
Edward Ross	U. S. Army Natick R&D Laboratories
R. Weiss	U. S. Army Waterways Experiment Station
I. M. Besieris	Virginia Polytechnic Institute
Werner Kohler	Virginia Polytechnic Institute
Michael Crandall	Mathematics Research Center
Donald Scott Stewart	University of Illinois
George Papanicolaou	New York University
Arthur Stuempfle	U. S. Army Chemical Systems Laboratory
Rao Yalamanchili	U. S. Army Armament R&D Command
Lee Segel	RPI and Weizmann Institute
Reza Malek-Madani	VPI & SU
S. H. Davis	Northwestern University
Daniel D. Joseph	University of Minnesota
Michael Renardy	University of Minnesota
Yuriko Renardy	University of Minnesota

Joan Armour	DRES DND Canada
Elizabeth B. Dussan V.	University of Pennsylvania
H. L. Frisch	State University of New York-Albany
L. B. Rall	Mathematics Research Center
D. A. Drew	RPI and Mathematics Research Center
Billy Jenkins	U. S. Army Missile Command
Joseph E. Matta	Chemical Systems Laboratory
Julian L. Davis	U. S. Army Armament R&D Command
Jean-Marc Vanden-Broeck	Mathematics Research Center
Donald L. Buttz	White Sands Missile Range
J. R. Brock	University of Texas at Austin
Eugene A. Margerum	U. S. Army Engineer Topographic Lab
Sanjoy Mitter	Massachusetts Institute of Technology
Angelina Buttz	EPCC
W. D. Foster	Armed Forces Institute of Pathology
Ram Srivastav	SUNY-Stony Brook
Peter Tikuisis	Dept. National Defence/Canada
Lang Mann Chang	Ballistic Research Laboratory
A. S. Galbraith	Retired
R. E. Meyer	University of Wisconsin
R. C. DiPrima	Rensselaer Polytechnic Institute
Ray Sedney	Ballistic Research Laboratory
R. L. Launer	U. S. Army Research Office
Jagdish Chandra	U. S. Army Research Office
Steve Wolff	U. S. Army Research Office
Bernard Fleishman	Rensselaer Polytechnic Institute

D. Tracey

Shih C. Chu

T. Posbergh

A. A. Khan

J. Zavada

Pak T. Yip

Paul Davis

William P. D'Amico

Eric Benck

Donald Neal

Aaron Das Gupta

Jim Greenberg

Charles Giardina

Frank P. Kuhl

Peter C. T. Chen

Donald L. Gilman

Miles C. Miller

Thorwald Herbert

William Saric

U. S. AMMRC

U. S. Army Armament R&D Command

U. S. Army Armament R&D Command

U. S. Army Concepts Analysis Agency

U. S. Army Armament R&D Command

USA ARRADCOM-FC&SCWSL

Worcester Polytechnic Institute

Ballistic Research Laboratory

Ballistic Research Laboratory

U. S. AMMRC

Ballistic Research Laboratory

National Science Foundation

Fairleigh-Dickinson University

U. S. Army Armament R&D Command

Benet Weapons Laboratory

Institute for Scientific Information

Chemical Systems Laboratory

VPI & SU

VPI & SU

UNCLASSIFIED

SECURITY CLASSIFICATION OF THIS PAGE (When Data Entered)

REPORT DOCUMENTATION PAGE		READ INSTRUCTIONS BEFORE COMPLETING FORM
1. REPORT NUMBER ARO Report 83-1	2. GOVT ACCESSION NO. AD-A128683	3. RECIPIENT'S CATALOG NUMBER
4. TITLE (and Subtitle) Transactions of the Twenty-Eighth Conference of Army Mathematicians		5. TYPE OF REPORT & PERIOD COVERED
7. AUTHOR(s)		6. PERFORMING ORG. REPORT NUMBER
9. PERFORMING ORGANIZATION NAME AND ADDRESS		8. CONTRACT OR GRANT NUMBER(s)
11. CONTROLLING OFFICE NAME AND ADDRESS Army Mathematics Steering Committee on Behalf of the Chief of Research, Development and Acquisition		10. PROGRAM ELEMENT, PROJECT, TASK AREA & WORK UNIT NUMBERS
14. MONITORING AGENCY NAME & ADDRESS (if different from Controlling Office) U. S. Army Research Office P. O. Box 12211 Research Triangle Park, NC 27709		12. REPORT DATE January 1983
		13. NUMBER OF PAGES 533
		15. SECURITY CLASS. (of this report) Unclassified
		15a. DECLASSIFICATION/DOWNGRADING SCHEDULE
16. DISTRIBUTION STATEMENT (of this Report) Approved for public release; distribution unlimited. The findings in this report are not to be construed as official Department of the Army position unless so designated by other authorized documents.		
17. DISTRIBUTION STATEMENT (of the abstract entered in Block 20, if different from Report)		
18. SUPPLEMENTARY NOTES This is a technical report resulting from the Twenty-Eighth Conference of Army Mathematicians. It contains most of the papers in the agenda of this meeting. These treat various Army applied mathematical problems.		
19. KEY WORDS (Continue on reverse side if necessary and identify by block number)		
Reynolds stress tensor inhomogeneous diffusion viscoelastic fluids ray tracing methods radiative transfer theory waveguide structures mass transport osmosis Newtonian flows flame problems eigenvalue problems aerosols two flow models cavitation flows	Composite materials finite difference methods stress problems Legendre functions porous medium equations spinning projectiles mobility problems stationary values of functionals encoded images filter models hyperbolic Volterra equations finite element methods Cauchy problem physical chemistry problems	

DATE  
FILMED  
8